Preface

Symmetry. Chaos. These are the things that have captured both the hearts and the minds of both of us.

Bob came to symmetry first through his studies of Lie groups and their applications in physics. Twenty years later he confronted chaos and began to try to tame it with the topological methods he brought from Lie group theory.

Christophe came to symmetry through a book by Claude Cohen-Tannoudji and Jean-Pierre Baton[1] and the lectures he attended in particle physics. A point always mentioned was "physics is invariant under symmetry transformations." In the beginning of his Ph.D. thesis, he immediately tried to apply this message when he started to investigate the Lorenz system, trying to answer Rössler's remark: "a trick which exploits the inherent symmetry between the two leaves of the flow, so that in effect only a single leaf needs to be considered, has yet to be found".[2]

When we met for the first time (Lille, 1996) Bob asked a question: What is the trick that Christophe was using to project one leaf onto the other: "Is there a link between your trick and a theorem by Cartan?" This "simple" question lead us to this book.

Since both of us chant the same mantra:

$$\text{Symmetry} + \text{Chaos} = \text{Beauty}$$

[1] C. Cohen-Tannoudji & J.-P. Baton, *L'horizon des Particules*, Gallimard, 1989.
[2] O. E. Rössler, An equation for continuous chaos, *Physics Letters A*, **57**(5), 397-398, 1976.

it was inevitable that we meet, and once met, formed a tightly bound, always excited state. This book is a consequence of our excitement.

This book is divided into three parts and an appendix. Part I consists of many concrete examples; Part II presents the foundations for applications of symmetry to nonlinear dynamics; Part III replaces groups (algebraic structures) with topological structures. The appendix brings together in one place all the equivariant dynamical systems (dynamical systems with symmetry) that have been discussed to date in the open literature.

One basic question that launched us on this project is: If an observed intensity $I(t) = |A(t)|^2$ behaves chaotically, how many *different* strange attractors can the (unobserved) amplitude $A(t)$ generate that are compatible with the strange attractor that is generated by the intensity data? Many similar questions arise about the relation between "symmetric" and "nonsymmetric" (cover and image) strange attractors that are identical at the local level but inequivalent at the global level. These questions are introduced in Chapter 1. The remainder of Part I illustrates these concepts in a large variety of ways by a large variety of examples. Simple symmetries and their relation to the cover and image problem are described in Chapters 2-4. Perestroikas—transformations induced by changing control parameters or operating conditions—are introduced in Chapter 5. Chapter 6 describes covers of autonomous dynamical systems, and Chapter 8 describes covers of nonautonomous dynamical systems. Symmetric intermittencies are treated in Chapter 7 and larger symmetries are treated in Chapter 9.

Part II is devoted to laying a foundation for the methods used in Part I. Not surprisingly, group theory plays a prominent role. Perhaps surprisingly, algebraic topology also plays a significant role. Along the way we extend some concepts from classical mathematics into new directions: Cauchy-Riemann symmetries out of the complex domain into the group and algebraic topology domains; continuations out of the analytic domain into the group and topological domains.

In Part III we do the unthinkable. We extend the role of symmetry by replacing symmetry groups by topological structures. There are clearly strange attractors with definite symmetry but without a symmetry group with which to express this symmetry. This possibility was a surprise to both of us, but the results show that this approach is here to stay.

The web sites of Bob[3] and Christophe[4] contain much material that is related in some way or other to this work.

This work was carried out during many visits of Bob to Christophe in Rouen, Christophe to Bob in Philadelphia, and both to our mutual friend and colleague, Marc Lefranc in Lille. The visits of Bob have been supported in part by Drexel University's grant of a sabbatical leave, the Centre National de la Recherche Scientifique, and the U.S. National Science Foundation. Bob thanks his colleagues M. Lefranc, S. Bielawski, T. D. Tsankov, A. Nishtala, N. Romanazzi, and T. Jones for fruitful

[3] http://lagrange.physics.drexel.edu and http://physics.drexel.edu/directory/faculty/Gilmore.html.
[4] http://www.koakidi.com/rubrique.php?id_rubrique=81.

interactions. Christophe extends his warm thanks to J. Maquet, C. Lainseck, J.-M. Malasoma, L. Achour, L. A. Aguirre, and O. E. Rössler for stimulating discussions.

Last, we thank our better halves. Bob thanks his wife Claire and the children, Marc and Keith: His queen Claire, for creating miraculous 10-15-course candlelight dinners in our tiny, marvelous French apartments after a hard day computing SVDs; Marc and Keith for providing both stimulation and enough time to complete this project. Most of the time this book was in gestation Christophe spent under a gray sky, but with its publication the sun has come out. Christophe thanks especially Valerie, who encouraged him "pour la dernière ligne droite." Christophe and Valerie eagerly await Valentin.

ROBERT GILMORE AND CHRISTOPHE LETELLIER

Rouen, Le Quattorze Juillet, 2006

Contents

Part I

Examples and Simple Applications

1

Introduction

The subject of this work is the description of physical systems that

1. possess symmetry
2. exhibit chaotic behavior

These systems are described by sets of nonlinear ordinary differential equations. The existence of a symmetry has a profound and far-reaching impact on the properties of the solutions of such equations. The presence of symmetry sometimes complicates and sometimes simplifies our understanding of the physical processes that generate chaotic behavior.

In the following sections we describe a number of physical systems with symmetry and present a number of mathematical reasons for studying the relation between symmetries and dynamical systems. We also outline the structure and contents of this book.

1.1 SWIFT SURVEY OF SYMMETRIES

In this section we briefly introduce a number of different physical systems that exhibit some type of symmetry. We also raise questions about the relation between

the physical system with symmetry and measured quantities, which may have no symmetry.

1.1.1 Lasers

In laser experiments, intensities ($I \approx |A|^2$) are usually measured, whereas the appropriate variables in any fundamental theory are the field amplitudes (A). Strange attractors constructed from intensity data do not have the same structure as those that are constructed from amplitude data (were the latter available). Some information has been "squared away" in the transition from amplitudes to intensities. A natural question then arises: what spectrum of strange attractors for amplitude behavior is compatible with the strange attractor constructed from observed intensity data?

1.1.2 Sunspot Data

These data exhibit an 11-year cycle (Fig. 1.1) and may possibly be chaotic. It is widely believed that sunspot numbers are closely related to a solar averaged magnetic field $\overline{B}$. This averaged field exhibits a 22-year cycle. Thus $n(t) \approx |\overline{B}|^2$. Some information about solar dynamics has been "squared away" in the observation of sunspot numbers (Fig. 1.1). What is the relation between the sunspot number cycle and the magnetic field cycle?

1.1.3 Paleomagnetic Data

These data have been observed in conjunction with seafloor spreading [131, 132]. In fact, they provide one of the strongest confirmations of the theory of continental drift. As the seafloor spreads, iron-rich magma beneath the seafloor rises to the seafloor surface where it cools below the Curie temperature. As it does, the iron is magnetized

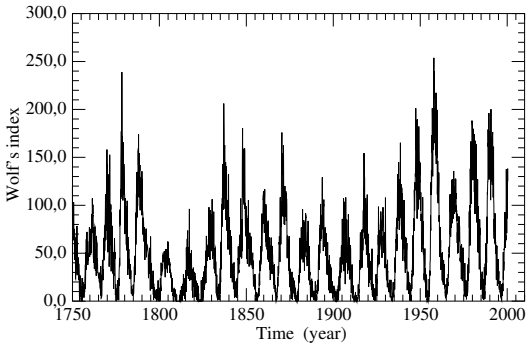

Fig. 1.1 Time series of the sunspot number at the surface of the sun.

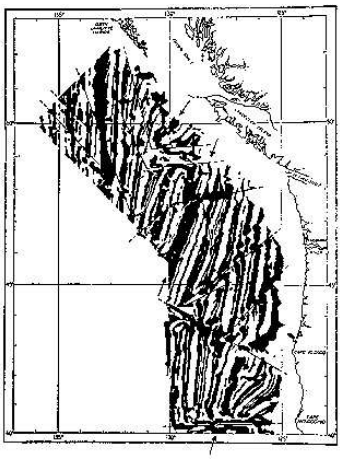

Fig. 1.2 Profile of the seafloor magnetic field near the Juan de Fuca plate off the coast of Washington. Dark and light stripes show current magnetic field polarity and reverse polarity. These alternate in a symmetric way around seafloor spreading centers. Reprinted from the article [131] with the permission of the journal *Science*.

in the direction of the earth's magnetic field at that time. [1]When the earth's magnetic field reverses, so also does the polarity of the cooled magma. Segments of seafloor on different sides of the spreading center exhibit a symmetry in the magnetic field reversals. These reversals are "unpredictable," indicating the possibility that the earth's magnetic field should be described by coupled ordinary differential equations that generate chaotic behavior. The polarity of the seafloor near the Juan de Fuca plate off the coast of Washington is shown in Fig. 1.2 [131]. Clearly apparent in this figure are alternations in the direction of the magnetic field polarity as well as an approximate symmetry around the seafloor spreading site.

A history of the earth's magnetic field reversals during the last 80 million years is presented in Fig. 1.3. This figure shows the polarity, not the magnitude, of the magnetic field. This behavior raises several questions: What is the mechanism that causes the earth's magnetic field to be bipolar? Is there any relation between the magnetic switching mechanisms that take place in the sun and the earth?

1.1.4 Fluid Experiments

The behavior of a fluid is governed by the Navier-Stokes equations. These partial differential equations are typically studied by introducing a set of spatial normal modes and then truncating the equations to obtain a set of coupled nonlinear ordinary

[1]S. C. Cande and D. V. Kent, Revised calibration of the geomagnetic polarity time scale for the Late Cretaceous and Cenozoic, *Journal of Geophysical Research*, **100**, 6093–6095, 1995. Data available at the website: http://www.earth.rochester.edu/agu/timescale.html.

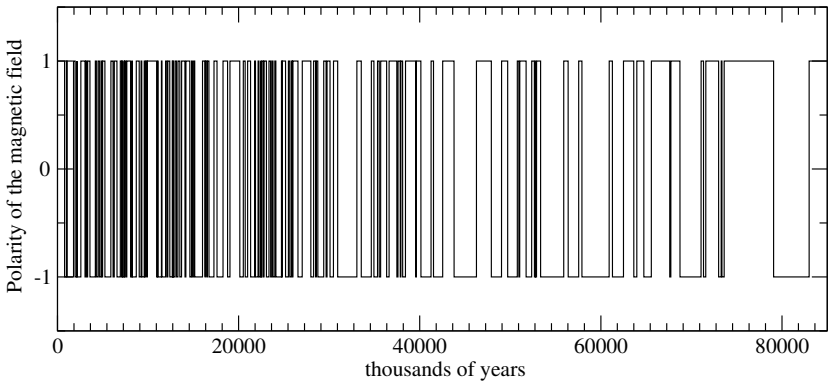

Fig. 1.3 Geomagnetic polarity for the Cenozoic period (present to 65 million years ago) and late Cretaceous periods. Plot shows polarity, not field amplitude.

differential equations. If the experimental conditions possess a symmetry, a suitable trunction of the Navier-Stokes equations will retain that symmetry. One of the most severe truncations of the Navier-Stokes equations consists of the Lorenz equations [78]. Several experiments have been carried out on fluid systems that are reasonably well described by these equations. Data and simulations can be plotted in many different ways. Three are shown in Fig. 1.4. They will be discussed in more detail throughout this book. For now we introduce the simple question: how are these three presentations of the data related? Is any one preferable to any other? Do they all contain the same information?

1.1.5 Electronic Circuits

Two circuit models (Fig. 1.5) that have a long history and that have been extensively studied were introduced by Duffing [28] and by van der Pol [129]. Both exhibit a two-fold symmetry. This symmetry greatly complicates attempts to determine the stretching and folding mechanisms that create chaotic behavior. The analysis of both systems is greatly simplified after the symmetry has been "eliminated." We will develop algorithmic methods to remove symmetry when it is present. We also introduce systematic ways to restore symmetry when it is absent.

1.2 DEEPER PROBE OF SYMMETRIES

In this section we investigate more deeply two classes of physical systems for the origin of symmetry. Specifically, we investigate fluids and lasers. Both are described by nonlinear partial differential equations. Under suitable assumptions and approximations, the partial differential equations can be reduced to a finite set of coupled nonlinear ordinary differential equations for a select number of modes. A "mode" is a macroscopically organized behavior for many microscopic elements. It is the

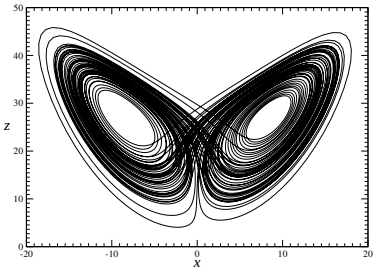

(a) Original phase space

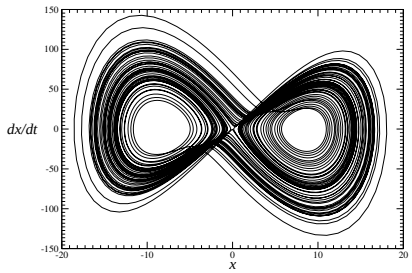

(b) x-induced phase space

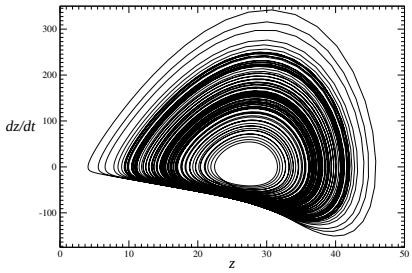

(c) z-induced phase space

Fig. 1.4 Different representations of the Lorenz attractor. The original phase portrait (a) has a rotation symmetry about the z-axis, the x-induced phase portrait (b) has an inversion symmetry, while the z-induced phase portrait (c) has no residual symmetry at all.

projected set of ordinary differential equations that exhibits the symmetry that forms the basic subject of this work.

We illustrate this procedure in this section by reducing the Navier-Stokes equations for a fluid to a familiar, severely truncated form (the Lorenz equations) and the Maxwell-Bloch equations for a laser to a severely truncated form (the "laser equations").

1.2.1 Navier-Stokes PDEs ⟶ Lorenz ODEs

Fluids are described by the Navier-Stokes partial differential equations

$$\begin{aligned} \rho\frac{\partial u_j}{\partial t} + \rho u_k \frac{\partial u_j}{\partial x_k} &= -\frac{\partial P}{\partial x_j} + \mu\nabla^2 u_j + \rho f_j \\ \frac{\partial T}{\partial t} + u_j \frac{\partial T}{\partial x_j} &= \kappa\nabla^2 T \\ \frac{\partial u_i}{\partial x_j} &= 0 \end{aligned} \tag{1.1}$$

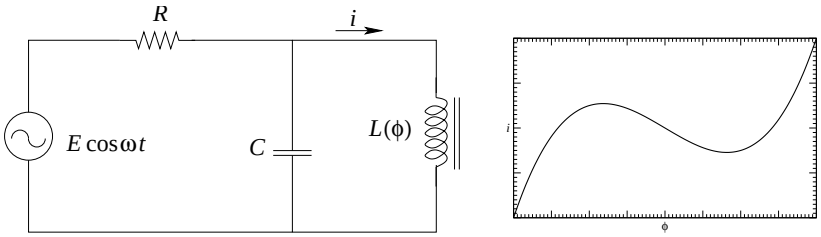

(a) Duffing system

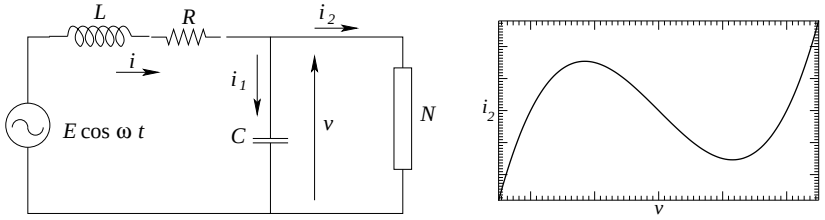

(b) van der Pol system

Fig. 1.5 Schematic diagrams of a series-resonance circuit with nonlinear inductance (a) corresponding to the Duffing system and of a forced self-oscillatory circuit (b) corresponding to the van der Pol type. The latter contains a negative-resistance element N which has a characteristic $i_2 = f(v)$ also shown.

In this set of equations

- $\boldsymbol{u} = \boldsymbol{u}(x) = (u_1, u_2, u_3)$ is the fluid velocity field
- $\rho(x, y, z)$ is the fluid density field
- $T = T(x, y, z)$ is the temperature field
- $P = P(x, y, z)$ is the pressure field
- f_j is the external force field
- μ is the dynamic viscosity
- κ is the coefficient of thermal conduction

The first equation is the equation of motion for the fluid velocity $\boldsymbol{u}(x)$. The second equation is the equation of motion for the temperature field, $T(\boldsymbol{x})$. The third equation is a constraint satisfied by incompressible fluids. These equations apply to the experiments shown in Fig. 1.6. Fig. 1.6(a) shows an experiment in which a fluid in a rectangular container is heated from below. A constant temperature difference ΔT is maintained between the lower surface at which heat is input and the upper surface at which heat is removed. This temperature difference establishes a thermal instability. Since the warmer liquid near the bottom is generally less dense than the cooler liquid above it, the warmer liquid will rise and the cooler liquid above it will descend when the heat is input at a greater rate than can be transferred from the lower to the upper surface by thermal conduction alone. When the fluid begins to move, it does so in coherent roll structures. The physics is invariant under reflections in a

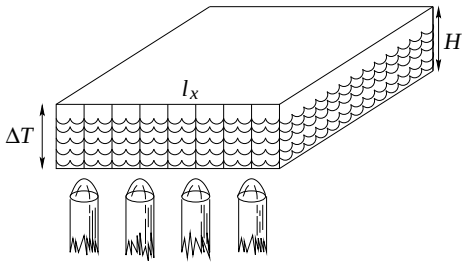

(a) Fluid in a flat rectangular container is heated from below.

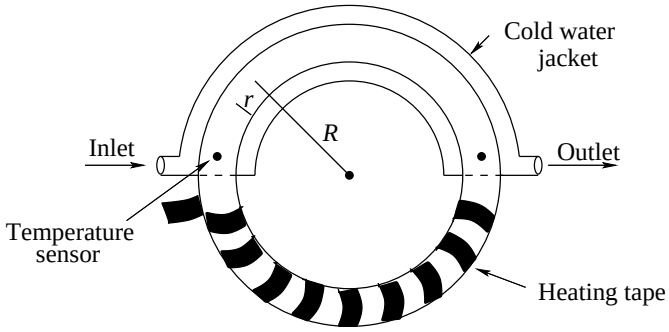

(b) Fluid in a torus is heated below and cooled above a horizontal plane.

Fig. 1.6 Two gravithermal fluid instabilities described by the Lorenz equations.

vertical plane through $\frac{1}{2}l_x$. Any projection of the partial differential equations to a set of ordinary differential equations must maintain this symmetry.

Similar arguments apply to the geometry shown in Fig. 1.6(b) [11]. In this case, a heating tape supplies heat along the lower half of the torus while a cooling jacket removes heat from the upper half of the torus. As in Fig. 1.6(a) a constant temperature difference ΔT is maintained between the lower and upper halves of the torus. The gravithermal instability will force a clockwise or counterclockwise rotation of the fluid in the torus when the temperature difference ΔT surpasses a critical value.

In both cases the experimental conditions are reflected by replacing the term ρf_i in Eq. (1.1) by $\rho g \epsilon \Delta T \delta_{i3}$, where g is the constant of gravitational acceleration of the earth's surface in the z ($i = 3$) direction and ϵ is the coefficient of thermal expansion.

The partial differential equations are reduced to a set of ordinary differential equations by introducing simplified expressions for the velocity and temperature fields [112]. For the experiment shown in Fig. 1.6(a) the velocity field is assumed to depend on the x- and z-variables only, and is expressed in terms of a stream function

$\Psi(x,z)$ by

$$\boldsymbol{u} = -\nabla\times(\hat{\mathbf{j}}\,\Psi(x,z))$$

so that $u_x = +\partial\Psi/\partial z$ and $u_z = -\partial\Psi/\partial x$. The stream function is subjected to the boundary conditions that the flow perpendicular to the surfaces, at the surfaces, vanishes. It is expanded in terms of normal modes (trigonometric functions) and truncated, keeping only the lowest order terms.

$$\Psi \approx \sqrt{2}X \sin\frac{\pi x}{l_x}\sin\frac{\pi z}{H}$$

The temperature field is treated similarly

$$T - T_{av} \approx \sqrt{2}Y\cos\frac{\pi x}{l_x}\sin\frac{\pi z}{H} - Z\sin\frac{2\pi z}{H}$$

The lowercase letters (x,y,z) parametrize space coordinates. $T_{av}(z)$ varies linearly between the fixed temperature at the lower and upper boundaries of the fluid. The uppercase letters (X,Y,Z) describe the amplitudes of the normal modes in the three-mode truncation of the Navier-Stokes equations. The resulting set of ordinary differential equations is [78]

$$\begin{aligned}\frac{dX}{dt} &= -\sigma X + \sigma Y\\ \frac{dY}{dt} &= RX - Y - XZ\\ \frac{dZ}{dt} &= -bZ + XY\end{aligned} \tag{1.2}$$

in suitable units of time. This set of equations is underchanged ("equivariant") under the symmetry $(X,Y,Z)\to(-X,-Y,Z)$.

The Lorenz equations (1.2) fail to describe fluid motion in the experiment shown in Fig. 1.6(a) when the imposed temperature difference ΔT becomes so large that the coherent roll structures break up. They provide a valid description for fluid flow in the experiment shown in Fig. 1.6(b) for much large temperature differences.

1.2.2 Maxwell-Bloch Equations ⟶ Laser Equations

The electromagnetic field is described by Maxwell's equations and the motion of matter is described by Newton's equations classically, or the Bloch equations when matter is described quantum mechanically. The Maxwell-Bloch equations for an electromagnetic field interacting with matter in a laser cavity are

$$\begin{aligned}\frac{\partial D}{\partial t} &= \frac{2i}{\hbar}\left(\bar{\mu}\mathcal{E}P^* - \bar{\mu}\mathcal{E}^*P\right) - \gamma_{\|}D + \Lambda\\ \frac{\partial P}{\partial t} &= -i(\omega-\omega_0)P - \frac{i}{\hbar}\bar{\mu}\mathcal{E}^*D - \gamma_{\perp}P\\ \frac{\partial \bar{\mathcal{E}}}{\partial t} &= -\frac{1}{2}\gamma_l\mathcal{E} + \frac{i\omega}{2\epsilon_0}N_0P\bar{\mu}\end{aligned} \tag{1.3}$$

In this coupled set of differential equations

- $\bar{\mathcal{E}}$ is the electric field amplitude $E(x,t) = \bar{\mathcal{E}} e^{i(kx-\omega t)}$
- P is the polarization amplitude for matter
- D is the population inversion: the difference between the number of atoms in the excited and ground states
- $\bar{\mu}$ is the electric dipole moment matrix element of an atom
- ϵ_0 is the vacuum dielectric constant
- $\gamma_{\|}, \gamma_{\perp}, \gamma_l$ are decay rates for the population inversion, polarization, and electric field, respectively
- N_0 is the number of atoms in the laser cavity
- ω_0 is one of the laser cavity resonances.

The partial differential equations that describe the electric field,

$$\left(\nabla^2 - \frac{1}{c^2}\frac{\partial^2}{\partial t^2}\right)\bar{E} = \frac{4\pi}{c^2}\frac{\partial \bar{j}(x)}{\partial t} + 4\pi\nabla\rho$$

have already been converted to ordinary differential equations through the slowly varying field amplitude ansatz $E(x,t) = \mathcal{E}(t)e^{i(kx-\omega t)}$.

The equations can be reduced in complexity by defining the cavity detuning as $\delta = \frac{\omega-\omega_0}{\omega_0}$, rescaling the time variable, and introducing complex variables e, p, and d. The resulting set of scaled ordinary differential equations consists of two complex equations and one real equation, as follows [139]

$$\begin{aligned}
\frac{\mathrm{d}e}{\mathrm{d}\tau} &= -\sigma(e-p) \\
\frac{\mathrm{d}p}{\mathrm{d}\tau} &= -(1-i\delta)p - ibdp + ed \\
\frac{\mathrm{d}d}{\mathrm{d}\tau} &= -\gamma\left[d - R + \frac{1}{2}(e^*p + ep^*)\right]
\end{aligned}$$

Here b describes the strengh of the dipole-dipole interaction. This set of equations is equivalent to a set of five real equations in the variables

$$\begin{aligned}
e &= x_1 + ix_2 \\
p &= y_1 + iy_2 \\
d &= z
\end{aligned}$$

The equations of motion for the five real variables x_i, y_i, z $(i = 1, 2)$ are

$$\begin{aligned}
\dot{x}_1 &= -\sigma(x_1 - y_1) \\
\dot{x}_2 &= -\sigma(x_2 - y_2) \\
\dot{y}_1 &= -y_1 - y_2(\delta - bz) + x_1 z \\
\dot{y}_2 &= -y_2 + y_1(\delta - bz) + x_2 z \\
\dot{z} &= -\gamma(z - R + x_1 y_1 + x_2 y_2)
\end{aligned}$$

This set of equations is invariant under the continuous rotation (or gauge) symmetry

$$e \to ee^{i\phi} \quad p \to pe^{i\phi} \quad d \to d$$

We will discuss continuous symmetries in Sections 9.1 and 9.2.

1.3 MATHEMATICAL MOTIVATION

It is customary that exciting physics drives the development of exciting mathematics. The problems superficially surveyed in Section 1.1 and more deeply probed in Sect. 1.2 are exciting—if for no other reason then we do not satisfactorily understand how to treat such systems.

Our study of dynamical systems with symmetry—and their counterparts without—has opened up a number of new developments on the mathematics side. We indicate several of these developments now.

1.3.1 Classification Theory

We are interested in classifying dynamical systems: in particular chaotic dynamical systems and the strange attractors that they create. A classification theory for strange attractors in $\mathbb{R}^3$, or more generally in three-dimensional manifolds, already exists [33, 34]. This classification theory depends heavily on topological structures called "branched manifolds" [14, 15]. We have observed that many inequivalent chaotic systems with symmetry project to the same, or equivalent, dynamical systems when the symmetry is removed [67]. Conversely, a dynamical system without symmetry can be lifted to many different inequivalent systems with a symmetry [35]. It is even possible that two lifts of a system without symmetry, with the same symmetry group, are not equivalent [21]. We would like to understand these details better. In particular, it is convenient to approach the classification of strange attractors in two steps:

1. Classify all strange attractors without symmetry.
2. Provide an algorithm for constructing all possible attractors with symmetry that can be obtained from the original nonsymmetric attractor.

Many of these ideas have their counterparts—or at least their analogs—in well-developed mathematical fields. For example, there is a well-codified study of Lie groups ("with symmetry") and locally isomorphic Lie groups "without symmetry." A particular example is $SU(2) \to SO(3)$, where $SU(2)$ is a "double cover" of $SO(3)$, and $SO(3)$ is the locally isomorphic image of $SU(2)$ [31]. Many of our results were obtained by trying to make the replacements

Lie Group Theory	$\longrightarrow$	Dynamical Systems Theory
Isomorphism	$\longrightarrow$	Diffeomorphism
Local Isomorphism	$\longrightarrow$	Local Diffeomorphism
Cover Group	$\longrightarrow$	Cover Dynamical System
Image Group	$\longrightarrow$	Image Dynamical System

There is a beautiful theorem in Lie group theory (Cartan's theorem) relating (simply connected) covering groups with their (multiply connected) homomorphic images. Driven by the desire not to let Lie group theory have the last word in beautiful theorems, we present the analog of Cartan's theorem for Dynamical Systems Theory in this book's final chapter.

1.3.2 Cover-Image Relations

Two of the simplest dynamical systems that exhibit chaotic behavior for certain ranges of the control parameter values are the Lorenz equations [78] and the Rössler equations [109]. It has long been known that there is a $2 \rightarrow 1$ relation between these two dynamical systems [90]. In fact, Rössler introduced his equations in order to simplify the study of chaotic dynamics [109]. He viewed his equation as "the square" of the Lorenz equations in counter-analogy with Dirac's view of his equations are "the square root" of the Schrödinger equation. In this sense, the Lorenz system is a double cover of the Rössler system in the same way that the Lie group $SU(2)$ is a double cover of the rotation group $SO(3)$, and the Dirac equation describes both electrons and their antiparticles, positrons, whereas the Pauli-Schrödinger equation describes just electrons. Conversely, there is a $2 \rightarrow 1$ mapping of the Lorenz attractor down to a Rössler-like attractor. This $2 \rightarrow 1$ projection is easily visualized by viewing the Lorenz attractor along the direction of a straight line through the two unstable foci. In this perspective, the two foci and their associated lobes fall on top of each other. There appear to be only two fixed points, the two superposed foci and the saddle at the origin. The attractor takes on the qualitative appearance of the Rössler attractor.

Three different representations of the Lorenz attractor have been presented in Fig. 1.4. Two of these attractors have "two holes" in them and one has "one hole" in the middle. The pair with two holes exhibit a symmetry: one has rotation symmetry, the other has inversion symmetry. How are they related? Do other sets of attractors share such properties?

The relation between the Lorenz attractor with two-fold symmetry and its projected image, without symmetry, was first put on a firm mathematical footing by Miranda and Stone [90]. This work is in fact just the tip of the iceberg [21, 34, 35, 67]. In the present work we try to look at the entire iceberg.

1.4 OVERVIEW OF THE BOOK

There is a very rich theory of dynamical systems with symmetry and closely related systems without (or with less) symmetry. There is a systematic way of "modding out" the symmetry to construct an image dynamical system. Conversely, a dynamical system with no symmetry can be "lifted" to a covering dynamical system with symmetry. There are essentially no limits on the type of symmetry the covering dynamical system can possess. In fact, surprisingly, it can possess many inequivalent covers, all with the same intrinsic symmetry group.

This book is divided into three parts:

Part I	Chapters 1–9	Examples & Simple Applications
Part II	Chapters 10–14	Group Theory Basics
Part III	Chapters 15–16	Symmetry Without Groups: Topology

In Part I we study a small number of basic dynamical systems, mostly in $\mathbb{R}^3$, mostly with two-fold symmetry. A systematic procedure is introduced for modding out the symmetry and constructing the dynamical system equations for the image without symmetry. This procedure is reversible and is used to construct covering dynamical systems with two-fold (or three-, or four-fold symmetry) from a dynamical system without symmetry. The relation between cover and image dynamical systems is studied at five levels

1. Relations among equations,
2. Relations between branched manifolds,
3. Relations between symbolic dynamics,
4. Relations between periodic orbits,
5. Indices relating covers and images.

Branched manifolds are "cardboard models" of the chaotic flow with a firm mathematical basis. Strange attractors in $\mathbb{R}^3$ have been classified by the branched manifolds they project to.

In many of the chapters in Part I we get the sense that there is a powerful, systematic mathematical theory underlying the procedures that have been introduced. Not only that, but these procedures have close connections with fundamental theorems from classical mathematics. All this is true. The deep connections with classical mathematics, and even the extension of the classical results into new realms, is developed in Part II.

In Part II we introduce the mathematical tools essential for the development of a proper understanding of the cover-image problem. The two basic tools are group theory and some essential components of algebaic geometry. These tools are used to provide a proper description of equivariant dynamical systems: that is, dynamical systems with a symmetry. The symmetry is removed by introducing a set of invariant coordinates that are polynomials in the original variables. The dynamical equations are re-expressed in terms of the invariant polynomials and generate a flow in this space of polynomials. In general, if the equivariant dynamical system is in $\mathbb{R}^N$, the invariant dynamical system is in $\mathbb{R}^K$, $K \geq N$. When $K > N$, the flow is restricted to an N-dimensional subspace by $K - N$ "constants of motion" of the invariant dynamics. These polynomial invariants are called "syzygies." Finally, the invariant flow in the N-dimensional manifold in $\mathbb{R}^K$ is projected to an N-dimensional space $\mathbb{R}^N$ by an appropriate choice of N linear combinations of the initial set of K invariant polynomials. This process is invertible, and can be used to construct covers from images.

Along the way we encounter four remarkable symmetries, already apparent (with careful study) in the examples studied in Part I. These are

1. Schur symmetries,
2. Cauchy-Riemann symmetries,

3. Clebsch-Gordon symmetries,
4. Continuations: Topological and Group.

The latter is an extension of the idea of analytic continuation.

The inverse problem, of constructing covers (or "lifts") of an image dynamical system, also includes delightful surprises. One of these is that an image dynamical system can have many inequivalent covers, all with the same symmetry group $\mathcal{G}$. These covers are distinguished by an index. The index has a topological interpretation, a group theory interpretation, and a dynamical interpretation. In fact, the index allows us to enumerate all possible inequivalent covers of a dynamical system. This is done in detail for low dimensional dynamical systems that can be described by branched manifolds.

In Part III we emerge from our earlier dependence on the group theory crutch. Group theory is a powerful tool for exploring the range and power of local diffeomorphisms. But there is an even more powerful tool for studying these many-to-one local diffeomorphisms. This is topology-specifically, the topology of the manifolds that contain flows that generate strange attractors. The boundaries of these manifolds are all tori with various numbers of holes in them. The flows dress the tori, and the canonically dressed tori can themselves be classified—classified in much the same way that branched manifolds and the periodic orbits they contain can be organized and classified. This is done in the last two chapters. We discuss not only the range of inequivalent covers that the standard stretch-and-fold mechanism (Smale horseshoe mechanism) can have ("All the covers of the Horseshoe"), but also discuss all the images that are diffeomorphic but not equivalent with the standard horseshoe ("Once a horseshoe—Always a horseshoe"). This treatment provides a direct response to a question often raised about the usefulness of the topological analysis approach to the analysis of chaotic experimental data: How much information about experimental chaotic data depends on the physics and how much depends on the embedding? We show in the final chapter that there are three degrees of freedom allowed by inequivalent embeddings: parity, global torsion, and knot type. But there is one degree of freedom that is rigidly fixed, independent of embedding — this is the *mechanism* that generates the chaotic behavior in the experimental system. This mechanism is represented by the template of the branched manifold that the strange attractor projects to.

In an appendix we pull together a large number of nonlinear dynamical systems that have been discussed in the literature. This potpourri should serve a valuable function, as it brings together in one place the large number of systems that have been studied in the recent past.

2

Simple Symmetries

2.1 EQUATIONS WITH TWO-FOLD SYMMETRY

In this section we describe the structure of equations with two-fold symmetry. This is done for three-dimensional dynamical systems since we would like to be able to visualize the strange attractors that they generate. In addition, this is the only dimension for which a satisfactory theory of chaos exists.

2.1.1 Rotation Symmetry

The Lorenz system [78]

$$\begin{aligned}\frac{dX}{dt} &= -\sigma X + \sigma Y \\ \frac{dY}{dt} &= RX - Y - XZ \\ \frac{dZ}{dt} &= -bZ + XY\end{aligned} \tag{2.1}$$

is equivariant under rotation by π radians about the Z-axis. The generator of this two-element group $\mathcal{R}_Z(\pi)$ is the 3×3 matrix, γ, that maps the coordinates $(X, Y, Z) \mapsto (-X, -Y, Z)$

$$\begin{bmatrix} -1 & 0 & 0 \\ 0 & -1 & 0 \\ 0 & 0 & 1 \end{bmatrix} \begin{bmatrix} X \\ Y \\ Z \end{bmatrix} = \begin{bmatrix} -X \\ -Y \\ +Z \end{bmatrix}$$

The matrix γ satisfies $\gamma^2 = I_3$. The action of γ, or $\mathcal{R}_Z(\pi)$, on the Lorenz equations, is

$$\gamma \frac{d}{dt} \begin{bmatrix} X \\ Y \\ Z \end{bmatrix} = \begin{bmatrix} f_1(\gamma \boldsymbol{X}) \\ f_2(\gamma \boldsymbol{X}) \\ f_3(\gamma \boldsymbol{X}) \end{bmatrix} = \begin{bmatrix} f_1(-X, -Y, +Z) \\ f_2(-X, -Y, +Z) \\ f_3(-X, -Y, +Z) \end{bmatrix}$$

$$\frac{d}{dt} \begin{bmatrix} -X \\ -Y \\ +Z \end{bmatrix} = \begin{bmatrix} -f_1(\boldsymbol{X}) \\ -f_2(\boldsymbol{X}) \\ +f_3(\boldsymbol{X}) \end{bmatrix}$$

In short, equivariance under $\mathcal{R}_Z(\pi)$ imposes conditions on the forcing functions f_1, f_2, and f_3

$$\begin{aligned} f_1(X,Y,Z) = \quad & -\sigma X + \sigma Y \quad && \to f_1(-X,-Y,Z) && = \quad -f_1(X,Y,Z) \\ & && && = \quad +\sigma X - \sigma Y \\ f_2(X,Y,Z) = \quad & RX - Y - XZ && \to f_2(-X,-Y,Z) && = \quad -f_2(X,Y,Z) \\ & && && = \quad -RX + Y + XZ \\ f_3(X,Y,Z) = \quad & -bZ + XY \quad && \to f_3(-X,-Y,Z) && = \quad +f_3(X,Y,Z) \\ & && && = \quad -bZ + XY \end{aligned}$$

With a view toward later developments, we point out here that the terms that appear in the forcing functions $f_i(X, Y, Z)$ are of two types:

1. Invariant under $R_Z(\pi)$: (Z, XY)
2. Not invariant under $R_Z(\pi)$: (X, Y, XZ).

Functions that are invariant under $\mathcal{R}_Z(\pi)$ include monomials of the form 1, Z, X^2, XY, Y^2, Z^2, X^2Z, etc. In fact, the most general invariant functions depend on only the four monomials Z, X^2, XY, and Y^2. Thus, the most general invariant function can be expressed in the form $g(Z, X^2, XY, Y^2)$. The three order-two invariant

polynomials X^2, XY, and Y^2 are *linearly* independent since the Jacobian

$$\begin{bmatrix} \dfrac{\partial}{\partial x} \\ \dfrac{\partial}{\partial y} \end{bmatrix} \begin{bmatrix} X^2 & XY & Y^2 \end{bmatrix} = \begin{bmatrix} 2X & Y & 0 \\ 0 & X & 2Y \end{bmatrix} \tag{2.2}$$

has maximal rank, but they are not *functionally* independent, since

$$(X^2)(Y^2) - (XY)^2 = 0 \tag{2.3}$$

Two elementary functions that are not invariant under $\mathcal{R}_Z(\pi)$ are X and Y. In fact, the most general function that is transformed to its negative under the group generator γ of $\mathcal{R}_Z(\pi)$ has the form $g_1(Z, X^2, XY, Y^2)X + g_2(Z, X^2, XY, Y^2)Y$. With this decomposition into invariant functions and noninvariant functions, the Lorenz equations can be expressed in the following form $[(X, Y, Z) = (X_1, X_2, X_3)]$

$$\begin{array}{rcccc} \dot{X}_1 &=& g_{11}X_1 + g_{12}X_2 & = & \begin{bmatrix} g_{11} & g_{12} & 0 \\ g_{21} & g_{22} & 0 \\ 0 & 0 & g_{33} \end{bmatrix} \begin{bmatrix} X_1 \\ X_2 \\ 1 \end{bmatrix} \\ \dot{X}_2 &=& g_{21}X_1 + g_{22}X_2 & = & \\ \dot{X}_3 &=& g_{33} \cdot 1 & & \end{array} \tag{2.4}$$

The invariant functions g_{**} depend on the four invariant monomials $(Z, X^2, XY, Y^2) = (X_3, X_1^2, X_1X_2, X_2^2)$.

Every three-dimensional dynamical system equivariant under the two-element rotation group $\mathcal{R}_Z(\pi)$ has the structure (2.4). For the Lorenz equations :

$$\begin{array}{rcccc} g_{11} &=& -\sigma & & \\ g_{12} &=& +\sigma & & \\ g_{21} &=& R - Z & = & R - X_3 \\ g_{22} &=& -1 & & \\ g_{33} &=& -bZ + XY & = & -bX_3 + X_1X_2 \end{array}$$

Another dynamical system in $\mathbb{R}^3$ with rotation symmetry $\mathcal{R}_Z(\pi)$ has been proposed by Burke and Shaw [70, 113]:

$$\begin{aligned} \dot{X} &= -S(X + Y) \\ \dot{Y} &= -Y - SXZ \\ \dot{Z} &= SXY + \mathcal{V} \end{aligned} \tag{2.5}$$

In the work that follows, we will often use these equations, together with the Lorenz equations, to emphasize similarities and differences among dynamical systems with identical symmetries.

2.1.2 Inversion Symmetry

The matrix generator, γ, for the two-element inversion group $\mathcal{P}$ in $\mathbb{R}^3$ is

$$\begin{bmatrix} -1 & 0 & 0 \\ 0 & -1 & 0 \\ 0 & 0 & -1 \end{bmatrix} \begin{bmatrix} X \\ Y \\ Z \end{bmatrix} = \begin{bmatrix} -X \\ -Y \\ -Z \end{bmatrix}$$

Functions g that are invariant under the action of this group are of even degree in the basic coordinates (X, Y, Z) : X^2, Y^2, Z^2, XY, YZ, ZX; $X^4, \ldots$ In fact, the polynomials of degree 2 are sufficient for the expression of any invariant function:

$$g = g(X^2, Y^2, Z^2, XY, YZ, ZX)$$

These six invariant polynomials of degree 2 are linearly independent but not functionally independent. They obey the three simple relations

$$\begin{array}{ll} (X^2)(Y^2) - (XY)^2 & = 0 \\ (Y^2)(Z^2) - (YZ)^2 & = 0 \\ (Z^2)(X^2) - (ZX)^2 & = 0 \end{array} \tag{2.6}$$

The three monomials $(X, Y, Z) = (X_1, X_2, X_3)$ are not invariant under $\mathcal{P}$: they are mapped into their negatives. The most general dynamical system in $\mathbb{R}^3$ equivariant under $\mathcal{P}$ is

$$\begin{array}{l} \dot{X}_1 = g_{11}X_1 + g_{12}X_2 + g_{13}X_3 \\ \dot{X}_2 = g_{21}X_1 + g_{22}X_2 + g_{23}X_3 \\ \dot{X}_3 = g_{31}X_1 + g_{32}X_2 + g_{33}X_3 \end{array} \quad \rightarrow \dot{X}_i = g_{ij}X_j$$

where g_{**} are functions of the six quadratic invariants.

Two dynamical systems in $\mathbb{R}^3$ with inversion symmetry are the Kremliovsky equations [54] and the induced Lorenz equations (cf. Eq. (2.8) below). The Kremliovsky equations are

$$\begin{array}{l} \dot{X} = -Y - Z \\ \dot{Y} = X + aY \\ \dot{Z} = bX + Z(X^2 - c) \end{array} \tag{2.7}$$

These equations were obtained from the Rössler equations by making minimal modifications (in the equation for $\dot{Z}$) to ensure an inversion symmetry.

The induced Lorenz equations arise in a very natural way when dynamics generated by a Lorenz mechanism are analyzed. Typically a single time series is recorded in many experiments. If the single time series $X(t)$ generated by a system satisfying Lorenz dynamics (1.2) is recorded, it is desirable to use this information to estimate the dynamics. One way to do this is to use as independent coordinates the observed time series $X(t)$ as well as the first and second derivatives

$$\begin{array}{l} X = X_1 = X(t) \\ Y = X_2 = \dot{X}(t) \\ Z = X_3 = \ddot{X}(t) \end{array}$$

The dynamical system equations described from the observed data must obey an inversion symmetry, since $X(t)$ has this symmetry. The dynamical system equations are

$$\begin{array}{rcl} \dot{X} & = & Y \\ \dot{Y} & = & Z \\ \dot{Z} & = & b\sigma(R-1)X - b(\sigma+1)Y - (b+\sigma+1)Z - X^2Y \\ & & -\sigma X^3 + \dfrac{Y\left[(\sigma+1)Y + Z\right]}{X} \end{array} \tag{2.8}$$

This set of equations is clearly equivariant under $(X, Y, Z) \to (-X, -Y, -Z)$. The third equation is also singular unless $Y[(\sigma + 1)Y + Z]/X$ is bounded as $|X| \to 0$.

Equations equivariant under $\mathcal{P}$ can be written in the matrix form

$$\frac{d}{dt}\begin{bmatrix} X \\ Y \\ Z \end{bmatrix} = \begin{bmatrix} g_{11} & g_{12} & g_{13} \\ g_{21} & g_{22} & g_{23} \\ g_{31} & g_{32} & g_{33} \end{bmatrix}\begin{bmatrix} X \\ Y \\ Z \end{bmatrix}$$

The 3×3 matrices of invariant functions for the Kremliovsky system are

$$\text{Kremliovsky: } \begin{bmatrix} 0 & -1 & -1 \\ 1 & a & 0 \\ b & 0 & X^2 - c \end{bmatrix}$$

and for the induced Lorenz system they are

Induced Lorenz:

$$\begin{bmatrix} 0 & 1 & 0 \\ 0 & 0 & 1 \\ b\sigma(R-1) - \sigma X^2 & -b(\sigma+1) - X^2 + \dfrac{(\sigma+1)Y + Z}{X} & -(\sigma + b + 1) \end{bmatrix}$$

These matrices are not unique because of the nonlinear relation (2.6) between the invariant quadratic polynomials.

2.1.3 Reflection Symmetry

The matrix generator, γ, for the two-element reflection group σ_Z in $\mathbb{R}^3$ is

$$\begin{bmatrix} +1 & 0 & 0 \\ 0 & +1 & 0 \\ 0 & 0 & -1 \end{bmatrix}\begin{bmatrix} X \\ Y \\ Z \end{bmatrix} = \begin{bmatrix} +X \\ +Y \\ -Z \end{bmatrix}$$

This group reflects points in $\mathbb{R}^3$ in the X-Y-plane $Z = 0$. The invariant polynomials are functions of X, Y, and Z^2. Every function mapped to its negative under σ_Z is of the form $g(X, Y, Z^2)Z$. The dynamical system equations equivariant under σ_Z have the form

$$\frac{d}{dt}\begin{bmatrix} X \\ Y \\ Z \end{bmatrix} = \begin{bmatrix} g_{11} & 0 \\ g_{21} & 0 \\ 0 & g_{32} \end{bmatrix}\begin{bmatrix} 1 \\ Z \end{bmatrix} \tag{2.9}$$

where $g_{*,*}$ are functions of X, Y, Z^2.

We will not spend much time studying systems equivariant under this symmetry group. The reason is that such dynamical systems cannot generate connected strange attractors with this symmetry.

The X-Y-plane $Z = 0$ is invariant under σ_Z. This means that $\dot{Z} = 0$ on this invariant set (provided g_{32} is nonsingular on this set). As a result, an initial condition in this plane must evolve to a point also in the plane ($Z = 0 \Rightarrow \dot{Z} = 0 \Rightarrow Z$ remains

0). We assume the dynamical system (2.9) possesses a strange attractor $\mathcal{A}$, and some point in this attractor has coordinates (X_0, Y_0, Z_0) with $Z_0 > 0$. Then the point $(X_0, Y_0, -Z_0)$ is also in a strange attractor $\bar{\mathcal{A}} = \sigma\mathcal{A}$, the "mirror image" attractor. The two attractors $\mathcal{A}$ and $\bar{\mathcal{A}}$ cannot be connected. They are disjoint. In order to be connected, some point in either must attempt to cross the plane $Z = 0$. However, once on the plane it becomes stuck in the plane forever. This conclusion depends on properties of the forcing functions g on the singular set. These properties are discussed in the following section.

This is the first instance in which properties of symmetry and topology have nontrivial consequences on the properties of strange attractors. Many more instances will follow.

2.2 EXISTENCE AND UNIQUENESS OF SOLUTIONS

A theorem of fundamental importance guarantees that solutions of a set of first-order ordinary differential equations $\frac{dx_i}{dt} = f_i(\boldsymbol{x})$ exist over a time interval and are unique during that interval. The theorem depends on a smoothness property.

Definition 2.1 *A dynamical system $\dot{\boldsymbol{x}} = \boldsymbol{f}(\boldsymbol{x})$ is Lipschitz in the neighborhood of a point $\boldsymbol{x}_0$ if*

$$|\boldsymbol{f}(\boldsymbol{x}) - \boldsymbol{f}(\boldsymbol{x}_0)| < K|\boldsymbol{x} - \boldsymbol{x}_0|$$

where K is a bounded real constant. Any reasonable measure of distance $|\boldsymbol{x} - \boldsymbol{x}_0|$ in $\mathbb{R}^n$ can be used.

The existence and uniqueness theorem is [5]:

Theorem 2.1 *If a dynamical system $\dot{\boldsymbol{x}} = \boldsymbol{f}(\boldsymbol{x})$ is Lipschitz in the neighborhood of a point $\boldsymbol{x}_0$, then there is a positive number s and*

EXISTENCE: *There is a function ϕ*

$$\phi(t) = (\phi_1(t), \phi_2(t), \ldots, \phi_n(t))$$

that satisfies the dynamical system equations

$$\frac{d\phi_i}{dt} = f_i(\phi_1(t), \phi_2(t), \ldots, \phi_n(t))$$

in the interval $-s \leq t \leq +s$.

UNIQUENESS: *The function $\phi(t)$ is unique.*

Remark: If $\boldsymbol{f}(\boldsymbol{x})$ is Lipschitz for all values of $\boldsymbol{x}$, then the solution can be extended to infinity in both directions. That is, a unique solution through any point exists for all time.

Remark: Dynamical systems with polynomial forcing functions $f_i(\boldsymbol{x})$ cannot be Lipschitz since $K \to \infty$ as $\boldsymbol{x}_0 \to \infty$. However, if motion occurs in a bounded domain

$|\boldsymbol{x}| < R < \infty$, the forcing functions for the system are Lipschitz on that domain, and there is a unique solution through each point that extends to $t \to \pm\infty$.

Remark: If the dynamical system equations $\dot{\boldsymbol{x}} = \boldsymbol{f}(\boldsymbol{x})$ are defined on a compact domain, for example a 3-sphere $S^3 \subset \mathbb{R}^4$, and the forcing functions do not have singularities, the system is Lipschitz.

Remark: All of the dynamical systems introduced so far have polynomial forcing functions with the exception of the induced Lorenz equations. In order for this system to be Lipschitz, we require

1. Motion occurs in a bounded domain
2. $\left|\dfrac{Y\left[(\sigma+1)Y+Z\right]}{X}\right| < K$ as $X \to 0$.

Without the latter condition solutions through the Y-Z plane $X = 0$ cannot be guaranteed.

2.3 SYMMETRY AND THE FUNDAMENTAL THEOREM

If an equivariant dynamical system is Lipschitz at $\boldsymbol{x}_0$, then it is Lipschitz at $\gamma\boldsymbol{x}_0$, where $\gamma\boldsymbol{x}_0$ is the image of $\boldsymbol{x}_0$ under the group operation γ. If $\phi = (\phi_1(t), \phi_2(t), \ldots, \phi_n(t))$ is the unique solution through $\boldsymbol{x}_0$, the unique solutions through $\gamma\boldsymbol{x}_0$, in systems with inversion, rotation, and reflection symmetry in $\mathbb{R}^3$ are:

$$\begin{aligned}
&\mathcal{P} && (-\phi_1(t), -\phi_2(t), -\phi_3(t)) \\
&\mathcal{R}_Z(\pi) && (-\phi_1(t), -\phi_2(t), +\phi_3(t)) \\
&\sigma_Z && (+\phi_1(t), +\phi_2(t), -\phi_3(t))
\end{aligned}$$

If the dynamical system is globally Lipschitz all solutions are extendable to $t \to \pm\infty$. Two possibilities occur for solutions $\phi(t)$ through a point $\boldsymbol{x}_0$ and $\gamma\phi(t)$ through $\gamma\boldsymbol{x}_0$. The solutions are either identical or disjoint. In the first case, the solution is called symmetric and

$$\gamma\phi(t) = \phi(t+T)$$

for some T. In the second case the two disjoint solutions form a symmetric pair of asymmetric solutions. In Fig. 2.1 we show a symmetric period-four orbit and an asymmetric pair of period-three orbits for the Lorenz system ("symmetric pair of asymmetric orbits").

Remark: The concept of symmetric solution set or symmetric pair (for order-two symmetry groups) of asymmetric solution sets extends from closed periodic orbits to fixed points, in one direction of complexity, and to strange attractors in the other direction of complexity. We investigate both in the following two sections.

2.4 FIXED POINT DISTRIBUTIONS

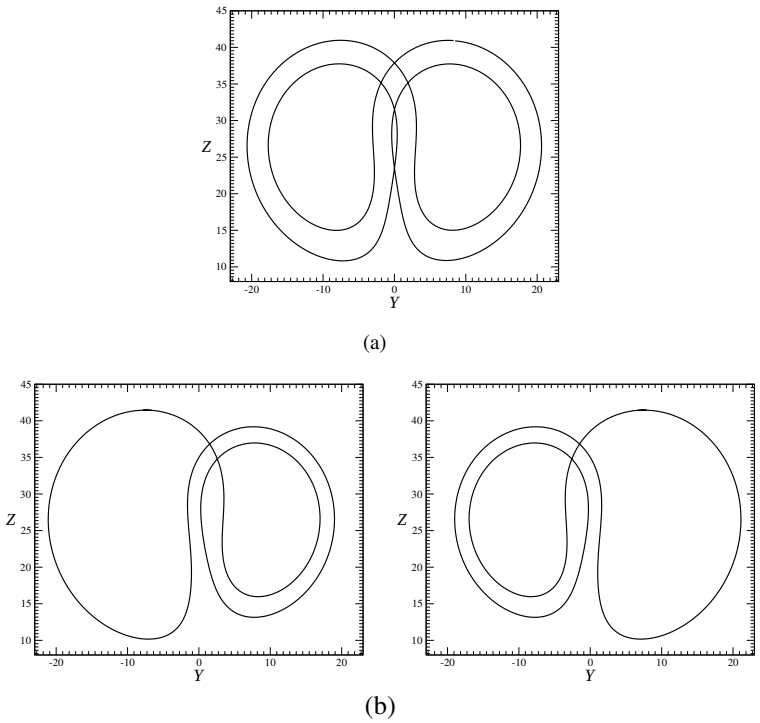

Fig. 2.1 (a) Symmetric period-four orbit of the Lorenz equations and (b) a pair of asymmetric period-three orbits.

Fixed points are points in the phase space at which motion vanishes: $\dot{x}_i = 0$, all i. Thus, fixed points occur at the zeroes of the forcing functions: $f_i(\boldsymbol{x}) = 0$. For relatively simple three-dimensional dynamical systems, the fixed points can be determined by solving the simultaneous nonlinear equations

$$\begin{aligned} f_1(x, y, z) &= 0 \\ f_2(x, y, z) &= 0 \\ f_3(x, y, z) &= 0 \end{aligned}$$

by brute strength methods. For the more sophisticated dynamical systems encountered in Part II, more sophisticated methods for solving these nonlinear equations will be introduced.

If $\boldsymbol{x}_0$ is a fixed point of a dynamical system equivariant under an order-two symmetry group with generator γ and relation $\gamma^2 = I$, then $\gamma\boldsymbol{x}_0$ is also a fixed point. Two types of fixed points exist, depending on whether $\gamma\boldsymbol{x}_0 \neq \boldsymbol{x}_0$ or $\gamma\boldsymbol{x}_0 = \boldsymbol{x}_0$. In the first case, the fixed points occur as a symmetric pair of asymmetric fixed points. In the second case, $\gamma\boldsymbol{x}_0 = \boldsymbol{x}_0$, the single fixed point is a symmetric fixed point. The term symmetric or asymmetric, when applied to a fixed point, depends on whether or not it occurs on the set of fixed points of the symmetry. This is the set of points left

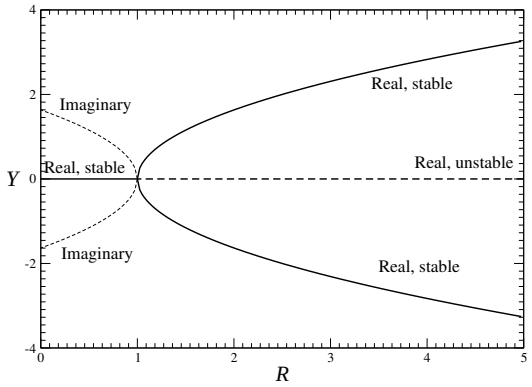

Fig. 2.2 Pitchfork bifurcation for the fixed points of the Lorenz dynamical system.

invariant by the operator γ: $\gamma \boldsymbol{x} = \boldsymbol{x}$. The fixed points, or invariant sets for the three maps $\mathcal{P}$, $\mathcal{R}_Z(\pi)$, and σ in $\mathbb{R}^3$ are

$\mathcal{P}$	$(0,0,0)$	origin
$\mathcal{R}_Z(\pi)$	$(0,0,Z)$	Z-axis
σ_Z	$(X,Y,0)$	X-Y plane-$Z=0$

The invariant sets are of dimension 0, 1, and 2, respectively. In particular for the Lorenz system symmetric fixed points occur on the Z-axis and pairs of asymmetric fixed points (X,Y,Z), $(-X,-Y,Z)$ occur off the Z-axis.

In general, a dynamical system with polynomial forcing terms can have only a finite number of fixed points. This number can be determined by sophisticated methods (cf. Chapter 12). However, not all the fixed points are real. We illustrate what typically occurs for the Lorenz system (2.1). The fixed points are determined by setting $X = Y$ (from $\dot{X} = 0$), $(R-1-Z)X = 0$ (from $\dot{Y} = 0$) and solving $X^2 = bZ$ (from $\dot{Z} = 0$). There is always a solution $X = Y = Z = 0$. For $Z > 0$ there are two real fixed points $X = Y = \pm\sqrt{bZ}$, $Z = R - 1$. For $bZ < 0$ there are two imaginary fixed points. As the control parameter increases through $R = +1$, the two imaginary fixed points become real in a pitchfork bifurcation. The evolution of the real fixed points in the phase space as a function of increasing control parameter R is shown in Fig. 2.2.

In general, when a single control parameter is varied, only fold (saddle-node) bifurcations occur. In a fold bifurcation two imaginary points collide with each other to become real fixed points. In a suitable coordinate system the fold bifurcation has the canonical dependence on a control parameter given by

$$\text{Fold Bifurcation:} \qquad A_2(x;\mu) = x^2 - \mu = 0, \qquad x_{f_p} = \pm\sqrt{\mu}$$

There are two imaginary solutions for $\mu < 0$ and two real fixed points for $\mu > 0$. The bifurcation occurs at $\mu = 0$ (Fig. 2.3(a)).

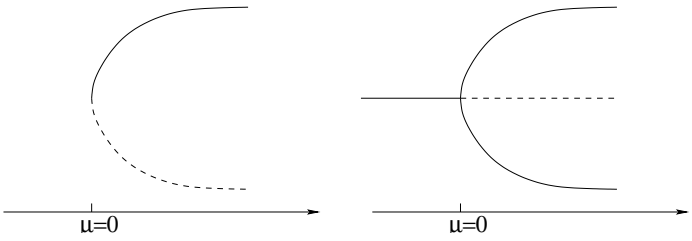

(a) A_2 or saddle-node bifurcation

(b) A_3 or pitchfork bifurcation

Fig. 2.3 There are two one-parameter bifurcations: (a) the fold A_2 and (b) the pitchfork A_3.

The pitchfork bifurcation has a canonical form, in a suitable coordinate system, given by

$$\text{Pitchfork Bifurcation:} \qquad A_3(x;\mu) = x^3 - \mu x = 0, \qquad x_{f_p} = 0, \pm\sqrt{\mu}$$

There is one real root, $x_{f_p} = 0$, for all values of μ. The other pair is imaginary, $x_{f_p} = \pm i\sqrt{-\mu}$ for $\mu < 0$, and real at $x_{f_p} = \pm\sqrt{\mu}$ for $\mu > 0$. The bifurcation occurs at $\mu = 0$ (Fig. 2.3(b)).

The pitchfork bifurcation is a special case of a more general family of singularities called cusp bifurcations [32]. These have canonical form

$$A_3(x;\mu,\epsilon) = x^3 - \mu x - \epsilon = 0$$

In general, the terms μ and ϵ depend on some control parameter s, so that the bifurcation of $x^3 - \mu(s)x - \epsilon(s) = 0$ is as shown in Fig. 2.4. If a symmetry exists that imposes some conditions on $A_3(x;\mu,\epsilon)$, for example $A_3(-x;\mu,\epsilon) = -A_3(x;\mu,\epsilon)$, then the coefficient ϵ is suppressed and one parameter paths in the space of control parameters cannot avoid the point $(\mu,\epsilon) = (0,0)$, where the pitchfork bifurcation takes place. The fixed points obey

$$V_3(x;\mu,0) = x^3 - \mu x = 0, \qquad x_{f_p} = \begin{matrix} +\sqrt{\mu} \\ 0 \\ -\sqrt{\mu} \end{matrix}$$

The general result for dynamical systems equivariant under a symmetry group with two operations is as follows. As the control parameters are varied, real fixed points are created or annihilated:

1. In fold bifurcations. The fold bifurcations occur in symmetric pairs. The fixed points do not occur on the invariant set.
2. In pitchfork bifurcations. The pitchfork bifurcation involves one fixed point on the invariant set. In general, the other two fixed points involved in the pitchfork bifurcation are a symmetric pair of asymmetric fixed points.

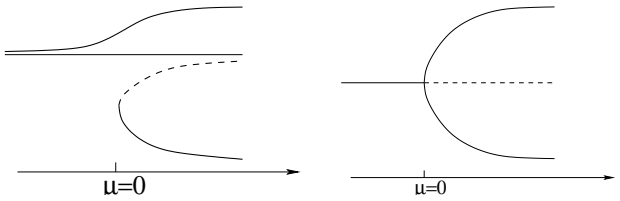

Fig. 2.4 (a) Path $[\mu(s), \epsilon(s)]$ through control parameter space of the cusp family produces only a saddle-node bifurcation. (b) Under symmetry restriction, a pitchfork bifurcation can occur.

Remark: Fold bifurcations are singularities of type A_2 and pitchfork bifurcations are a symmetry-restricted class of cusp bifurcations, which are singularities of type A_3.

Equivariant dynamical systems in $\mathbb{R}^3$ with two-fold symmetry exhibit fixed point bifurcations depending on the symmetry group as follows.

$\mathcal{P}$ Pitchfork bifurcations involve the fixed point at the origin and two symmetry-related fixed points (X, Y, Z), $(-X, -Y, -Z)$. Fold bifurcations occur in symmetric pairs and do not involve the fixed point at the origin.

$\mathcal{R}_Z(\pi)$ Pitchfork bifurcations involve a fixed point on the Z-axis $(0, 0, Z)$ and two symmetry-related points off the z-axis (X, Y, Z') and $(-X, -Y, Z')$. Fold bifurcations occur in symmetric pairs and involve two pairs of fixed points, off the Z-axis.

σ_Z Pitchfork bifurcations involve a point in the X-Y-plane $(X, Y, 0)$ and two mirror image points (X', Y', Z) and $(X', Y', -Z)$ off the symmetry plane. Fold bifurcations occur in symmetric mirror image pairs, one above, the other below the $Z = 0$ plane.

The structure of the flow on the invariant set is easily determined from the standard form of the equivariant dynamical system in the three cases:

$$\mathcal{P} \quad \frac{d}{dt}\begin{bmatrix} X \\ Y \\ Z \end{bmatrix} = \begin{bmatrix} g_{11} & g_{12} & g_{13} \\ g_{21} & g_{22} & g_{23} \\ g_{31} & g_{32} & g_{33} \end{bmatrix} \begin{bmatrix} X \\ Y \\ Z \end{bmatrix} \overset{(X,Y,Z)=(0,0,0)}{\longrightarrow} \begin{bmatrix} 0 \\ 0 \\ 0 \end{bmatrix}$$

$$\mathcal{R}_Z(\pi) \quad \frac{d}{dt}\begin{bmatrix} X \\ Y \\ Z \end{bmatrix} = \begin{bmatrix} g_{11} & g_{12} & 0 \\ g_{21} & g_{22} & 0 \\ 0 & 0 & g_{33} \end{bmatrix} \begin{bmatrix} X \\ Y \\ 1 \end{bmatrix} \overset{(X,Y,Z)=(0,0,Z)}{\longrightarrow} \begin{bmatrix} 0 \\ 0 \\ g_3(Z) \end{bmatrix}$$

$$\sigma_Z \quad \frac{d}{dt}\begin{bmatrix} X \\ Y \\ Z \end{bmatrix} = \begin{bmatrix} 0 & g_{12} \\ 0 & g_{22} \\ g_{31} & 0 \end{bmatrix} \begin{bmatrix} Z \\ 1 \end{bmatrix} \overset{(X,Y,Z)=(X,Y,0)}{\longrightarrow} \begin{bmatrix} g_{12}(X,Y) \\ g_{22}(X,Y) \\ 0 \end{bmatrix}$$

In all three cases, the flow, restricted to the invariant set, is completely *in* the invariant set. This is a general result, valid for all symmetry groups and any dimensional dynamical system.

Remark: The discussion above involves two different definitions of invariant set:

Invariant set for a group: This is the set of points that are fixed (mapped into themselves) under all of the group operations.

Invariant set for a flow: This is the set of points that are mapped into themselves under the flow.

We emphasize that these two definitions are highly intertwined.

2.5 CLASSIFICATION OF STRANGE ATTRACTORS

In the present work we will describe many inequivalent strange attractors. It is essential that we adopt some robust mechanism for identifying strange attractors. This classification must enable us to distinguish between equivalent and inequivalent strange attractors. One attractor is equivalent to another when there is a smooth transformation that takes one to the other in a continuous way. If such a smooth deformation does not exist, two strange attractors are not equivalent.

2.5.1 Background

During the early stages in the evolution of "chaos theory" two tools were widely used to analyze strange attractors. These were computation of the fractal dimensions and computation of the Lyapunov exponents.

Fractal dimension is a geometric measure. A strange attractor is built up by repeated occurrence of two operations: stretching and squeezing. The repetition of these two processes builds up a geometric structure that is self-similar: it looks the same at many magnification scales. Fractal dimension is in some way a measure of this self-similarity [95].

Lyapunov exponents are dynamical measures. Nearby points in phase space will be acted on in different ways by the flow. In practice, a sphere of initial conditions will be deformed approximately into an ellipsoid during a short time. The Lyapunov exponents are essentially the logarithms of the ratios of the principal axes of the ellipsoid to the radius of the original sphere. Positive Lyapunov exponents indicate directions in which expansion takes place; negative Lyapunov exponents indicate directions in which contraction takes place. When the flow shrinks volumes, the sum of the Lyapunov exponents is less than zero [34, 94, 137].

Fractal dimension estimates provide very little information about a dynamical system. Estimates of the spectrum of Lyapunov exponents provide somewhat more information. Both statistics are beset with problems:

- They require long (*very* long for fractal dimension calculations), clean (ditto) data sets.
- They require delicate and time consuming calculations that sometimes resemble a black art more than an algorithmic procedure.
- The calculations result in a real number (or numbers) with no error estimates.
- There is no independent way to assess this real number.
- There is no statistical theory for error estimation.
- The estimates are not robust under changes in operating conditions or parameter values.
- These estimates convey no information on "how to model the dynamics."

2.5.2 Topological Classification of Strange Attractors

The flows for the symmetric dynamical systems introduced so far (Fig. 2.5) clearly suggest what stretching and squeezing mechanisms act on the phase space flow to generate the strange attractor. For the cases shown it is possible to introduce a "cardboard model" to describe the nature of the flow and the stretching and squeezing mechanism that generates chaotic behavior. Cardboard models of the Lorenz, Burke and Shaw, induced Lorenz, and Kremliovsky flows are shown in Fig. 2.5. These flows are easy to describe by "cardboard models" because they are highly dissipative, or strongly volume contracting.

In fact, representing the flows on a strange attractor by a cardboard model does not depend on strong dissipation. There is a theorem that guarantees the existence of such a limiting model for flows in three dimensions [14, 15]. The theorem is due to Birman and Williams, the limiting model is called a branched manifold, or template, or knot-holder. Examples of branched manifolds are shown in Fig. 2.5.

A branched manifold is built up "Lego-style" from two basic units. These are shown in Fig. 2.6. One unit describes the stretching process, the other describes the squeezing process. On the left of Fig. 2.6 we show how a cube of initial conditions in $\mathbb{R}^3$ is deformed when one Lyapunov exponent (λ_1) is positive and the other (λ_3) is negative. The Lyapunov exponent λ_2 corresponding to the flow direction is zero:

$$\lambda_1 > \lambda_2 = 0 > \lambda_3$$

The flow is assumed to be dissipative

$$\lambda_1 + \lambda_2 + \lambda_3 < 0$$

In this cartoon, initial conditions are compressed into the plane of the page and stretched apart in the plane of the page. Eventually the flow will lead to different parts of the phase space. A singularity occurs at the tear point. This point describes an initial condition that flows to a fixed point. The sequence on the right of Fig. 2.6

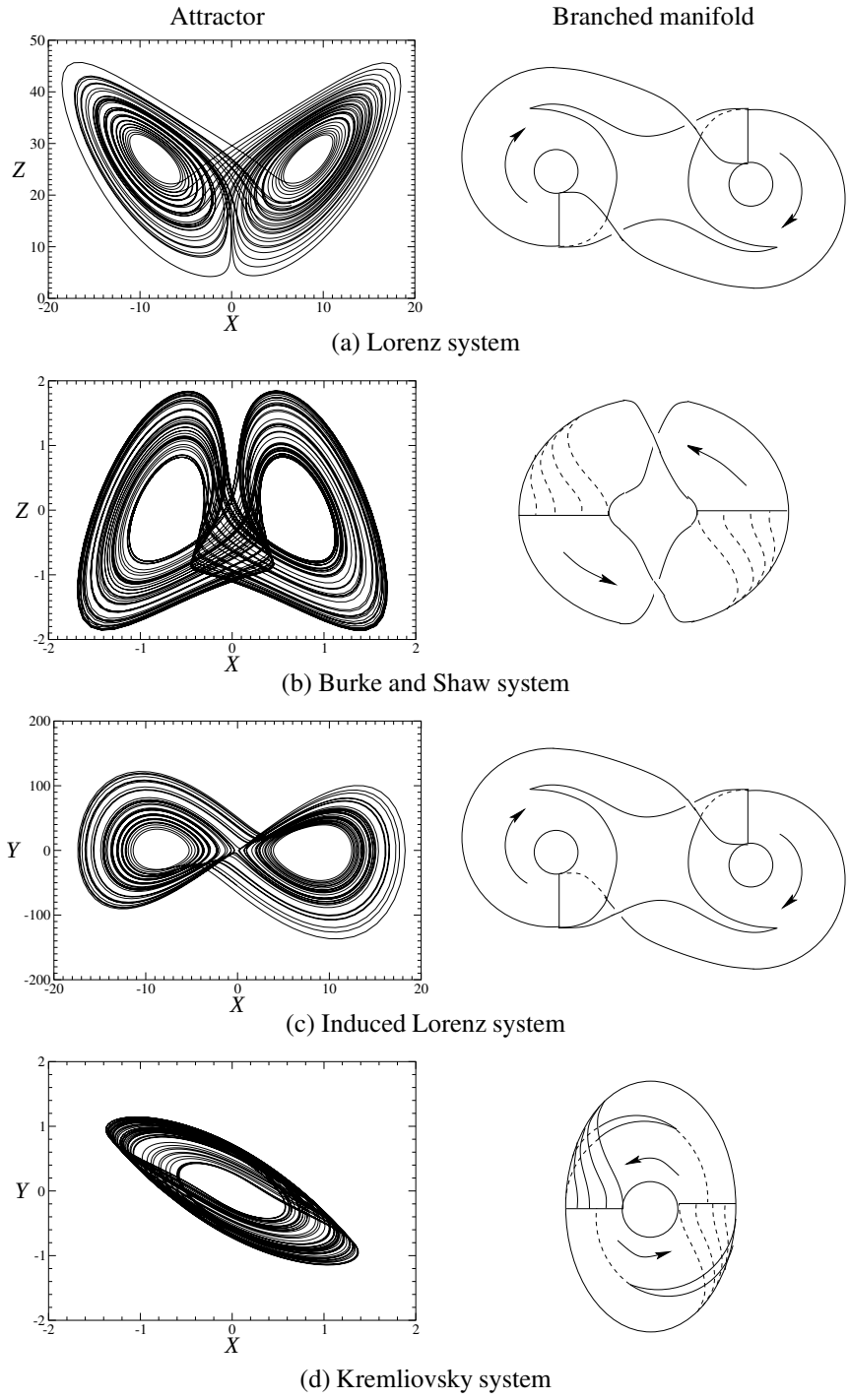

Fig. 2.5 Symmetric attractors (left) and their representations by branched manifolds (right). The Lorenz and the induced Lorenz attractors are generated by a tearing and squeezing mechanism, while the Burke and Shaw and the Kremliovsky attractors are generated by a folding and squeezing mechanism.

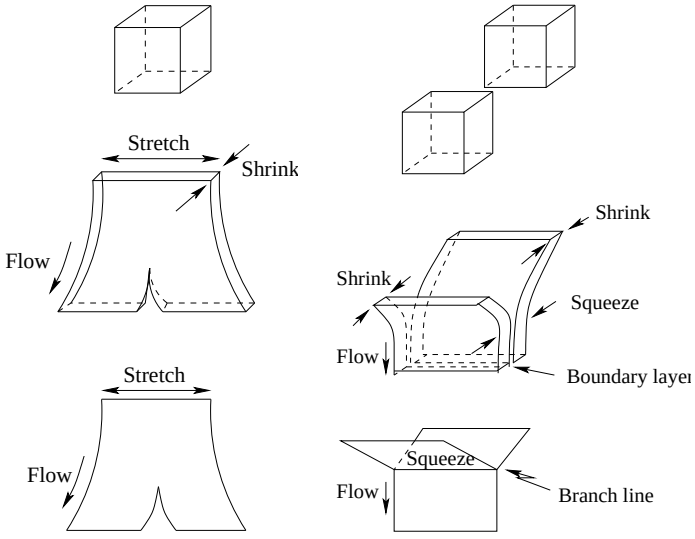

(a) Stretching mecanism (b) Squeezing mecanism

Fig. 2.6 Cartoons describing stretching (left) and squeezing (right). In both cases time evolves downward. In the case of stretching, a cube of initial conditions is deformed by being stretched in the direction of the page and shrunk (volume-decreasing transformation) in the transverse direction. Eventually distant parts of the cube of initial conditions are pulled off to different parts of the phase space. The tear point is an initial condition that flows to a fixed point. In the case of squeezing, two sets of initial conditions from distant parts of phase space are squeezed together. In the limit, they meet at a branch line. The two units at the bottom on the left and right can be used to describe the mechanism of every chaotic flow in three dimensions by plugging them together, Lego style, output to input, with no leftover free ends.

shows sets of initial conditions in two different parts of the phase space. The initial conditions (two cubes) are squeezed together under the flow. There is a singularity at the branch line, where the flows from two distant regions are joined.

The singularities—tear point and branch line— describe the stretching and the squeezing process that take place to generate a strange attractor. These two building blocks can be joined in many possible ways, subject to just two conditions:

1. Each outflow feeds into an inflow.
2. There are no free edges.

Every possible combination of these two building blocks represents a mechanism that generates a strange attractor [14, 15, 33, 34].

The Birman-Williams theorem is based on a useful identification. Two points, $\boldsymbol{x}$ and $\boldsymbol{y}$, in phase space are said to be equivalent if they have the "same future" [14, 15]. That is, the distance between the trajectories that start at equivalent points $\boldsymbol{x}$ and $\boldsymbol{y}$

shrinks to zero as $t \to \infty$. Formally we write

$$\boldsymbol{x} \approx \boldsymbol{y} \quad \text{if} \quad |\boldsymbol{x}(t) - \boldsymbol{y}(t)| \stackrel{t\to\infty}{\longrightarrow} 0 \tag{2.10}$$

By identifying equivalent points in a strange attractor we are in effect projecting the flow down along a stable manifold to a two-dimensional branched manifold. One dimension corresponds to the flow direction, the other to the stretching direction. The projection converts the flow to a "semiflow." This is a flow in which every point has a unique future but not a unique past. In fact, the past is unique up to the nearest branch line in its past.

A formal statement of the Birman-Williams theorem is as follows [14, 15].

Theorem 2.1 *Birman-Williams Theorem: Assume that a dissipative dynamical system in $\mathbb{R}^3$ has Lyapunov exponents that satisfy*

$$\lambda_1 > \lambda_2 = 0 > \lambda_3$$

$$\lambda_1 + \lambda_2 + \lambda_3 < 0$$

and generates a hyperbolic strange attractor. The identification (2.10) maps the strange attractor $\mathcal{SA}$ to a branched manifold $\mathcal{BM}$ and the flow Φ_t on $\mathcal{SA}$ to a semiflow $\bar{\Phi}_t$ on $\mathcal{BM}$. The periodic orbits in $\mathcal{SA}$ under the flow Φ_t correspond in a one-to-one way with the periodic orbits in $\mathcal{BM}$ under $\bar{\Phi}_t$ with one or two specified exceptions. On any finite subset of periodic orbits the correspondence can be taken to be via isotopy.

In plain English this theorem guarantees that a strange attractor $\mathcal{SA}$ can be projected down to a branched manifold $\mathcal{BM}$, and in this projection the number and type of periodic orbits as well as their topological organization is unchanged.

The condition that the strange attractor is hyperbolic can be relaxed. This theorem is even true for strange attractors in n-dimensional space provided that they are "strongly contracting" [33, 34, 89]. This means that the Lyapunov exponents satisfy

$$\lambda_1 > \lambda_2 > \lambda_3 \geq \cdots \geq \lambda_n$$

$$\lambda_1 + \lambda_2 + \lambda_3 < 0$$

In other words, $\lambda_1 > 0$, $\lambda_2 = 0$, $\lambda_3 < 0$, and $\lambda_1 + \lambda_3 < 0$. In such cases, the strange attractor can be squeezed into $\mathbb{R}^3$, or at least some three-dimensional manifold.

2.5.3 Extracting Branched Manifolds from Data

Branched manifolds are excellent tools for classifying strange attractors because the organization of the unstable periodic orbits is unchanged during the projection from the strange attractor to the branched manifold [87]. The organization of the unstable periodic orbits is determined by the topological indices of pairs of orbits: specifically, their Gaussian linking numbers [89, 116].

As a reminder, the key to classifying strange attractors is by "la seule brèche par où nous puissions essayer de pénétrer dans une place jusqu'ici réputée inabordable"—the topological organization of their unstable periodic orbits. This point was made by Poincaré over 100 years ago [100].

A strange attactor can be identified, or classified, by determining the branched manifold that it projects to. The identification is algorithmic. The algorithm has a finite, small number of steps. In the event that the analysis is carried out on a single time series $x(t)$ the steps are as follows [33,34]:

1. Unstable periodic orbits are extracted from the time series. The method of choice is the close returns procedure. This method identifies segments of the chaotic time series that are almost periodic, and which can serve as surrogates for unstable periodic orbits.
2. A three-dimensional embedding for the time series is constructed. The method of choice is the differential embedding x, $y = \dot{x}$, $z = \ddot{x}$ or the integral-differential embedding (y_1, y_2, y_3) where $y_2 = x$, $\dot{y}_1 = x$, and $\dot{x} = y_3$.
3. Linking numbers for pairs of the surrogate periodic orbits in the three-dimensional embedding space are computed.
4. The unstable periodic orbits are named by introducing a symbolic dynamics.
5. A branched manifold is proposed. Each branch is labeled by one of the symbols of the symbol set required to provide a unique identification for all the orbits.
6. Periodic orbits on the branched manifold are determined and their linking numbers are computed. They are compared with linking numbers for corresponding pairs of labeled surrogate orbits. Modifications in the proposed branched manifold and labeling of the surrogate periodic orbits are made until the two tables of linking numbers of orbits on the branched manifold and surrogate orbits extracted from the data are in agreement. Tables of linking numbers for the orbits to period five that exist in Smale horseshoe dynamics and in Lorenz dynamics are presented in the following subsection.
7. Usually the branched manifold can be identified by analyzing a small number of low period orbits. Here "period" is the number of letters in the symbol sequence that identifies an orbit. The identification of the branched manifold can be confirmed by comparing the linking numbers of all other pairs of surrogate orbits with the corresponding orbits on the branched manifold. Such confirmation steps are lacking in analyses using geometric (fractal dimension) and dynamical (Lyapunov exponent) tools.

Remark: The branched manifold used to described a flow may not be unique. Three descriptions of the flow on the Lorenz attractor are shown in Fig. 2.7. The first two involve a two-symbol dynamics. One branched manifold is related to the other by rotating one lobe through π radians about a horizontal axis. The second and third branched manifolds are essentially the same, but one uses two symbols, the other four. A transition matrix (Section 2.6) indicates how the branches flow onto each other.

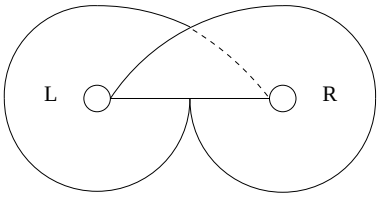

(a) Standard representation of the "Lorenz mask" by a cardboard model.

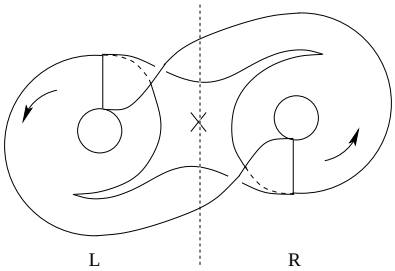

$$\begin{array}{c} \\ L \\ R \end{array} \begin{array}{c} \begin{array}{cc} L & R \end{array} \\ \begin{bmatrix} 1 & 1 \\ 1 & 1 \end{bmatrix} \end{array}$$

(b) The left-hand lobe of (a) is rotated about a horizontal axis. Symbols L and R describe the two foci.

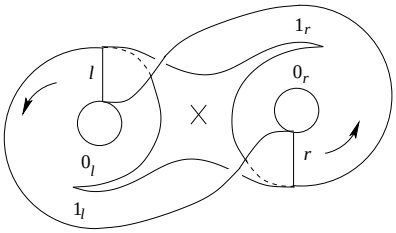

$$\begin{array}{c} \\ 0_l \\ 1_l \\ 0_r \\ 1_r \end{array} \begin{array}{c} \begin{array}{cccc} 0_l & 1_l & 0_r & 1_r \end{array} \\ \begin{bmatrix} 1 & 1 & 0 & 0 \\ 0 & 0 & 1 & 1 \\ 0 & 0 & 1 & 1 \\ 1 & 1 & 0 & 0 \end{bmatrix} \end{array}$$

(c) Same as (b), except that the symbols label the four branches instead of the two branch lines.

Fig. 2.7 Branched manifolds and their transition matrices for Lorenz dynamics.

2.5.4 Linking Number Tables

The locations of periodic orbits on branched manifolds are determined using standard kneading theory [86]. Once the trajectory of a periodic orbit has been determined, its linking number with other periodic orbits is easily computed simply by counting crossings. For the standard Smale horseshoe branched manifold, shown in Fig. 2.8(a), the periodic orbits are labeled by two symbols, 0 and 1. These indicate the branch that the trajectory flows through. For orbits to period five, the linking numbers are presented in Table 2.1. These linking numbers remain unchanged as long as the orbits exist. All crossings occur as the flow in the two branches approaches the branch line,

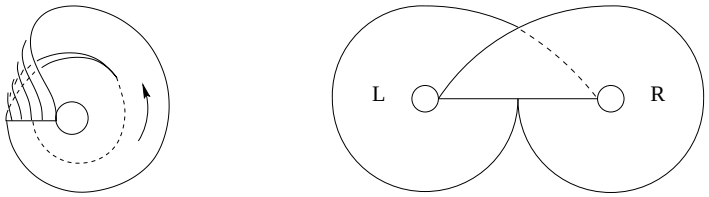

(a) Smale horseshoe dynamics (b) Lorenz dynamics

Fig. 2.8 Branched manifolds for (a) Smale horseshoe dynamics and (b) Lorenz dynamics.

Table 2.1 Linking numbers for orbits to period five in Smale horseshoe dynamics.

	$1s$	$1f$	2_1	$3f$	$3s$	4_1	4_2f	4_2s	5_3f	5_3s	5_2f	5_2s	5_1f	5_1s
0	0	0	0	0	0	0	0	0	0	0	0	0	0	0
1	0	0	1	1	1	2	1	1	1	1	2	2	2	2
01	0	1	1	2	2	3	2	2	2	2	3	3	4	4
001	0	1	2	2	3	4	3	3	3	3	4	4	5	5
011	0	1	2	3	2	4	3	3	3	3	5	5	5	5
0111	0	2	3	4	4	5	4	4	4	4	7	7	8	8
0001	0	1	2	3	3	4	3	4	4	4	5	5	5	5
0011	0	1	2	3	3	4	4	3	4	4	5	5	5	5
00001	0	1	2	3	3	4	4	4	4	5	5	5	5	5
00011	0	1	2	3	3	4	4	4	5	4	5	5	5	5
00111	0	2	3	4	5	7	5	5	5	5	6	7	8	9
00101	0	2	3	4	5	7	5	5	5	5	7	6	8	9
01101	0	2	4	5	5	8	5	5	5	5	8	8	8	10
01111	0	2	4	5	5	8	5	5	5	5	9	9	10	8

and all crossings are negative according to standard conventions. The minus sign $(-)$ has not been included in Table 2.1.

In the case of Lorenz dynamics, the corresponding knot-holder also has two branches. These are labeled L and R, and the knot-holder is shown in Fig. 2.8(b). All periodic orbits are composed of these two symbols. The linking numbers of all Lorenz orbits to period five are presented in Table 2.2. All crossings in this branched manifold are positive. The symmetry that is exhibited by the Lorenz equations and that is evident in its branched manifold can also be deduced from the table of linking numbers, Table 2.2. It is easily seen that if P_1 and P_2 are two orbits and $\overline{P}_1$ and $\overline{P}_2$ are the orbits obtained from P_1 and P_2 by interchanging the letters L and R,

$$\text{Link}(P_1, P_2) = \text{Link}(\overline{P}_1, \overline{P}_2) \tag{2.11}$$

For example Link($LLR, LLLR$) = 2 = Link($LRR, LRRR$). If rotation symmetry is replaced by inversion symmetry the relation above would be $\text{Link}(P_1, P_2) = -\text{Link}(\overline{P}_1, \overline{P}_2)$ (c.f., Fig. 4.6). The linking numbers for this symmetry are presented in Table 2.3. The projections of corresponding orbits with the two symmetries onto

Table 2.2 Linking numbers for orbits to period five in Lorenz dynamics.

	L	R	LR	3_1	3_2	4_1	4_2	4_3	5_1	5_2	5_3	5_4	5_5	5_6
L	0	0	0	0	0	0	0	0	0	0	0	0	0	0
R	0	0	0	0	0	0	0	0	0	0	0	0	0	0
LR	0	0	1	1	1	1	1	2	1	2	2	2	2	1
LLR	0	0	1	2	1	1	2	2	2	3	2	3	2	1
LRR	0	0	1	1	2	2	1	2	1	2	3	2	3	2
LRRR	0	0	1	1	2	3	1	2	1	2	3	2	3	3
LLLR	0	0	1	2	1	1	3	2	3	3	2	3	2	1
LLRR	0	0	2	2	2	2	2	3	2	3	3	4	4	2
LLLLR	0	0	1	2	1	1	3	2	4	3	2	3	2	1
LLLRR	0	0	2	3	2	2	3	3	3	4	3	5	4	2
LLRRR	0	0	2	2	3	3	2	3	2	3	4	4	5	3
LLRLR	0	0	2	3	2	2	3	4	3	5	4	6	4	2
LRRLR	0	0	2	2	3	3	2	4	2	4	5	4	6	3
LRRRR	0	0	1	1	2	3	1	2	1	2	3	2	3	4

the x-y plane are indistinguishable until the projections are dressed with crossing information.

Table 2.3 Linking numbers for orbits to period five in dynamics invariant under $\mathcal{P}$.

	L	R	LR	3_1	3_2	4_1	4_2	4_3	5_1	5_2	5_3	5_4	5_5	5_6
L	-	0	0	0	0	0	0	0	0	0	0	0	0	0
R	0	-	0	0	0	0	0	0	0	0	0	0	0	0
LR	0	0	-	0	0	0	0	0	0	0	0	0	0	0
LLR	0	0	0	-	0	0	-1	-1	-1	-1	-1	-1	0	0
LRR	0	0	0	0	-	1	0	1	0	1	1	0	1	1
LRRR	0	0	0	0	1	-	0	1	0	1	2	0	1	2
LLLR	0	0	0	-1	0	0	-	-1	-2	-2	-1	-1	0	0
LLRR	0	0	0	-1	1	1	-1	-	-1	0	0	-1	1	1
LLLLR	0	0	0	-1	0	0	-2	-1	-	-2	-1	-1	0	0
LLLRR	0	0	0	-1	1	1	-2	0	-2	-	0	-1	1	1
LLRRR	0	0	0	-1	1	2	-1	0	-1	0	-	-1	1	2
LLRLR	0	0	0	-1	0	0	-1	-1	-1	-1	-1	-	0	0
LRRLR	0	0	0	0	1	1	0	1	0	1	1	0	-	1
LRRRR	0	0	0	0	1	2	0	1	0	1	2	0	1	-

Remark 1: Equivariance in a dynamical system, in particular in covering dynamical systems, is reflected in the symmetries intrinsic to its table of linking numbers.

Remark 2: Since the Smale horseshoe branched manifold (Rössler system) does not have a two-fold symmetry, its table of linking numbers lacks a symmetry of type (2.11).

Remark 3: Group continuation of tables of linking numbers is not straightforward. This is seen by comparing Table 2.2 with Table 2.3.

2.5.5 Symmetry

When a three-dimensional system with a two-fold symmetry generates a strange attractor, either

1. the attractor possesses the two-fold symmetry
2. the attractor is disconnected and consists a symmetric pair of asymmetric attractors.

These properties are reflected in the branched manifold for the strange attractor. The branches must occur in symmetry-related pairs. The branched manifold for the strange attractor is either

1. connected and symmetric
2. not connected and consists of a symmetric pair of asymmetric branched manifolds.

Several branched manifolds of symmetric systems are shown in Fig. 2.5. Several representations of a branched manifold for Lorenz dynamics are shown in Fig. 2.7.

2.5.6 Application

The first topological analysis was carried out on chaotic data generated by the Belousov-Zhabotinskii chemical reaction [89]. A set of data segments that served as surrogates for unstable periodic orbits was extracted from the long, very clean scalar time series [115]. These data segments were located by the method of close returns before the data were embedded in a three-dimensional phase space.

Subsequently a suitable three-dimensional embedding was constructed. This embedding was an integro-differential embedding. The embedding showed that the reconstructed attractor "had a hole in the middle" so that a Poincaré surface of section could easily be constructed. A return map onto the Poincaré surface of section was similar to that shown in Fig. 3.9(b). Specifically:

1. It was almost one-dimensional, showing that the system was highly dissipative;
2. It had two branches, showing that two symbols sufficed to encode the trajectory, and all periodic orbits.

Data segments that intersected the Poincaré section p times before (almost) closing were identified as period-p orbits, and a symbolic encoding was tentatively given according to whether the intersection occurred in the orientation-perserving (0) or -reversing (1) branch of the return map. The linking numbers of all pairs of orbits were computed in this embedding. These linking numbers are presented for the subset of experimental orbits, up to period five, in Table 2.4.

Table 2.4 Linking numbers for orbits extracted from data generated by the Belousov-Zhabotinskii reaction, up to period five.

	1	01	011	0111	01011
1	0	1	1	2	2
01	1	1	2	3	4
011	1	2	2	4	5
0111	2	3	4	5	8
01011	2	4	5	8	8

Since the branched manifold describing the dynamics has two branches, it was possible to determine it using information determined from the linking numbers of only three periodic orbits. The three orbits of lowest period (1, 01, 011) were used in this determination. Their linking numbers are shown in the 3×3 submatrix in the upper left corner of Table 2.4. On the basis of these three linking numbers (self-linking numbers were neglected) the appropriate branched manifold was identified. This was the Smale horseshoe branched manifold, shown in Fig. 2.8(a). Using this branched manifold, the linking numbers of all other surrogate orbits were computed and compared with those calculated directly from the surrogate orbit segments. This comparison serves as a double-check on the validity of the branched manifold identification. This identification is vastly overdetermined and the comparison serves as a rejection criterion for the double problem of determining the correct branched manifold as well as the correct labeling for the surrogate orbits. Three linking numbers (1, 1, 2) of the three lowest period orbits (1, 01, 011) were used to determine the linking numbers of all nine surrogate orbits up to period eight. The three off-diagonal integers correctly predicted the remaining $\frac{1}{2}9 \times 8 - 3 = 33$ integers.

2.6 SYMBOLIC DYNAMICS

Each branch of a branched manifold is identified by a symbol label. If the original dynamical system has two-fold symmetry, the branches and branch labels must exhibit this symmetry.

The strange attractor generated by the Lorenz system at standard parameter values $R = 28$, $\sigma = 10$, $b = 8/3$ (Fig. 2.5(a)) has two lobes. They are related to each other by the rotation symmetry, $\mathcal{R}_Z(\pi)$. The branched manifold for this strange attractor (Fig. 2.7(a)) has two branches. These can conveniently be labeled L, R. Every orbit on the branched manifold can be represented symbolically by an infinite string composed of the two letters L and R. In principle, after the trajectory passes through branch L it may return to L or to pass to R. Similarly for R. The transition matrix describing dynamics on this branched manifold is

	L	R
L	1	1
R	1	1

Lorenz dynamics can also be described by the four-branched manifold shown in Fig. 2.7(c). The transition matrix for this four-branch template is

	0_l	1_l	0_r	1_r
0_l	1	1	0	0
1_l	0	0	1	1
0_r	0	0	1	1
1_r	1	1	0	0

This means that after transiting 0_l the dynamics can enter branch 0_l (again) or 1_l but not branches 0_r and 1_r. Similarly after traveling through branch 1_l the dynamics must enter branch 0_r or 1_r.

2.7 PERIODIC ORBITS

Trajectories of initial conditions in strange attractors are simpler to study when the trajectory can be expressed as a symbol sequence. The same is true for semiflows on a branched manifold. In both cases the space is partitioned into a set of subspaces, each labeled by a different symbol. The flow through each subset is labeled by the name of the subset. For a branched manifold the subsets consist of the different branches.

A periodic orbit returns to its initial condition infinitely often. The symbol sequence representing a periodic orbit therefore repeats infinitely often. For example, the symbol sequence

$$\ldots \text{L R L L R L L R L L R L} \ldots$$

describes the period-three orbit $(\text{LLR})^\infty$ in the Lorenz attractor. Two other equivalent representations of the same orbit are $(\text{LRL})^\infty$ and $(\text{RLL})^\infty$. Usually some convention (such as lexigraphic) is chosen to provide a unique naming mechanism for periodic orbits.

In a representation of Lorenz dynamics using a four-branch manifold the following equivalence exists for the period-three orbit LLR:

LLR	$0_l\ 1_l\ 1_r$
LRL	$1_l\ 1_r\ 0_l$
RLL	$1_r\ 0_l\ 1_l$

We return now to the question of whether the solutions $\phi(t)$ and $\gamma\phi(t)$ (cf. Section 2.3) of the equivariant equations belong to the same or different trajectories. This question is simple to resolve for periodic orbits. We illustrate for Lorenz dynamics—the argument is unchanged for other two-fold symmetries. The operator γ acts in symbol space

$$\begin{aligned} \mathrm{L} &\xrightarrow{\gamma} \mathrm{R} \\ \mathrm{R} &\xrightarrow{\gamma} \mathrm{L} \end{aligned}$$

to map a segment in the left half space into the right half space, and vice versa. It therefore acts on periodic orbits as well:

$$\mathrm{LLR} \xrightarrow{\gamma} \mathrm{RRL}$$

Periodic orbits are either symmetric or occur in asymmetric pairs. An orbit of odd period cannot be symmetric. Therefore odd period orbits occur in symmetric pairs. The symbol sequence for an even period orbit of period $2p$ can be written in the form $(\mathrm{S}_1\mathrm{S}_2)$. Here $\mathrm{S}_1\mathrm{S}_2$ are symbol sequences of length p. If S_1=S_2, the orbit is $(\mathrm{S}_1)^2$ — that is, its minimal period is p, not $2p$. Therefore $\mathrm{S}_1 \neq \mathrm{S}_2$. If $\mathrm{S}_2 = \gamma\mathrm{S}_1$, the orbit is symmetric, if not, it is asymmetric

$\mathrm{S}_2 = \gamma\mathrm{S}_1$	Symmetric
$\mathrm{S}_2 \neq \gamma\mathrm{S}_1$	Asymmetric

Example The period-three orbits (LLR) and (RRL) form a symmetric pair of asymmetric period three orbits. The orbit LRLR is actually a period-two orbit LR. This period-two orbit is symmetric. The period-four orbit LLRR is symmetric, since RR = γ(LL). The period-four orbit LLLR is not symmetric since LR $\neq \gamma$ (LL): its symmetric partner is RRRL. All these orbits can be labeled using the four symbols 0_l 1_l 0_r 1_r.

LR	$1_l\ 1_r$
LLR	$0_l\ 1_l\ 1_r$
RRL	$0_r\ 1_r\ 1_l$
LLRR	$0_l\ 1_l\ 0_r\ 1_r$
LLLR	$0_l\ 0_l\ 1_l\ 1_r$
RRRL	$0_r\ 0_r\ 1_r\ 1_l$

Remark: If the period of a symmetric orbit is T, then $\gamma\phi(t) = \phi(t + \frac{1}{2}T)$.

2.8 TOPOLOGICAL ENTROPY

Not every orbit that exists in the branched manifold can be found in the strange attractor. However, those that exist in the strange attractor are organized topologically exactly as their counterparts in the branched manifold are organized.

Topological entropy measures the growth in the number of orbits of period p with the period [3]. In general, the period p, topological entropy h_T, and the number, $N(p)$, of different orbits of period p are related by

$$\begin{aligned} N(p) &\approx e^{ph_T} \\ h_T &= \lim_{p\to\infty} \frac{1}{p} \log N(p) \end{aligned}$$

Since there are generally more orbits on a branched manifold than in the strange attractor from which it is projected (the branched manifold is hyperbolic and the strange attractor is generally not), the topological entropy of the branched manifold serves as an upper bound for the topological entropy of the parent strange attractor. The topological entropy of a branched manifold is easily computed from the transition matrix. Specifically, it is the logarithm of the largest eigenvalue [34]. The transition matrices, their eigenvalue spectra, and the topological entropy for the two branched manifold representations of Lorenz dynamics shown in Fig. 2.7(b) and 2.7(c) are

Symbols	Transition matrix	Eigenvalue spectrum	h_T
L R	$\begin{bmatrix} 1 & 1 \\ 1 & 1 \end{bmatrix}$	2, 0	$\log 2$
$0_l\ 1_l\ 0_r\ 1_r$	$\begin{bmatrix} 1 & 1 & 0 & 0 \\ 0 & 0 & 1 & 1 \\ 0 & 0 & 1 & 1 \\ 1 & 1 & 0 & 0 \end{bmatrix}$	2, 0, 0, 0	$\log 2$

It is a general result that the topological entropy of the branched manifold describing a strange attractor is independent of the choice of the number of branches and the symbol assignments.

2.9 RETURN MAPS

Poincaré introduced an ingenious method for simplifying the analysis of low dimensional flows [100]. He introduced a "surface of section," now universally called a Poincaré section. The section is constructed in such a way that the flow always intersects the surface transversally from the same side. An initial condition on the surface is mapped back to the surface under the flow. Study of the flow is simplified by studying the first-return map of the surface of section back to itself.

There is always a problem of determining when, where, and how a Poincaré section can be constructed. For flows that are embedded in a toroidal phase space $\mathbb{R}^2 \times S^1$ Poincaré sections can be chosen as planes of constant phase angle $\varphi \in S^1$, $0 \leq \varphi < 2\pi$.

For three-dimensional flows that generate strange attractors there is a concise answer to these questions. The strange attractor is projected down to a branched manifold. The Poincaré section for the branched manifold is the union of the branch lines. It is a disconnected set if there are two or more branch lines. For the original flow the Poincaré section is the inverse image of the branched manifold's Poincaré section. Specifically it consists of the set of all points that project to the branch lines of the branched manifold under the Birman-Williams projection (2.10).

For Lorenz dynamics the branched manifold shown in Fig. 2.7(a) has a single branch line while the representations of the dynamics shown in Fig. 2.7(b) and (c) has two branch lines. In the first case, the Poincaré section has one component. The intersection of the strange attractor with this surface is in fact disconnected. In

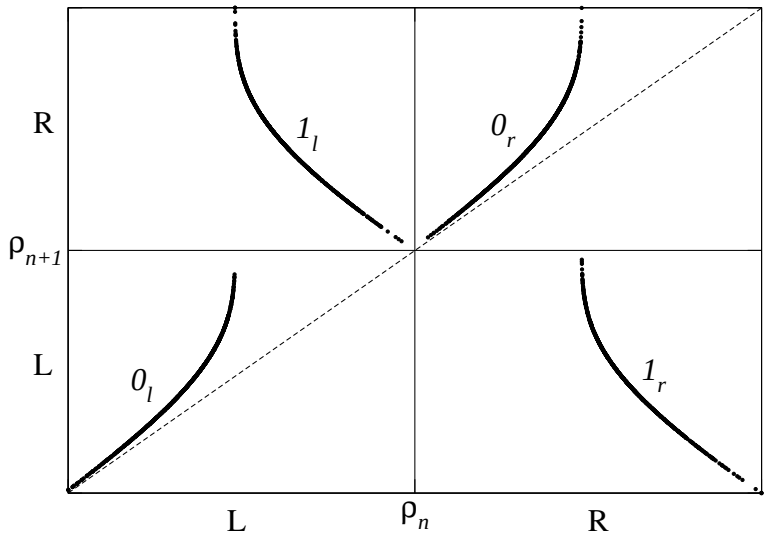

Fig. 2.9 First-return map to the Poincaré section for the Lorenz system. The dynamics is represented by the branched manifold shown in Fig. 2.7(b) or (c).

the second and third cases the Poincaré section is the union of two disconnected components.

Once the Poincaré section has been constructed, the return map can be constructed. We illustrate for the Lorenz flow as described by the branched manifold shown in Fig. 2.7(c). There are two symmetry-related branch lines. These are labeled L and R. The return map on these branch lines is shown in Fig. 2.9. Distances along the branch lines are measured from inside to outside. This figure merely shows the obvious. Initial conditions along L near the inside map back to L, those farther than halfway along L map to R in an orientation-reversing way. Similarly for R. Each component of this first return map can be identified with one of the four symbols 0_l 1_l 0_r 1_r, as shown in this figure.

Closed orbits of period 2, 3, 4, ..., p are determined by constructing the second, third, fourth, ..., pth return maps from the first return map, and identifying the intersection of these return maps with the diagonal. As an example, in Fig. 2.10 we show the third-return map constructed from Fig. 2.9. The six intersections with the diagonal indicate the intersection of the two period-three orbits LLR and RRL with the branch lines L and R.

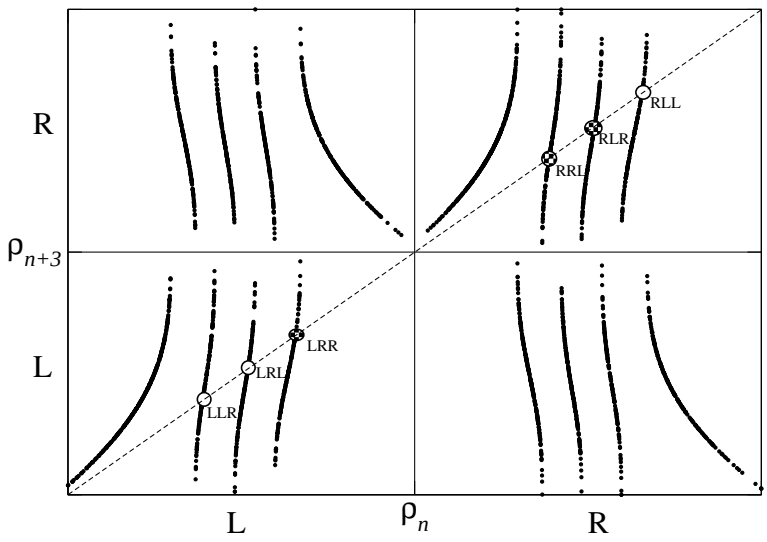

Fig. 2.10 Third-return map to the Poincaré section for the Lorenz system.

3

Image Dynamical Systems

3.1 DIFFEOMORPHISMS: GLOBAL AND LOCAL

Dynamical systems can be studied in any coordinate system. If $x_1, x_2, x_3, \ldots, x_n$ is one coordinate system in $\mathbb{R}^n$ and $u_1, u_2, u_3, \ldots, u_n$ is another, related to the first by transformations

$$\begin{aligned} u_1 &= u_1(x_1, x_2, x_3, \ldots, x_n) \\ \vdots \quad &\vdots \quad \vdots \\ u_n &= u_n(x_1, x_2, x_3, \ldots, x_n), \end{aligned}$$

the dynamical equations of motion in the ***x***-coordinate system

$$\frac{dx_j}{dt} = F_j(\boldsymbol{x})$$

can easily be expressed in the $\boldsymbol{u}$-coordinate system by elementary calculus (chain rule)

$$\frac{du_i}{dt} = \frac{\partial u_i}{\partial x_j}\,\frac{dx_j}{dt} = \frac{\partial u_i}{\partial x_j} F_j(\boldsymbol{x}) = g_i(\boldsymbol{u}) \tag{3.1}$$

As long as the Jacobian of the transformation is nonsingular *everywhere* ($\det\left(\frac{\partial u_i}{\partial x_j}\right) \neq 0$) this transformation can be inverted everywhere

$$\frac{dx_j}{dt} = \frac{\partial x_j}{\partial u_i}\, g_i(\boldsymbol{u}) = \left(\frac{\partial u}{\partial x}\right)^{-1}_{ji} g_i(\boldsymbol{u}) = F_j(\boldsymbol{x})$$

The two dynamical systems are equivalent. If $\det\left(\frac{\partial u_i}{\partial x_j}\right) > 0$ the two are topologically equivalent; if $\det\left(\frac{\partial u_i}{\partial x_j}\right) < 0$ they are topological images of each other—that is, one is"left-handed," the other "right handed" (in R^3 the quotations can be removed).

The principle reason for introducing a nonsingular change of variables is to simplify analysis. As an example, in Fig. 3.1(a) we show a phase space projection of laser data on the I-N plane or u-w plane, where I (u) is the observed laser intensity and $N(z)$ is the population inversion. There are long stretches of time during which the laser intensity is close to zero. The topological organization of data segments with low intensity is difficult to discern in this projection. Topological organization is simpler to discern when data along the I-axis are stretched out. A simple smooth stretch is provided by a logarithmic transformation

$$(x, y) = (I, N) \rightarrow (u, v) = (\log(I), N).$$

In this coordinate system topological analyses are simpler to carry out than in the original coordinate system. However, the data are compressed in a positive direction. An even better smooth transformation is $(I, N) \mapsto (I + \log(I), N)$. The transformation from (I, N) to $(I + \log(I), N)$ is shown in Fig. 3.1(b).

A smooth everywhere nonsingular invertible transformation (3.1) is called a global diffeomorphism. Since the dynamical systems $\dot{x}_j = F_j(\boldsymbol{x})$ and $\dot{u}_i = g_i(\boldsymbol{u})$ are equivalent (up to handedness) global diffeomorphisms are not adequate for relating a dynamical system with symmetry to a closely related system (image system) without symmetry.

Dynamical systems with symmetry can be mapped to closely related systems without symmetry by introducing transformations that are diffeomorphisms *almost* everywhere. For such mappings the Jacobian of the transformation is nonsingular *almost* everywhere. It vanishes on a set of measure zero.

In this chapter and the next we introduce the relation between equivariant dynamical systems and their images, invariant dynamical systems. The coordinates for the equivariant dynamical system are capitalized, those for the invariant dynamical system are in lowercase letters. In these two chapters we concentrate on three dimensional dynamical systems, so the coordinates are

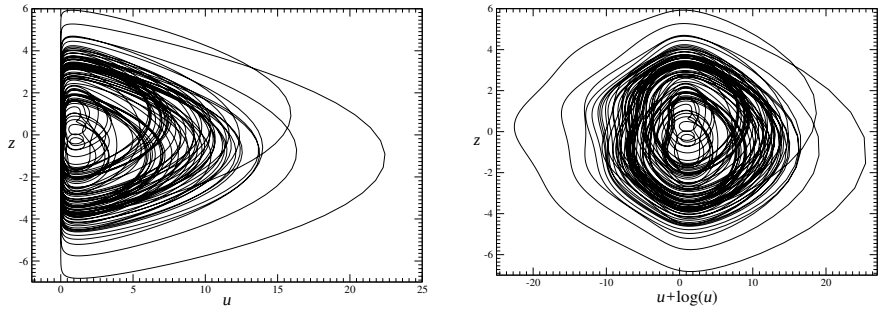

(a) u-z plane

(b) $(u + \log u)$-z plane

Fig. 3.1 $\dot{u} = [z - A\cos(\Omega t)]u$, $\dot{z} = (1 - \epsilon_1 z) - (1 + \epsilon_2 z)u$ with $\epsilon_1 = 0.03$, $\epsilon_2 = 0.009$, $\Omega = 1.5$ and $A = 1.06$. The initial conditions are $u_0 = 1.0$ and $z_0 = 4.2$. (a) Plot in the u-z plane. (b) Plot in the $u + \log(u)$-z plane.

Equivariant coordinates	Invariant coordinates
(X_1, X_2, X_3)	(u_1, u_2, u_3)
or	or
(X, Y, Z)	(u, v, w)

The relation between the equivariant and image invariant dynamical systems is in general

$$\frac{dX_j}{dt} = F_j(\boldsymbol{X}) \qquad \frac{du_i}{dt} = g_i(\boldsymbol{u})$$

$$\frac{du_i}{dt} = \frac{\partial u_i}{\partial X_j} F_j(\boldsymbol{X}) \qquad \frac{dX_j}{dt} = \left(\frac{\partial u_i}{\partial X_j}\right)^{-1} g_i(\boldsymbol{u})$$

If γ is an element of the symmetry group, not the identity, then

$$\gamma(X_1, X_2, X_3) \neq (X_1, X_2, X_3)$$
$$\gamma(u_1, u_2, u_3) = (u_1, u_2, u_3)$$

In short, the coordinates (u_1, u_2, u_3) are invariant coordinates.

We will spend the rest of this chapter learning how to construct invariant coordinates $\boldsymbol{u}$ from equivariant coordinates $\boldsymbol{X}$ and the equivariance group $\mathcal{G}$. This information will then be used to construct image equations from equivariant coordinates, and to relate the properties of the solutions of the image equations to the properties of the solutions of the equivariant equations. In particular, we consider relations between

- fixed points
- periodic orbits
- branched manifolds
- symbolic dynamics
- topological entropy
- Poincaré sections

3.2 2 → 1 LOCAL DIFFEOMORPHISMS

In this section we introduce the $2 \rightarrow 1$ local diffeomorphisms used to construct image dynamical systems from equivariant dynamical systems where the symmetry group $\mathcal{G}$ is of order 2. This is done carefully for the rotation group $\mathcal{R}_Z(\pi)$, more quickly for the inversion group $\mathcal{P}$ and the reflection group σ_Z.

We can divide the elementary polynomials $X^a Y^b Z^c$ ($a \geq 0$, $b \geq 0$, $c \geq 0$) into two sets: one that is invariant under $\mathcal{R}_Z(\pi)$ and the rest. Up to degree 2, this decomposition is

	Invariant under $\mathcal{R}_Z(\pi)$	Not invariant under $\mathcal{R}_Z(\pi)$
degree 1	Z	X, Y
degree 2	Z^2, X^2, XY, Y^2	ZX, ZY

We truncate this decomposition at degree 2 because the group $\mathcal{R}_Z(\pi)$ has order 2 (two operations). There is a theorem to the effect that this is sufficient (Noether's theorem, cf. Part II) for constructing all invariant and covariant (noninvariant) polynomials.

These nine polynomials are all *linearly* independent. However, they are not all *functionally* independent. For example, the second-degree polynomial Z^2 is the square of the first-degree polynomial. More interesting is the relation among the three other quadratic invariants. Only two are functionally independent, for

$$(X^2)(Y^2) - (XY)^2 = 0$$

Every invariant polynomial of any degree can be expressed as a function of the four invariants Z, X^2, XY, Y^2, of which only three are functionally independent. We can write for $\gamma \in \mathcal{R}_Z(\pi)$

$$\gamma F(X, Y, Z) = F(X, Y, Z) \Rightarrow F(X, Y, Z) = g(Z, X^2, XY, Y^2)$$

An *arbitrary* polynomial in (X, Y, Z) can be expressed in terms of invariant polynomials and the basic noninvariant functions X, Y in the following way

$$F(X, Y, Z) = g_X(Z, X^2, XY, Y^2)X + g_Y(Z, X^2, XY, Y^2)Y + g_1(Z, X^2, XY, Y^2)1$$

An invariant coordinate system can be constructed from the invariant polynomials of lowest degree. We choose $Z = u_3 = w$ as one of the invariant coordinates. The other pair can be chosen as suitable linear combinations of the three quadratic invariants involving X and Y. We choose

$$\begin{aligned} u_1 &= X^2 - Y^2 \\ u_2 &= 2XY \\ u_3 &= Z \end{aligned} \tag{3.2}$$

The Jacobian of this transformation is

$$\frac{\partial u_i}{\partial X_j} = \begin{bmatrix} 2X & -2Y & 0 \\ 2Y & 2X & 0 \\ 0 & 0 & 1 \end{bmatrix} \xrightarrow{\det} 4(X^2 + Y^2)$$

The Jacobian is singular on the Z-axis. The Z-axis is the singular set of the symmetry group $\mathcal{R}_Z(\pi)$ as well as of the local diffeomorphism (3.2).

Remark 1: The singular set of the group action is the set of fixed points—in the present case this is the Z axis. The singular set of the diffeomorphism is the set of points on which the Jacobian vanishes. It is not always true that the singular set of the group action and of its local diffeomorphism coincide.

Remark 2: The Jacobian of the inverse transformation $X = X(\boldsymbol{u})$, $\frac{\partial X_j}{\partial u_i}$, can be computed in two ways:

1. Compute the inverse of $\frac{\partial u_i}{\partial X_j}$: $\left[\frac{\partial u_i}{\partial X_j}\right]^{-1}$.
2. Solve for the X_j as a function of the u_i and compute the derivative: $\frac{\partial X_j(\boldsymbol{u})}{\partial u_i}$.

The second method is generally far harder than the first.

Similar results hold for the inversion and reflection groups. Both are also of order two, so analysis of polynomials to degree 2 is sufficient.

For $\mathcal{P}$ the invariant and covariant polynomials are

	Invariant under $\mathcal{P}$	Not invariant under $\mathcal{P}$
degree 1		X, Y, Z
degree 2	$X^2, XY, XZ, Y^2, YZ, Z^2$	

Three relations exist among the six invariant quadratic polynomials:

$$\begin{aligned}(X^2)(Y^2) - (XY)^2 &= 0\\ (Y^2)(Z^2) - (YZ)^2 &= 0\\ (Z^2)(X^2) - (ZX)^2 &= 0\end{aligned}$$

Invariant polynomials of any degree can expressed in terms of the six invariant degree-2 polynomials

$$\gamma F(X,Y,Z) = F(X,Y,Z) \Rightarrow F(X,Y,Z) = g(X^2, Y^2, Z^2, XY, YZ, ZX)$$

The most general polynomial is

$$\begin{aligned}F(X,Y,Z) &= \textstyle\sum_{i=1}^{3} g_{X_i}(X^2, Y^2, Z^2, XY, YZ, ZX)X_i\\ &\quad + g_1(X^2, Y^2, Z^2, XY, YZ, ZX)1\end{aligned}$$

Three invariant coordinates (u_1, u_2, u_3) can be chosen as linear combinations of the six invariant polynomials. We always attempt to find a choice that covers the entire space $\mathbb{R}^3(\boldsymbol{u})$. That is, given any values of the invariant coordinates (u_1, u_2, u_3) we can always find two real preimages (X_1, X_2, X_3) or one doubly degenerate preimage. A useful choice of coordinates is

$$\begin{aligned}u_1 &= X^2 - Y^2\\ u_2 &= 2XY\\ u_3 &= (X - Y)Z\end{aligned}$$

The Jacobian of this local diffeomorphism is

$$\frac{\partial u_i}{\partial X_j} = \begin{bmatrix} 2X & -2Y & 0 \\ 2Y & 2X & 0 \\ Z & -Z & X-Y \end{bmatrix} \xrightarrow{\det} 4(X^2+Y^2)(X-Y)$$

The singular set of the group $\mathcal{P}$ is the origin (0,0,0) while the singular set of this transformation is the union of the Z-axis $X^2+Y^2=0$ with the plane $X-Y=0$.

For the reflection group σ_Z the invariant and covariant polynomials are

	Invariant under σ_Z	Not invariant under σ_Z
degree 1	X, Y	Z
degree 2	X^2, XY, Y^2, Z^2	XZ, YZ

Invariant polynomials are functions of the three lowest degree invariants X, Y, and Z^2

$$\gamma F(X,Y,Z) = F(X,Y,Z) \Rightarrow F(X,Y,Z) = g(X,Y,Z^2)$$

There are no relations between the three invariant polynomials X, Y, and Z^2. An arbitrary function can be written

$$F(X,Y,Z) = g_Z(X,Y,Z^2)Z + g_1(X,Y,Z^2)\cdot 1$$

A simple coordinate transformation is

$$\begin{aligned} u_1 &= X \\ u_2 &= Y \\ u_3 &= Z^2 \end{aligned}$$

The Jacobian of this transformation is

$$\frac{\partial u_i}{\partial X_j} = \begin{bmatrix} 1 & 0 & 0 \\ 0 & 1 & 0 \\ 0 & 0 & 2Z \end{bmatrix} \xrightarrow{\det} 2Z$$

In this case the singular sets of the group and the diffeomorphism are equal.

3.3 IMAGE EQUATIONS

Invariant equations or image equations are simple to construct from the equivariant equations once the local diffeomorphism has been constructed. We illustrate this procedure with some care for the Lorenz equations before briefly presenting the results for several other equivariant dynamical systems.

3.3.1 Lorenz Equations: $\mathcal{R}_Z(\pi)$

Under the local diffeormorphism (3.2) the dynamical system equations are

$$\begin{aligned}
\frac{d}{dt}\begin{bmatrix} u \\ v \\ w \end{bmatrix} &= \frac{d}{dt}\begin{bmatrix} X^2 - Y^2 \\ 2XY \\ Z \end{bmatrix} = \begin{bmatrix} 2X & -2Y & 0 \\ 2Y & 2X & 0 \\ 0 & 0 & 1 \end{bmatrix}\begin{bmatrix} \dot{X} \\ \dot{Y} \\ \dot{Z} \end{bmatrix} \\
&= \begin{bmatrix} 2X & -2Y & 0 \\ 2Y & 2X & 0 \\ 0 & 0 & 1 \end{bmatrix}\begin{bmatrix} -\sigma X + \sigma Y \\ RX - Y - XZ \\ -bZ + XY \end{bmatrix} \\
&= \begin{bmatrix} -(\sigma+1)u + (\sigma - R)v + vw + (1-\sigma)\rho \\ (R-\sigma)u - (\sigma+1)v - uw + (R+\sigma)\rho - \rho w \\ -bw + \frac{1}{2}v \end{bmatrix}
\end{aligned} \tag{3.3}$$

These equations have been expressed in terms of the three variables u, v, and w as well as the one *linear* combination of the original invariants X^2, XY, and Y^2 that does not occur among the basic invariant coordinates:

$$\rho = X^2 + Y^2 = \sqrt{u^2 + v^2}$$

Remark: We emphasize here that the "extra coordinate" that appears in the invariant equations is *linear* in the original invariants. Because of the relations that exist among $u_1 = X^2 - Y^2$, $u_2 = 2XY$, and $\rho = (X^2 + Y^2)$, this last coordinate can be expressed as a *radical* function of the invariant coordinates ($\rho = \sqrt{u^2 + v^2}$). This observation generalizes widely.

In Fig. 3.2, we show an X-Z projection of the Lorenz strange attractor and a v-w projection of the image attractor. Below each we provide a description of the dynamics by a branched manifold. The image branched manifold is that for a Smale horseshoe stretch and fold mechanism, as exhibited by the Rössler equations, for example.

3.3.2 Burke and Shaw Equations: $\mathcal{R}_Z(\pi)$

The Burke and Shaw equations (2.5) can be treated identically:

$$\begin{aligned}
\frac{d}{dt}\begin{bmatrix} u \\ v \\ w \end{bmatrix} &= \begin{bmatrix} 2X & -2Y & 0 \\ 2Y & 2X & 0 \\ 0 & 0 & 1 \end{bmatrix}\begin{bmatrix} -SX - SY \\ -Y - SXZ \\ SXY + \mathcal{V} \end{bmatrix} \\
&= \begin{bmatrix} -(S+1)u - S(1-w)v + (1-S)\rho \\ S\,(1-w)\,u - (S+1)v - S\,(1+w)\,\rho \\ \frac{S}{2}v + \mathcal{V} \end{bmatrix}
\end{aligned} \tag{3.4}$$

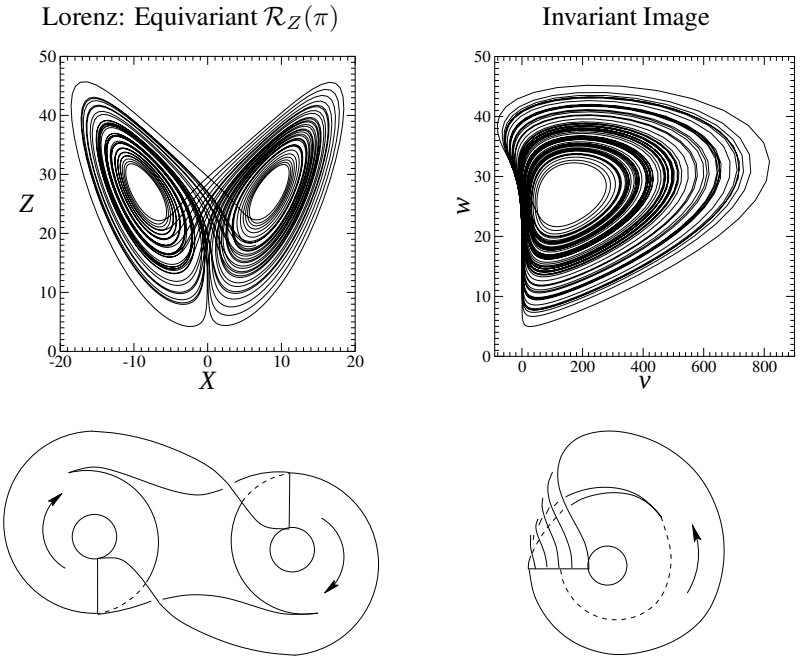

Fig. 3.2 Top: Strange attractors generated by $\mathcal{R}_Z(\pi)$ equivariant Lorenz equations (1.2) and invariant image equations (3.3). Parameter values: $R = 28.0$; $\sigma = 10.0$; $b = 8/3$. Bottom: Branched manifolds for these two strange attractors.

The flow generated by the Burke and Shaw equations (2.5) and the image equations (3.4) are shown in Fig. 3.3. The branched manifolds for the two strange attractors are shown below the two attractors. The image branched manifold describes a single stretch and fold mechanism, but with an additional half twist. This describes a reverse horseshoe.

3.3.3 General Case: $\mathcal{R}_Z(\pi)$

The most general dynamical system equivariant under $\mathcal{R}_Z(\pi)$ in $\mathbb{R}^3$ has the structure

$$\frac{d}{dt}\begin{bmatrix} X \\ Y \\ Z \end{bmatrix} = \begin{bmatrix} g_{XX} & g_{XY} & 0 \\ g_{YX} & g_{YY} & 0 \\ 0 & 0 & g_{ZZ} \end{bmatrix} \begin{bmatrix} X \\ Y \\ 1 \end{bmatrix}$$

In this expression the invariant functions g can be expressed as a function of the three invariant coordinates $\boldsymbol{u} = (u_1, u_2, u_3) = (u, v, w)$ and the radical $\rho = \sqrt{u^2 + v^2}$.

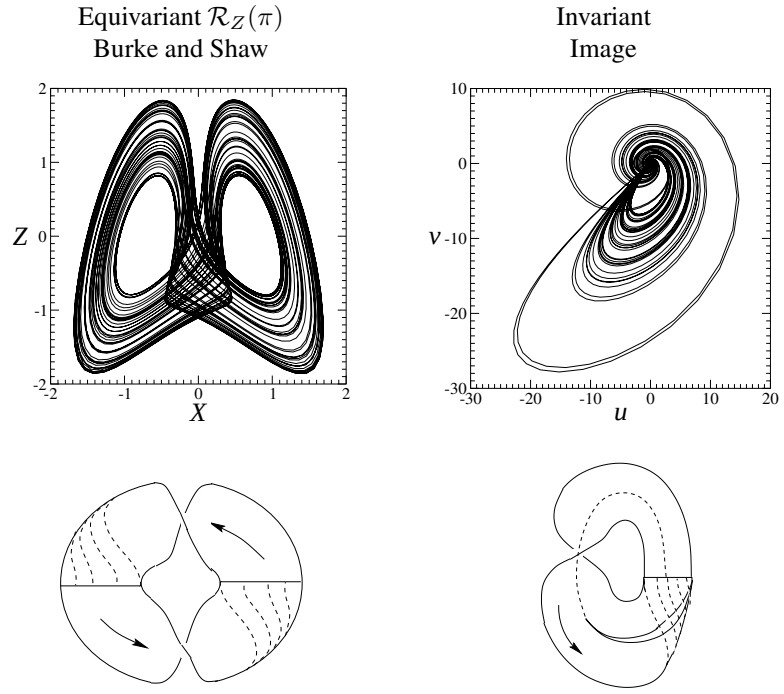

Fig. 3.3 Top: Strange attractors generated by $\mathcal{R}_Z(\pi)$ equivariant Burke and Shaw equations (2.5) and invariant image equations (3.4). Parameter values: $V = 4.271$; $S = 10.0$. Bottom: Branched manifolds for these two strange attractors.

The invariant equations are

$$\frac{d}{dt}\begin{bmatrix} u \\ v \\ w \end{bmatrix} = \frac{d}{dt}\begin{bmatrix} X^2 - Y^2 \\ 2XY \\ Z \end{bmatrix} = \begin{bmatrix} 2X & -2Y & 0 \\ 2Y & 2X & 0 \\ 0 & 0 & 1 \end{bmatrix}\begin{bmatrix} g_{XX}X + g_{XY}Y \\ g_{YX}X + g_{YY}Y \\ g_{ZZ} \end{bmatrix}$$

$$= \begin{bmatrix} +g_{XX} + g_{YY} & g_{XY} - g_{YX} & 0 & +g_{XX} - g_{YY} & 0 \\ -g_{XY} + g_{YX} & g_{XX} + g_{YY} & 0 & +g_{XY} + g_{YX} & 0 \\ 0 & 0 & 0 & 0 & g_{ZZ} \end{bmatrix}\begin{bmatrix} u \\ v \\ w \\ \rho_1 \\ 1 \end{bmatrix}$$

3.3.4 General Case: $\mathcal{P}$

Two dynamical systems that we have introduced so far that have inversion symmetry are the induced Lorenz system (2.8) and the Kremliovsky equations (2.7). The image equations of both systems are a mess to compute without some guidance. We provide

that here by giving a general formulation for the image equations of an inversion equivariant dynamical system.

The three invariant coordinates and the three radicals are

Invariant coordinates	Radicals (X)	Radicals (u)
$u_1 = X^2 - Y^2$	$\rho_1 = X^2 + Y^2$	$= \sqrt{u_1^2 + u_2^2}$
$u_2 = 2XY$	$\rho_2 = Z^2$	$= \frac{u_3^2}{u_1^2}\left(\sqrt{u_1^2 + u_2^2} + u_2\right)$
$u_3 = (X - Y)Z$	$\rho_3 = (X + Y)Z$	$= \frac{u_3}{u_1}\left(\sqrt{u_1^2 + u_2^2} + u_2\right)$

The equivariant equations are

$$\frac{d}{dt}\begin{bmatrix} X \\ Y \\ Z \end{bmatrix} = \begin{bmatrix} g_{XX} & g_{XY} & g_{XZ} \\ g_{YX} & g_{YY} & g_{YZ} \\ g_{ZX} & g_{ZY} & g_{ZZ} \end{bmatrix}\begin{bmatrix} X \\ Y \\ Z \end{bmatrix}$$

The image equations are

$$\frac{d}{dt}\begin{bmatrix} u \\ v \\ w \end{bmatrix} = \begin{bmatrix} 2X & -2Y & 0 \\ 2Y & 2X & 0 \\ Z & -Z & X - Y \end{bmatrix}\begin{bmatrix} g_{XX} & g_{XY} & g_{XZ} \\ g_{YX} & g_{YY} & g_{YZ} \\ g_{ZX} & g_{ZY} & g_{ZZ} \end{bmatrix}\begin{bmatrix} X \\ Y \\ Z \end{bmatrix}$$

After some extensive computations, these reduce to

$$\frac{d}{dt}\begin{bmatrix} u \\ v \\ w \end{bmatrix} = \begin{bmatrix} 2g_{11} & -2g_{22} & 0 & 2g_{12} - 2g_{21} & 2g_{13} & -2g_{23} \\ 2g_{21} & +2g_{12} & 0 & 2g_{11} + 2g_{22} & 2g_{23} & +2g_{13} \\ & & & & +g_{11} & +g_{12} \\ g_{31} & -g_{32} & g_{13} - g_{23} & +g_{32} - g_{31} & -g_{21} & -g_{22} \\ & & & & +g_{33} & -g_{33} \end{bmatrix}\begin{bmatrix} X^2 \\ Y^2 \\ Z^2 \\ XY \\ XZ \\ YZ \end{bmatrix}$$

The mapping is completed by the transformation

$$2\begin{bmatrix} X^2 \\ Y^2 \\ Z^2 \\ XY \\ XZ \\ YZ \end{bmatrix} = \begin{bmatrix} 1 & 0 & 0 & 1 & 0 & 0 \\ -1 & 0 & 0 & 1 & 0 & 0 \\ 0 & 0 & 0 & 0 & 2 & 0 \\ 0 & 1 & 0 & 0 & 0 & 0 \\ 0 & 0 & 1 & 0 & 0 & 1 \\ 0 & 0 & -1 & 0 & 0 & 1 \end{bmatrix}\begin{bmatrix} u \\ v \\ w \\ \rho_1 \\ \rho_2 \\ \rho_3 \end{bmatrix}$$

The image of the Kremliovsky equations is

$$\frac{d}{dt}\begin{bmatrix} u \\ v \\ w \end{bmatrix} = \begin{bmatrix} au - 2v - w - a\rho_1 - \rho_3 \\ 2u + av + w - \rho_3 \\ \frac{1}{2}b(\rho_1 + u) - \frac{1}{2}bv + w\left[\frac{1}{2}(\rho_1 + u) - c\right] \end{bmatrix} \tag{3.5}$$

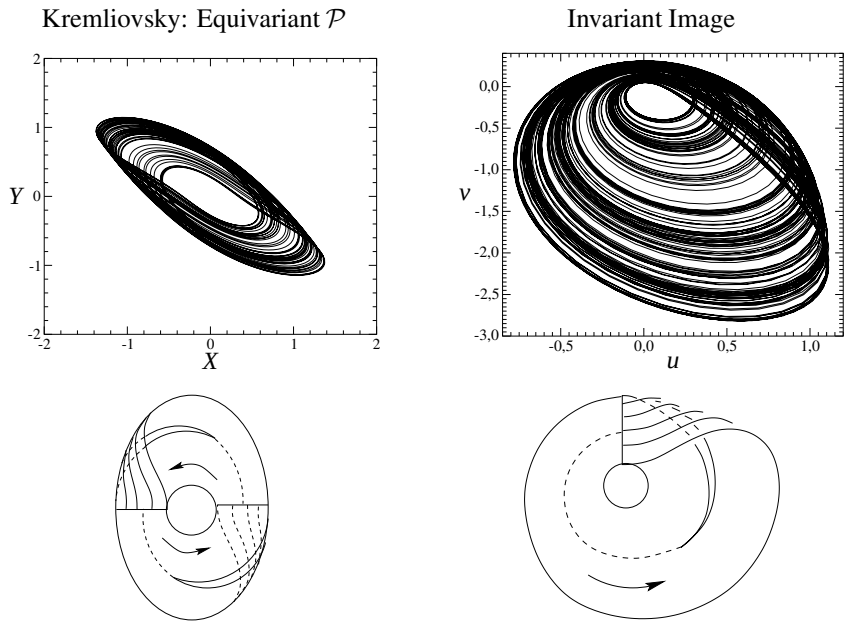

Fig. 3.4 Top: Strange attractors generated by $\mathcal{P}$ equivariant Kremliovsky equations (2.7) and invariant image equations. Parameter values: $a = 0.911$; $b = 0.9547623431$; $c = 2.192954632$. Bottom: Branched manifolds for these two strange attractors.

The strange attractors generated by the Kremliovsky equations (2.7) and the image equations (3.5) are projected onto the X-Y and u-v planes, respectively, in Fig. 3.4. Below each strange attractor is the branched manifold that describes the dynamics.

A similar computation has been carried out for the induced Lorenz equations (2.8). The equivariant attractor is projected onto the X-Y (X-$\dot{X}$) plane and the image attractor is projected onto the u-v plane in Fig. 3.5. Below each strange attractor we show the branched manifold that describes the flow.

3.3.5 General Case: σ_Z

For completeness we treat dynamical systems equivariant under the reflection group σ_Z. Strange attractors generated by such dynamical systems cannot be connected: they consist of an attractor and its disconnected mirror image.

The equivariant equations are

$$\frac{d}{dt}\begin{bmatrix} X \\ Y \\ Z \end{bmatrix} = \begin{bmatrix} 0 & g_{X1} \\ 0 & g_{Y1} \\ g_{ZZ} & 0 \end{bmatrix} \begin{bmatrix} Z \\ 1 \end{bmatrix}$$

The invariant functions g are functions of the three invariant monomials X, Y, and Z^2 that are functionally independent. Under the $2 \to 1$ local diffeomorphism $(u, v, w) =$

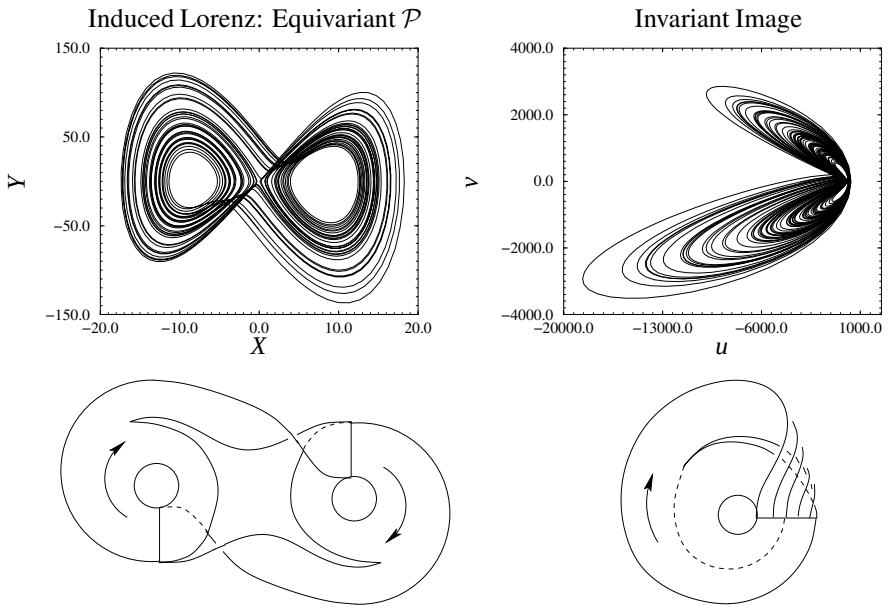

Fig. 3.5 Top: Strange attractors generated by $\mathcal{P}$ equivariant induced Lorenz equations (2.8) and invariant image equations. Parameter values: $R = 28.0$; $\sigma = 10.0$; $b = 8/3$. Bottom: Branched manifolds for these two strange attractors.

(X, Y, Z^2) the image equations are

$$\frac{d}{dt}\begin{bmatrix} u \\ v \\ w \end{bmatrix} = \begin{bmatrix} 1 & 0 & 0 \\ 0 & 1 & 0 \\ 0 & 0 & 2Z \end{bmatrix} \begin{bmatrix} 0 & g_{X1} \\ 0 & g_{Y1} \\ g_{ZZ} & 0 \end{bmatrix} \begin{bmatrix} Z \\ 1 \end{bmatrix} = \begin{bmatrix} g_{X1} \\ g_{Y1} \\ 2Z^2 g_{ZZ} \end{bmatrix}$$

A double cover of a Smale horseshoe template with reflection symmetry is shown in Fig. 3.6. Since the reflection plane is an invariant plane, it cannot intersect the chaotic attractor or its branched manifold. As a consequence, the double cover consists of two disconnected components. One of the components is a rescaled version ($Z = \sqrt{w}$) of the original attractor. The other component is its mirror image in the $Z = 0$ plane.

3.4 FIXED POINT DISTRIBUTIONS

Fixed points of equivariant dynamical systems map to fixed points of their image systems. For symmetry groups of order two, two cases arise.

1. If $\boldsymbol{X}_0$ is a fixed point and its image $\gamma\boldsymbol{X}_0$ under the symmetry is different, $\gamma\boldsymbol{X}_0 \neq \boldsymbol{X}_0$, both $\boldsymbol{X}_0$ and $\gamma\boldsymbol{X}_0$ map to the same fixed point in the image dynamics.
2. If $\boldsymbol{X}_0$ is in the set left invariant by the symmetry group, $\gamma\boldsymbol{X}_0 = \boldsymbol{X}_0$, the fixed point in the image dynamics has only one corresponding fixed point in the covering dynamics.

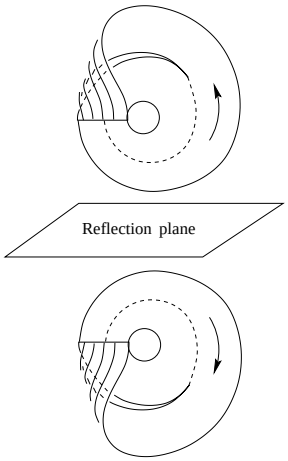

Fig. 3.6 Template representation of the cover of a Smale horseshoe with reflection symmetry.

For the three order-two symmetry groups in $\mathbb{R}^3$ the fixed point sets are

Group		Fixed Points		Dimension
Reflection	σ_Z	$(X, Y, 0)$	X-Y plane	2
Rotation	$\mathcal{R}_Z(\pi)$	$(0, 0, Z)$	Z-axis	1
Inversion	$\mathcal{P}$	(0,0,0)	Origin	0

For the reflection group σ_Z a fixed point in the X-Y plane $Z = 0$ will map into the image plane $w = 0$. However, since the $Z = 0$ plane is invariant under σ_Z, the dynamics in the plane is confined to the plane. As a result chaotic behavior in this invariant set is not possible. The mapping of the $Z = 0$ plane to the $w = 0$ plane is one-to-one. If there is a fixed point at (X_0, Y_0, Z_0) $(Z_0 \neq 0)$ off the $Z = 0$ plane, there is another at $(X_0, Y_0, -Z_0)$. The two fixed points map to the same fixed point $(u_0 = X_0, v_0 = Y_0, w_0 = Z_0^2)$.

For the rotation group $\mathcal{R}_Z(\pi)$, fixed points on the Z-axis map to fixed points on the w axis. Each fixed point on the w-axis has a single inverse image (preimage), since the mapping from the Z-axis to the w-axis is one-to-one. Each fixed point off the Z axis has a different image under $\mathcal{R}_Z(\pi)$: (X_0, Y_0, Z_0) and $\gamma(X_0, Y_0, Z_0) = (-X_0, -Y_0, Z_0)$. The two fixed points map to a single image fixed point off the w-axis.

The Lorenz dynamical system has three fixed points. One (the origin) lies on the Z-axis. This symmetric fixed point maps to a fixed point on the w-axis (the origin). The other pair of fixed points maps to a single fixed point off the $w = 0$ axis. The symmetric pair of asymmetric *real* fixed points map into the v-w plane $u = 0$. In fact, the imaginary fixed point pair maps into the same plane. The pitchfork bifurcation maps to a transverse bifurcation under this $2 \rightarrow 1$ local diffeomorphism. This is illustrated in Fig. 3.7.

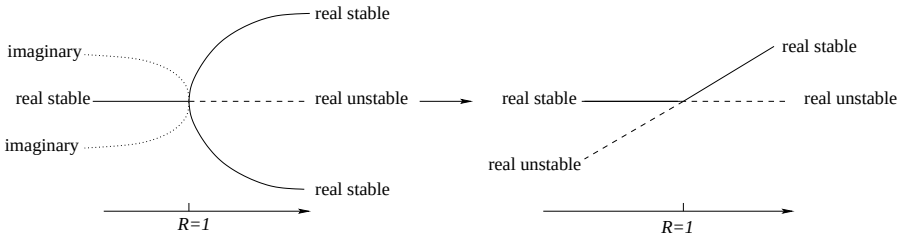

Fig. 3.7 A pitchfork bifurcation in the cover dynamics becomes a transverse bifurcation in the image dynamics.

The inversion symmetry $\mathcal{P}$ fixes only the single point (0,0,0). The origin in the equivariant system maps to the origin in the image system. All the other points in the image system have two preimages in the covering system. If the covering system has $2n$ fixed points, the image system has n. If the covering system has $2n + 1$ fixed points, the image system has $n + 1$.

3.5 BRANCHED MANIFOLDS AND THEIR IMAGES

Strange attractors generated by equivariant dynamical systems are described by branched manifolds that are mapped into themselves by the symmetry group. For each order-2 symmetry group a branched manifold has an even number of branches.

We are particularly interested in equivariant branched manifolds that are connected. Those equivariant under σ_Z are not. For the other symmetry groups that we have studied there are more interesting possibilities.

Equivariant strange attractors and their branched manifolds have been shown in Figs. 3.2, 3.3, 3.4, and 3.5. A number of lessons can be drawn from these figures. First, the branches occur in pairs. In the figures (cf. Fig. 2.7), they have been labeled by the symbols L and R. More generally, they are labeled by the elements of the symmetry group. One branch is chosen and labeled by the group operation I. This is mapped to other branches by the remaining group operations. Each group operation maps the original branch to a different branch which is labeled by that group operation. This process is repeated until all branches have been labeled.

As an example, it is possible to use two symbols, L and R, to label the branched manifold of the Lorenz attractor (Fig. 3.2 and Fig. 2.7(b)). The branch L is the image of branch R under $\gamma \in \mathcal{R}_Z(\pi)$. Similarly, R is the image of L under the same group operation.

It is also possible to use four symbols 0_l, 1_l, 0_r, and 1_r to label this branched manifold, as shown in Fig. 2.7(c). The pair 0_l, 0_r is symmetry related, as is the second pair 1_l, 1_r.

The second labeling scheme is preferable when describing the relation between cover and image dynamical systems. The branched manifold of the image attractor has two branches that are labeled 0 and 1. These integers label the local torsion of the

period-one orbit in the branch. Local torsion is a measure of how much the flow twists in the neighborhood of a periodic orbit. It is measured in units of π. Local torsion 1 means that a point just to one side of a period 1 orbit returns, after one period, just to the other side of that orbit. Local torsion is easily seen from the twisting of the branches of the branched manifold.

For the Lorenz system the branches 0_l and 0_r map under the local diffeomorphism to the branch 0 in the image branched manifold. Similarly, the branches 1_l and 1_r map to 1. The transition matrix collapses as follows

$$\begin{array}{c|cccc} & 0_l & 0_r & 1_l & 1_r \\ \hline 0_l & 1 & 0 & 1 & 0 \\ 0_r & 0 & 1 & 0 & 1 \\ 1_l & 0 & 1 & 0 & 1 \\ 1_r & 1 & 0 & 1 & 0 \end{array} \quad \rightarrow \quad \begin{array}{c|cc} & 0 & 1 \\ \hline 0 & 1 & 1 \\ 1 & 1 & 1 \end{array} \tag{3.6}$$

In effect, the local diffeomorphism erases the group action information (l, r): $0_l, 0_r \rightarrow 0$ and $1_l, 1_r \rightarrow 1$.

These remarks hold for all the other cover-image branched manifold pairs related by $2 \rightarrow 1$ local diffeomorphisms, as shown in Figs. 3.2, 3.3, 3.4, and 3.5. If the image has n branches, labeled A, B, C, ... then its double cover has $2n$ branches labeled A_l, A_r; B_l, B_r; C_l, C_r; ... or A_I, A_γ; B_I, B_γ; C_I, C_γ; ...

The Burke and Shaw dynamical system has four branches that can preferably be labeled 1_l, 1_r, 2_l, 2_r (Fig. 3.3). Its image is a reverse Smale horseshoe with branches 1 and 2. The $2 \rightarrow 1$ local diffeomorphism produces the following collapse: $1_l, 1_r \rightarrow 1$ and $2_l, 2_r \rightarrow 2$. The transition matrix reduces as follows under the action of the local diffeomorphism

$$\begin{array}{c|cccc} & 1_l & 1_r & 2_l & 2_r \\ \hline 1_l & 0 & 1 & 0 & 1 \\ 1_r & 1 & 0 & 1 & 0 \\ 2_l & 0 & 1 & 0 & 1 \\ 2_r & 1 & 0 & 1 & 0 \end{array} \quad \rightarrow \quad \begin{array}{c|cc} & 1 & 2 \\ \hline 1 & 1 & 1 \\ 2 & 1 & 1 \end{array} \tag{3.7}$$

We should point out here, forcefully, that the Lorenz and the Burke and Shaw dynamical systems share the same symmetry group and more or less the same image. However, the two systems are not equivalent (even disregarding the difference in local torsion), as is indicated by their transition matrices. There is no smooth transformation that maps one into the other. This suggests that a given dynamical system without symmetry can be the image of more than one inequivalent equivariant dynamical system, each with the same symmetry group. It also suggests that somehow the two equivariant dynamical systems (the Lorenz and the Burke and Shaw) can be mapped into each other by some analog of "analytic continuation" which, for want of a better term, we christen "group continuation." Both inferences are correct and will be elaborated in Chapter 14.

3.6 SYMBOLIC DYNAMICS

Every trajectory in a strange attractor can be encoded by a symbol sequence. This is true for every trajectory on a branched manifold under a semiflow. The symbol sequence of a trajectory in a strange attractor is the same as the symbol sequence for the image of that trajectory under the Birman-Williams projection, in the attractor's branched manifold. The symbol sequence is exactly the itinerary of the trajectory through the labeled branches of the branched manifold.

There are several possible ways to label branches in a branched manifold. We have described two for the Lorenz attractor in Sections 2.5 and 3.5. For example, a piece of a trajectory labeled

$$\text{L R R L L L R R } \ldots$$

passes through the left-hand branch, then goes around the right hand branch twice followed by three cycles around the left hand branch, ... Comparing Fig. 2.7(b) and 2.7(c) it is easy to see that a cycle around L is equivalent to a cycle around 0_l or 1_l. If the following symbol is L, then the trajectory cycles through the branch 0_l. If the subsequent symbol is R the trajectory cycles through 1_l. The following identification is valid

$$\begin{array}{ll} \text{L L} \leftrightarrow 0_l & \text{R L} \leftrightarrow 1_r \\ \text{L R} \leftrightarrow 1_l & \text{R R} \leftrightarrow 0_r \end{array}$$

The two symbol sequences are equivalent

$$\begin{array}{cccccccc} \text{L} & \text{R} & \text{R} & \text{L} & \text{L} & \text{L} & \text{R} & \text{R} \ldots \\ 1_l & 0_r & 1_r & 0_l & 0_l & 1_l & 0_r & *_r \ldots \end{array}$$

where $* = (0, 1)$ cannot be assigned on the basis of the information present.

Both encoding methods are adequate to identify trajectories and periodic orbits in Lorenz dynamics. The latter coding procedure is vastly preferable in discussing the relation between equivariant dynamical systems and their image dynamical systems. The reason is that the coding symbols carry one piece of information about the symmetry group $\mathcal{G}$ (l, r or I, γ) and one piece of information about the image dynamical system (branch labels 0 and 1).

In discussing relations between equivariant dynamical systems and their images we will always use a coding procedure that carries information about the equivariance group $\mathcal{G}$ and the image dynamical system. In particular, the code labels for the Lorenz and the Burke and Shaw dynamical systems are 0_l, 1_l, 0_r, 1_r and 1_l, 2_l, 1_r, 2_r. The transition matrix for these two dynamical systems are the 4×4 matrices given in (3.6) and (3.7).

For the induced Lorenz system, equivariant under $\mathcal{P}$, the coding symbols remain 0_l, 1_l, 0_r, 1_r. This procedure is very general, and extends easily to arbitrary symmetry groups and image dynamical systems. This will be described in more detail in Chapter 6 and more generally in Chapter 13.

Remark: We call symbols that carry information about both the symmetry group and the image dynamical system a **symmetry-adapted symbolic dynamics**, or **dressed symbolic dynamics**.

3.7 PERIODIC ORBITS

Closed orbits of minimal period p in the equivariant system are mapped to closed orbits of period p or $p/2$ in the image system. We illustrate for orbits in the Lorenz dynamical system.

Period p	Symbolic Sequence L R	Symbolic Sequence $0_l\ 1_l\ 0_r\ 1_r$	Image
2	L R	$1_l\ 1_r$	$1\ 1 \rightarrow 1 \times 2$
3	L L R	$0_l\ 1_l\ 1_r$	0 1 1
3	R R L	$0_r\ 1_r\ 1_l$	0 1 1
4	L L R R	$0_l\ 1_l\ 0_r\ 1_r$	$0\ 1\ 0\ 1 \rightarrow 01 \times 2$
4	L L L R	$0_l\ 0_l\ 1_l\ 1_r$	0 0 1 1
4	R R R L	$0_r\ 0_r\ 1_r\ 1_l$	0 0 1 1

This table illustrates the general principle. Mapping to the image system simply removes the group indices (l, r) on the symmetry adapted symbols. A symmetric orbit of period $2p$ is mapped twice (indicated by $\times\ 2$) onto an image orbit of period p. A symmetric pair of asymmetric orbits of period p (e.g., $0_l\ 1_l\ 1_r$ and $0_r\ 1_r\ 1_l$; $0_l\ 0_l\ 1_l\ 1_r$ and $0_r\ 0_r\ 1_r\ 1_l$) are mapped to the same image orbit (e.g., 011; 0011). Symmetric pairs of asymmetric orbits are obtained by the exchange $l \leftrightarrow r$ on the symmetry adapted symbols. A symmetric orbit in the equivariant system has symbol sequence $S\bar{S}$, where S is a symbol sequence of minimal period p and $\bar{S}$ is obtained from S by switching symbols $l \leftrightarrow r$. The transition from the pth symbol S to the first symbol of γS must be allowed by the transition matrix.

These statements hold for all orbits in all order-two equivariant systems.

Remark: In many cases we have a spectrum of periodic orbits in the image dynamical system and would like to know their parentage—that is, what are their parents in the equivariant system.

The question is not difficult to answer when the cover satisfies Lorenz dynamics. If the image orbit of period p has an odd number of symbols 1, then the covering orbit has either

1. period p and an odd number of symbols 1, or
2. period $2p$ and an even number of symbols 1.

In the first case there is an odd number of symbols 1_l and 1_r. This means that an orbit segment that begins in the left-hand lobe winds up on the right-hand lobe after p periods. It cannot be closed. Therefore case 2 is the only possibility.

The result relating orbits in Lorenz-like branched manifold with orbits in the image branched manifold are as follows.

1. All nodes (odd number of symbols 1) of period p are images of one orbit of period $2p$. If the symbol name of the image is S, the symbol name of its cover is $S_*\bar{S}_*$. Here S_* is the "dressed" form of S. A group label (l or r) is affixed

to the first letter in S, and symbols are affixed to the remaining $p-1$ symbols in S according to the transition matrix. $\bar{S}_*$ is γS_*.

2. All regular saddles (even number of symbols 1) of period p are images of two symmetry-related orbits of period p in the cover. If S is the symbol name of the image orbit, the two cover orbits are S_* and $\gamma S_* = \bar{S}_*$.

Example: In the Smale horseshoe branched manifold the period-three saddle node pair is 011 and 001. The two orbits that cover the saddle are $0_l 1_l 1_r$ and $0_r 1_r 1_l$. The single orbit that covers the node is $0_l 0_l 1_l 0_r 0_r 1_r$.

Remark 1: The relation between orbits in the image and the cover is different for the Burke and Shaw attractor and its image. These relations will be explained in detail in Section 4.9.

Remark 2: The topological entropy of any system with Lorenz-like dynamics is the same as the topological entropy of its image. The number of orbits of period p in the Lorenz system grows like $N_L(p) \approx e^{ph_T(L)}$, while the growth rate in the image Smale horseshoe system grows like $N_S(p) \approx e^{ph_T(S)}$. In the latter, roughly half of the period-p orbits are saddles and half are nodes. As a result we estimate

$$\begin{aligned} N_L(p) &\approx 2 \times \frac{1}{2} N_S(p) + \frac{1}{2} N_S\left(\frac{1}{2}p\right) \\ e^{ph_T(L)} &\approx e^{ph_T(S)} + \frac{1}{2} e^{\frac{1}{2}ph_T(S)} \\ h_T(L) &= \lim_{p\to\infty} \frac{1}{p} \log e^{ph_T(S)} \left[1 + \frac{1}{2e^{\frac{1}{2}ph_T(S)}}\right] \\ &= h_T(S) \end{aligned}$$

The result is insensitive to the assumed 50-50 decomposition.

Remark 3: More generally the topological entropy of the image of an equivariant strange attractor is the same as the topological entropy of the equivariant strange attractor.

Remark 4: Periodic orbits are created and/or annihilated when control parameters are varied. In the highly dissipative limit (with negative Schwartzian derivative), they are created in a very specific order—the U Sequence order—in the transition from the "laminar" (nonchaotic) to the "hyperbolic" (fully chaotic) limit. By lifting the orbits from the image to the covering dynamical system we have a very specific algorithm for the order of orbit creation in equivariant systems that cover Rössler-like dynamical systems that have a logistic-like return map.

Two types of bifurcations occur repeatedly in the transition from laminar to chaotic behavior in dynamical systems described by a single stretch and fold (horseshoe) mechanism associated with a return map with a negative Schwarzian derivative. These are the saddle-node bifurcations and period-doubling bifurcations. They have their counterparts in covering systems with Lorenz-type branched manifolds. We illustrate with the period-three orbits.

Type Bifurcation	Orbit Symbol Image	Orbit Symbol Cover
Saddle-Node	011	$0_l1_l1_r + 0_r1_r1_l$
	001	$0_l0_l1_l0_r0_r1_r$
Period-Doubling	001	$0_l0_l1_l0_r0_r1_r$
	001011	$0_l0_l1_l0_r1_r1_l0_r0_r1_r0_l1_l1_r$

Covering a saddle-node bifurcation of two period-p orbits in the image system is a bifurcation that creates two period-p orbits and one period-$2p$ orbit in the cover. Covering a period-doubling bifurcation from a period-p to period-$2p$ orbit in the image system is a period-doubling bifurcation from a period-$2p$ to a period-$4p$ orbit in the cover. Saddle-node and period-doubling bifurcations lift in a different way to equivariant dynamical systems that possesses a Burke and Shaw type branched manifold.

3.8 POINCARÉ SECTIONS AND FIRST-RETURN MAPS

The first-return map for the image is constructed easily from the first-return map from the cover. We illustrate for the equivariant Lorenz system.

The $2 \to 1$ local diffeomorphism maps the two branch lines l and r in the equivariant system to a single branch line in the image dynamical system. We therefore identify the two segments L and R along the horizontal axis in Fig. 2.9, and the two branch lines along the return (vertical) axis in the same figure. This maps the four panels in Fig. 2.9 or Fig. 3.8(a) down to a single panel showing the return map from the Poincaré section (single branch line) onto itself in the image dynamics. This is shown in Fig. 3.8. The return map in Fig. 3.8(b) has a cusp type singularity. This is a significant indication that "tearing" occurs in the cover [21, 75]. Tearing means that the flow is split into two parts that move to different regions of the phase space. Tearing occurs as the flow approaches a singularity—in this case a fixed point at the origin splits the flow.

The same computation is repeated for the Burke and Shaw dynamical system in Fig. 3.9. For this system (cf. Fig. 3.3) the Poincaré section can be chosen as the union of two disconnected and symmetry related components. In this case an initial condition on one component maps to the other component. This is the reason for the "off-diagonal" structure of the return map in Fig. 3.9(a). Both components of the Poincaré section in the cover map to the single component in the image, as above for the Lorenz dynamical system. However, in this case the return map for the image shows a fold rather than a cusp singularity. The fold means that there is no tearing taking place in the covering dynamical system: chaos is generated by an iterated double fold.

Remark 1: Qualitatively speaking, as the flow spirals away from an unstable focus, it accelerates when a tearing mechanism is involved in the generation of chaotic

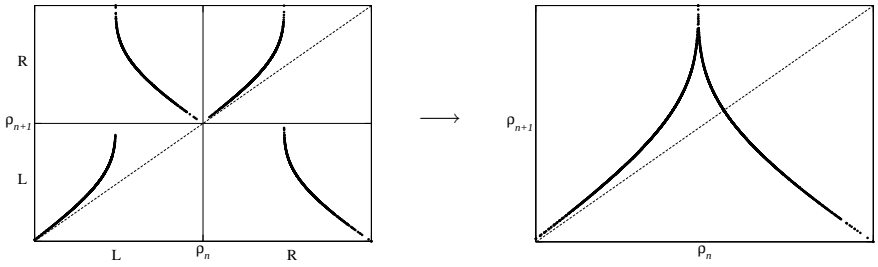

(a) (b)

Fig. 3.8 First-return maps in cover and image. (a) The Poincaré section in the equivariant Lorenz system consists of two disconnected components (cf. Fig. 2.9). Both components are mapped to the single component of the image (b). The return map shows a cusp-like singularity. This indicates that a "tearing" mechanism operates in the cover.

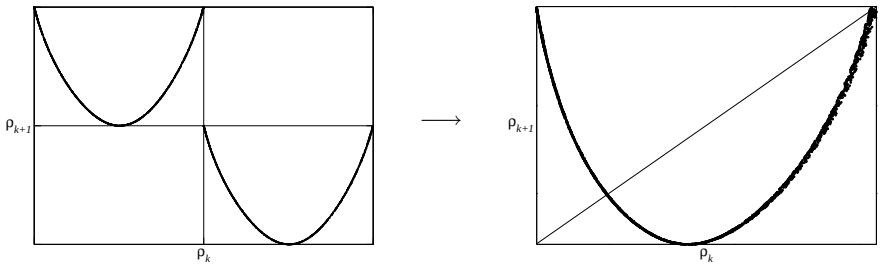

(a) (b)

Fig. 3.9 First-return maps in cover and image. (a) The Poincaré section in the equivariant Burke and Shaw system can be chosen as two disconnected components. Both components are mapped to the single component of the image (b).

behavior, but it decelerates in preparation for a folding process when the latter is involved in the generation of chaos. Acceleration or deceleration is directly related to the slope of the return map in the neighborhood of its maximum or minimum. In fact, the slope is zero at the turning point for folding mechanisms.

Remark 2: When the image shows that only folding takes place in the cover, the two components of the Poincaré section can be moved around the attractor to form a single component Poincaré section. For the Burke and Shaw attractor the return map on this Poincaré section shows four branches.

Remark 3: The Poincaré section for the Burke and Shaw attractor can be chosen differently: as a single component transverse to the flow. In Chapter 15 we will introduce an altorithm for properly choosing the Poincaré section for a flow in $\mathbb{R}^3$.

3.9 TIPS FOR INTEGRATION

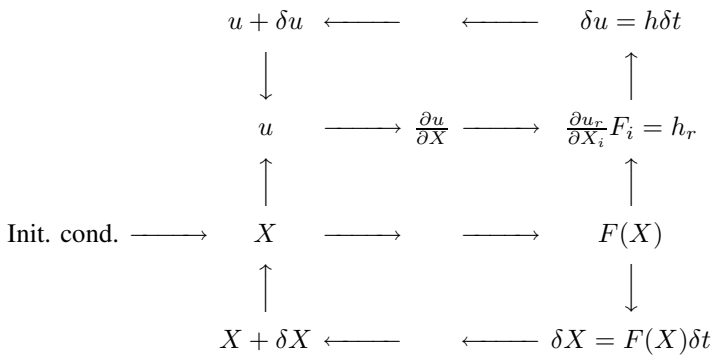

Fig. 3.10 Equivariant Integrator → Invariant Integrator. Lower loop shows the steps in a typical code for integrating equivariant dynamical systems. Upper loop shows modifications needed to integrate invariant dynamical systems.

It is useful to have an algorithmic procedure for constructing an image flow from a covering dynamical system, and vice versa. In this section we describe the modifications required to convert a numerical procedure which integrates an equivariant flow to one which generates the image flow. We describe the reverse procedure in Chapter 4.

First, we assume a program has been developed for integrating the equivariant equations. This consists of the following steps:

1. From X, evaluate $F(X)$.
2. Evaluate $\delta X = F(X)\delta t$.
3. Evaluate $X(t + \delta t) = X(t) + \delta X$.
4. Replace $X(t)$ by $X(t + \delta t)$.
5. Return to Step 1.

This sequence is shown in the lower loop in Fig. 3.10. To convert this program to one that integrates the image equations, we include the following steps:

1. Evaluate $u(t) = u(X(t))$.
2. Evaluate $\partial u/\partial X$.
3. Evaluate $h_r(u; r(u)) = (\partial u_r/\partial X_i)\, F_i(X)$.
4. Evaluate $\delta u = h(u)\delta t$.
5. Evaluate $u(t + \delta t) = u(t) + \delta u$.
6. Replace $u(t)$ by $u(t + \delta t)$ and continue.

This second algorithm is shown in the upper loop in Fig. 3.10. In fact, at each time step, it is sufficient to map $X(t)$ to its image $u(t)$. This simpler variant is shown in Fig. 3.11.

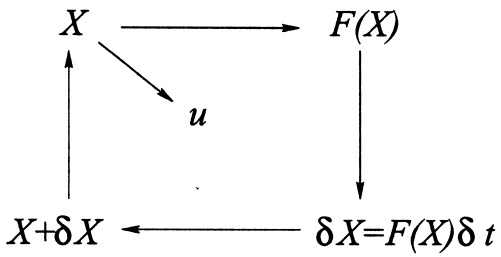

Fig. 3.11 Simple method for computing image dynamical system.

4

Covers

Every covering dynamical system has a unique image. The same is not true for images. Every image dynamical system has many different inequivalent equivariant covers.

We make these statements more precise. Every dynamical system $\dot{X}_i = F_i(\boldsymbol{X})$ equivariant under symmetry group $\mathcal{G}$ has a unique image dynamical system $\dot{u}_j = g_j(\boldsymbol{u})$. The image is obtained by introducing invariant coordinates $u_j = u_j(\boldsymbol{x})$. The two dynamical systems are *locally* diffeomorphic but not *globally* diffeomorphic. Conversely, a dynamical system $\dot{u}_j = g_j(\boldsymbol{u})$ without symmetry can be "lifted" to a covering dynamical system with symmetry group $\mathcal{G}$ by introducing a set of coordinates X_i with suitable transformation properties under $\mathcal{G}$.

The covering dynamical system $\dot{X}_i = F_i(\boldsymbol{X})$ is equivariant under $\mathcal{G}$ and locally diffeomorphic to the image dynamical system $\dot{u}_j = g_j(\boldsymbol{u})$. Each different symmetry group $\mathcal{G}$ gives rise to an inequivalent covering dynamical system. However, it is

possible that the image system $\dot{u}_j = g_j(\boldsymbol{u})$ has many *different* inequivalent covers with the *same* symmetry group $\mathcal{G}$. This possibility depends on the existence of certain topological indices [35,67].

4.1 LOCAL DIFFEOMORPHISMS

The relation between equivariant and invariant coordinates was described in Chapter 3. To recapitulate briefly, if X_i are equivariant coordinates, invariant coordinates u_j are linear combinations of polynomials invariant under $\mathcal{G}$ that are constructed from the X_i. The equivariant dynamical system $\dot{X}_i = F_i(\boldsymbol{X})$ and invariant dynamical system $u_j = g_j(\boldsymbol{u})$ are related by a local diffeomorphism

$$\frac{du_j}{dt} = \frac{\partial u_j}{\partial X_i}\frac{dX_i}{dt} = \frac{\partial u_j}{\partial X_i}F_i(\boldsymbol{X})$$

This local one-to-one map is invertible almost everywhere, so that the equivariant dynamical system can be recovered from the invariant dynamical system in a straightforward way

$$\frac{dX_i}{dt} = \frac{\partial X_i}{\partial u_j}\frac{du_j}{dt} = \left(\frac{\partial u}{\partial X}\right)^{-1}_{ij} g_j(\boldsymbol{u})$$

Example 1: A convenient set of coordinates invariant under $\mathcal{R}_Z(\pi) : (X, Y, Z) \to (-X, -Y, Z)$ is

$$\begin{aligned} u &= X^2 - Y^2 \\ v &= 2XY \\ w &= Z \end{aligned}$$

The image equations for the Lorenz system are

$$\frac{d}{dt}\begin{bmatrix} u \\ v \\ w \end{bmatrix} = \begin{bmatrix} -(\sigma+1)u + (\sigma - R)v + vw + (1-\sigma)\rho \\ (R-\sigma)u - (\sigma+1)v - uw + (R+\sigma)\rho - \rho w \\ -bw + \frac{1}{2}v \end{bmatrix}$$

where $\rho = \sqrt{u^2 + v^2}$. These equations can be lifted using the inverse of the Jacobian

$$\frac{\partial \boldsymbol{u}}{\partial \boldsymbol{X}} = \begin{bmatrix} 2X & -2Y & 0 \\ 2Y & 2X & 0 \\ 0 & 0 & 1 \end{bmatrix}$$

to the original Lorenz equations in (X, Y, Z).

Example 2: By a similar argument, the image of the Burke and Shaw system (2.5) is

$$\frac{d}{dt}\begin{bmatrix} u \\ v \\ w \end{bmatrix} = \begin{bmatrix} -(S+1)u - S(1-w)v + (1-S)\rho \\ S\,(1-w)\,u - (S+1)v - S\,(1+w)\,\rho \\ \frac{S}{2}v + \mathcal{V} \end{bmatrix}$$

These image equations can be lifted back up to the original Burke and Shaw equations.

Now suppose that we encounter a dynamical system $u_j = g_j(\boldsymbol{u})$ without symmetry. We have no knowledge of how it is obtained from an equivariant dynamical system, or even if it is obtained from a covering dynamical system by a local diffeomorphism. In principle it should be possible to lift this invariant dynamical system to a cover with any symmetry that we please. Even more to the point, we can lift this invariant system—or any dynamical system equivalent to it—to a cover with preassigned symmetry. Systems equivalent to the original system $du_j/dt = g_j(\boldsymbol{u})$ are obtained through global diffeomorphisms involving the simplest case: rigid rotation and displacement of the origin. For the present purposes it is sufficient to consider only rigid displacements of the origin

$$u' = u'(\boldsymbol{u})$$
$$u'_i = u_i - (u_i)_0$$

For this simple case, lifts of the dynamical system

$$\dot{u}'_j = g'_j(\boldsymbol{u}')$$

to equivariant dynamical systems with symmetry group σ_Z, $\mathcal{R}_Z(\pi)$, and $\mathcal{P}$ are given by the following maps

	$u' = u - u_0$	$v' = v - v_0$	$w' = w - w_0$
σ_Z	X	Y	Z^2
$\mathcal{R}_Z(\pi)$	$X^2 - Y^2$	$2XY$	Z
$\mathcal{P}$	$X^2 - Y^2$	$2XY$	$(X - Y)Z$

We will show that different choices for the location of the rotation axis parallel to w and through the point (u_0, v_0) for covers with $\mathcal{R}_Z(\pi)$ symmetry produce inequivalent covers of the Rössler system.

4.2 SINGULAR SETS

The Jacobian $\frac{\partial u_i}{\partial X_j}$ has zeroes, so its inverse has singularities. The Jacobians, their inverses, and the singular sets for the three local diffeomorphisms for σ_Z, $\mathcal{R}_Z(\pi)$, and $\mathcal{P}$ are

$$\frac{\partial \boldsymbol{u}}{\partial \boldsymbol{X}} \qquad \left(\frac{\partial \boldsymbol{u}}{\partial \boldsymbol{X}}\right)^{-1}$$

$$\sigma_Z \quad \begin{bmatrix} 1 & 0 & 0 \\ 0 & 1 & 0 \\ 0 & 0 & 2Z \end{bmatrix} \quad \begin{bmatrix} 1 & 0 & 0 \\ 0 & 1 & 0 \\ 0 & 0 & \frac{1}{2Z} \end{bmatrix}$$

Singular set: $X - Y$-plane $Z = 0$

$$\mathcal{R}_Z(\pi) \qquad \begin{bmatrix} 2X & -2Y & 0 \\ 2Y & 2X & 0 \\ 0 & 0 & 1 \end{bmatrix} \qquad \begin{bmatrix} \dfrac{X}{2\rho^2} & \dfrac{Y}{2\rho^2} & 0 \\ -\dfrac{Y}{2\rho^2} & \dfrac{X}{2\rho^2} & 0 \\ 0 & 0 & 1 \end{bmatrix}$$

Singular set: Z-axis
$\rho^2 = X^2 + Y^2 = 0$

$$\mathcal{P} \qquad \begin{bmatrix} 2X & -2Y & 0 \\ 2Y & 2X & 0 \\ Z & -Z & X-Y \end{bmatrix} \qquad \begin{bmatrix} \dfrac{X}{2\rho^2} & \dfrac{Y}{2\rho^2} & 0 \\ -\dfrac{Y}{2\rho^2} & \dfrac{X}{2\rho^2} & 0 \\ \dfrac{X+Y}{Y-X}\dfrac{Z}{2\rho^2} & \dfrac{Z}{2\rho^2} & \dfrac{1}{X-Y} \end{bmatrix}$$

Singular set: plane $X = Y$
Z-axis
$\rho^2 = X^2 + Y^2 = 0$

Lifting a dynamical system $\dot{u}_j = g_j(\boldsymbol{u})$ to a covering dynamical system with preassigned symmetry follows a standard prescription. We illustrate for the reflection group. The equations for the equivariant covering system are

$$\frac{d}{dt}\begin{bmatrix} X \\ Y \\ Z \end{bmatrix} = \begin{bmatrix} 1 & 0 & 0 \\ 0 & 1 & 0 \\ 0 & 0 & 2Z \end{bmatrix}^{-1} \begin{bmatrix} g_1(u,v,w) \\ g_2(u,v,w) \\ g_3(u,v,w) \end{bmatrix} = \begin{bmatrix} g_1(X,Y,Z^2) \\ g_2(X,Y,Z^2) \\ \frac{1}{2Z}g_3(X,Y,Z^2) \end{bmatrix}$$

If $g_3(X,Y,Z^2)$ is not of the form $Z^2 h_3(X,Y,Z^2)$, with $h_3(X,Y,Z^2)$ of polynomial form, then the equation of motion for Z has a singularity at $Z = 0$. The existence and uniqueness theorem is not applicable. If $g_3(u,v,w) = Z^2 h_3(X,Y,Z^2)$, then

$$\frac{dZ}{dt} = \frac{1}{2} Z h_3(X,Y,Z^2)$$

and the plane $Z = 0$ is an invariant set. In either case the reflection plane chosen to implement the symmetry should avoid all points in the strange attractor:

$$w = 0 \text{ plane} \bigcap \text{ Strange Attractor } = \emptyset$$

If this is not the case, the covering equations are either not Lipschitz or else will not generate a locally diffeomorphic cover of the original dynamical system.

Example: The Rössler equations are

$$\begin{aligned} \dot{u} &= -v - w \\ \dot{v} &= u + av \\ \dot{w} &= b + w(u - c) \end{aligned} \tag{4.1}$$

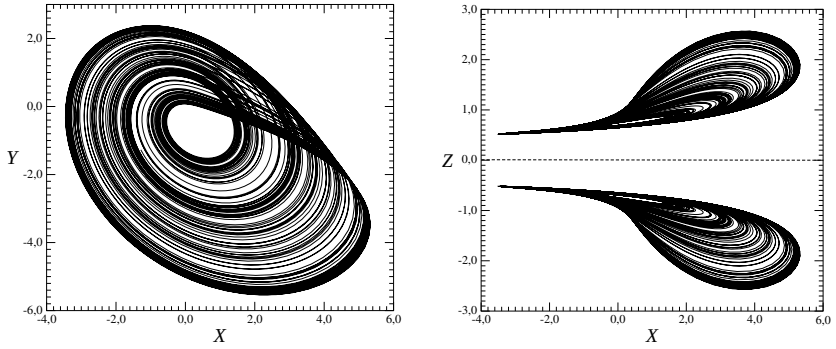

(a) X-Y plane projection (b) X-Z plane projection

Fig. 4.1 The two paired chaotic attractors generated by the double cover of the Rössler system under a reflection symmetry. Parameter values $(a, b, c) = (0.415, 2.0, 4.0)$ for equations (4.2). (a) X-Y projection. (b) X-Z projection.

The equivariant double cover with reflection symmetry in the X-Y plane $Z = 0$ is

$$\begin{aligned} \dot{X} &= -Y - Z^2 \\ \dot{Y} &= X + aY \\ \dot{Z} &= \frac{1}{2Z}\left(b + Z^2(X - c)\right) = \frac{b}{2Z} + \frac{1}{2}Z(X - c) \end{aligned} \tag{4.2}$$

Two projections of this double cover of the Rössler attractor are shown in Fig. 4.1.

The singularity on approach to the plane $Z = 0$ is evident. If we were to displace the origin, so that the new coordinate system is

$$\begin{aligned} u' &= u \\ v' &= v \\ w' &= w - w_0 \end{aligned}$$

with w_0 slightly greater than b, then the reflection plane would intersect the strange attractor, the equivariant equations would be

$$\begin{aligned} \dot{X} &= -Y - (Z^2 + w_0) \\ \dot{Y} &= X - aY \\ \dot{Z} &= \frac{b}{2Z} + \frac{1}{2Z}(Z^2 + w_0)(X - c) \end{aligned}$$

and the cover would not be locally diffeomorphic with the original dynamical system.

4.3 LIFTS TO ROTATION INVARIANT SYSTEMS: TOPOLOGICAL INDICES

Lifts to rotation equivariant dynamical systems exhibit a much wider spectrum of possibilities than σ_Z-equivariant lifts. The reason is that the singular set of the diffeomorphism for rotation invariant lifts is the Z-axis, while it is a plane for σ_Z-invariant lifts. The plane divides $\mathbb{R}^3$ into two disjoint open sets that have only the plane in common. Lifts are disconnected. In the rotation invariant case the rotation axis is a one-dimensional set. Closed orbits encircle this invariant set in different ways, depending on the choice of rotation axis in the original space $\mathbb{R}^3(u, v, w)$.

A closed orbit S_* in the cover that encircles the Z-axis n times maps to a closed orbit S in the image. Two possibilities occur:

1. The orbit S_* is not symmetric. The two orbits S_* and $\bar{S}_* = \gamma S_*$, both of period p, map to the same orbit S in the image. The orbit S has period p and winds around the w-axis $2n$ times.
2. The orbit is symmetric, $S_*\bar{S}_*$, and of even period $2p$. It encircles the Z-axis n times. The symmetric orbit projects to an orbit SS of (nonminimal) period $2p$ that winds around the w-axis $2n$ times. The image S of minimal period p winds around the w-axis n times.

Topological considerations guarantee that dynamical systems $\dot{u}_j = g_j(\boldsymbol{u})$ without symmetry can have many different, inequivalent lifts. The different lifts depend on the placement of the w-axis in the space $\mathbb{R}^3(u, v, w)$. In particular, the lifts depend on how the unstable periodic orbits in the image strange attractor are linked with the rotation axis.

4.4 BRANCHED MANIFOLDS

These considerations can be made more precise by recalling that the set of unstable periodic orbits in a strange attractor is specified by the branched manifold that the attractor projects to (under Eq. (2.10)), and that classifies the strange attractor. We illustrate the subtleties of the topological index by discussing a simple but important case: lifts of the Smale horseshoe branched manifold.

This manifold is shown in Fig. 4.2. Each of the two branches supports a period-one orbit. In this figure we illustrate four different ways that the rotation axis w in $\mathbb{R}^3(u, v, w)$ can be oriented with respect to this 2-branched manifold without intersecting either branch. The topology of the lift is determined by the way that the two period-one orbits wind around the rotation axis. This is specified by a topological index (n_0, n_1). The integer n_0 is the number of times the period-one orbit 0, the period-one orbit in branch 0, winds around the w-axis. This in turn is the linking number of the orbit 0 with the w-axis, closed by return path from $(u, v, w) = (0, 0, Z)$ $(Z \to +\infty)$ to $(0, 0, Z)$ $(Z \to -\infty)$. The integer n_1 is defined similarly for the period-one orbit in branch 1.

Remark: If the branched manifold of the image system has b branches, the topological index consists of b integers.

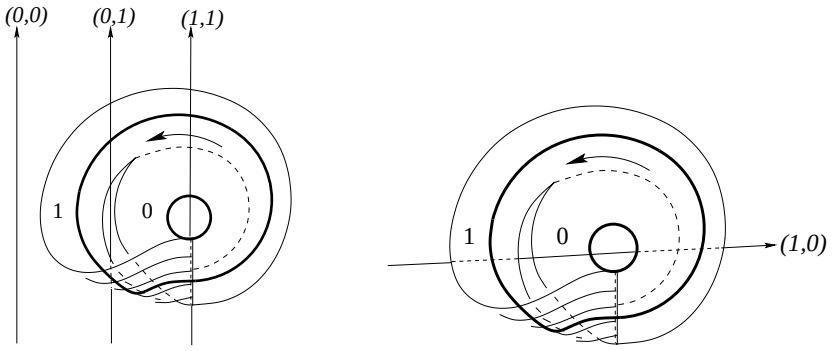

(a) cases (0,0), (0,1) and (1,1) (b) case (1,0)

Fig. 4.2 Two-branch Smale horseshoe template. The period-one orbit in each branch is shown by a heavy line. The rotation axis $(0, 0, w)$ in (u, v, w) space can link the period-one orbits 0 and 1 in the four ways shown. The four axes are labeled by their linking numbers (n_0, n_1) with the two period-one orbits. These axes have been chosen to be disjoint from the strange attractor's branched manifolds: 0 or 1. (a) The three cases (0,0), (0,1), and (1,1) are shown. (b) In the case (1,0), the rotation axis passes behind branch 1, in front of branch 0, then through the hole in the middle of the attractor and behind both branches.

Four inequivalent rotation-equivariant lifts of the Smale horseshoe branched manifold are shown in Fig. 4.3. For each, the topological index of the image is given.

In the first case $(n_0, n_1) = (0, 0)$ (Fig. 4.3(a)). Neither of the period-one orbits in the Smale horseshoe template circles the w-axis. The rotation axis is "outside" the strange attractor. The double cover is rotation invariant. It consists of two disconnected branched manifolds, each having two branches, each being one-to-one diffeomorphic with the original Smale horseshoe branched manifold.

A symmetry adapted branch labeling scheme is used. Branches in the cover that map to branch 0 in the image are labeled 0 and dressed by a group index or equivalent index: 0_l and 0_r. Similarly, for the other pair of branches: 1_l and 1_r. The transition matrix for this (disconnected) four-branch template is

$$\begin{array}{c|cccc} & \bar{0}_l & \bar{1}_l & \bar{0}_r & \bar{1}_r \\ \hline \bar{0}_l & 1 & 1 & 0 & 0 \\ \bar{1}_l & 1 & 1 & 0 & 0 \\ \bar{0}_r & 0 & 0 & 1 & 1 \\ \bar{1}_r & 0 & 0 & 1 & 1 \end{array} \tag{4.3}$$

In the second case $(n_0, n_1) = (0, 1)$ (Fig. 4.3(b)). Branch 1 in the image links the w-axis once and branch 0 does not. The covering template has four branches: one $(\bar{0}_l)$ exists on the left, its image $(\bar{0}_r)$ on the right, one branch $(\hat{1}_l)$ extends from the left to the right, and its image $(\hat{1}_r)$ under $\mathcal{R}_Z(\pi)$. Under projection, the image of the two branches $\bar{0}_l$, $\bar{0}_r$ in the cover branched manifold is the branch 0 in the Smale horseshoe

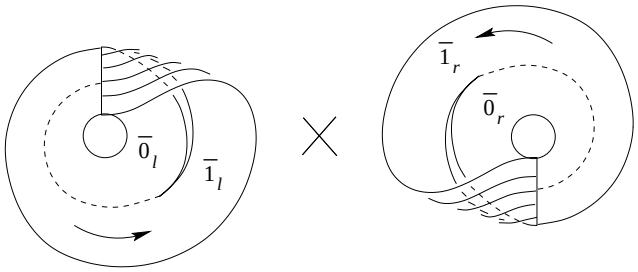

(a) $(n_0, n_1) = (0, 0)$

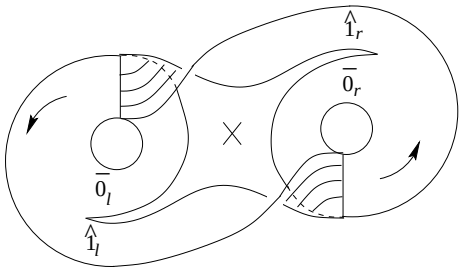

(b) $(n_0, n_1) = (0, 1)$

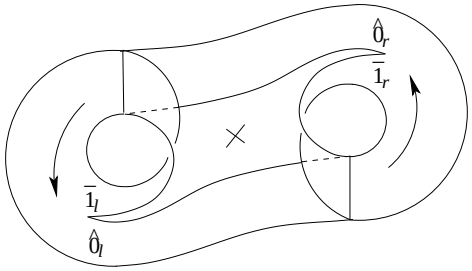

(c) $(n_0, n_1) = (1, 0)$

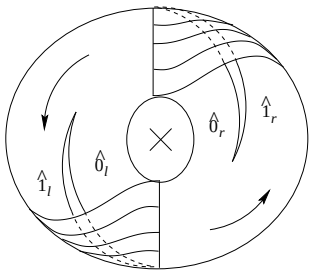

(d) $(n_0, n_1) = (1, 1)$

Fig. 4.3 Branched manifolds for four inequivalent double covers of the Smale horseshoe template. Each cover is equivariant under rotations by π around an axis through $\times$. The four different double covers are identified by their topological index (n_0, n_1).

template. The branches $\hat{1}_l$, $\hat{1}_r$ both map to the branch 1 in the image template. The period-one orbit $\bar{0}_l$ and its counterpart $\bar{0}_r$ do not link the Z-axis ($n = 0$). Both map to the period-one orbit 0 in the horseshoe template, which does not link the w-axis ($n_0 = 0$). There is one period-two orbit $\hat{1}_l\hat{1}_r$ in the cover template. This links the Z-axis once ($n = 1$). This orbit maps twice onto the period-one orbit 1 in the horseshoe template ($\hat{1}_l\hat{1}_r \to 11$), which links the w-axis twice ($n = 2$). The period-one orbit 1 links the w-axis only once ($n_1 = 1$).

These arguments can be run backward. Since $n_0 = 0$, the period-one orbit 0 in the horseshoe lifts to two symmetry-related orbits $\bar{0}_l$, $\bar{0}_r$, which do not link the Z-axis. Since $n_1 = 1$, the period-one orbit 1 in the horseshoe lifts to "half a closed orbit" $\hat{1}_l$ or $\hat{1}_r$, which is then closed by adjoining the complementary symmetry-related segment ($\hat{1}_r$ or $\hat{1}_l$). This closed orbit $\hat{1}_l\hat{1}_r$ in the cover links the Z-axis with $n = 1$. That is, the period-"two" orbit 11 in the image, with $n = n_1 + n_1 = 2$, lifts to the period-two orbit $\hat{1}_l\hat{1}_r$ with $n = 1$ in the cover.

The transition matrix for this cover of the Smale horseshoe template is

	$\bar{0}_l$	$\hat{1}_l$	$\bar{0}_r$	$\hat{1}_r$
$\bar{0}_l$	1	1	0	0
$\hat{1}_l$	0	0	1	1
$\bar{0}_r$	0	0	1	1
$\hat{1}_r$	1	1	0	0

(4.4)

The third and fourth cases are analyzed similarly. The third case $(n_0, n_1) = (1, 0)$ is shown in Fig. 4.3(c). For all practical purpose it is the "dual" to the case shown in Fig. 4.3(b). The period-one orbits in the cover $\bar{1}_l$ and $\bar{1}_r$ do not link the Z-axis, while the period-two orbit $\hat{0}_l\ \hat{0}_r$ in the cover maps to 00 in the image.

The transition matrix is

	$\hat{0}_l$	$\bar{1}_l$	$\hat{0}_r$	$\bar{1}_r$
$\hat{0}_l$	0	0	1	1
$\bar{1}_l$	1	1	0	0
$\hat{0}_r$	1	1	0	0
$\bar{1}_r$	0	0	1	1

(4.5)

In the fourth case, shown in Fig. 4.3(d), both branches in the image link the rotation axis. The topological index is (1,1), so orbit segments $\hat{0}_l$, $\hat{1}_l$, $\hat{0}_r$, and $\hat{1}_r$ are not closed. The period-two orbits $\hat{0}_l\hat{0}_r$ and $\hat{1}_l\hat{1}_r$ map to the orbits 00 and 11. The transition matrix is

	$\hat{0}_l$	$\hat{1}_l$	$\hat{0}_r$	$\hat{1}_r$
$\hat{0}_l$	0	0	1	1
$\hat{1}_l$	0	0	1	1
$\hat{0}_r$	1	1	0	0
$\hat{1}_r$	1	1	0	0

(4.6)

The Smale horseshoe template lifts to four inequivalent branched manifolds that are equivariant under the group $\mathcal{R}_Z(\pi)$ by choosing the rotation axis w to have

topological index $(n_0, n_1) = (0, 0)$, (0,1), (1,0), and (1,1) with the two branches of the horseshoe template (or the period-one orbits in these branches). Other values of the topological index generate other inequivalent double covers of the horseshoe.

The symmetry adapted labeling scheme has been augmented with yet another symbol ($\bar{}$ and $\hat{}$), depending on the value of the topological index: $n = 0 \leftrightarrow \bar{}$, $n = 1 \leftrightarrow \hat{}$. This symbol summarizes the information available from the transition matrix. A superscript $\bar{}$ signifies that there is no transition from left to right; $\hat{}$ signifies that there is a transition $l \leftrightarrow r$. We summarize four transition matrices here for ease of comparison. This comparison suggests the proper generalization when the image branched manifold has three or more branches. It also suggests the generalization when n_0 is odd ($n_0 = \ldots, -1, 1, 3, \ldots$ are similar) or even ($n_0 = \ldots, -2, 0, +2, \ldots$ are similar).

$(n_0, n_1) = (0, 0)$

	$\bar{0}_l$	$\bar{1}_l$	$\bar{0}_r$	$\bar{1}_r$
$\bar{0}_l$	1	1	0	0
$\bar{1}_l$	1	1	0	0
$\bar{0}_r$	0	0	1	1
$\bar{1}_r$	0	0	1	1

$(n_0, n_1) = (0, 1)$

	$\bar{0}_l$	$\hat{1}_l$	$\bar{0}_r$	$\hat{1}_r$
$\bar{0}_l$	1	1	0	0
$\hat{1}_l$	0	0	1	1
$\bar{0}_r$	0	0	1	1
$\hat{1}_r$	1	1	0	0

$(n_0, n_1) = (1, 1)$

	$\hat{0}_l$	$\hat{1}_l$	$\hat{0}_r$	$\hat{1}_r$
$\hat{0}_l$	0	0	1	1
$\hat{1}_l$	0	0	1	1
$\hat{0}_r$	1	1	0	0
$\hat{1}_r$	1	1	0	0

$(n_0, n_1) = (1, 0)$

	$\hat{0}_l$	$\bar{1}_l$	$\hat{0}_r$	$\bar{1}_r$
$\hat{0}_l$	0	0	1	1
$\bar{1}_l$	1	1	0	0
$\hat{0}_r$	1	1	0	0
$\bar{1}_r$	0	0	1	1

(4.7)

There are no other transition matrices for two paires of symbols (0,1) (l, r) with $l \leftrightarrow r$ symmetry. Only the lift $(n_0, n_1) = (1, 1)$ does not possess period-one orbits with this symbolic dynamics.

Remark 1: Comparison of Fig. 3.2 and Fig. 4.3(b) shows that the Lorenz template is topologically equivalent to the double cover of the horseshoe template (branch labels (0,1)) with $\mathcal{R}_Z(\pi)$ symmetry and topological index $(n_0, n_1) = (0, 1)$. Comparison of Fig. 3.3 with Fig. 4.3(d) shows that the Burke and Shaw branched manifold is topologically equivalent to the double cover of the reverse horseshoe template (branch labels (1,2)) with $\mathcal{R}_Z(\pi)$ symmetry and topological index $(n_1, n_2) = (1, 1)$. These two $\mathcal{R}_Z(\pi)$ equivariant dynamical systems therefore differ from each other in two distinct ways:

1. In the topology of their image, which have branches with local torsion (0,1) and (1,2).
2. In their topological indices which are $(n_0, n_1) = (0, 1)$ and $(n_1, n_2) = (1, 1)$.

Remark 2: It is clear by inspection that to each of the four branched manifolds shown in Fig. 4.3 with $\mathcal{R}_Z(\pi)$ symmetry there corresponds exactly one branched manifold with $\mathcal{P}$ symmetry. Topological indices can be used to classify and distinguish $\mathcal{R}_Z(\pi)$ equivariant as well as $\mathcal{P}$-equivariant branched manifolds.

Remark 3: Corresponding $\mathcal{R}_Z(\pi)$-equivariant and $\mathcal{P}$-equivariant branched manifolds relate in a one-to-one way dynamical systems that are topologically globally inequivalent but that are locally equivalent everywhere. A one-to-one mapping between two dynamical systems with globally distinct topologies is called "group continuation." This is described in more detail in Section 14.4.3.

4.5 PERIODIC ORBITS

Periodic orbits in a strange attractor for the dynamical system $\dot{u}_j = g_j(\boldsymbol{u})$ without symmetry can be lifted to periodic orbits in a covering system $\dot{X}_i = F_i(\boldsymbol{X})$ with symmetry in an algorithmic way.

The algorithm is very simple for the reflection group σ_Z. The double cover is disconnected and consists simply of two disjoint copies of the original strange attractor. Orbits in the image attractor appear with unchanged names in the cover attractor, in pairs. For example, an orbit 011 in a Smale horseshoe attractor is lifted to the pair $\bar{0}_l\bar{1}_l\bar{1}_l$ and $\bar{0}_r\bar{1}_r\bar{1}_r$ in the disconnected double cover, one orbit in each of the two covering attractors.

Similar remarks hold for double cover with $\mathcal{R}_Z(\pi)$ and $\mathcal{P}$ symmetry and topological index (0,0), which are also disconnected.

In the more general case when the symmetry group is $\mathcal{R}_Z(\pi)$ or $\mathcal{P}$ and the topological index is not zero the "lifting rules" are also simple. An orbit S of period p in the invariant dynamical system is lifted to an orbit in the equivariant strange attractor as follows:

1. Obtain S_* from S by dressing each symbol in the name of the orbit S by a group index (l, r) and a topological index $(\bar{}, \hat{})$. The dressing is unique once the first symbol has been dressed.

2. If there is an even number of topological indices $\hat{}$ in S_*, the lifted trajectory is closed and of period p. The orbit is asymmetric, and its symmetry-related partner is γS_*.

3. If there is an odd number of topological indices $\hat{}$ in S_*, the lifted trajectory is "half a closed orbit." The closed lifted orbit is $S_*(\gamma S_*)$, of period $2p$. It is symmetric.

To illustrate these simple rules, we construct the periodic orbits that cover the period-3 saddle node pair 011 and 001 in a Smale horseshoe template. This is done for covers with $\mathcal{R}_Z(\pi)$ or $\mathcal{P}$ symmetry and four topological indices

Topological index	Symmetry adapted symbols	Cover of 100	Cover of 101
(0,0)	$\bar{0}_l, \bar{1}_l, \bar{0}_r, \bar{1}_r$	$\bar{1}_l\bar{0}_l\bar{0}_l + \bar{1}_r\bar{0}_r\bar{0}_r$	$\bar{1}_l\bar{0}_l\bar{1}_l + \bar{1}_r\bar{0}_r\bar{1}_r$
(0,1)	$\bar{0}_l, \hat{1}_l, \bar{0}_r, \hat{1}_r$	$\hat{1}_l\bar{0}_r\bar{0}_r\hat{1}_r\bar{0}_l\bar{0}_l$	$\hat{1}_r\bar{0}_l\hat{1}_l + \hat{1}_l\bar{0}_r\hat{1}_r$
(1,0)	$\hat{0}_l, \bar{1}_l, \hat{0}_r, \bar{1}_r$	$\bar{1}_l\hat{0}_l\hat{0}_r + \bar{1}_r\hat{0}_r\hat{0}_l$	$\bar{1}_l\hat{0}_l\bar{1}_r\bar{1}_r\hat{0}_r\bar{1}_l$
(1,1)	$\hat{0}_l, \hat{1}_l, \hat{0}_r, \hat{1}_r$	$\hat{1}_r\hat{0}_l\hat{0}_r\hat{1}_l\hat{0}_r\hat{0}_l$	$\hat{1}_r\hat{0}_l\hat{1}_r\hat{1}_l\hat{0}_r\hat{1}_l$

4.6 POINCARÉ SECTIONS AND FIRST-RETURN MAPS

Poincaré sections and return maps can be lifted from image to covering systems. We illustrate the procedure for the Rössler dynamical system and for its double covers with $\mathcal{R}_Z(\pi)$ symmetry and topological indices (0,0), (0,1), (1,0), and (1,1).

The Poincaré section for the Rössler system is the set of points that project to a branch line in its branched manifold. Since the Rössler system is highly dissipative for the normal range of its control parameter values, we can use the intersection of the attractor with a half-plane hinged on the Z-axis as the branch line. The return map is shown in Fig. 4.4. The two parts of the branch line that provide initial conditions for flows through the orientation preserving branch 0 and the orientation-reversing branch 1 are clearly labeled 0 and 1.

Double covers of the Smale horseshoe template have four branches and two disconnected branch lines, labeled l and r. Return maps describe how initial conditions on the two branch lines map to the two branch lines. Four symmetry-adapted symbols suffice to label all orbits in the cover uniquely. They also suffice to construct the return maps in all double covers. The four return maps are presented in Fig. 4.5. We describe the construction of the return map for the double cover with topological index $(n_0, n_1) = (0, 1)$. The others are constructed with the same ease.

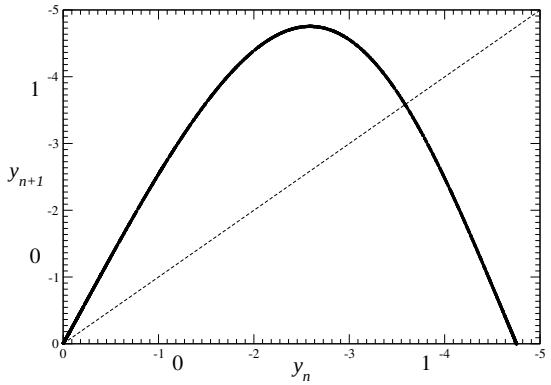

Fig. 4.4 First return map to a Poincaré section of the Rössler system. Parameter values: $(a, b, c) = (0.432, 2.0, 4.0)$.

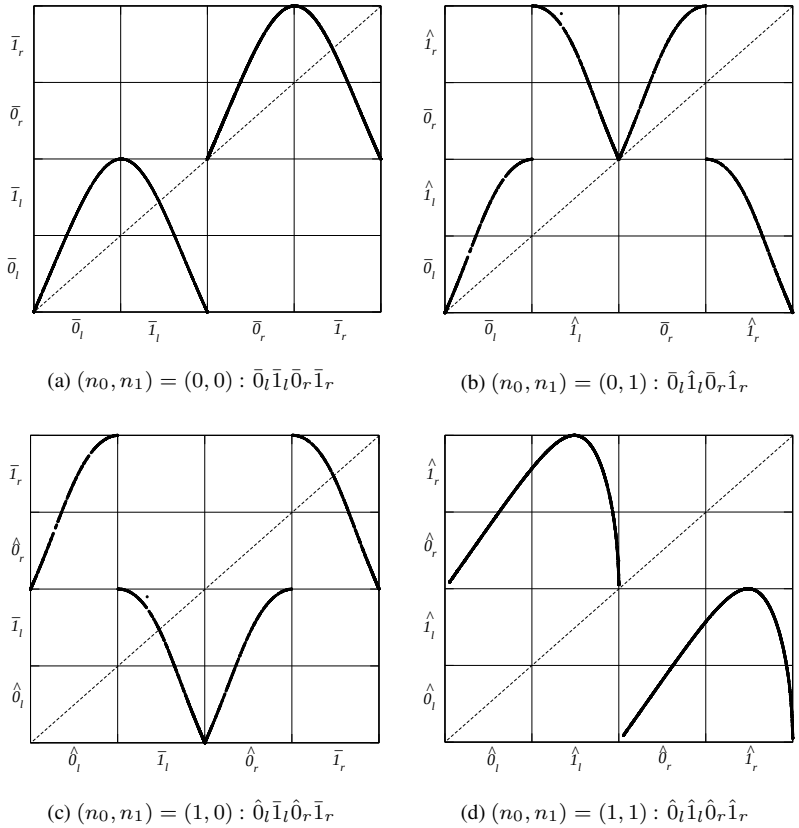

(a) $(n_0, n_1) = (0, 0) : \bar{0}_l \bar{1}_l \bar{0}_r \bar{1}_r$

(b) $(n_0, n_1) = (0, 1) : \bar{0}_l \hat{1}_l \bar{0}_r \hat{1}_r$

(c) $(n_0, n_1) = (1, 0) : \hat{0}_l \bar{1}_l \hat{0}_r \bar{1}_r$

(d) $(n_0, n_1) = (1, 1) : \hat{0}_l \hat{1}_l \hat{0}_r \hat{1}_r$

Fig. 4.5 First-return map to a Poincaré section of the two-fold covers of the Rössler system. For each of the four $\mathcal{R}_Z$ equivariant double covers we show the topological index (n_0, n_1) and the four symbols required to specify any trajectory.

The transition matrix for the cover with topological index $(n_0, n_1) = (0, 1)$ is given in Eq. (4.4). It can also be inferred from the symmetry-adapted symbols $\bar{0}_l$, $\hat{1}_l$, $\bar{0}_r$, $\hat{1}_r$. Either way, points on the half line 0_l on the left-hand branch map to the branch line l while points on the other part of l, labeled 1_l, map to branch r. This is summarized on the left-hand side of the return map shown in Fig. 4.5(b). The right-hand side is similarly constructed.

4.7 FRACTAL DIMENSIONS AND LYAPUNOV EXPONENTS

Fractal dimensions are invariant under diffeomorphisms and local diffeomorphisms. Therefore the spectrum of fractal dimensions of an attractor obtained from the invari-

ant dynamical system $\dot{u}_j = g_j(\boldsymbol{u})$ is the same as the spectrum of fractal dimensions of any of its covers obtained from equivariant dynamical system equations $\dot{X}_i = F_i(\boldsymbol{X})$.

Similar arguments apply to the spectrum of Lyapunov exponents of images and their covers.

Local Lyapunov exponents are treated similarly. If $\boldsymbol{X}_0$ and $\gamma\boldsymbol{X}_0$ are two points in the cover with the same image $\boldsymbol{u}_0$, then the spectrum of local Lyapunov exponents is the same at all three points. This remains true even in the singular case $\boldsymbol{X}_0 = \gamma\boldsymbol{X}_0$.

4.8 CONTINUATIONS

In Fig. 4.3 we show branched manifolds for four topologically inequivalent double covers of the Smale horseshoe branched manifold. Each of these double covers is equivariant under the same symmetry group of rotations $\mathcal{R}_Z$ about a different Z-axis. In Fig. 3.4, we show a double cover of the Smale horseshoe branched manifold with inversion symmetry, $\mathcal{P}$. The four double covers of Fig. 4.3 and the double cover of Fig. 3.4 are all locally diffeormorphic to the image dynamical system with Smale horseshoe template. Therefore they are all locally diffeomorphic with each other. This means that there is a local diffeomorphism between any pair of these dynamical systems.

The relation among these dynamical systems is comparable to the relation between two different functions of a complex variable that are analytic continuations of each other. In the case of dynamical systems, there are two different "continuation mechanisms":

1. topological continuation
2. group continuation.

We describe both now.

4.8.1 Topological Continuation

An image dynamical system $\underline{D}$ can have many distinct covers $D_{1\mathcal{G}}$, $D_{2\mathcal{G}}$, ..., all equivariant under $\mathcal{G}$, distinguished from each other by some index, i. Fig. 4.3 illustrates the case where $\underline{D}$ has Smale horseshoe dynamics and the four double covers with $\mathcal{R}_Z$ symmetry are distinguished by a topological index (n_0, n_1). The cover-image relations are summarized by

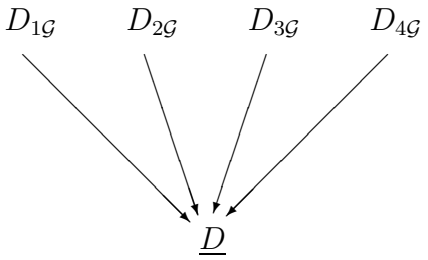

Each $\mathcal{D}_i$ is locally diffeomorphic with $\underline{\mathcal{D}}: \mathcal{D}_{i_\mathcal{G}} \overset{\text{local}}{\longleftrightarrow} \underline{\mathcal{D}}$. As a result, each $\mathcal{D}_{i_\mathcal{G}}$ is locally diffeomorphic with every other $\mathcal{D}_{j_\mathcal{G}}$.

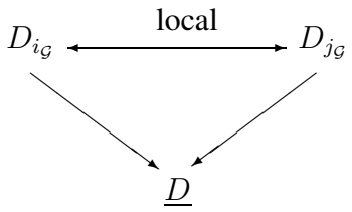

4.8.2 Group Continuation

An image dynamical system $\underline{\mathcal{D}}$ can have covers with different symmetry groups $\mathcal{H}$ and $\mathcal{G}$. Fig. 4.3(d) and Fig. 3.4 illustrate this case where $\underline{\mathcal{D}}$ has Smale horseshoe dynamics and the double covers have rotation ($\mathcal{R}_Z$) and inversion ($\mathcal{P}$) symmetry and the same topological index. This relation is shown in Fig.4.6.

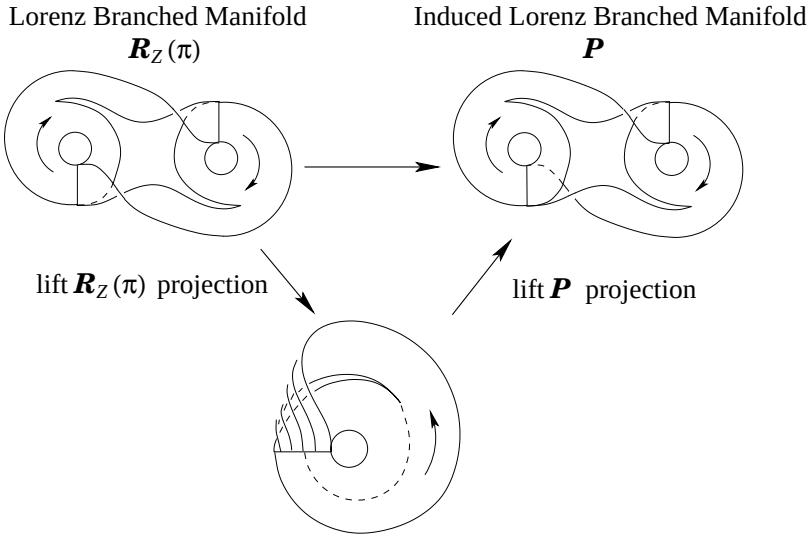

Fig. 4.6 Group continuation. The $\mathcal{R}_Z$ equivariant lift of the Smale horseshoe with index $(n_0, n_1) = (0, 1)$ (left) is projected to the Smale horseshoe (center), then lifted to the double cover equivariant under $\mathcal{P}$ with index (0,1) (right).

The group continuation relation is

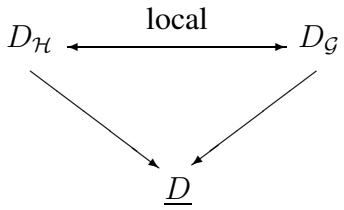

This means that $\mathcal{D}_{\mathcal{H}}$ is the cover of $\underline{\mathcal{D}}$ with equivariance group $\mathcal{H}$, $\mathcal{D}_{\mathcal{G}}$ is the cover of $\underline{\mathcal{D}}$ with equivariance group $\mathcal{G}$, and all three dynamical systems $\mathcal{D}_{\mathcal{H}}$, $\mathcal{D}_{\mathcal{G}}$, and $\underline{\mathcal{D}}$ are locally isomorphic.

Group continuation can be carried out whenever two distinct groups have the same order and the equivariant covers have the same topological index. This concept is not restricted to the order-two groups $\mathcal{R}_Z(\pi)$ and $\mathcal{P}$ acting in $\mathbb{R}^3$.

4.9 HORSESHOE VERSUS REVERSE HORSESHOE

The Lorenz system (1.2) and the Burke and Shaw system (2.5) are both equivariant under $\mathcal{R}_Z(\pi)$. As previously remarked, they differ in two ways.

1. The Lorenz system has topological index $(n_0, n_1) = (0, 1)$ (cf. Fig. 3.2) while the Burke and Shaw system has topological index $(n_1, n_2) = (1, 1)$ (cf. Fig. 3.3).
2. The image of the Lorenz attractor is a Smale horseshoe (cf. Fig. 3.2) while that of the Burke and Shaw attractor is a reverse horseshoe (cf. Fig. 3.3).

The branched manifold for the Smale horseshoe has two branches with local torsion 0 and 1, while that of the reverse horseshoe has two branches with local torsion 1 and 2. Both are subtemplates of a larger branched manifold (part of a "gateau roulé") with three branches having local torsions 0,1,2 [33,34,36,37].

In Fig. 4.7 we show the images of the Lorenz attractor (top/left) and the Burke and Shaw attractor (top/right). Below the image of the Lorenz system (Fig. 4.7(a)) we show the two-fold covers with topological indices $(n_0, n_1) = (1, 1)$ (Fig. 4.7(c)) and (0,1) (Fig. 4.7(e)). Both covers exhibit $\mathcal{R}_Z$ symmetry. Two two-fold covers of the Burke and Shaw image (Fig. 4.7(b)) are also shown. The cover with index $(n_1, n_2) = (1, 1)$, which is the original Burke and Shaw system, is shown in Fig. 4.7(d). The cover with index (1,0) is shown in Fig. 4.7(f). The covers in Fig. 4.7(e) and (f) both have the property that the odd parity period-one orbit circles the rotation axis but the even parity orbit does not. All six attractors shown in Fig. 4.7 are inequivalent. The three on the left are locally diffeomorphic, as are the three on the right.

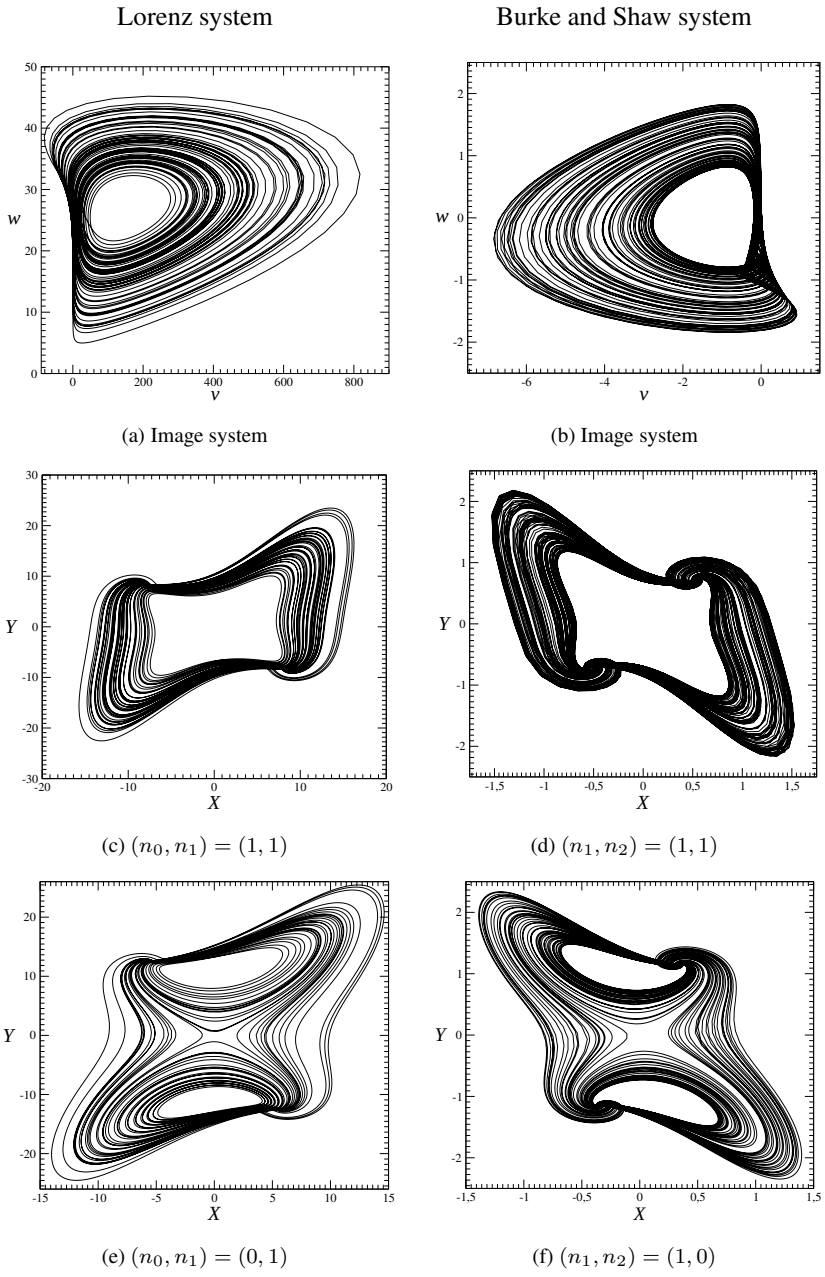

Fig. 4.7 Images of (a) the Lorenz system and (b) the Burke and Shaw system. The first is a horseshoe, the second is a reverse horseshoe. Two double covers of each are shown. The topological indices (n_0, n_1) for the covers of the proto Lorenz system in (a) are (c) (1,1) and (e) (0,1). The topological indices (n_1, n_2) for the covers of the proto Burke and Shaw system in (b) are (d) (1,1) and (f) (1,0).

(n_0, n_1)	(0,0)	(0,1)	(1,0)	(1,1)
$R_Z(\pi)$	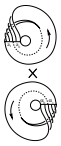 ?	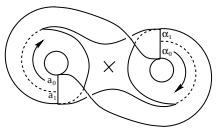 Lorenz system	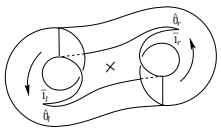 Lorenz dual	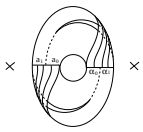 Burke and Shaw
$\mathcal{P}$	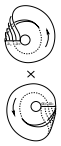 Chua	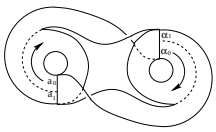 Induced Lorenz	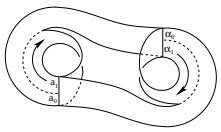 ?	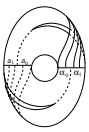 Kremliovsky

Fig. 4.8 Lifts of the Smale horseshoe template. Top row: $\mathcal{G} = \mathcal{R}_Z(\pi)$. Bottom row: $\mathcal{G} = \mathcal{P}$. Columns left to right: topological index of lift: (n_0, n_1) = (0,0), (0,1), (1,0), (1,1).

4.10 LIFTS OF THE SMALE HORSESHOE

As can be seen by now, even the simplest image dynamical system can have many inequivalent covers. The covers can differ either by symmetry group or by topological index, or both. In Fig. 4.8 we illustrate this idea by showing eight inequivalent lifts of the Smale horseshoe branched manifold. Four covers are equivariant under $\mathcal{G} = \mathcal{R}_Z(\pi)$ while the other four are equivariant under $\mathcal{G} = \mathcal{P}$. For each of the two equivariance groups, covers with the four topological indices (n_0, n_1) = (0,0), (0,1), (1,0), (1,1) are presented. When the resulting branched manifolds have previously been encountered, they are identified by their appropriate names.

4.11 TIPS FOR INTEGRATION

It is useful to have an algorithmic procedure for constructing a covering flow from an image flow. We assume that a procedure has been developed for integrating the image equations. This is shown in the lower loop in Fig. 4.9. To convert this program to one that integrates the equivariant equations, we modify it as follows:

1. Initiate the integration by choosing a value of X at $t = 0$, and construct an initial condition for the u integration routine.
2. Evaluate $\partial u_r / \partial X_i$ at $X(t)$.
3. Evaluate the inverse of this nonsingular matrix, $(\partial u / \partial X)^{-1}$.
4. Evaluate $F_i(x) = (\partial u / \partial X)^{-1}_{ir} h_r(u; r(u))$.
5. Evaluate $X(t + \delta t) = X(t) + F(X)\delta t$.

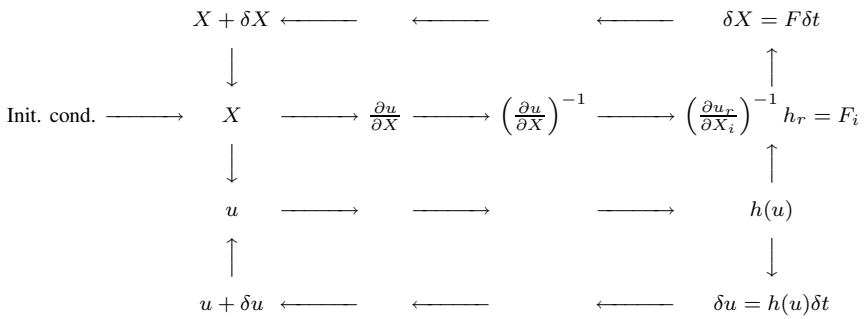

Fig. 4.9 Invariant Integrator → Equivariant Integrator. Lower loop shows the steps in a typical code for integrating invariant dynamical systems. Upper loop shows modifications needed to integrate equivariant dynamical systems.

6. Replace $X(t)$ by $X(t + \delta t)$.
7. Return to Step 2.

Using this procedure, it is a very simple matter to construct covers of an image dynamical system with inequivalent symmetries. The only change occurs in Step 2, where the Jacobian of the transformation is computed. The Jacobian varies from group to group and index to index.

5

Peeling Bifurcations

In Chapter 4 we saw that a dynamical system can have many inequivalent double covers, each with the same symmetry group. This was shown explicitly for double covers of a dynamical system exhibiting horseshoe dynamics. The four distinct double covers all possessed $\mathcal{R}_Z(\pi)$ symmetry but possessed different topological indices (n_0, n_1). The rotation axis of the symmetry group $\mathcal{R}_Z(\pi)$ linked the image dynamical system in four ways (cf. Fig. 4.2). In creating these four distinct double covers we were careful that the rotation axis did not intersect the strange attractor. This is possible at the level of a branched manifold description of the dynamics and sometimes possible for real strange attractors. But it is not always possible. For example, there is usually no clear gap in a (Rössler-like) strange attractor between orbit segments that project to the branches 0 and 1 under the Birman-Williams projection.

In this chapter we explore what happens when the rotation axis intersects the strange attractor. This is done at five levels of detail:

- Strange attractors
- Branched manifolds
- Transition matrices
- Return maps
- Periodic orbits

In particular, we will discuss a new type of global bifurcation. This occurs as the axis about which the rotation symmetry $\mathcal{R}_Z(\pi)$ is exhibited sweeps across the strange attractor. This is called a "peeling bifurcation" because of the deformation that is induced in the flow in the neighborhood of the rotation singularity.

5.1 STRUCTURAL STABILITY

"Structural stability" is a sophisticated mathematical concept with an intuitively simple interpretation. It means, roughly but accurately, that quantitatively small perturbations have quantitatively small consequences [32]. In particular, quantitatively small perturbations have no *qualitative* consequences.

For the cases at hand, structural stability has the following meaning and consequences. For an image system with horseshoe dynamics, choose the w-axis to go through the "hole in the middle," as shown for the axis labeled $(1,1)$ in Fig. 4.2. The two-fold cover with rotation symmetry $\mathcal{R}_Z(\pi)$ about the $Z = w$-axis is shown in Fig. 4.3(d). If we perturb the w-axis in Fig. 4.2 slightly, the 2-fold cover in Fig. 4.3(d) will be slightly perturbed, but not qualitatively changed. Such quantitative perturbations produce no qualitative changes. In particular, there are no changes in: the number of periodic orbits; the topological organization of these orbits; or the transition matrix. We say that the lift of the branched manifold in Fig. 4.2 using the w-axis labeled $(1,1)$ to the double cover shown in Fig. 4.3(d) is *structurally stable*.

The same arguments apply to lifts using the other axes in Fig. 4.2. The lift using axis $(0,0)$ to the double cover with index $(n_0, n_1) = (0,0)$ in Fig. 4.3(a) is structurally stable.

If there is a gap in the attractor, as shown for the branched manifold in Fig. 4.2, then an axis passing through this gap will generate a double cover in a structurally stable way. That is, sufficiently small perturbations of the rotation axis will remain in the gap and the double cover will not be qualitatively changed by the perturbation. The gap between the branches 0, 1 in the branched manifold in Fig. 4.2 allows the construction of the two inequivalent double covers with indices $(n_0, n_1) = (0,1)$ [Fig. 4.3(b)] and $(1,0)$ [Fig. 4.3(c)].

However, for typical strange attractors, such as the Rössler attractor, gaps are hard to find (i.e., don't usually exist) between orbit sequences that project to different branches under the Birman-Williams projection. In these cases the double covers, such as $(0,1)$ and $(1,0)$, are not structurally stable.

The four double covers of the two-branched manifold (Fig. 4.2) with topological indices $(n_0, n_1) = (0,0),\ (0,1),\ (1,0),\ (1,1)$ can be regarded as structurally stable limits in a continuous series of covers of this manifold in which the $w = Z$ rotation axis is allowed to sweep across the attractor. We study the "perestroika" (unfolding, transition [32]) of these double covers in the remainder of this chapter.

5.2 THE PERESTROIKA FROM (1,1) TO (0,1)

In this section we investigate the perestroika that occurs as the rotation axis moves from the structurally stable limit $(1,1)$ to the structurally stable limit $(0,1)$. The progression of the rotation axis from the inside to the outside of the attractor is quantitatively described by a real number f (cf. Fig. 5.1). Inside the attractor $f = 0$. Outside, $f = 1$. In the hole between branches 0 and 1, $f = \frac{1}{2}$.

5.2.1 Branched Manifolds

In Fig. 5.1(a) we show a branched manifold for a dynamical system that exhibits horseshoe dynamics. The w-axis is shown intersecting branch 0 in this branched manifold. In Fig. 5.1(b) we show the double cover of this branched manifold. The double cover is structurally unstable.

In the structurally stable double cover with topological index $(n_0, n_1) = (1,1)$, the branch line l is the source for initial conditions that flow through branches $\hat{0}_l$ and $\hat{1}_l$ to branch line r. Similarly, branch line r feeds branch line l. When the rotation axis is moved into branch 0 of the horseshoe template, the rotation axis Z intersects flows whose initial conditions are on the half branch lines 0_l and 0_r in the double cover and $0 < f < \frac{1}{2}$. The rotation axis splits the flow whose initial conditions are on 0_l into two subbranches. One, $\bar{0}_l$, is the source for a flow that returns to branch line l. The remainder, $\hat{0}_l$, provides initial conditions that continue to flow to branch line r. The split between the two subbranches, $\bar{0}_l, \hat{0}_l$ is marked by the point f on the branch line 0_l. This point is the initial condition on the branch line that flows to the singular rotation axis. This flow is shown by a dashed curve in Fig. 5.1(b). The location of the rotation axis is indicated by an $\times$ in this figure. By symmetry, similar

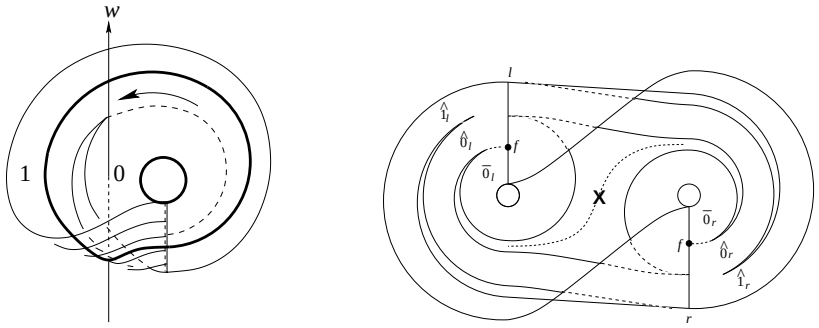

(a) Horseshoe branched manifold (b) Double cover of (a)

Fig. 5.1 (a) Horseshoe branched manifold. The w-axis intersects branch 0. (b) Double cover of (a). Branches $0_l, 0_r$ are each split into two subbranches: $0_l \to \bar{0}_l, \hat{0}_l$ and $0_r \to \bar{0}_r, \hat{0}_r$. The points f are initial conditions in the half branch lines $0_l, 0_r$ that flow to the singularity at the location of the Z rotation axis.

remarks hold for branch line r. The number $2f$, $0 \leq 2f \leq 1$, represents the fraction of initial conditions that return to the source branch line. For $f = 0$, there is no flow through subbranches $\bar{0}_l, \bar{0}_r$ while for $f = \frac{1}{2}$ there is no flow through the subbranches $\hat{0}_l, \hat{0}_r$. The value of f for orbits up to period 6 in structurally unstable covers of the Rössler attractor is given in the left half of Table 5.1 [65].

Table 5.1 Periodic points of period less than 6 for the orbits embedded within the chaotic Rössler attractor for $(a, b, c) = (0.43295, 2.0, 4.0)$. The symbol name of each periodic orbit is listed under S. The fraction of periodic points that return to the source branch line 0_l, 0_r in the cover is $2f$, $0 \leq f \leq \frac{1}{2}$ (left columns). The fraction that returns to the source line 1_l, 1_r is $2(f - \frac{1}{2})$, $\frac{1}{2} \leq f \leq 1$ (right columns). The coordinate y_n in the Poincaré section is also given.

S	y_n	f	S	y_n	f
0	−0.0032	0.0192	11000	−2.7936	0.5192
00001	−0.1382	0.0384	1100	−2.9270	0.5384
00011	−0.1632	0.0576	11001	−2.9817	0.5576
0001	−0.3421	0.0769	110	−3.1522	0.5769
00010	−0.3601	0.0961	11011	−3.1902	0.5961
00011	−0.4255	0.1153	1101	−3.2155	0.6153
0011	−0.4485	0.1346	11010	−3.2911	0.6346
00111	−0.6175	0.1538	11011	−3.5096	0.6538
00101	−0.6920	0.1730	1	−3.5850	0.6730
001	−0.8208	0.1923	1110	−3.7368	0.6923
0010	−0.8930	0.2115	11110	−3.7466	0.7115
00100	−0.9397	0.2307	11100	−3.8248	0.7307
00110	−1.1097	0.2500	10100	−4.1071	0.7500
0011	−1.1693	0.2692	10110	−4.1698	0.7692
011	−1.2731	0.2884	10	−4.2028	0.7884
01101	−1.3392	0.3076	1011	−4.2892	0.8076
01111	−1.4481	0.3269	10111	−4.3258	0.8269
0111	−1.5688	0.3461	10110	−4.3586	0.8461
01110	−1.6183	0.3653	101	−4.3783	0.8653
01010	−1.7912	0.3846	100	−4.5124	0.8846
01	−1.8566	0.4038	10010	−4.5494	0.9038
01011	−1.9555	0.4230	10011	−4.5720	0.9230
010	−2.1139	0.4423	1001	−4.6193	0.9423
01001	−2.1531	0.4615	1000	−4.6533	0.9615
0100	−2.2862	0.4807	10001	−4.7046	0.9807
01000	−2.3983	0.5000	10000	−4.7132	1.0000

5.2.2 Transition Matrices

The transition matrices for the branched manifold shown in Fig. 5.1(a) is a 6×6 matrix:

		$2f$ $\bar{0}_l$	$1-2f$ $\hat{0}_l$	$\hat{1}_l$	$2f$ $\bar{0}_r$	$1-2f$ $\hat{0}_r$	$\hat{1}_r$
$2f$	$\bar{0}_l$	1	1	1			
$1-2f$	$\hat{0}_l$				1	1	1
	$\hat{1}_l$				1	1	1
$2f$	$\bar{0}_r$				1	1	1
$1-2f$	$\hat{0}_r$	1	1	1			
	$\hat{1}_r$	1	1	1			

$f = 0 \swarrow (1,1)$ $\qquad$ $(0,1) \searrow f = \dfrac{1}{2}$

	$\hat{0}_l$	$\hat{1}_l$	$\hat{0}_r$	$\hat{1}_r$
$\hat{0}_l$			1	1
$\hat{1}_l$			1	1
$\hat{0}_r$	1	1		
$\hat{1}_r$	1	1		

	$\bar{0}_l$	$\hat{1}_l$	$\bar{0}_r$	$\hat{1}_r$
$\bar{0}_l$	1	1		
$\hat{1}_l$			1	1
$\bar{0}_r$			1	1
$\hat{1}_r$	1	1		

The 6×6 transition matrix for the 6-branch manifold is expressed in terms of f. In the limit $f = 0$, the rows and columns $\bar{0}_l, \bar{0}_r$ can be eliminated from the 6×6 transition matrix, and the 4×4 transition matrix for the double cover with topological index $(n_0, n_1) = (1,1)$ is recovered. In the same way, in the limit $2f = 1$, the rows and columns $\hat{0}_l, \hat{0}_r$ can be eliminated from the 6×6 transition matrix, and the 4×4 matrix for the double cover with $(n_0, n_1) = (0,1)$ is recovered.

5.2.3 Return Maps

The first-return map for the 6×6 branched manifold shown in Fig. 5.1(b) is shown in Fig. 5.2. This figure is constructed as follows. The first-return map for the double cover with topological index $(n_0, n_1) = (1,1)$ is constructed [Fig. 4.5(d)]. In the return map initial conditions on branch line l flow to r, and vice versa. In the structurally unstable double cover the parts of the two branch lines l, r labeled 0 are separated by the point f. The part of the return map above $\bar{0}_l$ is moved down, from the branch line r to branch line l. This is indicated by the downward pointing arrow. Similarly, the part of the return map over $\bar{0}_r$ is moved upward from the branch line l to the branch line r. In the limits $f \to 0$ and $f \to \frac{1}{2}$, we recover the first-return maps for the structurally stable double covers with topological indices $(n_0, n_1) = (1,1)$ [Fig. 4.5(d)] and (0,1) [Fig. 4.5(b)].

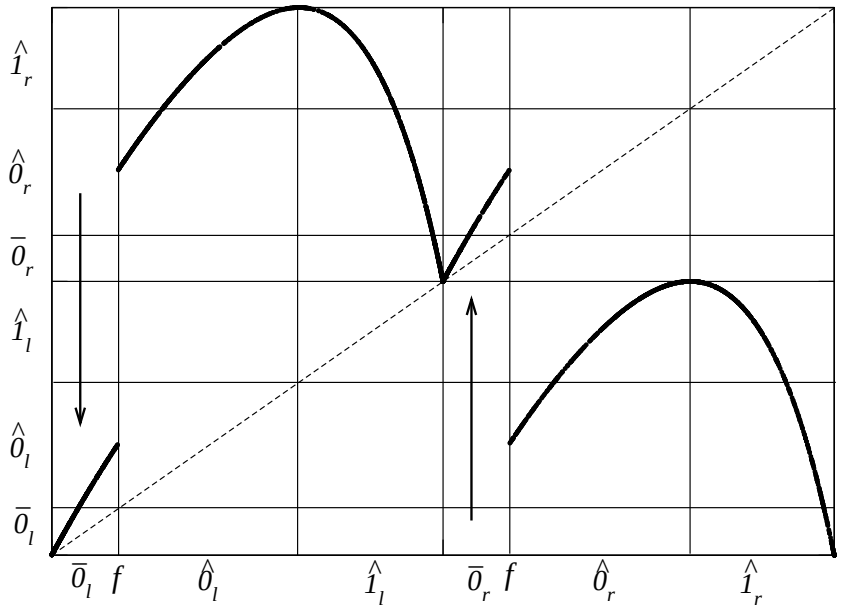

Fig. 5.2 Return map for the branched manifold in Fig. 5.1(b). It is obtained from the return map for the structurally stable double cover with topological index $(n_0, n_1) = (1, 1)$ by moving the part of the return map over $\bar{0}_l$ from branch r to branch l (downward arrow), and similarly for $\bar{0}_r$ (upward arrow).

5.2.4 Periodic Orbits

Moving the rotation axis w across the image dynamical system has absolutely no effect on the image dynamics. However, there is a profound effect in the cover. In particular, lifts of periodic orbits in the cover are dramatically rearranged as the rotation axis (Z) traverses the orbit in the cover.

We illustrate the nature of this reorganization by example. We choose the period-5 orbit 00101 in the image horseshoe template. This lifts to the period-10 orbit in the double cover $(n_0, n_1) = (1, 1)$:

$$00101 \longrightarrow \hat{0}_l\hat{0}_r\hat{1}_l\hat{0}_r\hat{1}_l\ \hat{0}_r\hat{0}_l\hat{1}_r\hat{0}_l\hat{1}_r \tag{5.1}$$

As the rotation axis is moved from the center to the gap between branches 0 and 1 in the image branched manifold, it will cut the image orbit three times. In general, it is not possible to predict the order in which the axis will intersect the three segments labeled 0 in the period-5 orbit. However, in the highly dissipative limit the order of these segments is prescribed by U-Sequence Theory [34]. The axis meets the segments in the order (a, b, c, d):

$$\begin{array}{ccccccccccc} & & 00101 & & 01010 & & 01001 & & 10100 & & 10010 \\ a & \bullet & & b & \bullet & c & \bullet & d & \bullet & & \bullet \end{array} \tag{5.2}$$

The locations a, b, c, d of the rotation axis are shown in Fig. 5.3 by a small $\times$. This gives rise to the following orbit rearrangement in the double cover

$w-$axis	Orbit
a	$\hat{1}_r\hat{0}_l\hat{0}_r\hat{1}_l\hat{0}_r\hat{1}_l\hat{0}_r\hat{0}_l\hat{1}_r\hat{0}_l$
b	$\hat{1}_r\bar{0}_l\hat{0}_l\hat{1}_r\hat{0}_l \ + \ \hat{1}_l\bar{0}_r\hat{0}_r\hat{1}_l\hat{0}_r$
c	$\hat{1}_r\bar{0}_l\bar{0}_l\hat{1}_l\hat{0}_r\hat{1}_l\bar{0}_r\bar{0}_r\hat{1}_r\hat{0}_l$
d	$\hat{1}_r\bar{0}_l\bar{0}_l\hat{1}_l\bar{0}_r \ + \ \hat{1}_l\bar{0}_r\bar{0}_r\hat{1}_r\bar{0}_l$

(5.3)

As the w-axis cuts successive segments of the period-5 orbit 00101 in the image, its covering orbit alternates successively between a symmetric period-10 orbit and a symmetric pair of asymmetric period-5 orbits in a regular and predictable way. These orbits in the cover are shown in Fig. 5.3.

5.3 THE PERESTROIKA FROM (0,1) TO (0,0)

The perestroika described in the previous section can be continued beyond the gap between branches 0 and 1 in the image dynamical system. In this section we describe the perestroika that takes place between the two structurally stable limits with $(n_0, n_1) = (0, 1)$ and $(0, 0)$. This occurs as the rotation axis w moves across the branch labeled 1 in the image dynamical system, and the fraction f increases from $\frac{1}{2}$ to 1.

5.3.1 Branched Manifolds

In Fig. 5.4(a) we show the horseshoe branched manifold, together with a rotation axis through the branch labeled 1 in this branched manifold. The branched manifold for the structurally unstable double cover is shown in Fig. 5.4(b). In this branched manifold the (semi)flow originating on the parts $\bar{0}_l, \bar{0}_r$ of the left and right branch lines is unaffected by the location of the Z-axis. However, the half branch lines $1_l, 1_r$ are split into two subbranches $\bar{1}_l, \hat{1}_l$ and $\bar{1}_r, \hat{1}_r$. As the rotation axis is moved from the gap between branches 0 and 1 ($f = \frac{1}{2}$) to outside the image attractor ($f = 1$), the size of the branches $\bar{1}_l, \bar{1}_r$ increases from 0 while the size of the branches $\hat{1}_l, \hat{1}_r$ decreases to 0. The point f along the parts $1_l, 1_r$ of the branch lines l, r is the initial condition on the branch line that flows to the singularity presented by the Z rotation axis. As before, $f = \frac{1}{2}$ and $f = 1$ are two structurally stable limits $(n_0, n_1) = (0, 1)$ and $(0, 0)$.

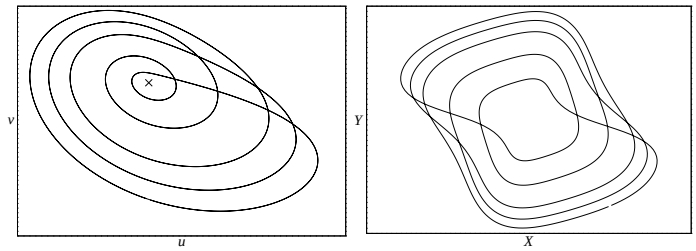

(a) Location a: $\mu = 0.0$

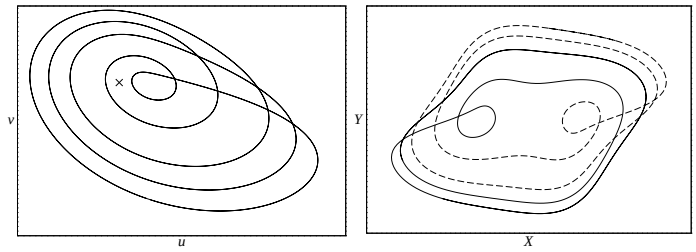

(b) Location b: $\mu = -0.90$

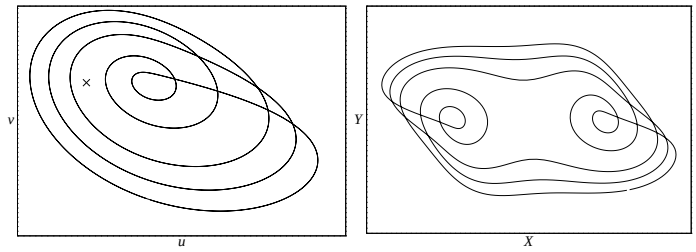

(c) Location c: $\mu = -1.90$

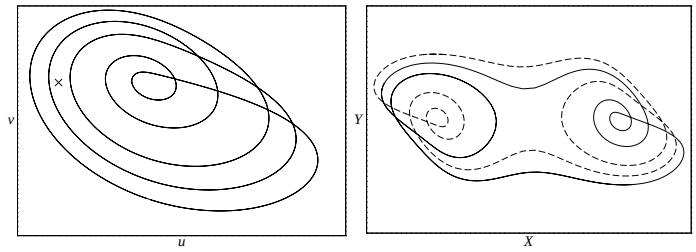

(d) Location d: $\mu = -2.75$

Fig. 5.3 Perestroika of the double cover of 10010. As the rotation axis sweeps past the three segments labeled 0 in this orbit, major changes in the topology of the orbit take place. (a) – (d) correspond to lines (a) – (d) in Eq. (5.3). These periodic orbits were obtained by integrating Eqs. (5.8) and (5.9).

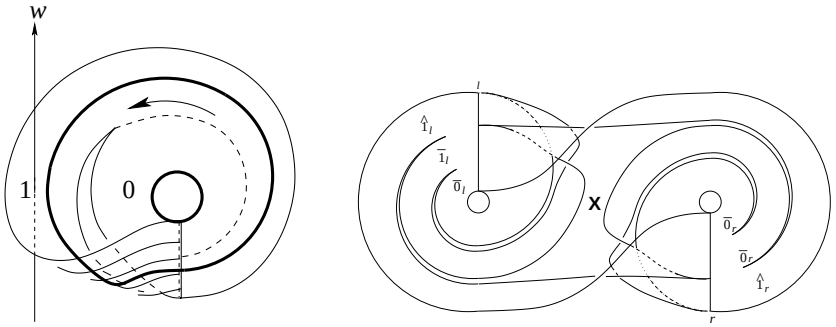

(a) Horseshoe branched manifold (b) Double cover of (a)

Fig. 5.4 (a) Horseshoe branched manifold. The w-axis intersects branch 1. (b) Double cover of (a). Branches $1_l, 1_r$ are each split into two subbranches: $1_l \to \bar{1}_l, \hat{1}_l$ and $1_r \to \bar{1}_r, \hat{1}_r$. The points f are initial conditions in the half branch lines $1_l, 1_r$ that flow to the singularity at the location of the Z rotation axis.

5.3.2 Transition Matrices

The transition matrix for the 6 branch covering template shown in Fig. 5.4(b) is

		$\bar{0}_l$	$2f-1$ $\bar{1}_l$	$2(1-f)$ $\hat{1}_l$	$\bar{0}_r$	$2f-1$ $\bar{1}_r$	$2(1-f)$ $\hat{1}_r$
	$\bar{0}_l$	1	1	1			
$2f-1$	$\bar{1}_l$	1	1	1			
$2(1-f)$	$\hat{1}_l$				1	1	1
	$\bar{0}_r$				1	1	1
$2f-1$	$\bar{1}_r$				1	1	1
$2(1-f)$	$\hat{1}_r$	1	1	1			

$$f = \frac{1}{2} \swarrow (0,1) \qquad (0,0) \searrow f = 1$$

	$\bar{0}_l$	$\hat{1}_l$	$\bar{0}_r$	$\hat{1}_r$
$\bar{0}_l$	1	1		
$\hat{1}_l$			1	1
$\bar{0}_r$			1	1
$\hat{1}_r$	1	1		

	$\bar{0}_l$	$\bar{1}_l$	$\bar{0}_r$	$\bar{1}_r$
$\bar{0}_l$	1	1		
$\bar{1}_l$	1	1		
$\bar{0}_r$			1	1
$\bar{1}_r$			1	1

In the limits $f \to \frac{1}{2}$ and $f \to 1$ the transition matrices for the double covers with indices $(n_0, n_1) = (0,1)$ and $(0,0)$ are recovered, as shown.

5.3.3 Return Maps

The return map for the 6-branched manifold shown in Fig. 5.4(b) is presented in Fig. 5.5. This return map is constructed following the procedure used to construct the return map shown in Fig. 5.2. The return map for the structurally stable 4-branched manifold with $(n_0, n_1) = (0, 1)$ is modified by dividing the branches $1_l, 1_r$ into two parts each: $1_l \rightarrow \bar{1}_l, \hat{1}_l$ and $1_r \rightarrow \bar{1}_r, \hat{1}_r$. The division is indicated by the point labeled f. Parts of the return map originating from $\bar{1}_l$ flow back to the branch line l. Therefore that part of the return map of the branched manifold $(0, 1)$ over $\bar{0}_l$ is moved from branch line r to branch line l. This is shown by the downward arrow in Fig. 5.5. The same arguments are used for the part of the return map over $\bar{1}_r$ (upward arrow). The return map shown in Fig. 5.5 interpolates between the return map for the 4-branch manifold with topological index $(n_0, n_1) = (0, 1)$ [Fig. 4.5(b)] and the return map for the disconnected double cover with $(n_0, n_1) = (0, 0)$ [Fig. 4.5(a)].

5.3.4 Periodic Orbits

As the rotation axis continues to cross branch 1 of the image dynamical system, it will intersect segments of periodic orbits labeled by the symbol 1. Once again the order in

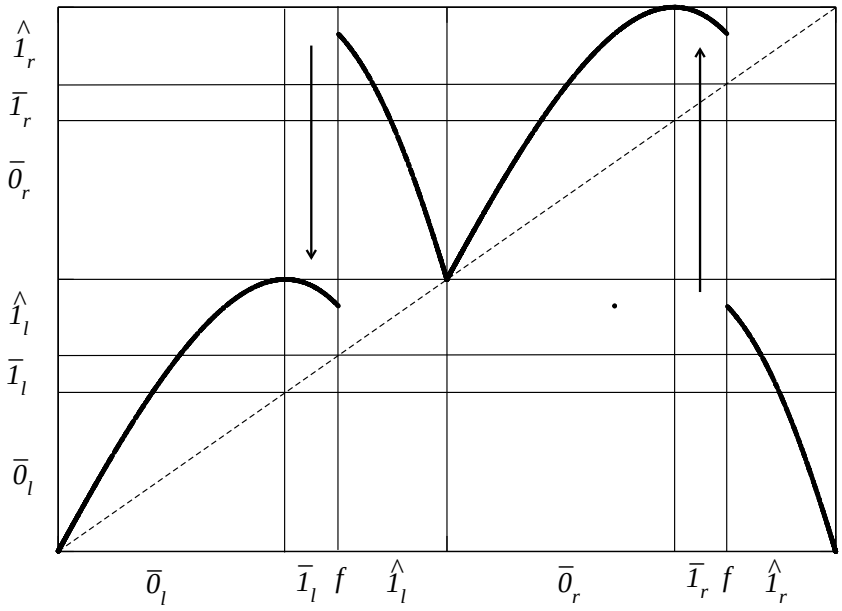

Fig. 5.5 Return map for the branched manifold in Fig. 5.4(b). It is obtained from the return map for the structurally stable double cover with topological index $(n_0, n_1) = (0, 1)$ by moving the part of the return map over $\bar{1}_l$ from branch r to branch l (downward arrow), and similarly for $\bar{1}_r$ (upward arrow).

which these segments are intersected depends on the (dissipation of the) dynamical system. In the highly dissipative limit the order is prescribed by U-Sequence Theory. For the period-5 orbit 10010 this order is alphabetical, as shown.

$$\begin{array}{ccccccccc} 00101 & & 01010 & & 01001 & & 10100 & & 10010 \\ \bullet & & \bullet & & \bullet & d & \bullet & e & \bullet & f \end{array} \tag{5.4}$$

The locations of the rotation axis corresponding to d, e, and f are shown in Fig. 5.6 by $\times$. The orbit reorganization that occurs in the perestroika as f increases from $\frac{1}{2}$ to 1 is

w-axis	Orbit
d	$\hat{1}_r\bar{0}_l\bar{0}_l\hat{1}_l\bar{0}_r \ + \ \hat{1}_l\bar{0}_r\bar{0}_r\hat{1}_r\bar{0}_l$
e	$\hat{1}_r\bar{0}_l\bar{0}_l\bar{1}_l\bar{0}_l\hat{1}_l\bar{0}_r\bar{0}_r\bar{1}_r\bar{0}_r$
f	$\bar{1}_r\bar{0}_r\bar{0}_r\bar{1}_r\bar{0}_r \ + \ \bar{1}_l\bar{0}_l\bar{0}_l\bar{1}_l\bar{0}_l$

(5.5)

This completes our study of the perestroika of orbits. The rearrangement in the orbits that cover 00101 in the horseshoe during the perestroika leading from the cover $(1,1)$ through the cover $(0,1)$ to the disconnected cover $(0,0)$ is shown in two parts. The first part, the transition from (1,1) to (0,1), is shown in Eq. (5.3) and Fig. 5.3. The second part, the transition from (0,1) to (0,0), is shown in Eq. (5.5) and Fig. 5.6.

5.4 STRUCTURALLY UNSTABLE STRANGE ATTRACTORS

A one-parameter family of double covers of the Rössler attractor exhibits all of the bifurcations described in Sections 5.2 and 5.3.

In order to exhibit these bifurcations we first displace the origin of coordinates of the Rössler attractor, $(u,v,w) \to (u+u_0, v+v_0, w+w_0)$. In this coordinate system the equations of motion are

$$\begin{array}{rcl} \dot{u} &=& -v-w \qquad\qquad\qquad\qquad - \quad v_0 - w_0 \\ \dot{v} &=& u+av \qquad\qquad\qquad\qquad + \quad u_0 + av_0 \\ \dot{w} &=& b+w(u+u_0-c)+w_0u \quad + \quad w_0(u_0-c) \end{array} \tag{5.6}$$

Next, we choose the origin at the fixed point at the center of the "hole in the middle."

$$u_0 = -av_0 = aw_0 = (c-\sqrt{c^2-4ab})/2$$

With this new choice of origin the equations are

$$\begin{array}{rcl} \dot{u} &=& -v-w \\ \dot{v} &=& u+av \\ \dot{w} &=& \tilde{b}u+w(u-\tilde{c}) \end{array} \tag{5.7}$$

where $\tilde{b}=w_0$ and $\tilde{c}=c-u_0$.

We would like to construct double covers of this attractor by choosing a rotation axis parallel to the w-axis passing through the point $(\mu,0)$ in the (u,v) plane. Rather

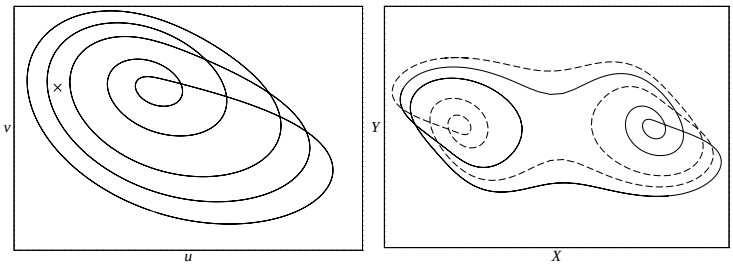

(a) Location d: $\mu = -2.75$

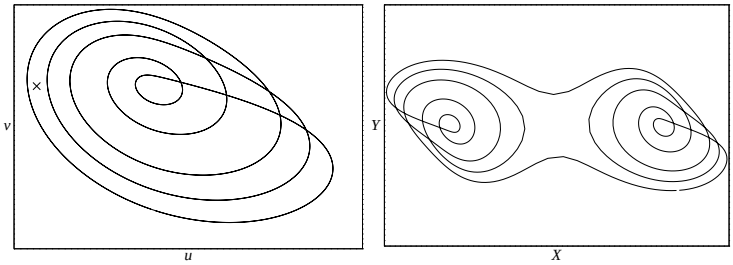

(b) Location e: $\mu = -3.35$

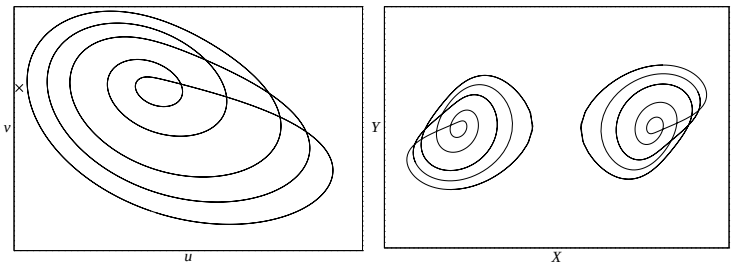

(c) Location f: $\mu = -3.85$

Fig. 5.6 Perestroika of the double cover of 10010. As the rotation axis sweeps past the two segments labeled 1 in this orbit, major changes in the topology of the orbit take place. (d) – (f) correspond to lines (d) – (f) in Eq. (5.5). These periodic orbits were obtained by integrating Eqs. (5.8) and (5.9).

than do this, we displace the attractor to this point and construct a double cover with $\mathcal{R}_Z(\pi)$ symmetry about the w-axis. The image equations are

$$\begin{aligned} \dot{u} &= -v - w \\ \dot{v} &= u + av + \mu \\ \dot{w} &= \tilde{b}(u + \mu) + w(u - \tilde{c} + \mu) \end{aligned} \tag{5.8}$$

The covering equations are

$$\begin{aligned} \dot{X} &= \frac{1}{2r^2}\left[-r^2 Y + X\left(2aY^2 - Z\right) + \mu Y\right] \\ \dot{Y} &= \frac{1}{2r^2}\left[r^2 X + Y\left(2aX^2 + Z\right) + \mu X\right] \\ \dot{Z} &= \tilde{b}\left(X^2 - Y^2 + \mu\right) + Z\left(X^2 - Y^2 - \tilde{c} + \mu\right) \end{aligned} \tag{5.9}$$

where $r^2 = X^2 + Y^2$.

The image equations (5.7) are integrated for standard values $(a, b, c) = (0.432, 2.0, 4.0)$ of the control parameters. This image is shown in Fig. 5.7. The double cover equations (5.9) were integrated for the same standard values and a sequence of different values of the displacement parameter μ. These μ values are also indicated in Fig. 5.7. For $\mu = 0$ the double cover is structurally stable with topological index $(n_0, n_1) = (1, 1)$. For μ large the double cover is structurally stable and disconnected, with topological index $(0, 0)$. As μ changes from zero to large (and negative) the double cover becomes structurally unstable and undergoes a series of bifurcations. The results are summarized in Fig. 5.8. In the top row we show double covers with four branches and topological indices $(n_0, n_1) = (1, 1)$ [(a), $\mu = 0.0$], (0,1) [(c), $\mu = -2.083$], and (0,0) [(e), $\mu = -4.166$]. In the second row, below and between the structurally stable strange attractors, are structurally unstable attractors with six branches. The attractor (b) ($\mu = -0.84548$) interpolates between the limits $(n_0, n_1) = (1, 1)$ and (0,1) while the other attractor (d) ($\mu = -3.14674$) interpolates between the limits $(n_0, n_1) = (0, 1)$ and (0,0).

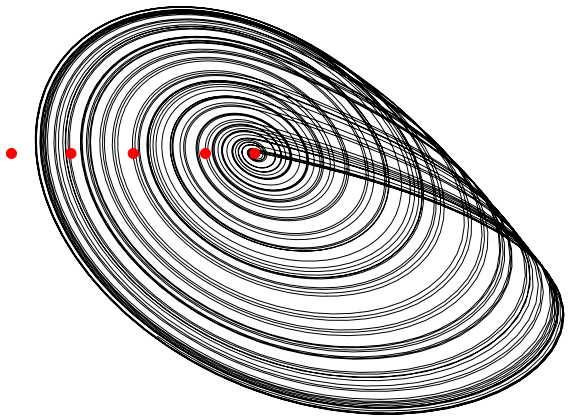

Fig. 5.7 Projections of the Rössler attractor with control parameter values $(a, b, c) = (0.432, 2, 4)$. Also shown are the five values of $\mu = 0.0$, $\mu = -0.84548$, $\mu = -2.083$, $\mu = -3.14674$, and $\mu = -4.166$ (represented by circles from right to left) at which the double covers shown in Fig. 5.8 are computed.

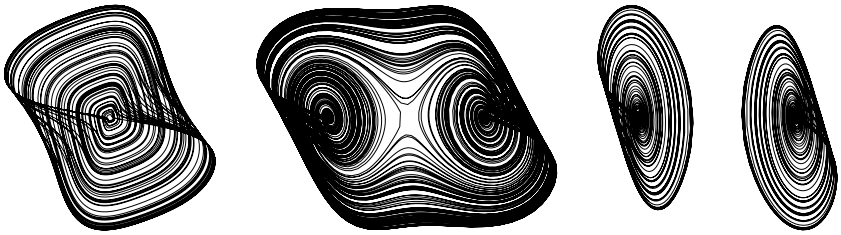

(a) $\mu = 0.0$ (b) $\mu = -2.083$ (c) $\mu = -4.166$

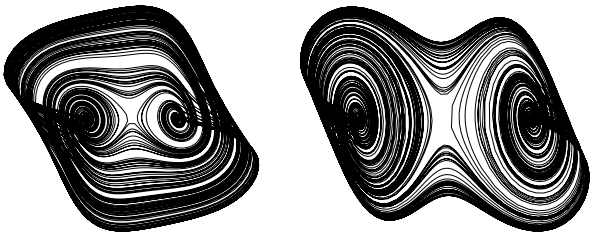

(d) $\mu = -0.84548$ (e) $\mu = -3.14674$

Fig. 5.8 Five double cover strange attractors for the Rössler equations (5.7) with $\mathcal{R}_Z$ symmetry. These are obtained by displacing the origin of coordinates along the u-axis. (a), (c), (e) are 4-branch, structurally stable double covers. (b), (d) are structurally unstable 6-branch double covers. The structurally unstable double covers interpolate between the two structurally stable double covers above them.

We emphasize again that the placement of the w-axis has no effect on the nature of the flow in the image dynamical system. The bifurcation takes place only in the covering dynamical system: The image remains unperturbed during displacement of the symmetry axis. The bifurcation is caused by sweeping a splitting axis (the symmetry axis) through the covering flow from the inside to the outside of the flow.

5.5 THE PEELING BIFURCATION

The "peeling bifurcation" gets its name from the deformation induced in the flow by the splitting (rotation) axis. This deformation can be seen clearly in Fig. 5.8(d). A schematic representation is presented in Fig. 5.9. This figure shows that the flow is split by the singularity. The part of the flow passing to the left of the axis flows to the neighborhood of the focus on the left. That part of the flow passing to the right of the singularity remains in the neighborhood of the focus on the right, shown as a small circle. The flow passes around the focus, moves underneath the part of the flow that passed to the left of the splitting axis, and joins it at a branch line.

This is the type of deformation that an apple skin experiences when it is peeled from an apple. Hence the descriptive title: "peeling bifurcation."

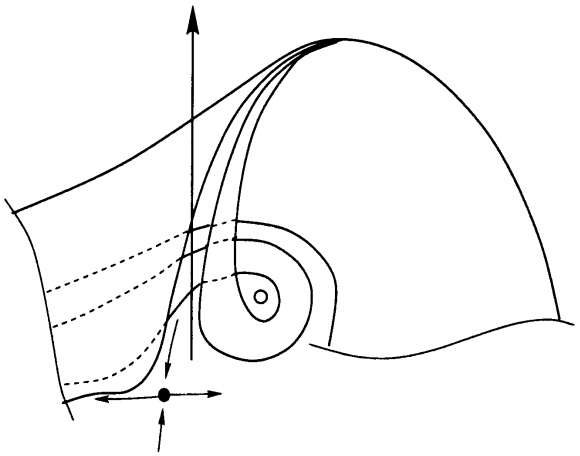

Fig. 5.9 Schematic representation of the flow in the neighborhood of the rotation axis. The deformation is the same as that experienced by the skin of an apple when it is peeled.

Peeling bifurcations annihilate branches one pair at a time, and create new branches, one pair at a time. They are therefore responsible for massive orbit extinctions. When a pair of branches is annihilated, all orbits carrying a symbol for either branch must be annihilated. Nevertheless, the orbits themselves are not destroyed—they are simply required to visit a new branch. During the entire peeling bifurcation, orbits are simply "rearranged" in the covering dynamical system as seen in Figs. 5.3 and 5.6. This occurs in such a way that the topological entropy remains unchanged during the bifurcation.

5.6 APPLICATION: SUNSPOT COVERS

We illustrate the usefulness of the peeling bifurcation by returning to the sunspot data (cf., Section 1.1). In that brief description we stated that the observables were the sunspot numbers but the physics driving this phenomenon seems to be magnetic field strength. We illustrate in this Section one possible way to recover information that is "squared away" from observed data.

The sunspot data are reproduced in Fig. 5.10. A solid curve representing a smoothing of the data is superposed on the data. We will work with the smoothed data. The smoothing was obtained as follows. First, a monthly averaged sunspot number is computed for each month in the sample. This average is computed using the Wolf index $R(t) = k(10g + f)$, where g counts the number of sunspot groups and f counts the number of individual sunspots per month. The factor k is a normalization term. Compensations must be made for the problem that the data are not of uniform quality going back to the year 1750—a significant improvement in the quality of the recorded data occurred in 1850. The description of these compensations is contained in [62].

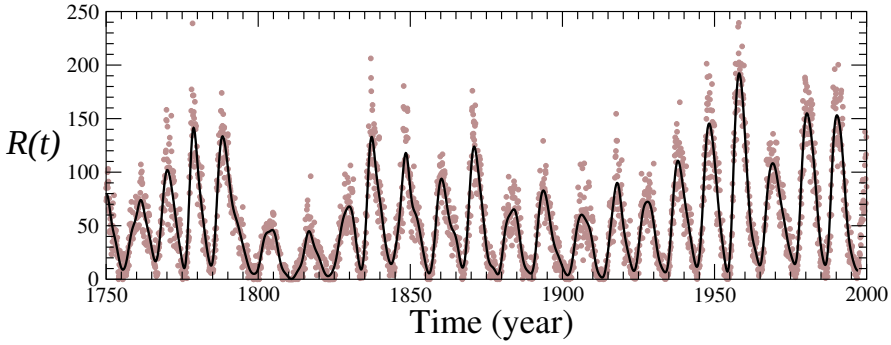

Fig. 5.10 Dots: monthly averaged sunspot data using Wolf's index. Solid curve: data smoothed using a low-pass filter followed by a 30-month moving window average.

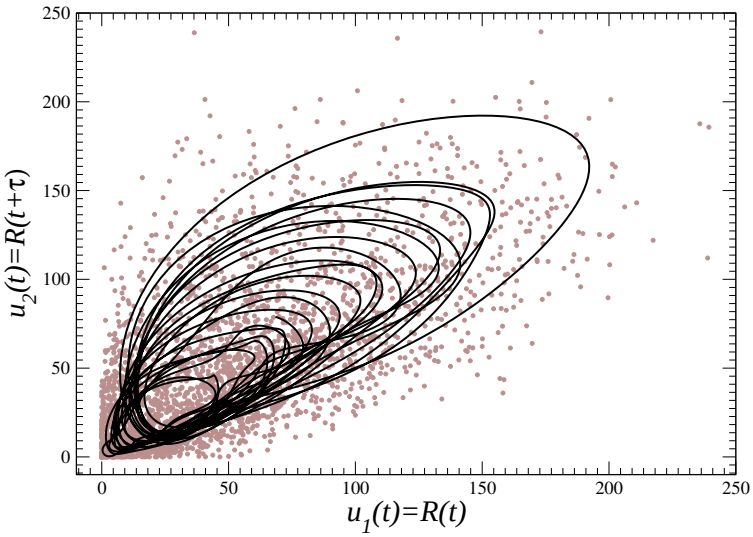

Fig. 5.11 Time-delay embedding of the smoothed scalar time series shown in Fig. 5.10 with delay $\tau = 16$ months. There are 23 cycles since 1750. Monthly Wolf index values are also shown in this projection.

The monthly averaged data showed high-frequency fluctuations, which were removed with a low-pass filter using standard Fourier techniques. The filtered data were further smoothed by using a moving window average with width w_s, where w_s was chosen as 30 months (about a quarter of the 11-year cycle) to produce the solid curve shown in Fig. 5.10. Efforts were taken to ensure that the results presented below are not artifacts of the filtering-smoothing procedures.

In order to carry out a dynamical analysis the scalar time series must be embedded in a phase space of suitable dimension. The default embedding procedure was used—this is the time delay. A projection of the time delay embedding onto the first two

coordinates is shown in Fig. 5.11. The time delay used is $\tau = 16$ months. This projection is superposed on a projection of the unsmoothed data (gray dots). The projected time series using this embedding exhibits a "hole in the middle" so that a Poincaré section can easily be constructed. Further tests (false nearest neighbor test [1], correlation dimension estimate [95], self-intersection test [126]) revealed that three dimensions suffice for an embedding of this time series.

A series of double covers of the attractor shown in Fig. 5.11 is presented in Fig. 5.12. These covers all possess rotation invariance under $\mathcal{R}_Z(\pi)$. To construct these covers the rotation axis was moved from the origin in Fig. 5.12(a), into the attractor in Fig. 5.12(b), and finally into the hole in the middle of the attractor in Fig. 5.12(c). If X or Y or some reasonable linear combination is taken as a representation of the magnetic field, these three covers show the field is confined to positive (or negative) values for the double cover in Fig. 5.12(a), shows "unpredictable" alternation between positive and negative values during alternating 11-year cycles in Fig. 5.12(b), and predictable alternation after every 11-year cycle in Fig. 5.12(c).

The X and Y coordinates of the double cover with index $(n_0, n_1) = (1, 1)$ can be used to represent the magnetic field responsible for generating sunspots. We choose $B(t) = X\cos(\theta) + Y\sin(\theta)$, with $\theta = \pi/4$ radians to project onto the diagonal, to represent $B(t)$ for the cover constructed in Fig. 5.12(c), since this is the only cover that guarantees alternation of the magnetic field after each 11-year sunspot

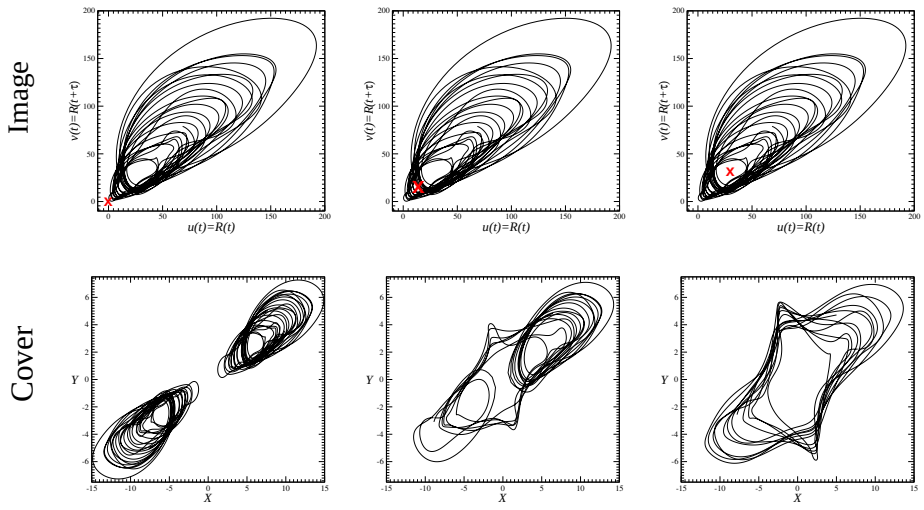

(a) $u_0 = 0$ (b) $u_0 = 15$ (c) $u_0 = 30$

Fig. 5.12 Different topologically inequivalent covers of the phase portrait reconstructed from the sunspot numbers using the delay coordinates. The location of the singularity—indicated by the $\times$ — is displaced in the plane $\mathbb{R}^2(u, v)$ along the bisecting line.

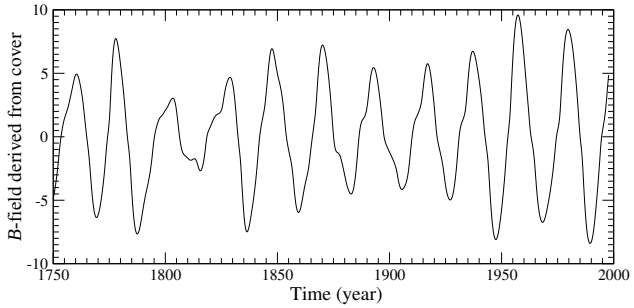

Fig. 5.13 Plot of $B(t) = X\cos(\theta) + Y\sin(\theta)$ for the cover shown in Fig. 5.12(c). Another trace that is the reflection image ($B(t) \to -B(t)$) is also possible. For this plot $\theta = \pi/4$.

cycle. The results are shown in Fig. 5.13. Since delay coordinates have been used to construct an embedding, rather than coordinates depending on a specific time (such as differential coordinates), it is not straightforward to synchronize features of the sunspot data (maxima and minima) with corresponding features of the $B(t)$ curve, such as maxima, minima, and zero-crossings.

6

Three-Fold and Four-Fold Covers

6.1 IMAGE DYNAMICAL SYSTEMS

In this chapter we will describe three-fold and four-fold covers of image dynamical systems. It is possible to numerically generate strange attractors equivariant under the groups $\mathcal{C}_3$, $\mathcal{C}_4$, and $\mathcal{V}_4$. This is done by lifting image dynamical systems without symmetry. In this section we present three canonical image dynamical systems. One is the Rössler attractor, the other two are images of equivariant dynamical systems. The strange attractors for all three dynamical systems without symmetry are shown in Fig. 6.1.

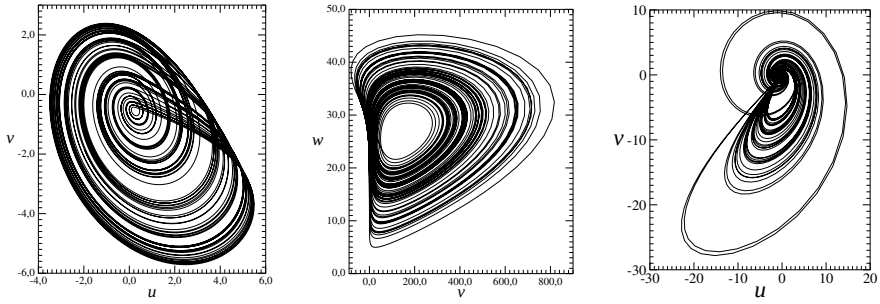

(a) Rössler system (b) Proto–Lorenz system (c) Proto–Burke and Shaw system

Fig. 6.1 Image systems. Parameter values: $(a, b, c) = (0.4332, 2.0, 4.0)$ in Equ. (6.1a); $(R, \sigma, b) = (28.0, 10.0, 8/3)$ in Eq. (6.1b); $(S, \mathcal{V}) = (10.0, 4.271)$ in Eq. (6.1c).

6.1.1 Rössler System

The centered Rössler equations used to describe the new global bifurcation (cf. Eq. (5.8)) are repeated here for convenience:

$$\begin{aligned} \dot{u} &= -v - w \\ \dot{v} &= u + av + \mu \\ \dot{w} &= \tilde{b}(u + \mu) + w(u - \tilde{c} + \mu) \end{aligned} \tag{6.1a}$$

In this set of equations the origin of coordinates has been moved to the fixed point (u_0, v_0, w_0), $\tilde{b} = w_0$, $\tilde{c} = c - u_0$, and μ is the displacement of the rotation axis along the u-axis. The Rössler attractor is shown in Fig. 6.1(a) for control parameter values $(a, b, c) = (0.432, 2.0, 4.0)$ and $\mu = 0.0$ [35].

6.1.2 Proto–Lorenz System

The proto-Lorenz equations are obtained from the Lorenz equations by modding out the symmetry in the usual way. They are (cf. Eq. 3.3)

$$\begin{aligned} \dot{u} &= (-\sigma - 1)u + (\sigma - R)v + vw + (1 - \sigma)\rho \\ \dot{v} &= (R - \sigma)u - (\sigma + 1)v - uw + (R + \sigma)\rho - \rho w \\ \dot{w} &= -bw + \tfrac{1}{2}v \end{aligned} \tag{6.1b}$$

where $\rho = \sqrt{u^2 + v^2}$. The proto-Lorenz attractor is shown in Fig. 6.1(b) for control parameter values $(R, \sigma, b) = (28, 10, 8/3)$.

6.1.3 Proto–Burke and Shaw Equations

These equations are obtained from the Burke and Shaw equations (2.5) by modding out the symmetry. They are (cf. Eq. 3.4)

$$\begin{aligned} \dot{u} &= -(S+1)u - S(1-w)v + (1-S)\rho \\ \dot{v} &= S(1-w)u - (S+1)v - S(1+w)\rho \\ \dot{w} &= \tfrac{S}{2}v + \mathcal{V} \end{aligned} \tag{6.1c}$$

The proto–Burke and Shaw attractor is shown in Fig. 6.1(c) for control paramter values $(S, \mathcal{V}) = (10, 4.271)$.

6.2 N-FOLD COVERS AND COMPLEX VARIABLES

The astute reader will have noticed by this time that there is a close connection between n-fold covers and complex variables. The relation between the coordinates X, Y in the covering space and the coordinates u, v in the image space is [67,90]

$$\begin{aligned} u_n = \quad \Re z^n = \Re(X+iY)^n = \quad \tfrac{1}{2}(z^n + \bar{z}^n) \quad &= \rho^n \cos\ n\phi \\ v_n = \quad \Im z^n = \Im(X+iY)^n = \quad \tfrac{1}{2i}(z^n - \bar{z}^n) \quad &= \rho^n \sin\ n\phi \end{aligned} \tag{6.2}$$

where $z = X + iY = \rho e^{i\phi}$. This relation can be adapted for all integer values of $n \geq 1$.

To be specific, we assume that the image equations are as usual

$$\frac{d}{dt}\begin{bmatrix} u \\ v \\ w \end{bmatrix} = \begin{bmatrix} f_1(u,v,w) \\ f_2(u,v,w) \\ f_3(u,v,w) \end{bmatrix} = \begin{bmatrix} f_1(\rho^n \cos n\phi, \rho^n \sin n\phi, Z) \\ f_2(\rho^n \cos n\phi, \rho^n \sin n\phi, Z) \\ f_3(\rho^n \cos n\phi, \rho^n \sin n\phi, Z) \end{bmatrix} \tag{6.3}$$

We have introduced a polar decomposition

$$z = X + iY = \rho e^{i\phi} \Longrightarrow u + iv = (\rho e^{i\phi})^n = \rho^n \cos n\phi + i\rho^n \sin n\phi$$

The equations for the variables X, Y are easily expressed in polar coordinates

$$\begin{aligned} \frac{d}{dt}(X+iY) &= \left(\frac{\partial z^n}{\partial z}\right)^{-1} \frac{d}{dt}(u+iv) \\ (\dot{\rho} + i\dot{\phi}\rho)e^{i\phi} &= \frac{1}{n\rho^{n-1}e^{i(n-1)\phi}}(f_1 + if_2) \end{aligned} \tag{6.4}$$

The real and imaginary parts give the dynamical equations for ρ and ϕ

$$\begin{aligned} \begin{bmatrix} \dot{\rho} \\ \rho\dot{\phi} \end{bmatrix} &= \frac{1}{n\rho^{n-1}} \begin{bmatrix} \cos n\phi & \sin n\phi \\ -\sin n\phi & \cos n\phi \end{bmatrix} \begin{bmatrix} f_1 \\ f_2 \end{bmatrix} \\ \dot{Z} \quad &= \quad f_3(\rho^n \cos n\phi, \rho^n \sin n\phi, Z) \end{aligned} \tag{6.5}$$

Example: For the Rössler equations

$$\begin{aligned} f_1(u,v,w) &= -v-w &\to& -\rho^n \sin n\phi - Z \\ f_2(u,v,w) &= u+av &\to& \rho^n \cos n\phi + a\rho^n \sin n\phi \\ f_3(u,v,w) &= b+w(u-c) &\to& b+Z(\rho^n \cos n\phi - c) \end{aligned}$$

Equations describing the three-fold covers and four-fold covers of the image dynamical systems can be obtained from (6.5) by setting $n = 3$ or 4 and expressing the result in terms of the equivariant coordinates (X, Y, Z).

The covering equations can be systematically expressed in terms of the functions $u_n = \Re(X + iY)^n$ and $v_n = \Im(X + iY)^n$, with

n	u	v
2	$X^2 - Y^2$	$2XY$
3	$X^3 - 3XY^2$	$3X^2Y - Y^3$
4	$X^4 - 6X^2Y^2 + Y^4$	$4X^3Y - 4XY^3$

(6.6)

These functions, and the function R, with $R^2 = X^2 + Y^2$, are used to construct explicit realizations of the three-fold and the four-fold covers of the Rössler, proto–Lorenz, and proto–Burke and Shaw dynamical systems.

6.2.1 Covers of the Rössler Equations

The n-fold cover of the Rössler equations simplifies to

$$\begin{aligned} \frac{d}{dt}(X+iY) &= \frac{i(X+iY)}{n} + \frac{\bar{z}^{n-1}}{nR^{2(n-1)}}(-Z+iav_n) \\ \dot{Z} &= b + Z(u_n - c) \end{aligned} \tag{6.7a}$$

For $n = 3$ and $n = 4$ the equations for X, Y, Z are

$$\begin{aligned} \dot{X} &= -\frac{Y}{3} + \frac{-u_2 Z + v_2(av_3)}{3R^4} \\ \dot{Y} &= +\frac{X}{3} + \frac{+v_2 Z + u_2(av_3)}{3R^4} \\ \dot{Z} &= b + Z(u_3 - c) \end{aligned} \tag{6.7b}$$

and

$$\begin{aligned}
\dot{X} &= -\frac{Y}{4} + \frac{-u_3 Z + v_3(a v_4)}{4R^6} \\
\dot{Y} &= +\frac{X}{4} + \frac{+v_3 Z + u_3(a v_4)}{4R^6} \\
\dot{Z} &= b + Z(u_4 - c)
\end{aligned} \tag{6.7c}$$

6.2.2 Covers of the Proto-Lorenz Equations

The n-fold cover of the proto-Lorenz equations simplifies to

$$\begin{aligned}
\frac{d}{dt}(X+iY) &= \frac{i(X+iY)[-(\sigma+1) - i(\sigma - R + Z)]}{n} + \\
&\quad \frac{\bar{z}^{n-1}}{nR^{n-2}}[(1-\sigma) + i(\sigma + R - Z)] \\
\dot{Z} &= bZ + \tfrac{1}{2} v_n
\end{aligned} \tag{6.8a}$$

For $n = 3$ and $n = 4$ the equations for X, Y, Z are

$$\begin{aligned}
\dot{X} &= -\frac{(\sigma+1)X}{3} + \frac{(\sigma - R + Z)Y}{3} + \frac{+u_2(1-\sigma) + v_2(\sigma + R - Z)}{3R} \\
\dot{Y} &= -\frac{(\sigma - R + Z)X}{3} - \frac{(\sigma+1)Y}{3} + \frac{-v_2(1-\sigma) + u_2(\sigma + R - Z)}{3R} \\
\dot{Z} &= bZ + \tfrac{1}{2} v_3
\end{aligned} \tag{6.8b}$$

and

$$\begin{aligned}
\dot{X} &= -\frac{(\sigma+1)X}{4} + \frac{(\sigma - R + Z)Y}{4} + \frac{+u_3(1-\sigma) + v_3(\sigma + R - Z)}{4R^2} \\
\dot{Y} &= -\frac{(\sigma - R + Z)X}{4} - \frac{(\sigma+1)Y}{4} + \frac{-v_3(1-\sigma) + u_3(\sigma + R - Z)}{4R^2} \\
\dot{Z} &= bZ + \tfrac{1}{2} v_4
\end{aligned} \tag{6.8c}$$

6.2.3 Covers of the Proto–Burke and Shaw System

The n-fold cover of the proto–Burke and Shaw equations simplifies to

$$\begin{aligned} \frac{d}{dt}(X+iY) &= \frac{i(X+iY)[-(S+1)+iS(1-Z)]}{n} + \\ &\qquad \frac{\bar{z}^{n-1}}{nR^{n-2}}[(1-S)-iS(1+Z)] \\ \dot{Z} &= \mathcal{V}+\tfrac{S}{2}v_n \end{aligned} \tag{6.9a}$$

For $n=3$ and $n=4$ the equations for X, Y, Z are

$$\begin{aligned} \dot{X} &= -\frac{(S+1)X}{3} - \frac{S(1-Z)Y}{3} + \frac{+u_2(1-S)-v_2S(1+Z)}{3R} \\ \dot{Y} &= +\frac{S(1-Z)X}{3} - \frac{(S+1)Y}{3} + \frac{-v_2(1-S)-u_2S(1+Z)}{3R} \\ \dot{Z} &= \mathcal{V}+\frac{S}{2}v_3 \end{aligned} \tag{6.9b}$$

and

$$\begin{aligned} \dot{X} &= -\frac{(S+1)X}{4} - \frac{S(1-Z)Y}{4} + \frac{+u_3(1-S)-v_3S(1+Z)}{4R^2} \\ \dot{Y} &= +\frac{S(1-Z)X}{4} - \frac{(S+1)Y}{4} + \frac{-v_3(1-S)-u_3S(1+Z)}{4R^2} \\ \dot{Z} &= \mathcal{V}+\frac{S}{2}v_4 \end{aligned} \tag{6.9c}$$

6.3 COVERS WITH $\mathcal{C}_3$ SYMMETRY

6.3.1 The Group

The rotation group $\mathcal{C}_3$ acts in $\mathbb{R}^3$ according to the defining matrix representation:

$$\begin{bmatrix} X \\ Y \\ Z \end{bmatrix}' = \begin{bmatrix} \cos\theta & \sin\theta & 0 \\ -\sin\theta & \cos\theta & 0 \\ 0 & 0 & 1 \end{bmatrix} \begin{bmatrix} X \\ Y \\ Z \end{bmatrix}$$

where angle $\theta = 0, \frac{2\pi}{3}, \frac{4\pi}{3}$ or $\theta = \frac{2\pi}{3}k$, $k = 0, 1, 2$.

6.3.2 Invariant Polynomials

Up to degree 3, polynomials invariant and covariant under $\mathcal{C}_3$ (independent of Z) are

Degree	Invariant Polynomials	Covariant Polynomials
1		X, Y
2	X^2+Y^2	$X^2-Y^2, 2XY$
3	$X^3-3XY^2, 3X^2Y-Y^3$	$X(X^2+Y^2), Y(X^2+Y^2)$

The three invariant polynomials in X and Y are linearly independent but not functionally independent, for

$$(X^3-3XY^2)^2+(3X^2Y-Y^3)^2=(X^2+Y^2)^3$$

Every invariant polynomial in X, Y, and Z can be written as a function of polynomials that are invariant under $\mathcal{C}_3$:

$$g(X^2+Y^2, X^3-3XY^2, 3X^2Y-Y^3, Z)$$

Every polynomial in the three variables X, Y, Z can be written in the form

$$\sum_{\alpha=0}^{6} g_\alpha(X^2+Y^2, X^3-3XY^2, 3X^2Y-Y^3, Z)C_\alpha(X,Y)$$

where $C_\alpha(X,Y)$ are six ($1 \le \alpha \le 6$) covariant polynomials of degree ≤ 3, or the invariant 1 ($\alpha = 0$). In fact, it is sufficient to include only the first four covariant polynomials of degree ≤ 2.

6.3.3 The Jacobian

It is useful to choose as invariant coordinates:

$$\begin{array}{lll} u = u_1 = & X^3-3XY^2 \\ v = u_2 = & 3X^2Y-Y^3 \\ w = u_3 = & Z \end{array}$$

The Jacobian of this local diffeomorphism is

$$J=\frac{\partial \boldsymbol{u}}{\partial \boldsymbol{X}}=\begin{bmatrix} 3X^2-3Y^2 & -6XY & 0 \\ 6XY & 3X^2-3Y^2 & 0 \\ 0 & 0 & 1 \end{bmatrix} \xrightarrow{\det} 9(X^2+Y^2)^2$$

The singular set of this transformation is the Z-axis $X = Y = 0$.

6.3.4 Covering Equations

The equations $\dot{\boldsymbol{u}} = g_i(\boldsymbol{u})$ of an invariant dynamical system can be lifted to equations for a three-fold cover in the usual way

$$\frac{d}{dt}\begin{bmatrix} X \\ Y \\ Z \end{bmatrix} = \begin{bmatrix} 3X^2 - 3Y^2 & -6XY & 0 \\ 6XY & 3X^2 - 3Y^2 & 0 \\ 0 & 0 & 1 \end{bmatrix}^{-1} \begin{bmatrix} g_1(\boldsymbol{u}) \\ g_2(\boldsymbol{u}) \\ g_3(\boldsymbol{u}) \end{bmatrix}$$

The inverse of this Jacobian is

$$\begin{bmatrix} 3X^2 - 3Y^2 & -6XY & 0 \\ 6XY & 3X^2 - 3Y^2 & 0 \\ 0 & 0 & 1 \end{bmatrix}^{-1} = \begin{bmatrix} \dfrac{X^2 - Y^2}{3\rho^4} & \dfrac{2XY}{3\rho^4} & 0 \\ -\dfrac{2XY}{3\rho^4} & \dfrac{X^2 - Y^2}{3\rho^4} & 0 \\ 0 & 0 & 1 \end{bmatrix}$$

where $\rho^2 = X^2 + Y^2$. These relations have been implemented in Section 6.2 to construct the covering equations of the Rössler, proto–Lorenz, and proto–Burke and Shaw equations with $\mathcal{C}_3$ symmetry.

6.3.5 Topological Index

The singular set of the Jacobian of the local diffeomorphism links every periodic orbit in any strange attractor generated by the invariant equations $\dot{\boldsymbol{u}}_j = g_j(\boldsymbol{u})$. If the rotation axis is disjoint from the attractor, the linking number of any orbit with this axis can be determined from the linking numbers of the basic period-one orbits in the image attractor. If the image attractor has b branches, then b linking numbers of the corresponding period-one orbits with the Z-axis (closed with a return at "infinity") constitute a topological index. The index applies to the image attractor but it provides a great deal of information about the covering attractor.

As an example, if the strange attractor generated by the invariant dynamical equations is classified by a template with four branches, each labeled by its local torsion (1, 2, 3, 4), the topological index of the image attractor is the set (n_1, n_2, n_3, n_4).

6.3.6 Covering Branched Manifolds

If the image branched manifold has b branches, its 3-fold cover has $3b$ branches. In particular, 3-fold covers of the Smale horseshoe branched manifold have six branches.

It is useful to label the branches using a group label. For example, the two branches 0 and 1 of a Smale horseshoe template are lifted to six branches in any three-fold cover. These can be labeled variously $0_{\mathbb{I}}, 1_{\mathbb{I}}$; $0_\gamma, 1_\gamma$; $0_{\gamma^2}, 1_{\gamma^2}$ or $0_0,\ 1_0$; $0_1, 1_1$; 0_2, 1_2. The symmetry-adapted labeling scheme displays information about the image—in the symbols for the image branched manifold—and some information about the symmetry group. However, this information is not complete: Information about the transition matrix is missing.

This information is provided by the topological index. For the Smale horseshoe this index is (n_0, n_1). Three-fold lifts obtained from rotations about axes with different topological indices generate topologically inequivalent covers. For example, the three-fold cover with topological index $(n_0, n_1) = (0, 0)$ consists of three disjoint copies of a Smale horseshoe branched manifold. Three-fold covers with indices (0,1) and (1,1) are shown in Fig. 6.2. The branched manifold for the attractors shown in Fig. 6.2(a) and 6.2(b) are shown in Fig. 6.3(a) and 6.3(b).

The reverse horseshoe branched manifold has two branches with local torsions 1 and 2. Its three-fold cover with topological index (1, 2) is shown in Fig. 6.4. This three-fold cover has three branch lines b_0, $b_1 = \gamma b_0$, $b_2 = \gamma^2 b_0$. Each is divided into two parts labeled by the symbols 1, 2. They label their images in the image branched

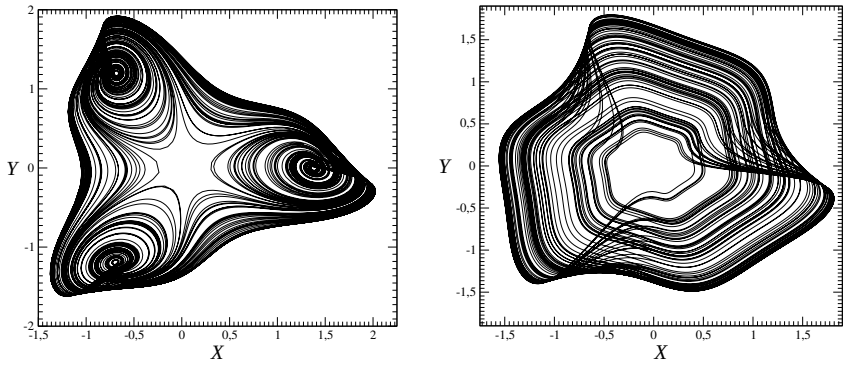

(a) $(n_0, n_1) = (0, 1)$ (b) $(n_0, n_1) = (1, 1)$

Fig. 6.2 Three-fold covers of the centered Rössler system.

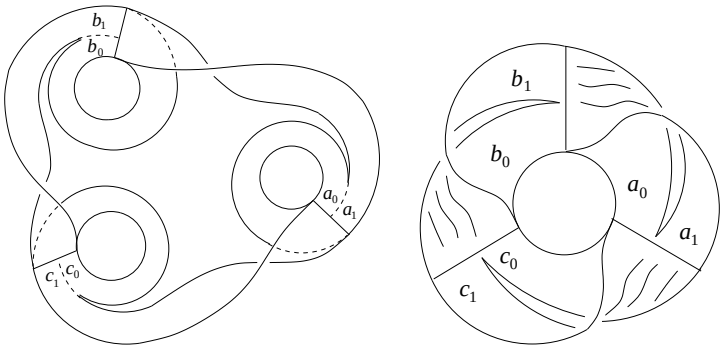

(a) $(n_1, n_2) = (0, 1)$ (b) $(n_1, n_2) = (1, 1)$

Fig. 6.3 Branched manifolds for three-fold covers of the Rössler system shown in Fig. 6.2.

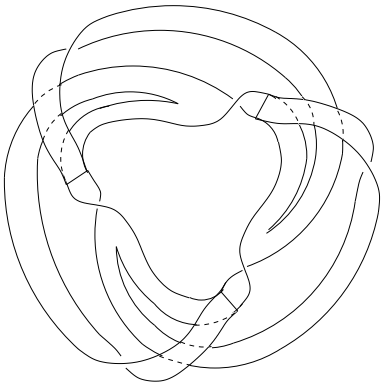

Fig. 6.4 Branched manifold for three-fold cover of the reverse horseshoe with topological index $(n_1, n_2) = (1, 2)$.

manifold. Initial conditions on 1_0 flow to branch b_1. The branch connecting 1_0 with b_1 has a half twist. Initial conditions on 2_0 flow to branch $b_2 = \gamma^2 b_0$ with a full twist. The flow from b_1 and b_2 are symmetry-related to the flow from b_0, as follows:

$$\begin{aligned} \gamma(1_0 \to b_1) &\Rightarrow 1_1 \to b_2 \\ \gamma(2_0 \to b_2) &\Rightarrow 2_1 \to b_{3=0} \end{aligned}$$

$$\begin{aligned} \gamma^2(1_0 \to b_1) &\Rightarrow 1_2 \to b_0 \\ \gamma^2(2_0 \to b_2) &\Rightarrow 2_2 \to b_1 \end{aligned}$$

6.3.7 Symmetry-Adapted Labeling

The symmetry-adapted symbol scheme provides three pieces of information.

1. A symbol describes the image of a branch under the $3 \to 1$ local diffeomorphism.
2. A group label distinguishs the three branches related to each other under a rotation.
3. A second group label. This describes which branches a given branch flows into.

We illustrate by example. The three-fold cover of the 2-branch Smale horseshoe with branch labels 0 and 1 has six branches. They are labeled $0_{(g_i)}, 1_{(g_i)}, g_i = \mathbb{I}, \gamma, \gamma^2$; $i = (0, 1, 2)$. The three-fold cover with topological index $(n_0, n_1) = (0, 0)$ consists of three disjoint copies of the horseshoe. Branch $0_{(g_0)}$ flows into $0_{(g_0)}$ and $1_{(g_0)}$. So also does $1_{(g_0)}$. These two branches, *and their connectivity*, are then labeled $0_{(g_0,g_0)}$ and $1_{(g_0,g_0)}$. Similarly, branches $0_{(g_1)}$, $1_{(g_1)}$ map to themselves and are labeled $0_{(g_1,g_1)}$, $1_{(g_1,g_1)}$. The labels for the third pair are $0_{(g_2,g_2)}$, $1_{(g_2,g_2)}$.

The three-fold cover with topological index $(n_0, n_1) = (0, 1)$ has a different set of labels. Branch $0(g_i)$ flows back to branch $0(g_i)$, $1(g_i)$, so is labeled $0(g_i, g_i)$. Branch $1(g_0)$ flows into branches $0(g_1)$ and $1(g_1)$. It is labeled $1(g_0, g_1)$. Similarly, we have $1(g_1, g_2)$ and $1(g_2, g_3 = g_0)$. The following table gives some indications of the relations between topological indices and symmetry adapted labeling schemes using two group labels

(n_0, n_1)			
(0,0)	$0_{(g_0,g_0)}$	$0_{(g_1,g_1)}$	$0_{(g_2,g_2)}$
	$1_{(g_0,g_0)}$	$1_{(g_1,g_1)}$	$1_{(g_2,g_2)}$
(0,1)	$0_{(g_0,g_0)}$	$0_{(g_1,g_1)}$	$0_{(g_2,g_2)}$
	$1_{(g_0,g_1)}$	$1_{(g_1,g_2)}$	$1_{(g_2,g_0)}$
(0,2)	$0_{(g_0,g_0)}$	$0_{(g_1,g_1)}$	$0_{(g_2,g_2)}$
	$1_{(g_0,g_2)}$	$1_{(g_1,g_0)}$	$1_{(g_2,g_1)}$

In this symmetry-adapted labeling scheme, the first group operation identifies distinct branches that are mapped into each other by the symmetry group. The second group index identifies the image of that branch under the dynamics: that is, it determines the transition matrix.

Remark: In quantum mechanics the Wigner-Eckart theorem allows decomposition of a matrix element of a system with symmetry into the product of two factors: one depending on geometry, the other contains the physics. The symmetry-adapted labeling scheme using two group operations effects the same type of decomposition. The first group operation "is geometry." It serves to label equivalent branches. The second group operation "is dynamics." It identifies where the flow goes to after it leaves each branch.

In Fig. 6.5(a) we show a gateau roulé branched manifold [33, 34]. There is one branch line and three branches a_j, $j = 0, 1, 2$. Branch j has local torsion j (or $j\pi$). In Fig. 6.5(b) we show a double cover of this branched manifold with $\mathcal{R}_Z$ symmetry and topological index $(n_0, n_1, n_2) = (0, 1, 1)$, and in Fig. 6.5(c) we show a cover of the gateau roulé with $\mathcal{C}_3$ symmetry, three branch lines, 9 branches, and topological index $(n_0, n_1, n_2) = (0, 1, 1)$.

6.3.8 Transition Matrices

Symmetry-adapted labels lead directly to transition matrices, and vice versa. The two are complementary ways of describing equivariant dynamics. In Table 6.3.8 we present the transition matrices for the three-fold cover of the horseshoe branched manifold with topological index $(n_0, n_1) = (0, 1)$ and the reverse horseshoe with topological index $(n_1, n_2) = (1, 2)$.

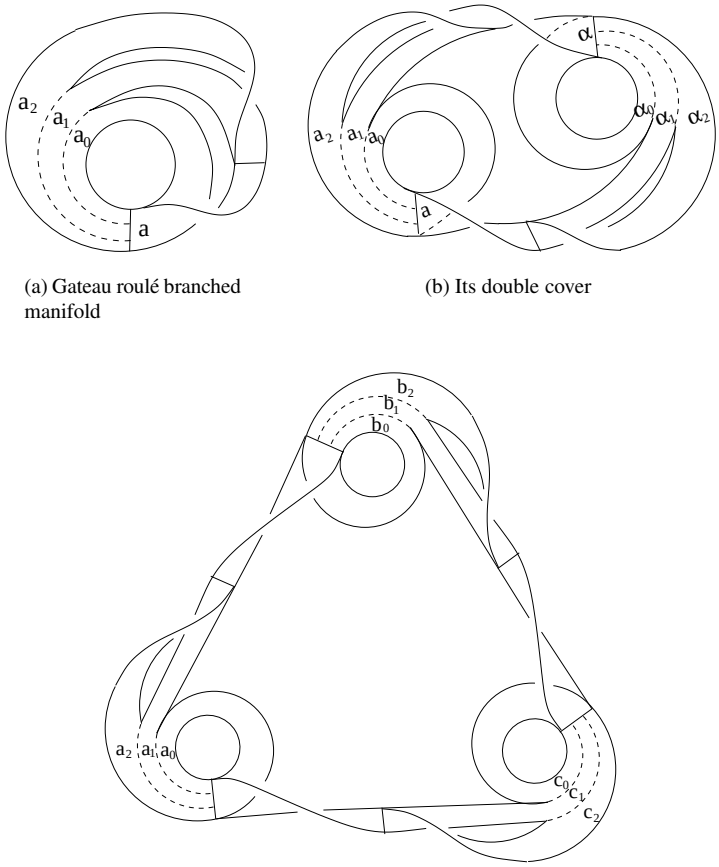

(a) Gateau roulé branched manifold

(b) Its double cover

(c) Its triple cover

Fig. 6.5 (a) Gateau roulé branched manifold, also called a scroll template. (b) Double cover under $\mathcal{R}_Z(\pi)$ and (c) triple cover under $\mathcal{C}_3$ of the 3-branched scroll template with topological index $(n_0, n_1, n_2) = (0, 1, 1)$.

6.3.9 Periodic Orbits

Periodic orbits in the image can be lifted to periodic orbits in the covering system in an algorithmic way using symmetry-adapted symbols. We provide two sets of examples before stating the algorithm [35].

In the first example, we consider a three-fold cover of a Smale horseshoe branched manifold. The branches of the horseshoe have local torsion 0, 1 and are so labeled. The topological index of the image is $(n_0, n_1) = (0, 1)$. The branched manifold for the cover is shown in Fig. 6.3(a).

Table 6.1 The symmetry-adapted labeling scheme leads directly to transition matrices. Left: Transition matrix for the 3-fold cover of the horseshoe with topological index $(n_0\,, n_1) = (0, 1)$. Right: Transition matrix for the 3-fold cover of the reverse horseshoe with topological index $(n_1, n_2) = (1, 2)$.

		$\mathbb{I}=0$		$C_3^1=1$		$C_3^2=2$	
		0_0	1_0	0_1	1_1	0_2	1_2
$\mathbb{I}=0$	0_0	1	1	0	0	0	0
	1_0	0	0	1	1	0	0
$C_3^1=1$	0_1	0	0	1	1	0	0
	1_1	0	0	0	0	1	1
$C_3^2=2$	0_2	0	0	0	0	1	1
	1_2	1	1	0	0	0	0

		$\mathbb{I}=0$		$C_3^1=1$		$C_3^2=2$	
		1_0	2_0	1_1	2_1	1_2	2_2
$\mathbb{I}=0$	1_0	0	0	1	1	0	0
	2_0	0	0	0	0	1	1
$C_3^1=1$	1_1	0	0	0	0	1	1
	2_1	1	1	0	0	0	0
$C_3^2=2$	1_2	1	1	0	0	0	0
	2_2	0	0	1	1	0	0

We now attempt to construct the triple covers of the period-4 saddle-node pair 1001 and 1000 as well as the period-4 orbit 1011 in the primary period-doubling cascade. As a first step, we dress the image symbols 0,1 with two group labels. The topological index $n_0 = 0$ indicates that branch $0_{(i,*)}$ returns to itself, so the group symbol pair is $0_{(i,i)}$, $i = 0, 1, 2$. The index $n_1 = 1$ indicates that branch $1_{(i,*)}$ flows to the next branch, so that the group symbol pair is $1_{(i,i+1)}$ (all integers are mod 3). We now construct the periodic orbits covering 1011. We begin in the cover with an initial condition on $1_{(0,1)}$ and proceed from there

$$1011 \to \underline{1_{(0,1)}\ 0_{(1,1)}\ 1_{(1,2)}\ 1_{(2,0)}}\ 1_{(0,1)}\ 0_{(1,1)}\ 1_{(1,2)} \text{ etc.}$$

This cover goes through four branches in the covering branched manifold before repeating. It has period 4. The totality of the three-fold covers of a period-4 orbit have 12 ($= 4 \times 3$) symbols. We therefore expect two more period-4 covering orbits, related to the first by the symmetry operations of the group $\mathcal{C}_3$. The three covering orbits are

$$1011 \overset{\text{lifts to}}{\longrightarrow} \begin{array}{l} 1_{(\underline{0}1)}\ 0_{(11)}\ 1_{(12)}\ 1_{(2\underline{0})} \\ 1_{(\underline{1}2)}\ 0_{(22)}\ 1_{(20)}\ 1_{(0\underline{1})} \\ 1_{(\underline{2}0)}\ 0_{(00)}\ 1_{(01)}\ 1_{(1\underline{2})} \end{array}$$

The lifts of the period-4 saddle and node are constructed similarly, but are of period 12:

$$1001 \overset{\text{lifts to}}{\longrightarrow} 1_{(\underline{0}1)}\ 0_{(11)}\ 0_{(11)}\ 1_{(12)}\ \ 1_{(20)}\ 0_{(00)}\ 0_{(00)}\ 1_{(01)}\ \ 1_{(12)}\ 0_{(22)}\ 0_{(22)}\ 1_{(2\underline{0})}$$

$$1000 \overset{\text{lifts to}}{\longrightarrow} 1_{(\underline{0}1)}\ 0_{(11)}\ 0_{(11)}\ 0_{(11)}\ \ 1_{(12)}\ 0_{(22)}\ 0_{(22)}\ 0_{(22)}\ \ 1_{(20)}\ 0_{(00)}\ 0_{(00)}\ 0_{(0\underline{0})}$$

We observe that the signature for closure in the covering orbit is that the last group symbol is equal to the first group symbol. These symbols have been underlined in the five covering orbits computed above.

As a second example, we treat a three-fold cover of the reverse horseshoe. The reverse horseshoe has two branches with local torsions 1, 2. The topological index is (n_1, n_2). To illustrate the richness of cover possibilities, we choose the topological index to be $(n_1, n_2) = (1, 2)$. The branched manifold for this three-fold cover with this index is illustrated in Fig. 6.4. Symbolic dynamics in the image contains symbols 1 and 2. Symmetry adapted symbols in the cover include the six symbols $1_{(i,i+1)}$, $2_{(i,i+2)}$, again mod 3. In this example, we determine the covers of the period-4 saddle-node pair 2112, 2122 and the period-4 orbit in the primary (reverse) cascade: 2111. Proceeding as before for the period-4 orbit, in the saddle-node pairs we find

$$2111 \overset{\text{lifts to}}{\longrightarrow} 2_{(\underline{0}2)}\ 1_{(20)}\ 1_{(01)}\ 1_{(12)}\ \ 2_{(21)}\ 1_{(12)}\ 1_{(20)}\ 1_{(01)}\ \ 2_{(10)}\ 1_{(01)}\ 1_{(12)}\ 1_{(2\underline{0})}$$

For the two period-4 orbits we find

$$2112 \overset{\text{lifts to}}{\longrightarrow} \begin{array}{l} 2_{(\underline{0}2)}\ 1_{(20)}\ 1_{(01)}\ 2_{(1\underline{0})} \\ 2_{(\underline{1}0)}\ 1_{(01)}\ 1_{(12)}\ 2_{(2\underline{1})} \\ 2_{(\underline{2}1)}\ 1_{(12)}\ 1_{(20)}\ 2_{(0\underline{2})} \end{array}$$

$$2122 \overset{\text{lifts to}}{\longrightarrow} 2_{(\underline{0}2)}\ 1_{(20)}\ 2_{(02)}\ 2_{(21)}\ \ 2_{(10)}\ 1_{(01)}\ 2_{(10)}\ 2_{(02)}\ \ 2_{(21)}\ 1_{(12)}\ 2_{(21)}\ 2_{(1\underline{0})}$$

In this case, the orbit in the cascade has one covering orbit of period 12. The period-4 saddle 2112 has three symmetry-related period-4 covering orbits, while its node partner 2122 has a single covering orbit of period 12.

The general algorithm for lifting periodic orbits in the image to their covering orbits is as follows:

1. Write down the symbol code, S, for the image orbit. Repeat the symbol sequence S as often as necessary.
2. Replace the first symbol in S by its symmetry adapted symbol in the cover. Begin anywhere in the cover, specified by group operator g_i.
3. The first symbol g_i forces a unique sequence of group operations in the covering sequence.
4. Stop when the last group label in $(S)^m$ is equal to the first group label in S, for some $m = 1, 2, \ldots$

This algorithm has been used in the two examples for three-fold covers presented above. It is valid for all symmetry groups. The construction of periodic orbits in two-fold covers is a special case of this algorithm.

In Fig. 6.6 we show lifts of four orbits in the Rössler attractor to a three-fold cover with topological index $(n_0, n_1) = (0, 1)$. The period-1 orbit 1 lifts to a period-3 orbit and the period-2 orbit 10 lifts to a period-6 orbit. The period-3 saddle node pair both lift to period-9 orbits. In Fig. 6.7 we show lifts of the same four orbits to the three-fold cover with topological index $(n_0, n_1) = (1, 1)$. Once again 1 lifts to a period-3 orbit and 10 lifts to a period-6 orbit. However, the saddle node pair 101, 100 both lift to three period-3 orbits, only one of which is shown for the saddle 101 and node 100.

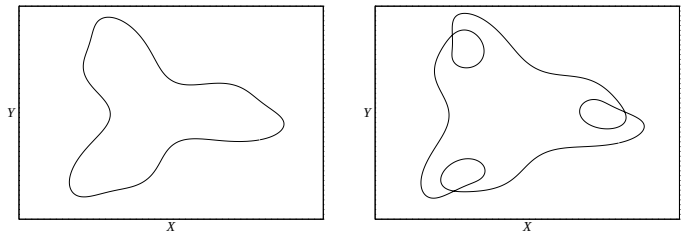

(a) Period-1 orbit (1) (b) Period-2 orbit (10)

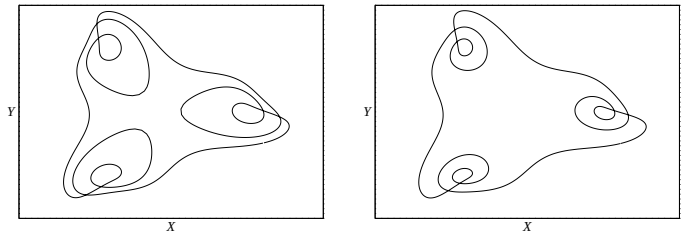

(c) Period-3 orbit (101) (d) Period-3 orbit (100)

Fig. 6.6 Lifts of orbits into three-fold covers of Rössler system with topological index $(n_1, n_2) = (0, 1)$.

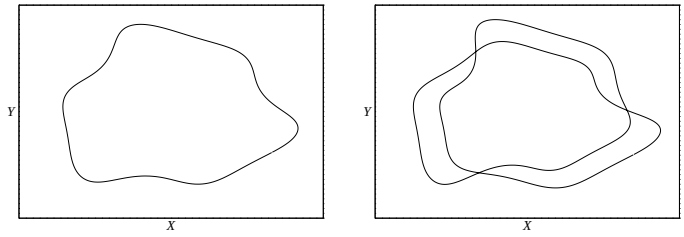

(a) Period-1 orbit (1) (b) Period-2 orbit (10)

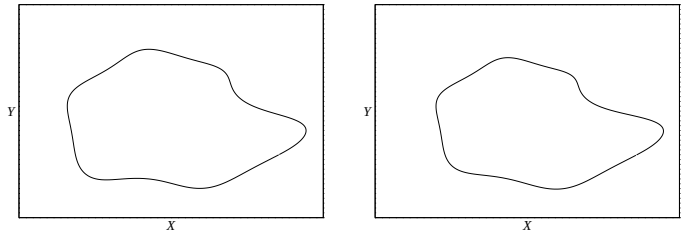

(c) Period-3 orbit (101) (d) Period-3 orbit (100)

Fig. 6.7 Lifts of orbits into three-fold covers of Rössler system with topological index $(n_1, n_2) = (1, 1)$. In (c) and (d) only one of the three different, symmetry-related orbits is shown.

6.3.10 Linking Numbers

Linking numbers for pairs of periodic orbits on the image branched manifold can be computed algorithmically. This, in fact, is one of the primary reasons for describing strange attractors in $\mathbb{R}^3$ by their branched manifolds.

Linking numbers of lifts of periodic orbits can easily be inferred from the linking numbers of the image pair. Assume that two orbits, P and Q, have linking number Link(P, Q). How is the linking number of the three-fold lifts $\bar{P}$, $\bar{Q}$ related to Link(P, Q)?

The linking numbers are half the signed number of crossings in the projection down to the u-v plane (in the image) or the X-Y plane (in the cover). Each crossing in the u-v-plane has three preimages in the covering space, so that

$$\text{Link}(\bar{P}, \bar{Q}) = 3\text{Link}(P, Q)$$

The covering orbit $\bar{P}$ either has three times the period of P or consists of three disconnected components $\bar{P}_i$, $i = 0, 1, 2$, that are symmetry related and have the same period as P (since 3 is prime). If $\bar{P}$ and $\bar{Q}$ are both connected, Link$(\bar{P}, \bar{Q}) =$ 3Link(P, Q). If one is connected ($\bar{Q}$) and one is disconnected ($\bar{P} = \cup \bar{P}_i$), then for each i

$$\text{Link}(\bar{P}_i, \bar{Q}) = \text{Link}(P, Q)$$

If both are disconnected

$$\sum_{i,j=0}^{2} \text{Link}(\bar{P}_i, \bar{Q}_j) = 3\text{Link}(P, Q)$$

In Fig. 6.8 we show the link of the lifts of the orbits 1, 10 in the Rössler attractor to three-fold covers with topological index $(n_0, n_1) = (0, 1)$ and $(1, 1)$. In the image, Link$(1, 10) = 1$, so in both cases the linking number of the period-3 and period-6 orbits are 3.

6.3.11 Poincaré Sections and First-Return Maps

As usual, the Poincaré section in the image lifts to the Poincaré section in the cover. In the cover, the Poincaré section is the union of three disjoint components when the Poincaré section in the image is connected.

Again as usual, it is useful to consider the Poincaré section in the branched manifold representation of the strange attractor. It is simply the union of the branch line(s). If there is one branch line in the image branched manifold, there are n branch lines in the n-fold cover. The Poincaré sections for the strange attractors are the "inverse image" of the branch lines: that is, the set of all points in $\mathbb{R}^3$ that project to the branch lines under the Birman-Williams projection.

We construct the Poincaré sections and the first-return maps from the two covers treated in Section 6.3.6. The return map for a typical Smale horseshoe template is shown in Fig. 6.9(a). For its three-fold cover with topological index $(n_0, n_1) = (0, 1)$

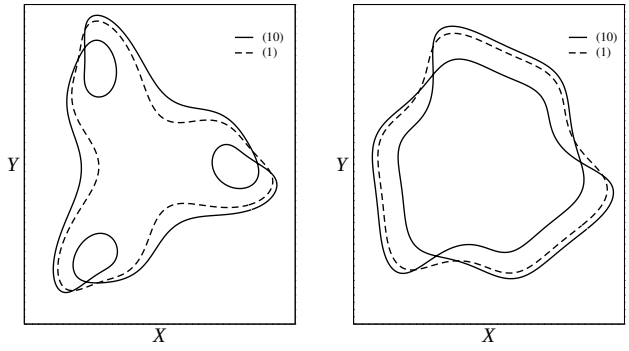

(a) $(n_0, n_1) = (0, 1)$ (b) $(n_0, n_1) = (1, 1)$

Fig. 6.8 Links of three-fold lifts of Rössler orbits.

the return map is shown in Fig. 6.9(c). Recall that in the cover, the symbol 0 reinjects to the same spatial domain while the symbol 1 reinjects to the following domain.

The first return map for the reverse horseshoe is shown in Fig. 6.9(b). For the three-fold cover with topological index $(n_1, n_2) = (1, 2)$ the return map is shown in Fig. 6.9(d).

6.4 COVERS WITH $\mathcal{C}_4$ SYMMETRY

Four-fold covers equivariant under $\mathcal{C}_4$ can be studied by methods essentially identical to those used to study three-fold covers with the difference that 3 is prime and $4 = 2\times 2$ is not. This produces one notable difference: four-fold covers of a period p orbit can consist of

1. One symmetric orbit of period $4p$.
2. Two asymmetric orbits of period $2p$.
3. Four asymmetric orbits of period p

We follow the procedure used in Section 6.3, omitting extended explanations when redundent.

6.4.1 The Group

The group $\mathcal{C}_4$ acts on three space $\mathbb{R}^3$ as follows

$$\begin{bmatrix} X \\ Y \\ Z \end{bmatrix}' = \gamma \begin{bmatrix} X \\ Y \\ Z \end{bmatrix} = \begin{bmatrix} 0 & 1 & 0 \\ -1 & 0 & 0 \\ 0 & 0 & 1 \end{bmatrix} \begin{bmatrix} X \\ Y \\ Z \end{bmatrix} = \begin{bmatrix} Y \\ -X \\ Z \end{bmatrix}$$

The four group operations are γ, γ^2, γ^3, $\gamma^4 = \gamma^0 = \mathbb{I}$.

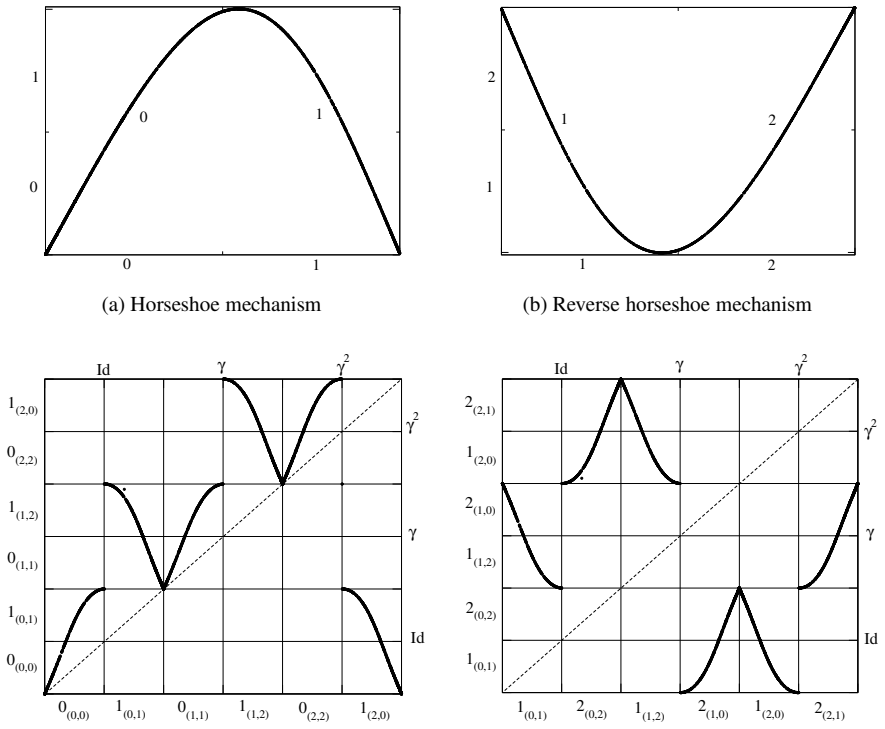

(a) Horseshoe mechanism

(b) Reverse horseshoe mechanism

(c) Lift of (a) into 3-cover with index $(0, 1)$

(d) Lift of (b) into 3-cover with index $(1, 2)$

Fig. 6.9 First-return map of the three-fold covers. (a) Return map for a simple stretch and fold (horseshoe) mechanism. (c) Lift of (a) to a three-fold cover with topological index $(n_0, n_1) = (0, 1)$. (b) Return map for a reverse horseshoe. Branches have local torsion 1,2 as indicated. (d) Lift to three-fold cover with topological index $(n_1, n_2) = (1, 2)$.

6.4.2 Invariant and Covariant Polynomials

The decomposition into invariant and covariant polynomials (independent of Z) is

Degree	Invariant Polynomials	Covariant Polynomials
1		X, Y
2	$X^2 + Y^2$	$X^2 - Y^2, 2XY$
3		$X(X^2 + Y^2), Y(X^2 + Y^2),$ $X(X^2 - Y^2), Y(X^2 - Y^2)$
4	$X^4 - 6X^2Y^2 + Y^4,$ $4(X^3Y - XY^3), X^4 + Y^4$	$XY(X^2 + Y^2)$ $X^4 - Y^4$

The four invariant polynomials of degree 4 are functionally dependent

$$\begin{array}{rcl} 4X^4 - (X^4 - 6X^2Y^2 + Y^4) + 4Y^4 & = & 3(X^2 + Y^2)^2 \\ (X^4 - 6X^2Y^2 + Y^4)^2 + \left[4(X^3Y - XY^3)\right]^2 & = & (X^2 + Y^2)^4 \end{array}$$

Every polynomial in the three variables X, Y, Z can be written in the form

$$\sum_{\alpha=0} g_\alpha \left(X^2 + Y^2,\ X^4 - 6X^2Y^2 + Y^4,\ 4(X^3Y - XY^3), Z\right) C_\alpha(X, Y,)$$

where $C_0 = 1$ and

$$C_\alpha = X,\ Y,\ X^2 - Y^2,\ 2XY,\ X(X^2 - Y^2),\ Y(X^2 - Y^2)$$

6.4.3 The Jacobian

A useful choice of invariant coordinates is

$$\begin{array}{rcccl} u = u_1 = & X^4 - 6X^2Y^2 + Y^4 & = & \Re(X + iY)^4 \\ v = u_2 = & 4(X^3Y - XY^3) & = & \Im(X + iY)^4 \\ w = u_3 = & Z & & \end{array}$$

With these coordinates, the Jacobian of the $4 \to 1$ local diffeomorphism is

$$\frac{\partial \boldsymbol{u}}{\partial \boldsymbol{X}} = \begin{bmatrix} 4X^3 - 12XY^2 & -12X^2Y + 4Y^3 & 0 \\ 12X^2Y - 4Y^3 & 4X^3 - 12XY^2 & 0 \\ 0 & 0 & 1 \end{bmatrix} \xrightarrow{\det} 16(X^2 + Y^2)^3$$

The singular set of this diffeomorphism is the Z-axis $X = Y = 0$.

6.4.4 Covering Equations

These are obtained from the inverse of the Jacobian. Specifically

$$\frac{d}{dt}\begin{bmatrix} X \\ Y \\ Z \end{bmatrix} = \begin{bmatrix} \dfrac{4X^3 - 12XY^2}{16\rho^6} & \dfrac{12X^2Y - 4Y^3}{16\rho^6} & 0 \\ \dfrac{-12X^2Y + 4Y^4}{16\rho^6} & \dfrac{4X^3 - 12XY^2}{16\rho^6} & 0 \\ 0 & 0 & 1 \end{bmatrix} \begin{bmatrix} \dot{u} \\ \dot{v} \\ \dot{w} \end{bmatrix}$$

where $\rho^2 = X^2 + Y^2$. These relations have been implemented in Section 6.2 to construct the covering equations of the Rössler, proto-Lorenz, and proto-Burke and Shaw equations with $\mathcal{C}_4$ symmetry.

6.4.5 Topological Index

Since the rotation axis is once again the singular set, the topological index for $\mathcal{C}_4$-invariant covers has identical properties as the topological index for $\mathcal{C}_3$-invariant covers. Recall that the topological index applies to the *image* dynamical system and the rotation axis of the symmetry group. Two four-fold covers of the Rössler strange attractor with topological index $(n_0, n_1) = (0, 1)$ and (1,1) are shown in Fig. 6.10(a) and 6.10(b).

6.4.6 Covering Branched Manifolds

Branched manifolds for the covers with topological index $(n_0, n_1) = (0, 1)$ and $(1, 1)$, shown in Fig. 6.10, are shown in Fig. 6.11.

6.4.7 Symmetry-Adapted Labeling

If the image strange attractor, or its template, has P branches A, B, $\ldots$, P, then its four-fold cover has $4P$ branches. A partial symmetry-adapted labeling scheme involves symbols $A_{(i,*)}$, $B_{(i,*)}$, $\ldots$, $P_{(i,*)}$, where $i = 0, 1, 2, 3$ labels the four group operations $\gamma^0 = \mathbb{I}, \gamma^1 = \gamma, \gamma^2, \gamma^3$. The unspecified labels $*$ indicate which of the four regions of the space the branch $A_{(i,*)}$, $B_{(i,*)}$, $\ldots$, $P_{(i,*)}$ flows into. This information is provided by the topological index.

For the Smale horseshoe template with branches 0 and 1 labeled by their local torsion and topological index $(n_0, n_1) = (0, 1)$, the eight branches in the four-fold cover are

$$\begin{array}{cccc} 0_{(0,0)} & 0_{(1,1)} & 0_{(2,2)} & 0_{(3,3)} \\ 1_{(0,1)} & 1_{(1,2)} & 1_{(2,3)} & 1_{(3,0)} \end{array}$$

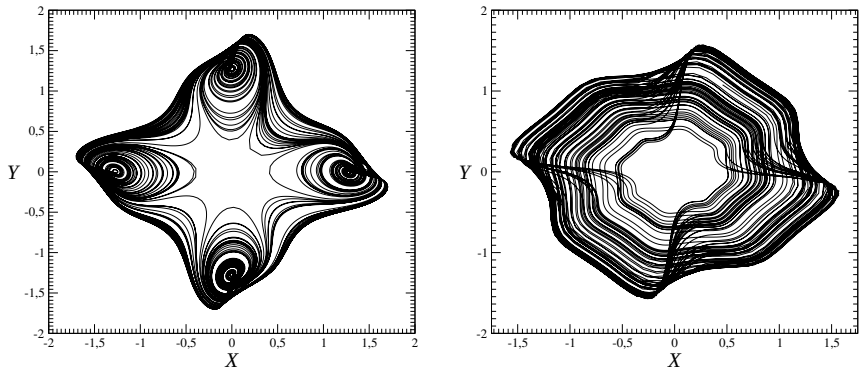

(a) $(n_1, n_2) = (0, 1)$ (b) $(n_1, n_2) = (1, 1)$

Fig. 6.10 Four-fold covers of the Rössler equations.

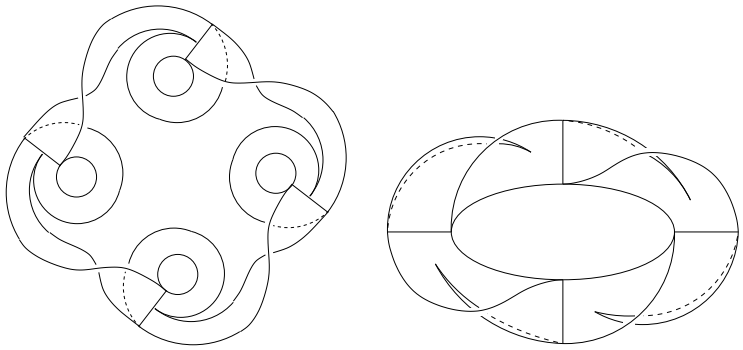

(a) $(n_0, n_1) = (0, 1)$ (b) $(n_0, n_1) = (1, 1)$

Fig. 6.11 Branched manifolds for two four-fold covers of the Rössler system shown in Fig. 6.10.

For the inverse horseshoe with branches 1 and 2 and topological index $(n_1, n_2) = (1, 2)$ the eight branches are

$$\begin{array}{cccc} 1_{(0,1)} & 1_{(1,2)} & 1_{(2,3)} & 1_{(3,0)} \\ 2_{(0,2)} & 2_{(1,3)} & 2_{(2,0)} & 2_{(3,1)} \end{array}$$

6.4.8 Transition Matrices

In Table 6.2 we present the transition matrices for the four-fold covers of the horseshoe branched manifold with topological index $(n_0, n_1) = (0, 1)$ and the reverse horseshoe with topological index $(n_1, n_2) = (1, 2)$.

6.4.9 Periodic Orbits

Covers of periodic orbits are constructed using the algorithm presented in Section 6.3.9 [35]. The three period-four orbits 1000, 1001, and 1011 lift to orbits in the cover with $(n_0, n_1) = (0, 1)$ as follows:

$$\begin{array}{lll} 1000 \overset{\text{lifts to}}{\longrightarrow} & 1_{(\underline{0}1)}\ 0_{(11)}\ 0_{(11)}\ 0_{(11)} & 1_{(12)}\ 0_{(22)}\ 0_{(22)}\ 0_{(22)} \\ & 1_{(23)}\ 0_{(33)}\ 0_{(33)}\ 0_{(33)} & 1_{(30)}\ 0_{(00)}\ 0_{(00)}\ 0_{(0\underline{0})} \\ 1001 \overset{\text{lifts to}}{\longrightarrow} & 1_{(\underline{0}1)}\ 0_{(11)}\ 0_{(11)}\ 1_{(12)} & 1_{(23)}\ 0_{(33)}\ 0_{(33)}\ 1_{(3\underline{0})} \\ & 1_{(\underline{1}2)}\ 0_{(22)}\ 0_{(22)}\ 1_{(23)} & 1_{(30)}\ 0_{(00)}\ 0_{(00)}\ 1_{(3\underline{1})} \\ 1011 \overset{\text{lifts to}}{\longrightarrow} & 1_{(\underline{0}1)}\ 0_{(11)}\ 1_{(12)}\ 1_{(23)} & 1_{(30)}\ 0_{(00)}\ 1_{(01)}\ 1_{(02)} \\ & 1_{(23)}\ 0_{(33)}\ 1_{(30)}\ 1_{(01)} & 1_{(12)}\ 0_{(22)}\ 1_{(23)}\ 1_{(3\underline{0})} \end{array}$$

Table 6.2 The symmetry-adapted labeling scheme leads directly to transition matrices. Left: Transition matrix for the 4-fold cover of the horseshoe with topological index $(n_0, n_1) = (0, 1)$. Right: Transition matrix for the 4-fold cover of the reverse horseshoe with topological index $(n_1, n_2) = (1, 2)$.

		$\mathbb{I}$		C_4		C_4^2		C_4^3	
		0_0	1_0	0_1	1_1	0_2	1_2	0_3	1_3
$\mathbb{I}$	0_0	1	1	0	0	0	0	0	0
	1_0	0	0	1	1	0	0	0	0
C_4^1	0_1	0	0	1	1	0	0	0	0
	1_1	0	0	0	0	1	1	0	0
C_4^2	0_2	0	0	0	0	1	1	0	0
	1_2	0	0	0	0	0	0	1	1
C_4^3	0_3	0	0	0	0	0	0	1	1
	1_3	1	1	0	0	0	0	0	0

		$\mathbb{I}$		C_4		C_4^2		C_4^3	
		1_0	2_0	1_1	2_1	1_2	2_2	1_3	2_3
$\mathbb{I}$	1_0	0	0	1	1	0	0	0	0
	2_0	0	0	0	0	1	1	0	0
C_4^1	1_1	0	0	0	0	1	1	0	0
	2_1	0	0	0	0	0	0	1	1
C_4^2	1_2	0	0	0	0	0	0	1	1
	2_2	1	1	0	0	0	0	0	0
C_4^3	1_3	1	1	0	0	0	0	0	0
	2_3	0	0	1	1	0	0	0	0

The period-4 node 1000 lifts to a connected period 4×4 orbit. Its partner, the period-4 saddle 1001, lifts to two asymmetric period 4×2 orbits. The orbit 1011 in the primary cascade lifts to a single connected period 4×4 orbit.

In Fig. 6.12 we show lifts of the four orbits 1, 10, 100, and 101 to a four-fold cover with index $(n_0, n_1) = (0, 1)$. The three orbits 1, 10, and 100 lift to single orbits of four times the basic period, while the period-three orbit 101 lifts to a pair of period-six orbits, only one of which is shown in this figure. In Fig. 6.13 the same four orbits are lifted to the cover with topological index $(n_0, n_1) = (1, 1)$. The odd period orbits lift to orbits of period $4p$, while the period-2 orbit 10 lifts to a pair of period-4 orbits, only one of which is shown.

A similar construction for the reverse horseshoe (1,2) with topological index $(n_1, n_2) = (1, 2)$ and a corresponding spectrum of orbits can be carried out. The fully dressed symbols are

$$\begin{array}{cccc} 1_{(0,1)} & 1_{(1,2)} & 1_{(2,3)} & 1_{(3,0)} \\ 2_{(0,2)} & 2_{(1,3)} & 2_{(2,0)} & 2_{(3,1)} \end{array}$$

The lifts of the corresponding three orbits 1222, 1221, and 1211 are

$$\begin{array}{lll} 1222 \overset{\text{lifts to}}{\longrightarrow} & 1_{(\underline{0}1)}\ 2_{(13)}\ 2_{(31)}\ 2_{(13)} & 1_{(30)}\ 2_{(02)}\ 2_{(20)}\ 2_{(02)} \\ & 1_{(23)}\ 2_{(31)}\ 2_{(13)}\ 2_{(31)} & 1_{(12)}\ 2_{(20)}\ 2_{(02)}\ 2_{(2\underline{0})} \\ 1221 \overset{\text{lifts to}}{\longrightarrow} & 1_{(\underline{0}1)}\ 2_{(13)}\ 2_{(31)}\ 1_{(12)} & 1_{(23)}\ 2_{(31)}\ 2_{(13)}\ 1_{(3\underline{0})} \\ & 1_{(\underline{1}2)}\ 2_{(20)}\ 2_{(02)}\ 1_{(23)} & 1_{(30)}\ 2_{(02)}\ 2_{(20)}\ 1_{(3\underline{1})} \\ 1211 \overset{\text{lifts to}}{\longrightarrow} & 1_{(\underline{0}1)}\ 2_{(13)}\ 1_{(30)}\ 1_{(01)} & 1_{(12)}\ 2_{(20)}\ 1_{(01)}\ 1_{(02)} \\ & 1_{(23)}\ 2_{(31)}\ 1_{(12)}\ 1_{(23)} & 1_{(30)}\ 2_{(02)}\ 1_{(23)}\ 1_{(3\underline{0})} \end{array}$$

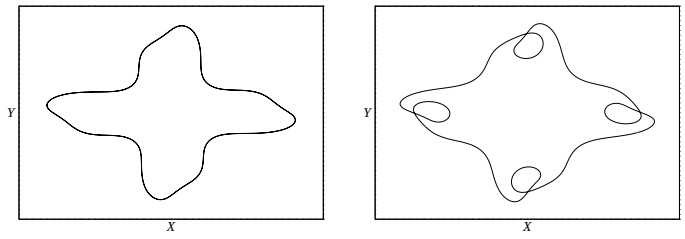

(a) Period-1 orbit (1) (b) Period-2 orbit (10)

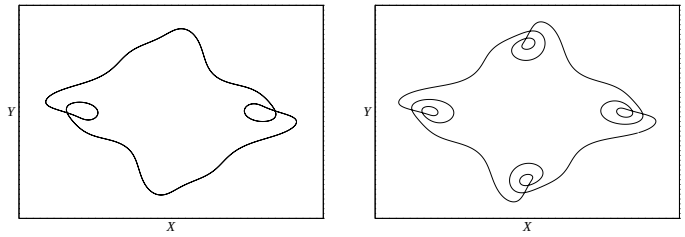

(c) Period-3 orbit (101) (d) Period-3 orbit (100)

Fig. 6.12 Lifts of four orbits into four-fold covers of Rössler system with topological index $(n_0, n_1) = (0, 1)$.

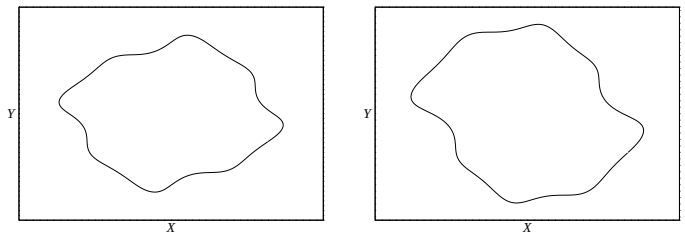

(a) Period-1 orbit (1) (b) Period-2 orbit (10)

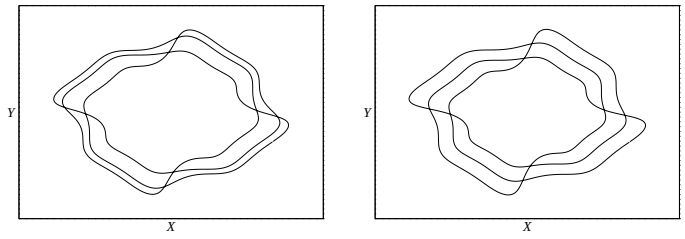

(c) Period-3 orbit (101) (d) Period-3 orbit (100)

Fig. 6.13 Lifts of the same four orbits into four-fold covers of Rössler system with topological index $(n_0, n_1) = (1, 1)$. The orbit in (b) has one symmetry-related partner that is not shown.

The node 1222 lifts to a period-16 orbit, its partner saddle 1221 lifts to two period-8 orbits, and the period-4 orbit 1211 in the reverse cascade lifts to a period-16 orbit.

6.4.10 Linking Numbers

If P and Q are orbits of periods p and q in the image, their covers $\bar{P}$ and $\bar{Q}$ are described by $4p$ and $4q$ symbols. $\bar{P}$ may consist of

1. One long connected orbit of period $4p$
2. Two disconnected orbits of period $2p = \cup_{i=1}^{2} \bar{P}_i$
3. Four disconnected orbits of period $p = \cup_{i=1}^{4} \bar{P}_i$

If $\bar{P}$ and $\bar{Q}$ are connected,

$$\text{Link}(\bar{P}, \bar{Q}) = 4\text{Link}(P, Q)$$

If $\bar{Q}$ is connected and $\bar{P}$ is disjoint $\bar{P} = \cup_{i=1}^{2 \text{ or } 4} \bar{P}_i$, then

$$\text{Link}(\cup \bar{P}_i, \bar{Q}) = \sum_{i=1} \text{Link}(\bar{P}_i, \bar{Q})$$

If $\bar{P}$ has two components, then for each

$$\text{Link}(\bar{P}_i, \bar{Q}) = 2\text{Link}(P, Q) \quad i = 1, 2$$

If $\bar{P}$ has four components,

$$\text{Link}(\bar{P}_i, \bar{Q}) = \text{Link}(P, Q) \quad i = 1, 2, 3, 4$$

In the more general case

$$\text{Link}(\bar{P}, \bar{Q}) = \sum_{i=1}^{2 \text{ or } 4} \sum_{j=1}^{2 \text{ or } 4} \text{Link}(\bar{P}_i, \bar{Q}_j) = 4\text{Link}(P, Q)$$

In Fig. 6.14 we show the link of lifts of the period-one and -two orbits 1, 10 in the Rössler attractor to covers with index $(n_0, n_1) = (0, 1)$ and (1,1). In the Rössler attractor $\text{Link}(1, 10) = 1$. In the cover with $(n_0, n_1) = (0, 1)$ the two orbits 1 and 10 lift to two orbits of periods 4 and 8. These two orbits have linking number equal to 4. In the cover with $(n_0, n_1) = (1, 1)$ the orbit 1 lifts to a period-four orbit while the orbit 10 lifts to a pair of period-four orbits. Each of the two period-four lifts of 10 has linking number equal to 2 with the period-four lift of 1.

6.4.11 Poincaré Sections and First-Return Maps

The return maps for the Smale horseshoe branched manifold and its four-fold cover with $\mathcal{C}_4$ symmetry and topological index $(n_0, n_1) = (0, 1)$ are shown in Fig. 6.15(a) and Fig. 6.15(c). For the reverse horseshoe and its four-fold cover with topological index $(n_1, n_2) = (1, 2)$ they are shown in Fig. 6.15(b) and Fig. 6.15(d).

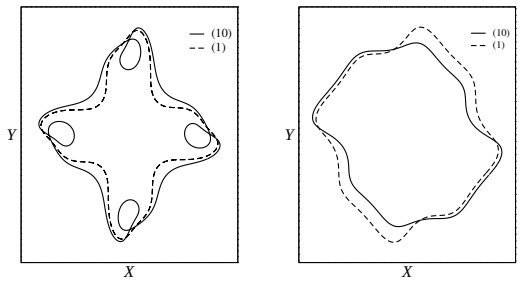

(a) $(n_0, n_1) = (0, 1)$ (b) $(n_0, n_1) = (1, 1)$

Fig. 6.14 Links of orbits in four-fold covers of the Rössler system.

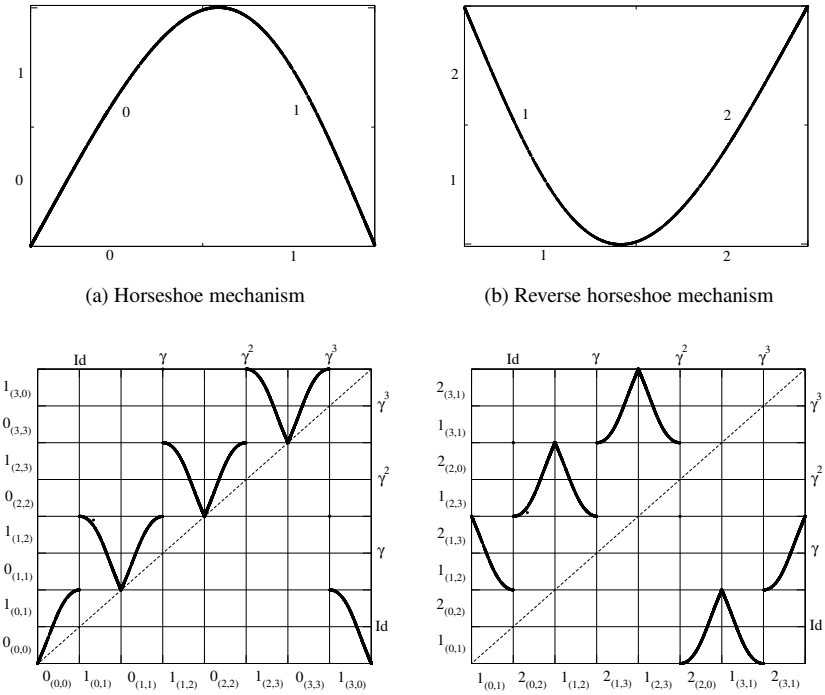

(a) Horseshoe mechanism (b) Reverse horseshoe mechanism

(c) Four-fold cover of (a) with index $(0, 1)$ (d) Four-fold cover of (b) with index $(1, 2)$

Fig. 6.15 First-return map of (a) the horseshoe and (b) reverse horseshoe. (c) First-return map of the four-fold cover for the Rössler attractor with topological index $(n_0, n_1) = (0, 1)$. (d) First return map for the four-fold cover of a reverse horseshoe with topological index $(1, 2)$.

6.5 COVER COMPARISONS

In this section we compare the dynamical and the topological properties of the three image dynamical systems that are discussed in Section 6.1. For each, three types of comparisons are made.

1. We compare two-fold, three-fold, and four-fold covers with two different topological indices.
2. We compare lifts of the period-1 orbit, the period-2 orbit and the two period-3 orbits into covers with $\mathcal{C}_n$ symmetry, with $n = 2, 3, 4$.
3. We compare links of lifts of the period-1 and period-2 orbits.

6.5.1 Rössler System

The Rössler equations, and their n-fold covers, are given in Section 6.2, and for $n = 3,\ 4$ in Sections 6.3, 6.4.

6.5.1.1 Cover Attractors Fig. 6.16 displays strange attractors that are two-fold, three-fold, and four-fold covers of the Rössler attractor. The covers are equivariant under $\mathcal{C}_n$. The topological indices are $(0, 1)$ (left column) and $(1, 1)$ (right column).

6.5.1.2 Lifts of Low Period Orbits Lifts of the low period orbits 1, 10, 101, 100 into covers equivariant under $\mathcal{C}_n$ with topological index $(n_0, n_1) = (0, 1)$ are shown in Fig. 6.17. The same orbits, lifted into covers with index $(n_0, n_1) = (1, 1)$ are shown in Fig. 6.18. In both figures the orbits 1, 10, 101, and 100 are shown in the left hand column. Their lifts to two-fold covers, three-fold covers, and four-fold covers are shown in the succeeding columns.

In $\mathcal{C}_n$ equivariant covers of the Rössler attractor, lifts of orbits of period p have a total of $pn = p|\mathcal{C}_n|$ symbols. The lift may be a single connected symmetric orbit of period np, it may consist of n symmetry-related copies of an asymmetric period p orbit, or may be any allowed intermediate case. The lifts of the orbits 1, 10, 101, 100, in the lift with index $(n_0, n_1) = (0, 1)$ have minimal periods

Image	Period	Two-fold cover	Three-fold cover	Four-fold cover
1	1	2	3	4
10	2	4	6	8
101	3	3	9	6
100	3	6	9	12

The lifts of these same orbits into the cover with index $(n_0, n_1) = (1, 1)$ have periods

Image	Period	Two-fold cover	Three-fold cover	Four-fold cover
1	1	2	3	4
10	2	2	6	4
101	3	6	3	12
100	3	6	3	12

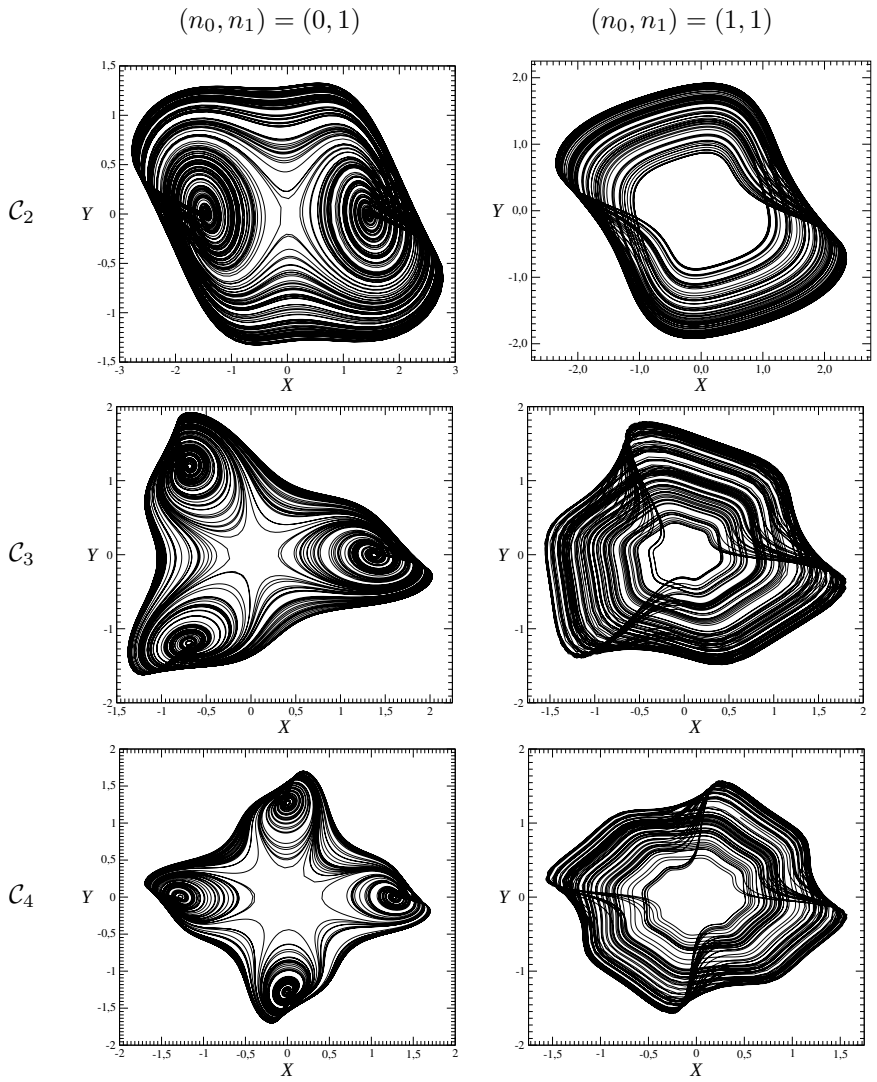

Fig. 6.16 Two-, three-, and four-fold covers of the Rössler equations with topological indices $(n_0, n_1) =$ (0,1) and (1,1).

6.5.1.3 Links of Lifts

In the Rössler attractor

$$\text{Link}\,(1, 01) = 1$$

The lifts of these orbits into n-fold covers, $n = 2, 3, 4$, with topological indices $(n_0, n_1) = (0, 1)$ and $(1, 1)$, are shown in Fig. 6.19. The links of these lifts can be determined by inspection of these projections.

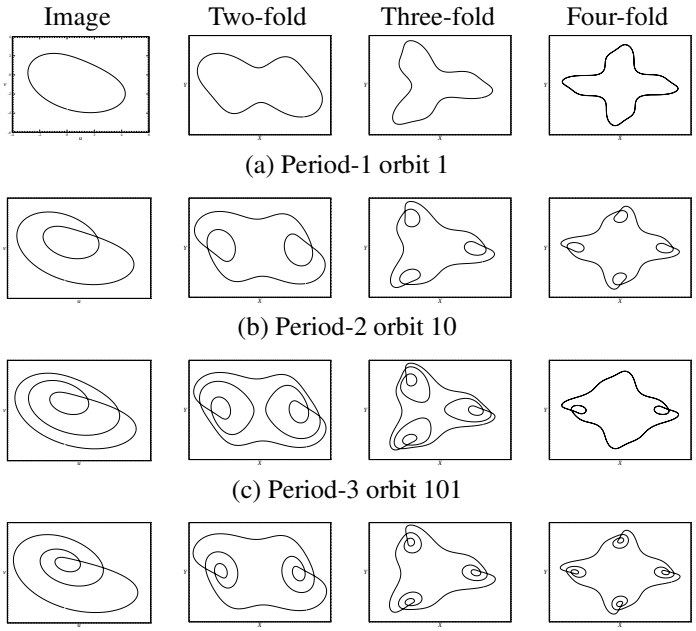

(a) Period-1 orbit 1

(b) Period-2 orbit 10

(c) Period-3 orbit 101

(d) Period-3 orbit 100

Fig. 6.17 Periodic orbits for the Rössler system and its different covers with indices $(n_0, n_1) = (0, 1)$.

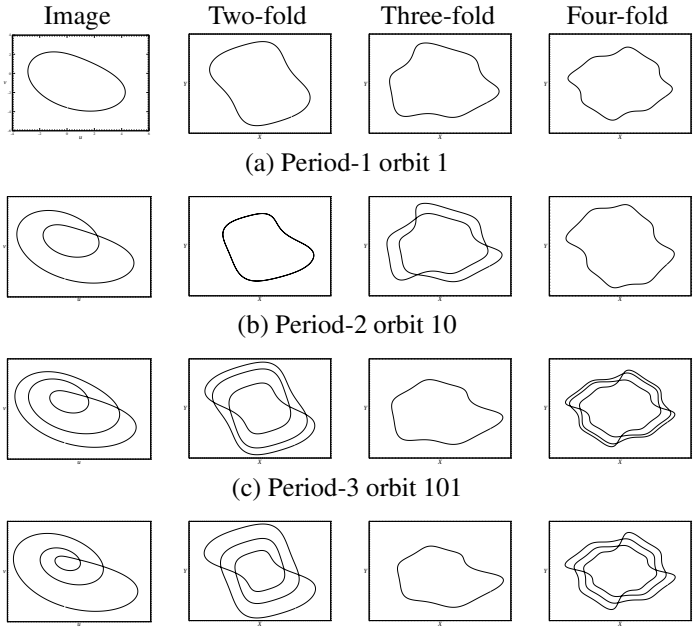

(a) Period-1 orbit 1

(b) Period-2 orbit 10

(c) Period-3 orbit 101

(d) Period-3 orbit 100

Fig. 6.18 Periodic orbits of the Rössler system and its different covers with indices $(n_0, n_1) = (1, 1)$. When more than one cover orbit exists, only one is shown.

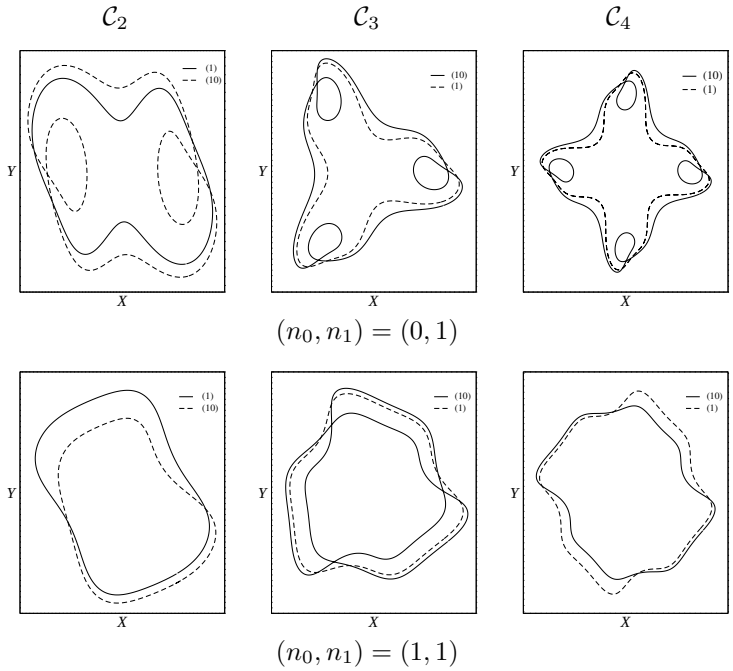

Fig. 6.19 Links of orbits that cover 1 and 10 in two-, three-, and four-fold covers of the Rössler system. Top: linking numbers are 2, 3, 4. Bottom: 1, 3, 2.

In the case with index $(0, 1)$ the image orbit 1 lifts to a period-2 orbit in the two-fold cover, a period-3 orbit in the three-fold cover, and a period-4 orbit in the four-fold cover. The orbit 10 of period-2 lifts to orbits of periods 4, 6, and 8, respectively. The linking numbers of the lifted orbits are 2, 3, and 4, as can be confirmed directly by counting crossings. Things are slightly different in the covers with topological index (1,1). In the two-fold cover 1 and 10 both lift to period-two orbits with linking number 1. In the three-fold cover 1 and 10 lift to orbits of periods 3 and 6. The linking number of these two covering orbits is 3. However, the orbit 10 lifts to two disconnected orbits of period-4. One of these orbits is shown in Fig. 6.17. The linking number of this orbit with the period 4 lift of the image orbit 1 is $2 = \frac{1}{2} \times 4$, as can be verified directly by counting crossings.

6.5.2 Proto–Lorenz System

The proto-Lorenz equations, and their n-fold covers, are given in Section 6.2. We remark that one of the two-fold covers of the proto-Lorenz equations is the original Lorenz system. However, the proto-Lorenz equations have alternative two-fold covers, differing by the equivariance group $(\mathcal{R}_Z \to \mathcal{P})$ and topological index $(n_0, n_1) = (0, 1) \to (1, 1)$. One of the double covers of the original Lorenz sys-

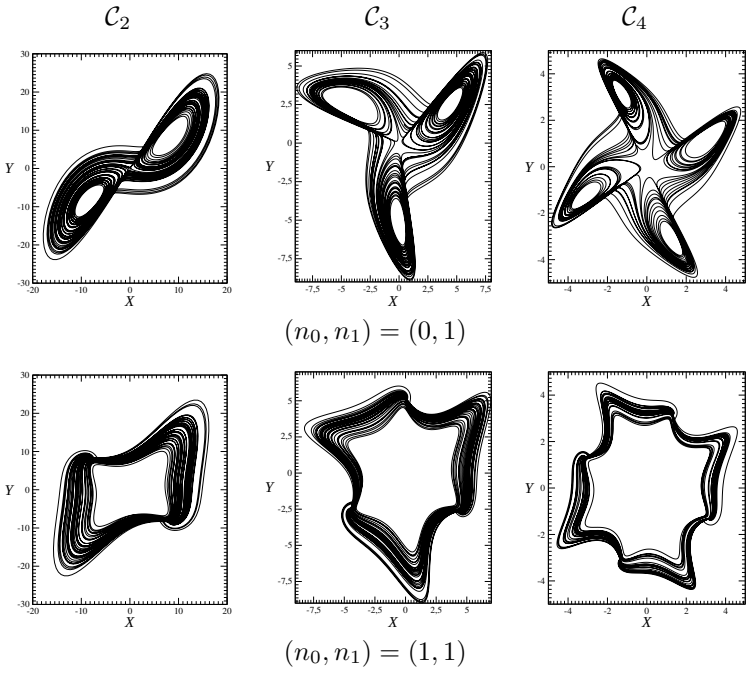

Fig. 6.20 Two-, three-, and four-fold covers of the proto-Lorenz equations.

tem is one of the four-fold covers of the proto-Lorenz system. Again, both have a spectrum of inequivalent covers. We finally remark that "the" three-fold cover of the proto-Lorenz system can be regarded as a "$\frac{3}{2}$" cover of the original Lorenz system.

6.5.2.1 Cover Attractors Fig. 6.20 displays strange attractors that are two-fold, three-fold, and four-fold covers of the proto-Lorenz attractor. The covers are equivariant under $\mathcal{C}_n$. Their topological indices are $(n_0, n_1) = (0, 1)$ (top row) and (1,1) (bottom row). The covering attractor with $\mathcal{C}_2$ symmetry and topological index $(n_0, n_1) = (0, 1)$ is the original Lorenz attractor.

6.5.2.2 Lifts of Low Period Orbits Lifts of the orbits up to period 3 into attractors that cover the proto-Lorenz attractor with $\mathcal{C}_n$ symmetries are shown in Figs. 6.21 and 6.22. The orbits shown in Fig. 6.21 are into a cover with index $(0, 1)$; those in Fig. 6.22 are into a cover with index $(1, 1)$.

The periods of the orbits in the cover $(0, 1)$ are

Image	Period	Two-fold cover	Three-fold cover	Four-fold cover
1	1	2	3	4
10	2	4	6	8
101	3	3	9	6
100	3	6	9	12

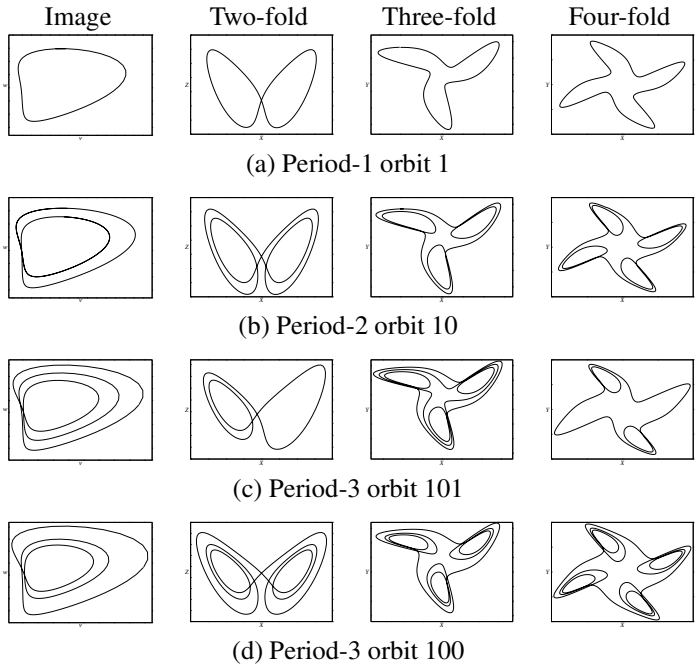

Fig. 6.21 Periodic orbits for the proto-Lorenz system and its different covers with indices $(n_0, n_1) = (0, 1)$.

The image orbit 101 lifts to a pair of period-6 orbits in the four-fold cover. The pair is symmetry-related. Only one is shown in Fig. 6.21. In Fig. 6.22 we show lifts of the same four low period orbits to covers of the proto-Lorenz attractor with topological index $(n_0, n_1) = (1, 1)$. The periods of the covering orbits are

Image	Period	Two-fold cover	Three-fold cover	Four-fold cover
1	1	2	3	4
10	2	2	6	4
101	3	6	3	12
100	3	6	3	12

In this case the four-fold lift of 10 consists of two disconnected, symmetry-related period-four orbits. There are three symmetry-related three-fold covers of 101 and 100, all of period three.

6.5.2.3 Links of Lifts Links of the lifts of the orbits 1 and 10 in the proto-Lorenz system are shown in Fig. 6.23. The lifts are into covers with $\mathcal{C}_n$ symmetry, $n = 2, 3, 4$ and topological indices $(0, 1)$ and $(1, 1)$.

In Fig. 6.23 we show links of the lifts of the two orbits 1, 10 in the proto-Lorenz attractor. The links are shown in the two-fold, three-fold, and four-fold

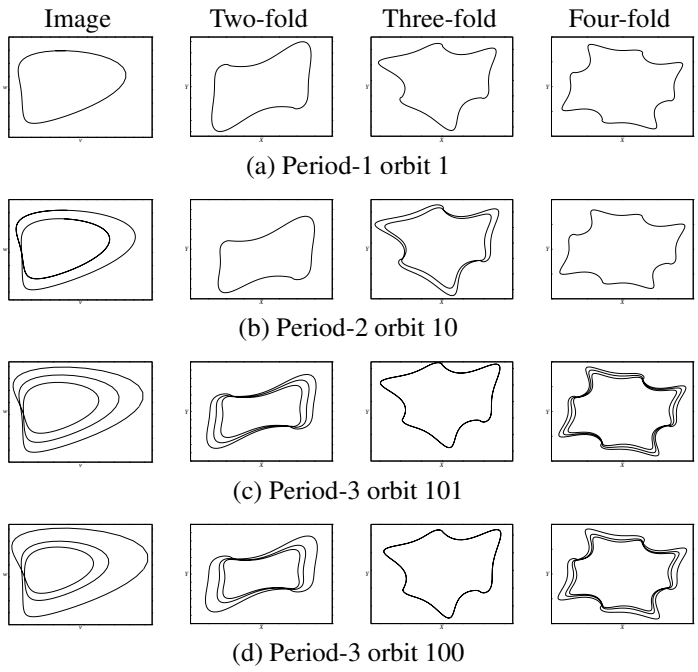

Fig. 6.22 Periodic orbits for the proto-Lorenz system and its different covers with indices $(n_0, n_1) = (1, 1)$.

covers with topological index $(n_0, n_1) = (0, 1)$ and $(1, 1)$. In the cover with index $(n_0, n_1) = (0, 1)$, the orbit 1 lifts to orbits of periods 2, 3, and 4 (respectively) and the orbit 10 lifts to orbits of periods 4, 6, and 8. The linking numbers of the lifts are therefore

$$\text{Link}(\bar{1}, \overline{10}) = n \times \text{Link}(1, 10)$$

where $n = 2, 3, 4$ for two-fold, three-fold, and four-fold lifts. Similar results hold for the two-fold and three-fold lifts of $1, 10$ to covers with index $(n_0, n_1) = (1, 1)$. However, in this case the period-2 orbit 10 lifts to two asymmetric orbits of period-4 in the four-fold cover. The linking number of the period-4 lifts of 10 with the lift of 1 is therefore 2. This can be verified by direct counting of the signed crossings in Fig. 6.23.

6.5.3 Proto–Burke and Shaw System

The proto–Burke and Shaw equations and their n-fold covers are given in Section 6.2. As for the proto-Lorenz equations, one of the two-fold covers of the proto–Burke and Shaw equations is the original Burke and Shaw set of equations.

6.5.3.1 Cover Attractors Fig. 6.24 displays strange attractors that are two-fold, three-fold, and four-fold covers of the proto–Burke and Shaw attractor. The covers are

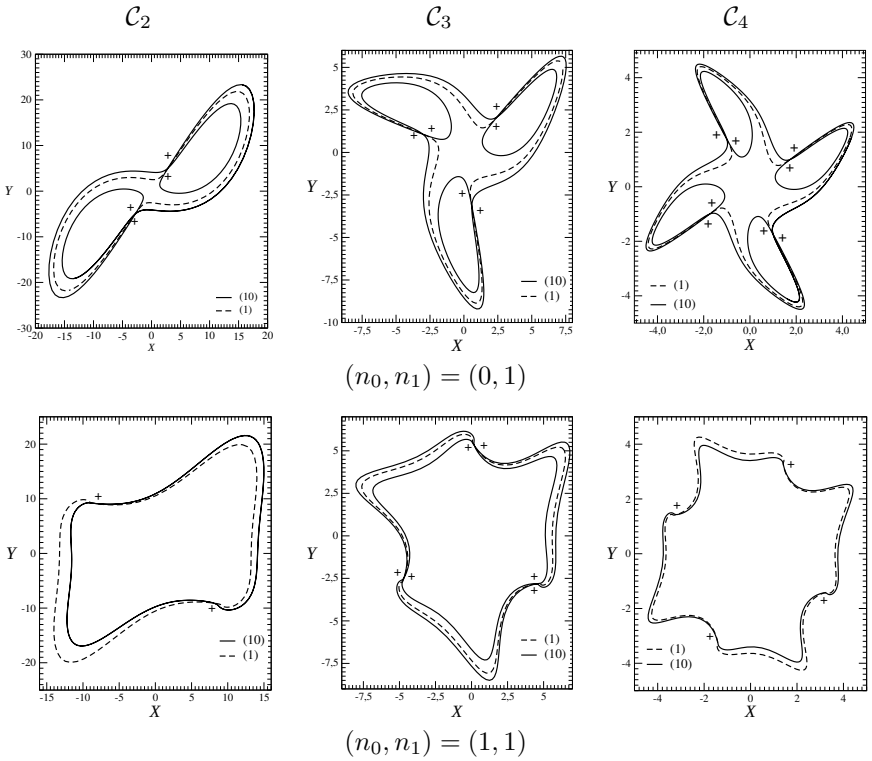

Fig. 6.23 Link of orbits that cover 1 and 10 in two-, three-, and four-fold covers of the proto-Lorenz system.

equivariant under $\mathcal{C}_n$. Their topological indices are $(n_1, n_2) = (1, 0)$ (top row) and $(1, 1)$ (bottom row). The original covering attractor with $\mathcal{C}_2$ symmetry and topological index $(n_1, n_2) = (1, 1)$ is essentially the original Burke and Shaw attractor.

6.5.3.2 Lifts of Low Period Orbits The proto–Burke and Shaw attractor is described by a reverse horseshoe branched manifold. The two branches have local torsion 1 and 2. Therefore, all periodic orbits have the symbol sequences composed of these two symbols.

Lifts of the orbits up to period 3 into attractors that cover the proto–Burke and Shaw attractor with $\mathcal{C}_n$ symmetry are shown in Figs. 6.25 and 6.26. The orbits shown in Fig. 6.25 are into a cover with index $(n_1, n_2) = (1, 0)$; those in Fig. 6.26 are into a cover with index $(1, 1)$.

The four orbits 1, 12, 121, and 122 from the proto–Burke and Shaw system in the covers with index (1,0) have periods as follows

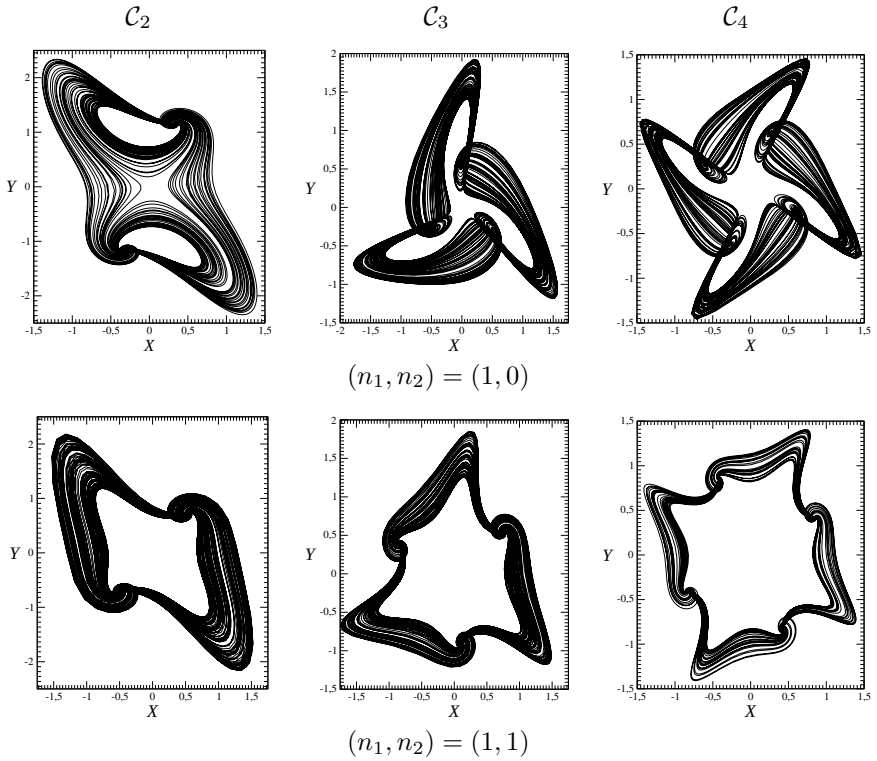

Fig. 6.24 Two-, three-, and four-fold covers of the proto–Burke and Shaw equations.

	Image	Two-fold cover	Three-fold cover	Four-fold cover
1	1	2	3	4
12	2	4	6	8
122	3	6	9	12
121	3	3	9	6

The image orbit 121 lifts to a pair of orbits in both the two-fold cover and the four-fold cover. In all other cases shown, the image orbit of period-p lifts to a cover orbit of period np in the n-fold cover.

Lifts of the orbits 1, 12, 121, and 122 to the cover with topological index $(n_1, n_2) = (1, 1)$ are shown in Fig. 6.26. These orbits have periods as follows

	Image	Two-fold cover	Three-fold cover	Four-fold cover
1	1	2	3	4
12	2	2	6	4
121	3	6	3	12
122	3	6	3	12

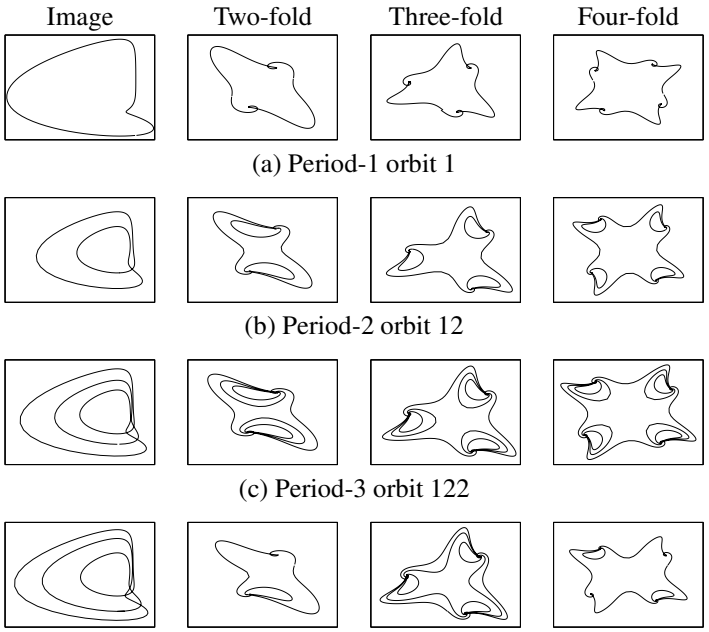

Fig. 6.25 Periodic orbits for the proto–Burke and Shaw system and its different covers with indices $(n_1, n_2) = (1, 0)$.

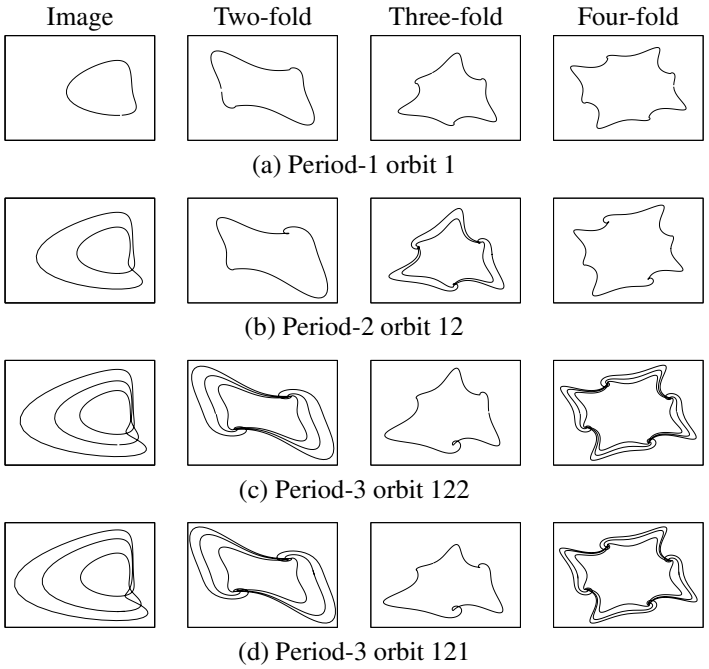

Fig. 6.26 Periodic orbits for the proto–Burke and Shaw system and its different covers with indices $(n_1, n_2) = (1, 1)$.

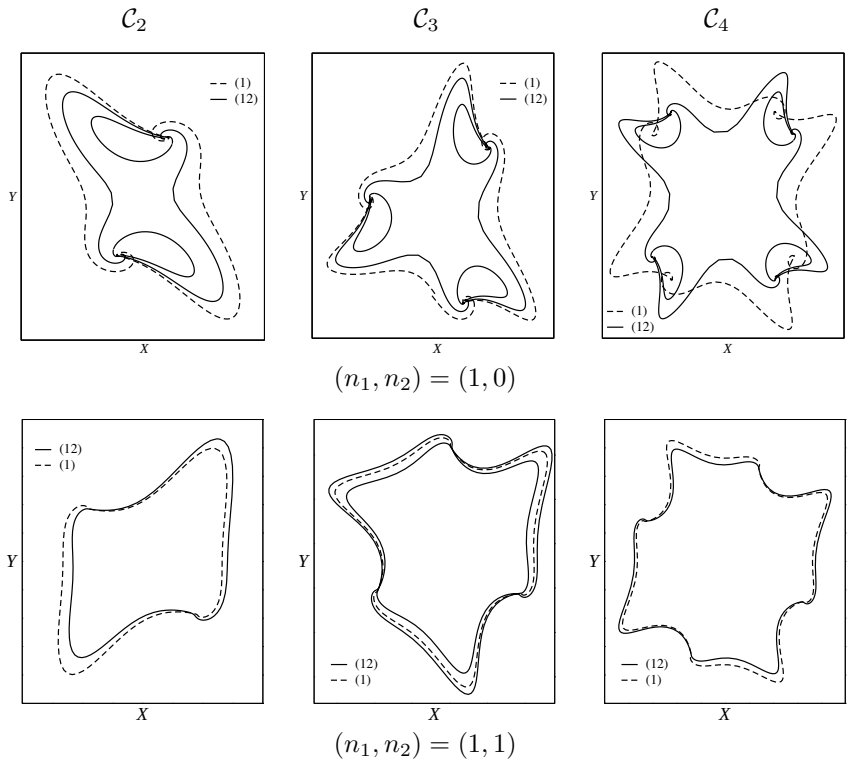

Fig. 6.27 Links of orbits that cover 1 and 12 in two-, three-, and four-fold covers of the proto–Burke and Shaw system.

In this case the period-2 orbit 12 lifts to two orbits of period-2 in the two-fold cover and two orbits of period-4 in the four-fold cover, while both period-3 orbits lift to three symmetry-related period-3 orbits in the three-fold cover.

6.5.3.3 Links of Lifts In Fig. 6.27 we show the period-1 orbit 1 and the period-2 orbit 12 in the proto–Burke and Shaw system as well as the lifts of these two orbits to the two-fold, three-fold, and four-fold covers with topological indices $(n_1, n_2) = (1, 0)$ and $(n_1, n_2) = (1, 1)$. In the image, $\text{Link}(1, 12) = 1$. The orbit 1 lifts to orbits of period n in the n-fold cover with both indices $(n_1, n_2) = (1, 0)$ and $(n_1, n_2) = (1, 1)$. In the case with $(n_1, n_2) = (1, 0)$ the period-two orbit lifts to single orbits in the covers with periods $2n = 4, 6, 8$. The linking numbers with the lifts of 1 are $2, 3, 4$, respectively, as seen in the top line of Fig. 6.27. In the cover with $(n_1, n_2) = (1, 1)$ the period-2 orbit 12 lifts to: two period-2 orbits in the two-fold cover; one period-6 orbit in the three-fold cover; two period-4 orbits in the four-fold cover. The linking numbers of the covering orbits in the two-fold, three-fold, and four-fold covers 1, 3, and 2, respectively, as seen in the bottom line of Fig. 6.27.

6.6 COVERS WITH $\mathcal{V}_4$ SYMMETRY

6.6.1 The Group

The four-group V_4 ("vier gruppe") has four group operations, the identity, two generators, σ_1 and σ_2, and their product $\sigma_1\sigma_2$. The generators satisfy the relations $\mathbb{I} = \sigma_1^2 = \sigma_2^2 = (\sigma_1\sigma_2)^2$. This group can be implemented in $\mathbb{R}^3$ as the group of rotations by π radians about the X-, Y- and Z-axes. The matrix representation of this group is

$$\begin{matrix}\mathbb{I}\\ \begin{bmatrix}1&0&0\\0&1&0\\0&0&1\end{bmatrix}\end{matrix} \quad \begin{matrix}\mathcal{R}_X(\pi)\\ \begin{bmatrix}+1&0&0\\0&-1&0\\0&0&-1\end{bmatrix}\end{matrix} \quad \begin{matrix}\mathcal{R}_Y(\pi)\\ \begin{bmatrix}-1&0&0\\0&+1&0\\0&0&-1\end{bmatrix}\end{matrix} \quad \begin{matrix}\mathcal{R}_Z(\pi)\\ \begin{bmatrix}-1&0&0\\0&-1&0\\0&0&+1\end{bmatrix}\end{matrix}$$

Any two distinct rotations can be chosen as σ_1 and σ_2.

6.6.2 Invariant Polynomials

The invariant polynomials are

$$p_1 = X^2, \;\; p_2 = Y^2, \;\; p_3 = Z^2, \;\; p_4 = XYZ$$

The quartic invariants are all products of quadratic invariants. The four basic invariant polynomials above obey one syzygy

$$(X^2)(Y^2)(Z^2) - (XYZ)^2 = p_1p_2p_3 - p_4^2 = 0$$

The ring of covariant polynomials consists of 1, X, Y, Z, XY, YZ, ZX, all cubic terms except XYZ. The quartic terms in the ring $X^{n_1}Y^{n_2}Z^{n_3}$ must have at least one n_i odd.

The generating function for the number of invariants of degree d is

$$f(X) = \sum N(d)X^d = \frac{1}{4}\sum_{g_i}\frac{1}{\det[I_3 - x\mathcal{R}(g_i)]} = \frac{1+x^3}{(1-x^2)^3}$$

This shows that there are three independent quadratic terms (X^2, Y^2, Z^2), and the cubic terms obey the syzygy $p_4^2 = p_1p_2p_3$.

6.6.3 Invariant Coordinates

It is useful to choose an invariant coordinate system as the following linear combination of the quadratic and cubic invariant polynomials

$$\begin{aligned} u_1 &= \tfrac{1}{2}(X^2 - Y^2)\\ u_2 &= \tfrac{1}{2}(X^2 + Y^2 - 2Z^2)\\ u_3 &= XYZ \end{aligned}$$

Every point in $\mathbb{R}^3(\boldsymbol{u})$ has an inverse image in $\mathbb{R}^3(\boldsymbol{X})$. This is obtained from

$$X = \pm\sqrt{Z^2 + u_2 + u_1}$$

$$Y = \pm\sqrt{Z^2 + u_2 - u_1}$$

The value of Z is determined from

$$u_3 = \sqrt{Z^2 + u_2 + u_1}\,\sqrt{Z^2 + u_2 - u_1}\,Z$$

This equation has a unique solution, as can easily be seen. If $u_3 > 0$, the solution is in the positive octant $(X, Y, Z) = (+, +, +)$. If $u_3 < 0$ the solution is in the octant (+,+,−); The unique solution is mapped into the three additional inverse images by the three rotation operations

$$\begin{array}{cccccc} & & \mathbb{I} & \mathcal{R}_X(\pi) & \mathcal{R}_Y(\pi) & \mathcal{R}_Z(\pi) \\ (+++) & \rightarrow & (+++) & (+--) & (-+-) & (--+) \\ (++-) & \rightarrow & (++-) & (+-+) & (-++) & (---) \end{array}$$

The four inverse images in the top line map to the upper half $(u_3 > 0)$ of $\mathbb{R}^3(\boldsymbol{u})$. The bottom line maps to the lower half of this space.

6.6.4 The Jacobian

The Jacobian of the $4 \rightarrow 1$ local diffeomorphism of $\mathbb{R}^3(\boldsymbol{X})$ onto $\mathbb{R}^3(\boldsymbol{u})$ is

$$\frac{\partial \boldsymbol{u}}{\partial \boldsymbol{X}} = \begin{bmatrix} X & -Y & 0 \\ X & Y & -2Z \\ YZ & ZX & XY \end{bmatrix} \xrightarrow{\det} 2(X^2Y^2 + Y^2Z^2 + Z^2X^2)$$

The determinant vanishes when any two of the three quadratic invariants X^2, Y^2, Z^2 are zero. Specifically, it is

$$\underset{\mathcal{R}_X(\pi)}{Y^2 + Z^2 = 0} \quad \cup \quad \underset{\mathcal{R}_Y(\pi)}{Z^2 + X^2 = 0} \quad \cup \quad \underset{\mathcal{R}_Z(\pi)}{X^2 + Y^2 = 0}$$

In short, it is the union of three rotation axes. The singularities reflect the symmetry of the group.

6.6.5 Covering Equations

The dynamical equations for a four-fold cover with symmetry group $\mathcal{V}_4$ are

$$\frac{d}{dt}\begin{bmatrix} X \\ Y \\ Z \end{bmatrix} = \frac{1}{2(X^2 + Y^2 + Z^2)}\begin{bmatrix} X(Y^2 + 2Z^2) & XY^2 & 2YZ \\ -Y(X^2 + 2Z^2) & X^2Y & 2ZX \\ Z(X^2 - Y^2) & -Z(X^2 + Y^2) & 2XY \end{bmatrix}\begin{bmatrix} \dot{u}_1 \\ \dot{u}_2 \\ \dot{u}_3 \end{bmatrix}$$

A strange attractor in the image space can be lifted to a covering attractor by integrating these equations following the prescription of Fig. 4.9. An initial condition in the covering space is chosen to initiate the computation. This is needed to evaluate the u_i, which are then used to evaluate the $\dot{u}_i$. We use this procedure to lift the Rössler attractor to various covers.

6.6.6 Topological Index

The V_4-symmetric covers of the Rössler attractor are distinguished by the linking numbers of the period-one orbits $0, 1$ with the three rotation axes. The topological index is a six-component object:

$$\boldsymbol{n} = [n_x, n_y, n_z] = [(n_{0X}, n_{1X}), (n_{0Y}, n_{1Y}), (n_{0Z}, n_{1Z})].$$

Branch	Axis		
0	n_{0X}	n_{0Y}	n_{0Z}
1	n_{1X}	n_{1Y}	n_{1Z}

The cover contains four branch lines labeled by the group operations. The transition matrix is determined by the topological index. The cover may be connected or disconnected according to the topological index. In Fig. 6.28 we show how the branch lines are labeled. For the cover with topological index

	X	Y	Z
0	0	0	1
1	0	1	1

(6.10)

the orbit 0 does not circle the X- or Y-axis, but does circles the Z-axis. As a result, the image of the half branch line $0_{\mathbb{I}}$ under the flow is the branch line in $\mathcal{R}_Z : 0_Z, 1_Z$. Similarly, the images of the other symbols 0_* under the flow are $\mathcal{R}_Z 0_* = 0_{\mathcal{R}_Z *}, 1_{\mathcal{R}_Z *}$. The orbit 1 does not circle the X-axis but circles both the Y- and Z-axes. The image of the half branch line $1_{\mathbb{I}}$ under the flow is $\mathcal{R}_Y \mathcal{R}_Z 1_{\mathbb{I}} = 0_{\mathcal{R}_Y \mathcal{R}_Z \mathbb{I}}, 1_{\mathcal{R}_Y \mathcal{R}_Z \mathbb{I}} = 0_X, 1_X$.

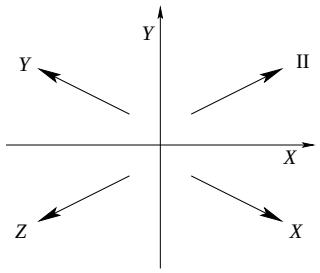

Fig. 6.28 Labeling of the four different branch lines of the $\mathcal{V}_4$ cover of the Rössler system.

In a similar way the images of the other three symbols are $\mathcal{R}_Y\mathcal{R}_Z 1_X = (0,1)_{\mathbb{I}}$, $\mathcal{R}_Y\mathcal{R}_Z 1_Y = (0,1)_Z$, $\mathcal{R}_Y\mathcal{R}_Z 1_Z = (0,1)_Y$.

In summary

$$\begin{array}{llll} 0_{\mathbb{I}} \to 0_Z, & 1_Z & \quad 1_{\mathbb{I}} \to 0_X, & 1_X \\ 0_X \to 0_Y, & 1_Y & \quad 1_X \to 0_{\mathbb{I}}, & 1_{\mathbb{I}} \\ 0_Y \to 0_X, & 1_X & \quad 1_Y \to 0_Z, & 1_Z \\ 0_Z \to 0_{\mathbb{I}}, & 1_{\mathbb{I}} & \quad 1_Z \to 0_Y, & 1_Y \end{array}$$

6.6.7 Transition Matrix

The transition matrix for this cover is

		$\mathbb{I}$		$\mathcal{R}_X$		$\mathcal{R}_Y$		$\mathcal{R}_Z$	
		0	1	0	1	0	1	0	1
$\mathbb{I}$	0	0	0	0	0	0	0	1	1
	1	0	0	1	1	0	0	0	0
$\mathcal{R}_X$	0	0	0	0	0	1	1	0	0
	1	1	1	0	0	0	0	0	0
$\mathcal{R}_Y$	0	0	0	1	1	0	0	0	0
	1	0	0	0	0	0	0	1	1
$\mathcal{R}_Z$	0	1	1	0	0	0	0	0	0
	1	0	0	0	0	1	1	0	0

For this topological index the cover is connected. This can be seen at two levels: every branch line is visited from an initial condition on any branch line, and the transition matrix cannot be put in block-diagonal form. Another way to look at this is that it is possible to find a path from any branch line to any other branch line. The eigenvalues of this transition matrix are $(2,0,0,0,0,0,0,-2)$. The topological entropy is $\log 2$.

6.6.8 Branched Manifold

The Rössler attractor can be lifted to a cover with $\mathcal{V}_4$ symmetry and index (6.10) by placing the rotation axis as shown in Fig. 6.29. The cover branched manifold has $\mathcal{V}_4$ symmetry. It is difficult to represent this branched manifold in planar projection. For this reason a topologically accurate distortion is presented in Fig. 6.30.

6.6.9 Another Cover

In a different case, we choose topological index

	X	Y	Z
0	0	0	1
1	0	0	0

For this index, the transition matrix is

		$\mathbb{I}$		$\mathcal{R}_X$		$\mathcal{R}_Y$		$\mathcal{R}_Z$	
		0	1	0	1	0	1	0	1
$\mathbb{I}$	0	0	0	0	0	0	0	1	1
	1	1	1	0	0	0	0	0	0
$\mathcal{R}_X$	0	0	0	0	0	1	1	0	0
	1	0	0	1	1	0	0	0	0
$\mathcal{R}_Y$	0	0	0	1	1	0	0	0	0
	0	0	0	0	0	1	1	0	0
$\mathcal{R}_Z$	0	1	1	0	0	0	0	0	0
	1	0	0	0	0	0	0	1	1

This cover is disconnected. The branch lines $\mathbb{I}, Z$ are connected by the transition matrix. The branch lines X and Y are also connected. The two pairs of branch lines $(\mathbb{I}, \mathcal{R}_Z)$ and $(\mathcal{R}_X, \mathcal{R}_Y)$ are disconnected from each other. These two components are equivariant under $\mathcal{R}_Z(\pi)$. They are mapped into each other by $\mathcal{R}_X$ and $\mathcal{R}_Y$.

6.6.10 Comparison of Attractors

Attractors with two different topological indices are shown in three different projections in Fig. 6.31. The attractor shown in Fig. 6.31(a) is disconnected. It is the $\mathcal{V}_4$ equivariant cover of the Rössler attractor with y displaced to $y - 1$. This component is equivariant under the subgroup $\{\mathbb{I}, R_X(\pi)\}$ and mapped into its symmetric partner by the two group operations $\{R_Y, R_Z\}$. The attractor in Fig. 6.31(b) consists of one connected component that is equivariant under $\mathcal{V}_4$. It is the $\mathcal{V}_4$ equivariant cover of the Rössler attractor with y displaced to $y - 1$ and z displaced to $z - 1$.

The time series for the three coordinates $X(t), Y(t), Z(t)$ for the latter attractor are shown in Fig. 6.32.

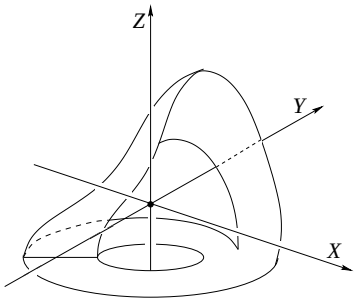

Fig. 6.29 Configuration of the rotation axes in the image space for the $\mathcal{V}_4$ cover of the Rössler system, with index (6.10).

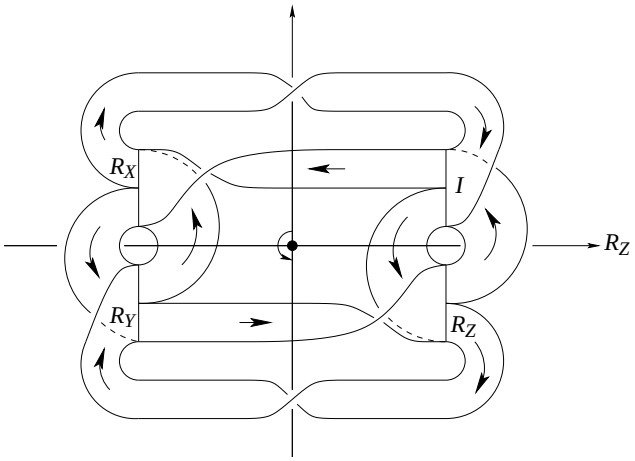

Fig. 6.30 Branched manifold of the $\mathcal{V}_4$ cover of the Rössler system with index (6.10).

Periodic orbits in the image can lifted in the cover following the prescription provided in Fig. 4.9.

The period-3 saddle-node pair 100, 101 in the image, shown in Fig. 6.33, lift to orbits in the $\mathcal{V}_4$ equivariant cover with topological index (6.10) that are shown in Fig. 6.34. The symbolic dynamics of the lifted orbits are

$$\begin{aligned} 100 \rightarrow \quad & 1_{(\underline{\mathbb{I}},R_x)}0_{(R_x,R_y)}0_{(R_y,R_x)}1_{(R_x,\mathbb{I})}0_{(\mathbb{I},R_z)}0_{(R_z,\underline{\mathbb{I}})} \\ & 1_{(\underline{R_y},R_z)}0_{(R_z,\mathbb{I})}0_{(\mathbb{I},R_z)}1_{(R_z,R_y)}0_{(R_y,R_x)}0_{(R_x,\underline{R_y})} \end{aligned}$$

$$\begin{aligned} 101 \rightarrow \quad & 1_{(\underline{\mathbb{I}},R_x)}0_{(R_x,R_y)}1_{(R_y,R_z)}1_{(R_z,R_y)}0_{(R_y,R_x)}0_{(R_x,\underline{\mathbb{I}})} \\ & 1_{(\underline{R_x},R_y)}0_{(R_y,R_x)}1_{(R_x,R_y)}1_{(R_y,R_z)}0_{(R_z,\mathbb{I})}1_{(\mathbb{I},\underline{R_x})} \end{aligned}$$

Each period-3 orbit in the image lifts to a pair of symmetry related orbits in the cover. The two lifts of 100 are invariant under $\{\mathbb{I}, R_x\}$ while the two lifts of 101 are invariant under a different symmetry subgroup $\{\mathbb{I}, R_z\}$.

6.7 NONCOMMUTATIVITY OF LIFTS

We have until now described covers of image dynamical systems without symmetry. It is possible to construct covers of image dynamical systems with symmetry—systems that are already covers of systems without (or with less) symmetry. This raises the question: Suppose an image dynamical system equivariant under $\mathcal{G}_1$ is lifted to a cover equivariant under $\mathcal{G}_2$. Do we recover the same dynamics if the order of the groups $\mathcal{G}_1$ and $\mathcal{G}_2$ is reversed? We show that the answer is "No" even in the simplest case where the two equivariance groups are equal, $\mathcal{G}_1 = \mathcal{R}_Z(\pi)$, $\mathcal{G}_2 = \mathcal{R}_Z(\pi)$. The reason is that a cover is determined by two input pieces of data: a symmetry group $\mathcal{G}$ and an index.

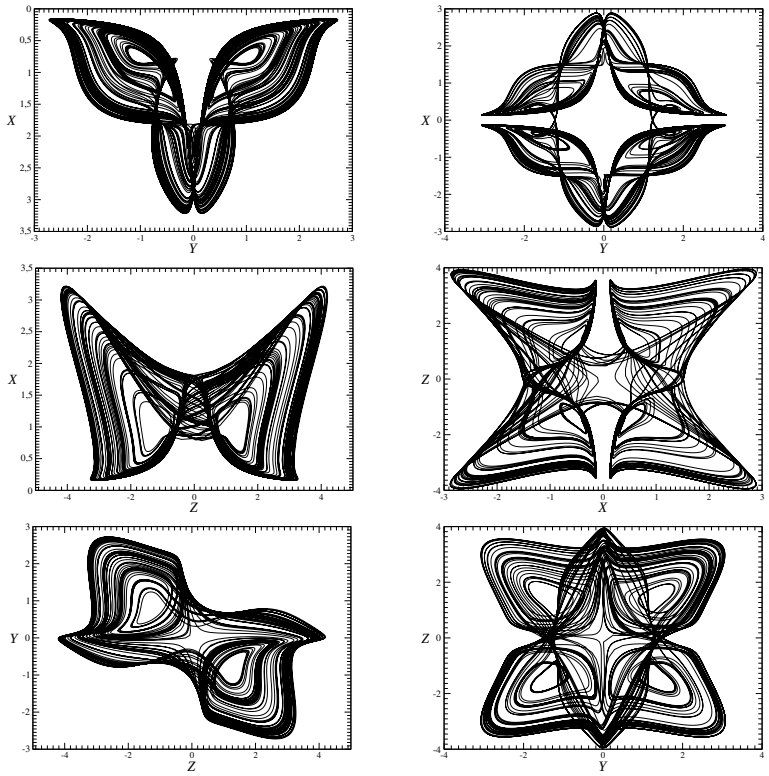

(a) Two disconnected attractors coexist (b) A single connected attractor

Fig. 6.31 $\mathcal{V}_4$ equivariant cover of the Rössler attractor $(a = 0.420)$ for two different displacements of the rotation axes. Case (a) $y \mapsto y - 1$. Case (b) $y \mapsto y - 1$ and $z \mapsto z + 1$. The rotation axis is located in the branch 0 of the image attractor.

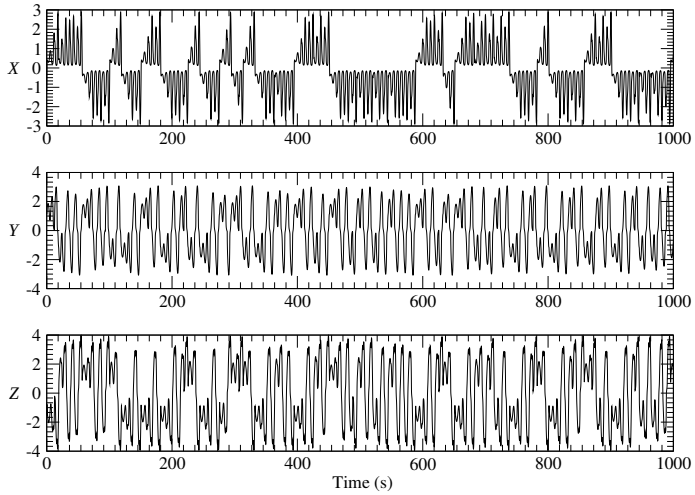

Fig. 6.32 The time series for the connected $\mathcal{V}_4$ equivariant cover of the Rössler attractor shown in Fig. 6.31(b).

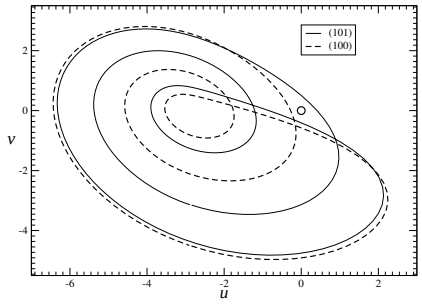

Fig. 6.33 Period-3 orbits embedded within the Rössler attractor. The rotation axis is located between them. Thus the orbits are organized in a different way in the cover space $\mathbb{R}^3(X, Y, Z)$.

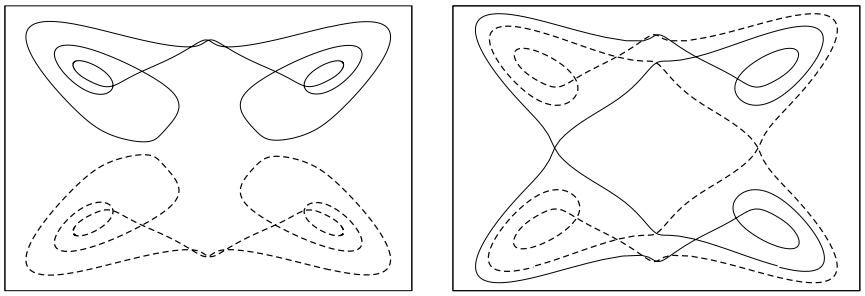

(a) (100) (b) (101)

Fig. 6.34 Covers of the period-3 orbits extracted from the Rössler system for $a = 0.432$. Pairs of periodic orbits are shown in the X-Z plane projection. The $\mathcal{V}_4$ equivariant cover is shown in Fig. 6.31(b).

Two topologically inequivalent lifts of the proto-Lorenz system are shown in Fig. 6.35(a) and (b). Since they are two-fold covers of a system with one branch line, both have two branch lines. They are labeled l and r. Each has two parts labeled 0 and 1. These labels identify branches in the image branched manifold. The two lifts differ by their topological index. The 2×2 transition matrix for the two branch image and its two lifts to the $\mathcal{R}_Z(\pi)$ equivariant covers with indices $(n_0, n_1) = (0, 1)$ and (1,1) are

	0	1
0	1	1
1	1	1

(0,1) (1,1)

	l		r	
	0	1	0	1
0	1	1	0	0
1	0	0	1	1
0	0	0	1	1
1	1	1	0	0

	l		r	
	0	1	0	1
0	0	0	1	1
1	0	0	1	1
0	1	1	0	0
1	1	1	0	0

Two $\mathcal{R}_Z(\pi)$ equivariant double covers of the attractor shown in Fig. 6.35(a) are now constructed. In one, the rotation axis is taken in the hole near the branch line r. This double cover is shown in Fig. 6.35(c). In this double cover the two branch lines l_0, l_1 cover branch line l in the image in Fig. 6.35(a). Similarly, the two branch lines r_0, r_1 cover in r in Fig. 6.35(a). The second double cover of the attractor in Fig. 6.35(a) is obtained using the same symmetry axis used to lift the proto-Lorenz attractor to the double cover shown in Fig. 6.35(a). The rotation axis passes through the origin in the X-Y plane. This double cover is shown in Fig. 6.35(e). Once again, the two branch lines l_0, l_1 cover l and r_0, r_1 cover r. The 4×4 transition matrix for the attractor in Fig. 6.35(a) lifts to the two 8×8 matrices for the attractors shown in Fig. 6.35(c) and (e) as follows

	l		r	
0	1	1	0	0
1	0	0	1	1
0	0	0	1	1
1	1	1	0	0

Axis in lobe (c)

Axis at origin (e)

	l_0		r_0		l_1		r_1	
	0	1	0	1	0	1	0	1
0	1	1	0	0	0	0	0	0
1	0	0	1	1	0	0	0	0
0	0	0	0	0	0	0	1	1
1	0	0	0	0	1	1	0	0
0	0	0	0	0	1	1	0	0
1	0	0	0	0	0	0	1	1
0	0	0	1	1	0	0	0	0
1	1	1	0	0	0	0	0	0

	l_0		r_0		l_1		r_1	
	0	1	0	1	0	1	0	1
0	1	1	0	0	0	0	0	0
1	0	0	1	1	0	0	0	0
0	0	0	1	1	0	0	0	0
1	0	0	0	0	1	1	0	0
0	0	0	0	0	1	1	0	0
1	0	0	0	0	0	0	1	1
0	0	0	0	0	0	0	1	1
1	1	1	0	0	0	0	0	0

Branched manifolds for the two attractors shown in Fig. 6.35(c) and (e) are presented in Fig. 6.36. These branched manifolds are clearly inequivalent.

Two double covers of the attractor shown in Fig. 6.35(b) can be constructed by similar methods. The attractor has two branch lines, again labeled l, r. Its two double covers both have four branch lines, again labeled l_0, l_1 and r_0, r_1. The two double covers of Fig. 6.35(b) that we consider are obtained with a rotation axis at the origin (Fig. 6.35(d)) and with the axis in the attractor (Fig. 6.35(f)). The 4×4 transition

matrix for the attractor in Fig. 6.35(b) lifts to the two 8×8 transition matrices for its double covers as follows

	l		r	
	0	1	0	1
0	0	0	1	1
1	0	0	1	1
0	1	1	0	0
1	1	1	0	0

Axis at origin (d)

	l_0		r_0		l_1		r_1	
	0	1	0	1	0	1	0	1
0	0	0	1	1	0	0	0	0
1	0	0	1	1	0	0	0	0
0	0	0	0	0	1	1	0	0
1	0	0	0	0	1	1	0	0
0	0	0	0	0	0	0	1	1
1	0	0	0	0	0	0	1	1
0	1	1	0	0	0	0	0	0
1	1	1	0	0	0	0	0	0

Axis in lobe (f)

	l_0		r_0		l_1		r_1	
	0	1	0	1	0	1	0	1
0	0	0	1	1	0	0	0	0
1	0	0	1	1	0	0	0	0
0	1	1	0	0	0	0	0	0
1	0	0	0	0	1	1	0	0
1	0	0	0	0	0	0	1	1
0	0	0	0	0	0	0	1	1
0	0	0	0	0	1	1	0	0
1	1	1	0	0	0	0	0	0

These four 8×8 transition matrices are all inequivalent. There is no reordering of the row and columns, or branch labels, that maps one into any of the others. The simplest way to see this is to compute a spectrum of invariants for these matrices. A useful spectrum is the trace of various power of these matrices: $\mathrm{Tr}\mathcal{M}^k$. We provide the traces for the two 4×4 matrices, and four 8×8 matrices, of the attractors shown in Fig. 6.35 as well as for the 2×2 Smale horseshoe matrix, up to $k = 8$:

Attractor	1	2	3	4	5	6	7	8
Smale horseshoe	2	4	8	16	32	64	128	256
Fig. 6.35(a)	2	4	8	16	32	64	128	256
Fig. 6.35(b)	0	8	0	32	0	128	0	512
Fig. 6.35(c)	2	4	8	16	32	64	128	256
Fig. 6.35(d)	4	4	4	8	24	64	144	288
Fig. 6.35(e)	0	0	0	64	0	0	0	1024
Fig. 6.35(f)	0	8	0	32	0	128	0	512

It is clear from this result that the two double covers are inequivalent and the four covers of covers are all inequivalent. This test does not distinguish between Fig. 6.35(a) and Fig. 6.35(c). Since Fig. 6.35(a) is a double cover and Fig. 6.35(c) is a 4-fold cover,the two cannot be globally equivalent. Similarly for Fig. 6.35(b) and Fig. 6.35(f).

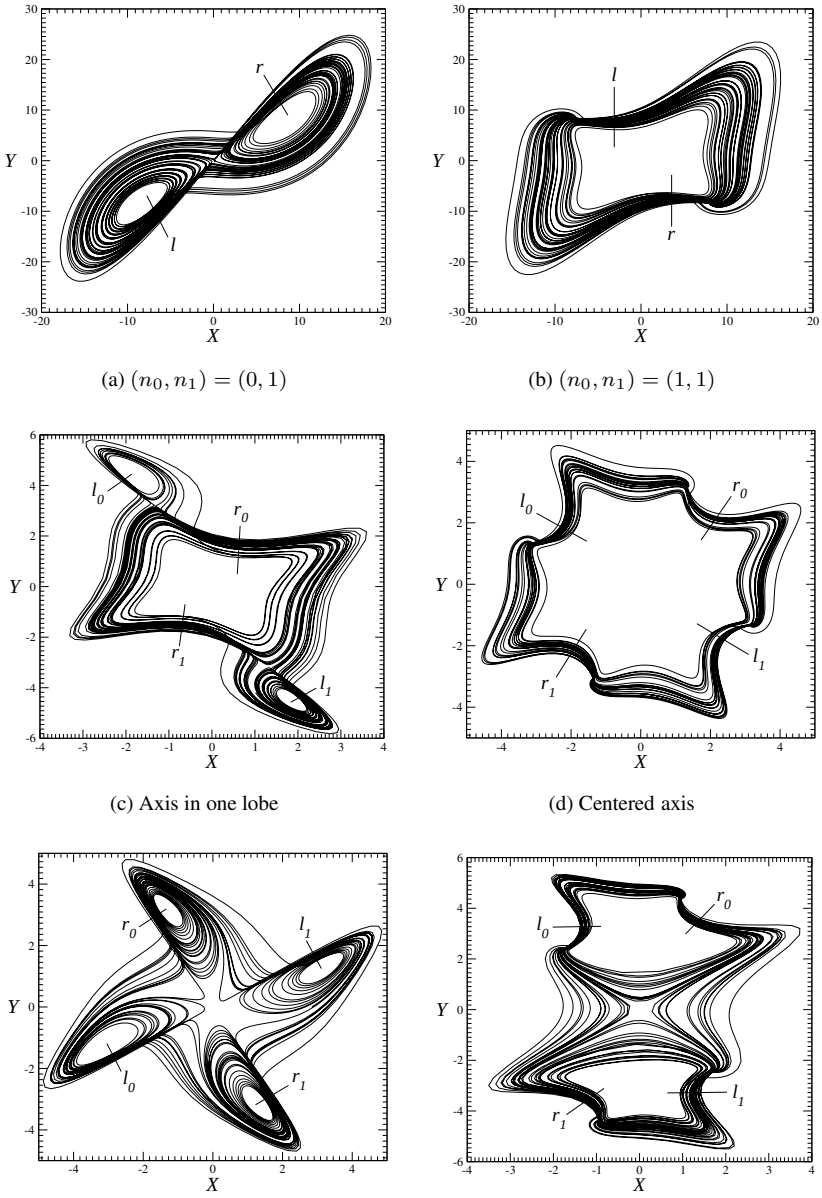

(a) $(n_0, n_1) = (0, 1)$

(b) $(n_0, n_1) = (1, 1)$

(c) Axis in one lobe

(d) Centered axis

(e) Axis at the origin

(f) Axis in the attractor

Fig. 6.35 Covers of covers of the proto-Lorenz equations. Double covers of the proto-Lorenz equations with index $(n_0, n_1) = (0, 1)$ (a) and $(n_0, n_1) = (1, 1)$ (b). (c), (e): Two inequivalent double covers of (a). (d), (f): Two inequivalent double covers of (b). All six attractors are topologically inequivalent.

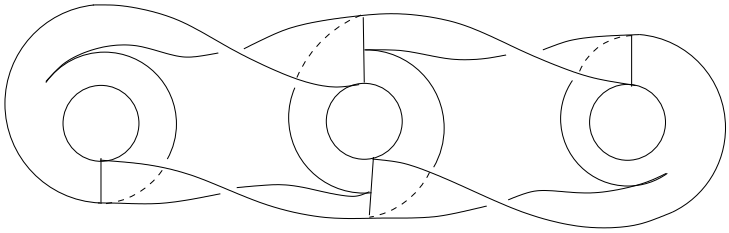

(a) $G = R_Z(\pi)$ but the symmetry axis passes through one of the foci.

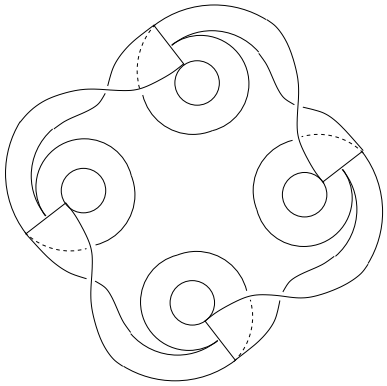

(b) The four-fold cover of the Smale horseshoe branched manifold is a double cover of its double cover, the Lorenz branched manifold. The symmetry axis passes through the origin.

Fig. 6.36 Two inequivalent covers of Lorenz dynamics. (a) Branched manifold for the strange attractor of Fig. 6.35(c) while (b) is the branched manifold for the strange attractor of Fig. 6.35(e).

Remark: The four 4-fold covers can be distinguished by the bounding tori that surround them (cf. Chapter 15). We present here the genus and labeling of the bounding tori that enclose each of these four branched manifolds.

Figure	Genus	Label
Fig. 6.35(c)	5	$ABCB$
Fig. 6.35(d)	5	$ABCD$
Fig. 6.35(e)	1	
Fig. 6.35(f)	3	AB

The matrix invariants $\mathrm{Tr}\mathcal{M}^k$ are not useless. They provide information about the number of distinct orbits of period p (p symbols) that can exist in an attractor. In brief, $\mathrm{Tr}\mathcal{M}^k$ is the number of initial conditions that return to themselves after k forward iterations. For example, for $k = 4$ there are $16 = 2^4 = \mathrm{Tr}\mathcal{M}^4$ initial conditions

in the horseshoe template that are closed after 4 periods. These 16 initial conditions include the two initial conditions for the two period-one orbits $0, 1$ and the two initial conditions $01, 10$ for the single period two orbit. This leaves $12 = 16-(2\times 1+1\times 2)$ initial conditions that return to themselves in four periods. There are distributed among the $12/4 = 3$ period-4 orbits. If $n(p)$ is the number of orbits of smallest period p, then

$$p \times n(p) = \mathrm{Tr}\mathcal{M}^p - \left(\sum_{k|p} k \times n(k) \right)$$

Here $k|p$ means "k divides p" (evenly). This recursion is used to compute the number of orbits of period p (≤ 8) for the horseshoe template, its two double covers shown in Fig. 6.35(a) and (b), and the two double covers ((c) and (e) of (a), (d) and (f) of (b)) of these double covers.

Attractor	1	2	3	4	5	6	7	8
Smale horseshoe	2	1	2	3	6	9	18	30
Fig. 6.35(a)	2	1	2	3	6	9	18	30
Fig. 6.35(b)	0	4	0	6	0	20	0	60
Fig. 6.35(c)	2	1	2	3	6	9	18	30
Fig. 6.35(d)	4	0	0	1	4	10	20	35
Fig. 6.35(e)	0	0	0	16	0	0	0	120
Fig. 6.35(f)	0	4	0	6	0	20	0	60

6.8 MATRIX INDEX FOR LIFTS OF PERIODIC ORBITS

It is possible to develop a simple algorithm for computing the period of the lift of any image orbit into a $\mathcal{G}$-equivariant cover with any index. The magic ingredients are group theory and matrix multiplication. This algorithm facilitated construction of the periodic tables in Sections 6.5.1.2, 6.5.2.2, and 6.5.3.2.

Group operations play two roles in describing orbits in covering dynamical systems with symmetry.

1. They label distinct but equivalent regions in the phase space for the covering dynamical system. For three-dimensional dynamical systems, they label the branch lines in the symmetry-related parts of the phase space.
2. They describe the destination of the flow once it leaves a branch line.

These two functions represent symmetry and dynamics in a very real way.

The two functions are illustrated for 3-fold covers in Section 6.3.9 and for 4-fold covers in Section 6.4.9. In the cases studied in these sections the image branched manifold had one branch line and two branches. In order to raise an orbit in the image attractor to an orbit in the covering attractor, each symbol in the image orbit was assigned two indices. Both indices were group operations. The first group

operation identified which of the equivalent domains of the phase space acted as the *source* for the flow. The second group operation indicated the *destination* of the flow. To be specific, the first image orbit described in Section 6.3.9 was 1011, and was lifted to a 3-fold cover with topological index $(n_0, n_1) = (0, 1)$. The symbol 0 (in the image) picked up indices $0_{(g_i,g_i)}$ in the cover and the symbol 1 in the image picked up indices $1_{(g_i,g_{i+1})}$ in the cover. The symbols in the image dynamical system are "dressed" when lifted to symbols for dynamics in the cover.

Construction of orbits in the cover amounts to *matrix multiplication*. This has a simple interpretation. If the flow begins from the half branch line labeled 1 in the region of phase space identified by group operation g_1, it must flow to the region of phase space identified by group label g_2 ($1_{(g_1,g_2)}$ or $1_{(1,2)}$). The flow next emanates from the half branch line (0 or 1) labeled with group index g_2, and flows where directed:

$$1_{(1,2)}0_{(2,2)} \qquad \text{or} \qquad 1_{(1,2)}1_{(2,0)} \tag{6.11}$$

In this way the construction of a covering orbit reduces to matrix multiplication. The algorithm is as follows.

1. Write down the symbol name for the image orbit of period p.
2. Replace each symbol by its "dressed" counterpart: a $|\mathcal{G}| \times |\mathcal{G}|$ matrix. The $|\mathcal{G}| \times |\mathcal{G}|$ matrix for each symbol in the image is determined by the index of the cover.
3. Multiply the matrices.

If the trace of the product of these p $|\mathcal{G}| \times |\mathcal{G}|$ matrices is $n > 0$, there are n covering orbits of period p.

If the trace of the product is zero, square this matrix and take its trace. If this trace is $n > 0$, there are $\frac{1}{2}n$ periodic orbits of period $2p$. The enumeration of the orbit spectrum continues in this fashion (cube, trace, divide by 3, etc.) until all periodic orbits have been identified. All orbits have been identified when the total symbol count is $|\mathcal{G}|p$.

Example 1. For the 3-fold cover of the Smale horseshoe with index $(n_0, n_1) = (0, 1)$ (Section 6.3.9) the dressing is

$$0 \longrightarrow \begin{bmatrix} 1 & 0 & 0 \\ 0 & 1 & 0 \\ 0 & 0 & 1 \end{bmatrix} \qquad\qquad 1 \longrightarrow \begin{bmatrix} 0 & 1 & 0 \\ 0 & 0 & 1 \\ 1 & 0 & 0 \end{bmatrix} \tag{6.12}$$

The row and column labels for these 3×3 matrices are the three group operations $g_0,\ g_1,\ g_2$.

The matrix describing the lift of 1011 is the appropriate product of the two dressed matrices above:

$$\begin{array}{ccc} 1011 & \rightarrow & \begin{bmatrix} 0 & 1 & 0 \\ 0 & 0 & 1 \\ 1 & 0 & 0 \end{bmatrix} \begin{bmatrix} 1 & 0 & 0 \\ 0 & 1 & 0 \\ 0 & 0 & 1 \end{bmatrix} \begin{bmatrix} 0 & 1 & 0 \\ 0 & 0 & 1 \\ 1 & 0 & 0 \end{bmatrix} \begin{bmatrix} 0 & 1 & 0 \\ 0 & 0 & 1 \\ 1 & 0 & 0 \end{bmatrix} \\ \downarrow & & \downarrow \\ M_{(1011)} & = & \begin{bmatrix} 1 & 0 & 0 \\ 0 & 1 & 0 \\ 0 & 0 & 1 \end{bmatrix} \end{array} \tag{6.13}$$

Since the trace of $M_{(1011)}$ is 3, the image orbit lifts to three closed period-4 orbits in the cover. For the orbit 1001 we find by similar arguments

$$\begin{array}{ccc} 1001 & \rightarrow & \begin{bmatrix} 0 & 1 & 0 \\ 0 & 0 & 1 \\ 1 & 0 & 0 \end{bmatrix} \begin{bmatrix} 1 & 0 & 0 \\ 0 & 1 & 0 \\ 0 & 0 & 1 \end{bmatrix} \begin{bmatrix} 1 & 0 & 0 \\ 0 & 1 & 0 \\ 0 & 0 & 1 \end{bmatrix} \begin{bmatrix} 0 & 1 & 0 \\ 0 & 0 & 1 \\ 1 & 0 & 0 \end{bmatrix} \\ \downarrow & & \downarrow \\ M_{(1001)} & = & \begin{bmatrix} 0 & 0 & 1 \\ 1 & 0 & 0 \\ 0 & 1 & 0 \end{bmatrix} \end{array} \tag{6.14}$$

The trace of $M_{(1001)}$ is zero, so there are no period-four orbits in the lift of this orbit. Further, the square of this matrix is also traceless, while the cube has trace = 3. Thus, there are no closed period-8 orbits covering 1001. There is $1 = \frac{1}{3} \times 3$ closed orbit of period 12 that covers 1001 in this lift. There are no other orbits covering 1001, since $12 = |\mathcal{C}_3| \times p = 3 \times 4$.

Example 2. For the 4-fold cover of the reverse horseshoe with topological index $(n_1, n_2) = (1, 2)$ (Section 6.4.9), the dressing is

$$1 \longrightarrow \begin{bmatrix} 0 & 1 & 0 & 0 \\ 0 & 0 & 1 & 0 \\ 0 & 0 & 0 & 1 \\ 1 & 0 & 0 & 0 \end{bmatrix} \qquad 2 \longrightarrow \begin{bmatrix} 0 & 0 & 1 & 0 \\ 0 & 0 & 0 & 1 \\ 1 & 0 & 0 & 0 \\ 0 & 1 & 0 & 0 \end{bmatrix} \tag{6.15}$$

The products of the dressed symbols for the three period-4 orbits 1222, 1221, and 1211 are

$$\begin{array}{ccc} 1222 & 1221 & 1211 \\ \downarrow & \downarrow & \downarrow \\ M_{(1222)} & M_{(1221)} & M_{(1211)} \\ \| & \| & \| \\ \begin{bmatrix} 0 & 0 & 0 & 1 \\ 1 & 0 & 0 & 0 \\ 0 & 1 & 0 & 0 \\ 0 & 0 & 1 & 0 \end{bmatrix} & \begin{bmatrix} 0 & 0 & 1 & 0 \\ 0 & 0 & 0 & 1 \\ 1 & 0 & 0 & 0 \\ 0 & 1 & 0 & 0 \end{bmatrix} & \begin{bmatrix} 0 & 1 & 0 & 0 \\ 0 & 0 & 1 & 0 \\ 0 & 0 & 0 & 1 \\ 1 & 0 & 0 & 0 \end{bmatrix} \end{array} \tag{6.16}$$

The 4×4 matrix $M_{(1222)}$ representing the lift of 1222 is traceless. Further, it is cyclic, so that its square and cube are also traceless, while its fourth power is the identity matrix. As a result, in this cover the period-4 image orbit 1222 has no covering orbits of periods 4, 8, or 12, and $1 = \frac{1}{4} \times \mathrm{tr} M^4_{(1222)}$ covering orbit of period $4 \times 4 = 16$. The same is true, word for word, of the orbit 1211.

For the image orbit 1221 the matrix $M_{(1221)}$ is also traceless. However, its square is the identity matrix, so that there are $2 = \frac{1}{2} \times \mathrm{tr} M^2_{(1221)}$ covering orbits of period 8. One of these orbits has an initial condition in region g_0 that flows to region g_2 after four periods, and returns to region g_0 after another 4 periods. The second period-8 orbit oscillates between regions identified by g_1 and g_3 every four periods. This information can be read off directly from the matrix $M_{(1221)}$.

7

Multichannel Intermittency

7.1 REVIEW OF INTERMITTENCY

Intermittent behavior has been observed under a wide variety of circumstances. Typically, the following behavior is observed. The physical system behaves in a regular, predictable way for a reasonable period of time. Over a rather short period of time, the system departs from regularity and may even behave in a very irregular, highly unpredictable way. Eventually the system returns to the original type of regular behavior and the cycle repeats. The durations of the periods of regular and irregular behaviors are not predictable but the statistics of these time intervals are predictable and vary smoothly with the control parameters.

Intermittency is intimately associated with the change in stability of a periodic orbit. It is observed just after an orbit loses its stability and there are no other accessible stable periodic orbits. Three types of intermittency have been identified [101], depending on how the stable periodic orbit loses its stability. These are described in terms of the Floquet multiplier of a map related to the dynamics. In particular, they are related to how the Floquet multiplier crosses from the interior of the unit circle in the complex plane. They are illustrated in Fig. 7.1 and summarized here:

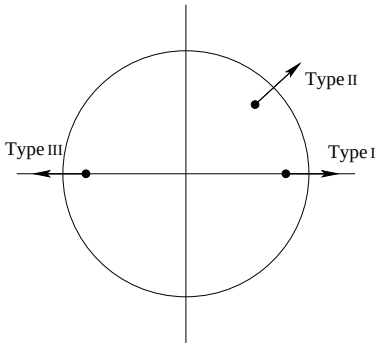

Fig. 7.1 Intermittency type is determined by how the Floquet multiplier of a periodic orbit crosses the unit circle boundary.

- Type I: $\lambda \to 1^+$
- Type II: $\lambda = \rho e^{\pm i\varphi},\ \rho \to 1^+$
- Type III: $\lambda \to -1^-$

In particular, Type I intermittency is associated with the destruction of a stable node during a saddle-node bifurcation. It is this type of intermittency that concerns us in this chapter.

7.2 INTERMITTENCY AND SADDLE-NODE BIFURCATIONS

We illustrate the idea of Type I intermittency by using the logistic map $x_{n+1} = a - x_n^2$. Fig. 7.2 is a bifurcation diagram of this map in the neighborhood of the period-3 window. The saddle-node bifurcation that creates the period-3 saddle-node pair occurs at $a = 7/4$. After the bifurcation, the period-3 node is clearly apparent in this window. It eventually undergoes period-doubling bifurcations to period $6, 12, \ldots, 3 \times 2^n$. What concerns us is what happens before the window, for $a < 7/4$. The bifurcation diagram in Fig. 7.2 shows that there is a nonuniform density in the state variable x.

The density variation is positive in the neighborhood of the emergent period-3 orbits. Not only that, the density variation grows systematically [$\rho(x_3) \approx |a - a_3|^{-\frac{1}{2}}$] as the control parameter a approaches the bifurcation value $a_3 = 7/4$ from below, where x_3 is any of the three values of x where the degenerate saddle-node pair is created at $a = a_3$.

The origin of this nonuniform density variation is illustrated in Fig. 7.3. In this figure we show the third iterate of the logistic map $x_{n+3} = f^{(3)}(x_n, a)$, for $a < a_3$ (Fig. 7.3(a)) and for $a > a_3$ (Fig. 7.3(b)). In Fig. 7.3(b) an initial condition is shown as it relaxes to the stable period-3 orbit. In Fig. 7.3(a) an initial condition has no stable periodic orbit to relax to. Instead, it gets trapped for a long time in a thin channel between $f^{(3)}(x_n, a)$ and the diagonal $x_{n+3} = x_n$. The thinner the channel,

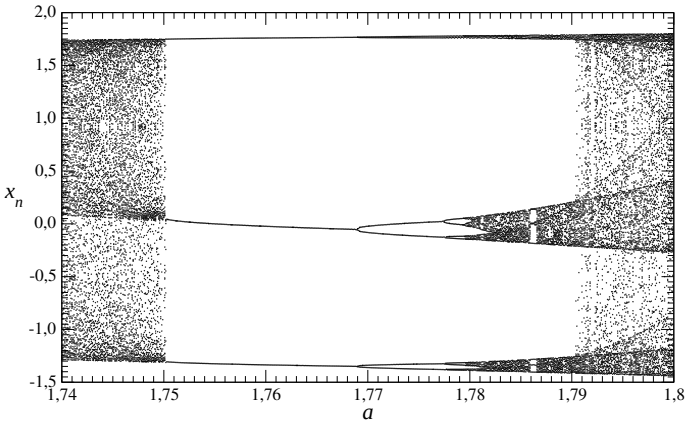

Fig. 7.2 Bifurcation diagram of the logistic map in the neighborhood of the period-3 window at $a = 7/4$.

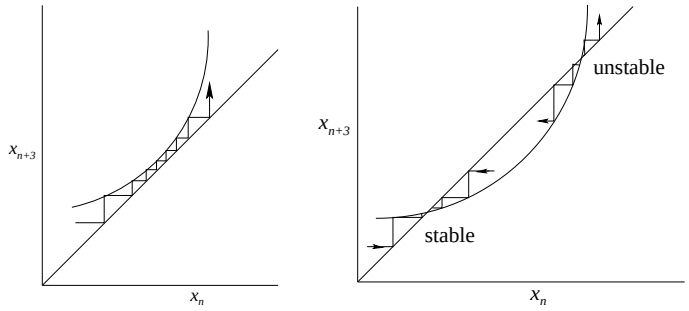

(a) Before the bifurcation: $a < a_3$

(b) After the bifurcation: $a > a_3$

Fig. 7.3 (a) Before the bifurcation an initial condition gets trapped in the neighborhood of the period-3 orbit for a long time. (b) After the bifurcation an initial condition moves to the stable period-3 orbit.

the longer the state variable gets trapped in that region. Since the channel width depends on $a < a_3$ like $|a - a_3|^{\frac{1}{2}}$, the time spent in this region behaves like its reciprocal: $T \approx |a - a_3|^{-\frac{1}{2}}$. And since the time spent in this region of space is like the (invariant) probability density, we see that the density statistics on the near side of the saddle-node bifurcation should be nonuniform, with maxima centered around the three values of x_3, and with maximum amplitude behaving like $|a - a_3|^{-\frac{1}{2}}$.

There is another useful way to look at the relation across the bifurcation value a_3. On one side, $a > a_3$, there is real pair of orbits: an unstable saddle and a stable node. We see only the node in the bifurcation diagram in Fig. 7.2. On the other side, $a < a_3$, there is "an imaginary period-3 orbit pair." As $a \to a_3$, the "imaginary part"

of these orbits approaches 0 (cf. Fig. 7.3(a)). The delta-function density for $a > a_3$, and the nonuniform density spiking around the x_3 values as $a \to a_3$, are analytic continuations of each other. To put this in another way, as a decreases below a_3 the two real orbits are killed and only their "ghost orbits" remain. These ghost orbits are responsible for the intermittency that occurs just before the saddle-node bifurcation. It is the imminent creation of a stable period-3 orbit that entrains a point in phase space to the neighborhood of the imaginary period-3 orbit — for a longer and longer time as a approaches a_3.

7.3 INTERMITTENCY IN EQUIVARIANT DYNAMICAL SYSTEMS

Intermittency occurs in flows as well as maps. For example, period-3 intermittency can be seen in the Rössler attractor just before the saddle-node bifurcation that creates the period-3 saddle-node pair. The mechanism is the same as that described for maps in the previous section.

Most of the flows that have been studied are highly dissipative. For such flows it is rare to have coexisting attractors. For less dissipative attractors the following possibility exists. For some control parameter value a, the system supports two stable nodes, n_1 and n_2 of periods p_1 and p_2. As a is decreased to $a - \epsilon$, both nodes are destroyed in saddle-node bifurcations, and there are no accessible stable periodic orbits. The system can then exhibit two "intermittency channels." One channel is associated with n_1, the second with n_2. As a point in phase space falls into the neighborhood of n_1, it follows closely the trajectory of n_1 for a while before departing for elsewhere. Eventually the wandering point falls into the neighborhood of n_1 or n_2 again and is enslaved by that ghost orbit. In effect, the phase space point traces out the orbits n_1 and n_2 very clearly in its wanderings.

The problem with this scenario is that it is not easy to find dynamical systems with coexisting stable periodic orbits that undergo saddle-node bifurcations at nearby control parameter values.

This is not a significant difficulty for equivariant dynamical systems. Such systems can exhibit symmetry-related periodic orbits. When they exist, they are guaranteed to undergo saddle-node bifurcations at the same control parameter values.

Our understanding of equivariant dynamical systems allows us to develop a strategy for studying multichannel intermittency using the degrees of freedom that are available. These degrees of freedom are

1. Control parameter values. In particular we identify control parameter values where saddle-node bifurcations of low period orbits occur. Then we move the control parameters to "ghost-orbit" values.
2. $\mathcal{G}$. This determines the symmetry of the equivariant dynamical system.
3. Topological index. This can be chosen to guarantee specific low period orbits have multiple distinct covers, and that the strange attractor they occur in is connected. This will guarantee that coexisting "ghost orbits" are accessible from each other.

In the following two sections we apply this strategy in two ways. In Section 7.4 we begin with an equivariant dynamical system—the Lorenz system—and search for parameter values at which symmetry-related pairs of asymmetric orbits are created in pairs of saddle-node bifurcations. In Section 7.5 we begin with an image dynamical system—the Rössler attractor—where the spectrum of saddle-node bifurcations has long been known. Then we lift to covers with $\mathcal{C}_2$, $\mathcal{C}_3$, and $\mathcal{C}_4$ symmetry and choose the topological index so that the lifts of the real orbits (and their "ghost" analytic continuations) are disconnected. Both approaches lead to multichannel intermittency.

7.4 TWO-CHANNEL INTERMITTENCY IN THE LORENZ ATTRACTOR

The Lorenz system [78] is one of the first systems in which a Type I intermittency has been investigated [83]. Depending on the control parameter values, the attractor is either fully symmetric, that is, globally unchanged under the action of the symmetry, or asymmetric. In the latter case, two attractors coexist in the phase space, one being mapped to the other under the group action. In this case symmetry-related orbits are not accessible to each other. For this reason, we do not further consider disconnected attractors.

In the work that follows we explore ranges of control parameter values in which low period windows exist. These windows are bounded on both sides by chaotic regions in which the strange attractor exhibits the full symmetry of the equivariance group.

The first observation of an intermittent behavior was done for $(R, \sigma, b) = (166.1, 10, 8/3)$. For these control parameter values, a single stable limit cycle $LLRR$ exists in the periodic window. It is symmetric, that is, left globally unchanged under the action of the symmetry (Fig. 7.4(a)). Thus, a unique reinjection channel is observed for the virtual symmetric periodic orbit. In the image system there is one reinjection channel to the virtual period-2 orbit 10 shown in Fig. 7.4(b).

In the periodic window at $R = 100.795$ there are two symmetry-related period-3 orbits LLR and RRL (Fig. 7.5) created by simultaneous saddle-node bifurcations from the virtual orbits. The key point is that the disconnected virtual orbits occur in a strange attractor (Fig. 7.6) that is globally invariant under the action of $\mathcal{R}_Z$. The two virtual orbits are accessible to each other, and the trajectory is "arbitrarily" reinjected into one of the two channels. Consequently, the laminar phases are associated with a trajectory visiting the neighborhood of either of the two symmetry-related virtual orbits LLR or RRL. Two different kinds of laminar phase can thus be distinguished (Fig. 7.7).

Fig. 7.7(a) reproduces the time series of $X(t)$. In one mode (solid curve in Fig. 7.5) $-35 \leq X(t) \leq +25$, while for the other mode (dashed), by symmetry, $-25 \leq X(t) \leq +35$. The intersections with a well-chosen plane can also be used to distinguish the two channels. An intersection plane is shown in Fig. 7.5. The Z-values are recorded as the trajectory passes through this section with $X \sim -22$ and $\dot{X} < 0$. The two reinjection channels appear in the neighborhoods of the (single)

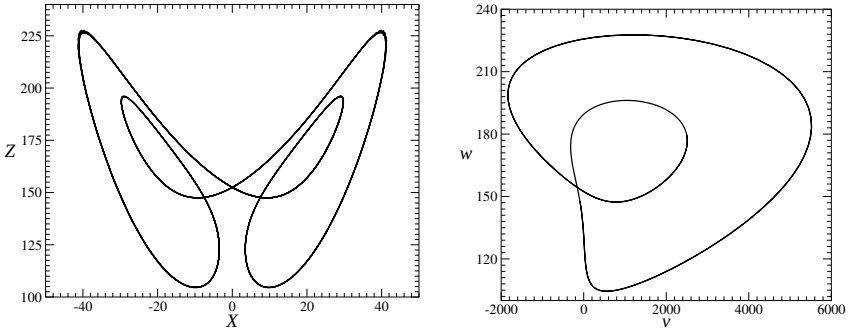

(a) Original phase space $\mathbb{R}^3(X, Y, Z)$ (b) Image phase space $\mathbb{R}^3(u, v, w)$

Fig. 7.4 (a) The period-4 limit cycle $LLRR$ observed in the original phase space $\mathbb{R}^3(X, Y, Z)$ and (b) its image 01 in the image phase space $\mathbb{R}^3(u, v, w)$. Parameter values: $(R, \sigma, b) = (166.1, 10, 8/3)$.

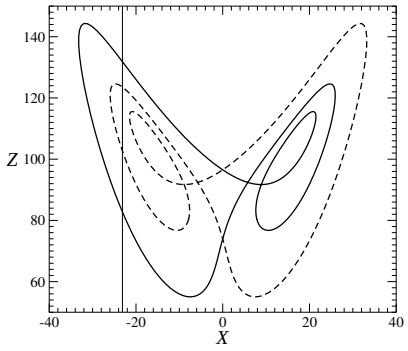

Fig. 7.5 The coexisting asymmetric period-3 limit cycles LLR and RRL generated by the Lorenz system. The initial conditions are related by the γ-matrix. Parameter values: $(R, \sigma, b) = (100.795, 10, 8/3)$.

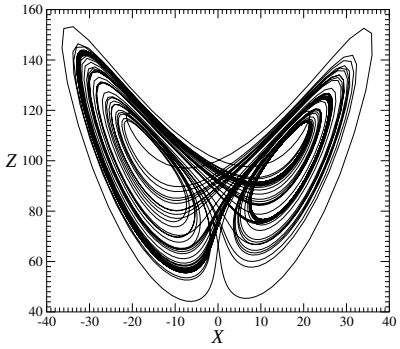

Fig. 7.6 Chaotic attractor, globally invariant under the action of the γ-matrix, generated by the Lorenz system. Chaotic bursts from the two asymmetric laminar phases LLR and RRL occur in this symmetric attractor. Parameter values: $(R, \sigma, b) = (100.799, 10, 8/3)$.

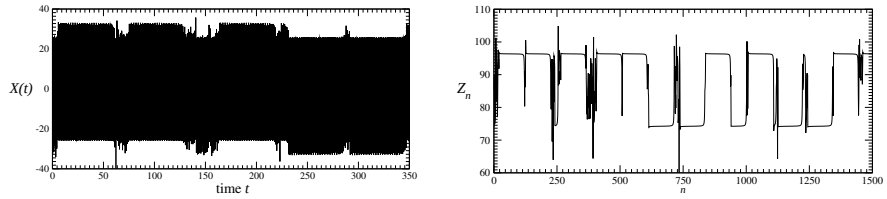

(a) Time series (b) Intersections with the Poincaré section

Fig. 7.7 Intermittent behavior with two reinjection channels in the Lorenz system. Parameter values: $(R, \sigma, b) = (100.799, 10, 8/3)$. The Poincaré section is shown in Fig. 7.5.

intersections of the two period-3 orbits with this plane: at $Z \approx 96$ (dashed) and $Z \approx 80$ (solid).

When the intermittent behavior is investigated in the image system, the symmetry properties are modded out and the 2-channel Type I intermittency does not present any difference with the common Type I intermittency as observed in any system without any symmetry properties. Indeed, a single type of laminar phase is observed as suggested by the chaotic attractor of the image, which does not have any residual symmetry (Fig. 7.8(a)). Both asymmetric orbits of the original phase space $\mathbb{R}^3(X, Y, Z)$ (Fig. 7.5) are mapped to the same period-3 orbit in the image phase space $\mathbb{R}^3(u, v, w)$. The laminar phase is described by a single virtual orbit, 011, which is the image of both LLR and RRL.

Since in the image system, the stable limit cycle has a period equal to 3, a third-return map to a Poincaré section has to be computed in the image system (Fig. 7.8(b)). In such a third-return map, three tangencies to the bisector are clearly identified at $\nu \simeq 1000, 1540$, and 3200. They correspond to the three periodic points of the limit cycle to appear. Note that when the original Lorenz system is investigated, the third-return map is much more difficult to obtain. A third-return map should present 2×3 tangencies with the bisector, three points being associated with each asymmetric limit cycle observed for $R = 100.795$ (Fig. 7.5).

7.5 INTERMITTENCY IN COVERS OF THE RÖSSLER SYSTEM

We can construct Type I intermittency with n reinjection channels in n-fold covers of a simple dynamical system [76]. We choose the simplest—the Rössler system. We construct n-fold covers with rotation symmetry, $\mathcal{C}_n$. We also are free to choose the

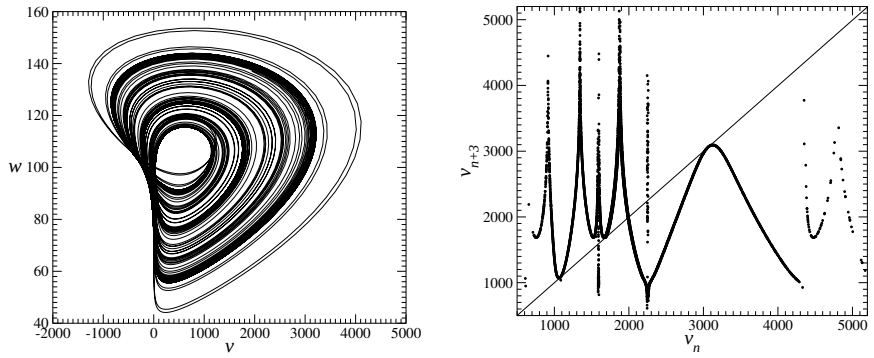

(a) Phase portrait

(b) Third-return map

Fig. 7.8 (a) Chaotic attractor generated by the Lorenz system projected to the image system without any residual symmetry. Parameter values: $(R, \sigma, b) = (100.799, 10, 8/3)$. (b) Third-return map to a Poincaré section of the image attractor.

rotation symmetry axis $\mathcal{R}_Z(\pi)$: this is equivalent to choosing the topological index of the cover. In particular this allows us to guarantee that the cover of an orbit of period p has n components, symmetry related, each of period-p, each accessible from the other.

7.5.1 Two-Fold Cover

The equations for the two-fold cover of the Rössler system (4.1) are [67]

$$\begin{cases} \dot{X} = \dfrac{1}{2\rho^2}\left[-\rho^2 Y + X\left(2aY^2 - Z\right) + \mu Y\right] \\ \dot{Y} = \dfrac{1}{2\rho^2}\left[\rho^2 X + Y\left(2aX^2 + Z\right) + \mu X\right] \\ \dot{Z} = \tilde{b}\left(X^2 - Y^2 + \mu\right) + Z\left(X^2 - Y^2 - \tilde{c} + \mu\right) \end{cases} \tag{7.1}$$

where $\rho^2 = X^2 + Y^2$. The chaotic attractor generated by these covering equations is globally invariant under a rotation symmetry $\mathcal{R}_Z(\pi)$ (Fig. 7.9). For $(a, b, c) \simeq (0.4, 2.0, 4.0)$ it remains connected for $\mu = 0.0$ down to $\mu = -4.0$.

We would like to investigate the Type I intermittency observed for $a \approx 0.4091$, just before the period-3 window. When $\mu = 0$, the rotation axis is located at the origin of the phase space $\mathbb{R}^3(u, v, w)$. The period-3 limit cycle observed in the image Rössler system is thus "lifted" to a single symmetric period-6 orbit in the 2-fold cover (Fig. 7.10(a)). Since a single stable limit cycle exists, Type I intermittency with a single channel is observed (Fig. 7.11(a)).

In order to change the number of stable limit cycles which coexist in the covering phase space for a control parameter value corresponding to a periodic window, it is

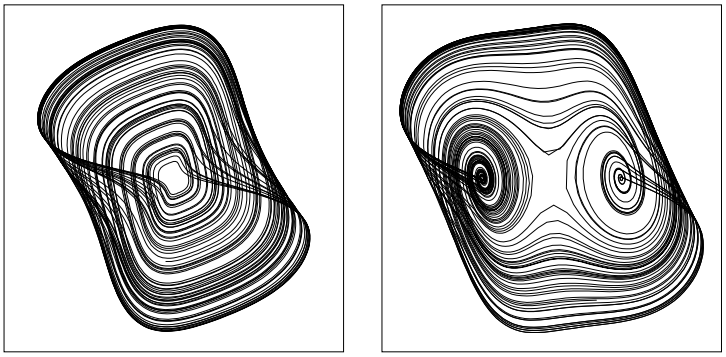

(a) $\mu = 0.0$ (b) $\mu = -1.5$

Fig. 7.9 Chaotic attractor generated by the 2-fold cover of the Rössler system. Both attractors are globally invariant under the rotation $\mathcal{R}_Z(\pi)$. (a) $\mu = 0.0$, (b)$\mu = -1.5$. Parameter values: $(a, b, c) = (0.432, 2.0, 4.0)$.

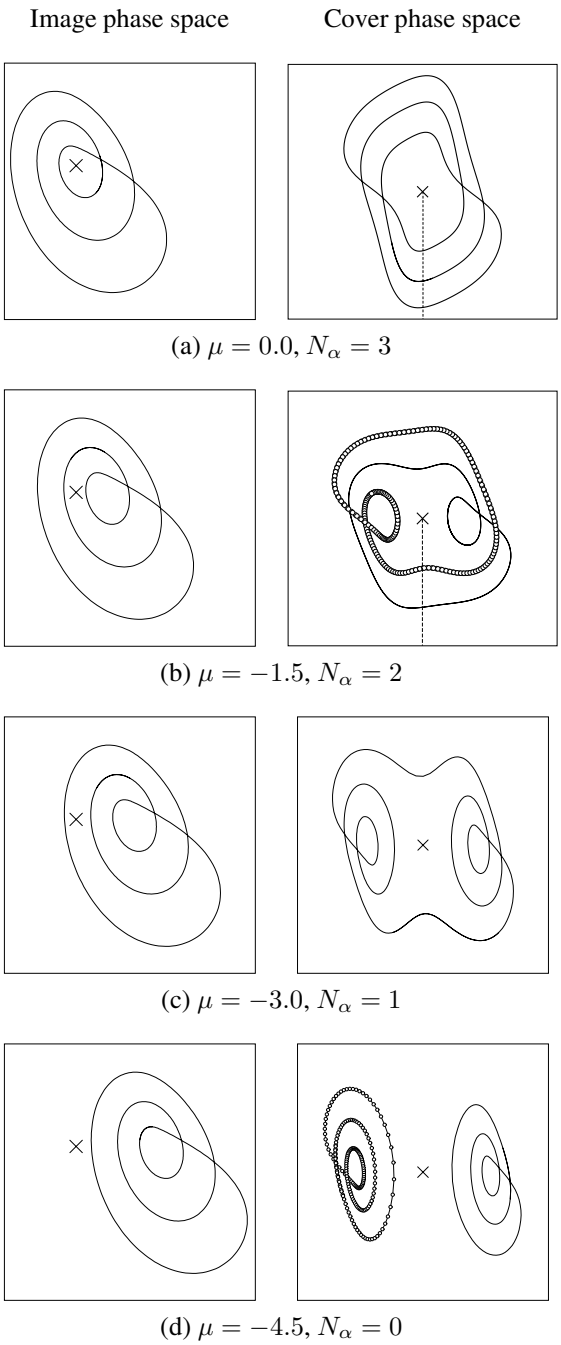

Fig. 7.10 Transformation of the period-3 orbits generated by the 2-fold cover of the Rössler system under the peeling bifurcation when μ is varied. The location of the rotation axis is designated by the symbol $\times$. Parameter values: $(a, b, c) = (0.4096, 2.0, 4.0)$.

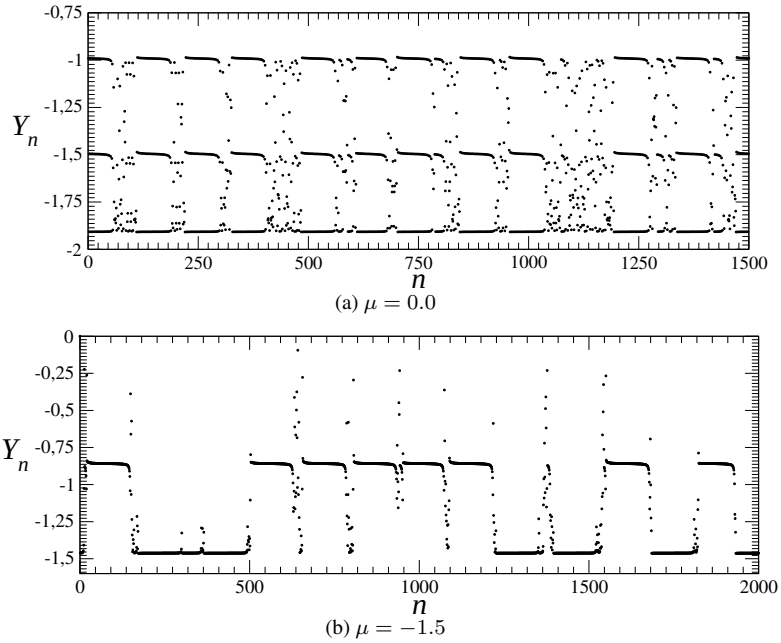

Fig. 7.11 Intersections with the Poincaré section corresponding to the case where one orbit (a) and two orbits (b) are associated with the period-3 window. The Poincaré sections are shown in Fig. 7.10(a) and (b). In the first case, intermittency with a single channel is observed. In the second case, two channels are identified and, consequently, two different laminar phases are described. Parameter values: $(a, b, c) = (0.409109, 2.0, 4.0)$.

sufficient to displace the rotation axis along the u-axis [35]. Indeed, when the rotation axis intersects the chaotic attractor, the flow of the cover is deformed like the deformation of an apple skin when the apple is peeled (cf. Fig. 5.9). We now review what happens to the period-3 orbit when the μ-parameter is progressively decreased (cf. Section 5.4). When the rotation axis is displaced toward the left side of the u-axis ($\mu = -1.5$), it intersects a segment of the orbit in the image space $\mathbb{R}^3(u, v, w)$. One revolution of the image periodic orbit does not encircle the rotation axis anymore (Fig. 7.10(b)). We introduce a topological index, N_α, which defines the number of times the orbit encircles the rotation axis. This index is decreased by one each time the rotation axis passes through the period-3 image orbit. After the first intersection, the period-3 image orbit is lifted into a symmetric pair of period-3 orbits (Fig. 7.10(b)). The topological index N_α of this pair of periodic orbits is equal to 2, as in the image space.

As μ continues to decrease, the rotation axis cuts the image period-3 orbit a second time. At $\mu = -3.0$ (Fig. 7.10(c)) $N_\alpha = 1$ and the period-3 image orbit is lifted to a single symmetric period-6 covering orbit. Finally, after the third crossing, at

$\mu = -4.5$ (Fig. 7.10(d)) $N_\alpha = 0$ and the period-3 image orbit is lifted to a pair of symmetry-related cover orbits. For slightly smaller μ values the attractor becomes disconnected, with each component exhibiting a single channel intermittency.

In this sequence, there is a single reinjection channel for $\mu = 0.0$ and $\mu = -3.0$ (Fig. 7.10(a) and (c)) since the covering orbit is connected in a symmetric strange attractor. There are two reinjection channels at $\mu = -1.5$ since the cover consists of two disconnected symmetry-related orbits in a symmetric connected attractor. Finally, there is one reinjection channel (in each attractor) for $\mu < -4.5$, since the cover of the period-3 orbit consists of two symmetry-related orbits, but the covering attractor is itself not connected. It consists of two asymmetric symmetry-related attractors, each containing one of the two symmetry-related orbits. The $X(t)$ time series for one ($\mu = 0.0$) and two ($\mu = -1.5$) reinjection channels are shown in Fig. 7.11(a) and (b).

The Poincaré sections for the attractors at $\mu = 0.0$ and $\mu = -1.5$ are shown on the right in Fig. 7.10(a) and (b). For $\mu = 0.0$, where a single period-6 orbit exists, it intersects the Poincaré section at three points. This accounts for the three plateaux in Fig. 7.11(a). For $\mu = -1.5$, the two period-3 orbits each intersect the Poincaré section once. This is why each plateau in Fig. 7.11(b) indicates a different reinjection channel.

7.5.2 Three-Fold Cover

A similar process can be observed in the three-fold cover of the centered Rössler system. The chaotic attractor generated by the three-fold cover of the centered Rössler system is shown in Fig. 7.12(a) and (b) for two different values of μ.

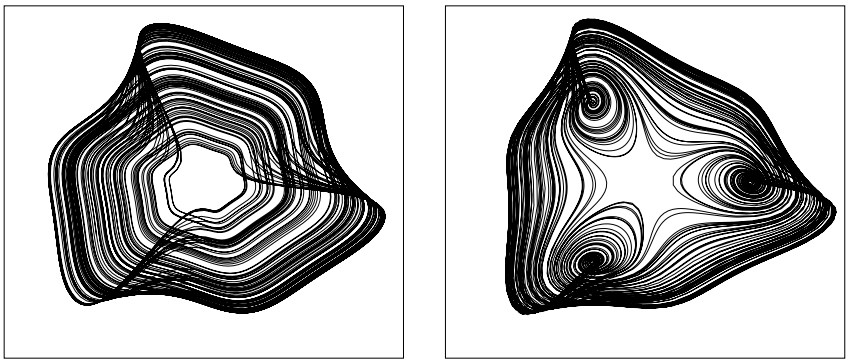

(a) $\mu = 0.0$ (b) $\mu = -1.15$

Fig. 7.12 Chaotic attractor generated by the 3-fold cover of the Rössler system for (a) $\mu = 0.0$ and (b) $\mu = -1.15$. Parameter values: $(a, b, c) = (0.432, 2.0, 4.0)$.

When the rotation axis is displaced, the attractor generated by the three-fold cover is deformed as shown in Fig. 7.12(b). Since this is a three-fold cover, up to three limit cycles may coexist in the cover space $\mathbb{R}^3(X, Y, Z)$ (Fig. 7.13(a)). Depending on the location of the rotation axis, three period-3 (Fig. 7.13(a)) or one period-9 (Fig. 7.13(b)) limit cycles are observed. In both cases, the limit cycles are embedded in a connected attractor globally invariant under the rotation symmetry $\mathcal{R}_Z(\frac{2\pi}{3})$. Consequently, depending on μ, one or three types of laminar phases may be observed. An example with the three types of laminar phases is shown in Fig. 7.14.

7.5.3 Four-Fold Cover

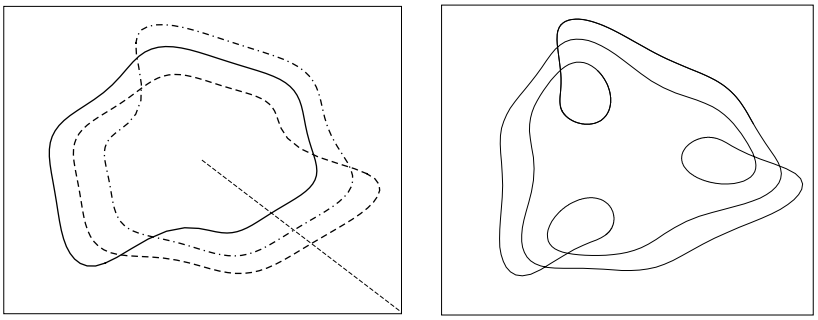

(a) $\mu = 0.0$ (b) $\mu = -1.15$

Fig. 7.13 At $(a, b, c) = (0.4096, 2.0, 4.0)$ the Rössler system has a stable period-3 orbit. (a) This is lifted to three coexisting disconnected symmetry-related period-3 orbits for $\mu = 0.0$ and (b) one single symmetric period-9 orbit for $\mu = -1.15$.

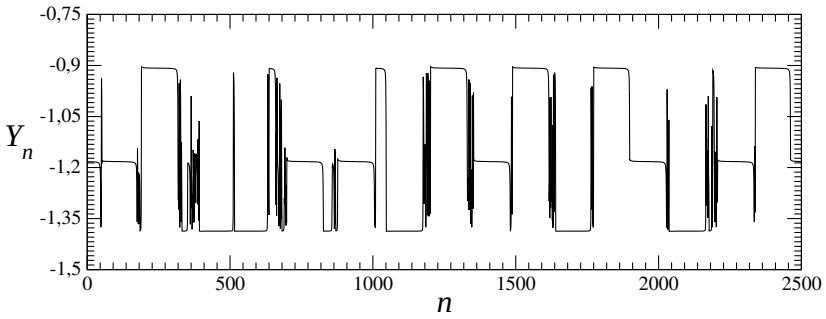

Fig. 7.14 Intersections with the Poincaré section corresponding to the case where three orbits are associated with the period-3 window. The Poincaré section is shown in Fig. 7.13(a). Three channels are identified and, consequently, three different laminar phases are described. Parameter values: $(a, b, c) = (0.409109, 2.0, 4.0)$.

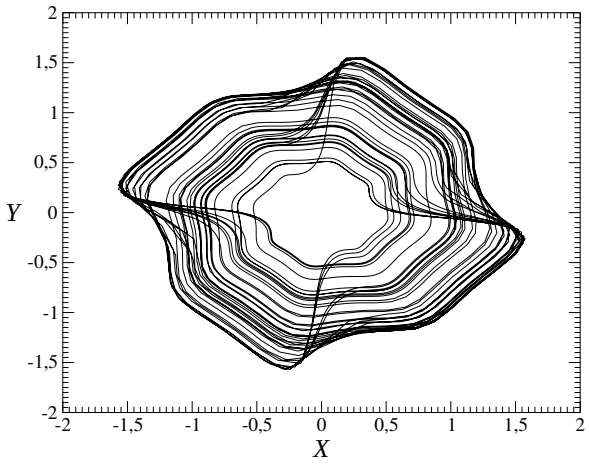

Fig. 7.15 Chaotic attractor generated by the 4-fold cover of the centered Rössler system with $\mu = 0.0$. Parameter values: $(a, b, c) = (0.432, 2.0, 4.0)$.

A richer case is obtained with the four-fold cover. The $\mathcal{C}_4$-equivariant attractor is shown in Fig. 7.15 for $\mu = 0.0$. Rather than investigating the period-3 window, it is more interesting to investigate the period-4 window for $a = 0.425$. This limit cycle is encoded by the sequence (1000) in the image space. When $\mu = 0.0$, there are four coexisting symmetry-related period-4 limit cycles (Fig. 7.16(a)). When the rotation axis is displaced, peeling bifurcations occur. The topological index is changed, as is the number of coexisting limit cycles. For instance, after two peeling bifurcations ($\mu = -1.15$), the topological index is decreased by two and two symmetry-related period-8 limit cycles coexist in the cover space $\mathbb{R}^3(X, Y, Z)$ (Fig. 7.16(b)). After a third peeling bifurcation ($\mu = -2.5$), the topological index N_α is equal to 1 and a single symmetric period-16 limit cycle is observed (Fig. 7.16(c)). Thus, depending on the location of the rotation axis, one, two, or four limit cycles may coexist in the cover space. Therefore one, two or four types of laminar phases may be observed (Fig. 7.17). In all of these cases, the chaotic bursts occur on a connected strange attractor that is globally unchanged under the action of the rotation symmetry $\mathcal{R}_Z(\frac{2\pi}{4})$, so separate ghost orbits are accessible from each other.

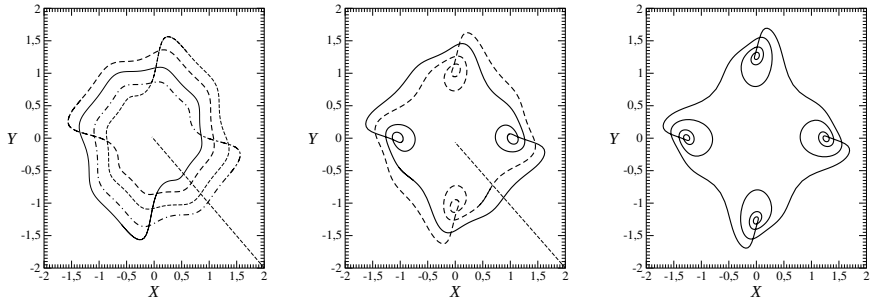

(a) $\mu = 0.0$, $N_\alpha = 4$ (b) $\mu = -1.15$, $N_\alpha = 2$ (c) $\mu = -2.50$, $N_\alpha = 1$

Fig. 7.16 At $(a, b, c) = (0.425, 2.0, 4.0)$ the Rössler attractor has a stable period-4 limit cycle (0001). This is lifted to: (a) four symmetry-related period-4 orbits for $\mu = 0.0$; (b) two symmetry-related period-8 orbits for $\mu = -1.15$; (c) one symmetric period-16 orbit for $\mu = -2.50$.

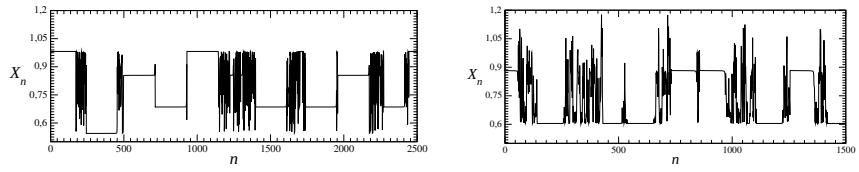

(a) $\mu = 0.0$ (b) $\mu = -1.15$

Fig. 7.17 Intersections with the Poincaré section corresponding to the case where four orbits (a) and two orbits (b) are associated with the period-4 window. The Poincaré sections are shown in Fig. 7.16(a) and (b). In the first case, an intermittency with four channels is observed. In the second case, two channels are identified and, consequently, two different laminar phases are described. Parameter values: $(a, b, c) = (0.42486152.0, 4.0)$.

8

Driven Two-Dimensional Dynamical Systems

8.1 STRUCTURE OF DYNAMICAL SYSTEMS

There is a general structure theory for dynamical systems—sets of coupled nonlinear ordinary differential equations—that remains to be worked out. This theory takes the form of the structure theory that is well known for algebraic systems—in particular, the structure theory that exists for groups and their representations. Groups may be nonsemisimple, semisimple, or simple [31]. Representations of groups can be reducible, fully reducible, or irreducible. We will adopt the language of representations to describe the structure theory for dynamical systems, on the grounds that such equations form *representations* of physical processes. We summarize schematically the structure theory for groups, representations, and dynamical systems in Table 8.1. Without explaining the meaning of these terms for groups and their representations,

Table 8.1 The structure theory of groups, representations, and dynamical systems is summarized schematically.

Group	Representation	Dynamical System	Structure
Nonsemisimple	Reducible	Reducible	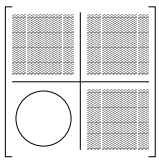
Semisimple	Fully Reducible	Fully Reducible	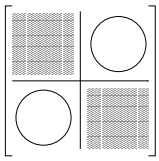
Simple	Irreducible	Irreducible	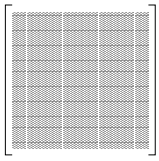

we will make their meaning clear in the definition of the corresponding structure for dynamical systems.

In order to describe the structure of a dynamical system, we assume that the coordinates $x = (x_1, x_2, \ldots, x_n) \in \mathbb{R}^n$ can be transformed in a globally smooth way to a new set of coordinates, $(x) \rightarrow (u, v)$, with $u = (u_1, u_2, \ldots, u_{n_1}) \in \mathbb{R}^{n_1}$ and $v = (v_1, v_2, \ldots, v_{n_2}) \in \mathbb{R}^{n_2}$, and $n_1 + n_2 = n$. We assume $n_1 \neq 0$ and $n_2 \neq 0$.

8.1.1 Reducible

A dynamical system is reducible if in this new coordinate system the equations of motion assume the form

$$\begin{aligned} \frac{du}{dt} &= f_1(u, v) \\ \frac{dv}{dt} &= f_2(-, v) \end{aligned} \tag{8.1}$$

In the equations above $f_2(-, v)$ means that the source function f_2 depends on v but does not depend on the coordinates u.

This structure means that the equations for the subset of coordinates v can be solved independently of the coordinates u. If any solution of $dv/dt = f_2(-, v)$ from a given initial condition, v_0, is known, that solution $v(t; v_0)$ can be substituted into the first of the dynamical system equations to give

$$\frac{du}{dt} = f_1(u, v) \rightarrow \frac{du}{dt} = f_1(u, v(t; v_0)) = \tilde{f}_1(u, t)$$

In short, the "v subsystem" acts to *drive* the "u subsystem." In this chapter we will deal with driven dynamical systems. The driven (u) subsystem is typically a two-dimensional nonlinear oscillator with inversion symmetry and the v subsystem will be a relatively simple dynamical system: the Rössler attractor, the Lorenz attractor, run at parameter values or initial conditions that give either periodic orbits or chaotic orbits, and a harmonic oscillator.

8.1.2 Fully Reducible

With the notation above, a dynamical system is fully reducible if

$$\begin{aligned} \frac{du}{dt} &= f_1(u, -) \\ \frac{dv}{dt} &= f_2(-, v) \end{aligned} \tag{8.2}$$

In this case, the v subsystem can be integrated independently of the u subsystem, *and* the u subsystem can be integrated independently of the v subsystem. Both may be treated independently. This simplifies greatly the treatment of the larger dynamical system.

8.1.3 Irreducible

If no transformation $(x) \rightarrow (u, v)$ exists, the original dynamical system is called irreducible. Up to now, the only dynamical systems that we have treated have been irreducible.

Remark: Both in the theory of groups and the theory of representations (of groups) there are algorithms for determining whether a structure is reducible, fully reducible, or irreducible. If the structure is reducible, there are algorithms for carrying out the reduction to reduced or fully reduced form. Such algorithms are currently lacking in dynamical systems theory. The formulation of such algorithms for dynamical systems will represent a major milestone in the development of this theory.

8.2 ENTRAINMENT AND SYNCHRONIZATION

It often happens that a physical system is governed by equations of the form

$$\frac{dx}{dt} = f(x) \tag{8.3}$$

where the function $f(x)$ is unknown. Data generated by this physical system are used to create models of the dynamics

$$\frac{dy}{dt} = g(y) \tag{8.4}$$

where the model variables y_i correspond to the physical variables x_i. When this is possible, the important question is: How good is the model?

8.2.1 Entrainment

One way to answer this question is to carry out an entrainment test [98]. In such a test, the data are used to "drive" the model. In short, the two dynamical systems $f(x)$ and $g(y)$ are coupled together to form a reducible dynamical system with the structure

$$\begin{aligned} \frac{dy}{dt} &= g(y) + \lambda(x-y) &&= f_1(y,x) \\ \frac{dx}{dt} &= f(x) &&= f_2(-,x) \end{aligned} \tag{8.5}$$

Even the simplest linear coupling term has a tensor structure: $dy/dt = g(y) + \lambda(x - y) \rightarrow dy_i/dt = g_i(y) + \sum_j \lambda_{ij}(x_j - y_j)$. If the model $g(y)$ is "close to" the real physics $f(x)$—this means that $g(x) - f(x)$ is "small" in some sense—the differences $x_j(t) - y_j(t)$ will remain close to zero after transients caused by poor choice of initial conditions have died out. An entrainment test involves a plot of each $y_j(t)$ against the corresponding $x_j(t)$. If all λ are small and all plots $y_j(t)$ vs. $x_j(t)$ are almost diagonal, the model $g(y)$ can be considered as a good representation of the physics $f(x)$.

At the present time we do not have a theory for the dependence of the difference $y_j(t) - x_j(t)$ on λ as a function of the goodness of the model $g(x) - f(x)$. We do have such a theory for linear systems. It is embodied in χ^2 tests.

8.2.2 Synchronization

When data $x_j(t)$ generated by a physical system are maintained offline, models $g(y)$ that are developed to describe the physics can only be tested using the entrainment test described above. However, when an experiment is maintained online, the model output can be fed back into the experimental system to create an irreducible dynamical system from the two components of the fully reduced system:

$$\begin{aligned} \frac{dy}{dt} &= g(y) + \lambda(x-y) &&= f_1(y,x) \\ \frac{dx}{dt} &= f(x) + \lambda(y-x) &&= f_2(y,x) \end{aligned} \tag{8.6}$$

In this case if the model is a close representation of the physics, for small values of λ the linear combination $\frac{1}{2}(x+y)$ will approximate both x and y, and the linear

combination $\frac{1}{2}(x-y)$ will approximate zero. In fact, as λ decreases from "large" to zero there will be a bifurcation from $x-y=0$ to $x-y\neq 0$. The locus of this bifurcation in the λ parameter space can be used as a measure of the "goodness" of the model.

As for the entrainment test, so for this synchronization test: at the present time we do not have a theory for the relation between the goodness of a model and the values at which this symmetry-breaking bifurcation occurs. The synchronization test will be discussed in more detail in Section 9.4.

8.3 DRIVING SYSTEMS

The driven two-dimensional oscillators that we study in detail are the van der Pol, Duffing, and Takens-Bogdanov oscillators. These are treated in detail in Sections 8.5, 8.6, and 8.7. In this section we describe the systems used to drive the two dimensional oscillators. We will force them with three different systems: the Rössler and Lorenz systems and the harmonic oscillator. Each of these systems is described briefly now.

8.3.1 Rössler System

The Rössler equations [109]

$$\begin{aligned} \dot{u} &= -v-w \\ \dot{v} &= u+av \\ \dot{w} &= b+w(u-c) \end{aligned} \tag{8.7}$$

exhibit a series of strange attractors and periodic windows as the control parameters are varied. For the most part, we keep the control parameters $(b,c)=(2.0,4.0)$ fixed and scan the parameter a. A bifurcation diagram is shown in Fig. 8.1. For $a=0.3$ this dynamical system has a limit cycle. The projection of the limit cycle on the u-v plane is shown in Fig. 8.2(a), while the power spectrum is shown in Fig. 8.2(b). The first sharply defined peak in the power spectrum occurs for at $\omega=0.175$. We use this to define the fundamental frequency of the Rössler period-one limit cycle. The limit cycle has both even and odd higher harmonics at $n\omega$, $n=2,3,\ldots$.

8.3.2 Lorenz System

The Lorenz system [78]

$$\begin{aligned} \dot{u} &= -\sigma u+\sigma v \\ \dot{v} &= Ru-v-uw \\ \dot{w} &= -bw+uv \end{aligned} \tag{8.8}$$

has been discussed extensively in earlier chapters. We briefly review its most important properties here. It possesses rotation symmetry $\mathcal{R}_Z(\pi)$ around the-Z axis. For $R>1$ and $(\sigma,b)=(10,8/3)$ there are three real fixed points. The fixed point at the origin is a saddle, and for $R>1.345$ the pair of symmetry-related fixed points

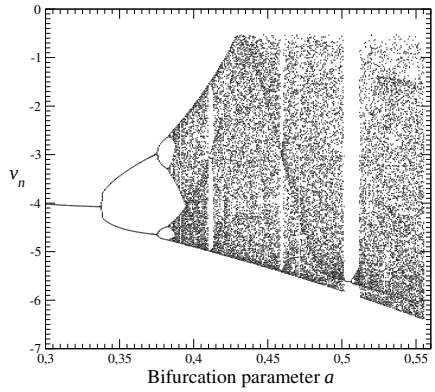

Fig. 8.1 Bifurcation diagram for the Rössler attractor for $(b, c) = (2.0,\ 4.0)$.

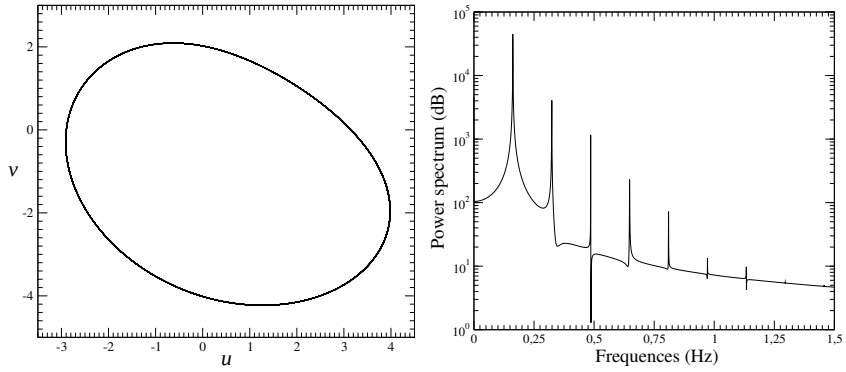

(a) Period-one limit cycle (b) Power spectrum

Fig. 8.2 (a) The Rössler dynamical system exhibits a period-one limit cycle for $(a, b, c) = (0.3, 2, 4)$. (b) The power spectrum of $u(t)$ shows the first sharply defined peak at $\omega = 0.175$. This is taken as the fundamental frequency of the periodic Rössler drive.

become foci that are stable for $R < 24.74$ and unstable for larger values of R. The angular frequency of the two unstable foci determine to a large extent the characteristic time of the Lorenz attractor. This angular frequency is a function of R that can be well approximated by the cubic regression

$$\omega(R) = 7.1931 + 13.32(R/100) - 2.8107(R/100)^2 + 0.29525(R/100)^3 \quad (8.9)$$

The angular frequency $\omega(R)$ and its approximation by this cubic function is shown in Fig. 8.3.

The Lorenz equations exhibit a series of strange attractors and periodic windows as the control parameters are varied. For the most part, we keep the control parameters

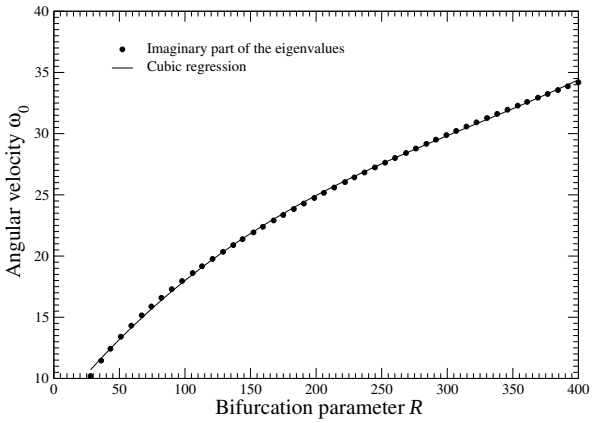

Fig. 8.3 Imaginary part of the complex eigenvalue of the unstable saddle foci of the Lorenz system. $(\sigma, b) = (10, 8/3)$.

$(\sigma, b) = (10.0, 8/3)$ fixed and scan the parameter R. A bifurcation diagram is shown in Fig. 8.4. For $R = 350$ this dynamical system has a limit cycle. As R decreases below ~ 315 a symmetry-breaking bifurcation to two asymmetric, but symmetry-related, orbits takes place. Only one of the two stable periodic orbits appears in the bifurcation diagram in the range $240 < R < 315$. The other can be seen by different choice of initial conditions.

The projection of the limit cycle at $R = 350$ on the u-v plane is shown in Fig. 8.5(a), while the power spectrum is shown in Fig. 8.5(b). The first sharply defined peak in the power spectrum occurs at $\omega = 2.5$. We use this to define the fundamental frequency, ω, of the Lorenz period-one limit cycle. The limit cycle has no even harmonics because of its symmetry. The odd harmonics have exponentially decreasing amplitudes.

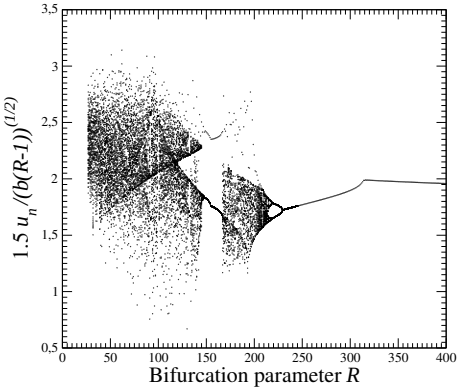

Fig. 8.4 Bifurcation diagram for the Lorenz system for $(\sigma, b) = (10.0,\ 8/3)$.

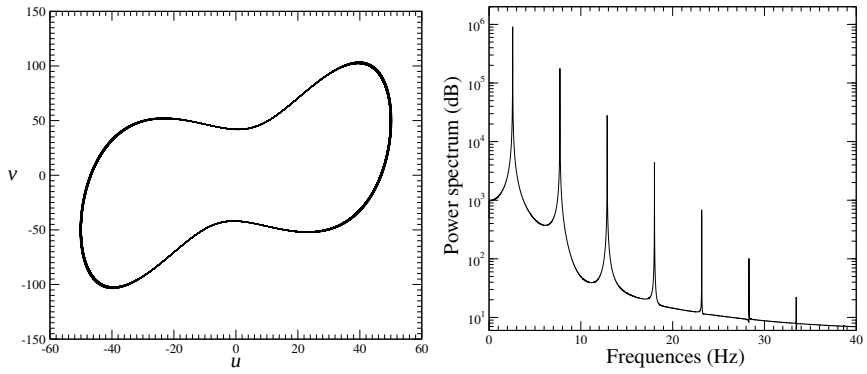

(a) Period-one limit cycle (b) Power spectrum

Fig. 8.5 (a) The Lorenz system exhibits a period-one limit cycle for $(R,\ \sigma,\ b) = (350, 10, 8/3)$. (b) The power spectrum of $u(t)$ shows the first sharply defined peak at $\omega = 2.5$. This is taken as the fundamental frequency of the periodic Lorenz drive.

A Lorenz orbit of topological period p is labeled by p symbols. The corresponding temporal period is $T_p \simeq 2\pi p/\omega(R)$ and the angular frequency is $\omega_p \simeq \omega(R)/p$. When driving a two-dimensional nonlinear oscillator with a Lorenz orbit of topological period p we always compare the driving frequency $\omega(R)/p$ to the fundamental frequency ω_1 of the driven system.

8.3.3 Harmonic Oscillator

The harmonic oscillator equations of motion, in symmetric form, are $\dot{u} = \omega v$, $\dot{v} = -\omega u$. In order to put these driving equations in a form as close as possible to the form given below to the two-dimensional nonlinear oscillators, we write these equations as

$$\begin{aligned} \dot{u} &= v \\ \dot{v} &= -\omega^2 u \end{aligned} \tag{8.10}$$

The phase space trajectories are circles, and the power spectrum of $u(t)$ and $v(t)$ contains exactly one peak at ω.

We point out explicitly here that in this case the driving system contains only two equations. These equations cannot generate a strange attractor. By the Poincaré-Bendixon theorem [5] two coupled ordinary differential equations can have as invariant sets only fixed points and limit cycles. The harmonic equations are particularly slippery: they are structurally unstable. They generate a one-parameter family of limit cycles: the continuous parameter is A, the radius of the limit cycle. Typical nonlinear two-dimensional systems generate only isolated limit cycles that alternate in their stability. For this reason, the behavior of two-dimensional nonlinear oscillators when driven harmonically is somewhat different from their behavior when driven

by a system that generates dynamically stable and structurally stable limit cycles, as do the Rössler and Lorenz systems for certain parameter value ranges. As a consequence, we must be careful to specify initial conditions (of the harmonic oscillator) in many of the bifurcation diagrams that we present that are based on harmonic drives.

8.4 UNDRIVEN NONLINEAR OSCILLATORS

8.4.1 Linear Oscillators

We begin with a simple linear harmonic oscillator without damping. The equation of motion is

$$\ddot{x} + \omega^2 x = 0 \qquad \text{or} \qquad \begin{aligned} \dot{x} &= p \\ \dot{p} &= -\omega^2 x \end{aligned} \tag{8.11}$$

We begin adding complications by including damping:

$$\ddot{x} + \gamma\dot{x} + \omega^2 x = 0 \qquad \text{or} \qquad \begin{aligned} \dot{x} &= p \\ \dot{p} &= -\omega^2 x - \gamma\dot{x} \end{aligned} \tag{8.12}$$

Damping occurs for $\gamma > 0$. If $\gamma < 0$ the system is "self-excitatory."

8.4.2 Nonlinear Oscillators

The general two-dimensional nonlinear oscillator can be written in the form

$$\ddot{x} + f_1(x,\dot{x})\dot{x} + f_2(x,\dot{x})x = 0 \qquad \text{or} \qquad \begin{aligned} \dot{x} &= p \\ \dot{p} &= -f_1(x,\dot{x})p - f_2(x,\dot{x})x \end{aligned} \tag{8.13}$$

For the linear oscillator with damping, $f_1(x,\dot{x}) = \gamma$ and $f_2(x,\dot{x}) = \omega^2$.

8.4.3 Fixed Points

The fixed points of the nonlinear oscillator (8.13) occur for $p = 0$ and $f_2(x,0)x = 0$. One fixed point occurs at the origin $(x,p) = (0,0)$. Other fixed points occur along the x-axis $p = 0$ at the zeroes of $f_2(x,0)$, if such zeroes exist. At the off-origin fixed points $x_0 \neq 0$, $f_2(x_0,0) = 0$.

8.4.4 Stability of Fixed Points

The stability properties of the fixed point at the origin are determined from the eigenvalues of the stability matrix

$$\begin{aligned} &\begin{bmatrix} 0 & 1 \\ -f_2(0,0) & -f_1(0,0) \end{bmatrix} \\ &\Rightarrow \lambda_\pm = -\frac{1}{2}f_1(0,0) \pm i\sqrt{f_2(0,0) - \left(\frac{1}{2}f_1(0,0)\right)^2} \end{aligned} \tag{8.14}$$

The fixed point at the origin is stable if $f_1(0,0) > 0$ and it is a focus if $f_2(0,0) - (\frac{1}{2}f_1(0,0))^2 > 0$.

At a fixed point $(x_0, p = 0)$ with $x_0 \neq 0$, the stability properties are determined by the eigenvalues of the stability matrix. They are

$$\lambda_\pm = -\frac{1}{2}\mathrm{Tr} \pm \sqrt{\left(\frac{1}{2}\mathrm{Tr}\right)^2 - \mathrm{Det}} \qquad \text{where} \qquad \begin{aligned} \mathrm{Tr} &= -f_1(x_0,0) \\ \mathrm{Det} &= x_0 \frac{\partial f_2(x_0,0)}{\partial x} \end{aligned} \tag{8.15}$$

8.4.5 Global Stability Conditions

The global stability of the nonlinear oscillator

$$\begin{aligned} \dot{x} &= y \\ \dot{y} &= -y f_1(x,y) - x f_2(x,y) \end{aligned}$$

is determined by perturbing from the Hamiltonian limit. To do this, it is useful to introduce a function $F_2(x,y)$ defined by

$$dF_2(x,y) = x f_2(x,y)\, dx$$

If we construct a function $H(x,y) = \frac{1}{2}y^2 + F_2(x,y)$, the Hamiltonian equations of motion derived from $H(x,y)$ are

$$\frac{dx}{dt} = +\frac{\partial H}{\partial y} = y$$

$$\frac{dy}{dt} = -\frac{\partial H}{\partial x} = -x f_2(x,y)$$

The Hamiltonian function can be treated as an energy that is conserved when the dissipative function $f_1(x,y) = 0$. The phase portraits of the four nonlinear oscillators in the absence of dissipation are shown in the left-hand column of Fig. 8.6. These contours are simply constant energy surfaces.

When dissipation is added, the rate of change of the energy function is

$$\frac{d}{dt}\left\{\frac{1}{2}\dot{x}^2 + F_2(x,y)\right\} = -\dot{x}^2 f_1(x,y)$$

This dissipation term breaks the closed contours. If the energy function $H(x,y)$ is bounded below, arbitrary initial conditions relax to some bounded domain in the phase space. This is the case for the Duffing, van der Pol, and Rayleigh oscillators. The energy function for the Takens-Bogdanov oscillator is not bounded below, so some initial conditions can escape to infinity. It is for this reason that study of the dynamics of this oscillator is somewhat delicate. The phase portraits for these four oscillators with dissipation are shown in the right-hand column of Fig. 8.6.

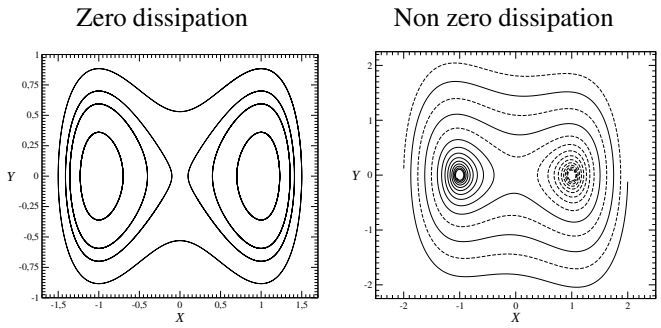

(a) Duffing system

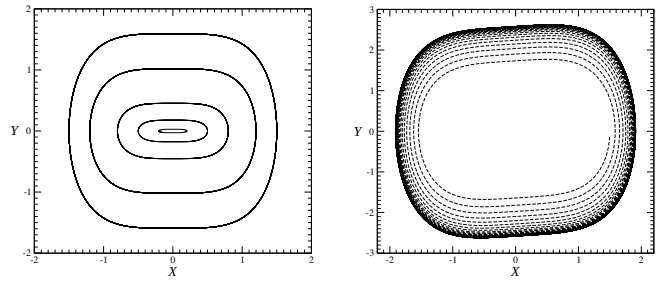

(b) van der Pol system

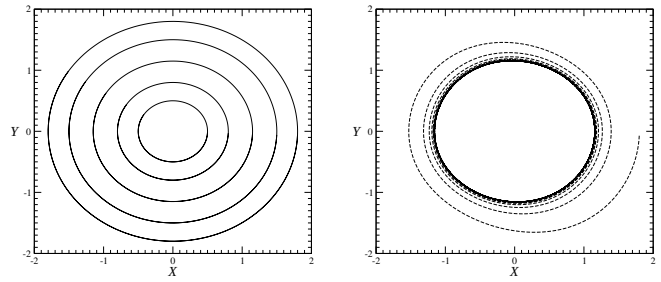

(c) Rayleigh system

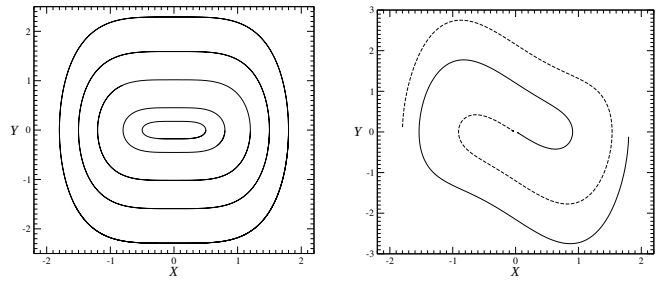

(d) Takens-Bogdanov system

Fig. 8.6 Phase portraits for Duffing, van der Pol, Rayleigh, and Takens-Bogdanov oscillators. Left: conservative limit. Right: with dissipation.

8.4.6 Symmetry

We are particularly interested in two-dimensional nonlinear oscillators with a twofold symmetry. The physically important symmetry is the inversion symmetry: $(x, p) \rightarrow (-x, -p)$. To ensure this symmetry, the two functions f_1 and f_2 must both be even: $f_i(-x, -p) = +f_i(x, p)$. Several widely studied oscillators possess this symmetry: the Duffing, the van der Pol, the Rayleigh, and the Takens-Bogdanov oscillators. Their forcing functions are collected in Table 8.2.

8.4.7 Origins of These Nonlinear Oscillators

Two of the three nonlinear oscillators that we study in detail in this chapter (the van der Pol and the Duffing oscillators) had their origins in classical nonlinear circuits. The third nonlinear oscillator was studied by mathematicians searching for canonical forms for nonlinear oscillators that exhibit degenerate bifurcations and include as special cases the bifurcations intrinsic to the van der Pol and Duffing oscillators.

8.4.7.1 Van der Pol Oscillator The van der Pol equation was introduced to study oscillations in an electronic circuit containing a nonlinear resistance [129,130]. Such a circuit is shown in Fig. 1.5(b). The nonlinear element at that time was a triode vacuum tube. A nonlinear characteristic of the form $V \simeq -\alpha i + \beta i^3$, $\alpha, \beta > 0$, guarantees self-excitations through an effective negative resistance at low current flows and a positive resistance (a stability condition) at high current flows. A very similar equation had previously been proposed by Rayleigh to describe self-sustained sound vibrations [104].

The van der Pol equations, in standard form, are

Table 8.2 Important nonlinear oscillators $\ddot{X} + f_1\dot{X} + f_2X = 0$ are defined by different functions.

Equations	$f_1(X, Y)$	$f_2(X, Y)$
Duffing	μ	$-(1 - X^2)$
van der Pol	$-\mu(1 - X^2)$	1 or X^2
Rayleigh	$-\mu\left(1 - \frac{1}{3}Y^2\right)$	1
Takens-Bogdanov	$\nu + X^2$	$\mu - X^2$

$$\begin{aligned}\dot{x} &= y \\ \dot{y} &= \alpha y - x^2 y - x\end{aligned}$$

This two-dimensional dynamical system has a single fixed point at $(x, y) = (0, 0)$. The stability of this fixed point is determined by the eigenvalues of the flow linearized about the fixed point. The Jacobian is

$$J = \begin{bmatrix} 0 & 1 \\ -2xy - 1 & \alpha \end{bmatrix} \xrightarrow{(0,0)} \begin{bmatrix} 0 & 1 \\ -1 & \alpha \end{bmatrix} \qquad \lambda_{\pm} = \frac{1}{2}\alpha \pm \sqrt{(\frac{1}{2}\alpha)^2 - 1}$$

The fixed point is stable if $\alpha < 0$ and unstable if $\alpha > 0$. For $|\frac{1}{2}\alpha| > 1$ the fixed point is a node, for $|\frac{1}{2}\alpha| < 1$ it is a focus. As α increases through 0 the fixed point undergoes a Hopf bifurcation, changing from a stable to an unstable node and creating a stable limit cycle that models self-excitatory behavior.

8.4.7.2 Duffing Oscillator Duffing studied electrical circuits of the type shown in Fig. 1.5(a) [28]. Such circuits exhibit bistable behavior. The Duffing equations are typically used to model electrical or mechanical systems that have two symmetry-related ground states separated by an unstable equilibrium. These equations have been used to model the dynamics of buckled beams and beams subject to magnetic fields [8, 42].

The Duffing equations, in canonical form, are

$$\begin{aligned}\dot{x} &= y \\ \dot{y} &= \mu y - \frac{\partial V(x;\alpha)}{\partial x} \qquad V(x;\alpha) = \frac{1}{2}\alpha x^2 + \frac{1}{4}x^4\end{aligned}$$

The fixed points occur along the line $y = 0$ at the equilibria of the potential $V(x; \alpha)$. There is one equilibrium at $x = 0$ for $\alpha > 0$ and this equilibrium is stable. For $\alpha < 0$ there are three equilibria, an unstable one at $x = 0$ and two stable symmetry-related equilibria at $x = \pm\sqrt{-\alpha}$. As α decreases through 0 the potential exhibits a pitchfork (symmetry-restricted cusp, Ginzburg-Landau) bifurcation.

8.4.7.3 Takens-Bogdanov Oscillator The Takens-Bogdanov dynamical system is motivated less by physical than by mathematical considerations. The objective was to seek canonical forms for a nonlinear oscillator with a doubly degenerate eigenvalue [17, 120]. Unfoldings of this canonical germ include, as special cases, the van der Pol and the Duffing oscillators. The general dynamical system considered was of the form

$$\begin{aligned}\dot{x} &= y \\ \dot{y} &= f(x, y) \qquad f(-x, -y) = -f(x, y)\end{aligned}$$

If the source function $f(x, y)$ is assumed to be (real) analytic, and expanded in an ascending power series, the expansion contains two linear terms, four cubic terms, six fifth-degree terms, ...

$$\begin{aligned}\dot{x} &= y \\ \dot{y} &= \mu_1 x + \mu_2 y + \alpha x^3 + \beta x^2 y + \gamma x y^2 + \delta y^3 + \ldots\end{aligned}$$

The origin $(x, y) = (0, 0)$ is clearly a fixed point. All other fixed points lie along the line $y = 0$. If it is desired to study dynamics and bifurcations in the neighborhood of the origin, it is useful to truncate this expansion beyond the cubic terms. This was done by Takens and Bogdanov. They then sought coordinate transformations to bring the cubic terms to a canonical form, which is

$$\begin{aligned} \dot{x} &= y \\ \dot{y} &= \mu_1 x + \mu_2 y \mp x^3 + x^2 y \end{aligned}$$

The fixed points occur at the solutions of $x(\mu_1 \mp x^2) = 0$, or $x = 0$ and $x = \pm\sqrt{\pm\mu_1}$. As μ_1 passes through 0 there is a forward or reverse pitchfork bifurcation, depending on which of the two canonical forms ($\mp x^3$) is chosen. This system also exhibits Hopf bifurcations. Fig. 8.7 shows a series of phase portraits exhibited by the canonical form with $\dot{y} = \mu_1 x + \mu_2 y - x^3 + x^2 y$ as a function of increasing control parameter μ_1 for $\mu_2 < 0$. A stable fixed point ($\mu_1 < 0$) undergoes a pitchfork bifurcation as μ_1 increases through 0. As μ_1 continues to increase, a Hopf bifurcation occurs at the two off-origin fixed points $(x, y) = (\pm\sqrt{\mu_1}, 0)$ as $\mu_1 + \mu_2$ increases through 0. These two fixed points become unstable foci and are surrounded by stable limit cycles. For a somewhat larger value of μ_1 the two limit cycles meet at the origin in a nonlocal bifurcation (homoclinic connection [17,39,42,120]), and then grow to surround the origin.

This normal form has been used to describe a sequence of bifurcations observed in several fluid systems [93].

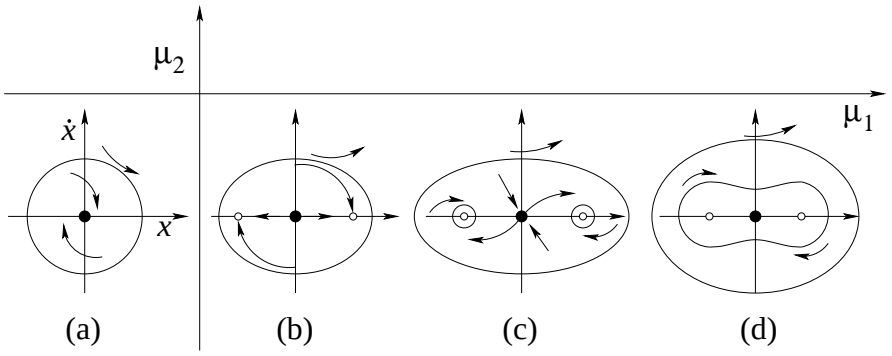

Fig. 8.7 Phase portraits of the Takens-Bogdanov normal form (with $-$ sign) showing a sequence of bifurcations as μ_1 increases with $\mu_2 < 0$. (a) Stable fixed point at the origin undergoes a pitchfork bifurcation at $\mu_1 = 0$ to produce (b) three fixed points, two stable nodes surrounding a saddle. The stable nodes become stable foci, then undergo Hopf bifurcations at $\mu_1 + \mu_2 = 0$ to produce (c) two unstable foci surrounded by two stable limit cycles. After a homoclinic connection a single stable limit cycle (d) encloses the two unstable foci and single saddle.

8.5 THE VAN DER POL OSCILLATOR

The equations that define the van der Pol oscillator are

$$\begin{aligned} \dot{x} &= y \\ \dot{y} &= \mu(1-\beta x^2)y - x^n \end{aligned} \tag{8.16}$$

The integer n is usually taken as $n = 1$ or $n = 3$, and β is taken as $+1$ in Table 8.2. The Rayleigh oscillator is closely related to the van der Pol oscillator. The van der Pol oscillator in z with $\beta = 1$, and $n = 1$ is obtained from the Rayleigh oscillator by taking the time derivative of the latter and setting $z = \dot{x}$.

The undriven van der Pol oscillator has a single fixed point at the origin that is unstable for $\mu < 0$. For $\mu > 0$ this set of equations has a limit cycle. A limit cycle is shown in Fig. 8.8(a) for $\mu = 0.48$, $\beta = 1$, and $n = 3$. The period of this limit cycle is $T = 3.903$, corresponding to a fundamental frequency of $f_1 = 0.256$ and angular frequency $\omega_1 = 1.608$. The power spectrum for the x-coordinate of this limit cycle is shown in Fig. 8.8(b). This figure shows that only odd angular frequencies contribute to the structure of this limit cycle, as the principal Fourier components are ω_1, $\omega_3 = 3\omega_1$, and $\omega_5 = 5\omega_1$. This occurs because the forcing terms are odd. A three-term Fourier expansion of $x(t)$ and $y(t)$ provides an excellent representation of this limit cycle.

The fundamental frequency f_1 depends on the parameter μ. This dependence is shown in Fig. 8.9, and is given analytically by the cubic regression

$$\omega_1 = 1.6163 + 0.0080136\mu - 0.046403\mu^2 + 0.0051574\mu^3 \tag{8.17}$$

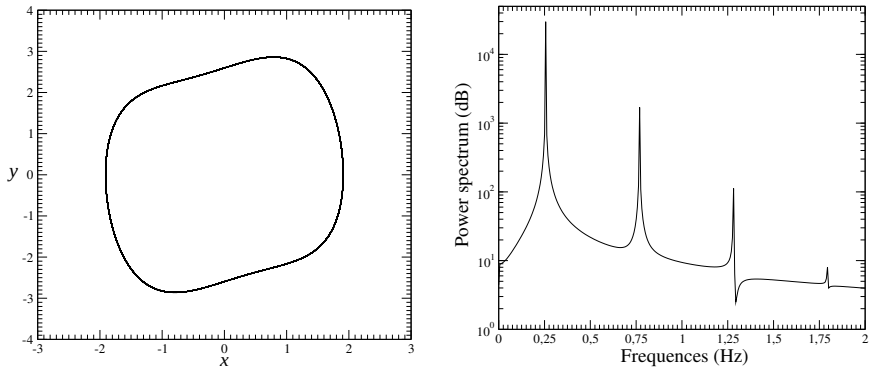

(a) Limit cycle (b) Power spectrum

Fig. 8.8 (a) Limit cycle solution $(x(t), y(t))$ to the van der Pol equations. (b) Power spectrum of $x(t)$. The fundamental frequency is $f_1 = 0.256$ and only odd harmonics are present. Parameter values: $(\mu, \beta, n) = (0.48, 1, 3)$.

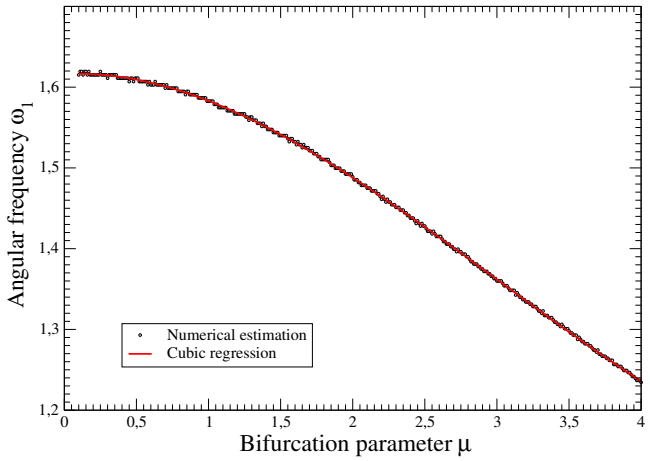

Fig. 8.9 Dependence of the fundamental angular frequency of the van der Pol oscillator on the parameter μ for $(\beta, n) = (1, 3)$.

It is useful to know the dependence of the fundamental frequency on the parameters of the nonlinear oscillator, as the response of the oscillator, with fundamental frequency f_1, to a driving system with a fundamental frequency f, depends to a large extent on the ratio f/f_1.

8.5.1 Rössler Drive

Roughly and accurately speaking, any dynamical system can be used to drive any other. In this section we use the Rössler system to drive the van der Pol nonlinear oscillator. The arrangement is

$$\begin{array}{ccc} \text{Driving System} & \longrightarrow & \text{Driven System} \\ \text{= Rossler} & & \text{= van der Pol} \end{array}$$

$$\begin{aligned} \dot{u} &= -v - w \\ \dot{v} &= u + av \\ \dot{w} &= b + w(u - c) \end{aligned} \qquad \begin{aligned} \dot{x} &= y \\ \dot{y} &= \mu(1 - \beta x^2)y - x^n + \rho u \end{aligned} \tag{8.18}$$

In this set of equations we have used a simple linear drive in the equation describing the acceleration (second equation). The coupling parameter $\rho = 1$. We will reverse the sign of the coupling later to make a point about symmetry.

The Rössler equations were integrated at control parameter values $(a, b, c) = (0.3, 2, 4)$ to generate a period-one orbit. This orbit was used to drive the van der Pol system using the coupling shown in Eq. (8.18). The Rössler orbit was renormalized (in time) before being used to drive the van der Pol oscillator. As the ratio of the driving frequency ω of the Rössler orbit to the fundamental frequency ω_1 of the van der Pol oscillator varied, $\delta = \omega/\omega_1$, the response of the driven system to the drive

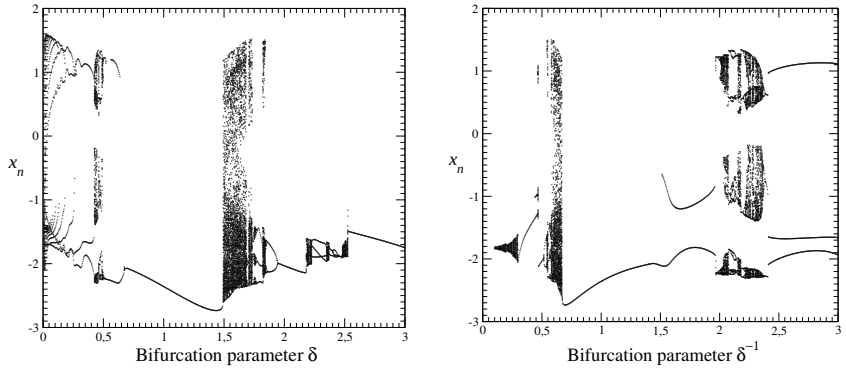

(a) Versus δ (b) Versus $1/\delta$

Fig. 8.10 The van der Pol system is driven by a period-1 orbit generated by the Rössler system. The bifurcation diagram shows the response of the van der Pol system as a function of (a) the frequency ratio $\delta = \omega/\omega_1$ and (b) its inverse δ^{-1}. Other parameter values: $(a, b, c) = (0.3, 2, 4)$ and $(\mu, \beta, n) = (0.48, 1, 3)$.

varied from simple to complex. The bifurcation diagram shown in Fig. 8.10 describes this variation. The coordinate x_n of the intersection of the trajectory with the plane $y = 0$, $\dot{y} > 0$, is plotted as a function of this ratio. This plot shows that the driven system exhibits a simple limit cycle in a broad range of values around $\delta = 1,\ 2,\ 3$. One of these limit cycles is shown in Fig. 8.11(a). Limit cycles are also obtained for subharmonic driving. Two of these are shown for $\delta = 0.6$ in Fig. 8.11(b) and for $\delta = 1/3$ in Fig. 8.11(c). They exhibit two and three intersections with the plane $y = 0$, $\dot{y} > 0$, as can be seen in both Fig. 8.10 and Fig. 8.11(b) and 8.11(c).

As the driving system goes through a sequence of bifurcations, so also does the driven system. We show this in Fig. 8.11 and Fig. 8.12. Fig. 8.12(a) shows the bifurcation diagram for the Rössler attractor as a function of the parameter a for $(b, c) = (2, 4)$. There is a period-one orbit for $a < 0.335$. We choose $a = 0.3$ and show three limit cycles obtained by driving the van der Pol system at frequency ratios $\delta = 1.0$ (Fig. 8.11(a)), $\delta = 0.6$ (Fig. 8.11(b)), and $\delta = 1/3$ (Fig. 8.11(c)). The period-one limit cycle is symmetric but the period-two and period-three limit cycles are not: we show the two symmetry-related limit cycles in Fig. 8.11(b) and (c). The bifurcation diagrams based on these three limit cycles are shown in Figs. 8.12(b), (c), and (d) as a function of increasing values of the Rössler control parameter a. It should be observed that the alternation of chaotic behavior and periodic windows is the same in the driven van der Pol system as it is in the Rössler attractor. The principal difference is that a period-p orbit for the Rössler system generates orbits of periods p, $2p$, and $3p$ in the driven van der Pol system for driving frequency ratios $\delta = 1,\ 0.6$, and $1/3$.

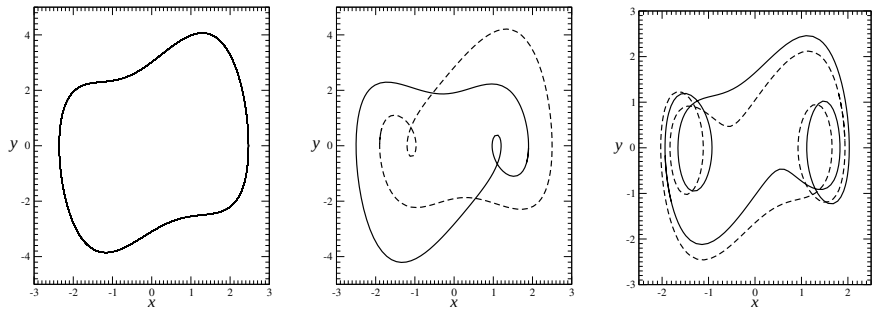

(a) Period-1: $\delta = 1$ (b) Period-2: $\delta = 0.6$ (c) Period-3: $\delta = 1/3$

Fig. 8.11 Limit cycles of the driven van der Pol system for different values of δ. The symmetric partners of the period-two and period-three limit cycles are shown. Other parameter values: $(a, b, c) = (0.3, 2, 4)$ and $(\mu, \beta, n) = (0.48, 1, 3)$.

We close this section with a discussion of symmetry. To be accurate, there is none. However, this is not a useful way to look at the coupling of two dynamical systems. We show in Fig. 8.13 two strange attractors that are closely related: they are "rotation-symmetric." Both are obtained by running the Rössler system in a periodic region, with $(a, b, c) = (0.3, 2, 4)$ and coupling with a frequency ratio $\omega/\omega_1 = \delta = 0.4$ that generates chaotic behavior. The two attractors are obtained by simultaneously changing their initial conditions and the sign of the coupling strength ρ. It is clear from this figure that the two attractors are related by a rotation through π radians about an axis through the origin perpendicular to the x-y plane.

8.5.2 Lorenz Drive

We now use the Lorenz system to drive the van der Pol oscillator. The coupled equations are

$$\begin{array}{ccc} \text{Driving System} & \longrightarrow & \text{Driven System} \\ \text{= Lorenz} & & \text{= van der Pol} \end{array}$$

$$\begin{aligned} \dot{u} &= -\sigma u + \sigma v & \qquad \dot{x} &= y \\ \dot{v} &= Ru - v - uw & \qquad \dot{y} &= \mu(1 - \beta x^2)y - x^n + \rho \frac{\alpha}{\sqrt{b(R-1)}} u \\ \dot{w} &= -bw + uv \end{aligned} \tag{8.19}$$

As with the driving Rössler system, we rescale the time parameter of the driving Lorenz attractor to the fundamental frequency of the van der Pol oscillator. In addition, we couple the $u(t)$ dependence into the van der Pol oscillator with a parameter-dependent coupling constant proportional to $(R-1)^{-1/2}$. This is done to maintain a rough amplitude independence of the driving term within the range of the R parameter. This subtle feature was unnecessary when driving with the Rössler attractor, since the

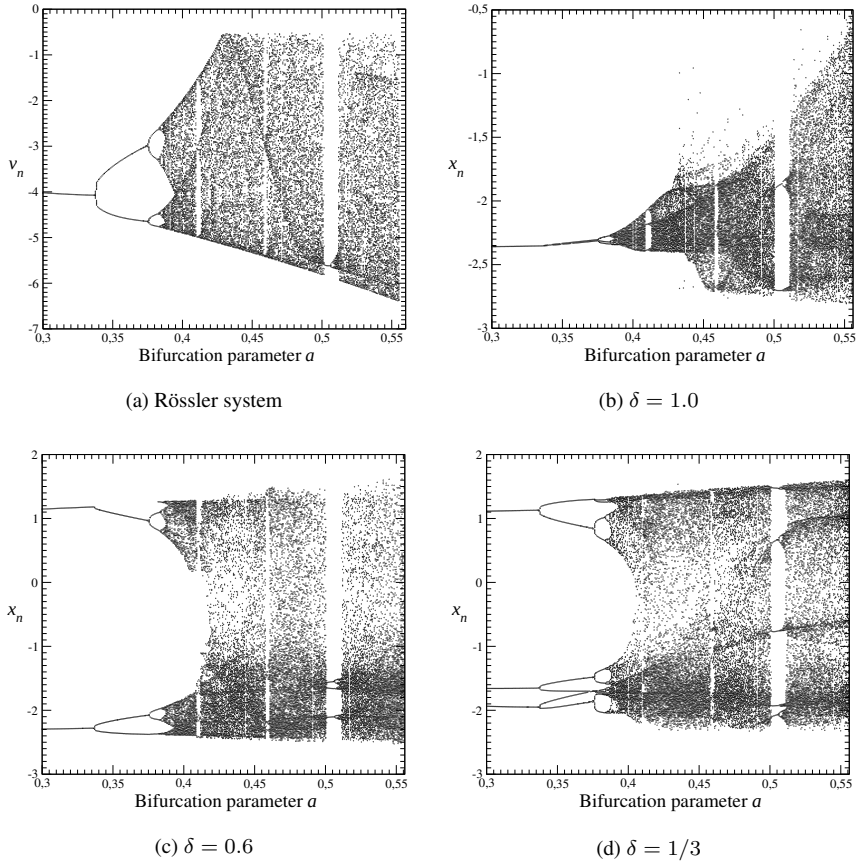

(a) Rössler system

(b) $\delta = 1.0$

(c) $\delta = 0.6$

(d) $\delta = 1/3$

Fig. 8.12 (a) Bifurcation diagram for the Rössler attractor for $(b, c) = (2, 4)$. Bifurcation diagrams for the responding van der Pol oscillator for (b) $\delta = 1.0$, (c) $\delta = 0.6$, and (d) $\delta = 1/3$. Other parameter values: $(a, b, c) = (0.3, 2, 4)$ and $(\mu, \beta, n) = (0.48, 1, 3)$.

diameter of that attractor did not vary by more than 25% over the range of the control parameters studied. With the coupling of the form $u(t)/\sqrt{R-1}$ introduced in Eq. (8.19), the amplitude of the driving term does not vary by more than 50% over the range of the R parameter that is studied. We choose as scaling parameter $\alpha = 1.5$ and introduce $\rho = \pm 1$ for the same reasons we introduced ρ in Eq. (8.18).

When the driving frequency ω is approximately equal to the natural frequency of the van der Pol oscillator, the response to a periodic drive is a period-one limit cycle. As the frequency mismatch becomes significant, chaotic behavior alternates with entrainment having limit cycle behavior. This is shown in the bifurcation diagrams of Fig. 8.14. We plot intersections of the attractor with the half-line $y = 0$, $\dot{y} > 0$, in the x-y phase plane of the van der Pol oscillator. The diagram shows that a series

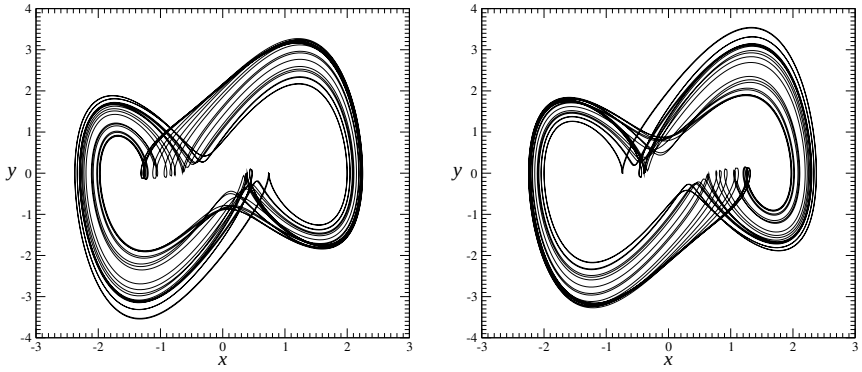

(a) $(x_0, y_0) = (0.0, +0.75)$, $\rho = -1$ (b) $(x_0, y_0) = (0.0, -0.75)$, $\rho = +1$

Fig. 8.13 Two chaotic attractors generated by the Rössler-driven van der Pol equations with $\delta = 0.4$ are related by rotation symmetry. They differ by initial conditions of the van der Pol attractor $[(x_0, y_0) \rightarrow (-x_0, -y_0)]$ and the sign of the coupling term ρ. Parameter values: $(a, b, c) = (0.3, 2, 4)$ and $(\mu, \beta, n) = (0.48, 1, 3)$.

of period-p limit cycles occurs for $\delta = \omega/\omega_1 \simeq p^{\pm 1}$. Three of these limit cycles are shown in Fig. 8.15.

A strange attractor based on each of these limit cycles is obtained as the Lorenz bifurcation parameter R is varied. The bifurcation diagram for the Lorenz attractor is shown in Fig. 8.16. The bifurcation diagrams presented in Fig. 8.16(b), (c), and (d) are based on the period-one, -two, and -three limit cycles. These diagrams show intersections of the $x(t), y(t)$ trajectory in the van der Pol phase space with the line $y = 0$, $\dot{y} > 0$. The alternation of chaotic behavior and periodic windows in all four bifurcation diagrams is similar.

Since the van der Pol oscillator has inversion symmetry, symmetry-related initial conditions can generate either a single symmetric attractor or two asymmetric, but symmetry-related, attractors. Two such attractors are shown in Fig. 8.17.

8.5.3 Harmonic Drive

The driven van der Pol equations are usually studied when the periodic driving function is harmonic: $\sin(\omega t)$ or $\cos(\omega t)$. The coupling is sometimes placed in the velocity term (first equation), sometimes in the acceleration (second) equation. We perform the coupling in the same way as we treated the Rössler and Lorenz driving conditions. The harmonic equations are written explicitly and one of the two coordinates is coupled linearly into the acceleration equation for the van der Pol oscillator. This

arrangement is shown explicitly in Eq. (8.20).

$$\begin{array}{ccc} \text{Driving System} & \longrightarrow & \text{Driven System} \\ \text{= Harmonic Oscillator} & & \text{= van der Pol} \end{array}$$

$$\begin{array}{rclcrcl} \dot{u} & = & v & & \dot{x} & = & y \\ \dot{v} & = & -\omega^2 u & & \dot{y} & = & \mu(1-\beta x^2)y - x^n + u \end{array} \tag{8.20}$$

The van der Pol oscillator was driven by a periodic orbit with initial conditions $(u_0, v_0) = (5.0, 0.0)$. The response is plotted as a function of the frequency ratio $\delta = \omega/\omega_1$ in Fig. 8.18. This figure shows that limit cycles are entrained in the neighborhood of integer values of δ and δ^{-1}.

As the frequency ratio δ varies the driven system goes through a series of bifurcations that involve a series of entrained periodic windows alternating with chaotic behavior. Limit cycles of periods one, two, and three are shown in Fig. 8.19 for decreasing values of δ. The period-one and period-three limit cycles are symmetric while the period-two limit cycles occur as a symmetry-related pair.

A bifurcation diagram for the harmonically driven van der Pol oscillator is shown in Fig. 8.20. In this case the bifurcation parameter is the amplitude of the harmonic limit cycle. This is simply the initial condition A, where $(u_0, v_0) = (A, 0)$. The harmonic drive has only three degrees of freedom to play with. One is the frequency ω; the bifurcation diagram as a function of ω has been presented in Fig. 8.18. The second and third degrees of freedom are the radius of the circular orbit and the initial phase. The bifurcation diagram as a function of the radius for initial phase $= 0$ is presented in Fig. 8.20. The bifurcation diagram shows intersections of the trajectory

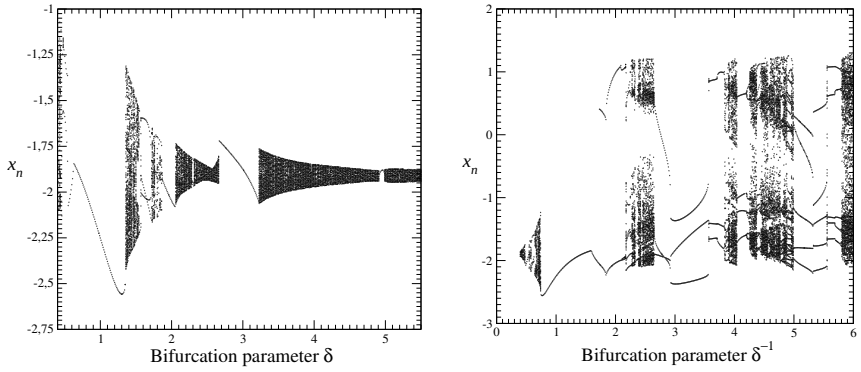

(a) versus δ (b) versus $1/\delta$

Fig. 8.14 The van der Pol system is driven by a periodic orbit generated by the Lorenz system. The bifurcation diagram shows the response of the van der Pol system as a function of (a) the frequency ratio $\delta = \omega/\omega_1$ and (b) its inverse δ^{-1}. Other parameter values: $(R, \sigma, b) = (350, 10, 8/3)$ and $(\mu, \beta, n) = (0.48, 1, 3)$.

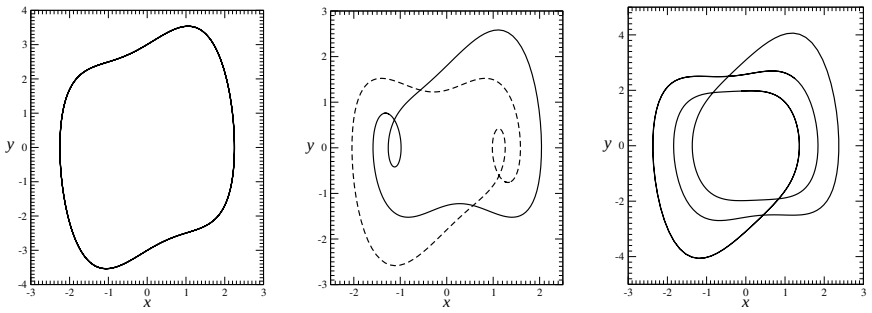

(a) $\delta = 1$ (b) $\delta = 1/2$ (c) $\delta = 1/3$

Fig. 8.15 Limit cycles of the van der Pol system driven by a periodic orbit of the Lorenz system for (a) $\delta = 1$, (b) $\delta = 1/2$, (c) $\delta = 1/3$. The period-one and -three limit cycles are symmetric and the two symmetry-related period-two limit cycles are shown. Other parameter values: $(R, \sigma, b) = (350, 10, 8/3)$ and $(\mu, \beta, n) = (0.48, 1, 3)$.

with the half-line $y = 0$, $\dot{y} < 0$, $x \geq 0$ in the (x, y) phase space of the van der Pol oscillator.

This figure shows that the response appears to be chaotic even for very small values of A, with a series of periodic windows of increasing width up to $A \simeq 2.6$, where a period-one orbit is entrained. This undergoes a period-doubling bifurcation into chaos at $A \simeq 3.5$, after which there is an alternation between periodicity and chaos up to $A \simeq 8.0$. One of the chaotic attractors generated in the construction of this bifurcation diagram is shown in Fig. 8.21.

Since the van der Pol oscillator has planar inversion symmetry, two symmetry-related strange attractors can be generated from symmetry-related initial conditions. Such a pair is shown in Fig. 8.22.

The periodically driven van der Pol oscillator generates low-dimensional strange attractor. This attractor can be embedded in a three-dimensional phase space. Since the drive is periodic, the phase space can be taken as $R^2 \times S^1$. In such a phase space, Poincaré sections are planes of constant phase: $\omega t = \text{const mod } 2\pi$. In order to visualize this strange attractor, cross sections obtained by intersections with Poincaré sections can be constructed. In fact, by taking a series of cross sections with constantly increasing phase, it is possible to visualize how the attractor evolves in time. A motion picture of this sort is shown in Fig. 8.23. This motion picture shows that the stretching and squeezing occurs by "pulling out" part of the surface and squeezing it back along a remaining part of this surface. The cross section in each cut has a fractal structure in the transverse ("radial") direction and is smooth in the transverse ("angular") direction.

Application of the Birman-Williams theorem maps this strange attractor to a branched manifold whose intersection with almost any Poincaré section is topologically a circle S^1. The attractor can be embedded in a solid torus $D^2 \times S^1$, where D^2

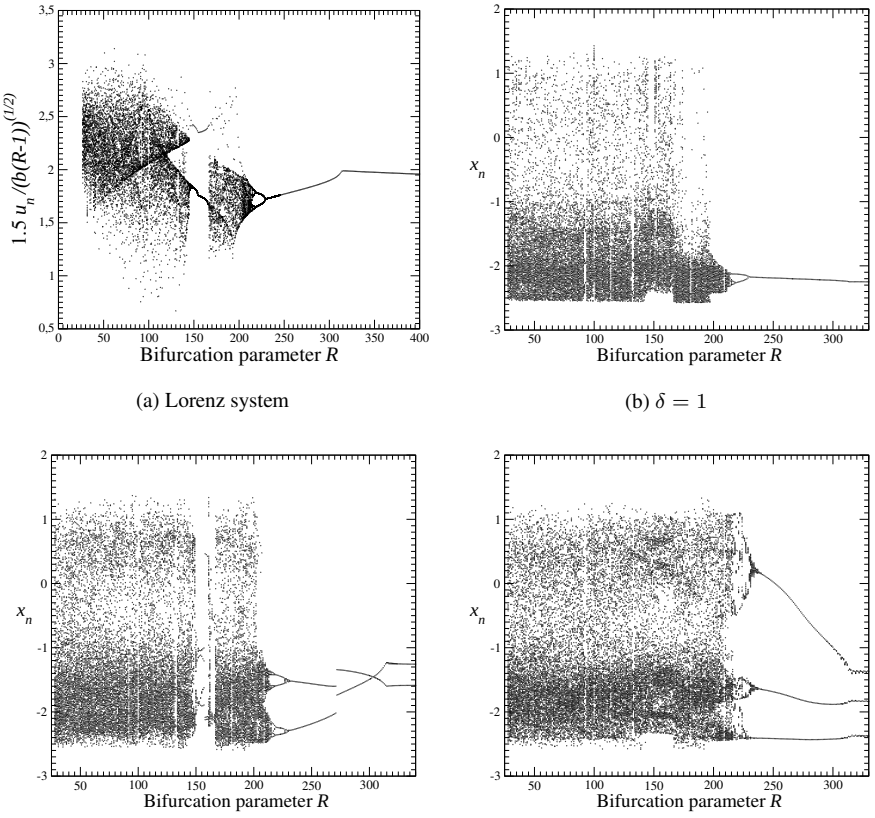

(a) Lorenz system

(b) $\delta = 1$

(c) $\delta = 1/2$

(d) $\delta = 1/3$

Fig. 8.16 (a) Bifurcation diagram for the Lorenz attractor for $(\sigma, b) = (10, 8/3)$. Bifurcation diagrams for the responding van der Pol oscillator for (b) $\delta = 1.0$, (c) $\delta = 1/2$, and (d) $\delta = 1/3$. Other parameter values: $(\mu, \beta, n) = (0.48, 1, 3)$.

is a disk. The interior of the disk can be removed, so that the strange attractor can be contained in an "annular torus." This is a solid torus from which a smaller solid torus has been removed from the inside. The global topology of the three-dimensional manifold that contains the van der Pol strange attractor differs substantially from the global topology of neighborhoods that contain any of the other strange attractors previously described in this work.

8.6 THE DUFFING OSCILLATOR

The equations that define the Duffing oscillator are

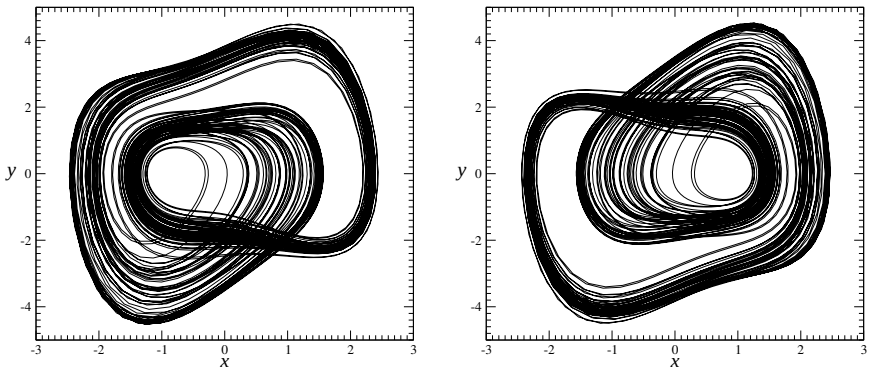

(a) $(x_0, y_0), (u_0, v_0, w_0) = (0, 0.75), (0.4, 0.4, 0.4)$

(b) $(x_0, y_0), (u_0, v_0, w_0) = (0, -0.75, -0.4), (-0.4, 0.4)$

Fig. 8.17 Two chaotic attractors generated by the Lorenz-driven van der Pol equations are related by rotation symmetry. They differ by initial conditions of the van der Pol attractor $[(x_0, y_0) \rightarrow (-x_0, -y_0)]$ and the sign of the coupling term ρ. Parameter values: $(R, \sigma, b) = (210, 10, 8/3)$ and $(\mu, \beta, n) = (0.48, 1, 3)$, $\delta = 1/3$.

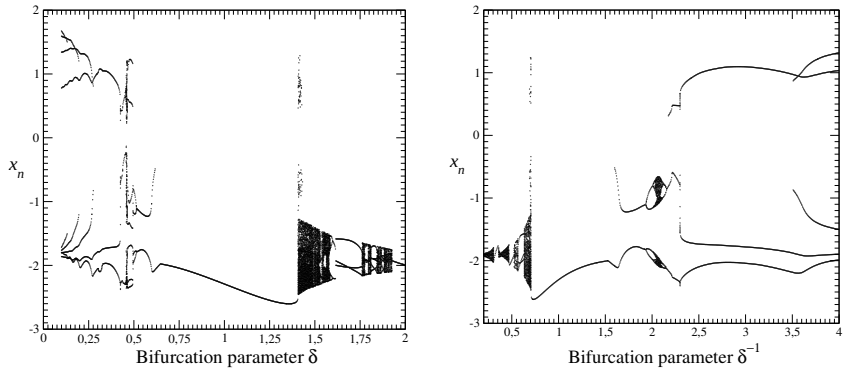

(a) versus δ

(b) versus $1/\delta$

Fig. 8.18 The van der Pol system is driven by a harmonic drive. The bifurcation diagram shows the response of the van der Pol system as a function of (a) the frequency ratio $\delta = \omega/\omega_1$ and (b) its inverse δ^{-1}. Other parameter values: $(\mu, \beta, n) = (0.48, 1, 3)$. Initial conditions: $(u_0, v_0) = (5.0, 0.0)$.

$$\begin{aligned} \dot{x} &= y \\ \dot{y} &= \mu y + x - x^3 \end{aligned} \tag{8.21}$$

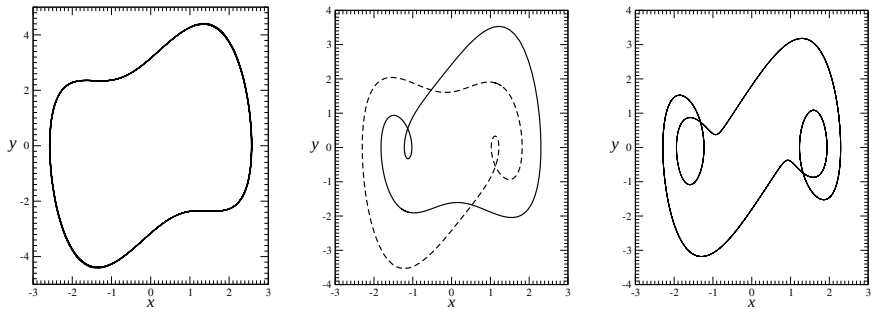

(a) $\delta = 1$ (b) versus $\delta = 0.5714$ (c) versus $\delta = 1/3$

Fig. 8.19 Three limit cycles for the harmonically driven van der Pol oscillator for different values of δ. (a) $\delta = 1$, $(x_0, y_0) = (0, 0.75)$ and $(u_0, v_0) = (5, 0)$. (b) $\delta = 0.5714$, $(x_0, y_0) = (-1.219, 0.0086)$ and $(u_0, v_0) = (-0.397, 2.573)$. (c) $\delta = 1/3$, $(x_0, y_0) = (0, 0.75)$ and $(u_0, v_0) = (5, 0)$. Other parameter values: $(\mu,\ \beta,\ n) = (0.48,\ 1,\ 3)$.

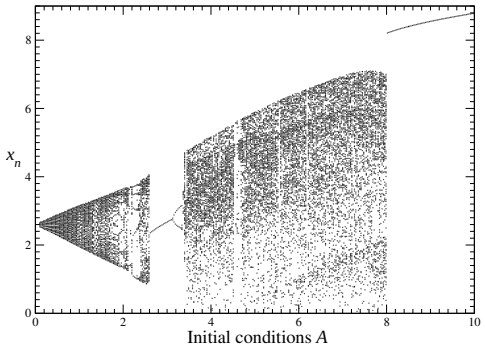

Fig. 8.20 Sensitivity to initial conditions $u_0 = A$ of the van der Pol oscillator driven by a harmonic oscillator. Parameter values: $(\mu, \beta, n) = (0.48, 1, 3)$, $\delta = 1.8$, and $(u_0, v_0) = (A, 0)$.

The undriven Duffing oscillator has three fixed points for all values of the control parameter μ. One occurs at the origin. Its eigenvalues are $\lambda_\pm = \frac{1}{2}\mu \pm [(\frac{1}{2}\mu)^2 + 1]^{1/2}$. This is a regular saddle for all values of μ. The other two fixed points occur on the x-axis at $(x, y) = (\pm 1, 0)$. The eigenvalues are $\lambda_\pm = \frac{1}{2}\mu \pm [(\frac{1}{2}\mu)^2 - 2]^{1/2}$. For $|\mu| < 2\sqrt{2}$ this is a focus: stable if $\mu < 0$ and unstable if $\mu > 0$. The decay of a trajectory to the stable focus at $(1, 0)$ is shown in Fig. 8.24(a). The dependence of the natural frequency $\omega_1(|\mu|)$ around the foci, stable or unstable, is shown as a function of the bifurcation parameter μ in the range $0 < \mu < 2\sqrt{2}$ in Fig. 8.24(b).

The undriven Duffing oscillator can be considered as exhibiting a dynamic Ginzburg-Landau transition as a function of the linear part of the odd driving term $ax - x^3$. We will typically operate the Duffing oscillator in the regime where the fixed point at

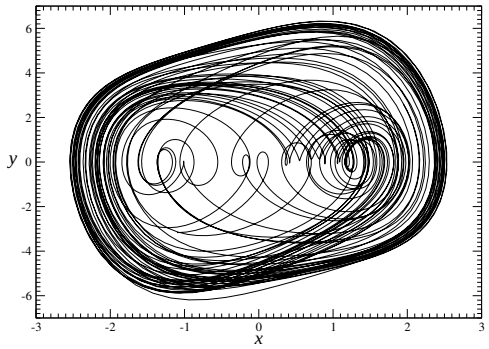

Fig. 8.21 Chaotic attractor solution to the van der Pol oscillator driven by a harmonic oscillator. Parameter values: $(\mu, \beta, n) = (0.48, 1, 3)$, $\delta = 1.8$, and $(u_0, v_0) = (5, 0)$.

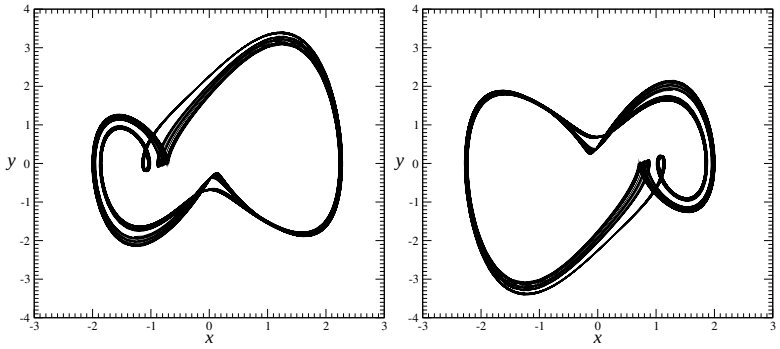

Fig. 8.22 Two chaotic attractors generated by the harmonically driven van der Pol equations are related by rotation symmetry. They differ by initial conditions of the van der Pol attractor $[(x_0, y_0) \rightarrow (-x_0, -y_0)]$ and the sign of the coupling term ρ. Parameter values: $(\mu, \beta, n) = (0.48, 1, 3)$, $\delta = 0.4917$ and $(u_0, v_0) = (3.0, 0.0)$.

the origin is unstable and the two symmetry-related fixed points at $x = \pm 1$ are stable foci ($-2\sqrt{2} < \mu < 0$).

8.6.1 Rössler Drive

We drive the Duffing oscillator with the output of the Rössler dynamical system in the same way that we drove the Duffing oscillator with the Rössler system. More specifically, the coupling is given by

$$\text{Driving System = Rössler} \quad \longrightarrow \quad \text{Driven System} \;=\; \text{Duffing}$$

$$\begin{aligned} \dot{u} &= -v - w \\ \dot{v} &= u + av \\ \dot{w} &= b + w(u - c) \end{aligned} \qquad\qquad \begin{aligned} \dot{x} &= y \\ \dot{y} &= \mu y + x - x^3 + \rho u \end{aligned} \tag{8.22}$$

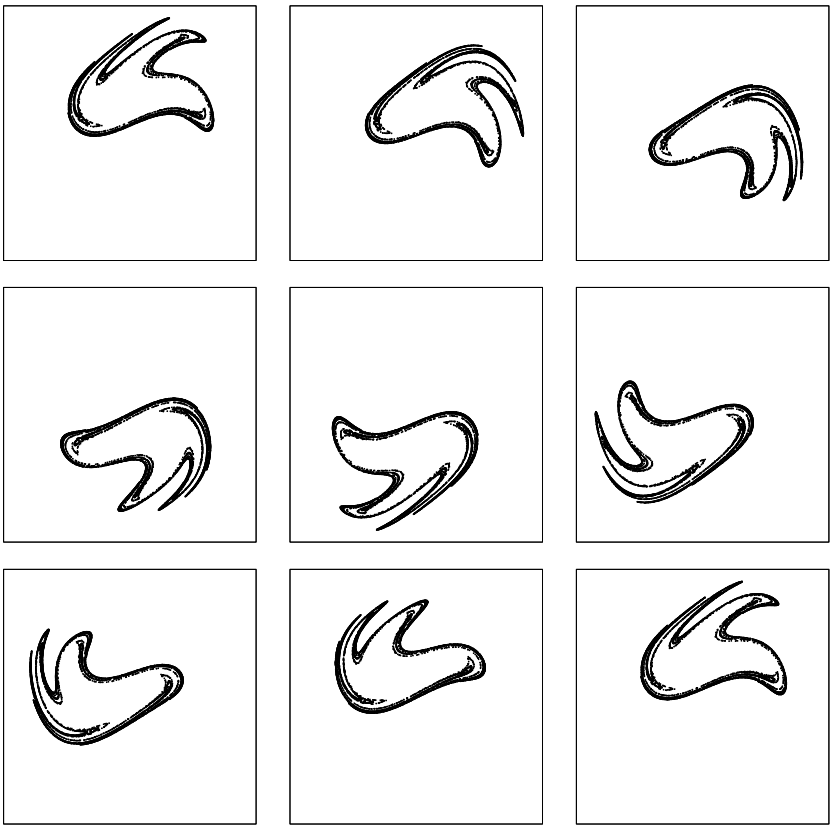

Fig. 8.23 Motion picture of the van der Pol oscillator driven by a harmonic oscillator. Eight equally spaced Poincaré sections are shown. Phase increases by $2\pi/8$ radians from left to right, top to bottom. Intersections π radians out of phase show rotation (inversion) symmetry. Parameter values: $(\mu, \beta, n) = (0.48, 1, 3)$, $\delta = 1.8$, and $(u_0, v_0) = (5, 0)$.

We have again used a simple linear drive in the equation describing the acceleration (second equation). The coupling parameter $\rho = 1$.

The Rössler equations were again integrated at control parameter values $(a, b, c) = (0.3, 2, 4)$ to generate a period-one orbit. The Rössler orbit was renormalized (in time) before being used to drive the Duffing oscillator. As the ratio of the driving frequency ω of the Rössler orbit to the fundamental frequency ω_1 of the Duffing oscillator varies, $\delta = \omega/\omega_1$, the Duffing oscillator undergoes a series of bifurcations. These are shown in Fig. 8.25.

The plots show that the driven system exhibits a simple limit cycle in a broad range of values around $\delta = 1,\ 2,\ 3$. Limit cycles are also obtained for subharmonic driving. Three of these are shown for $\delta = 1.0$ in Fig. 8.26(a), $\delta = 0.6$ in Fig. 8.26(b),

and for $\delta = 0.4$ in Fig. 8.26(c). In each case the limit cycle is asymmetric, and its symmetry-related partner is also shown.

As the driving system undegoes a series of bifurcations, so also does the driven system. In Fig. 8.27(a) we reproduce the bifurcation diagram for the Rössler attractor (cf. also Fig. 8.12(a)). As the control parameter a is scanned, the Duffing oscillator undergoes a series of bifurcations that is similar for all values of the frequency ratio

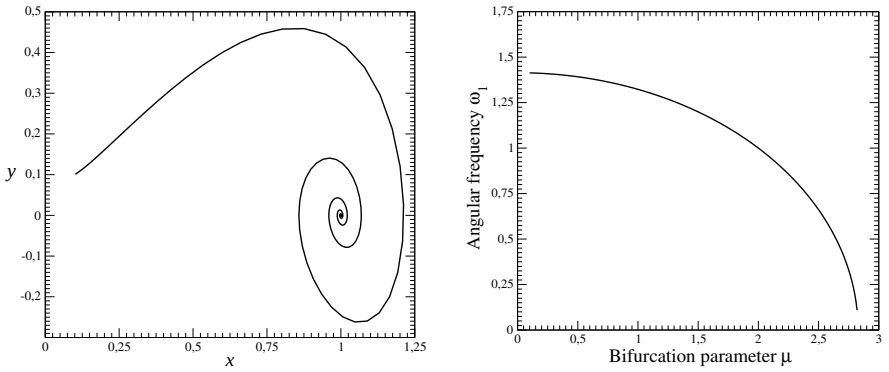

(a) x-y phase space (b) Natural frequency ω

Fig. 8.24 (a) Trajectory of decaying orbit in the x-y phase space of the undriven Duffing oscillator. (b) The natural frequency is $\omega = \sqrt{2 - (\mu/2)^2}$.

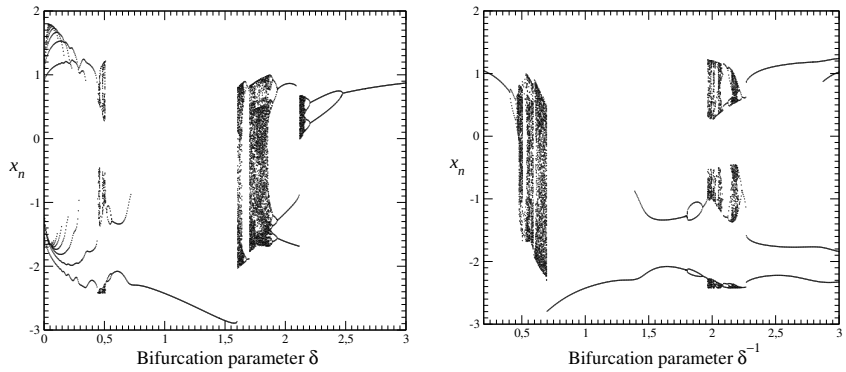

(a) Versus δ (b) Versus $1/\delta$

Fig. 8.25 The Duffing system is driven by a period-one orbit generated by the Rössler system. The bifurcation diagram shows the response of the Duffing system as a function of (a) the frequency ratio $\delta = \omega/\omega_1$ and (b) its inverse δ^{-1}. Other parameter values: $(a, b, c) = (0.3, 2, 4)$ and $\mu = 0.523$.

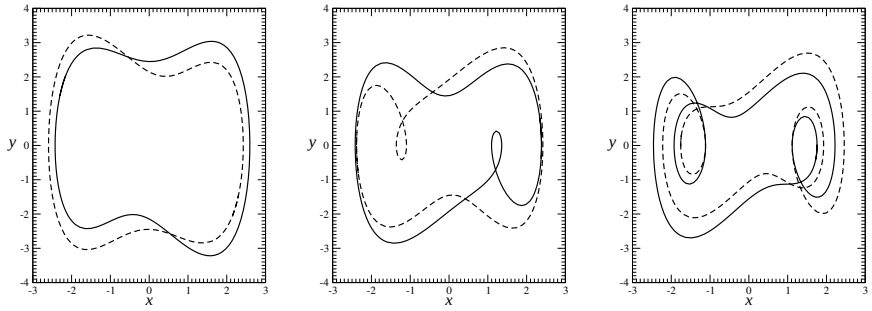

(a) Period-1 cycle: $\delta = 1$

(b) Period-2 cycle: $\delta = 0.6$

(c) Period-3 cycle: $\delta = 0.4$

Fig. 8.26 Limit cycles of the driven Duffing system for different values of δ. The symmetric partner of each limit cycle is shown. Other parameter values: $\mu = 0.523$, and $(a, b, c) = (0.3, 2, 4)$.

δ. The results are shown for $\delta = 1.0$ in Fig. 8.27(b), $\delta = 0.6$ in Fig. 8.27(c), and $\delta = 0.4$ in Fig. 8.27(d). It is clearly possible to make a correlation among the windows in each of these bifurcation diagrams.

Once again there is no symmetry in this coupled pair of dynamical systems. Nevertheless, once again it is possible to exhibit some symmetry. In Fig. 8.28 we show two strange attractors that are closely related: they are "rotation-symmetric." Both are obtained by running the Rössler system in a periodic region, with $(a, b, c) = (0.3, 2, 4)$ and coupling with a frequency ratio $\omega/\omega_1 = \delta = 1.61$. The two attractors are obtained by simultaneously changing their initial conditions and the sign of the coupling strength ρ. It is clear from this figure that the two attractors are related by a rotation through π radians about an axis through the origin perpendicular to the x-y plane.

8.6.2 Lorenz Drive

We couple the Lorenz driving system into the responding Duffing oscillator in the same way that we coupled the Lorenz drive into the van der Pol oscillator. The coupled equations are

$$\begin{array}{ccc} \text{Driving System} & \longrightarrow & \text{Driven System} \\ \text{= Lorenz} & & \text{= Duffing} \\ \dot{u} = -\sigma u + \sigma v & & \dot{x} = y \\ \dot{v} = Ru - v - uw & & \dot{y} = \mu y + x - x^3 + \rho \frac{\alpha}{\sqrt{b(R-1)}} u \\ \dot{w} = -bw + uv & & \end{array} \tag{8.23}$$

The response of the Duffing system is similar to that of the van der Pol oscillator. As the bifurcation parameter $\delta = \omega/\omega_1$ varies, a sequence of periodic windows

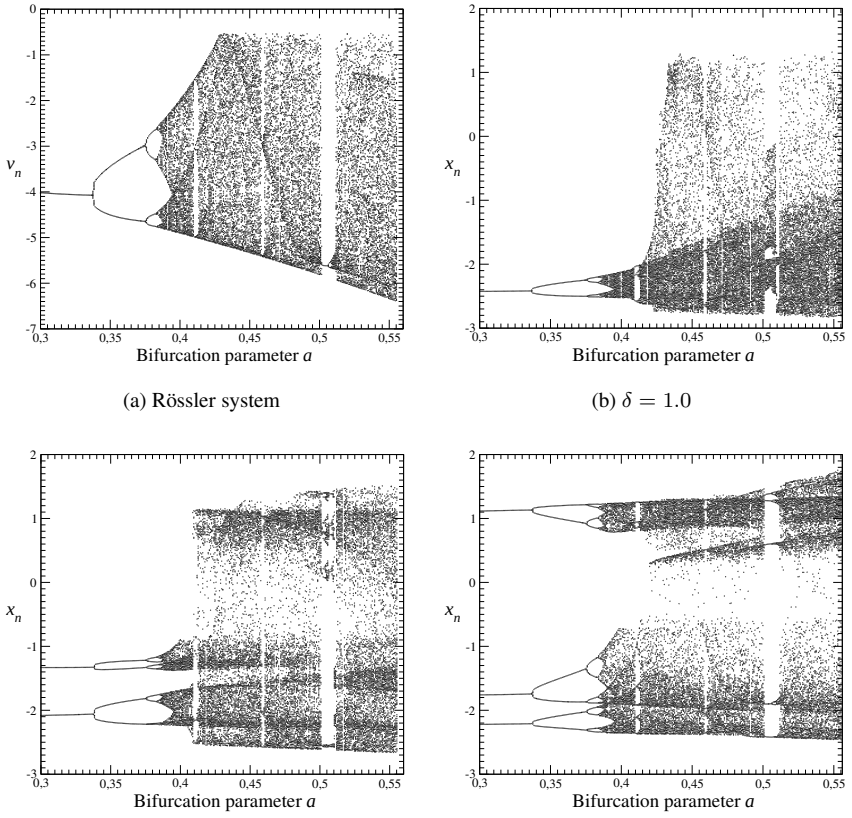

Fig. 8.27 Bifurcation diagram for the Rössler attractor for $(b, c) = (2, 4)$. Bifurcation diagrams for the responding Duffing oscillator for (b) $\delta = 1.0$, (c) $\delta = 0.6$, and (d) $\delta = 0.4$. Other parameter values: $\mu = 0.523$ and $(a, b, c) = (0.3, 2, 4)$.

alternates with chaotic behavior. Bifurcation diagrams for the Duffing oscillator driven by a periodic orbit of the Lorenz dynamical system are shown as a function of the bifurcation parameter δ in Fig. 8.29(a) and its inverse δ^{-1} in Fig. 8.29(b). The bifurcation diagram of Fig. 8.29(a) show broad regions around $\delta = 1.0$ with a period-one orbit, regions around $\delta = 1.5$ with a period-three orbit, around $\delta = 2.0$ with a period-two orbit, and above $\delta = 2.0$ with a period-one orbit. There are subharmonic entrainments as well. Near $\delta^{-1} = n$ there are periodic orbits of period n. Three of these are shown in Fig. 8.30. As before, the odd subharmonics are symmetric and the even subharmonics occur in symmetry-related pairs.

As the control parameter R of the Lorenz system is scanned, the responding Duffing oscillator undergoes a corresponding series of bifurcations. In Fig. 8.31(a) we show

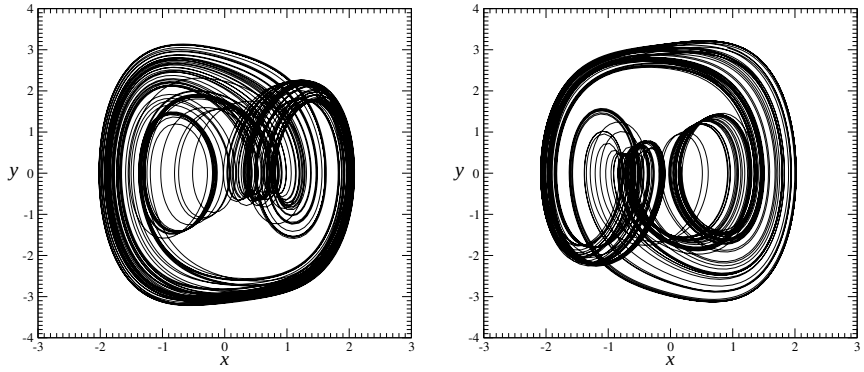

(a) $y_0 = 0.1$ and $\rho = +1$ (b) $y_0 = -0.1$ and $\rho = -1$

Fig. 8.28 Two chaotic attractors generated by the Lorenz-driven Duffing equations with $\delta = 1.61$ are related by rotation symmetry. They differ by initial conditions of the Duffing attractor $[(x_0, y_0) \rightarrow (-x_0, -y_0)]$ and the sign of the coupling term ρ. Parameter values: $\mu = 0.523$ and $(a, b, c) = (0.3, 2, 4)$.

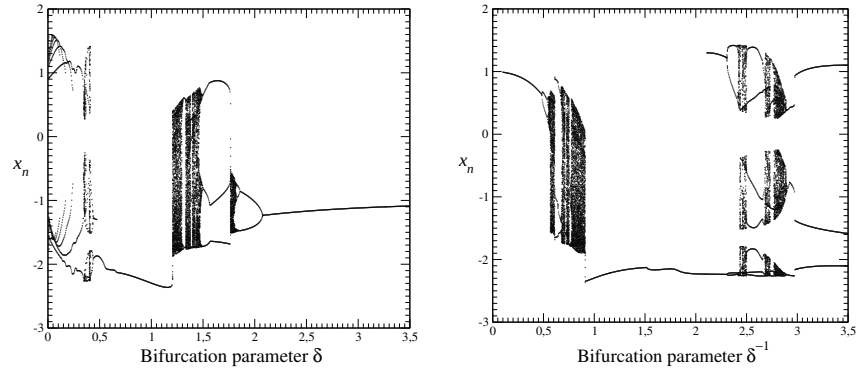

(a) versus δ (b) versus $1/\delta$

Fig. 8.29 The Duffing system is driven by a periodic orbit generated by the Lorenz system. The bifurcation diagram shows the response of the Duffing system as a function of the frequency ratio $\delta = \omega/\omega_1$. Other parameter values: $(R, \sigma, b) = (350, 10/8/3)$ and $\mu = 0.523$.

the bifurcation diagram for the Lorenz oscillator, and in Fig. 8.31(b)–(d) we show the bifurcation diagrams for the responding Duffing oscillator for frequency ratios $\delta = 1, 0.44$, and $1/3$. As the Lorenz attractor settles into a period-one limit cycle for $R > 340$, the response is entrained in orbits of periods one, two, and three, respectively.

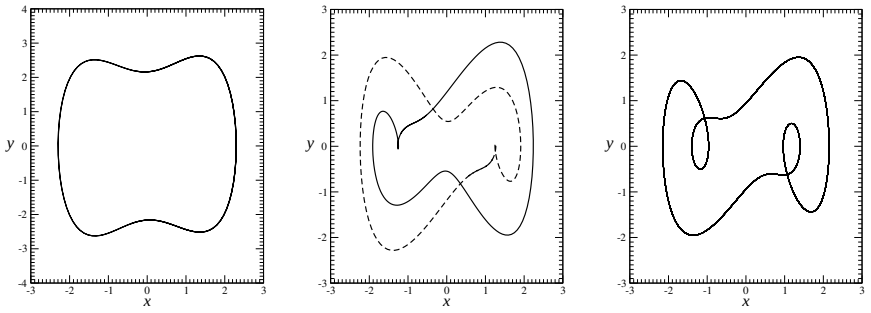

(a) $\delta = 1$ (b) $\delta = 0.44$ (c) $\delta = 1/3$

Fig. 8.30 Limit cycles of the Duffing system driven by a periodic orbit of the Lorenz system for (a) $\delta = 1$, (b) $\delta = 0.44$, (c) $\delta = 1/3$. The period-one and -three limit cycles are symmetric and the two symmetry-related period-two limit cycles are shown. Other parameter values: $\mu = 0.523$, and $(R, \sigma, b) = (350, 10, 8/3)$.

Once again it is possible to exhibit some symmetry. In Fig. 8.32 we show two strange attractors that are closely related: they are "rotation-symmetric." Both are obtained by running the Lorenz system in a periodic region, with $(R, \sigma, b) = (350, 10, 8/3)$ and coupling with a frequency ratio $\omega/\omega_1 = \delta = 1.77$. The two attractors are obtained by simultaneously changing their initial conditions and the sign of the coupling strength ρ. It is clear from this figure that the two attractors are related by a rotation through π radians about an axis through the origin perpendicular to the x-y plane.

8.6.3 Harmonic Drive

A harmonic drive is coupled into the Duffing oscillator in the usual way. The coupled system is explicitly

$$\begin{array}{ccc} \text{Driving System} = & \longrightarrow & \text{Driven System} = \\ \text{Harmonic Oscillator} & \longrightarrow & \text{Duffing Oscillator} \end{array}$$

$$\begin{array}{rclcrcl} \dot{u} &=& v & & \dot{x} &=& y \\ \dot{v} &=& -\omega^2 u & & \dot{y} &=& \mu y + x - x^3 + u \end{array} \tag{8.24}$$

The response of the Duffing oscillator depends on the ratio of the driving frequency to the natural frequency of the Duffing oscillator. The bifurcation diagram of the Duffing oscillatoris plotted as a function of the ratio $\delta = \omega/\omega_1$ in Fig. 8.33(a) and its inverse δ^{-1} in Fig. 8.33(b). As usual, broad periodic windows can be seen at sub- and super-harmonic integer values. Three limit cycles are shown explicitly in Fig. 8.34.

Since the harmonic drive is structurally unstable, the driving term can have arbitrary amplitude. If we fix the frequency ratio δ and vary the driving amplitude, the response of the Duffing oscillator will exhibit a series of bifurcations, just as the van der Pol oscillator does. In Fig. 8.35 we show this bifurcation diagram as a function of the initial condition of the driving linear oscillator. By choosing an initial condition in

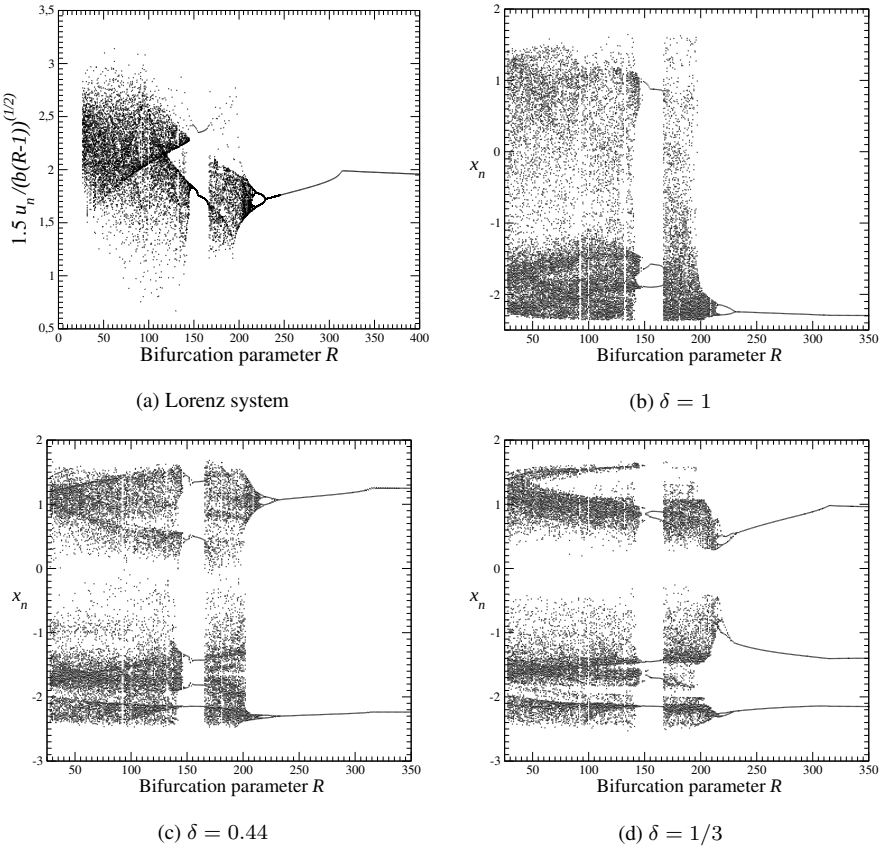

(a) Lorenz system

(b) $\delta = 1$

(c) $\delta = 0.44$

(d) $\delta = 1/3$

Fig. 8.31 (a) Bifurcation diagram for the Lorenz attractor for $(\sigma, b) = (10, 8/3)$. Bifurcation diagrams for the responding Duffing oscillator for (b) $\delta = 1.0$, (c) $\delta = 0.44$, and (d) $\delta = 1/3$. Other parameter values: $(R, \sigma, b) = (350, 10, 8/3)$ and $\mu = 0.523$.

the chaotic part of such a bifurcation diagram, we can construct a chaotic attractor. The one shown in Fig. 8.36 appears to be symmetric. Chaotic attractors generated in this way need not be symmetric: often they occur in symmetry-related pairs. The pair can be exhibited explicitly by the usual procedure of choosing symmetrically related initial conditions. Such a pair is shown in Fig. 8.37.

The periodically driven Duffing oscillator generates a low-dimensional strange attractor that exists in a phase space with the topology $D^2 \times S^1$, where D^2 is a disk. In such a phase space, Poincaré sections are planes of constant phase: $\omega t = \text{const} \mod 2\pi$. We can visualize this strange attractor by taking a series of freeze frames at equal angular intervals, as we did for the van der Pol attractor. This motion picture is shown in Fig. 8.38. This motion picture shows that the stretching and squeezing

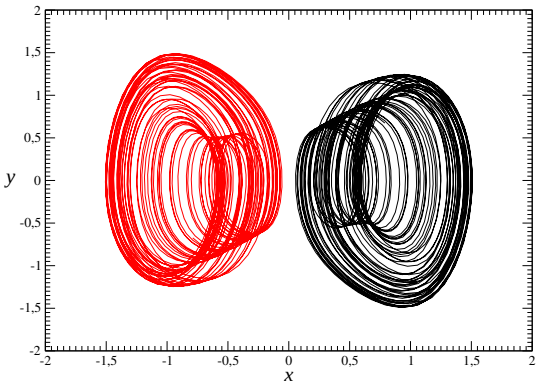

Fig. 8.32 Two chaotic attractors generated by the Lorenz-driven Duffing equations are related by rotation symmetry. They differ by initial conditions $[(x_0, y_0) \rightarrow (-x_0, -y_0)]$ and the sign of the coupling term ρ. Parameter values: $\mu = 0.523$, $(R, \sigma, b) = (350, 10, 8/3)$ and $\delta = 1.77$.

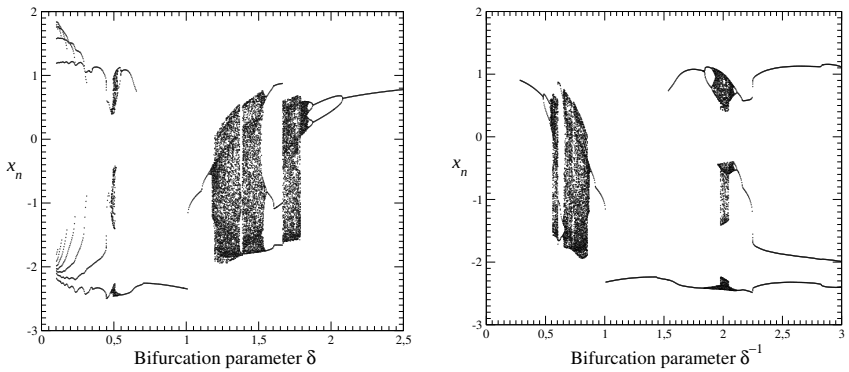

(a) Versus δ (b) Versus $1/\delta$

Fig. 8.33 The Duffing system is driven by a harmonic drive. The bifurcation diagram shows the response of the Duffing system as a function of the frequency ratio $\delta = \omega/\omega_1$. Other parameter values: $\mu = 0.523$. Initial conditions: $(x_0, y_0) = (0.1, 0.1)$ and $(u_0, v_0) = 2.0, 0.0)$.

occurs by stretching and rolling alternating parts of the surface separated by $\omega t = \pi$. The cross section in each cut has a fractal structure in the transverse direction and is smooth in the other direction.

8.7 THE TAKENS-BOGDANOV OSCILLATOR

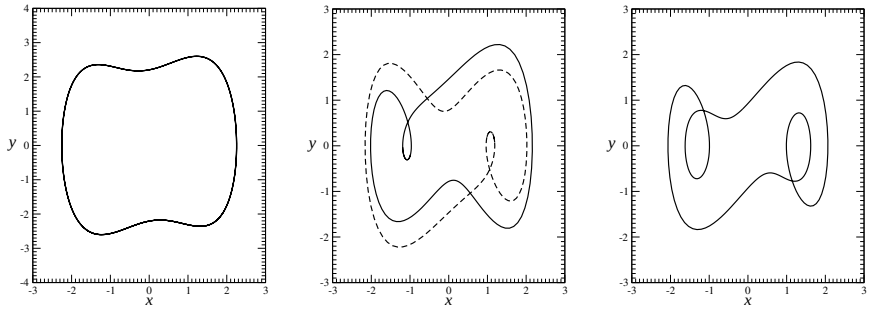

(a) $\delta = 1$ (b) $\delta = 1/2$ (c) $\delta = 1/3$

Fig. 8.34 Limit cycles of the Duffing system driven by a harmonic drive for (a) $\delta = 1$, (b) $\delta = 1/2$, (c) $\delta = 1/3$. Other parameter values: $\mu = 0.523$. Initial conditions: $(x_0, y_0) = (0.1, 0.1)$ and $(u_0, v_0) = 2.0, 0.0)$.

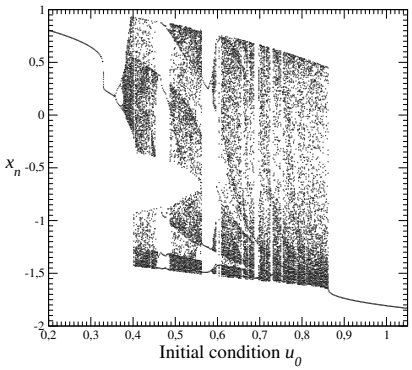

Fig. 8.35 Sensitivity to the initial condition $(u_0, 0)$ for the Duffing system driven by a harmonic oscillator. Parameter values $\mu = 0.523$ and $\delta = 0.7195$.

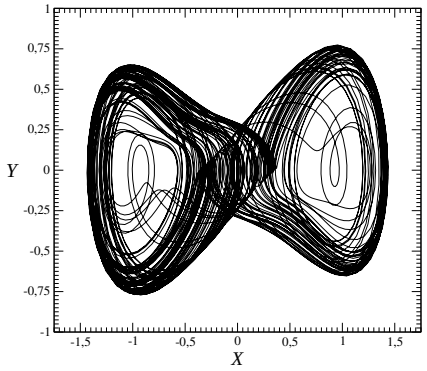

Fig. 8.36 Chaotic attractor solution to the Duffing oscillator driven by a harmonic oscillator. Parameter values: $\mu = 0.523$ and $\delta = 0.68$. Initial conditions: $(x_0, y_0), (u_0, v_0) = (0.1, 0.1), (0.4, 0)$.

A degenerate saddle with inversion symmetry has normal form

$$\begin{aligned} \dot{x} &= y \\ \dot{y} &= x^2 y - x^3 \end{aligned}$$

A universal unfolding of the flow in the neighborhood of this degenerate saddle has the Takens-Bogdanov normal form

$$\begin{aligned} \dot{x} &= y \\ \dot{y} &= \mu x + \nu y + x^2 y - x^3 \end{aligned} \tag{8.25}$$

This unfolding preserves the inversion symmetry of the original degenerate sadddle.

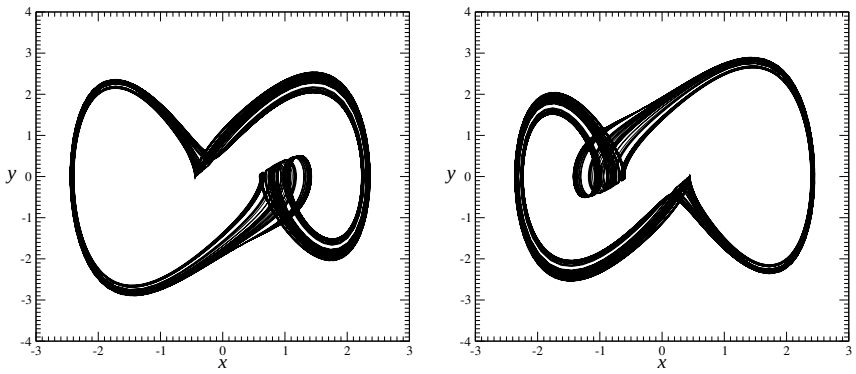

Fig. 8.37 Pair of chaotic attractor solutions to the Duffing system driven by a harmonic drive. Parameter values: $\mu = 0.523$ and $\delta = 0.512$. Initial conditions: $(x_0, y_0) = (0.1, 0.1)$ and $(u_0, v_0) = (2.0, 0.0)$.

The nonlinear oscillator represented by equations (8.25) has a fixed point at the origin and two symmetric fixed points at $(x, y) = (\pm\sqrt{\mu}, 0)$ that are real if $\mu > 0$. The fixed point at the origin has eigenvalues $\lambda_\pm = \frac{1}{2}\nu \pm \sqrt{\left(\frac{1}{2}\nu\right)^2 + \mu}$. This fixed point is a saddle if $\mu > 0$. The other two fixed points have eigenvalues $\lambda_\pm = \frac{1}{2}(\mu + \nu) \pm \sqrt{\left(\frac{1}{2}(\mu + \nu)\right)^2 - 2\mu}$. These are foci for $8\mu > (\mu + \nu)^2$, stable or unstable depending on the sign of $\mu + \nu$. In order to create interesting dynamics, we will take $\mu + \nu$ positive, so that the two symmetric fixed points are unstable, and small, so that $(\mu + \nu)^2 < 8\mu$ and these unstable fixed points are unstable foci. The angular frequency of these unstable foci are plotted as a function of the unfolding parameter μ in Fig. 8.39

8.7.1 Rössler Drive

We drive the Takens-Bogdanov oscillator with a periodic orbit generated by the Rössler dynamical system, as was done previously for the van der Pol and the Duffing oscillators. The coupling is given explicitly by the equations

$$\begin{array}{ccc} \text{Driving System} & \longrightarrow & \text{Driven System} \\ \text{= Rössler} & & \text{= Takens-Bogdanov} \end{array}$$

$$\begin{aligned} \dot{u} &= -v - w \\ \dot{v} &= u + av \\ \dot{w} &= b + w(u - c) \end{aligned} \qquad \begin{aligned} \dot{x} &= y \\ \dot{y} &= \mu x + \nu y + x^2(y - x) + \rho u \end{aligned} \tag{8.26}$$

As the ratio of the driving frequency ω of the Rössler periodic orbit to the natural frequency ω_1 of the Takens-Bogdanov oscillator varies, a series of bifurcations takes place. The bifurcation diagram is shown as a function of the frequency ratio $\delta = \omega/\omega_1$ in Fig. 8.40(a) and as a function of the inverse ratio δ^{-1} in Fig. 8.40(b). These

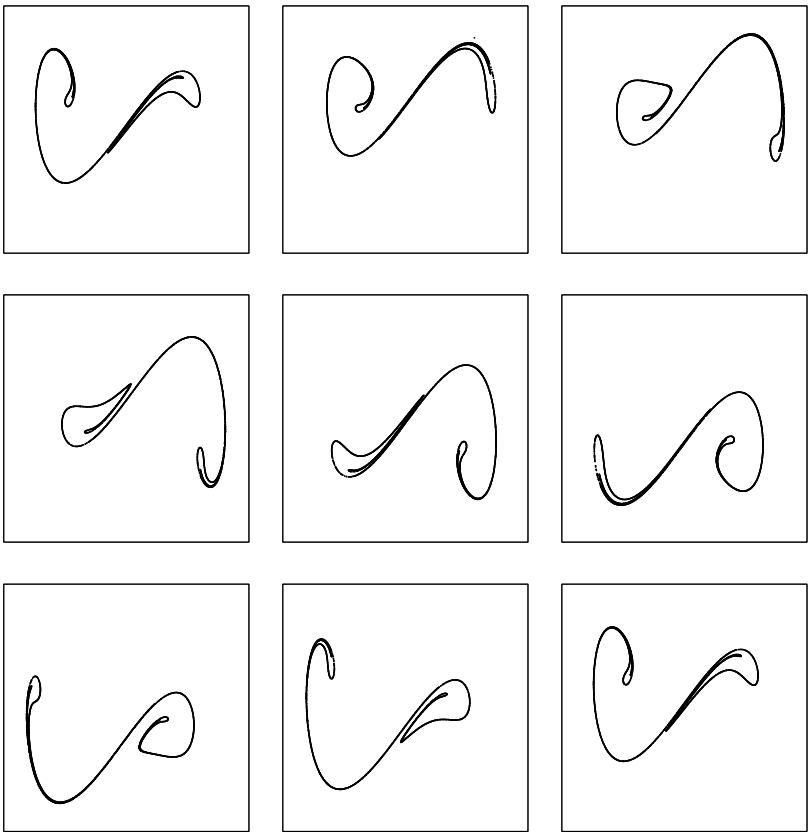

Fig. 8.38 Motion picture of the Duffing oscillator driven by a harmonic oscillator. Eight equally spaced Poincaré sections are shown. Phase increases by $2\pi/8$ radians from left to right, top to bottom. Intersections π radians out of phase show rotation (inversion) symmetry. Parameter values: $\mu = 0.523$ and $\delta = 0.68$. Initial conditions: $(x_0, y_0) = (0.1, 0.1)$ and $(u_0, v_0) = (0.4, 0.0)$.

bifurcation diagrams show the existence of entrained orbits of periods one, two, and three for $\delta = 1/1, 1/2$, and $1/3$. These orbits are shown in Fig. 8.41(a), (b), and (c). The orbits of period p occur in symmetric pairs. Both can be seen when the initial conditions are properly chosen.

In Fig. 8.42(a) we present a bifurcation diagram for the Rössler attractor, and in Figs. 8.42(b), (c), and (d) we show bifurcation diagrams for the Takens-Bogdanov oscillator that is driven by the $u(t)$ variable of the Rössler dynamical system. The bifurcation diagrams are shown for frequency ratios $\delta = 1.0, 0.5$, and 0.3. These show clearly the entrainment of period-one, -two, and -three orbits when the Rössler system exhibits a simple limit cycle. Period doubling behavior, chaotic behavior, and periodic windows are evident in these bifurcation diagrams.

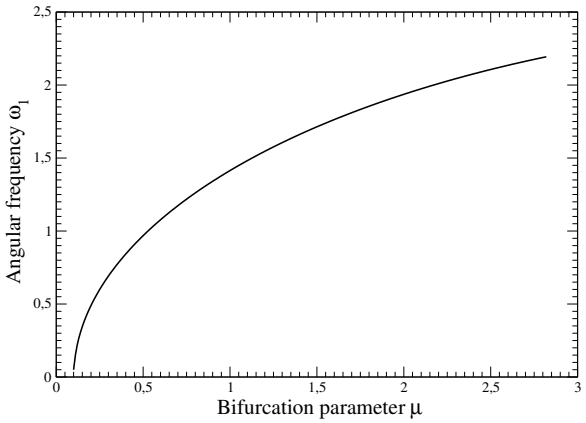

Fig. 8.39 Angular frequency around the unstable foci of the Takens-Bogdanov oscillator as a function of the parameter μ. Other parameter values: $\nu = -1$.

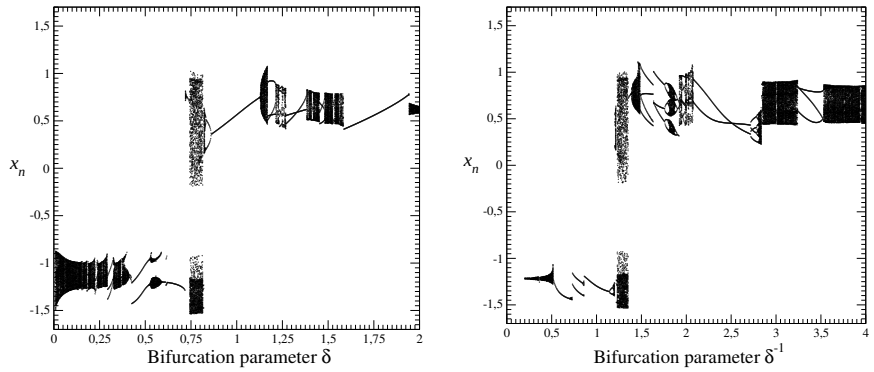

(a) Versus δ (b) Versus $1/\delta$

Fig. 8.40 Bifurcation diagrams of the Takens-Bogdanov system driven by a period-1 limit cycle of the Rössler system. Other parameter values: $\mu = 1.0434$, $\nu = -1$, and $\rho = 0.06$. Initial conditions: $(x_0, y_0, u_0, v_0, w_0) = -(\sqrt{\mu} + 0.01, -0.01, 0.4, 0.4, 0.4)$.

Strange attractors alternate with periodic windows in the periodically driven Takens-Bogdanov oscillator. In Fig. 8.43 we show one such strange attractor. It is projected onto the x-y plane in the phase space $D^2 \times S^1$, where D^2 is a disk in the x-y plane. The projection appears to possess inversion symmetry. This is in fact an indication of symmetry of the equations of motion under the transformation $(x, y, t) \to (-x, -y, t + \frac{1}{2}T)$.

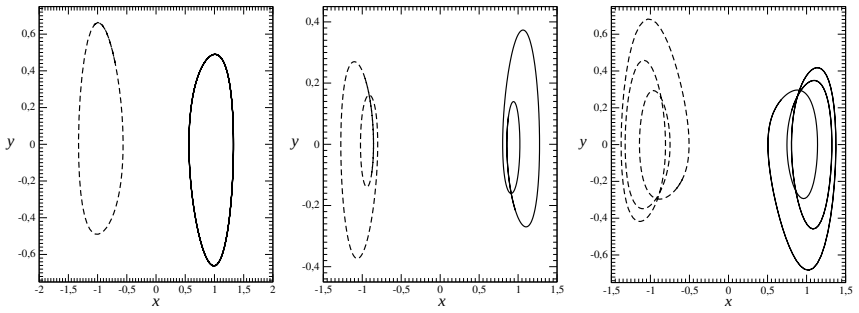

(a) Period-1 limit cycles: $\delta = 1$

(b) Period-2 limit cycles: $\delta = 1/2$

(c) Period-3 limit cycles: $\delta = 1/3$

Fig. 8.41 Limit cycles of the Takens-Bogdanov system driven by a limit cycle of the Rössler system for (a) $\delta = 1$, (b) $\delta = 1/2$, (c) $\delta = 1/3$. Other parameter values: $\mu = 1.0434$, $\nu = -1$, and $\rho = 0.06$. Initial conditions are $(x_0, y_0, u_0, v_0, w_0) = -(\sqrt{\mu} + 0.01, -0.01, 0.4, 0.4, 0.4)$ and the negatives of these values.

8.7.2 Lorenz Drive

Next, we use the Lorenz system to drive the Takens-Bogdanov oscillator. The coupled equations are

$$\begin{array}{ccc} \text{Driving System} & \longrightarrow & \text{Driven System} \\ \text{= Lorenz} & & \text{= Takens-Bogdanov} \\ \dot{u} = \ -\sigma u + \sigma v & & \dot{x} = \ y \\ \dot{v} = \ Ru - v - uw & & \dot{y} = \ \mu x + \nu y + x^2(y - x) + \rho \frac{\alpha}{\sqrt{b(R-1)}} u \\ \dot{w} = \ -bw + uv & & \end{array} \tag{8.27}$$

The driving term is treated in the same way as for the van der Pol and the Duffing oscillators, and for the same reasons.

As with the first two nonlinear oscillators, we drive the Takens-Bogdanov oscillator with a periodic orbit generated by the Lorenz dynamical system. This is the stable orbit that exists at $R = 350.0$. Once again we plot a bifurcation diagram of the responding nonlinear oscillator against the ratio, $\delta = \omega/\omega_1$, of the driving frequency to the natural frequency of the Takens-Bogdanov oscillator. However, with this oscillator there are coexisting stable invariant sets (strange attractors and limit cycles). Rather than plotting the response against both δ and δ^{-1}, we show the existence of multistable behavior by scanning δ in both the ascending and descending directions. These are shown in Fig. 8.44. The scan in the direction of increasing δ shows stable orbits of period p for $p = 1, 2, 3, 4$ and of periods 3 and 5 at $\delta = 3/2$ and $5/2$. For δ decreasing

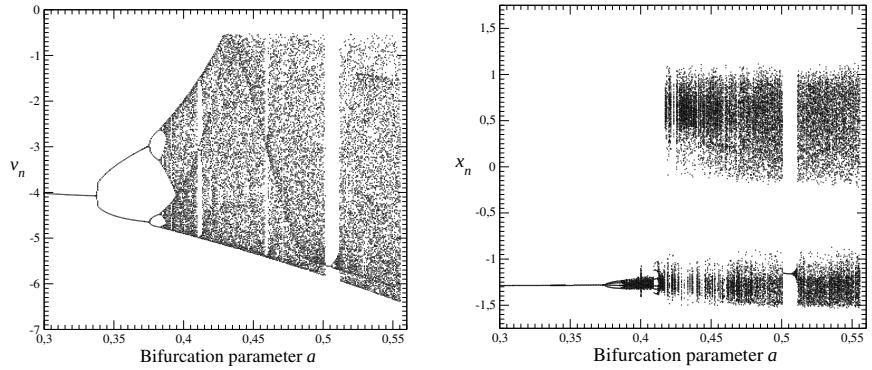

(a) Rössler system (b) $\delta = 1.0$

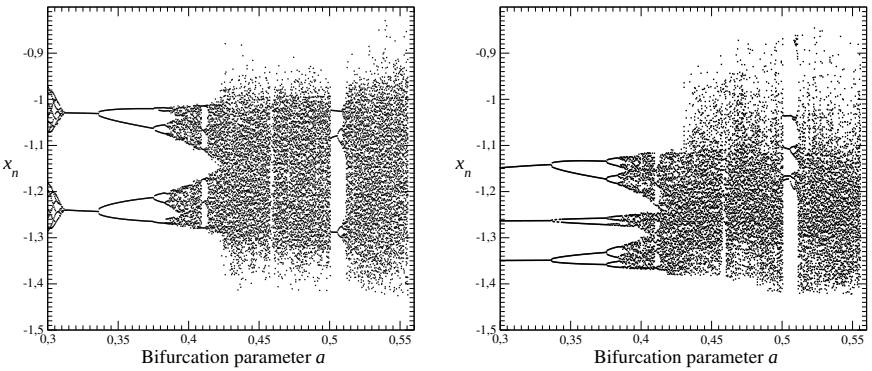

(c) $\delta = 0.5$ (d) $\delta = 0.3$

Fig. 8.42 Bifurcation diagram for the Rössler attractor for $(b, c) = (2, 4)$. Bifurcation diagrams for the responding Takens-Bogdanov oscillator for (b) $\delta = 1.0$, (c) $\delta = 0.5$ and (d) $\delta = 0.3$. Other parameter values: $\mu = 1.0434$, $\nu = -1$, and $\rho = 0.05$. Initial conditions: $(x_0, y_0, u_0, v_0) = -(\sqrt{\mu} + 0.01, -0.01, 0.4, 0.4, 0.4)$.

there are stable period-one limit cycles at $\delta = 2$ and $\delta = 1$ and a stable period-two limit cycle at $\delta = 3/2$.

Three of the low period limit cycles are shown in Fig. 8.45. These occur in disjoint pairs. They are not symmetric but are symmetry-related. The three limit cycles plotted here are for all practical purposes identical to the limit cycles obtained by driving the Takens-Bogdanov oscillator with a periodic orbit from the Rössler system (cf. Fig. 8.41).

Fig. 8.46(a) shows the standard bifurcation diagram for the Lorenz dynamical system, while Figs. 8.46(b), (c), and (d) show the bifurcation diagram for the responding Takens-Bogdanov oscillator. As a function of decreasing R, a bifurcation occurs in

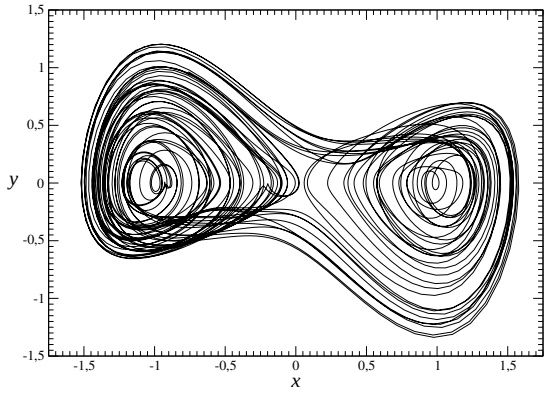

Fig. 8.43 Chaotic attractor generated by the Rössler-driven Takens-Bogdanov equations with $\delta = 0.78$. Other parameter values: $\mu = 1.0434$, $\nu = -1$, and $\rho = 0.05$. Initial conditions: $(x_0, y_0, u_0, v_0) = -(\sqrt{\mu} + 0.01, -0.01, 0.4, 0.4, 0.4)$.

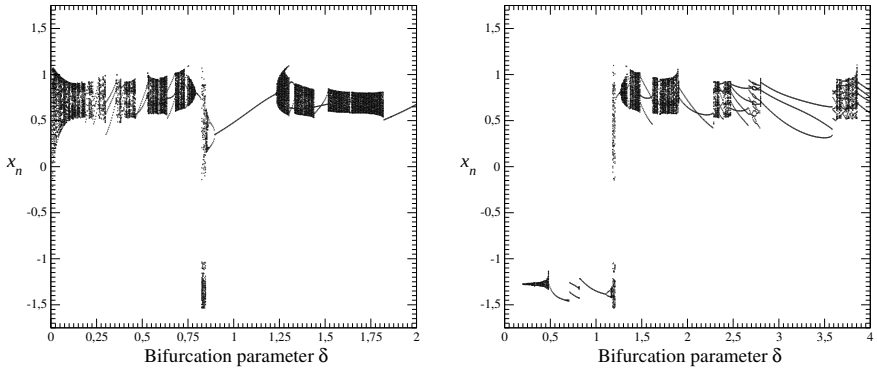

(a) Decreasing δ (b) Increasing δ

Fig. 8.44 Takens-Bogdanov system driven by the Lorenz system. Bifurcation diagram versus parameter δ. Other parameter values: $\mu = 1.0434$, $\nu = -1$, $\sigma = 10$, $b = 8/3$, and $R = 350$. Initial conditions as $(x_0, y_0, u_0, v_0, w_0) = (-\sqrt{\mu} + 0.01, -0.01, 0.4, 0.4, 0.4)$.

the Lorenz system at $R \simeq 315$. This bifurcation is not a period-doubling bifurcation, but rather a symmetry-breaking bifurcation. A symmetric limit cycle for $R > 315$ bifurcates to a symmetry-related pair of asymmetric limit cycles of approximately the same period as R decreases below the bifurcation value. It is for this reason that there appears to be no response in the entrained period-one orbit at this parameter value in Fig. 8.46(b) for $\delta = 1$, and only limited responses in Figs. 8.46(c) and (d) for $\delta = 0.44$, and $\delta = 1/3$. On the other hand, the period-doubling cascade into chaos ($R \simeq 230$) exhibited by either (in fact both) of the asymmetric orbits is clearly

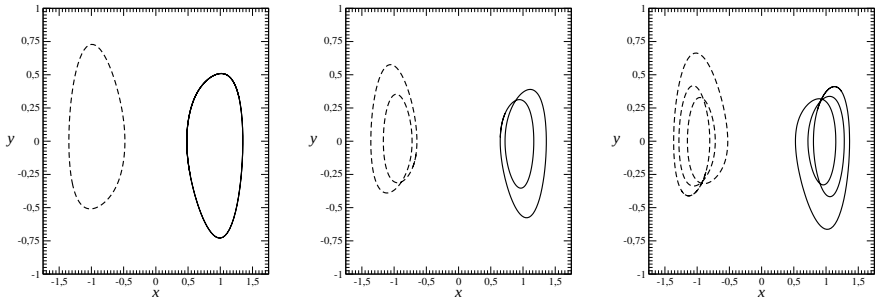

(a) $\delta = 1$ (b) $\delta = 1/2$ (c) $\delta = 1/3$

Fig. 8.45 Limit cycles of the Takens-Bogdanov system driven by a symmetric limit cycle of the Lorenz system for (a) $\delta = 1$, (b) $\delta = 1/2$, (c) $\delta = 1/3$. Other parameter values: $\mu = 1.0434$, $\nu = -1$, $\sigma = 10$, $b = 8/3$, $R = 350$, and $\rho = 0.0041$.

reflected in the bifurcation diagrams of the driven nonlinear oscillator for each of the three values of the frequency ratio.

Fig. 8.47 shows two chaotic attractors obtained from the driven Takens-Bogdanov oscillator. The ratio of the driving frequencies is one. The two chaotic attractors are symmetry-related. Both are based on "period-one" orbits. These are the two orbits that bifurcate from the symmetric period-one orbit as R decreases below $R \simeq 315$. The period-doubling bifurcation of each tends for "fatten up" the region they occupy in phase space, as shown in this figure.

8.7.3 Harmonic Drive

When the Takens-Bogdanov oscillator is driven by a harmonic oscillator, the driven equations can be taken in the form shown.

$$\begin{array}{ccc} \text{Driving System} & \longrightarrow & \text{Driven System} \\ \text{= Harmonic Oscillator} & & \text{= Takens-Bogdanov} \\ \dot{u} = v & & \dot{x} = y \\ \dot{v} = -\omega^2 u & & \dot{y} = \mu x + \nu y + x^2(y - x) + \rho u \end{array} \tag{8.28}$$

The bifurcation diagram of the Takens-Bogdanov oscillator as a function of the ratio $\delta = \omega/\omega_1$ ($\omega =$ driving frequency of harmonic oscillator, $\omega_1 =$ natural frequency of Takens-Bogdanov oscillator) is shown in Fig. 8.48(a) and as a function of δ^{-1} in Fig. 8.48(b). Both diagrams show the usual alternation between periodic and chaotic behavior. However, Fig. 8.48(b) shows clearly entrained period-p limit cycles for $\delta^{-1} = p = 1, 2, 3, 4$. A period-two subharmonic is clearly apparent in Fig. 8.48(a) for $\delta \simeq 1/2$.

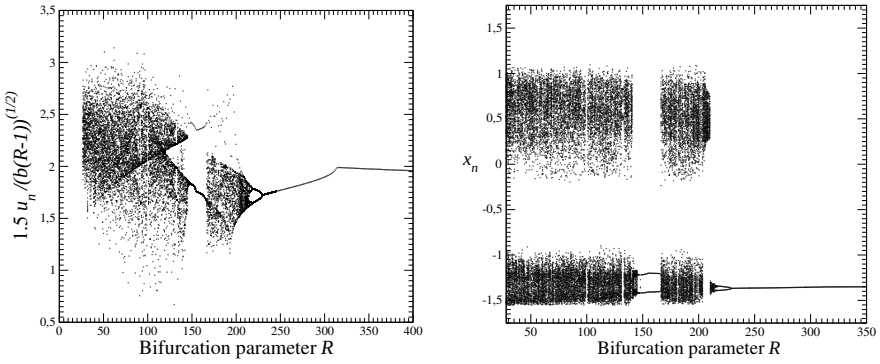

(a) Lorenz system (b) $\delta = 1$

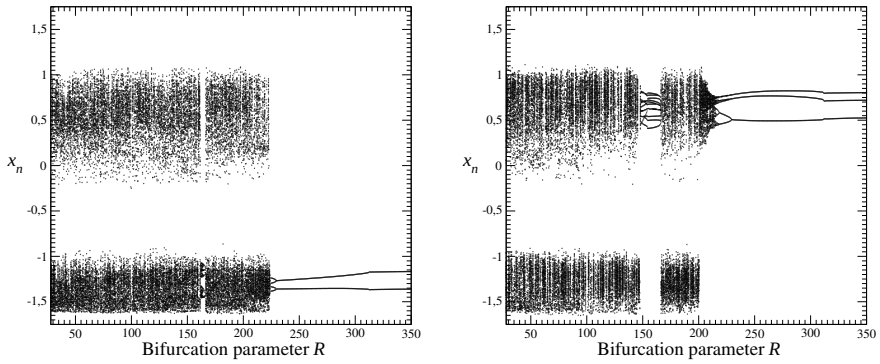

(c) $\delta = 0.44$ (d) $\delta = 1/3$

Fig. 8.46 (a) Bifurcation diagram for the Lorenz attractor for $(\sigma, b) = (10, 8/3)$. Bifurcation diagrams for the responding Takens-Bogdanov oscillator for (b) $\delta = 1.0$, (c) $\delta = 0.44$, and (d) $\delta = 1/3$. Other parameter values: $\mu = 1.0434$ and $\nu = -1$.

The limit cycles of periods $p = 1, 2, 3$ are shown in Fig. 8.49 for $\delta = 1/p$. As in the previous two cases, they are symmetry-related and reflect the symmetry of the driving equations under $(x, y, t) \to (-x, -y, t + \frac{1}{2}T)$.

The simple harmonic oscillator is structurally unstable. This is reflected in the response of the driven Takens-Bogdanov oscillator to changes in the amplitude of the driving term. A bifurcation diagram showing the response of this oscillator to changes in the amplitude of the harmonic oscillator drive is presented in Fig. 8.50. This diagram, like similar diagrams for the other nonlinear oscillators that are harmonically driven, shows an alternation between periodic and chaotic behavior.

Strange attractors that are generated by the harmonically driven Takens-Bogdanov oscillator exist as either asymmetric but symmetry-related pairs or as symmetric attractors. A symmetric attractor is shown for $\delta = 0.66$ in Fig. 8.51 and a symmetry-

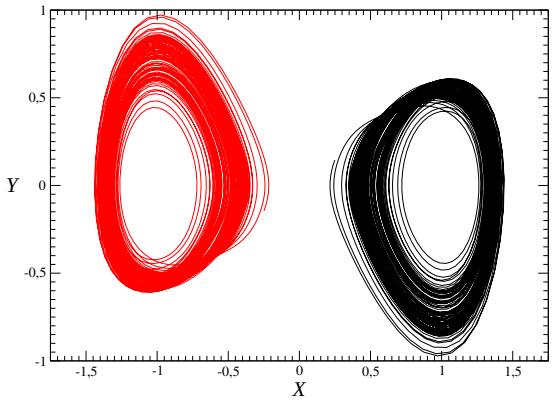

Fig. 8.47 Two chaotic attractors generated by the Lorenz-driven Takens-Bogdanov equations with $\delta = 1.0$. They differ by their initial conditions which are symmetry related. Other parameter values: $\mu = 1.0434$, $\nu = -1$, $\sigma = 10$, $b = 8/3$, $R = 210$, and $\rho = 0.0041$.

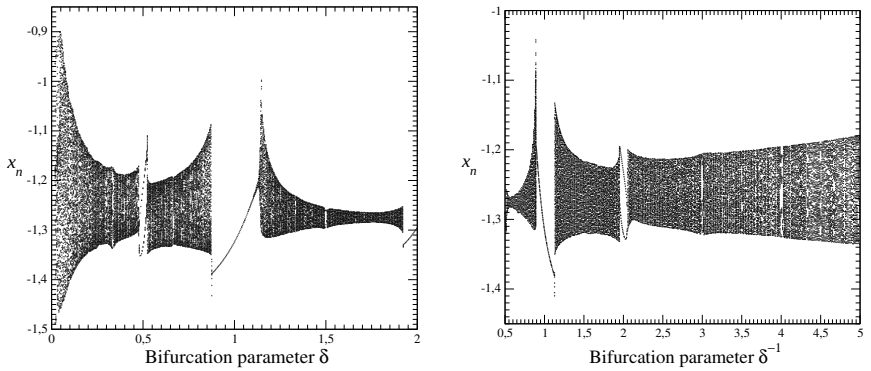

(a) Versus δ (b) Versus $1/\delta$

Fig. 8.48 Takens-Bogdanov system driven by an harmonic oscillator. Bifurcation diagram versus parameter δ (a) and versus $1/\delta$ (b). Other parameter values: $\mu = 1.0434$, $\nu = -1$, and $\rho = 0.4$. Initial conditions as $(x_0, y_0, u_0, v_0) = (-\sqrt{\mu} + 0.01, -0.01, 1, 0)$.

related pair, obtained by using symmetry-related initial conditions, is shown in Fig. 8.52.

Finally, Fig. 8.53 is a "motion picture" of the harmonically driven Takens-Bogdanov oscillator on an equally spaced sequence of Poincaré sections distributed around the solid torus $D^2 \times S^1$ that contains this strange attractor. This motion picture shares the same properties as do the motion pictures for the harmonically driven van der Pol and Duffing oscillators. Sections separated by half a period show the usual inversion symmetry: $(X, Y, t) \to (-X, -Y, t + \frac{1}{2}T)$.

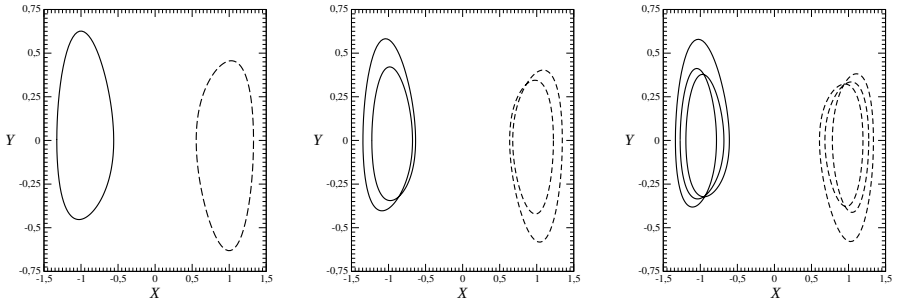

(a) $\delta = 1$ (b) $\delta = 1/2$ (c) $\delta = 1/3$

Fig. 8.49 Three limit cycles for the harmonically driven Takens-Bogdanov oscillator for different values of δ. (a) $\delta = 1$, (b) $\delta = 1/2$, (c) $\delta = 1/3$. Other parameter values: $\mu = 1.0434$, $\nu = -1$, and $\rho = 0.4$. Initial conditions as $(x_0, y_0, u_0, v_0) = (-\sqrt{\mu} + 0.01, -0.01, 1, 0)$.

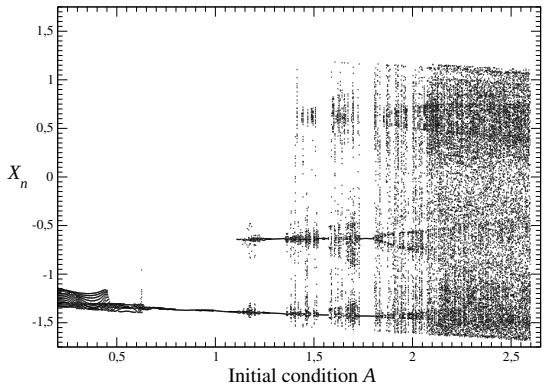

Fig. 8.50 Sensitivity to initial conditions $(u_0, v_0) = (A, 0)$ of the Takens-Bogdanov oscillator driven by a harmonic oscillator. Parameter values: $\mu = 1.0434$, $\nu = -1$, $\delta = 1$, and $\rho = 0.4$. Initial conditions as $(x_0, y_0, u_0, v_0) = (-\sqrt{\mu} + 0.01, -0.01, 1, 0)$.

8.8 MODDING OUT THE SYMMETRY

The motion pictures for the harmonically driven van der Pol, Duffing, and Takens-Bogdanov oscillators presented in Figs. 8.23, 8.38, and 8.53 show clearly that all three exhibit a two-fold symmetry, which is explicitly the invariance in $D^2 \times S^1$ of the driven system under the transformation $(X, Y, t) \rightarrow (-X, -Y, t + \frac{1}{2}T)$. The original dynamical system is an autonomous dynamical system in four variables, (X, Y) and (u, v), and the symmetry is an inversion symmetry in all four variables $(X, Y; u, v) \rightarrow (-X, -Y; -u, -v)$.

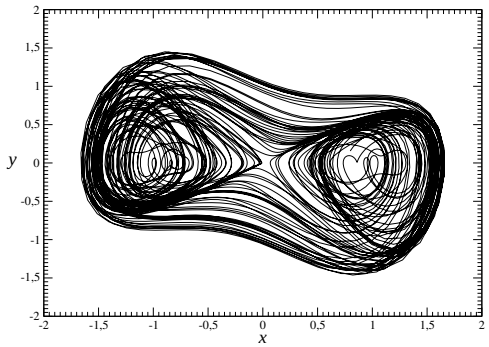

Fig. 8.51 Symmetric chaotic attractor solution to the Bogdanov-Takens oscillator driven by a harmonic oscillator. Parameter values: $(\mu, \nu, \rho) = (1.0434, -1, 1)$, $\delta = 0.66$, and $(u_0, v_0) = (0.45, 0)$.

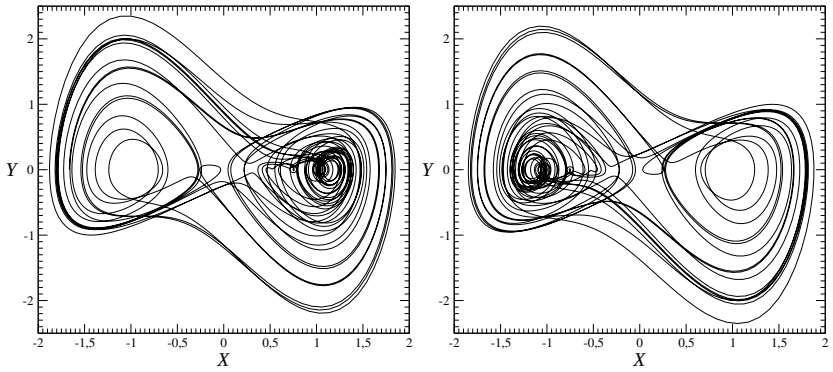

Fig. 8.52 Two chaotic attractors generated by the harmonically driven Takens-Bogdanov equations are related by rotation symmetry. They differ by initial conditions of the Takens-Bogdanov attractor. Parameter values: $\mu = 1.0434$, $\nu = -1$, $\rho = 0.4$, and $\delta = 10$.

We can mod out the symmetry by introducing 10 bilinear combinations of these four variables, in much the same way that we mod out a two-fold inversion symmetry in three variables (X, Y, Z) by introducing the six bilinear combinations X^2, Y^2, Z^2, XY, YZ, ZX (cf. Section 3.2). It is convenient to introduce some bookkeeping devices to keep the following computations in hand. To this end we introduce 2×2 matrix $\mathcal{X}$ for the nonlinear oscillator variables (X, Y)

$$\mathcal{X} = \begin{bmatrix} X & Y \\ -Y & X \end{bmatrix} = I_2 X + \sigma Y \quad \text{where} \quad \sigma = \begin{bmatrix} 0 & 1 \\ -1 & 0 \end{bmatrix} \tag{8.29}$$

and a similar matrix $\mathcal{U} = I_2 u + \sigma v$ for the harmonic oscillator variables (u, v). The 2×2 matrix σ $(= i\sigma_y)$ satisfies $\sigma^2 = -I_2$ and it commutes with I_2.

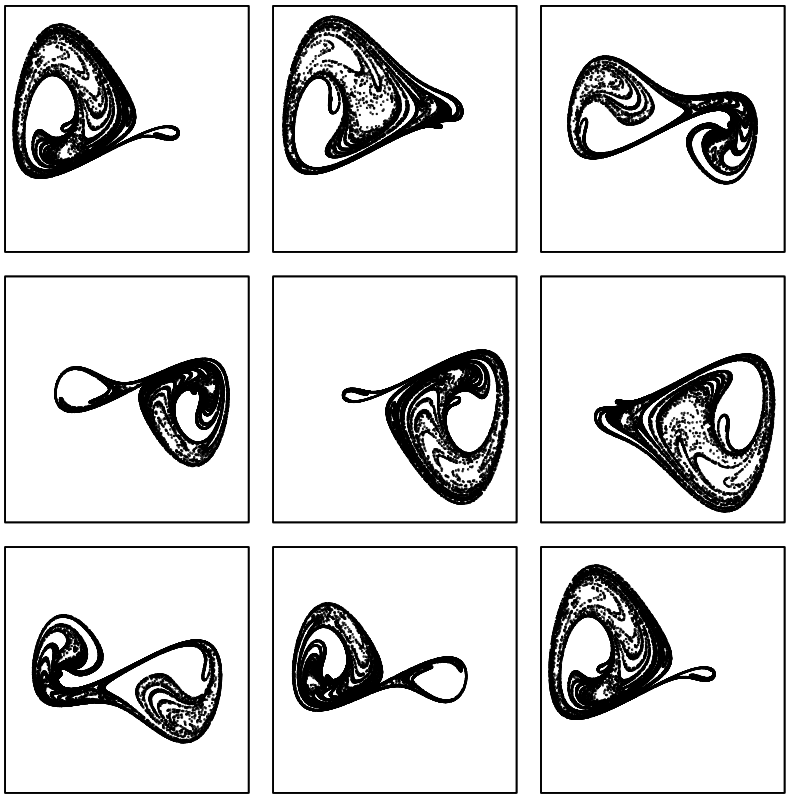

Fig. 8.53 Motion picture of the Bogdanov-Takens oscillator driven by a harmonic oscillator. Eight equally spaced Poincaré sections are shown. Phase increases by $2\pi/8$ radians from left to right, top to bottom. Sections separated by π radians show a rotation (inversion) symmetry. Parameter values: $(\mu, \nu, \rho) = (1.0434, -1, 0.4)$, $\delta = 10$, and $(X_0, Y_0, u_0, v_0) = (\sqrt{\mu} - 0.01, 0.01, -1, 0)$.

The square of $\mathcal{X}$ and the product of $\mathcal{X}$ with its adjoint provide the three bilinear products that can be constructed from these two variables, and similarly for $\mathcal{U}$:

$$\begin{array}{rclcrcl} \mathcal{X}^2 &=& I_2(X^2 - Y^2) + \sigma(2XY) & & \mathcal{X}\mathcal{X}^t &=& I_2(X^2 + Y^2) \\ \mathcal{U}^2 &=& I_2(u^2 - v^2) + \sigma(2uv) & & \mathcal{U}\mathcal{U}^t &=& I_2(u^2 + v^2) \end{array} \tag{8.30}$$

The four remaining bilinear combinations of these four variables, each involving one coordinate from the nonlinear oscillator and the other from the harmonic drive, can be obtained from products of $\mathcal{X}$ or $\mathcal{X}^t$ with $\mathcal{U}$ or $\mathcal{U}^t$. They are

$$\begin{array}{rcl} \mathcal{X}\mathcal{U} = \mathcal{U}\mathcal{X} &=& I_2(Xu - Yv) + \sigma(Xv + Yu) \\ \mathcal{X}\mathcal{U}^t = \mathcal{U}\mathcal{X}^t &=& I_2(Xu + Yv) + \sigma(Xv - Yu) \end{array} \tag{8.31}$$

Either of the two pairs of variables can be used to mod out the symmetry of the harmonically driven nonlinear oscillators. Each pair defines a rotating plane that we call the "van der Pol plane." It is the rotation of this plane that removes the two-fold symmetry.

In Fig. 8.54 we show the intersection of the $2 \rightarrow 1$ image of the van der Pol oscillator on eight equally spaced Poincaré sections around the solid torus $D^2 \times S^1$ using as coordinates $((Xu - Yv), (Xv + Yu))$. Since intersections on the Poincaré sections at $\omega t = \phi$ and $\omega t = \phi + \pi$ are identical, only the intersections for $\phi = k\pi/8$ are shown, $k = 0, 1, \ldots, 8$. In Fig. 8.55 we produce a similar mapping using the van der Pol coordinates $((Xu + Yv), (-Xv + Yu))$.

Remark 1: The van der Pol coordinates (X', Y') and (X'', Y'') can be written as

$$\begin{bmatrix} X' \\ Y' \end{bmatrix} = \begin{bmatrix} u & -v \\ v & u \end{bmatrix} \begin{bmatrix} X \\ Y \end{bmatrix} \qquad \begin{bmatrix} X'' \\ Y'' \end{bmatrix} = \begin{bmatrix} u & v \\ -v & u \end{bmatrix} \begin{bmatrix} X \\ Y \end{bmatrix}$$

Since $(u, v) = (\cos\theta, \sin\theta)$, $\theta = \omega t$ these represent transformations to rotating coordinate systems. The two planes rotate in opposite directions.

Remark 2: The two-fold symmetry described for the harmonic drive holds also for nonlinear oscillators driven by a periodic orbit of period T with an inversion symmetry: $(u(t + \frac{1}{2}T), v(t + \frac{1}{2}T)) = (-u(t), -v(t))$. The periodic orbit of the Lorenz system that was used to drive the nonlinear oscillators possesses this symmetry. As a result, motion pictures with a two-fold symmetry for the van der Pol, Duffing, and Takens-Bogdanov oscillators can be created by driving these systems with this Lorenz orbit. Further, these motion pictures are very similar to Figs. 8.23, 8.38, and 8.53.

Remark 3: In modding out the symmetry we identify two points (X, Y, t) and $(-X, -T, t + \frac{1}{2}T)$ in a torus $D^2 \times S^1(T)$ with a single point in a torus $D^2 \times S^1(\frac{1}{2}T)$ of "half the size": $(uX \mp vY, \pm vX + uY)$. Speaking roughly but accurately, we mod out the symmetry by:

a. cutting open the original torus and straightening it out along the time flow direction into a cylindrical shape;

b. giving it a full twist (or $2n + 1$ full twists) around this axis;

c. saving the first half ($0 \leq t \leq \frac{1}{2}T$) and "throwing away" the second half ($\frac{1}{2}T \leq t \leq T$), which is identical to the first half;

d. wrapping the remaining shortened cylinder ($0 \leq t \leq \frac{1}{2}T$) back up into a torus (of half the size) by identifying the ends at $t = 0$ and $t = \frac{1}{2}T$.

8.9 $\mathcal{C}_N$ SYMMETRIES

Periodically driven nonlinear oscillators in the solid torus $D^2 \times S^1$ with higher symmetries can be constructed systematically. This is done by combining the X and Y coordinates into a single complex variable $Z = X + iY$ in the usual way, and

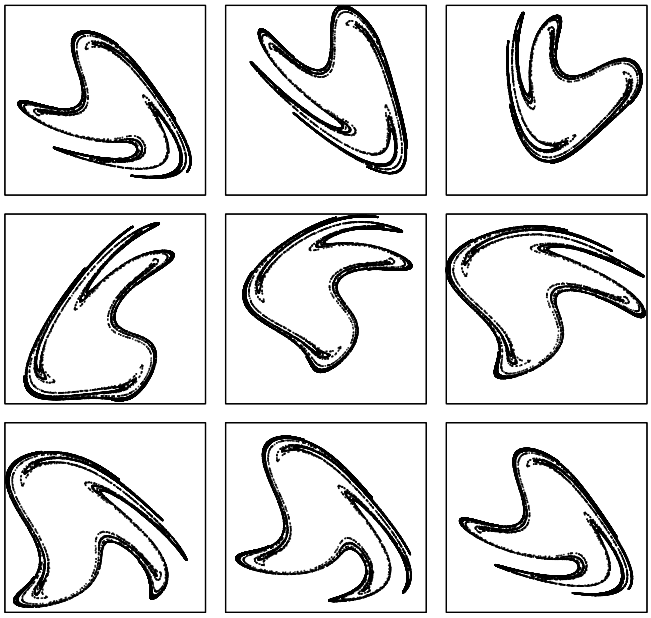

Fig. 8.54 Eight equally spaced sections from 0 to π radians around the torus $D^2 \times S^1$ of the $2 \rightarrow 1$ image of the harmonically driven van der Pol oscillator (cf. Fig. 8.23) using rotating van der Pol coordinates $(X', Y') = (uX - vY, vX + uY)$.

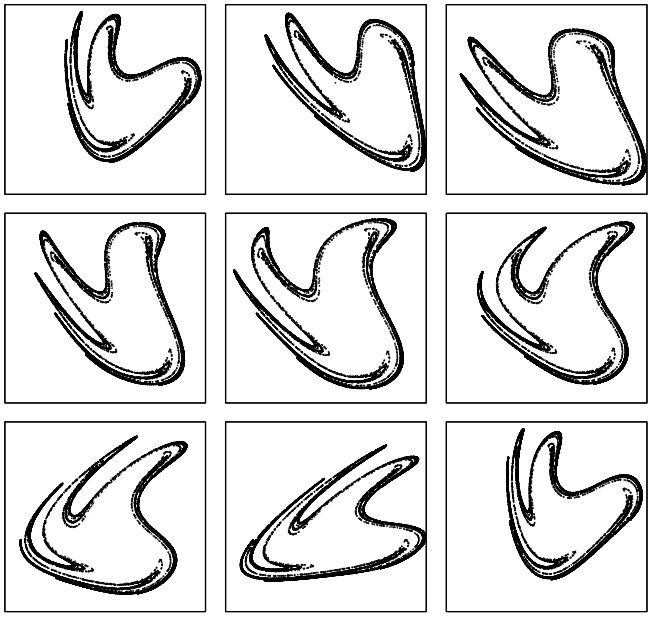

Fig. 8.55 Eight equally spaced sections from 0 to π radians around the torus $D^2 \times S^1$ of the $2 \rightarrow 1$ image of the harmonically driven van der Pol oscillator (cf. Fig. 8.23) using rotating van der Pol coordinates $(X'', Y'') = (uX + vY, -vX + uY)$.

then constructing an equation with the appropriate symmetry. For $\mathcal{C}_N$ invariance, the general equation is

$$\frac{dZ}{dt} = \gamma Z + Z f_1(\text{inv}) + (Z^*)^{N-1} g_{N-1}(\text{inv}) + Ae^{i\omega t} \tag{8.32}$$

where the two functions $f_1(\text{inv})$ and $g_{N-1}(\text{inv})$ depend on the invariants that can be constructed from powers of Z and Z^*. These are $(Z^N, Z^*Z, (Z^*)^N)$. This equation is invariant under $Z \to Ze^{2\pi i/N}$ and simultaneously $t \to t + \frac{1}{N}T$, where $\omega T = 2\pi$.

This model depends on the two arbitrary complex functions f_1 and g_{N-1} and the two complex constants γ and A. A can be taken to be real by choosing the phase of t. By choosing $\Re(\gamma) > 0$ we guarantee that the origin is an unstable fixed point, and by choosing the arbitrary functions f_1 and g_{N-1} so they become large and negative for $|Z|$ large, we guarantee that the motion is bounded.

To illustrate these ideas, we have chosen $N = 3$, $\gamma = 2.0$, $A = 5.5$, $f_1 = \beta Z^3 - \mu(Z^*Z)^2$, $g_2 = 0$, and $\omega = \pi/10$ for the general dynamical system in Eq. (8.32) and integrated these equations. For these parameter values these equations are stiff and thus delicate to integrate. Integration was carried out by reducing them to real form and driving the real and imaginary parts by coupling to harmonic terms. Specifically, the equations integrated are

$$\begin{aligned} \dot{X} &= \gamma X + X\left[\beta(X^3 - 3XY^2) - \mu(X^2+Y^2)^2\right] - Y\beta(3X^2Y - Y^3) + Au_1 \\ \dot{Y} &= \gamma Y + Y\left[\beta(X^3 - 3XY^2) - \mu(X^2+Y^2)^2\right] + X\beta(3X^2Y - Y^3) + Av_1 \end{aligned} \tag{8.33}$$

The independent harmonic drive satisfies $\dot{u} = \omega v, \dot{v} = -\omega u$. Initial conditions for the plot presented in Fig. 8.56(a) were $(X, Y) = (10^{-3}, 10^{-3})$ and $(u, v) = (1, 0)$. The control parameter values are given in the figure caption. It is seen from this figure that the strange attractor that is obtained in this way has a three-fold rotation symmetry in the sense that it is invariant under the simultaneous transformations $Z \to Ze^{2\pi i/3}$ and $t \to t + \frac{1}{3}T$. The $3 \to 1$ image of this attractor is plotted in Fig. 8.56(b). To construct this representation of the image, invariant coordinates $X^3 - 3XY^2$ and $3X^2Y - Y^3$ were used.

8.10 COVERS AND IMAGES IN THE TORUS

Harmonically driven two-dimensional nonlinear oscillators have the torus $D^2 \times S^1$ as their phase space. Some of these oscillators exhibit a symmetry under a simultaneous transformation in the disk D^2 and a time translation. These transformations typically have the form $(Z, t) \to (Ze^{i\phi}, t + (\phi/2\pi)T)$, using a complex variable $Z = X + iY$ in the plane, with $\phi = 2\pi/N$ for some integer N. Symmetric systems with these properties are described by Eq. (8.32). The van der Pol and Duffing oscillators are two examples of such systems with $N = 2$.

Such systems can be mapped to their images by the transformation $w = Z^N$. The equation of motion for w is invariant under $\mathcal{C}_1$: that is, there is generally no residual

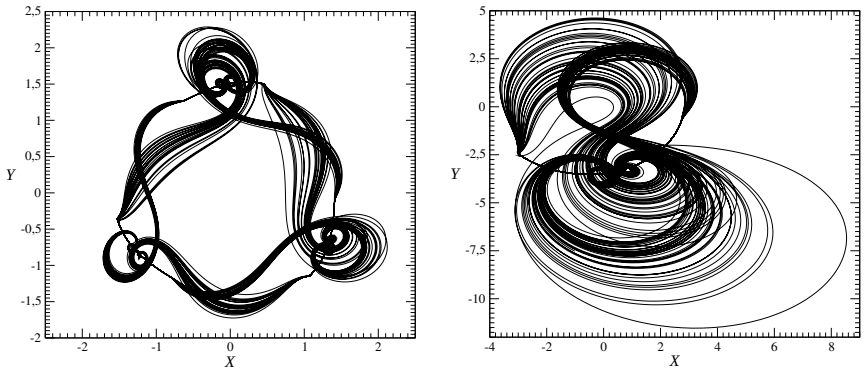

(a) (b)

Fig. 8.56 (a) Strange attractor with three-fold symmetry under the transformation $Z \to Ze^{2\pi i/3}$ and $t \to t + \frac{1}{3}T$. It is generated by Eq. 8.32 for $N = 3$. Parameter values: $\gamma = 2.0, A = 5.5, \omega = \pi/10, \mu = 0.235, \beta = 1.0$. Initial conditions: $(X, Y, t) = (10^{-3}, 10^{-3}, 0)$, as explained in the text. (b) $3 \to 1$ image attractor.

symmetry. This is easily seen from the equations of motion, for

$$\frac{dw}{dt} = NZ^{N-1}\frac{dZ}{dt} = NZ^{N-1}\left\{\gamma Z + Zf_1(\text{inv}) + (Z^*)^{N-1}g_{N-1}(\text{inv}) + Ae^{i\omega t}\right\} \tag{8.34}$$

Opening up the bracket leads to three terms. The first, $Z^N f_1$, is clearly invariant since $(Z^N, t) \to (Z^N e^{iN\phi}, t + N\phi)$ and $N\phi = 2\pi$. The second, $Z^{N-1}(Z^*)^{N-1}g_{N-1} = (Z^*Z)^{N-1}g_{N-1}$, is also clearly invariant. The third term is also, for under the group generator we find $Z^{N-1}e^{i\omega t} \to (Ze^{i\phi})^{N-1}e^{i\omega t+\phi} = Z^{N-1}e^{i\omega t}e^{iN\phi}$. Since $e^{iN\phi} = 1$, $w(t)$ is the $N \to 1$ image of the covering trajectory $Z(t)$.

It is useful to write $w(t)$ in polar form as

$$w(t) = \rho(t)e^{i\theta(t)} \tag{8.35}$$

In this representation, N-fold lifts are easily constructed by taking the Nth root:

$$Z(t) = \rho(t)^{1/N}e^{i\theta(t)/N} \tag{8.36}$$

In this way it is possible to construct an entire series of covers of the van der Pol and the Duffing equations. Formally take the square of the state variables (the coordinates $X^2 - Y^2$ and $2XY$ do this) to construct the mapping $Z \to w = Z^2$, then take the Nth root of this complex time series. This can be done even more directly from the original time series. For example, the triple cover of the proto–van der Pol attractor is the "$\frac{3}{2}$" cover of the original van der Pol attractor: $Z = X + iY \to (X + iY)^{3/2} = Z^{3/2}$. The "$\frac{3}{2}$" covers of the van der Pol and the Duffing oscillators are shown in Figs. 8.57 and 8.58.

These covers all look similar to those shown (for the van der Pol oscillator) in Figs. 8.54 and 8.55 when the torus angle is restricted from 0 to $2\pi/N$. For this reason we

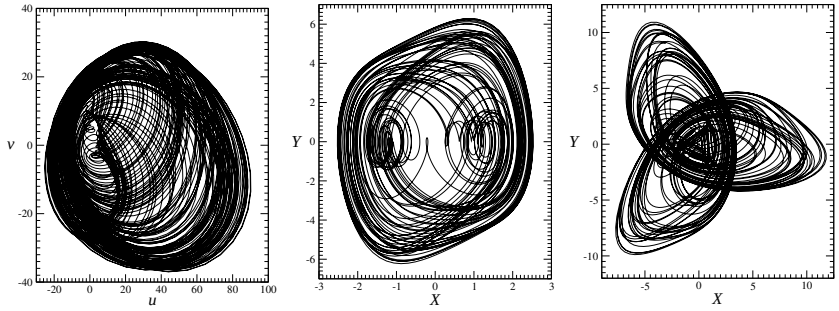

(a) Image (b) Original system (c) $\frac{3}{2}$ cover

Fig. 8.57 Projections onto the coordinate planes of attractors locally diffeomorphic with the van der Pol oscillator. (b) van der Pol oscillator, (a) image, (c) three-fold cover of image or "$\frac{3}{2}$" cover of the van der Pol attractor.

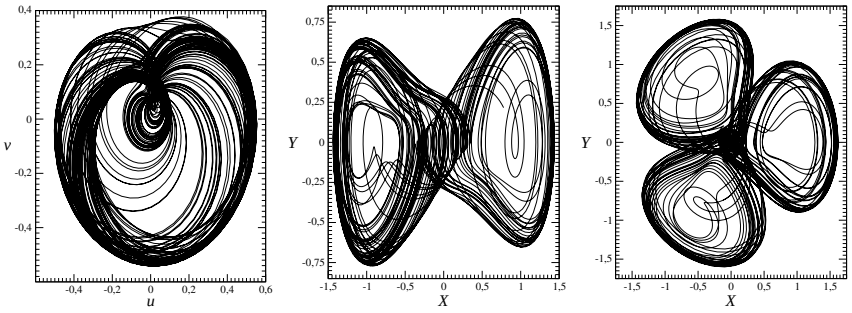

(a) Image (b) Original system (c) $\frac{3}{2}$ cover

Fig. 8.58 Projections onto the coordinate planes of attractors locally diffeomorphic with the Duffing oscillator. (b) Duffing oscillator, (a) image, (c) three-fold cover of image or "$\frac{3}{2}$" cover of the Duffing attractor.

plot the phase portraits $(X(t), Y(t))$ for the van der Pol oscillator and its image and "$\frac{3}{2}$" cover in Fig. 8.57(b), (a), and (c), respectively. The same is done in Fig. 8.58(b), (a), and (c) for the Duffing oscillator. These figures show clearly the symmetry under rotations of the coordinate plane about $2\pi/N$ radians for $N = 1, 2, 3$ in the three cases shown.

8.11 QUANTIZING CHAOS

In the closing section of this chapter we construct an entire family of strange attractors that are locally diffeomorphic with a single strange attractor. The members of this family are identified by two integers $n_1 \geq 1$ and n_2. Since these arise by imposing periodic boundary conditions, we call these integers *quantum numbers* for strange attractors.

To construct the members of this family we view a single strange attractor from various coordinate systems and then invoke the Equivalence Principle. This allows us to construct new strange attractors from old. The various transformations we use are to rotating coordinate systems. Along the way we introduce two simple measures as a way of characterizing the resulting strange attractors. These are dynamical measures, as opposed to topological indices that lead to the two integers n_1 and n_2.

A universal image attractor is identified and then lifted to a series of topologically inequivalent but globally diffeomorphic strange attractors and many $n_1 \rightarrow 1$ covers of the universal image attractor. These procedures can also be applied to certain autonomous dynamical systems, such as the Rössler attractor.

8.11.1 The Equivalence Principle

According to the Equivalence Principle, if two observers, $\mathcal{O}_1$ and $\mathcal{O}_2$, observe some process and "the rest of the universe" "looks the same" to both obsevers, then $\mathcal{O}_2$ can use the description of the process given by $\mathcal{O}_1$ to describe some other process, "and that process must exist" for $\mathcal{O}_2$.

Applied to strange attractors the Equivalence Principle provides the following information for us. We observe some process that generates a strange attractor, for example, the van der Pol equations in the natural (X, Y, t) coordinate system. A second observer $\mathcal{O}_2$ records this process from a different coordinate system. If the rest of the world looks the same from both coordinate systems, we can use the mathematical description of the process formulated by $\mathcal{O}_2$ to describe a process in our (X, Y, t) coordinate system to generate a strange attractor, and that attractor must exist.

This is not a useful way to generate strange attractors if the two are topologically equivalent. It is therefore of interest to choose coordinate transformations that lead to topologically inequivalent strange attractors. These are rotating coordinate transformations.

8.11.2 Rotating Transformations

We begin with a standard periodically driven dynamical system

$$\frac{d}{dt}\begin{bmatrix} X_1(t) \\ X_2(t) \end{bmatrix} = \begin{bmatrix} F_1(X_1, X_2) \\ F_2(X_1, X_2) \end{bmatrix} + \begin{bmatrix} t_1(t) \\ t_2(t) \end{bmatrix} \tag{8.37}$$

Here $t_i(t)$ are the periodic driving terms: $t_i(t + T_d) = t_i(t)$. The phase space is the torus $D^2 \times S^1$. If this dynamical system generates a strange attractor, the attractor

is periodic. More specifically the Ω-limit set is periodic. The relation between the geometric angle θ describing position along S^1 in the torus and the dynamical variable t is

$$\frac{\theta}{2\pi} = \frac{t}{T_d} \tag{8.38}$$

In a coordinate system (u_1, u_2, t) related to the original coordinate system (X_1, X_2, t) by the periodic transformation

$$\begin{aligned} u_i(t) &= R_{ij}(t)X_j(t) + d_i(t) \\ R_{ij}(t+T_d) &= R_{ij}(t) \\ d_i(t+T_d) &= d_i(t) \end{aligned} \tag{8.39}$$

the coordinates (X_1, X_2, t) are mapped to new coordinates (u_1, u_2, t) that also describe a strange attractor. If the transformation is a diffeomorphism, the new strange attractor has identical geometric (fractal) and dynamical (Lyapunov) measures as the original. However, it may not be topologically equivalent to the original.

To construct a series of topologically inequivalent attractors we choose homogeneous transformations ($d_i(t) = 0$) that are uniform rotations:

$$R_{ij}(t) = e^{\mathbf{\Omega} t} \quad \text{and} \quad d_i(t) = 0 \tag{8.40}$$

where $\mathbf{\Omega} = \omega \mathbf{L}$, $\omega = k\omega_d$, with k an integer and $\omega_d = 2\pi/T_d$, and $\mathbf{L} = \begin{bmatrix} 0 & 1 \\ -1 & 0 \end{bmatrix}$ is the infinitesimal generator for rotations in a plane. For this class of transformations $R(0) = I_2$, $R(T_d) = I_2$, and $R(t)$ goes through k full rotations as t increases through one period from $t = 0$ to $t = T_d$. As a result, the new strange attractor with coordinates (u_1, u_2, t) and the original strange attractor with coordinates (X_1, X_2, t) have global torsions differing by the integer k.

The dynamical equations for the new strange attractor are

$$\frac{d}{dt}\begin{bmatrix} u_1(t) \\ u_2(t) \end{bmatrix} = R(t)\begin{bmatrix} F_1(R^{-1}u) \\ F_2(R^{-1}u) \end{bmatrix} + R(t)\begin{bmatrix} t_1(t) \\ t_2(t) \end{bmatrix} + \mathbf{\Omega}\begin{bmatrix} u_1(t) \\ u_2(t) \end{bmatrix} \tag{8.41}$$

Of the three terms on the right: the first is the original driving term as seen in the rotating coordinate system; the second is the periodic drive, as seen also in the rotating coordinate system; the third is the usual Coriolis term.

In Fig. 8.59 we present images of the Duffing strange attractor ($k = 0$) and several of the strange attractors that have been generated from it by using uniformly rotating transformations. These attractors have been shown in a "toroidal" representation. We plot one of the two rotating coordinates ($u(t)$) vertically and the time direction horizontally for one period. The trace is shown darker ($v(t) > 0$) or lighter depending on the value of the second coordinate. These presentations show that the strange attractor becomes more "wound up" as $|k|$ increases.

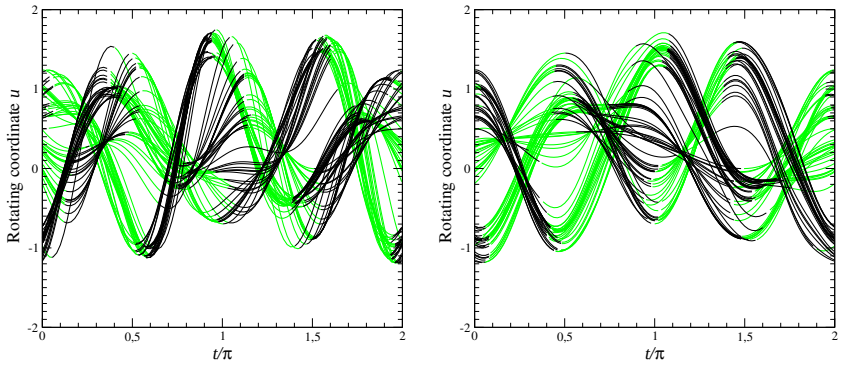

(a) Rotation index $k = -2$ (b) Rotation index $k = +2$

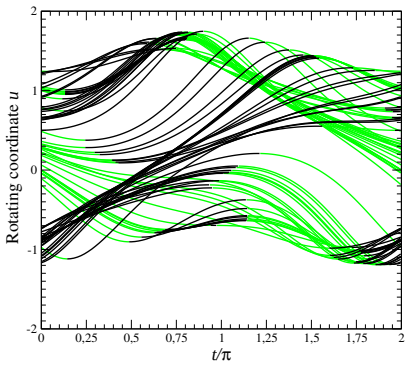

(c) Rotation index $k = 0$

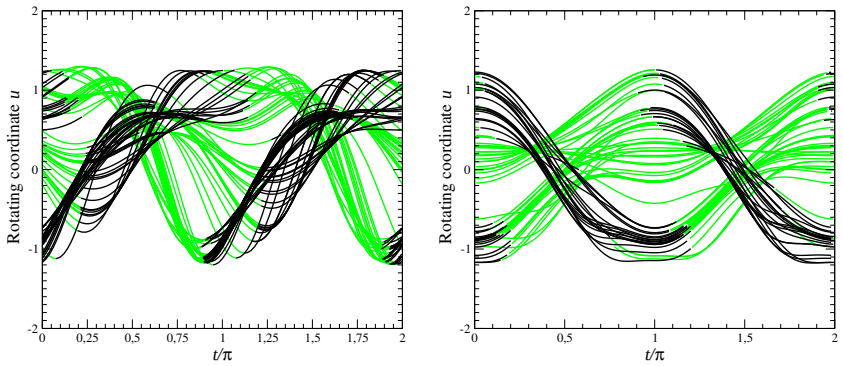

(d) Rotation index $k = -1$ (e) Rotation index $k = +1$

Fig. 8.59 Strange attractors obtained from the Duffing strange attractor using uniformly rotating coordinate transformations. Middle: The original strange attractor, toroidal representation. Top line: Lifts that are globally diffeomorphic with the original attractor. Bottom line: $2 \to 1$ images obtained by projections to planes subharmonically rotating in opposite directions. Parameter values: $(a, \delta, \omega, T) = (0.4, 0.4, 1.0, 2\pi)$. Rotation index $k = -2, -1, 0, +1, +2$.

8.11.3 Dynamical Measures

It is useful to introduce two classical-like measures for a periodically driven strange attractor. These are the mean torsion and energy integrals, defined by

$$\begin{aligned} L &= L(0) = \lim_{\tau\to\infty}\frac{1}{\tau}\int_0^\tau XdY - YdX \\ K &= K(0) = \lim_{\tau\to\infty}\frac{1}{\tau}\int_0^\tau \frac{1}{2}(\dot{X}^2+\dot{Y}^2)dt \end{aligned} \tag{8.42}$$

The first integral measures the rotation around the direction of flow. The second integral measures, in some rough sense, the "kinetic energy" associated with motion generating the strange attractor.

The integrals $L(\mathbf{\Omega})$ and $K(\mathbf{\Omega})$ for strange attractors generated from the original strange attractor by the uniformly rotating transformation are related to the integrals $L(0)$ and $K(0)$ by

$$\begin{aligned} L(\mathbf{\Omega}) = \langle u\dot{v} - v\dot{u}\rangle &= \langle X\dot{Y} - Y\dot{X}\rangle + \Omega\langle X^2+Y^2\rangle \\ &= L(0) + \Omega\langle R^2\rangle \\ K(\mathbf{\Omega}) = \frac{1}{2}\langle(\dot{u}^2+\dot{v}^2)\rangle &= \langle\frac{1}{2}(\dot{X}^2+\dot{Y}^2)\rangle + \Omega\langle X\dot{Y} - Y\dot{X}\rangle + \frac{1}{2}\Omega^2\langle X^2+Y^2\rangle \\ &= K(0) + \Omega L(0) + \frac{1}{2}\Omega^2\langle R^2\rangle \end{aligned} \tag{8.43}$$

The moment of inertia $\langle R^2\rangle = \langle X^2+Y^2\rangle = \lim_{\tau\to\infty}\frac{1}{\tau}\int_0^\tau(u(t)^2+v(t)^2)dt$ is invariant under rotating transformations.

In Fig. 8.60 we present the two classical integrals for the class of strange attractors obtained from the Duffing strange attractor using rotating transformations with integer index k, $-10 \le k \le +10$. The torsion integral has been scaled by $\omega_d\langle R^2\rangle$ to emphasize that its value increases by integer steps as the rotation ($\Omega = k\omega_d$) increases. The plots also show that the kinetic energy increases quadratically with the angular frequency.

8.11.4 Universal Image

The Duffing, van der Pol, and Takens-Bogdanov nonlinear oscillators have an inversion symmetry that leads to a two-fold internal symmetry over and above the periodic symmetry when the periodic drive also possesses a symmetry. This symmetry leads immediately to a symmetry in the rotating attractors:

$$(u, v, t) \to ((-)^{k+1}u, (-)^{k+1}v, t + \frac{1}{2}T_d) \tag{8.44}$$

For k even the rotating attractors have the same fundamental symmetry as the original attractor with $k = 0$. For k odd the attractors are invariant under the half-period

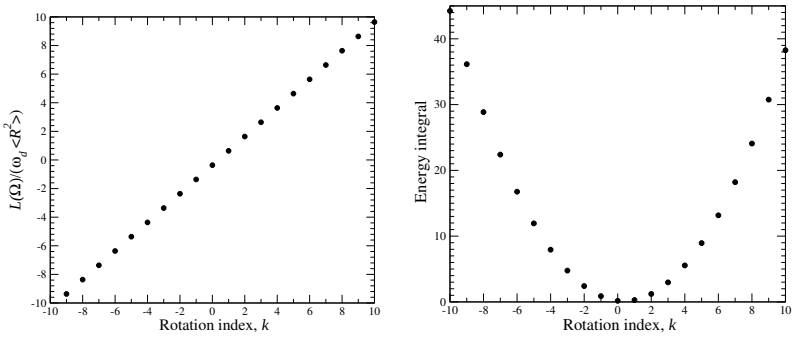

Fig. 8.60 Torsion and energy integrals for strange attractors created from the Duffing strange attractor ($k = 0$) using rotating transformations. The torsion integral is scaled by $\omega_d\langle R^2\rangle$ to emphasize the integer growth of $L(\mathbf{\Omega})$ with Ω. The attractors are all globally diffeomorphic and differ by their global torsion. Parameter values: $(a, \delta, \omega, T) = (0.4, 0.4, 1.0, 2\pi)$.

symmetry $(u, v, t) \rightarrow (+u, +v, t + \frac{1}{2}T_d)$. In some ways the attractors with k odd are "more fundamental" than those with k even. In fact, the latter can be considered as $2 \rightarrow 1$ covers of the odd-k attractors. Those with odd k have no residual internal symmetry.

We make these ideas more formal by defining a unique *universal image* strange attractor as the attractor with least symmetry and smallest value of the dynamical integrals. From Fig. 8.60 it is clear that the universal image of the Duffing attractor is the attractor obtained with $k = +1$.

8.11.5 Harmonic Maps

The universal image attractor can be used to construct an entire series of strange attractors that are closely related to the original strange attractor. To do this we use the uniformly rotating coordinate transformation Eq.(8.40), acting on the coordinates (u, v, t) of the universal image attractor. The driving frequency is $\omega_1 = 2\omega_d$ since the period of the universal image is half the period of the original attractor: $T_1 = \frac{1}{2}T_d$.

None of the attractors obtained by this means is equivalent to the original Duffing attractor.

8.11.6 Subharmonic Lifts and Quantum Numbers

In order to recover the original Duffing strange attractor from its universal image it is useful to:

1. allow the integer k used to define harmonic lifts to be replaced by a rational fraction p/q or n_2/n_1;
2. replace the source attractor on the right hand side of the rotation transformation equation Eq.(8.41) by the coordinates of the universal image attractor.

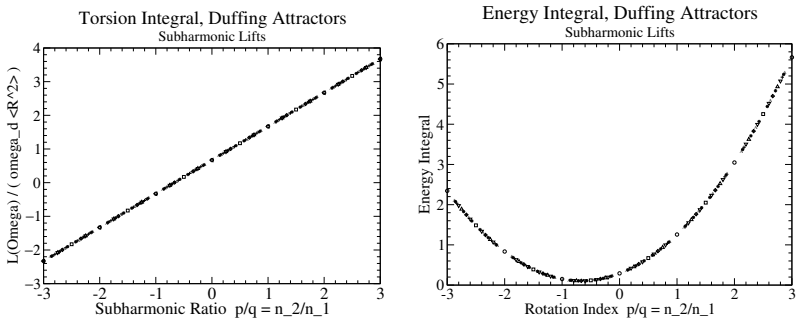

Fig. 8.61 Torsion and energy integrals for subharmonic lifts of the universal image of the Duffing attractor for $-3 \leq n_2/n_1 \leq +3$ and $1 \leq n_1 \leq 8$. The torsion integral is divided by by $\omega_1 \langle R^2 \rangle$: the scaled result is proportional to n_2/n_1 up to an additive constant. Parameter values: $(a, \delta, \omega, T) = (0.4, 0.4, 1.0, 2\pi)$.

The lift of the universal image strange attractor that is obtained by this subharmonic rotation is labeled by the index (n_1, n_2). The periodicity of the lifted attractor is $T_{(n_1,n_2)} = n_1 T_1$. Further, during the interval $0 \leq t \leq n_1 T_1$ the rotation increases by $2\pi n_2$ radians. The relation between the dynamical indices of the universal image attractor $L(\text{image})$ and $K(\text{image})$ and the indices of the covers obtained are

$$\begin{aligned} L(n_1, n_2) &= L(\text{image}) + \Omega \langle R^2 \rangle \\ K(n_1, n_2) &= K(\text{image}) + \Omega L(\text{image}) + \tfrac{1}{2}\Omega^2 \langle R^2 \rangle \end{aligned} \tag{8.45}$$

Here $\Omega = (n_2/n_1)\omega_1$.

Fig. 8.61 displays the values of the classical integrals for subharmonic lifts of the universal image Duffing attractor for $1 \leq n_1 \leq 8$ and $-3 \leq n_2/n_1 \leq +3$. The torsion integral depends linearly on $\Omega = (n_2/n_1)\omega_1$ and the energy integral depends quadratically on the rotation angular frequency. As before, the torsion integral is scaled by $\omega_1 \langle R^2 \rangle$ to emphasize its linear dependence on the rational fraction n_2/n_1.

The original Duffing attractor is the lift of the universal image with index $(n_1, n_2) = (2, -1)$. It is a $2 \to 1$ cover of the image. The subharmonic lifts with index (n_1, n_2) are n_1-fold covers of the universal image attractor. The relation between the geometric angle $\theta \in S^1$ in the torus $D^2 \times S^1$ and the dynamical variable t is

$$\frac{\theta}{2\pi} = \frac{t}{T_{(n_1,n_2)}} = \frac{t}{n_1 T_1} \tag{8.46}$$

There is a one to one correspondence between topologically distinct subharmonic lifts and pairs of integers (n_1, n_2) with $n_1 \geq 1$.

8.11.7 Application to Autonomous Systems

The distinction between autonomous and nonautonomous dynamical systems has been useful in the past, but it cannot be regarded as an absolute distinction. It is

possible to represent some nonautonomous dynamical systems in an autonomous form, and to express some autonomous dynamical systems in a nonautonomous form. This can be done when the autonomous dynamical system generates a strange attractor whose natural phase space is a torus with topology $D^2 \times S^1$.

We illustrate how to do this for the simplest of the autonomous dynamical systems: the Rössler attractor. The strange attractor generated by the Rössler equations for standard parameter values $(a, b, c) = (0.398, 2.0, 4.0)$ is shown projected onto the x-y plane on the left in Fig. 8.62. A toroidal representation of this strange attractor is presented on the right in this figure. The toroidal representation is constructed as follows. The autonomous phase space coordinates (x, y, z) are expressed as "$1\frac{1}{2}$ complex variables" by writing $x + iy = Ae^{i\phi}$, where the amplitude $A(\phi) > 0$ and $\tan(\phi) = y/x$. The angle $\phi(t)$ depends monotonically on the time coordinate t, and can be used to replace t. The three coordinates of the strange attractor are taken as $A(\phi) - \langle A \rangle$, the derivative $dA(\phi)/d\phi - \langle dA/d\phi \rangle$, and the geometric coordinate $\phi \bmod 2\pi$. The toroidal representation that is shown in Fig. 8.62 plots $A - \langle A \rangle$ against $\phi/2\pi$ mod 1, with darker parts where $dA/d\phi - \langle dA/d\phi \rangle > 0$ and lighter where $dA/d\phi - \langle dA/d\phi \rangle < 0$. As this attractor possesses no internal symmetry, it [or one of its harmonic lifts (k integer)] is the universal image attractor. Since it is clearly less wound up than any attractor created using a uniform rotation with $k \neq 0$, this is the universal image attractor.

The universal image can be lifted using either harmonic rotations (k integer) or subharmonic rotations. Attractors with index (n_1, n_2), $n_1 \geq 1$ are constructed using $\omega = (n_2/n_1)\omega_1$ as angular rotation frequencies. Several of these lifts are shown in Fig. 8.63.

In this final section we have shown that it is possible to create a two parameter family (n_1, n_2) of covers of an image dynamical system. The integer n_1 describes the order of the lift: the lift is an $n_1 \rightarrow 1$ cover of the universal image attractor. The integer n_2 describes the global torsion of the lift into the torus where $\theta/2\pi = t/(n_1 T_1)$. All attractors are locally diffeomorphic. As a result, they have identical spectra of geometric (fractal) invariants as well as dynamical invariants (Lyapunov exponents). Those with the same value of n_1 are globally diffeomorphic. Lifts with $(n_1, n_2) \neq (n_1, n_2)'$ are topologically distinct. The only way they can be distinguished from each other is through their topological invariants.

The covers of the Rössler system that we have created in this subsection are different from most of the covers that were described in Chapter 6, and those that will be described in Part III of this work. Most of the n-fold covers described in Chapter 6 exhibit n "ears," or formally, exist in bounding tori (cf., Chapter 15) of genus $g = n+1$. The exceptions include lifts with $\mathcal{C}_n$ symmetry, where the symmetry axis is inside both branches 0 and 1 of the Rössler attractor. This subset of lifts with $\mathcal{C}_n$ symmetry exists in a genus-one torus and corresponds exactly to the covers discussed above with $n_1 = n$ and $n_2 = 0$. Covers of the Rössler attractor (toroidal representation) with index (n_1, n_2) have 2^{n_1} branches and their Poincaré sections consist of a single plane. Covers with the same value of n_1 are globally diffeomorphic and differ from each other only by their global torsion, which is n_2.

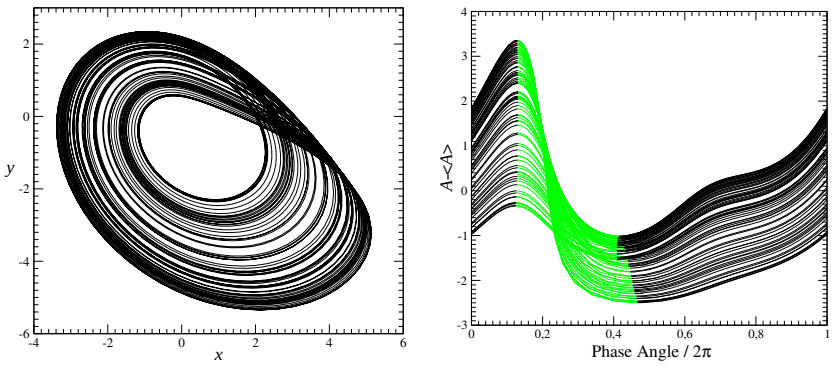

(a) Standard x-y projection in $\mathbb{R}^3$ (b) Toroidal representation

Fig. 8.62 (a) Projection of the strange attractor generated by the Rössler equations onto the x-y plane. The natural phase space is a torus $D^2 \times S^1$. (b) The Rössler strange attractor is shown in a toroidal representation. The natural variable $(A(\phi), dA/d\phi, \phi)$, with $0 \leq \phi < 2\pi$ and periodic boundary conditions. Parameter values: $(a, b, c) = (0.398, 2.0, 4.0)$.

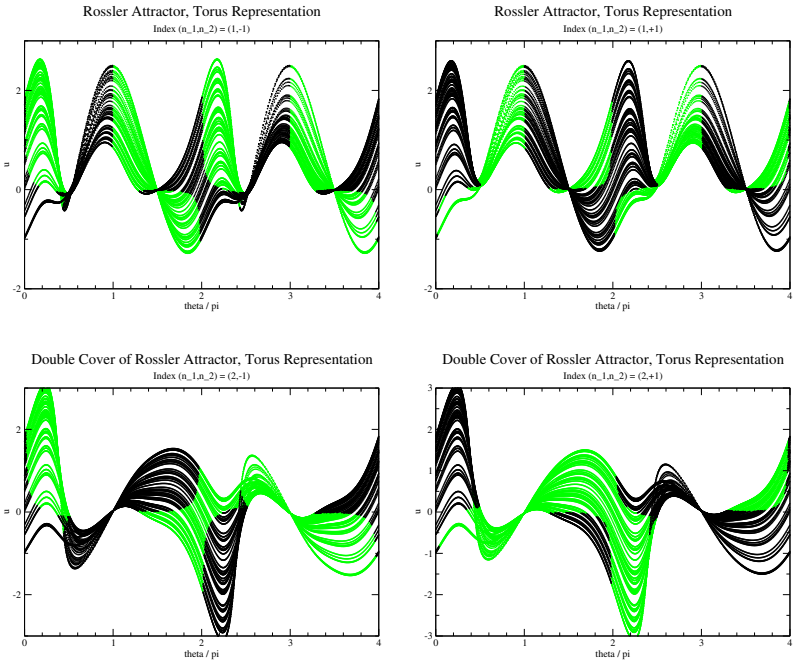

Fig. 8.63 Several harmonic and subharmonic lifts of the Rössler strange attractor are presented in toroidal representation. The covers with $n_1 = 1$ (top row) have period 2π while the covers with $n_1 = 2$ (bottom row) have period 4π. Parameter values: $(a, b, c) = (0.398, 2.0, 4.0)$.

9

Larger Symmetries

9.1 COMPLEX DYNAMICAL SYSTEMS

A large class of dynamical systems can be written in complex form

$$\dot{a}_i = A_{ij}a_j + A_{ijk}a_j^{(*)}a_k^{(*)} \tag{9.1}$$

These equations are truncations of nonlinear partial differential equations that support one or more propagating waves. They involve complex time-dependent amplitudes and possibly their complex conjugates. In these systems the complex amplitudes $a_j(t)$ are coupled to waves of the from $e^{i(k_j\boldsymbol{x}-\omega_j t)}$. When expressions of the form

$$u(\boldsymbol{x},t) = \sum a_j \Psi_j(\boldsymbol{x},t) = \sum a_j e^{i(k_j\boldsymbol{x}-\omega_j t)}$$

are substituted into the original partial differential equation and the spatial dependence is integrated out, coupled nonlinear equations of the form (9.1) result. If the partial differential equation has a quadratic nonlinearity, the projected coupled ordinary differential equations (9.1) contain only bilinear nonlinearities. In this section we will outline the general approach to the study of complex ordinary differential equations of type (9.1) when these equations exhibit a continuous symmetry. The approach will be illustrated by application to a four-wave mixing interaction in a plasma. The

interactions in a plasma between the electric field $\boldsymbol{E}(\boldsymbol{x},t)$ and the ion sound wave $\boldsymbol{u}(\boldsymbol{x},t)$ are described by the following partial differential equations

$$\nabla\cdot(i\partial_t+\Delta+i\tilde{\nu})\boldsymbol{E}=\nabla\cdot n\boldsymbol{E}$$
$$\left(\partial_t^2+2\tilde{\nu}_S\partial_t-\Delta\right)n=\Delta(\boldsymbol{E}\cdot\boldsymbol{E})$$

These are called Zakharov's equations [138].

9.1.1 Projection to Five Complex Dimensions

In the case that three propagating electric field modes $a_j e^{i(k_j\boldsymbol{x}-\omega_j t)}$ $(j=1,2,3)$ interact with a single ion acoustic wave $n(\boldsymbol{x},t)\approx n(t)e^{i(K\boldsymbol{x}-\Omega t)}$, the three mode amplitudes $a_i(t)$ each obey first-order equations and the acoustic mode amplitude obeys a second-order equation that can be written as a pair of first-order equations. The five resulting complex equations are

$$\begin{aligned}
\dot{a}_1&=-\nu_1 a_1+a_2a_4e^{-i\Delta t}\\
\dot{a}_2&=-\nu_2 a_2-a_1a_4^*e^{i\Delta t}+a_3a_4e^{-i\delta t}\\
\dot{a}_3&=-\nu_3 a_3-a_2a_4^*e^{i\delta t}\\
\dot{a}_4&=-2\nu_4 a_4+2i(a_4-a_5)\\
\dot{a}_5&=-\nu_4 a_4-a_1a_2^*e^{-i\Delta t}-a_2a_3^*e^{-i\delta t}
\end{aligned}\tag{9.2}$$

These equations exhibit a two-dimensional manifold of symmetries.

9.1.2 Symmetries

We begin our analysis of coupled complex ordinary differential equations by searching for sets of phase transformations $a_j\mapsto a_je^{i\theta_j}$ that leave these equations invariant. The angles θ_j are static (time independent). Under this transformation the equations are

$$\frac{d}{dt}a_i=A_{ij}a_je^{i(\theta_j-\theta_i)}+A_{ijk}a_j^{(*)}a_k^{(*)}e^{i(\pm\theta_j\pm\theta_k-\theta_i)}$$

The signs $(\pm)$ depend on whether the mode amplitude (+) or its complex conjugate $(-)$ appears in the equations. Each nonzero term A_{ij} $(j\neq i)$ and A_{ijk} in the dynamical system gives rise to a constraint on the allowed phase transformations. As an example, the three terms in the equations for $\frac{da_5}{dt}$ provide the following constraints on the phase angle θ_i:

$$\begin{aligned}
-\nu_4a_4:&\qquad \theta_4-\theta_5&=0\\
a_1a_2^*:&\qquad \theta_1-\theta_2-\theta_5&=0\\
a_2a_3^*:&\qquad \theta_2-\theta_3-\theta_5&=0
\end{aligned}$$

The entire set of phase constraints can be summarized by a matrix of phase relations, or simply a phase matrix MP. For the complex dynamical system (9.2) describing the

four-wave interaction, this phase matrix is

$$\begin{array}{cc} \text{Eq.} & \text{Term} \\ 1 & a_2a_4 \\ 2 & a_1a_4^* \\ 2 & a_3a_4 \\ 3 & a_2a_4^* \\ 4 & a_5 \\ 5 & a_4 \\ 5 & a_1a_2^* \\ 5 & a_2a_3^* \end{array} \begin{array}{c} \begin{array}{ccccc} \theta_1 & \theta_2 & \theta_3 & \theta_4 & \theta_5 \end{array} \\ \left[\begin{array}{ccccc} -1 & 1 & 0 & 1 & 0 \\ 1 & -1 & 0 & -1 & 0 \\ 0 & -1 & 1 & 1 & 0 \\ 0 & 1 & -1 & -1 & 0 \\ 0 & 0 & 0 & -1 & 1 \\ 0 & 0 & 0 & 1 & -1 \\ 1 & -1 & 0 & 0 & -1 \\ 0 & 1 & -1 & 0 & -1 \end{array}\right] \end{array} \left[\begin{array}{c} \theta_1 \\ \theta_2 \\ \theta_3 \\ \theta_4 \\ \theta_5 \end{array}\right] = 0 \tag{9.3}$$

The number of complex variables in the dynamical system is the maximum rank of the phase matrix. If the rank of the phase matrix is maximum the dynamical system has no continuous phase symmetry. If it is less than maximum, the dimension of the continuous symmetry group is the corank of this matrix (Complex dimension − Rank MP). This is the number of null vectors of MP. The matrix MP in (9.3) has rank 3, so that the dynamical system (9.2) has three independent phase angle degrees of freedom and a two-dimensional ($2 = 5 - 3$) group of symmetries whose generators are the null vectors of MP.

The three linearly independent row vectors and the two null vectors of the phase matrix (9.3) are

$$\begin{array}{c} \text{3 Independent Row Vectors} \\ \left[\begin{array}{ccccc} -1 & 1 & 0 & 1 & 0 \\ 0 & -1 & 1 & 1 & 0 \\ 0 & 0 & 0 & 1 & -1 \end{array}\right] \end{array} \qquad \begin{array}{c} \text{2 Null Vectors} \\ \left[\begin{array}{ccccc} 1 & 0 & -1 & 1 & 1 \\ 0 & -1 & 2 & -1 & -1 \end{array}\right] \end{array} \tag{9.4}$$

As usual, this decomposition into spanning vectors and null vectors represents a decomposition into dynamics and symmetry (Wigner-Eckart decomposition).

We discuss symmetry first. The dynamical system is invariant under phase changes represented by an arbitrary linear combination of the two null vectors. Choosing amplitudes α, β for these null vectors, the dynamics is invariant under the transformation

$$\left[\begin{array}{c} a_1 \\ a_2 \\ a_3 \\ a_4 \\ a_5 \end{array}\right] \mapsto \left[\begin{array}{c} a_1 e^{i\alpha} \\ a_2 e^{-i\beta} \\ a_3 e^{i(-\alpha+2\beta)} \\ a_4 e^{i(\alpha-\beta)} \\ a_5 e^{i(\alpha-\beta)} \end{array}\right]$$

As a result of this two-dimensional equivariance group, the complex five-dimensional system can be reduced to a real eight-dimensional dynamical system.

9.1.3 Dynamics

The dynamical equations of motion (9.2) can be integrated either as five complex equations or ten real equations. The evolution in the ten (or eight) dimensional phase

space is impossible to represent here. Instead, we show the time evolution of each of the five complex modes $a_1 \rightarrow a_5$ in Fig. 9.1(a)→(e). These projections exhibit several striking features:

1. The modes are locked. Each mode exhibits 90 maxima in $|a_i|$.
2. The phase angle for each mode can be decomposed into two parts

$$\theta_i = \Omega_i t + \Psi_i(t) \tag{9.5}$$

3. The slow part Ω_i can be taken as constant. It describes the slow rotation of the oscillation about the origin of each projection. For the five modes shown, $\Omega_1 > \Omega_2 > \Omega_4 \approx \Omega_5 > \Omega_3$.
4. The fast oscillations are of two types:

   Librations: $0 < \Psi < \pi$ for modes a_1, a_3.

   Rotations: Ψ increases approximately linearly for modes a_2, a_4, a_5.

These observations suggest that the dynamics will provide an even more significant simplification than symmetry in the description of this system.

9.1.4 Dynamics in Polar Coordinates

An alternative representation for the real eight-dimensional dynamical system could be constructed. A polar decomposition for each variable is introduced: $a_j \mapsto \rho_j e^{i\phi_j}$. In this decomposition $\rho_j \geq 0$, and both ρ_j and ϕ_j are explicitly time dependent. In this representation the dynamical system equations become

$$\dot{\rho}_i + i\dot{\varphi}_i\rho_i = A_{ij}\rho_j e^{i(\varphi_j - \varphi_i)} + A_{ijk}\rho_j\rho_k e^{i(\pm\varphi_j \pm \varphi_k - \varphi_i)}$$

The real and imaginary parts of each complex equation provide an equation for $\dot{\rho}_i$ and one for $\dot{\varphi}_i$. For the five-complex dimensional system there is one equation for each ρ_i. The five equations for the phase angle $\dot{\varphi}_i$ can be grouped into two subsets. One is a set of three dynamical phase angles Φ_i, $i = 1, 2, 3$. These are linear combinations of angles determined by the three linearly independent row vectors given in (9.4) and are

$$\begin{aligned}
\Phi_1 &= -\theta_1 + \theta_2 + \theta_4 - \Delta t \\
\Phi_2 &= -\theta_2 + \theta_3 + \theta_4 - \delta t \\
\Phi_3 &= \theta_4 - \theta_5
\end{aligned}$$

Two other linear combinations of the phase angles, Φ_j, $j = 4, 5$ represent the symmetries of the five complex equations. They are determined by the two null vectors in (9.4), and are

$$\begin{aligned}
\Phi_4 &= \theta_1 - \theta_3 + \theta_4 + \theta_5 \\
\Phi_5 &= -\theta_2 + 2\theta_3 - \theta_4 - \theta_5
\end{aligned}$$

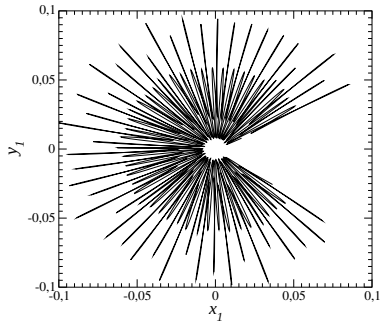

(a) Plane projection of mode a_1

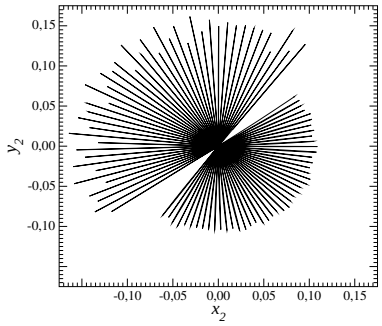

(b) Plane projection of mode a_2

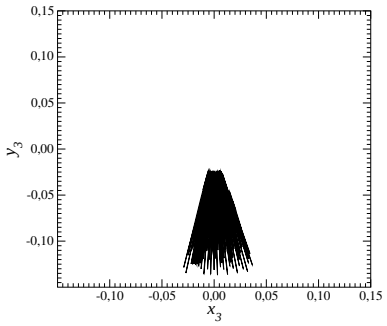

(c) Plane projection of mode a_3

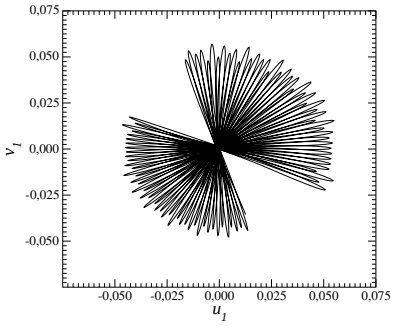

(d) Plane projection of mode a_4

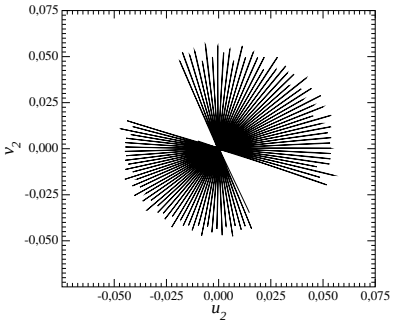

(e) Plane projection of mode a_5

Fig. 9.1 Plane projections of the chaotic attractor generated by the ten-dimensional system (9.2). The continuous rotation symmetry is easily identifed. Parameter values: $\nu_1 = 0.050$, $\nu_2 = -0.0345$, $\nu_3 = 0.03$, and $\nu_4 = 0.05$.

The eight dynamical variables satisfy the equations

$$\dot{\rho}_1 = -\nu_1\rho_1 + \rho_2\rho_4\cos\Phi_1$$
$$\dot{\rho}_2 = -\nu_2\rho_2 - \rho_1\rho_4\cos\Phi_1 + \rho_3\rho_4\cos\Phi_4$$
$$\dot{\rho}_3 = -\nu_3\rho_3 - \rho_2\rho_4\cos\Phi_2$$
$$\dot{\rho}_4 = -2(\nu_4\rho_4 + \rho_5\sin\Phi_3)$$
$$\dot{\rho}_5 = -\nu_4\rho_4\cos\Phi_3 - \rho_1\rho_2\cos(\Phi_1 - \Phi_3) - \rho_2\rho_3\cos(\Phi_2 - \Phi_3)$$

$$\dot{\Phi}_1 = -\Delta + 2\left(1 - \frac{\rho_5}{\rho_4}\cos\Phi_3\right) + \left(\frac{\rho_1\rho_4}{\rho_2} - \frac{\rho_2\rho_4}{\rho_1}\right)\sin\Phi_1 + \frac{\rho_3\rho_4}{\rho_2}\sin\Phi_2$$

$$\dot{\Phi}_2 = -\delta + 2\left(1 - \frac{\rho_5}{\rho_4}\cos\Phi_3\right) - \frac{\rho_1\rho_4}{\rho_2}\sin\Phi_1 + \left(\frac{\rho_2\rho_4}{\rho_3} - \frac{\rho_3\rho_4}{\rho_2}\right)\sin\Phi_2$$

$$\dot{\Phi}_3 = 2\left(1 - \tfrac{\rho_5}{\rho_4}\cos\Phi_3\right) + \nu_4\tfrac{\rho_4}{\rho_2}\sin\Phi_3 - \tfrac{\rho_1\rho_2}{\rho_5}\sin(\Phi_1 - \Phi_3) - \tfrac{\rho_2\rho_3}{\rho_5}\sin(\Phi_2 - \Phi_3)$$

The phase angles Φ_4, Φ_5 obey $\dot{\Phi}_4 = 0$, $\dot{\Phi}_5 = 0$.

9.1.5 Symmetry Reduction

There are systematic ways to reduce the dimension of complex dynamical systems of the type given in Eq. (9.1) by using the machinery described earlier for real dynamical systems. Invariant polynomials depending on the complex amplitudes are constructed as follows. One bilinear invariant can be constructed from each amplitude $a_j \mapsto a_j^* a_j$. Invariant polynomials depending on two or more amplitudes and their complex conjugates have the form

$$a_1^{n_1} a_2^{n_2} a_3^{n_3} a_4^{n_4} a_5^{n_5}$$

where a negative value of n_j means that $a_j^{n_j} \mapsto (a_j^*)^{(-n_j)}$. In order for this polynomial to be invariant, the exponents n_j must obey the following Diophantine equations

$$\begin{bmatrix} 1 & 0 & -1 & 1 & 1 \\ 0 & -1 & 2 & -1 & -1 \end{bmatrix} \begin{bmatrix} n_1 \\ n_2 \\ n_3 \\ n_4 \\ n_5 \end{bmatrix} = \begin{bmatrix} 0 \\ 0 \end{bmatrix} \tag{9.6}$$

This equation has three linearly independent sets of solutions. These are the three linearly independent sets of row vectors of the phase matrix (cf. Eq. (9.4)):

$$\begin{bmatrix} 1 & 0 & -1 & 1 & 1 \\ 0 & -1 & 2 & -1 & -1 \end{bmatrix} \begin{bmatrix} -1 & 0 & 0 \\ 1 & -1 & 0 \\ 0 & 1 & 0 \\ 1 & 1 & 1 \\ 0 & 0 & -1 \end{bmatrix} = \begin{bmatrix} 0 & 0 & 0 \\ 0 & 0 & 0 \end{bmatrix} \tag{9.7}$$

Each column of this 5×3 matrix defines an invariant polynomial. The three invariant polynomials are

$$a_1^* a_2 a_4\ ,\quad a_2^* a_3 a_4\ ,\quad a_4 a_5^*$$

Their complex conjugates are also invariant, as are all products of them, their complex conjugates, and the bilinear invariants $a_j^* a_j$.

The generating functions for invariant polynomials by degree consists of

1. One factor $\frac{1}{1-x^2}$ for each of the five bilinear invariants $a_j^* a_j$.
2. One factor $\frac{1}{1-x^2}$ for $a_4 a_5^*$ and one for $a_4^* a_5$.
3. One factor $\frac{1}{1-x^3}$ for $a_1^* a_2 a_4$, one for $a_2^* a_3 a_4$, and another for each complex conjugate.
4. One factor $1 + x^4$ in the numerator for the syzygy

$$(a_4 a_5^*)(a_4 a_5^*) - (a_4^* a_4)(a_5^* a_5) = 0$$

5. One factor $1 + x^6$ in the numerator for the syzygy

$$(a_1^* a_2 a_4)(a_1 a_2^* a_4) - (a_1^* a_1)(a_2^* a_2)(a_4^* a_4) = 0$$

   and another for the syzygy involving $a_2^* a_3 a_4$.

The generating function is

$$N(x,d) = \sum_{d=0} N(d) x^d = \frac{(1+x^4)(1+x^6)^2}{(1-x^2)^{5+2}(1-x^3)^{2\times 2}}$$

The invariant polynomials used for constructing an eight-dimensional image dynamical system are

$$\begin{aligned}
p_i &= a_i^* a_i && i = 1,2,3,4,5 \\
p_{6,r} &= a_4 a_5^* + a_4^* a_5 \\
p_{6,i} &= a_4 a_5^* - a_4^* a_5 \\
p_{7,r} &= a_1^* a_2 a_4 + a_1 a_2^* a_4^* \\
p_{7,i} &= a_1^* a_2 a_4 - a_1 a_2^* a_4^* \\
p_{8,r} &= a_2^* a_3 a_4 + a_2 a_3^* a_4^* \\
p_{8,i} &= a_2^* a_3 a_4 - a_2 a_3^* a_4^*
\end{aligned}$$

There are 11 basic invariant polynomials and three constraints. There are 11 real equations of motion, and the flow is restricted to an eight-dimensional subspace in $\mathbb{R}^{11}$. This subspace is defined by the real form of the syzygies

$$\begin{aligned}
p_{6,r}^2 + p_{6,i}^2 &= p_4^2 p_5^2 \\
p_{7,r}^2 + p_{7,i}^2 &= p_1^2 p_2^2 p_4^2 \\
p_{8,r}^2 + p_{8,i}^2 &= p_2^2 p_3^2 p_4^2
\end{aligned}$$

9.1.6 Dimensional Reduction

A reduction in dimension by two is possible because of the symmetries studied in Section 9.1.2. The reduction in dimension can be carried out using the 11 coordinates and three constraints determined in the preceeding section.

An even greater reduction in dimension can be effected, as we now show. The system (9.2) exhibits *dynamical symmetry*, as can be seen in Fig. 9.1. We can exploit this symmetry as follows. Instead of introducing a *polar* decomposition of the form

$$a_i \rightarrow \rho_i e^{i\theta_i} \tag{9.8}$$

where $\rho_i = |a_i|$ as done in Section 9.1.4, we introduce a decomposition of the form

$$a_i \rightarrow \rho_i e^{i\tilde{\theta}_i} \tag{9.9}$$

In this decomposition we absorb the fast variation of θ $(\psi_i(t))$ into the nonnegative amplitude $|a_i|$ to construct a slowly varying amplitude ρ_i that can assume negative as well as positive values. We also remove the slowly varying component of the phase Ω_i. This leaves us with a five-dimensional dynamical system with two different types of variables:

$$\begin{array}{ll} \text{even} & 0 < \rho_1,\ \rho_3 \\ \text{odd} & \rho_2,\ \rho_4,\ \rho_5 \end{array}$$

Once again, the evolution in this five-dimensional phase space is impossible to depict. It is not even clear that this dimension reduction produces a deterministic flow (no self-intersections in this projected flow). However, a projection of this five-dimensional flow onto the ρ_2-ρ_3 plane, shown in Fig. 9.2(a), shows that the flow is deterministic, and even low-dimensional. That is, the flow is effectively three-dimensional. Further evidence for the low dimensionality of this flow is the first-return map on the variable ρ_2, shown in Fig. 9.2(b).

The attractor is shown in Fig. 9.2(a) is one half of an equivariant attractor. The equivariance group is a discrete group of order two

$$(\rho_1, \rho_2, \rho_3, \rho_4, \rho_5) \xrightarrow{\mathcal{G}} (\rho_1, -\rho_2, \rho_3, -\rho_4, -\rho_5) \tag{9.10}$$

As the control parameter ν_2 is increased from $\nu_2 = -0.0345$ to $\nu_2 = -0.0343$ along the line $(\nu_1, \nu_2, \nu_3, \nu_4) = (0.05, \nu_2, 0.03, 0.05)$ in the control parameter space, an attractor merging (symmetry-restoring) crisis occurs. The equivariant connected attractor is shown in Fig. 9.3.

The topology of this attractor is the same as that of the Lorenz attractor. This can be made evident by identifying three of the five variables ρ with the X, Y, and Z variables of the Lorenz system. Under the identification $(\rho_2, \rho_4, \rho_3) \approx (X, Y, Z)$, it is possible to construct the image attractor under the usual local diffeomorphism

$$\begin{array}{rcl} u & = & \rho_2^2 - \rho_4^2 \\ v & = & 2\rho_2\rho_4 \\ w & = & \rho_3 \end{array} \tag{9.11}$$

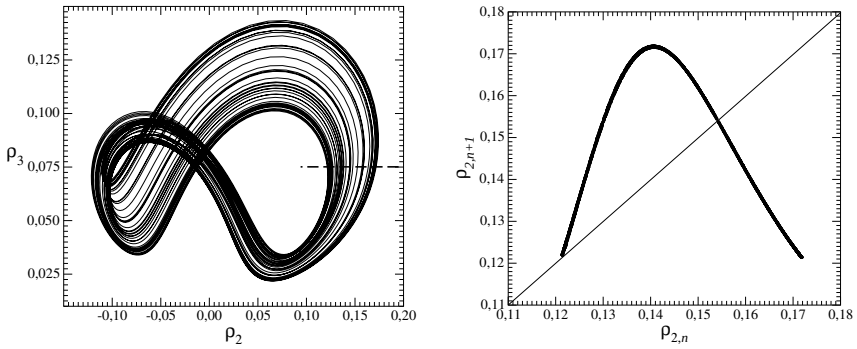

(a) ρ_2-ρ_3 plane projection (b) First-return map

Fig. 9.2 Chaotic behavior generated by the ten-dimensional system in the five real dynamical variables ρ_i. (a) Projection onto the ρ_2-ρ_3 plane is shown along with the Poincaré section. (b) The first-return map on the Poincaré section is a unimodal map with a differentiable maximum. Parameter values: $\nu_1 = 0.050$, $\nu_2 = -0.0345$, $\nu_3 = 0.03$, and $\nu_4 = 0.05$.

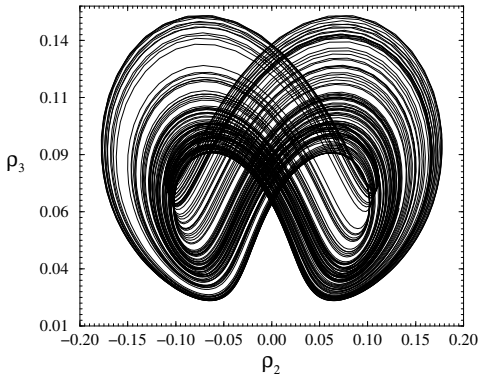

Fig. 9.3 Projection of the chaotic attractor onto the ρ_2-ρ_3 plane after the attractor merging crisis. Parameter values: $\nu_1 = 0.050$, $\nu_2 = -0.0343$, $\nu_3 = 0.03$, and $\nu_4 = 0.05$.

The projection of this image onto the (u, w) subspace is shown in Fig. 9.4. Branched manifolds for the strange attractors shown in Figs. 9.2, 9.3, and 9.4 are shown in Fig. 9.5.

9.2 CONTINUOUS ROTATIONS

Laser models are usually expressed in terms of the electric field $\boldsymbol{E}(\boldsymbol{x}, t)$, the polarisation of an optically active medium $\boldsymbol{P}(\boldsymbol{x}, t)$, and some variable that represents how the optically active medium is excited. When only one electric field mode is ex-

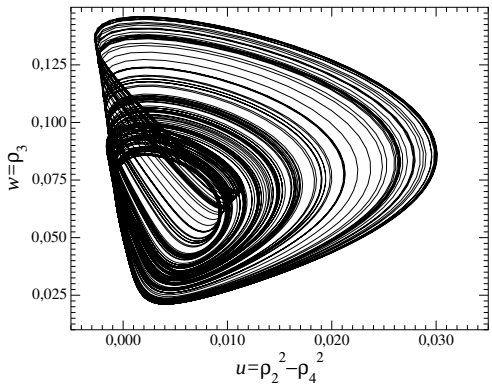

Fig. 9.4 Image of the chaotic attractor without any residual symmetry. Parameter values: $\nu_1 = 0.050$, $\nu_2 = -0.0343$, $\nu_3 = 0.03$, and $\nu_4 = 0.05$.

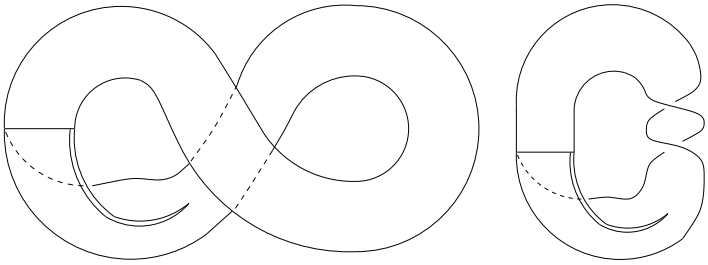

Branched manifold for Fig. 9.2(a) and its image.

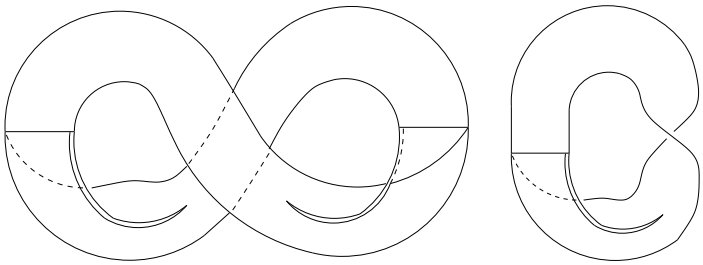

Branched manifold for Fig. 9.3 and its image as shown in Fig. 9.4.

Fig. 9.5 Branched manifolds for dimensionally reduced complex dynamical systems.

cited, the electric field can be represented by a single complex variable in the form $\boldsymbol{E}(\boldsymbol{x},t) = \boldsymbol{\epsilon}X(t)e^{i(k\cdot\boldsymbol{X}-\omega t)}$. Here the space-time dependence of the electric field mode is represented by the factor $e^{i(k\cdot\boldsymbol{X}-\omega t)}$ and $\boldsymbol{\epsilon}$ describes its polarization state. The complex variable $X(t)$ varies on a time scale much slower than the time scale for the propagating wave $[e^{i\omega t}]$. The polarization can be treated similarly.

9.2.1 Zeghlache-Mandel System

Following this procedure, Zeghlache and Mandel [139] proposed a laser model expressed in terms of two complex variables and one real variable ("$2\frac{1}{2}$ complex variables") as follows

$$\begin{aligned}\dot{X} &= -\sigma(1-i\delta)X + \sigma Y \\ \dot{Y} &= RX - (1+i\delta)Y - XZ \\ \dot{Z} &= -\gamma Z + \tfrac{1}{2}(X\bar{Y} + \bar{X}Y)\end{aligned} \tag{9.12}$$

In this model the complex variables X and Y represent the electric field $\boldsymbol{E}$ and the atomic polarization $\boldsymbol{P}$, which describes the response of the atomic system to the imposed electric field. The normalized population inversion is represented by the real variable Z. The control parameters $(R, \sigma = \frac{\gamma_E}{\gamma_P}, \gamma = \gamma_Z)$ represent the pump rate (R) and the relaxation (decay) rates of the electric field, polarization, and population inversion. The parameter δ is the detuning ratio, the difference between the pumping frequency ω and the empty cavity resonance frequency ω_0, normalized by ω_0: $\delta = (\omega - \omega_0)/\omega_0$. When $\delta = 0$ these equations reduce to the Lorenz equations if we interpret X and Y as real variables.

This dynamical system in $2\frac{1}{2}$ complex variables is written as a real five-dimensional dynamical system by expressing X and Y in terms of their real and imaginary parts $X = X_1 + iX_2$, $Y = Y_1 + iY_2$:

$$\begin{aligned}\dot{X}_1 &= -\sigma(X_1 + \delta X_2 - Y_1) \\ \dot{X}_2 &= -\sigma(X_2 - \delta X_1 - Y_2) \\ \dot{Y}_1 &= RX_1 - Y_1 + \delta Y_2 - X_1 Z \\ \dot{Y}_2 &= RX_2 - Y_2 - \delta Y_1 - X_2 Z \\ \dot{Z} &= -\gamma Z + (X_1 Y_1 + X_2 Y_2)\end{aligned} \tag{9.13}$$

9.2.2 Symmetries

These equations are invariant under the symmetry $U(1) : (X, Y, Z) \to (Xe^{i\theta}, Ye^{i\theta}, Z)$, as is easily verified. This symmetry is represented in the $2\frac{1}{2}$ and five dimensional

systems by the matrix equations

$$\begin{bmatrix} e^{i\theta} & 0 & 0 \\ 0 & e^{i\theta} & 0 \\ 0 & 0 & 1 \end{bmatrix} \begin{bmatrix} X \\ Y \\ Z \end{bmatrix} \qquad \begin{bmatrix} \cos\theta & \sin\theta & 0 & 0 & 0 \\ -\sin\theta & \cos\theta & 0 & 0 & 0 \\ 0 & 0 & \cos\theta & \sin\theta & 0 \\ 0 & 0 & -\sin\theta & \cos\theta & 0 \\ 0 & 0 & 0 & 0 & 1 \end{bmatrix} \begin{bmatrix} X_1 \\ X_2 \\ Y_1 \\ Y_2 \\ Z \end{bmatrix}$$

U(1) SO(2) (9.14)

The invariant set for this rotation is the Z-axis and the $U(1)$ or $SO(2)$ group action is represented by $\mathcal{R}_Z(\theta)$. The phase matrix for this dynamical system is determined from the three equations of (9.12)

$$\begin{array}{lll} \text{Eq.} & \text{Term} & \qquad\theta_1 \quad \theta_2 \\ 1 & Y & \begin{bmatrix} -1 & 1 \\ 1 & -1 \\ 1 & -1 \end{bmatrix} \begin{bmatrix} \theta_1 \\ \theta_2 \end{bmatrix} = 0 \\ 2 & X & \\ 3 & X\bar{Y} & \end{array} \tag{9.15}$$

The independent row vector and the null vector are

$$\begin{array}{cc} \text{Independent Row Vector} & \text{Null Vector} \\ \begin{bmatrix} 1 & -1 \end{bmatrix} & \begin{bmatrix} 1 & 1 \end{bmatrix} \end{array} \tag{9.16}$$

The symmetry is $(X_1 + iX_2, Y_1 + iY_2) = (a_1, a_2) \mapsto (a_1 e^{i\alpha}, a_2 e^{i\alpha})$. From the phase matrix we determine the invariant polynomials to be

$$\begin{array}{lll} a_1^* a_1 & \to X_1^2 + X_2^2 & = u_1 \\ a_2^* a_2 & \to Y_1^2 + Y_2^2 & = u_2 \\ a_1^* a_2 & \to (X_1 Y_1 + X_2 Y_2) + i(X_1 Y_2 - X_2 Y_1) & = u_3 + iu_4 \\ a_1 a_2^* & \to (X_1 Y_1 + X_2 Y_2) - i(X_1 Y_2 - X_2 Y_1) & = u_3 - iu_4 \end{array}$$

The invariant polynomial equations involve the five invariant polynomials $u_i (u_5 = Z)$ and one syzygy $u_1 u_2 - (u_3^2 u_4^2) = 0$. The four real equations in the polar representation involve the two positive radial variables ρ_1, ρ_2, the real variable ρ_3, and the phase difference $\Phi_1 = \phi_1 - \phi_2$.

9.2.3 Fixed Points

The fixed points are obtained as usual by setting all time derivatives equal to zero. There is always one fixed point at the origin $(X, Y, Z) = (0, 0, 0)$. If there is a second ("real") fixed point, it satisfies the relations

$$\begin{aligned} Z &= R - (1 + \delta^2) \\ |X| &= \sqrt{\gamma Z} \\ Y &= (1 - i\delta)X \end{aligned}$$

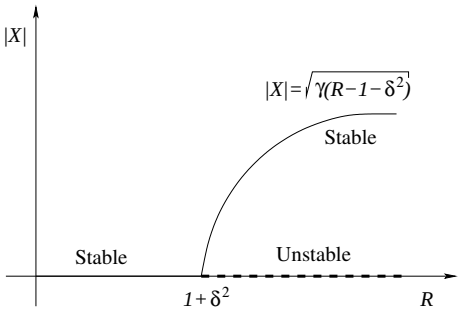

Fig. 9.6 Symmetry-restricted pitchfork bifurcation for the Zeghlache-Mandel equations as a function of increasing R.

The second "fixed point," is actually a continuous circle of fixed points. It bifurcates from the fixed point at the origin in a symmetry-restricted pitchfork bifurcation as R increases above $1 + \delta^2$. This bifurcation diagram is shown in Fig. 9.6. The fixed point at the origin is stable for $R < 1 + \delta^2$, unstable for $R > 1 + \delta^2$. The bifurcation circle [U(1)] of fixed points is stable for $R > 1 + \delta^2$. For $R < 1 + \delta^2$ it is a circle of imaginary fixed points.

Remark: Normally a pitchfork bifurcation involves a search for minima of the potential $V(x) = \frac{1}{4}x^4 + \frac{1}{2}\mu x^2$. There is one stable equilibrium at $x = 0$ for $\mu > 0$. There are three equilibria for $\mu < 0$, an unstable one at $x = 0$ and two stable equilibria at $x = \pm\sqrt{-\mu}$. If for some physical reason x must be positive or zero (e.g., x represents a radius) the pitchfork bifurcation is said to be symmetry-restricted.

9.2.4 Dynamics

The dynamics of the Zeghlache-Mandel equations can be determined, to some extent, by integrating this real five-dimensional system. Projections of the attractor into the electric field plane and polarization plane are shown in Fig. 9.7(a) and (b). Both projections are quite "spiky." However, the two projections are highly correlated, as can be seen by superposing one on the other. To emphasize this point, we show the Y_1 versus X_1 and Y_2 versus X_2 projections in Fig. 9.8(a) and (b). Both are strongly suggestive of the Lorenz attractor. This should not be too surprising, as these equations reduce to the Lorenz equations in the limit of zero detuning: $\delta \to 0$.

The evolution of the dynamics away from the Lorenz attractor is shown in Fig. 9.9. In the left column we shown the flow projected onto the (X, Z) plane as a function of increasing detuning. For $\delta = 0.002$ the projection is indistinguishable from the Lorenz attractor. As δ increases it appears that the attractor becomes somewhat "shaky."

When the detuning is increased up to $\delta = 0.69$, a quasi-periodic motion is observed (Fig. 9.9(c)). This is a two-frequency torus. These frequencies, f_x and f_y, are associated with the rotation occurring in the planes (X_1, X_2) and (Y_1, Y_2), re-

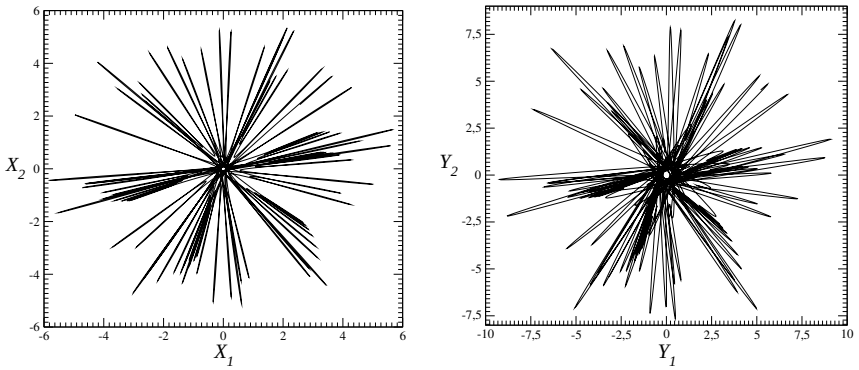

Fig. 9.7 Projections of the Zeghlache-Mandel attractor onto the (a) X_1-X_2 plane and (b) the Y_1-Y_2 plane. Parameter values: $R = 28.0$, $\gamma = 0.25$, $\delta = 0.10$, and $\sigma = 2.0$.

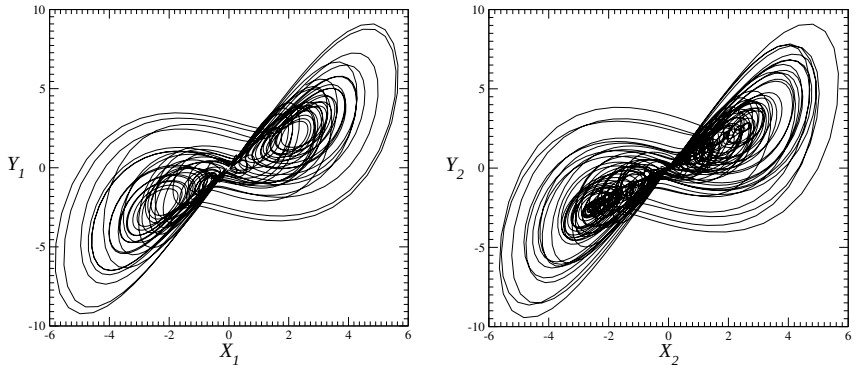

Fig. 9.8 Projections of the Zeghlache-Mandel attractor onto the (a) X_1-Y_1 plane and (b) the X_2-Y_2 plane. Parameter values: $R = 28.0$, $\gamma = 0.25$, $\delta = 0.10$, and $\sigma = 2.0$.

spectively. Both are associated with a continuous rotation around the axis Oz. Other types of quasi-periodic motions may be observed as exemplified with $\delta = 1.0$ (Fig. 9.9(d)).

In the right column of Fig. 9.9 we plot the Poincaré section in the polarization plane (Y_1, Y_2). Both directions of intersection of the flow with this plane are retained. The dashed curve represents the intersection of this plane with the circle of fixed points due to the continuous symmetry. The solid circles represent intersections of the quasiperiodic motions with the Poincaré section.

(a) $\delta = 0.002$

(b) $\delta = 0.1$

(c) $\delta = 0.69$

(d) $\delta = 1.0$

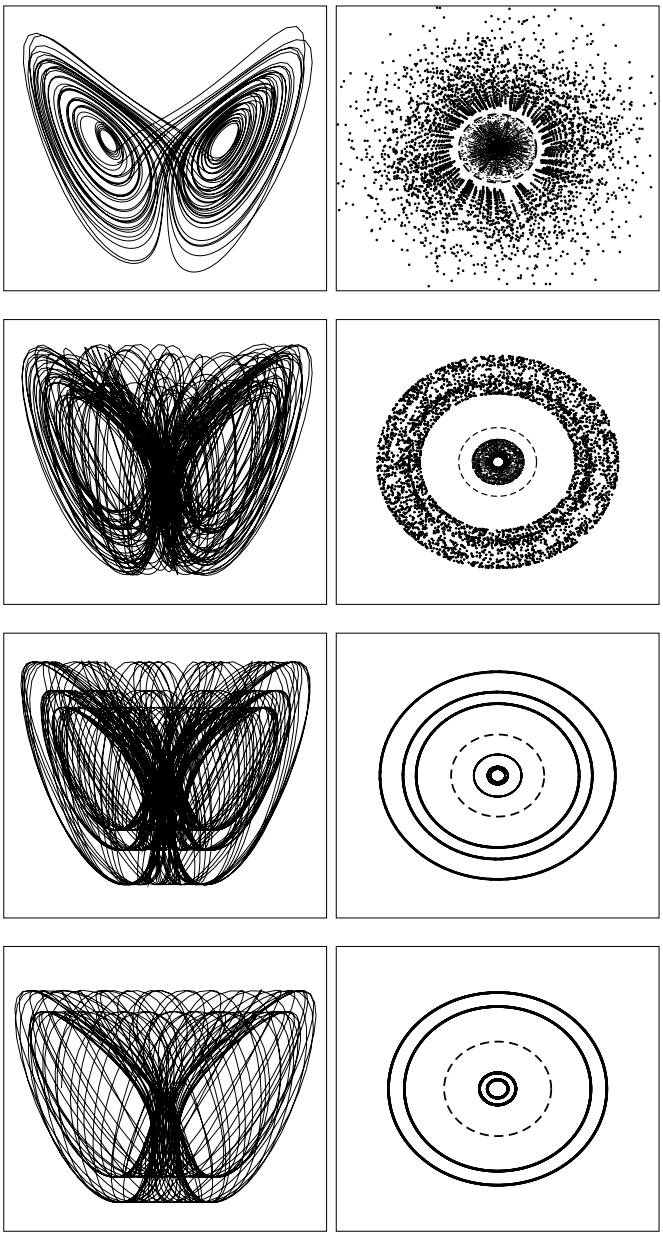

Fig. 9.9 Evolution of the dynamics as a function of the detuning δ. The left column corresponds to (X_1, Z) plane projections of the phase portraits embedded in the original phase space $\mathbb{R}^5(X_1, X_2, Y_1, Y_2, Z)$. The right column provides Poincaré sections in the plane (Y_1, Y_2). Both directions of intersections with a transverse plane are retained for these Poincaré sections. In the Poincaré section, the dashed line represents the section of the torus of fixed points. Parameter values: $R = 24.0$, $\sigma = 2.0$, and $\gamma = 0.25$.

9.2.5 Dynamics in Polar Coordinates

The reduced dynamical equations can also be expressed in a more traditional "polar" decomposition. We introduce new variables (ρ, ϕ) according to

$$\begin{aligned} X &= \rho_1 e^{i\phi_1} \\ Y &= \rho_2 e^{i\phi_2} \\ Z &= \rho_3 \end{aligned}$$

where $\rho_1 > 0$, $\rho_2 > 0$, and $-\infty < \rho_3 < \infty$. The dynamical system equations are invariant under the tranformation

$$\begin{aligned} X &\to X e^{i\theta} \\ Y &\to Y e^{i\theta} \end{aligned}$$

The equations can be expressed in terms of the three variables ρ_i $(i = 1, 2, 3)$ and one linear combination of the two angles: $\phi_1 - \phi_2$. An independent linear combination leaves the equations unchanged, and so is similar to a "Goldstone mode." The dynamical system equations in the new set of variable are

$$\begin{aligned} \dot{\rho}_1 &= -\sigma\Delta\cos\alpha + \sigma\rho_2\cos\Phi \\ \dot{\rho}_2 &= R\rho_1\cos\Phi - \Delta\cos\alpha\rho_2 - \rho_1\rho_2\cos\Phi \\ \dot{\rho}_3 &= -\gamma\rho_3 + \rho_1\rho_2\cos\Phi \\ \dot{\Phi} &= (\sigma+1)\Delta\sin\alpha - \left(\sigma\frac{\rho_2}{\rho_1} + R\frac{\rho_1}{\rho_2} - \frac{\rho_1\rho_3}{\rho_2}\right)\sin\Phi \end{aligned} \tag{9.17}$$

where we have defined

$$\begin{aligned} \Delta e^{i\alpha} &= 1 + i\delta \\ \Phi &= \phi_1 - \phi_2 \end{aligned}$$

Integration of the dynamical system equations in polar format (9.17) is much less stable than integration of the same equations in cartesian format (9.13).

9.2.6 Reduction of Dimension by Symmetry

It is useful to introduce invariant coordinates. They can be chosen as

$$\begin{aligned} u_1 &= X_1^2 + X_2^2 \\ u_2 &= Y_1^2 + Y_2^2 \\ u_3 &= X \cdot Y \quad = \quad X_1Y_1 + X_2Y_2 \\ u_4 &= X \times Y \quad = \quad X_1Y_2 - X_2Y_1 \\ u_5 &= Z \end{aligned} \tag{9.18}$$

These coordinates obey the following relation

$$\begin{aligned} \left(X_1^2 + X_2^2\right)\left(Y_1^2 + Y_2^2\right) - \left(X_1Y_1 + X_2Y_2\right)^2 - \left(X_1Y_2 - X_2Y_1\right)^2 &= 0 \\ u_1 \qquad\quad u_2 \quad - \quad u_3^2 \quad - \quad u_4^2 &= 0 \end{aligned} \tag{9.19}$$

The equations of motion for the five invariant coordinates are

$$\begin{aligned}
\dot{u}_1 &= -2\sigma u_1 + 2\sigma u_2 \\
\dot{u}_2 &= 2Ru_3 - 2u_2 - 2u_3u_5 \\
\dot{u}_3 &= (R - u_5)u_1 + \sigma u_2 - (\sigma + 1)(u_3 - \delta u_4) \\
\dot{u}_4 &= -(\sigma + 1)(u_4 + \delta u_3) \\
\dot{u}_5 &= -\gamma u_5 + u_3
\end{aligned}$$

It is a simple matter to verify that the constraint surface

$$u_1u_2 - u_3^2 - u_4^2 = 0$$

is invariant directly from these equations, for

$$\frac{d}{dt}(u_1u_2 - u_3^2 - u_4^2) = u_1\dot{u}_2 + \dot{u}_1u_2 - 2u_3\dot{u}_3 - 2u_4\dot{u}_4 = 0$$

As a result, the dynamics is confined to a four-dimensional subspace in $\mathbb{R}^5$.

Mapping to the image dynamical system simplifies the analysis of this dynamical system. A number of projections are shown in Fig. 9.10. The projections into the (u_1, u_2), (u_1, u_3) and especially the (u_1, u_5) and (u_3, u_4) planes clearly show a Rössler-type band with a simple folding. This suggests strongly that the dynamics is three dimensional.

9.2.7 Dynamical Reduction

This system exhibits a strong correlation between the electric field and the polarization. This correlation effectively reduces the dimension even below the minimum dimension (four) allowed by the symmetry restriction. The correlation reduces the dimension to three. To show this is the case, we constructed a differential embedding based on the Z coordinate. The projection of the attractor in the three-dimensional $(Z, \dot{Z}, \ddot{Z})$ space onto the $(Z, \dot{Z})$ plane is shown in Fig. 9.11(a). The return map on the $\dot{Z}$ coordinate for the Poincaré section is shown in Fig. 9.11(b). The cusped nature of the return map is very similar to the return map for the Lorenz attractor. It indicates that tearing occurs in the five-dimensional system.

As previously discussed, an image system will greatly simplify the analysis by disentangling the properties which are due to the symmetry. To mod out the symmetry properties, both static and dynamic, the image system induced by the Z variable and its successive time derivatives is used. Fig. 9.11 the dynamics can be described in a three-dimensional phase space spanned by the derivative coordinates $(x, y, z) = (Z, \dot{Z}, \ddot{Z})$. The phase portraits are similar to those generated by the image of the Lorenz system (1.4). A first-return map to the Poincaré section in Fig. 9.11(a) is shown in Fig. 9.11(b). The maximum of this map is a cusp, as usually observed for the Lorenz system. A sequence of attractors, return maps, and periodic orbits are shown in Fig. 9.12 for the differentially embedded attractor corresponding to the control parameters

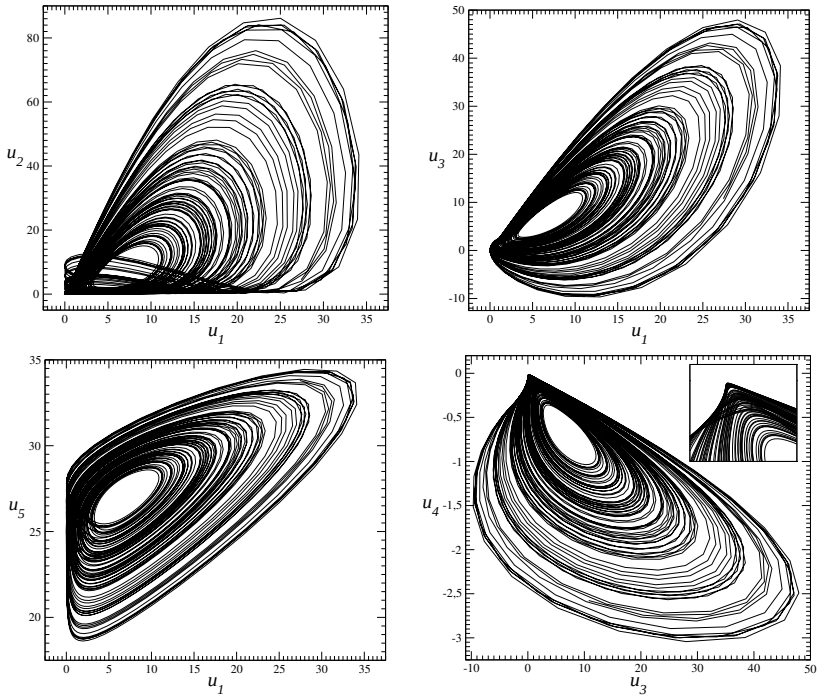

Fig. 9.10 Phase portraits of the image of the Zeghlache-Mandel equations for $R = 28.0$, $\gamma = 0.25$, $\delta = 0.10$, and $\sigma = 2.0$.

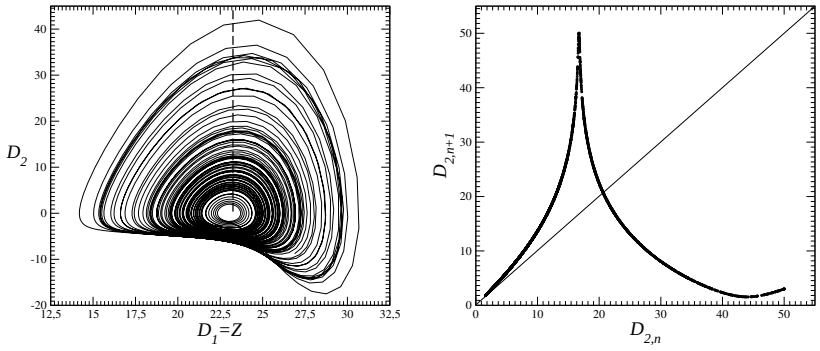

Fig. 9.11 Phase portrait and first return map for the image of the Zeghlache-Mandel equations for $R = 24.0$, $\gamma = 0.25$, $\delta = 0.01$ and $\sigma = 2.0$. Here $D_1 = Z$ and $D_2 = \dot{Z}$.

used for the cover attractor in Fig. 9.9. Fig. 9.13 provides a bifurcation diagram for the differentially embedded (image) attractor without symmetry. Period doubling cascades as well as some of the larger low-period windows are clearly visible in this bifurcation diagram. The branched manifold that describes this strange attractor is shown in Fig. 9.14.

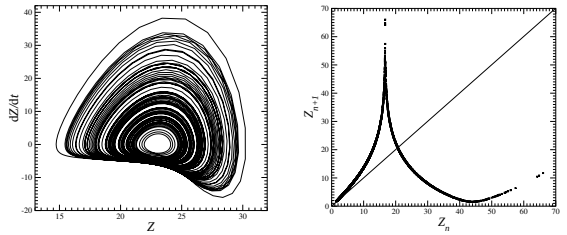

(a) $\delta = 0.002$

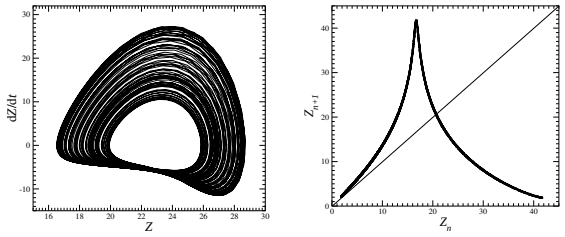

(b) $\delta = 0.1$

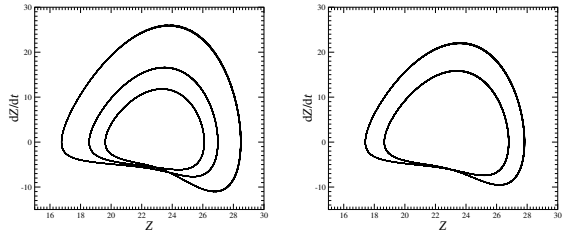

(c) $\delta = 0.69$ (d) $\delta = 1.0$

Fig. 9.12 Evolution of the dynamics as a function of the detuning δ. The attractors (a), (b) are obtained from a differential embedding. The projection onto the $(Z, \dot{Z})$ plane is shown. The dynamics is that of a Smale horseshoe. A return map on $\dot{Z}$ is given for each. Period-3 (c) and -2 (d) orbits are shown. Parameter values: $R = 24.0$, $\sigma = 2.0$, and $\gamma = 0.25$.

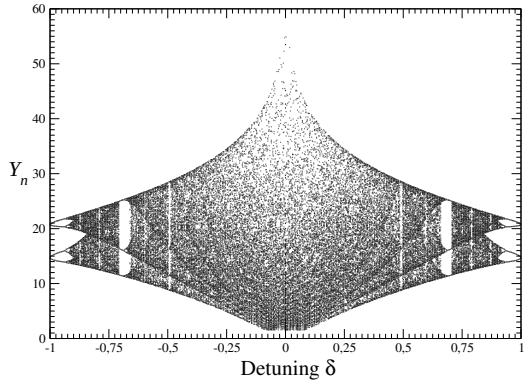

Fig. 9.13 Bifurcation diagram versus the detuning δ computed in the Poincaré section P_I of the image system.

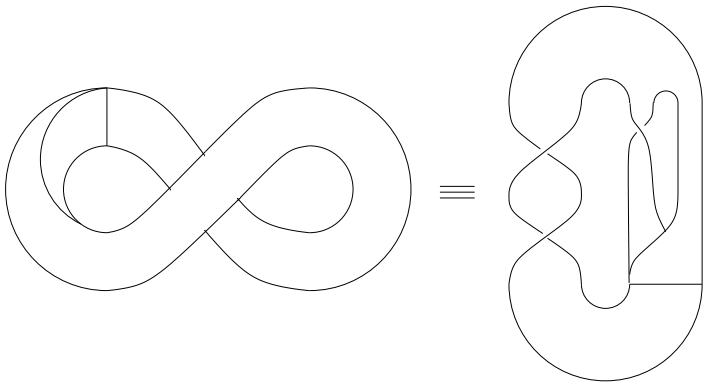

Fig. 9.14 Template of the chaotic attractor generated by the system (9.13) when the continuous symmetry is modded out. It is a reverse horseshoe template with a global torsion of one.

9.3 THOMAS' SYSTEM

A system with an $\mathcal{S}_6$ symmetry has been proposed by R. Thomas [122]:

$$\begin{aligned} \dot{x} &= -bx + ay - y^3 \\ \dot{y} &= -by + az - z^3 \\ \dot{z} &= -bz + ax - x^3 \end{aligned} \tag{9.20}$$

This dynamical system is invariant under the group $\mathcal{C}_3$ of rotations by $2\pi/3$ radians about the (1,1,1) axis that sends $(X, Y, Z) \mapsto (Y, Z, X)$ and the inversion group $\mathcal{P}$ that sends $(X, Y, Z) \mapsto (-X, -Y, -Z)$. The direct product of these two groups is $\mathcal{C}_3 \times \mathcal{P} = \mathcal{S}_6$. This group is generated by $S_6 = C_3 \times P$ consisting of a rotation by $2\pi/6$ radians about the (1,1,1) axis followed by an inversion. The matrix generator for this group is

$$\gamma = \begin{bmatrix} 0 & -1 & 0 \\ 0 & 0 & -1 \\ -1 & 0 & 0 \end{bmatrix} \tag{9.21}$$

with $\gamma^6 = \mathbb{I}$. This group is commutative.

9.3.1 Fixed Points

For all values of (a, b) the origin $(x, y, z) = (0, 0, 0)$ is a fixed point. It is 6-fold degenerate. The Jacobian is the cyclic matrix:

$$\mathcal{J} = \begin{bmatrix} -b & a & 0 \\ 0 & -b & a \\ a & 0 & -b \end{bmatrix} \tag{9.22}$$

with eigenvalues $-b+a\epsilon^j$ where $\epsilon = e^{\frac{2\pi i}{3}}$ and $j = 0, 1, 2$. There are two fixed points along the $(1, 1, 1)$ rotation axis at $x = y = z = \pm\sqrt{a-b}$. The eigenvalues at these fixed points are $-b + (3b - 2a)\epsilon^j$.

In general, this system has 27 fixed points. For $b = 0.3$ and $a = 1.1$ they are all real and tabulated below.

	x	y	z
F_0	0.0000	0.0000	0.0000
F_I	± 0.8944	± 0.8944	± 0.8944
F_{II}	± 1.0370 ± 0.0850 ± 0.3098	± 0.3098 ± 1.0370 ± 0.0850	± 0.0850 ± 0.3098 ± 1.0370
F_{III}	± 1.0128 ± 0.2502 ± 0.8653	± 0.8653 ± 1.0128 ± 0.2502	± 0.2502 ± 0.8653 ± 1.0128
F_{IV}	± 1.0953 ∓ 0.3643 ∓ 1.1746	∓ 1.1746 ± 1.0953 ∓ 0.3643	∓ 0.3643 ∓ 1.1746 ± 1.0953
F_V	± 1.1796 ∓ 1.1461 ± 0.8164	± 0.8164 ± 1.1796 ∓ 1.1461	∓ 1.1461 ± 0.8164 ± 1.1796

The eigenvalues for these fixed points are

F_I	$\lambda_{1,2}$	$=$	$+0.35 \pm 1.1258\, I$
	λ_3	$=$	-1.6
F_{II}	$\lambda_{1,2}$	$=$	$+0.31506 \pm 1.0653\, I$
	λ_3	$=$	-1.5301
F_{III}	$\lambda_{1,2}$	$=$	$-.93704 \pm 1.1034\, I$
	λ_3	$=$	$+0.97409$
F_{IV}	$\lambda_{1,2}$	$=$	$-1.1734 \pm 1.5128\, I$
	λ_3	$=$	$+1.4469$
F_V	$\lambda_{1,2}$	$=$	$+0.69404 \pm 1.7217\, I$
	λ_3	$=$	-2.2880

All of these fixed points are either stable foci with an unstable perpendicular direction or unstable foci with a stable perpendicular direction.

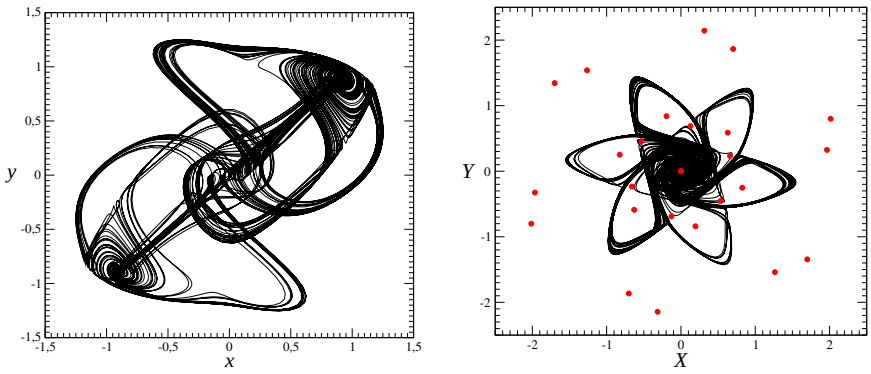

(a) Plane projection $\mathbb{R}^2(x, y)$ (b) Plane projection $\mathbb{R}^2(X, Y)$

Fig. 9.15 A single attractor generated by the Thomas system for $a = 1.1$. The 27 fixed points are shown in the plane projection $\mathbb{R}^2(X, Y)$. Note that points F_I cannot be distinguished from the point located at the origin of the projection $\mathbb{R}^2(X, Y)$.

9.3.2 Symmetry

In order to have a better representation of the symmetry properties, we use the coordinate transformation:

$$\begin{aligned} X &= \frac{\sqrt{3}}{2}(y - x) \\ Y &= z - \frac{x + y}{2} \\ Z &= x + y + z \end{aligned} \tag{9.23}$$

The Z-axis is the (1,1,1) rotation axis while the (X, Y) coordinates parametrize the plane through the origin perpendicular to the rotation axis. Projection of the attractor onto the X, Y plane clearly shows the 6-fold symmetry of the dynamical system. For example, a single connected attractor for $(a, b) = (1.1, 0.3)$ is shown in the x-y projection in Fig. 9.15(a) and X-Y plane in Fig. 9.15(b). The locations of the 27 fixed points are shown in the latter projection where their symmetry is apparent.

A projection of the $6 \mapsto 1$ image is obtained using the coordinate transformation:

$$\begin{aligned} u &= \Re(X + iY)^6 = X^6 - 15X^4Y^2 + 15X^2Y^4 - Y^6 \\ v &= \Im(X + iY)^6 = 6X^5Y - 20X^3Y^3 + 6XY^5 \end{aligned} \tag{9.24}$$

This projection is shown in Fig. 9.16. The inset to this figure shows the deformation of the image attractor in the neighborhood of the origin.

9.3.3 Bifurcation Studies

The bifurcation diagram for the equivariant system (9.20) is complicated and difficult to understand. The bifurcation properties of the $6 \mapsto 1$ image are *much* simpler to

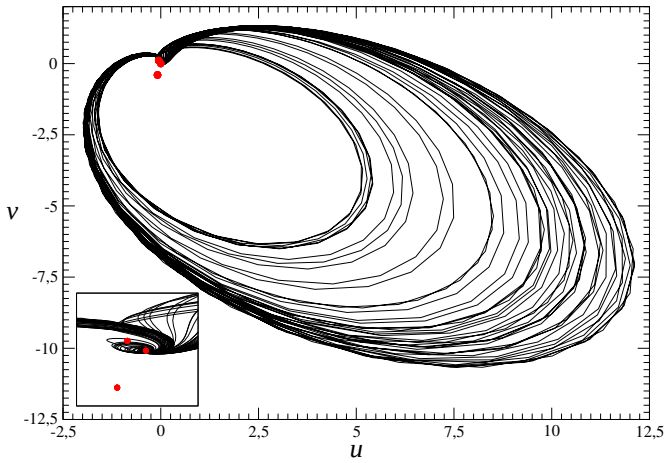

Fig. 9.16 Image of the single attractor generated by the Thomas system for $a = 1.1$.

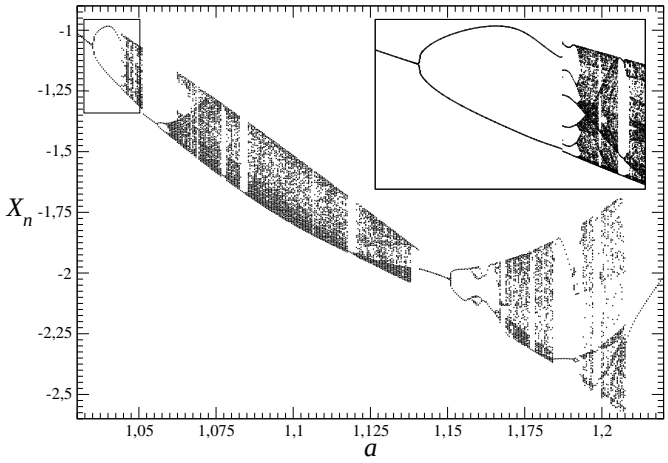

Fig. 9.17 Bifurcation diagram for the Thomas system versus a for $b = 0.3$.

visualize and interpret. The two systems are locally diffeomorphic: therefore very little information is lost in studying the simpler bifurcation diagram. A bifurcation diagram for the $6 \rightarrow 1$ image of the Thomas attractor, shown in Fig. 9.16 for $a = 1.1$, is presented in Fig. 9.17 as a function of a, $1.1 \leq a \leq 1.22$, for fixed value of $b = 0.3$. It should be clear from this figure that a bifurcation diagram based on the covering attractor would be practically impossible to disentangle.

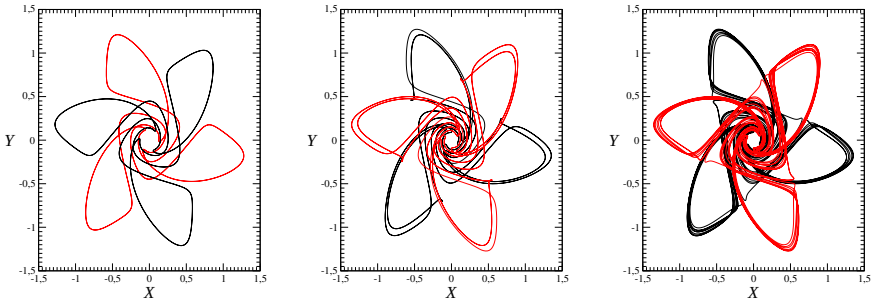

(a) Two symmetry-related period-three lifts of a period-1 limit cycle for $a = 1.030000$

(b) Two symmetry-related period-6 lifts of a period-2 limit cycle for $a = 1.044193$

(c) Two period-18 lifts of a period-6 limit cycle for $a = 1.044300$

Fig. 9.18 The period-1, -2, and -6 stable limit cycles shown at the beginning of the bifurcation diagram Fig. 9.17 of the image system lift to pairs of symmetry-related orbits in the cover. The covering orbits have three times the period of the image orbit.

9.3.4 Periodic Orbits

The bifurcation diagram shows that the image has a period-one orbit for $a = 1.03$ that undergoes a period-doubling bifurcation at $a \simeq 1.035$. A stable period-six orbit exists for a short range of a control parameter values slightly below $a = 1.05$. These orbits are simple to find in the image attractor, simply by allowing transients to die out. The image orbits can easily be lifted into the covering system by inverting the local diffeomorphism connecting the two. The lifted orbits are shown in Fig. 9.18. Fig. 9.18(a) shows that the period-one orbit lifts to a pair of symmetry-related period-three orbits in the covering system, while Fig. 9.18(b) shows that the period-two orbit in the image lifts to a pair of symmetry-related period-six orbits in the cover. The period-6 image orbit lifts to a pair of symmetry-related period-18 orbits in the cover, as shown in Fig. 9.18(c).

9.3.5 Period-Doubling Cascades

The bifurcation diagram shows that for a slightly greater than 1.05 a crisis occurs and the chaotic attractor becomes a repellor, as a globally attracting period-one orbit is created in a saddle-node bifurcation. This orbit undergoes a period-doubling cascade to create another strange attractor. Lifts of trajectories in this sequence are shown in Fig. 9.19. This time the period-one orbit lifts to six symmetry-related orbits in the cover. These are shown in Fig. 9.19(a). The six symmetry-related strange attractors (in the cover) that result at the end of this periodic doubling cascade are shown in Fig. 9.19(b). Finally, a first-return map for the image attractor shows that a simple

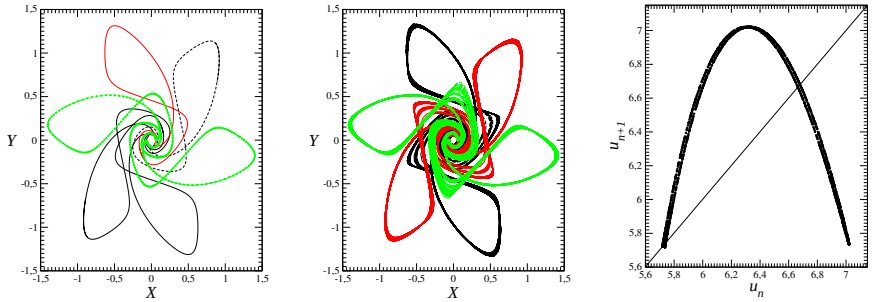

(a) 6 period-1 limit cycles for $a = 1.0550$

(b) 6 coexisting chaotic attractors for $a = 1.0623$

(c) First-return map of an attractor for $a = 1.0623$

Fig. 9.19 (a) Six period-1 limit cycles in the cover induce six simultaneous period-doubling cascades leading to (b) coexisting attractors. (c) Unimodal first-return map with a complete symbolic dynamics shows that the image strange attractor that appears in Fig. 9.16 is created by a simple horseshoe mechanism.

stretch-and-fold mechanism is at work to create chaos in the image of the Thomas dynamical system.

9.4 SYMMETRY BREAKING AND RESTORATION

9.4.1 Modeling

Model-making is a vast field. It usually proceeds along the following lines:

1. Construct a model, including some free parameters.
2. Fit observational data by adjusting the free parameters.
3. Determine if the fitted model is any good.

The first step in this process usually requires some insight into the physical processes responsible for the data that have been or will be observed. The second step usually involves some sort of optimization procedure, such as a least squares fit or a maximum liklihood estimate. This step determines the "best" model within the class that has been proposed. The fact that a particular model (including fitted parameters) is the best within the class being considered is no guarantee that the model is any good at all. This must be determined by some additional procedure. Unfortunately, this last step is often overlooked. Proper implementation of this step falls within the realm of the subject called statistics [102]. A number of statistical tests exist to determine the worthiness of a model. Roughly speaking, all depend on two assumptions:

1. The model is linear in some sense (general linear model).
2. Observational errors are normally distributed.

Chief among the goodness-of-fit tests is the χ^2 test.

In recent years a lot of effort has gone into the development of nonlinear models to describe physical systems that generate behavior that appears to be chaotic. At present there is no Nonlinear counterpart to the χ^2 test for linear models.

There is evidence that an entrainment test can be developed that will play the role, for nonlinear systems, that the χ^2 test currently plays for linear systems.

Suppose that a physical process is described by a set of coupled nonlinear ordinary differential equations depending on control parameters and having the form

$$\frac{dx_i}{dt} = f_i(x; c) \tag{9.25}$$

For the moment we assume that all components of the phase space vector $(x_1, x_2, \ldots, x_n)$ can be measured.

Next, assume that a set of coordinates $(y_1, y_2, \ldots, y_n)$ is introduced in an attempt to model the behavior of the corresponding coordinates in the physical phase space. Further, we guess a set of that equations provides a reasonable model for the physical behavior

$$\frac{dy_i}{dt} = f_i(y; c') \tag{9.26}$$

The fundamental question is: Is this model a good representation of the physical process? If yes: How good?

To approach this question, we observe

1. If the model is exact ($c' = c$) and
2. The initial conditions are identical ($y(0) = x(0)$)

then in principle for all future times $y(t) = x(t)$. Of course this is a nongeneric situation. If either of the two conditions above is not satisfied (normally both are not satisfied) the trajectories $x(t)$ in the physical phase space and $y(t)$ in the model phase space will eventually diverge—the worse the model/initial condition difference, the sooner the divergence.

9.4.2 Entrainment

In order to slow down or even prevent this divergence it is customary to add a perturbation to the model equations to "nudge" the model behavior closer to the observed physical behavior. The simplest class of perturbations is linear in the differences:

$$\frac{dy_i}{dt} = f_i(y; c') - \lambda_{ij}(y_j - x_j) \tag{9.27}$$

Even in this form the perturbation has a tensor structure, with n^2 components. A simpler class of pertrubations involves only the diagonal subset, where only differences of the jth variable are used to nudge the equation for the evolution of the jth variable. An even more economical class of perturbations involves the application of

perturbation terms to the special subset of the most observable coordinates [61], such as the x or y variables of the Rössler system.

When the control parameters are close in some sense ($\delta c = c' - c$ is small), then only a small value of the coupling parameter λ should be required to keep the model values $y(t)$ entrained with the observed values $x(t)$.

Entrainment tests can be carried out as follows. Fix $\lambda_i > 0$, $c' = c$, and $y(0) = x(0)$. Under these conditions $z(t) = y(t) - x(t)$ is zero. As δc increases, the state variable differences $|y_i(t) - x_i(t)|$ will slowly increase. The larger the value of λ, the larger the value of δc before this difference becomes too large.

The entrainment test as presented in Eq. (9.27) lacks a certain symmetry: the original dynamical system as represented by the forcing terms $f(x; c)$ and the model of it, as represented by the forcing terms $f(y; c')$ are not treated on an equal footing. The dynamical system represented by these equations is *reducible*. For this reason the difference $y_i - x_i$ may not vanish even when δc is small and the coupling coefficients λ are large.

9.4.3 Mutual Entrainment

To avoid this problem we propose a more symmetric version of the entrainment test using an *irreducible* description of the coupled dynamics. In this description the couple equations have the form

$$\begin{aligned} \frac{dx_i}{dt} &= f_i(x; c) - \lambda_i(x_i - y_i) \\ \frac{dy_i}{dt} &= f_i(y; c') - \lambda_i(y_i - x_i) \end{aligned} \tag{9.28}$$

This couple set of equations describes a $2n$-dimensional dynamical system with state variables $(x_1, x_2, \ldots, x_n; y_1, y_2, \ldots, y_n)$.

When $c' = c$ the coupled set of Eq. (9.28) has a two-fold symmetry under the permutation group P_2 that interchanges the x and y coordinates: $x \to y, y \to x$. It is useful to choose linear combinations of the coordinates that are adapted to this symmetry, namely $X_i = \frac{1}{2}(x_i + y_i)$ and $\delta_i = \frac{1}{2}(x_i - y_i)$. In this coordinate system the dynamical equations are

$$\begin{aligned} \frac{dX_i}{dt} &= \tfrac{1}{2}\left(f_i(X + \delta; c) + f_i(X - \delta; c)\right) \\ \frac{d\delta_i}{dt} &= \tfrac{1}{2}\left(f_i(X + \delta; c) - f_i(X - \delta; c)\right) - \lambda_i \delta_i \end{aligned} \tag{9.29}$$

This representation shows clearly that the n-dimensional subspace $(X, \delta = 0)$ is invariant: an initial condition in this submanifold will remain in this submanifold.

When $c' \neq c$ the two-fold symmetry is broken, but it is possible to hope that there still exists an n-dimensional invariant manifold for reasonably small values of the coupling parameter λ. Eventually, for fixed values of λ, when $\delta c = c' - c$ becomes

sufficiently large, it is expected that there is a bifurcation that allows motion to extend into a manifold of dimension d, $n < d \leq 2n$. The relation between the critical values of δc and λ at which such a bifurcation occurs is currently not known.

The entrainment statistic we propose is based on the kind of computation shown in Fig. 9.20. Two Rössler systems are coupled together as described in Equ. (9.28). The mean value of $|y_i(t) - x_i(t)|$, averaged over the attractor, is plotted as a function of the parameter difference $\delta a = a_{\rm model} - a_{\rm data}$ ($a_{\rm data} = 0.398$ and $(b, c)_{\rm model} = (b, c)_{\rm data} = (2.0, 4.0)$) for several values of the coupling strength λ. Coupling in the x-variable ($i = 1$) is shown in Fig. 9.20(a) and in the y-variable ($i = 2$) is shown in Fig. 9.20(b). These plots show that the average mean error falls off sharply as the control parameters of the model and the physical system approach equality, for fixed value of the coupling parameter λ. Read in the vertical direction, they show that for fixed value of the control parameter difference, increasing the coupling decreases the mean error.

Coupling of the z-variable ($i = 3$) does not produce similar results, as observability using the z variable is much degraded compared to observability using either of the other two variables [61]. This lack of symmetry in the three variables of the Rössler attractor is summarized in Fig. 9.21, which shows the mean error when the coupling is done separately in the x-, y-, and z-directions, all with the same numerical value of the coupling strength $\lambda_i = 0.15$. This figure shows pratically no response for coupling in the z direction as the model parameters sweep past the actual parameter values.

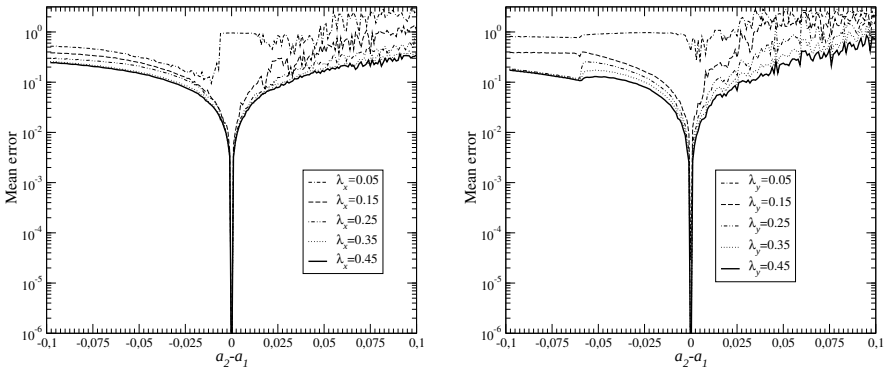

(a) Coupling in the x-variable (b) Coupling in the y-variable

Fig. 9.20 Mean error $|y_i(t) - x_i(t)|$ as a function of difference $\delta a = a_{\rm model} - a_{\rm data}$ for several values of the coupling constant. (a) $i = 1$, coupling in the x-variable. (b) $i = 2$, coupling in the y-variable.

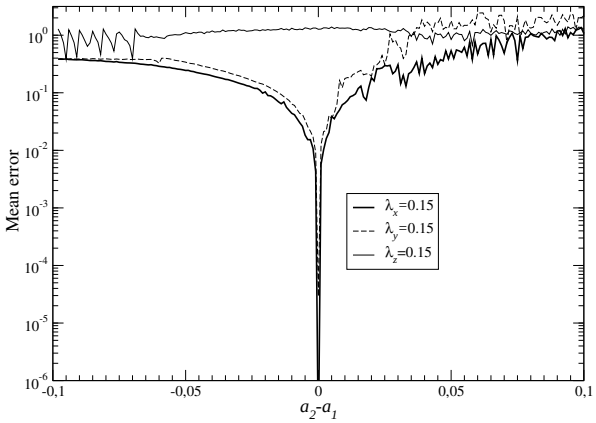

Fig. 9.21 Mean value of the error $|y_i(t) - x_i(t)|$ for coupling in the x-, y-, and z-directions.

Part II

Mathematical Foundations

10

Group Theory Basics

10.1 DYNAMICAL SYSTEMS

Dynamical systems are sets of first-order ordinary differential equations of the form

$$\frac{dx}{dt} = f(x; c) \tag{10.1}$$

The variables $x = (x_1, x_2, \cdots, x_n)$ are called *state variables*. They are coordinates of a point p contained in a suitable phase space: $x(p) = (x_1(p), x_2(p), \cdots, x_n(p))$. The phase space is a manifold that can have just about any topological structure. For example, in the simple case $n = 2$ the phase space can be a plane $\mathbb{R}^2$, a sphere S^2, a cylinder $\mathbb{R}^1 \times S^1$, a torus $S^1 \times S^1$, a Möbius strip, a Klein bottle, etc. Since our objective in this work is to study dynamical systems with symmetry (under *linear*

transformations), we constrain our study to dynamical systems in Euclidean spaces $\mathbb{R}^n$.

The parameters $c = (c_1, c_2, \cdots, c_k)$ are called *control parameters*. They are parameters that typically appear in the dynamical systems equations. For example, for the Lorenz equations (2.1) the three control parameters are $c = (c_1, c_2, c_3) = (R, \sigma, b)$ and for the Rössler equations (5.7) they are $c = (c_1, c_2, c_3) = (a, b, c)$. The control parameters are points in a k-dimensional manifold whose global topology is less important than that of the phase space.

The dynamical systems equations (10.1) are typically coupled nonlinear equations. They are deterministic under mild conditions on the source functions $f(x; c)$. Trajectories exist through any point at which a *Lipschitz condition* is satisfied. Such trajectories are locally extendable and unique. Specifically, the theorem is as follows [5].

Existence and Uniqueness Theorem: If the dynamical system $dx/dt = f(x; c)$ satisfies the Lipschitz condition

$$|f(x; c) - f(x_0; c)| < K(c)|x - x_0| \tag{10.2}$$

at x_0, then there is a positive number, s, and:

Existence: There is a set of functions $\phi(t) = (\phi_1(t), \phi_2(t), \cdots, \phi_n(t))$ that satisfies the dynamical system equations $d\phi_i(t)/dt = f_i(\phi(t); c)$ in the interval $-s \leq t \leq +s$, with $\phi(0) = x_0$.

Uniqueness: The function $\phi(t)$ is unique.

If the source functions $f(x; c)$ are Lipschitz everywhere:

$$|f(x; c) - f(x'; c)| < K(c)|x - x'| \qquad \text{all } x, x' \in \mathbb{R}^n \tag{10.3}$$

then a unique trajectory passes through every point in phase space and that trajectory can be extended in the forward direction to $t \to +\infty$ and in the reverse direction to $t \to -\infty$.

Many of the equations studied in this work have polynomial source functions. This means, in fact, that none of them satisfy the global Lipschitz conditions. Nevertheless, we can salvage the essential nature of the global theorem if motion occurs in an attractor that is bounded in phase space. Under this condition the Lipschitz condition is satisfied by polynomial source functions over any bounded domain in $\mathbb{R}^n$. Thus, if the source terms are polynomial and motion occurs in a bounded domain, a unique trajectory through any point exists and can be extended to $t \to \pm\infty$.

We point out here that many of the exciting results we have encountered occur because the source terms are not polynomial and contain singularities. The Lipschitz condition is not satisfied at such singularities. As a result, interesting things can and do happen.

Another result in a general theory of dynamical systems would be very nice to have. This is a general criterion under which it can be shown that motion occurs in a bounded domain. While this can be shown for certain classes of dynamical systems, such as the Lorenz and related equations, a general result of this type is currently not available.

10.2 CHANGE OF BASIS

The dynamical system equations (10.1) depend on the choice of coordinate system. They may appear complicated in some coordinate systems, less so in others. Following a time-honored principle of physics (Principle of Maximum Laziness) it is useful to learn how to transform a dynamical system from one coordinate system to another.

Rather than present the general theory, we present a simple 2-dimensional example from which the general result can easily be deduced. We treat a dynamical system on $\mathbb{R}^2$ given by

$$\begin{aligned} \frac{dx^1}{dt} &= -\alpha x^1 + a(x^2)^2 \\ \frac{dx^2}{dt} &= -\beta x^2 + b(x^1)^2 \end{aligned} \tag{10.4}$$

The phase space is described by a coordinate system with basis vectors $\mathbf{e}_1,\ \mathbf{e}_2$. In this basis the coordinates of any point p are $(x^1(p), x^2(p))$, as shown in Fig. 10.1. The vector describing the point $p \in \mathbb{R}^2$ is

$$\mathbf{e}_1 x^1(p) + \mathbf{e}_2 x^2(p) = \begin{pmatrix} \mathbf{e}_1 & \mathbf{e}_2 \end{pmatrix} \begin{bmatrix} x^1(p) \\ x^2(p) \end{bmatrix} \tag{10.5}$$

Remark: In this section *only* we change notation slightly, to conform with standard practice in linear vector space theory. We use superscripts for coordinates and subscripts to label basis vectors in linear vectors spaces ($\mathbb{R}^n$). This is done to emphasize the covariant-contravariant nature of the relation between coordinates and basis vectors.

Now we choose a new coordinate system with basis vectors $(\mathbf{e}_1', \mathbf{e}_2')$, related to the original basis vectors by a linear transformation

$$\begin{pmatrix} \mathbf{e}_1' & \mathbf{e}_2' \end{pmatrix} = \begin{pmatrix} \mathbf{e}_1 & \mathbf{e}_2 \end{pmatrix} \begin{bmatrix} \cos\theta & -\sin\theta \\ \sin\theta & \cos\theta \end{bmatrix} \tag{10.6}$$

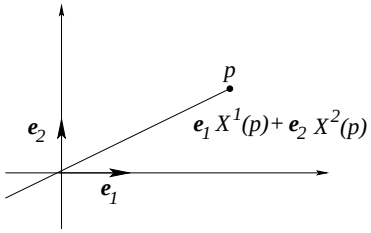

Fig. 10.1 Once a set of basis vectors $\mathbf{e}_1, \mathbf{e}_2$ has been defined in $\mathbb{R}^2$, the coordinates $x^1(p), x^2(p)$ of any point $p \in \mathbb{R}^2$ are defined.

How are the coordinates $x^{'1}(p), x^{'2}(p)$ related to the coordinates $x^1(p), x^2(p)$? This is easily answered by expressing the vector from the origin to p in matrix form in the two coordinate systems:

$$\begin{pmatrix} \mathbf{e}_1 & \mathbf{e}_2 \end{pmatrix} \begin{bmatrix} x^1 \\ x^2 \end{bmatrix} = \begin{pmatrix} \mathbf{e}_1^{'} & \mathbf{e}_2^{'} \end{pmatrix} \begin{bmatrix} x^{'1} \\ x^{'2} \end{bmatrix} \tag{10.7}$$

By substituting the linear relation (10.6) for the basis vectors into (10.7) and using linear independence arguments, we find

$$\begin{bmatrix} x^1 \\ x^2 \end{bmatrix} = \begin{bmatrix} \cos\theta & -\sin\theta \\ \sin\theta & \cos\theta \end{bmatrix} \begin{bmatrix} x^{'1} \\ x^{'2} \end{bmatrix} \tag{10.8}$$

More generally, if $\mathbf{e}_j^{'} = \mathbf{e}_i M^i_{\ j}$ defines the coordinate transformation, then $x^i = M^i_{\ j} x^{'j}$ shows the covariant-contravariant nature of the transformation between basis vectors and coordinates.

We can now use this information to determine what the dynamical system equations look like in the new coordinate system. It is sufficient to express the original variables x^1, x^2 in terms of the new variables. For the time derivatives we find

$$\begin{aligned} \frac{d}{dt}\begin{bmatrix} x^1 \\ x^2 \end{bmatrix} &= \frac{d}{dt}\begin{bmatrix} \cos\theta & -\sin\theta \\ \sin\theta & \cos\theta \end{bmatrix} \begin{bmatrix} x^{'1} \\ x^{'2} \end{bmatrix} \\ &= \begin{bmatrix} \cos\theta & -\sin\theta \\ \sin\theta & \cos\theta \end{bmatrix} \frac{d}{dt} \begin{bmatrix} x^{'1} \\ x^{'2} \end{bmatrix} \end{aligned} \tag{10.9}$$

As far as the source terms go, we find

$$\begin{bmatrix} -\alpha x^1 + a(x^2)^2 \\ -\beta x^2 + b(x^1)^2 \end{bmatrix} \longrightarrow \tag{10.10}$$

$$\begin{bmatrix} a[\sin^2\theta(x^{'1})^2 + 2\sin\theta\cos\theta x^{'1}x^{'2} + \cos^2\theta(x^{'2})^2] - \alpha(\cos\theta x^{'1} - \sin\theta x^{'2}) \\ b[\cos^2\theta(x^{'1})^2 - 2\sin\theta\cos\theta x^{'1}x^{'2} + \sin^2\theta(x^{'2})^2] - \beta(\sin\theta x^{'1} + \cos\theta x^{'2}) \end{bmatrix}$$

Untangling these results, we find

$$\frac{d}{dt}\begin{bmatrix} x^{'1} \\ x^{'2} \end{bmatrix} = g(x^{'1}, x^{'2}) \tag{10.11}$$

where $g(x^{'1}, x^{'2}) = \gamma^{-1} f(x \to \gamma x^{'})$ and $\gamma = \begin{bmatrix} \cos\theta & -\sin\theta \\ \sin\theta & \cos\theta \end{bmatrix}$.

The general result, for an arbitrary linear transformation γ defined by $x = \gamma x^{'}$ is that

$$\text{if} \quad \frac{dx}{dt} = f(x) \quad \text{then} \quad \frac{dx'}{dt} = g(x') = \gamma^{-1} f(x \to \gamma x') \tag{10.12}$$

This can be expressed in more elegant form as

$$\gamma g(x') = f(\gamma x') \tag{10.13}$$

10.3 SYMMETRY UNDER LINEAR TRANSFORMATIONS

In general, the form that the dynamical system equations take differs from coordinate system to coordinate system:

Original Coordinate System	Transformed Coordinate System
$\dfrac{dx}{dt} = f(x;c)$	$\dfrac{dx'}{dt} = g(x';c)$

(10.14)

$$g(x';c) = \gamma^{-1} f(\gamma x';c)$$

If $g(x;c) = f(x;c)$, things would be simpler. The two sets of equations would be identical. This provides a set of constraints on the structure and properties of dynamical systems that we explore in the remainder of Part II.

Definition: A dynamical system is *equivariant* under a linear transformation γ if $f(x;c) = g(x;c)$, or

$$\begin{aligned} \gamma f(x;c) &= f(\gamma x;c) \\ \text{or} \quad \gamma f(\gamma^{-1}x;c) &= f(x;c) \end{aligned} \tag{10.15}$$

Example: Suppose a dynamical system is equivariant under the linear transformation

$$\gamma = \begin{bmatrix} -\dfrac{1}{2} & -\dfrac{\sqrt{3}}{2} \\ +\dfrac{\sqrt{3}}{2} & -\dfrac{1}{2} \end{bmatrix} \tag{10.16}$$

obtained by setting $\theta = 2\pi/3$ in (10.9). This corresponds to a rotation by $2\pi/3$ radians about an axis perpendicular to the x-y plane through the origin. Assume that the dynamical system has fixed points at the origin $(0,0)$ and at some point on the x-axis $(x_0, 0)$. Then

1. Equivariance under γ (and γ^2) requires that there are two additional fixed points at the images of $(x_0, 0)$ under γ and γ^2: at $x_0(-\frac{1}{2}, -\frac{\sqrt{3}}{2})$ and $x_0(-\frac{1}{2}, +\frac{\sqrt{3}}{2})$.
2. The Jacobians $\partial f_i/\partial x_j$ at these three symmetric fixed points are related to each other by a similarity transformation. As a result, these three fixed points have identical stability properties.
3. Since the image of the origin under γ remains the origin, no new fixed points are generated from the origin by this linear transformation. This forces the Jacobian, $\partial f_i/\partial x_j$, evaluated at $(0,0)$, to be invariant under γ: $[\partial f_i/\partial x_j]_{(0,0)} = \gamma\,[\partial f_i/\partial x_j]_{(0,0)}\,\gamma^{-1}$.

Equivariance under a linear transformation imposes constraints on the form of the forcing functions in the dynamical systems equations. We illustrate this idea with a

simple example. We wish to show that the dynamical system

$$\frac{d}{dt}\begin{bmatrix} x \\ y \end{bmatrix} = \begin{bmatrix} -\alpha x + \beta(x^2 - y^2) \\ -\alpha y - 2\beta xy \end{bmatrix} \tag{10.17}$$

is invariant under the linear transformations γ and $\gamma^2 = \gamma^{-1}$, given in (10.16). Verification of this claim involves a straightforward substitution of the expression for (x, y) in terms of (x', y') given by

$$\begin{bmatrix} x \\ y \end{bmatrix} = \begin{bmatrix} -\frac{1}{2} & \pm\frac{\sqrt{3}}{2} \\ \mp\frac{\sqrt{3}}{2} & -\frac{1}{2} \end{bmatrix} \begin{bmatrix} x' \\ y' \end{bmatrix} \tag{10.18}$$

into the dynamical systems equations (10.17), and showing that the resulting equations have an identical form. There is nothing mysterious about this calculation. It is just long, boring, and subject to error.

We therefore choose to do this calculation using an elegant trick. This trick exploits a relation between rotation groups and complex numbers. Specifically, the linear transformation C_θ acting on the complex number $z = x + iy$ is simply a rotation: $C_\theta z = e^{i\theta} z$. The two equations above can be written as a single equation in one complex variable (cf. Eq. (8.34)):

$$\frac{d}{dt}(x + iy) = -\alpha(x + iy) + \beta(x^2 + y^2 - 2ixy) = -\alpha z + \beta \bar{z}^2 \tag{10.19}$$

where $\bar{z} = x - iy$ is the complex conjugate of z. The action of C_3 on this equation is

$$\begin{aligned} C_3 \frac{dz}{dt} &= C_3\left(-\alpha z + \beta \bar{z}^2\right) \\ e^{2\pi i/3}\frac{dz}{dt} &= -\alpha z e^{2\pi i/3} + \beta \bar{z}^2 e^{-4\pi i/3} \\ &= e^{2\pi i/3}\left(-\alpha z + \beta \bar{z}^2\right) \end{aligned} \tag{10.20}$$

As a result, the set of equations (10.17) is equivariant under the group $\mathcal{C}_3$.

Remark: There are systematic ways for determining the structure of equations that are equivariant under an arbitrary group $\mathcal{G}$. They are generalizations of the procedure we have just used for equations equivariant under the groups $\mathcal{C}_n$. As such, these methods can be regarded as generalizations of the methods of complex analysis that we have just exploited for the rotation groups.

We summarize the relation between a linear transformation γ and functions equivariant under γ in two suggestive ways.

Commutation: γ commutes with f, or γ *intertwines* f:

$$\gamma f = f\gamma \quad \text{or} \quad [\gamma, f] = 0$$

Similarity transform: f is invariant under a "similarity transform":

$$\gamma f \gamma^{-1} = f$$

10.4 GROUPS OF LINEAR TRANSFORMATIONS

In the previous section we hinted that a function f may be equivariant under more than one linear transformation. This is the case. In this section we show that the set of linear transformations that leave f unchanged in form forms a group. We also present many examples of possible invariance groups.

Suppose a function f is equivariant under linear transformations $\gamma_1, \gamma_2, \gamma_3, \cdots$. Then this set of linear transformations forms a group. To show this, we must show that the four axioms that define a group are satisfied. These are the axioms of (a) closure under multiplication; (b) associativity; (c) existence of an identity; and (d) existence of an inverse. The group multiplication in this case is matrix multiplication.

a. Closure: Since f is equivariant under γ_i and γ_j, $\gamma_i f(x) = f(\gamma_i x)$ and $\gamma_j f(x) = f(\gamma_j x)$. As a result

$$[\gamma_j \gamma_i]\, f(x) = \gamma_j \left[\gamma_i f(x)\right] = \gamma_j f(\gamma_i x) = f(\gamma_j \left[\gamma_i x\right]) = f([\gamma_j \gamma_i]\, x)$$

This means that if f is equivariant under γ_i and γ_j, it is also equivariant under their product $\gamma_j \gamma_i$.

b. Associativity: Matrix multiplication is associative:

$$(\gamma_i \gamma_j)\, \gamma_k = \gamma_i\, (\gamma_j \gamma_k)$$

c. Identity: The function is unchanged under "no change":

$$f(x) = I f(x) = f(Ix) = f(x)$$

d. Inverse: Every change of basis has an inverse. If the change of basis is represented by the matrix γ, the inverse change of basis is represented by the inverse matrix γ^{-1}, with $\gamma\gamma^{-1} = I$. Thus

$$f(x) = I f(x) = \gamma\gamma^{-1} f(x) = \gamma f(\gamma^{-1} x)$$

As a result, $\gamma^{-1} f(x) = f(\gamma^{-1} x)$.

Most of the groups that we will encounter satisfy a fifth condition:

$$\gamma_i \gamma_j = \gamma_j \gamma_i \qquad \text{all } i, j$$

Groups that satisfy this fifth condition are called *commutative* or *abelian*. While commutativity will simplify some of our results, we emphasize here that all results

developed later for equivariant covers hold for noncommutative as well as commutative groups.

We have already encountered a number of matrix groups. We review several groups here.

At the abstract level there is only one group of order 2. There is one *generator* A that obeys one *relation*: $A^2 = I$. The two group operations are $\{I, A\}$. In $\mathbb{R}^3$ this group has three different (faithful) matrix representations. In each, the identity operation I is represented by the identity matrix I_3, and the matrix representation of the generator defines action of the group in $\mathbb{R}^3$:

$$\begin{array}{cccc} & \sigma_Z & R_Z(\pi) & P \\ A \rightarrow & \begin{bmatrix} 1 & 0 & 0 \\ 0 & 1 & 0 \\ 0 & 0 & -1 \end{bmatrix} & \begin{bmatrix} -1 & 0 & 0 \\ 0 & -1 & 0 \\ 0 & 0 & 1 \end{bmatrix} & \begin{bmatrix} -1 & 0 & 0 \\ 0 & -1 & 0 \\ 0 & 0 & -1 \end{bmatrix} \end{array} \tag{10.21}$$

These three matrix represention of A define the groups σ_Z of reflections in the $Z = 0$ plane, $\mathcal{R}_Z(\pi)$ of rotations about the Z-axis by π radians, and $\mathcal{P}$ of spacial inversions.

There is one group of order three. It has one generator A that satisfies one relation: $A^3 = I$. The three group operations are $\{I, A, A^2\}$. This group has only one faithful (real) representation in $\mathbb{R}^3$. In this representation

$$A = \begin{bmatrix} -\frac{1}{2} & +\frac{\sqrt{3}}{2} & 0 \\ -\frac{\sqrt{3}}{2} & -\frac{1}{2} & 0 \\ 0 & 0 & 1 \end{bmatrix} \tag{10.22}$$

This is the group $\mathcal{C}_3$, consisting of rotations by $2\pi/3$ (and $4\pi/3$ and $6\pi/3 = 0$) radians about the Z-axis.

At the abstract level there are two groups of order four. One abstract group has one generator A that satisfies the single relation: $A^4 = I$. The four group operations are $\{I, A, A^2, A^3\}$. The other group ("four-group" or "viergruppe") has two generators A and B that satisfy three relations: $A^2 = I,\ B^2 = I$, and $AB = BA$. The four group operations are $\{I, A, B, AB\}$.

The first of these two groups has two different representations in $\mathbb{R}^3$. The matrix representatives of the generator A in these two representations are

$$\begin{array}{cc} C_4 & S_4 = \sigma_Z\, C_4 \\ \begin{bmatrix} 0 & 1 & 0 \\ -1 & 0 & 0 \\ 0 & 0 & 1 \end{bmatrix} & \begin{bmatrix} 0 & 1 & 0 \\ -1 & 0 & 0 \\ 0 & 0 & -1 \end{bmatrix} \end{array} \tag{10.23}$$

The group $\mathcal{C}_4$ with generator C_4 consists of rotations about the Z-axis through multiples of $\pi/2$ radians. The generator S_4 describes a rotation about the Z-axis through $\pi/2$ radians followed by a reflection in the $Z = 0$ plane. The groups with generator C_4 and S_4 are called (surprise!) $\mathcal{C}_4$ and $\mathcal{S}_4$, respectively.

The four-group with generators A and B also has two faithful representations in $\mathbb{R}^3$. In these representations the two linear operators A and B are reflections or rotations, and their product AB is a rotation.

$$
\begin{array}{lccc}
 & A & B & AB \\
 & \sigma_X & \sigma_Y & \mathcal{R}_Z \\
\text{Reflections} & \begin{bmatrix} -1 & 0 & 0 \\ 0 & +1 & 0 \\ 0 & 0 & +1 \end{bmatrix} & \begin{bmatrix} +1 & 0 & 0 \\ 0 & -1 & 0 \\ 0 & 0 & +1 \end{bmatrix} & \begin{bmatrix} -1 & 0 & 0 \\ 0 & -1 & 0 \\ 0 & 0 & +1 \end{bmatrix} \\
 & R_X & R_Y & R_Z \\
\text{Rotations} & \begin{bmatrix} +1 & 0 & 0 \\ 0 & -1 & 0 \\ 0 & 0 & -1 \end{bmatrix} & \begin{bmatrix} -1 & 0 & 0 \\ 0 & +1 & 0 \\ 0 & 0 & -1 \end{bmatrix} & \begin{bmatrix} -1 & 0 & 0 \\ 0 & -1 & 0 \\ 0 & 0 & +1 \end{bmatrix}
\end{array}
\tag{10.24}
$$

In the first representation the operators A and B describe reflections in the $X = 0$ and $Y = 0$ planes. Dynamical systems that are equivariant under this representation of the four-group have strange attractors that are of necessity disconnected because of the symmetry under the two reflections. This reduces our interest in this representation of the four-group.

In the second representation of the four-group the three operators A, B, AB describe rotations by π radians about the X-, Y-, and Z-axes. Dynamical systems equivariant under this group show exciting properties. In the future, when we refer to *the* four-group $\mathcal{V}_4$, we mean the representation generated by rotations.

10.5 PROPERTIES OF EQUIVARIANT DYNAMICAL SYSTEMS

For an equivariant dynamical system, dynamics in the neighborhood of a point $x \in \mathbb{R}^n$ looks the same as dynamics in the neighborhood of its image γx, $\gamma \in \mathcal{G}$. This observation has the following specific implications.

1. If x_0 is a fixed point, then γx_0 is a fixed point. At a fixed point, $f(x_0) = 0$. As a result, $f(\gamma x_0) = \gamma f(x_0) = \gamma 0 = 0$.

2. The Jacobian $[\partial f_i/\partial x_j]_{x_0}$ is related by a similarity transformation to the Jacobian at the image point:

$$
\left[\frac{\partial f_i}{\partial x_j}\right]_{\gamma x_0} = \gamma \left[\frac{\partial f_i}{\partial x_j}\right]_{x_0} \gamma^{-1} \tag{10.25}
$$

As a a result, if x_0 and γx_0 are fixed points, the eigenvalues of the Jacobians at x_0 and γx_0 are identical. Symmetry-related fixed points have identical stability

properties. In addition, the eigenvectors of the two Jacobians are related by the similarity transformation γ.

3. If x_0 is a fixed point that is left invariant under γ, then the Jacobian evaluated at that fixed point commutes with γ: $\left[\frac{\partial f_i}{\partial x_j}\right]_{x_0} = \gamma \left[\frac{\partial f_i}{\partial x_j}\right]_{x_0} \gamma^{-1}$.

4. If $\phi(t) = (\phi_1(t), \phi_2(t), \cdots, \phi_n(t))$ is a solution to $dx_i/dt = f_i(x;c)$ at x_0, then $\gamma\phi(t) = \left(\tilde{\phi}_1(t), \tilde{\phi}_2(t), \cdots, \tilde{\phi}_n(t)\right)$, $\tilde{\phi}_i(t) = \gamma_i{}^j \phi_j(t)$, is a solution to $dx_i/dt = f_i(x;c)$ at γx_0.

5. If x_0 is on a closed orbit $\phi(t)$, then γx_0 is on the closed orbit $\tilde{\phi}(t) = \gamma\phi(t)$. If $\phi(t)$ has period T, so that $\phi(t+T) = \phi(t)$, then $\tilde{\phi}(t)$ also has period T. The points x_0 and γx_0 may be on different orbits or on the same orbit. If they are on the same orbit, $\tilde{\phi}(t) = \phi(t+\tau)$, where $k\tau = T$ and k is an integer, $k > 1$.

6. If x_0 is "in" a strange attractor, γx_0 is also. By "in" we mean that a trajectory passes through x_0 which lies in the closure of a strange attractor. This includes all the unstable periodic orbits associated with ("in") the strange attractor.

7. A strange attractor of an equivariant dynamical system may have a single connected component. If the strange attractor possesses more than one (disconnected) component, the components are mapped into each other by symmetry group operations $\gamma \in \mathcal{G}$.

Example 1: The dynamical system (10.17) has a fixed point at the origin: $(x, y) = (0, 0)$. It is mapped into itself under the two operations γ and γ^2 given in (10.18). This fixed point is triply degenerate. There is a fixed point on the x-axis at $(x, y) = (\alpha/\beta, 0)$ if $\alpha \neq 0$ and $\beta \neq 0$ and α/β is real. Two additional fixed points occur at $\gamma^{\pm 1}(\alpha/\beta, 0) = \alpha/\beta(-\frac{1}{2}, \pm\frac{\sqrt{3}}{2})$. Each of these three symmetry-related fixed points is nondegenerate. The total number of fixed points, including degeneracy, is $6 = 3(1) + 1 \times (1 + 1 + 1) = 2|\mathcal{C}_3|$.

Example 2: The dynamical system defined by

$$\frac{d}{dt}\begin{bmatrix} x \\ y \\ z \end{bmatrix} = \begin{bmatrix} -\alpha_1 x + a_1 yz \\ -\alpha_2 y + a_2 zx \\ -\alpha_3 z + a_3 xy \end{bmatrix} \qquad \begin{matrix} \alpha_i \neq 0 \\ a_i \neq 0 \\ a_i' = a_i/\alpha_i > 0 \end{matrix} \tag{10.26}$$

is equivariant under the four group $\mathcal{V}_4$ defined in (9.24). There is one 4-fold degenerate fixed point at the origin $(x, y, z) = (0, 0, 0)$. The other four fixed points occur at

$$x = \pm\frac{1}{\sqrt{a_2' a_3'}} \qquad y = \pm\frac{1}{\sqrt{a_3' a_1'}} \qquad z = \pm\frac{1}{\sqrt{a_1' a_2'}} \tag{10.27}$$

where $xyz > 0$. That is, there is an even number of negative signs. The total number of fixed points, including degeneracy, is $8 = 4(1) + 1 \times (1 + 1 + 1 + 1) = 2|\mathcal{V}_4|$.

Generalization: If the image system has m fixed points, any of its covers with $\mathcal{G}$-fold symmetry has $m|\mathcal{G}|$ fixed points, counting degeneracy.

10.6 PARTITION OF PHASE SPACE

An equivariance group $\mathcal{G}$ partitions the phase space $\mathbb{R}^n$ into $|\mathcal{G}|$ equivalent domains. These are mapped into each other by the elements γ_i of the equivariance group. We say that these domains are symmetry-related. We show that these domains can be labeled by the $|\mathcal{G}|$ elements of the equivariance group.

Most points $x \in R^n$ satisfy the condition that $\gamma_i x \neq x$ for all $\gamma_i \in \mathcal{G}$, $(\gamma_i \neq I)$:

$$\gamma_i x \neq x \qquad \gamma_i \in \mathcal{G} \qquad \gamma_i \neq I \tag{10.28}$$

Points that obey this condition are called *generic* or *nonsingular* under the action of $\mathcal{G}$. Each such point occurs in a set of $|\mathcal{G}|$ points, technically called the *orbit* of x under $\mathcal{G}$. It is useful to partition the phase space into $|\mathcal{G}|$ open domains containing (almost) all the generic points. Each of the $|\mathcal{G}|$ points in the orbit of a generic point belongs to a different domain.

Example 1: The group $\mathcal{C}_n$ acts in $\mathbb{R}^3$ through the generator

$$\begin{bmatrix} \cos\theta & \sin\theta & 0 \\ -\sin\theta & \cos\theta & 0 \\ 0 & 0 & 1 \end{bmatrix} \qquad \theta = 2\pi/n \tag{10.29}$$

Singular points $(0, 0, z)$ occur on the z-axis. Each off-z-axis point occurs in an n-tuplet of symmetry-related points. The space $\mathbb{R}^3$ can be partitioned into n open sets by half-planes hinged on the z-axis and separated from each other by a dihedral angle $\theta = 2\pi/n$. The open domains do not include their boundary. The boundary of any domain consists of the two enclosing open half-planes (nonsingular points), as well as their intersection, the z-axis (singular points).

The $|\mathcal{G}|$ domains can be labeled by the group elements $\gamma_i \in \mathcal{G}$. We choose one of the open domains and call it the *fundamental domain*. The choice of fundamental domain is arbitrary (like the starting line on a circular track). This domain is labeled by the identity group operator: D_I. If $x \in D_I$, then $\gamma_i x$ is in a different domain $(\gamma_i \neq I)$. We label this domain D_{γ_i}:

$$x \in D_I \Rightarrow \gamma_i x \in D_{\gamma_i} \tag{10.30}$$

The group operations permute the domains among themselves. If $x \in D_{\gamma_i}$, then $x = \gamma_i y$, $y \in D_I$, so that

$$\gamma_j x = \gamma_j \left[\gamma_i y\right] = \left[\gamma_j \gamma_i\right] y \in D_{\gamma_j \gamma_i} \tag{10.31}$$

As a result, we can write

$$\gamma_j D_{\gamma_i} = D_{\gamma_j \gamma_i} \tag{10.32}$$

Thus, the action of the group $\mathcal{G}$ on the domain D_{γ_i} can be described in purely group theoretical terms, as follows

$$\gamma_j D_{\gamma_i} = D_{\gamma_k} \Gamma^{\mathrm{Reg}}_{ki}(\gamma_j) \tag{10.33}$$

The Regular $|\mathcal{G}| \times |\mathcal{G}|$ matrix representation $\Gamma^{\rm Reg}(\mathcal{G})$ of the group $\mathcal{G}$ is defined in terms of its matrix elements $\Gamma^{\rm Reg}_{ki}(g_\alpha)$ by

$$g_\alpha g_i = g_k \Gamma^{\rm Reg}_{ki}(g_\alpha) \qquad \begin{array}{rcl} = & 0 & \text{if } g_k \neq g_\alpha g_i \\ = & 1 & \text{if } g_k = g_\alpha g_i \end{array} \tag{10.34}$$

Example 2: For $\mathcal{C}_3$ the three symmetry-related domains are $D_I, D_{C_3}, D_{C_3^2}$. The operator C_3 maps $I \to C_3$, $C_3 \to C_3^2$, and $C_3^2 \to I$, so that the regular representation is

$$\begin{array}{c} \\ I \\ C_3 \\ C_3^2 \end{array} \begin{array}{c} \begin{array}{ccc} I & C_3 & C_3^2 \end{array} \\ \begin{bmatrix} 1 & 0 & 0 \\ 0 & 1 & 0 \\ 0 & 0 & 1 \end{bmatrix} \begin{bmatrix} 0 & 0 & 1 \\ 1 & 0 & 0 \\ 0 & 1 & 0 \end{bmatrix} \begin{bmatrix} 0 & 1 & 0 \\ 0 & 0 & 1 \\ 1 & 0 & 0 \end{bmatrix} \end{array} \tag{10.35}$$

Example 3: For $\mathcal{V}_4$ the 4×4 matrix representatives of the identity and three rotations are

$$\begin{array}{c} \\ I \\ R_x \\ R_y \\ R_z \end{array} \begin{array}{c} \begin{array}{c} I \end{array} \\ \begin{bmatrix} 1 & 0 & 0 & 0 \\ 0 & 1 & 0 & 0 \\ 0 & 0 & 1 & 0 \\ 0 & 0 & 0 & 1 \end{bmatrix} \end{array} \qquad \begin{array}{c} \\ I \\ R_x \\ R_y \\ R_z \end{array} \begin{array}{c} \begin{array}{c} R_x \end{array} \\ \begin{bmatrix} 0 & 1 & 0 & 0 \\ 1 & 0 & 0 & 0 \\ 0 & 0 & 0 & 1 \\ 0 & 0 & 1 & 0 \end{bmatrix} \end{array} \qquad \begin{array}{c} \begin{array}{c} R_y \end{array} \\ \begin{bmatrix} 0 & 0 & 1 & 0 \\ 0 & 0 & 0 & 1 \\ 1 & 0 & 0 & 0 \\ 0 & 1 & 0 & 0 \end{bmatrix} \end{array} \qquad \begin{array}{c} \begin{array}{c} R_z \end{array} \\ \begin{bmatrix} 0 & 0 & 0 & 1 \\ 0 & 0 & 1 & 0 \\ 0 & 1 & 0 & 0 \\ 1 & 0 & 0 & 0 \end{bmatrix} \end{array} \tag{10.36}$$

It is useful to describe the geometry of the various domains. In particular, it is useful to understand which domains are "close to" each other. Two domains in $\mathbb{R}^n$ are "close to" each other if their closures share an $n-1$ dimensional boundary.

Remark: This is useful definition, since a trajectory can leave one domain and enter an adjacent domain. By genericity, a one-dimensional trajectory and an $n-1$ dimensional boundary in $\mathbb{R}^n$ can intersect in a set of dimension $(n-1)+1-n=0$, that is, at isolated points. Trajectories do not generically intersect lower dimensional components of the boundary.

Example 4: For the group $\mathcal{C}_4$ acting in $\mathbb{R}^3$, the fundamental domain can be chosen as the union of the two open octants $D_I = (+++) \cup (++-)$. The octant $(++-)$ consists of all points with $x > 0$, $y > 0$, $z < 0$. We include in D_I all points in the boundary between these two octants: $(x, y, z = 0)$ with $x > 0, y > 0$. Then

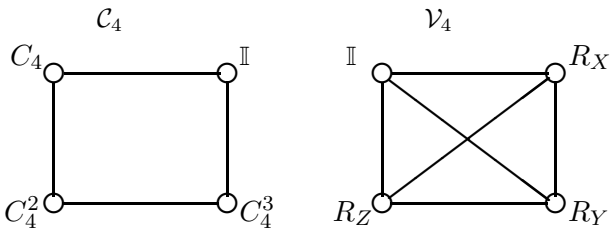

Fig. 10.2 Adjacency diagrams for the four domains in $\mathbb{R}^3(X, Y, Z)$ under the group (a) $\mathcal{C}_4$ and (b) $\mathcal{V}_4$.

$C_4 D_I = D_{C_4} = (-++) \cup (-+-)$. The four domains are

Domain Label	Domain
I	$(+++) \cup (++-)$
C_4	$(-++) \cup (-+-)$
C_4^2	$(--+) \cup (---)$
C_4^3	$(+-+) \cup (+--)$

(10.37)

Domain D_I shares two dimensional boundaries with domains D_{C_4} and $D_{C_4^3}$, but not with $D_{C_4^2}$. Similarly, D_{C_4} is not adjacent to $D_{C_4^3}$.

Similar results hold for $\mathcal{C}_n$, $n > 2$. The domain labeled by C_n^k is adjacent to the two domains labeled by $C_n^{k\pm1}$. Identical results hold for the groups $\mathcal{S}_{2n}$ with generators $A = \sigma_z C_{2n}$ and relations $A^{2n} = I$.

It is useful to summarize these geometric ("nearness") relations by an *adjacency diagram*. In an adjacency diagram the $|\mathcal{G}|$ domains are represented by small circles. Each circle (domain) is labeled by one of the group operations. If two domains are adjacent the circles representing them are connected by a straight line. The adjacency diagram for $\mathcal{C}_4$ is presented in Fig. 10.2(a).

For the four-group $\mathcal{V}_4$ generated by rotations in $\mathbb{R}^3$ the domain decomposition must be symmetric under interchange of the three rotation axes. That is, the domains D_{R_X}, D_{R_Y}, and D_{R_Z} must be rotated into each other under the action of the group $\mathcal{C}_3$ acting as a rotation group about the axis in the $(1, 1, 1)$ direction. A suitable choice of domains consists of the union of opposite octants, as follows:

Domain Label	Domain
I	$(+++) \cup (---)$
R_X	$(+--) \cup (-++)$
R_Y	$(-+-) \cup (+-+)$
R_Z	$(--+) \cup (++-)$

(10.38)

The adjacency diagram for $\mathcal{V}_4$ is shown in Fig. 10.2(b). Each domain is adjacent to every other domain.

10.7 REPRESENTATIONS OF GROUPS

In previous sections we have spoken of abstract groups. We have also spoken of the action of these groups as groups of linear transformations in n-dimensional linear vector spaces. The step from an abstract group to its concrete action on a space is through a set of matrices. These matrices are called a (matrix) *representation* of that group. There is a very elegant and beautiful theory of the matrix representations of groups. We summarize the most important aspects of that theory in the following subsections.

10.7.1 Definition of Representation

A representation of a group $\mathcal{G}$ is a mapping of each group element $g_i \in \mathcal{G}$ to an $n \times n$ invertible matrix $\Gamma(g_i)$:

$$g_i \longrightarrow \Gamma(g_i) \tag{10.39}$$

The group operations and their matrix representations must satisfy the group multiplication axioms:

$$g_i \circ g_j = g_k \Rightarrow \Gamma(g_i) \times \Gamma(g_j) = \Gamma(g_k) \tag{10.40}$$

Here $\circ$ is the combinatorial operation in the abstract group and $\times$ is the standard matrix multiplication operation.

10.7.2 Equivalent Representations

Two $n \times n$ matrix representations of a group $\mathcal{G}$, $\Gamma^{(a)}(\mathcal{G})$ and $\Gamma^{(b)}(\mathcal{G})$, are said to be *equivalent* if there is a nonsingular similarity transformation S for which

$$S\Gamma^{(a)}(g_i)S^{-1} = \Gamma^{(b)}(g_i) \qquad \text{all } g_i \in \mathcal{G} \tag{10.41}$$

The two sets of matrices, $\Gamma^{(a)}(g_i)$ and $\Gamma^{(b)}(g_i)$, act on n-dimensional spaces. Eq. (10.41) simply means that the two representations act in the same linear vector space, but are expressed with respect to different choice of basis vectors $\{\mathbf{e}_1, \mathbf{e}_2, \cdots, \mathbf{e}_n\}$ and $\{\mathbf{f}_1, \mathbf{f}_2, \cdots, \mathbf{f}_n\}$, where $\mathbf{e}_i = \mathbf{f}_j S^j_i$.

Example: In $\mathbb{R}^2$ the two element group $\{I, A\}$ has representations

$$\begin{array}{lcc} & I & A \\ \Gamma^{(a)} & \begin{bmatrix} 1 & 0 \\ 0 & 1 \end{bmatrix} & \begin{bmatrix} 1 & 0 \\ 0 & -1 \end{bmatrix} \\ \Gamma^{(b)} & \begin{bmatrix} 1 & 0 \\ 0 & 1 \end{bmatrix} & \begin{bmatrix} 0 & 1 \\ 1 & 0 \end{bmatrix} \end{array} \tag{10.42}$$

These two representations are equivalent under the similarity transformation $S = \frac{1}{\sqrt{2}}\begin{bmatrix} 1 & -1 \\ 1 & 1 \end{bmatrix}$. In $\mathbb{R}^3$ this same abstract group has two representations

$$\begin{array}{cccc} & I & & A \\ \Gamma^{(c)} & \begin{bmatrix} 1 & 0 & 0 \\ 0 & 1 & 0 \\ 0 & 0 & 1 \end{bmatrix} & & \begin{bmatrix} 1 & 0 & 0 \\ 0 & 1 & 0 \\ 0 & 0 & 1 \end{bmatrix} \\ \Gamma^{(d)} & \begin{bmatrix} 1 & 0 & 0 \\ 0 & 1 & 0 \\ 0 & 0 & 1 \end{bmatrix} & & \begin{bmatrix} 1 & 0 & 0 \\ 0 & 0 & 1 \\ 0 & 1 & 0 \end{bmatrix} \end{array} \tag{10.43}$$

that are not equivalent. It can easily be seen that there is no nonsingular matrix S for which $S\Gamma^{(c)}S^{-1} = \Gamma^{(d)}$. Simplest is to observe that tr $\Gamma^{(c)}(A) = 3$ while tr $\Gamma^{(d)}(A) = 1$. More subtle is the observation that $\Gamma^{(d)}$ is a faithful representation of $\{I, A\}$ while $\Gamma^{(c)}$ is not (cf. subsection 10.7.3 below).

10.7.3 Faithful Representations

A matrix representation of $\mathcal{G}$, $\Gamma(\mathcal{G})$, is said to be *faithful* if, by knowing the matrix $\Gamma(g_i)$, the group operation g_i is uniquely determined.

Example: The two-group $\{I, A\}$ has a matrix representation $\Gamma^{(c)}$ given in (10.43). This representation is not faithful. The representation $\Gamma^{(d)}$ is faithful.

10.7.4 Reducible Representations

So, how many faithful matrix representations does a group have? This is actually not a well-posed question: its answer cannot be given in terms of the properties of the group itself.

We temporarily delay treating this question until the following subsection. We first describe how the most general representations of a group are constructed.

Suppose $\mathcal{G}$ acts in an n-dimensional linear vector space through a matrix representation $\Gamma(\mathcal{G})$. We ask: is there some clever, or preferred, choice of basis vectors in this space? A preferred choice would reduce $\Gamma(\mathcal{G})$ to block diagonal form (cf. Table 8.1)

$$\Gamma(\mathcal{G}) \longrightarrow S\Gamma(\mathcal{G})S^{-1} = \begin{bmatrix} \Gamma^{(a)}(\mathcal{G}) & 0 \\ 0 & \Gamma^{(b)}(\mathcal{G}) \end{bmatrix} \tag{10.44}$$

If a similarity transformation S can be found that reduces $\Gamma(\mathcal{G})$ to block diagonal form, then $\Gamma(\mathcal{G})$ is said to be *reducible*. In this case $\Gamma^{(a)}(\mathcal{G})$ is an $n_1 \times n_1$ matrix representation of $\mathcal{G}$ acting on an n_1-dimensional subspace of the original n-dimensional space, and $\Gamma^{(b)}(\mathcal{G})$ is an $n_2 \times n_2$ matrix representation of $\mathcal{G}$ acting on an n_2-dimensional subspace, where $n_1 + n_2 = n$. The n_1- and n_2-dimensional subspaces are orthogonal.

This argument can be repeated on $\Gamma^{(a)}(\mathcal{G})$ and $\Gamma^{(b)}(\mathcal{G})$, and continued until the matrices on the diagonal are no longer reducible.

10.7.5 Irreducible Representations

Eventually, all the matrix representations along the diagonal are no longer reducible. These representations are said to be *irreducible*. The original matrix representation $\Gamma(\mathcal{G})$ is a *direct sum* of irreducible representations of $\mathcal{G}$. As a matter of fact, *every* matrix representation of $\mathcal{G}$ is (equivalent to) a direct sum of irreducible representations of $\mathcal{G}$. (These remarks hold for compact groups and for a large class of noncompact groups as well. Technically, the reducible representations are fully reducible for finite and compact groups.)

So the proper question is: How many inequivalent irreducible representations of $\mathcal{G}$ exist? The answer to this question depends entirely on the group $\mathcal{G}$, through its multiplication table. It is an "intrinsic" question: it does not depend at all on what kind of space (i.e., dimension) $\mathcal{G}$ acts on—or even if $\mathcal{G}$ acts on a linear vector space.

The answer to this question is well known for all the groups under consideration in this book.

- Every group has an unfaithful matrix representation, $\Gamma^{\mathrm{Id}}(g) = 1$, called the identity representation. It is unfaithful if $|\mathcal{G}| > 1$.
- If $\mathcal{G}$ is commutative, then there are exactly $|\mathcal{G}|$ inequivalent irreducible representations of $\mathcal{G}$, and they are all one-dimensional.
- Whether or not $\mathcal{G}$ is commutative, the total number of matrix elements in all its inequivalent irreducible representations $\Gamma^{(\lambda)}(\mathcal{G})$ is equal to the order of $\mathcal{G}$:

$$\sum_{\text{all irreps}} d_\lambda^2 = |\mathcal{G}| \tag{10.45}$$

  Here $\Gamma^\lambda(g)$ is $d_\lambda \times d_\lambda$ matrix representation of $\mathcal{G}$.

Elaboration: A finite group $\mathcal{G}$ can be considered as a set of $|\mathcal{G}|$ points: each group operation being a "point." Once we have a space of points, the urge to introduce a set of functions on this set of points ("function space") is irrepressible. In fact, each matrix element $\Gamma^\lambda_{ij}(g_\alpha)$ $(g_\alpha \in \mathcal{G})$ is a function on these $|\mathcal{G}|$ points. A function space with $|\mathcal{G}|$ points has $|\mathcal{G}|$ basis functions. The set of all d_λ^2 matrix elements for all inequivalent irreducible representations $\Gamma^\lambda(g)$ constitutes such a complete set. It is for these reason that $\sum_{\text{all irreps}} d_\lambda^2 = |\mathcal{G}|$. In addition to being complete these functions are orthogonal.

Warning: These remarks are true for irreducible representations over the field of complex numbers.

Examples: The two-element group $\{I, A\}$ has two inequivalent (unitary) irreducible representations

$\{I, A\}$	I	A
$\Gamma^{(1)}$	1	1
$\Gamma^{(2)}$	1	-1

(10.46)

The group $\mathcal{C}_3$ has three unitary irreducible representations

$$\begin{array}{c|ccc} \mathcal{C}_3 & I & C_3 & C_3^2 \\ \hline \Gamma^{(1)} & 1 & 1 & 1 \\ \Gamma^{(2)} & 1 & \epsilon & \epsilon^2 \\ \Gamma^{(3)} & 1 & \epsilon^2 & \epsilon \end{array} \qquad \epsilon = e^{2\pi i/3} \tag{10.47}$$

The group $\mathcal{C}_n$ has n unitary irreducible representations:

$$\mathcal{C}_n \longrightarrow \Gamma^{(k)}(C_n^j) = e^{2\pi ijk/n} \tag{10.48}$$

with $k = 0, 1, 2, \cdots, n-1, n \simeq 0$.

The four-group $\mathcal{V}_4 = \{I, A, B, AB\}$ ($A^2 = B^2 = I, AB = BA$) is commutative. Its four unitary irreducible representations are

$$\begin{array}{c|cccc} \mathcal{V}_3 & I & A & B & AB \\ \hline \Gamma^{(1)} & 1 & 1 & 1 & 1 \\ \Gamma^{(2)} & 1 & 1 & -1 & -1 \\ \Gamma^{(3)} & 1 & -1 & 1 & -1 \\ \Gamma^{(4)} & 1 & -1 & -1 & 1 \end{array} \tag{10.49}$$

The group of the square (Fig. 10.3) has as group operations the identity I, three rotations C_4^j, $j = 1, 2, 3$, two reflections in the x-and y-axes, and two reflections in the diagonals. If n_i are the dimensions of the irreducible representations,

$$\sum_i d_i^2 = |\mathcal{G}| = 8 \tag{10.50}$$

This group (every group) has one one-dimensional representation, the identity, with $d_1 = 1$. This group is noncommutative, so at least one representation must consist of $n \times n$ matrices, $n > 1$. There is only one way to satisfy the Diophantine equation above: $d_1 = d_2 = d_3 = d_4 = 1$ and $d_5 = 2$. This group has five inequivalent unitary irreducible representations.

10.7.6 Arbitrary Representations

An arbitrary representation $\Gamma(\mathcal{G})$ of $\mathcal{G}$ is equivalent to a direct sum of unitary irreducible representations of $\mathcal{G}$. If the irreducible representations are $\Gamma^{(1)}(\mathcal{G}), \Gamma^{(2)}(\mathcal{G}), \cdots, \Gamma^{(\omega)}(\mathcal{G})$, then

$$\Gamma(\mathcal{G}) \simeq \sum_{i=1}^{\omega} n_i \Gamma^{(i)}(\mathcal{G}) \tag{10.51}$$

The integers n_i indicate how often the irreducible representation $\Gamma^{(i)}$ occurs in the direct sum: $n_i \geq 0$.

Application: The two-group $\{I, A\}$ has two one-dimensional unitary irreducible representations. If $\Gamma(\mathcal{G})$ is a representation of $\{I, A\}$ acting in $\mathbb{R}^n$, then

$$\Gamma(\mathcal{G}) = n_1 \Gamma^{(1)}(\mathcal{G}) + n_2 \Gamma^{(2)}(\mathcal{G}), \qquad n_1 + n_2 = n \tag{10.52}$$

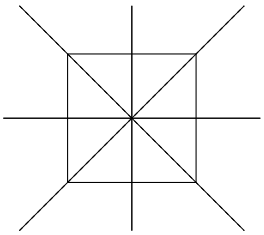

Fig. 10.3 The group of the square, $\mathcal{D}_4$, consists of the identity I, the three rotations C_4^j, $j = 1, 2, 3$, two reflections in the horizontal and vertical axes (solid lines), and two reflections in the diagonals (dashed lines).

As a result, there are exactly $n + 1$ inequivalent representations of the two element group $\{I, A\}$ acting in $\mathbb{R}^n$. One of these representations is unfaithful—the representation with $n_2 = 0$. The two-group has exactly n distinct (inequivalent) faithful representations when acting in $\mathbb{R}^n$. We have seen this result already in $\mathbb{R}^3$ (cf. Eqs. (10.21)).

10.7.7 Real Representations

We are primarily interested in the action of $\mathcal{G}$ through *real* linear transformations. We can construct real linear transformations from complex conjugate pairs of complex representations.

Example: For the group $\mathcal{C}_n$ the irreducible (complex) representations are $\Gamma^{(k)}(C_j) = e^{2\pi ijk/n}$. The representation with $k = 0$ is the identity, and if n is even, the representation with $k = n/2$ is real. The remaining representations are complex. However, the direct sum of the two one-dimensional representations k and $n - k$ is equivalent to a real 2×2 matrix representation

$$\begin{aligned} \Gamma^{(k)}(C_j) + \Gamma^{(n-k)}(C_j) &= \begin{bmatrix} e^{2\pi ijk/n} & 0 \\ 0 & e^{-2\pi ijk/n} \end{bmatrix} \\ &\simeq \begin{bmatrix} \cos\left(\frac{2\pi jk}{n}\right) & \sin\left(\frac{2\pi jk}{n}\right) \\ -\sin\left(\frac{2\pi jk}{n}\right) & \cos\left(\frac{2\pi jk}{n}\right) \end{bmatrix} \end{aligned} \tag{10.53}$$

This matrix representation is irreducible over the real numbers unless $k = 0$ or $k = n/2$.

As a special case, the group $\mathcal{C}_3$ has one real 1×1 matrix representation and one real 2×2 matrix representation. The latter is irreducible over the real field:

$\mathcal{C}_3$	I	C_3	C_3^2
$\Gamma^{(1)}$	(1)	(1)	(1)
$\Gamma^{(2)}$	$\begin{bmatrix} 1 & 0 \\ 0 & 1 \end{bmatrix}$	$\begin{bmatrix} \cos\left(\frac{2\pi}{3}\right) & +\sin\left(\frac{2\pi}{3}\right) \\ -\sin\left(\frac{2\pi}{3}\right) & \cos\left(\frac{2\pi}{3}\right) \end{bmatrix}$	$\begin{bmatrix} \cos\left(\frac{2\pi}{3}\right) & -\sin\left(\frac{2\pi}{3}\right) \\ +\sin\left(\frac{2\pi}{3}\right) & \cos\left(\frac{2\pi}{3}\right) \end{bmatrix}$

(10.54)

10.7.8 Important Representations

There are three important kinds of representations that we encounter frequently when we study the action of a symmetry group $\mathcal{G}$ in a space $\mathbb{R}^n$. These are: the identity representation; the defining representation; and the regular representation.

10.7.8.1 Identity Representation: In this representation every group operation $g_i \in \mathcal{G}$ is mapped into the unit matrix I_n:

$$g_\alpha \longrightarrow \Gamma^{\mathrm{Id}}(g_\alpha) = I_n \tag{10.55}$$

10.7.8.2 Defining Representation: The action of the group $\mathcal{G}$ on the coordinates $x_1, x_2, \cdots, x_n$ is through the defining matrix representation:

$$g_\alpha x_i \longrightarrow x_j \Gamma^{\mathrm{Def}}_{ji}(g_\alpha) = \Gamma^{\mathrm{Def}}_{ij}(g_\alpha^{-1}) x_j \tag{10.56}$$

Important Remark: A group $\mathcal{G}$ can act in $\mathbb{R}^n$ in many different ways, as we have already seen. The action of the group in $\mathbb{R}^n$ is defined through the matrix representation $\Gamma^{\mathrm{Def}}(\mathcal{G})$. For example, the two-group $\{I, A\}$ can act faithfully in $\mathbb{R}^3$ through three distinct defining representations (cf. (10.21)). The group $\mathcal{G}$ acts on the image dynamical system through the identity representation $\Gamma^{\mathrm{Id}}(\mathcal{G})$:

$$\begin{array}{c} \mathcal{G} \text{ acts on} \\ \\ \begin{array}{ll} \text{covering dynamical system} & \text{image dynamical system} \\ \\ \mathcal{G} \to \Gamma^{\mathrm{Def}}(\mathcal{G}) & \mathcal{G} \to \Gamma^{\mathrm{Id}}(\mathcal{G}) \end{array} \end{array} \tag{10.57}$$

10.7.8.3 Regular Representation: This representation describes the group multiplication law. As opposed to the previous two representations, which are in terms of $n \times n$ matrices acting on $\mathbb{R}^n$, (n not related to $\mathcal{G}$), the regular representation is given in terms of $|\mathcal{G}| \times |\mathcal{G}|$ matrices. The regular representation is defined by permutation matrices—matrices that contain one nonzero element $+1$ in each row and column. This representation is defined by

$$\begin{array}{rcl} g_\alpha g_i & = & g_j \Gamma^{\mathrm{Reg}}_{ji}(g_\alpha) \\ \\ \Gamma^{\mathrm{Reg}}_{ji}(g_\alpha) & = & \begin{array}{ll} 0 & g_j \neq g_\alpha g_i \\ 1 & g_j = g_\alpha g_i \end{array} \end{array} \tag{10.58}$$

The regular representation is faithful and can be used to reproduce the group multiplication table. We use the regular representation to describe how the symmetry-related open domains of $\mathbb{R}^n$ are mapped into each other under the group operations $g_i \in \mathcal{G}$ (cf. (10.34)).

Example: The four open domains of $\mathbb{R}^3$ that are related to each other under the (rotation) four-group $\mathcal{V}_4$ are labeled by the four operations I, R_x, R_y, R_z (cf. Eq. (10.24)). They are mapped into each other by the group operations in $\mathcal{V}_4$:

$$g_\alpha D_{g_i} = D_{g_j} \Gamma^{\mathrm{Reg}}_{g_j g_i}(g_\alpha) \tag{10.59}$$

The 4×4 matrices that constitute the regular representation of $\mathcal{V}_4$ are presented in Eq. (10.36). The regular representation of $\mathcal{V}_4$ is equivalent to the direct sum of its four irreducible representations in (10.49): $\Gamma^{\mathrm{Reg}} \simeq \Gamma^{(1)} + \Gamma^{(2)} + \Gamma^{(3)} + \Gamma^{(4)}$.

10.8 HOW MANY WAYS CAN A GROUP APPEAR?

The two-group $\{I, A\}$ can act faithfully in $\mathbb{R}^3$ in three inequivalent ways. Other groups can act in a multiplicity of inequivalent ways in $\mathbb{R}^N$. In this section we compute the number of inequivalent ways that a group can act in $\mathbb{R}^N$, for any group and any N.

To lay the groundwork for this analysis, we review how we determined that $\{I, A\}$ can act faithfully in $\mathbb{R}^N$ in N inequivalent ways. The action of $\{I, A\}$ is through a direct sum of its irreducible representations: $\Gamma = n_1\Gamma^{(1)} + n_2\Gamma^{(2)}$, where $\Gamma^{(1)}$ and $\Gamma^{(2)}$ are given in (10.46) and $n_1 + n_2 = N$. Two representations Γ and Γ' are inequivalent if $n_2 \neq n_2'$. The representation is faithful unless $n_2 = 0$.

It is possible to construct a *generating function* for the number of inequivalent representations of $\{I, A\}$ in $\mathbb{R}^N$ for any N. A generating function is a function that generates answers to appropriate questions. Generating functions are used widely in physics. For example, there is a generating function for Hermite polynomials $H_n(x)$:

$$e^{2tx-t^2} = \sum_{n=0}^{\infty} \frac{t^n}{n!} H_n(x) \tag{10.60}$$

This is to be interpreted as follows. The exponential on the left-hand side is to be expanded in a Taylor series expansion and the terms rearranged into an ascending power series in the variable t. The coefficient of $t^n/n!$ is the Hermite polynomial $H_n(x)$. To second order in t, this process is

$$e^{2tx-t^2} = 1 + t(2x) + \frac{t^2}{2}(4x^2 - 2) + \cdots \tag{10.61}$$

The first three Hermite polynomials are thus $H_0 = 1$, $H_1(x) = 2x$, and $H_2(x) = 4x^2 - 2$.

A generating function for groups is constructed as follows. For representation $\Gamma^{(i)}$ of dimension d_i we write the factor $\frac{1}{1-x^{d_i}\Gamma^{(i)}}$. When this is expanded we find

$$\frac{1}{1 - x^{d_i}\Gamma^{(i)}} = 1 + x^{d_i}\Gamma^{(i)} + x^{2d_i}(\Gamma^{(i)})^2 + x^{3d_i}(\Gamma^{(i)})^3 + \cdots \tag{10.62}$$

We interpret this expansion as follows. From the first nontrivial term $1x^{d_i}\Gamma^{(i)}$ we understand there is one (1) representation of dimension d_i (from x^{d_i}), and that representation is $\Gamma^{(i)}$. From the next term $1x^{2d_i}(\Gamma^{(i)})^2$ we understand there is one (1) representation of dimension $2d_i$ (x^{2d_i}), and that is $(\Gamma^{(i)})^2 \to \Gamma^{(i)} + \Gamma^{(i)}$.

The group $\{I, A\}$ has two irreducible representations. Every representation of $\{I, A\}$ is a direct sum of these two, with various multiplicities. The generating function for this group includes a factor for each irreducible representation with $d_1 = 1, d_2 = 1$:

$$G(\Gamma^{(1)}, \Gamma^{(2)}; x) = \frac{1}{1 - x\Gamma^{(1)}} \frac{1}{1 - x\Gamma^{(2)}} = 1 + x\left(\Gamma^{(1)} + \Gamma^{(2)}\right) + \tag{10.63}$$

$$x^2\left((\Gamma^{(1)})^2 + \Gamma^{(1)}\Gamma^{(2)} + (\Gamma^{(2)})^2\right) + \cdots + x^N\left(\sum_{n_1+n_2=N} (\Gamma^{(1)})^{n_1}(\Gamma^{(2)})^{n_2}\right) + \cdots$$

The coefficient of x^N informs us that there is one representation of dimension N of the form $(\Gamma^{(1)})^{n_1}(\Gamma^{(2)})^{n_2} \to n_1\Gamma^{(1)} + n_2\Gamma^{(2)}$ with $n_1 + n_2 = N$ for each choice of (n_1, n_2).

In order to count just the faithful representations, we must remove each of the unfaithful representations $(\Gamma^{(1)})^N(\Gamma^{(2)})^0$ from this sum. This is done by subtracting 1 from the factor $\frac{1}{1-x\Gamma^{(2)}}$, leaving as generating function for *faithful* representations of $\{I, A\}$ in $\mathbb{R}^N$

$$G(\Gamma^{(1)}, \Gamma^{(2)}; x) = \frac{1}{1 - x\Gamma^{(1)}}\left(\frac{1}{1 - x\Gamma^{(2)}} - 1\right) \tag{10.64}$$

If we are interested in just the *number* of faithful representations, rather than their detailed decomposition in terms of irreducible representations, we can drop the information provided by the representation symbols $\Gamma^{(i)}$. The generating function for the number of faithful representations of $\{I, A\}$ in $\mathbb{R}^N$ is

$$G_F(\mathcal{G} = \{I, A\}; x) = \frac{1}{1 - x}\left(\frac{1}{1 - x} - 1\right) = \sum_{N=1}^{\infty} Nx^N \tag{10.65}$$

In $\mathbb{R}^3$ ($x^{N=3}$) there are 3 (coefficient of x^3) faithful inequivalent representations of the two-group.

These arguments generalize to arbitrary groups. If a group has representations $\Gamma^{(i)}$ of dimension d_i, $i = 1, 2, \cdots$, the generating function for inequivalent faithful representations of dimension N is

$$G(\Gamma^{(1)}, \Gamma^{(2)}, \cdots; x) = \prod_{i\in\mathcal{U}} \frac{1}{1 - x^{d_i}\Gamma^{(i)}}\left(\prod_{j\in\mathcal{F}} \frac{1}{1 - x^{d_j}\Gamma^{(j)}} - 1\right) \tag{10.66}$$

Here $i \in \mathcal{U}$ means $\Gamma^{(i)}$ is not faithful (*u*nfaithful) and $j \in \mathcal{F}$ means $\Gamma^{(j)}$ is *f*aithful. If only the number of inequivalent faithful representations is required, the symbols Γ

can be dispensed with:

$$G_F(\mathcal{G};x)=\prod_{i\in\mathcal{U}}\frac{1}{1-x^{d_i}}\left(\prod_{j\in\mathcal{F}}\frac{1}{1-x^{d_j}}-1\right) \tag{10.67}$$

Remark: Only real representations should be used to determine the action of a group $\mathcal{G}$ on $\mathbb{R}^N$ through real representations. For example, the group $\mathcal{C}_3$ has one unfaithful representation of dimension 1 (the identity representation) and two faithful representations, both also of dimension 1. However, these are complex. Their direct sum is equivalent to a real faithful two-dimensional representation. As a result, the generating function for the number of real inequivalent faithful representations of $\mathcal{C}_3$ in $\mathbb{R}^N$ is $G_F(\mathcal{C}_3;x)=\frac{1}{1-x}\left(\frac{1}{1-x^2}-1\right)$.

Calculations can be expedited by introducing functions

$$h_i=h_i(x)=\frac{1}{1-x^i} \tag{10.68}$$

and expressing the generating functions in terms of products of these factors.

Example 1: The generating function for the group $\mathcal{C}_3$ is

$$G_F(\mathcal{C}_3;x)=h_1(h_2-1)=\frac{1}{1-x}\left(\frac{1}{1-x^2}-1\right)= \tag{10.69}$$

$$1x^2+x^3+2x^4+2x^5+3x^6+3x^7+4x^8+\cdots$$

Example 2: The group $\mathcal{G}=\mathcal{C}_{3v}$ is the group that leaves the equilateral triangle invariant. It has six group elements and three irreducible representations that satisfy $n_1^2+n_2^2+n_3^2=6, n_1=1, n_2=1, n_3=2$. The two one-dimensional representations are real and unfaithful, the two-dimensional representation is real and faithful. The generating function is

$$G_F(\mathcal{C}_{3v};x)=h_1^2\,(h_2-1)=\left(\frac{1}{1-x}\right)^2\left(\frac{1}{1-x^2}-1\right)= \tag{10.70}$$

$$1x^2+2x^3+4x^4+6x^5+9x^6+12x^7+16x^8+\cdots$$

Example 3: The group $\mathcal{D}_4$ leaves the square invariant. It consists of the identity, three rotations C_4^k, $k=1,2,3$, and two pairs of reflections. It has four unfaithful one-dimensional real representations and one faithful two-dimensional representation. The generating function is

$$G_F(\mathcal{D}_4;x)=h_1^4\,(h_2-1)=\left(\frac{1}{1-x}\right)^4\left(\frac{1}{1-x^2}-1\right)= \tag{10.71}$$

$$1x^2+4x^3+11x^4+24x^5+46x^6+80x^7+130x^8+\cdots$$

Example 4: The tetrahedral group $\mathcal{T}$ consists of 12 proper rotations that leave the regular tetrahedron invariant. This group has three unfaithful one-dimensional irreducible representations, A_1, E_+, E_-, and one faithful three-dimensional representation, T_1. The two representations E_+ and E_- are complex conjugates; their direct sum is equivalent to a 2 dimensional representation that is real, unfaithful, and irreducible over the reals. This gives three real irreducible representations for $\mathcal{T}$, and a generating function for faithful representations that is

$$G_F(\mathcal{T};x) = h_1 h_2 (h_3 - 1) = \frac{1}{1-x}\frac{1}{1-x^2}\left(\frac{1}{1-x^3} - 1\right) = \tag{10.72}$$

$$1x^3 + 1x^4 + 2x^5 + 3x^6 + 4x^7 + 5x^8 + \cdots$$

Example 5: The proper octahedral group $\mathcal{O}$ consists of the 24 proper rotations that leave the cube invariant. This group has five inequivalent unitary irreducible representations A_1, A_2, E, T_1, T_2 of dimensions $1,\ 1,\ 2,\ 3,\ 3$, respectively. All are real. The first three are unfaithful, the two three-dimensional representations are faithful. The generating function is

$$G_F(\mathcal{O};x) = (h_1)^2 h_2\left((h_3)^2 - 1\right) = \left(\frac{1}{1-x}\right)^2 \frac{1}{1-x^2}\left(\left(\frac{1}{1-x^3}\right)^2 - 1\right) = \tag{10.73}$$

$$2x^3 + 4x^4 + 8x^5 + 15x^6 + 24x^7 + 36x^8 + \cdots$$

The number of inequivalent ways the six groups discussed above can act faithfully in spaces $\mathbb{R}^N$, $N = 3, \cdots, 8$ is summarized below.

N	3	4	5	6	7	8
Group						
$\{I, A\}$	3	4	5	6	7	8
$\mathcal{C}_3$	1	2	2	3	3	4
$\mathcal{C}_{3v}$	2	4	6	9	12	16
$\mathcal{D}_4$	4	11	24	46	80	130
$\mathcal{T}$	1	1	2	3	4	5
$\mathcal{O}$	2	4	8	15	24	36

Remark: The Taylor series expansion of each of these generating functions can easily be computed. The following Maple program carries out this expansion for the last generating function.

```
> h1 := 1/(1 - x) : h2 := 1/(1 - x^2) : h3 := 1/(1 - x^3) :
> f := h1^2 * h2 * (h3^2 - 1);
```

$$\left(\frac{1}{1-x}\right)^2 \frac{1}{1-x^2}\left(\left(\frac{1}{1-x^3}\right)^2 - 1\right)$$

```
> taylor(f, x = 0, 10);
```

$$2x^3 + 4x^4 + 8x^5 + 15x^6 + 24x^7 + 36x^8 + 54x^9 + \mathcal{O}(x^{10})$$

10.9 SUBGROUPS AND COSETS

It frequently happens that we encounter a subset of group operations $\{g_1, g_2, \cdots, g_h\}$ that close under the group multiplication operation. This means that the product of any two operations in this set produces another operation in this set. When this is the case, it is easy to show that the identity operation $g_1 = I$ is in this set. So also is the inverse of every operation in this set. In short, this set is a group, $\mathcal{H}$. We call $\mathcal{H}$ a *subgroup* of $\mathcal{G}$ and write $\mathcal{H} \subseteq \mathcal{G}$. If $\mathcal{H}$ does not contain all the operations in $\mathcal{G}$, that is if $|\mathcal{H}| < |\mathcal{G}|$, then we call $\mathcal{H}$ a *proper* subgroup of $\mathcal{G}$ and write $\mathcal{H} \subset \mathcal{G}$.

Example: The subset $\{I, R_X\}$ of $\mathcal{V}_4$ is closed under the group multiplication. This subset forms a two-element subgroup of $\mathcal{V}_4$.

The order of a subgroup divides the order of its host group. If $n_\mathcal{G} = |\mathcal{G}|$ and $n_\mathcal{H} = |\mathcal{H}|$, then $n_\mathcal{G}/n_\mathcal{H} = n_\mathcal{C}$, where $n_\mathcal{C}$ is an integer. If $|\mathcal{H}| = |\mathcal{G}|$, $n_\mathcal{C} = 1$, otherwise $n_\mathcal{C} > 1$.

The subgroup $\mathcal{H}$ can be used to partition the group $\mathcal{G}$ into $n_\mathcal{C}$ subsets, each containing $n_\mathcal{H}$ group operations. This decomposition can be carried out as follows. The group operations $g_1, g_2, \cdots, g_{n_\mathcal{G}}$ are written out, and those that belong to the subgroup $\mathcal{H}$ are removed from this list. For simplicity, we assume the group operations are numbered so that the first $n_\mathcal{H}$ belong to the subgroup $\mathcal{H}$. One group operation (ω_2) is chosen from the remaining $n_\mathcal{G} - n_\mathcal{H}$ group elements. This group operation is multiplied by all the $n_\mathcal{H}$ operations in the subgroup $\mathcal{H}$. These $n_\mathcal{H}$ operations are all different from the first set of $n_\mathcal{H}$ removed from the list of group operations. They are removed, leaving $n_\mathcal{G} - 2n_\mathcal{H}$ group operations. This procedure is repeated. During the last sweep through this process, the group operation $\omega_{n_\mathcal{C}}$ multiplies $g_1, \cdots, g_h$ to reproduce the last set of $n_\mathcal{H}$ group operations. Every group operation can then be represented uniquely in the form (identifying $\omega_1 = I$)

$$g_k = \omega_\alpha g_j \qquad \begin{array}{rcl} \alpha & = & 1, 2, \cdots, n_\mathcal{C} \\ j & = & 1, 2, \cdots, n_\mathcal{H} \end{array} \tag{10.74}$$

The subsets $\omega_\alpha g_1, \omega_\alpha g_2, \cdots, \omega_\alpha g_h = \omega_\alpha \circ \{g_1, g_2, \cdots, g_h\}$ are called *cosets*. Each coset has $|\mathcal{H}|$ group operations in it. The group operations $\{\omega_1, \omega_2, \cdots, \omega_{n_\mathcal{C}}\}$ are called *coset representatives*. The set of coset representatives is usually denoted $\mathcal{C} = \mathcal{G}/\mathcal{H}$. We have the result that $|\mathcal{G}/\mathcal{H}| = |\mathcal{G}|/|\mathcal{H}|$.

Example: The group $\mathcal{V}_4$ acting in $\mathbb{R}^3$ possesses the four group operations $\{I, R_X, R_Y, R_Z\}$. Assume a subgroup $\mathcal{H}$ contains the two operations $\{I, R_X\}$. This is the first coset in a coset deomposition. Removing these two operations from the four belonging to $\mathcal{V}_4$ leaves two: $\{R_Y, R_Z\}$. We can choose either of the group operations in this coset to represent this coset. We arbitrarily choose R_Z. Then the two group operations in this coset can be written as the product of this coset representative R_Z with each of the two subgroup operations I and R_X in turn:

$$R_Z\{I, R_X\} = \{R_Z, R_Y\} \tag{10.75}$$

If we were to choose R_Y rather than R_Z to represent this coset, we would obtain the same two group operations, but in a different order:

$$R_Y\{I, R_X\} = \{R_Y, R_Z\}$$

The idea of coset decomposition can be simply assimilated by pointing out that every operation in a group can be identified with a "matrix element" in an $n_{\mathcal{C}} \times n_{\mathcal{H}}$ matrix:

$$\begin{array}{c|cccccc} & g_1 = I & g_2 & \cdots & g_j & \cdots & g_{n_{\mathcal{H}}} \\ \hline \omega_1 = I & \omega_1 g_1 & g_2 & \cdots & g_j & \cdots & g_{n_{\mathcal{H}}} \\ \omega_2 & \omega_2 & \omega_2 g_2 & \cdots & \omega_2 g_j & \cdots & \omega_2 g_{n_{\mathcal{H}}} \\ \vdots & \vdots & \vdots & \ddots & \vdots & \ddots & \vdots \\ \omega_\alpha & \omega_\alpha & \omega_\alpha g_2 & \cdots & \omega_\alpha g_j & \cdots & \omega_\alpha g_{n_{\mathcal{H}}} \\ \vdots & \vdots & \vdots & \ddots & \vdots & \ddots & \vdots \\ \omega_{n_{\mathcal{C}}} & \omega_{n_{\mathcal{C}}} & \omega_{n_{\mathcal{C}}} g_2 & \cdots & \omega_{n_{\mathcal{C}}} g_j & \cdots & \omega_{n_{\mathcal{C}}} g_{n_{\mathcal{H}}} \end{array} \tag{10.76}$$

Since $\omega_1 = g_1 = I$, the group labels identifying the rows and columns are redundent, and the entire coset decomposition can be written in matrix form where the top row lists the subgroup operations and the left-hand column provides the coset representatives.

Example: The subgroup decomposition for $\mathcal{V}_4$ described above is simply:

$$\begin{bmatrix} I & R_X \\ R_Z & R_Y \end{bmatrix} \tag{10.77}$$

From this, we see $\mathcal{H} = \{I, R_X\}$ and the two coset representatives are $\omega_1 = I, \omega_2 = R_Z$. Each row contains a coset. Each row is obtained by multiplying the coset representative at the left of the row into the subgroup operations in the top row.

Remark: Coset decompositions can be constructed by reversing the order of multiplication: $g_k = g_j \omega_\alpha$. The decomposition is then represented by an $n_{\mathcal{H}} \times n_{\mathcal{C}}$ matrix. If the group $\mathcal{G}$ is commutative, the two matrices describing these *left*- and *right*-coset decompositions are transposes of each other. If $\mathcal{G}$ is not commutative, these two matrices are not transposes of each other.

10.10 SINGULAR SETS

There are two types of singular sets associated with equivariant dynamical systems. One is topological, the other is algebraic. The topological singular set depends on the equivariance group and its defining matrix representation in $\mathbb{R}^N$. The algebraic singular set depends on the local diffeomorphism chosen to mod out the symmetry group. The topological singular set is a subset of the algebraic singular set:

$$\text{Singular set of} \quad \mathcal{G} \quad \subseteq \quad \text{Singular set of} \quad \frac{\partial f}{\partial x} \tag{10.78}$$

Although the two singular sets are often equal, we show below that this is not always the case.

The topological singular set is determined by looking for the fixed points of each linear transformation $\gamma_i \in \Gamma^{\mathrm{Def}}(\mathcal{G})$. A point x is a fixed point of γ_i if $\gamma_i x = x$. The topological singular set is the union of the set of fixed points for all the equivariance transformations γ_i, $\gamma_i \neq I_N$.

Example 1: The singular set of the inversion group $\mathcal{P}$ acting on $\mathbb{R}^3$ is determined from the singular set of the single group operation P:

$$\begin{bmatrix} -1 & 0 & 0 \\ 0 & -1 & 0 \\ 0 & 0 & -1 \end{bmatrix} \begin{bmatrix} x_1 \\ x_2 \\ x_3 \end{bmatrix} = \begin{bmatrix} x_1 \\ x_2 \\ x_3 \end{bmatrix} \Rightarrow x_1 = x_2 = x_3 = 0 \tag{10.79}$$

The topological singular set of $\mathcal{P}$ acting in $\mathbb{R}^3$ is the origin.

The algebraic singular set is the set of points on which the Jacobian of the local diffeomorphism that mods out the symmetry vanishes.

The algebraic singular set for the inversion group $\mathcal{P}$ acting in $\mathbb{R}^3$ must be larger than the topological singular set. The invariant polynomials are all of second degree: $X^2, XY, Y^2, \cdots$. All matrix elements in the Jacobian must therefore be linear in the coordinates. The determinant of the Jacobian must therefore be a homogeneous polynomial of degree 3. The only homogeneous degree 3 function that has a single singular point at the origin is $(X^2 + Y^2 + Z^2)^{3/2}$. This is not a polynomial. For this reason, in this case the topological singular set is a proper subset of the algebraic singular set.

Equality of the two singular sets (a common occurrence) is shown for the group $\mathcal{V}_4$ in the following example.

Example 2: The topological singular set of the four-group $\mathcal{V}_4$ in $\mathbb{R}^3$ generated by rotations consists of the union of the X-, Y-, and Z-axes. A useful $4 \rightarrow 1$ local diffeomorphism that mods out the $\mathcal{V}_4$ symmetry in $\mathbb{R}^3$ is

$$\begin{aligned} f_1 &= \tfrac{1}{2}(X^2 - Y^2) \\ f_2 &= \tfrac{1}{2}(X^2 + Y^2 - 2Z^2) \\ f_3 &= XYZ \end{aligned} \tag{10.80}$$

The Jacobian of this transformation is

$$\left[\frac{\partial f_i}{\partial x_j}\right] = \begin{bmatrix} X & -Y & 0 \\ X & Y & -2Z \\ YZ & ZX & XY \end{bmatrix} \xrightarrow{\det} 2(X^2Y^2 + Y^2Z^2 + Z^2X^2) \tag{10.81}$$

The Jacobian vanishes on the Z-axis $X = 0, Y = 0$. It also vanishes on the X- and Y-axes. The algebraic singular set is the union of the three rotation axes. For this equivariance group, the algebraic and topological singular sets are the same.

10.11 ORBITS (KINETICS AND DYNAMICS)

"Orbit" is a technical term that has different meanings in the theory of groups and the theory of dynamical systems. The difference between the two meanings is very much like the difference between kinematics and dynamics in physics. Since we are combining the theory of groups with the theory of dynamical systems, the two concepts of orbits will be strongly linked.

In group theory the orbit of a point $x \in \mathbb{R}^N$ is the set of points $\gamma_i x$, $\gamma_i \in \mathcal{G}$. In general, most points $x \in \mathbb{R}^N$ have full orbits: the set of points $\gamma_i x$ consists of $|\mathcal{G}|$ distinct symmetry-related points. If x is a point that does not have a full orbit, there is at least one $\gamma_i \in \mathcal{G}$, $\gamma_i \neq I_N$, that leaves x fixed: $\gamma_i x = x$. In fact, the set of $\gamma_i \in \mathcal{G}$ that leaves x fixed is a subgroup $\mathcal{H} \subseteq \mathcal{G}$. If the fixed point subgroup $\mathcal{H}$ of x is larger than the identity subgroup I_N, x is a singular point. Not only is it a singular point under the group action (topological singularity), but by the inclusion (10.78) it is a singular point of any local diffeomorphism that mods out the symmetry. The orbit of any singular point $x \in R^N$ is the orbit of x under the coset representatives of $\mathcal{G}/\mathcal{H}$. There are $|\mathcal{G}|/|\mathcal{H}|$ distinct points in the orbit of x under $\mathcal{G}$ when x is singular.

An orbit in a dynamical system is a solution $\phi(t)$ of the dynamical system equations $dx_i/dt = f_i(x;c)$. We usually mean *closed* orbits: trajectories that return to their starting point after a finite time T, the (minimum) period of the orbit: $\phi(t+T) = \phi(t)$.

If x_0 is a nonsingular point on a dynamical orbit, then $\gamma_i x_0$ is also on a dynamical orbit, for each $\gamma_i \in \mathcal{G}$. There are $|\mathcal{G}|$ symmetry-related points $\gamma_i x_0$. The point $\gamma_i x_0$ is on the orbit $\gamma_i \phi(t)$. The main question is whether the orbits $\phi(t)$ and $\gamma_i \phi(t)$ consist of the same set of points or a different set of points.

If h points $x_0 = I_N x_0 = \gamma_1 x_0, \gamma_2 x_0, \cdots, \gamma_h x_0$ are on the same orbit they constitute a subgroup $\mathcal{H} \subseteq \mathcal{G}$. If $x_0 = \phi(0)$, the remaining $h-1$ symmetry-related points occur at $\phi(\frac{i}{h}T)$, $i = 1, 2, \cdots, h-1$. There are $n_{\mathcal{C}} - 1$ additional orbits that are symmetry-related to the orbit $\phi(t)$, where $n_{\mathcal{C}} = |\mathcal{G}/\mathcal{H}|$. These orbits are obtained from the orbit $\phi(t) = \phi_1(t)$ by operating on $\phi_1(t)$ with the coset representatives ω_α: $\phi_\alpha(t) = \omega_\alpha \phi_1(t)$. Along the orbit $\phi_\alpha(t)$ the h points $\omega_\alpha \circ \{\gamma_1, \gamma_2, \cdots, \gamma_h\} x_0$ occur at $\phi_\alpha(\frac{i}{h}T)$.

Example: Assume $\phi_1(t)$ is a closed orbit of period T for a dynamical system equivariant under $\mathcal{V}_4$. Assume that $\phi_1(0) = x_0$, and that the point $R_X x_0 \neq x_0$ also lies on this orbit, but the two other symmetry-related points $R_Y x_0$ and $R_Z x_0$ do not lie on this orbit. Then $\phi_1(\frac{1}{2}T) = R_X x_0$. The orbit $\phi_2(t) = R_Y \phi_1(t)$ has period T, with $\phi_2(0) = R_Y x_0$ and $\phi_2(\frac{1}{2}T) = R_Z x_0$. If we choose R_Z instead of R_Y as the representative of the second coset, then $\tilde{\phi}_2(t) = R_Z \phi_1(t)$ has the property that $\tilde{\phi}_2(0) = R_Z x_0$ and $\tilde{\phi}_2(\frac{1}{2}T) = R_Y x_0$

Remark: The ideas expressed in the example above can be carried out in more detail when the symbol sequence of the periodic orbit(s) is known in the image space.

11

Invariant Polynomials

11.1 INVARIANT POLYNOMIALS

Our ultimate goal is to find the relation between equivariant dynamical systems and locally identical ("locally diffeomorphic") invariant dynamical systems. This is the cover and image problem. The image dynamical system is always expressed in terms of *invariant polynomials*. The cover dynamical system is expressed in terms of *equivariant polynomials*. It is the objective of this chapter to describe invariant polynomials, equivariant polynomials, and their properties.

11.1.1 What Are They?

Invariant polynomials are unchanged under all the group operations. If γ_i is a matrix in the defining representation $\Gamma^{\mathrm{Def}}(\mathcal{G})$ and $p_\alpha(X)$ is an invariant polynomial, the condition

$$p_\alpha(\gamma_i X) = p_\alpha(X) \qquad \text{all } \gamma_i \in \Gamma^{\mathrm{Def}}(\mathcal{G}) \tag{11.1}$$

defines an invariant polynomial.

Example: Under the operations $C_3^{\pm 1}$ of $\mathcal{C}_3$ acting in $\mathbb{R}^2$ the coordinates X and Y transform as

$$\begin{bmatrix} X \\ Y \end{bmatrix}' = \begin{bmatrix} -\frac{1}{2} & \pm\frac{\sqrt{3}}{2} \\ \mp\frac{\sqrt{3}}{2} & -\frac{1}{2} \end{bmatrix} \begin{bmatrix} X \\ Y \end{bmatrix} = \begin{bmatrix} -\frac{1}{2}X \pm \frac{\sqrt{3}}{2}Y \\ \mp\frac{\sqrt{3}}{2}X - \frac{1}{2}Y \end{bmatrix} \tag{11.2}$$

Neither X nor Y is an invariant polynomial. Neither are the polynomials X^2, XY, Y^2. However, $p_1(X,Y) = X^2 + Y^2$ is invariant, since

$$p_1(X',Y') = X'^2 + Y'^2 = \left(-\frac{1}{2}X \pm \frac{\sqrt{3}}{2}Y\right)^2 + \left(\mp\frac{\sqrt{3}}{2}X - \frac{1}{2}Y\right)^2 =$$

$$X^2 + Y^2 = p_1(X,Y) \tag{11.3}$$

It can also be verified that the cubic polynomials $p_2(X,Y) = X^3 - 3XY^2$ and $p_3(X,Y) = 3X^2Y - Y^3$ are invariant polynomials.

Remark: Products of invariant polynomials are also invariant polynomials. Thus, it is an easy matter to construct some higher degree invariant polynomials as products of p_1, p_2, and p_3, as shown below

Degree	Polynomial
4	p_1^2
5	p_1p_2, p_1p_3
6	$p_1^3, p_2^2, p_2p_3, p_3^2$

(11.4a)

In fact, not all the degree-6 polynomials are independent, for

$$p_1^3 = (X^2+Y^2)^3 = (X^3 - 3XY^2)^2 + (3X^2Y - Y^3)^2 = p_2^2 + p_3^2 \tag{11.4b}$$

Of the four $6th$ degree polynomials, only 3 are linearly independent.

Invariant polynomials up to degree three are given for some simple groups in $\mathbb{R}^3$:

Group	Degree 1	2	3
σ_Z	X, Y	Z^2, X^2, XY, Y^2	$X^iY^j(i+j=3), Z^2X, Z^2Y$
$\mathcal{R}_Z$	Z	X^2, XY, Y^2, Z^2	Z^3, ZX^2, ZXY, ZY^2
$\mathcal{P}$	–	$X^2, Y^2, Z^2, XY, YZ, ZX$	–
$\mathcal{C}_3$	Z	Z^2, X^2+Y^2	$X^3 - 3XY^2, 3X^2Y - Y^3$ $Z^3, Z(X^2+Y^2)$

(11.5)

11.1.2 How to Construct Invariant Polynomials

It is well known that any real function $f(X)$ of a single real variable X, defined on the symmetric interval $(-a, +a)$, can be written as a superposition of an even function

and an odd function

$$\begin{aligned} f(X) &= f_{\rm even}(X) + f_{\rm odd}(X) \\ f_{\rm even}(X) &= \frac{1}{2}[f(X) + f(-X)] \\ f_{\rm odd}(X) &= \frac{1}{2}[f(X) - f(-X)] \end{aligned} \tag{11.6}$$

Perhaps not quite so well known is that the odd function averages to zero under the group inversion operation $P : X \to -X$:

$$\sum_{g\in\mathcal{G}} g f_{\rm odd}(X) = (I+P)\, f_{\rm odd}(X) = f_{\rm odd}(+X) + f_{\rm odd}(-X) = 0 \tag{11.7}$$

This result is a special case of a much more general result, valid for any group $\mathcal{G}$ [25]. Every polynomial $p(X)$ of several variables $X = (X_1, X_2, \cdots, X_N)$ can be decomposed into a sum of two polynomials

$$p(X) = p_{\rm inv}(X) + p_{\rm cov}(X) \tag{11.8}$$

One is invariant under the group operations. The other averages to zero under the group operations.

This theorem allows us to construct invariant polynomials by averaging. The invariant part of any polynomial is constructed by the following averaging procedure

$$\langle p(X)\rangle = \frac{1}{|\mathcal{G}|}\sum_{\gamma\in\mathcal{G}} p(\gamma X) \tag{11.9}$$

The left-hand side is simply the invariant part of any polynomial, since

$$\langle p(X)\rangle = \langle p_{\rm inv}(X) + p_{\rm cov}(X)\rangle = \langle p_{\rm inv}(X)\rangle + 0 = p_{\rm inv}(X) \tag{11.10}$$

The right-hand side of (11.9) is interpreted as follows. Compute the polynomial $p(\gamma X)$ for each $\gamma \in \mathcal{G}$, sum the $|\mathcal{G}|$ resulting polynomials, and divide by the order of $\mathcal{G}$.

Definition: The operator $\left(\frac{1}{|\mathcal{G}|}\sum_{\gamma\in\mathcal{G}}\gamma\right) p(X)$ is called the *Reynold's operator*.

Example: We apply the Reynold's operator for the group $\mathcal{C}_3$ to the polynomial X^2:

$$\begin{aligned} \frac{1}{|\mathcal{G}|}\sum_{\gamma\in\mathcal{G}}\gamma X^2 &= \frac{1}{3}\left\{X^2 + \left(-\frac{1}{2}X + \frac{\sqrt{3}}{2}Y\right)^2 + \left(-\frac{1}{2}X - \frac{\sqrt{3}}{2}Y\right)^2\right\} \\ &= \frac{1}{2}(X^2+Y^2) \end{aligned} \tag{11.11}$$

This operator projects XY to the invariant 0 and Y^2 to the invariant polynomial $\frac{1}{2}(X^2+Y^2)$.

```
> with(linalg):
> n:=4:
> Gamma[1]:=matrix(3,3,[[0,1,0],[-1,0,0],[0,0,-1]]);
```

$$\Gamma_1 = \begin{bmatrix} 0 & 1 & 0 \\ -1 & 0 & 0 \\ 0 & 0 & -1 \end{bmatrix}$$

```
> for i from 2 to n do
     Gamma[i]:=multiply(Gamma[i-1],Gamma[1]):
  od:
> V:=matrix(3,1,[[x],[y],[z]]):
> F(X,Y,Z):=X^2*Z;
```

$$F(X,Y,Z) = X^2 Z$$

```
> f(x,y,z):=0:
  for i from 1 to n do
     VP:=multiply(Gamma[i],V):
     xpr:=VP[1,1]: ypr:=VP[2,1]: zpr:=VP[3,1]:
     f(x,y,z):=f(x,y,z)
         +subs(X=xpr,Y=ypr,Z=zpr,F(X,Y,Z)):
  od:
  simplify(%/n);
```

$$-\frac{1}{2}zx^2 + \frac{1}{2}zy^2$$

Fig. 11.1 Program for projecting symmetric part of a polynomial $f_{\rm inv}(x,y,z)$ from the polynomial $f(x,y,z)$. The matrix Γ_1 is the generator for the action of $\mathcal{S}_4$ on $\mathbb{R}^3$.

The Maple code shown in Fig. 11.1 can be used to project the invariant part out of any polynomial. The first line loads the linear algebra package. The computation is done for a group with one generator Γ_1 and one relation $\Gamma_1^4 = Id.$ The second and third lines introduce the order ($n = 4$) of this group and its generator. The matrix is echoed back as a self-consistency check. This is the generator for the group $\mathcal{S}_4$. The next line is a short "do" loop that generates the matrix representatives of the remaining three group operations. The line following introduces the three coordinates (x, y, z) in $\mathbb{R}^3$ as the matrix V.

The function from which the symmetrized part is to be projected out is finally introduced. In the case shown it is X^2Z. For technical purposes the polynomial is expressed in terms of capitals. The last line contains the do loop that projects out the symmetric part of the polynomial $F(X,Y,Z) = X^2Z$. It is $\frac{1}{2}(-x^2 + y^2)z$.

11.1.3 How Many Invariant Polynomials Are There?

As (11.5) shows, the number of invariant polynomials of any degree depends in detail on the equivariance group. For some purposes, we would like to be able to count the

number of functionally independent invariant polynomials as a function of symmetry group $\mathcal{G}$, more specifically its defining representation $\Gamma^{\mathrm{Def}}(\mathcal{G})$ in $\mathbb{R}^N$, and the degree d.

It is possible to construct a generating function to do the counting. The generating function is

$$f(u;\Gamma^{\mathrm{Def}}(\mathcal{G})) = \frac{1}{|\mathcal{G}|}\sum_{g\in\mathcal{G}}\frac{1}{\det|I_N - u\Gamma^{\mathrm{Def}}(g)|} = \sum_{d=0}^{\infty} n(d)u^d \tag{11.12}$$

In this expression $n(d)$ is the number of functionally independent invariant polynomials of degree d and u is an indeterminant.

This generating function can be derived from the Reynold's projection operator. The basic idea is similar to that used to construct generating functions for representations of a group $\mathcal{G}$ in $\mathbb{R}^N$ from knowledge of its irreducible representations.

Example 1: For the two-element group $\mathcal{R}_Z$ acting in $\mathbb{R}^3$ we find

$$f(u;\mathcal{R}_Z) = \frac{1}{2}\left\{\left|I_3 - u\begin{bmatrix}1&0&0\\0&1&0\\0&0&1\end{bmatrix}\right|^{-1} + \left|I_3 - u\begin{bmatrix}-1&0&0\\0&-1&0\\0&0&1\end{bmatrix}\right|^{-1}\right\} =$$

$$\frac{1}{2}\left\{\frac{1}{(1-u)^3} + \frac{1}{(1-u)(1+u)^2}\right\} = \frac{1+u^2}{(1-u)^3(1+u)^2} \tag{11.13}$$

The generating functions for the three order-2 groups in $\mathbb{R}^3$ are

$\mathcal{G}$	σ_Z	$\mathcal{R}_Z$	$\mathcal{P}$
$f(u,\mathcal{G})$	$\dfrac{1}{(1-u)^3(1+u)^1}$	$\dfrac{1+u^2}{(1-u)^3(1+u)^2}$	$\dfrac{1+3u^2}{(1-u)^3(1+u)^3}$

(11.14)

The coefficients $n(d)$ of the powers u^d for these three generating functions are

	0	1	2	3	4	5	6	7	8	9	10
σ_Z	1	2	4	6	9	12	16	20	25	30	36
$\mathcal{R}_Z$	1	1	4	4	9	9	16	16	25	25	36
$\mathcal{P}$	1	0	6	0	15	0	28	0	45	0	66

(11.15)

Example 2: The generating function for polynomials invariant in X and Y under $\mathcal{C}_3$ acting in $\mathbb{R}^2$ is computed by summing three terms:

$$f(u;\mathcal{C}_3) = \frac{1}{3}\left(\frac{1}{\det[I_2 - uI_2]} + \frac{1}{\det[I_2 - uM]} + \frac{1}{\det[I_2 - uM^2]}\right)$$

where M is the 2×2 matrix generator of this group, given in (11.2). The determinant is invariant under similarity transformations, so that we can do this computation by

diagonalizing M and M^2 (separately!). The eigenvalues of M and M^2 are equal: the two eigenvalues are $\epsilon = e^{2\pi i/3}$ and ϵ^*. As a result, the generating function is

$$f(u;\mathcal{C}_3) = \frac{1}{3}\left(\frac{1}{(1-u)^2} + \frac{2}{(1-\epsilon u)(1-\epsilon^* u)}\right) = \frac{1-u+u^2}{(1-u)^2(1+u+u^2)} \tag{11.16}$$

The Taylor series expansion of this function is

$$f(u;\mathcal{C}_3) = 1+1u^2+2u^3+1u^4+2u^5+3u^6+2u^7+3u^8+4u^9+3u^{10}+\cdots \tag{11.17}$$

We point out that the coefficient of u^6 indicates that there are three independent degree-6 invariant polynomials in X and Y. The list given in (11.4a) includes four, among which there is one constraint, (11.4b). This constraint indicates that of these four, only three are *functionally* independent. The generating function for this group, acting in $\mathbb{R}^3$ instead of $\mathbb{R}^2$, is obtained by multiplying the $\mathbb{R}^2$ generating function $f(u;\mathcal{C}_3)$ given above by the factor $\frac{1}{1-u}$.

Extended Remark: We can develop an appreciation for the algorithm (11.12) for constructing generating functions $f(u;\Gamma^{\rm Def}(\mathcal{G}))$ from the following considerations. A generating function for monomials in $\mathbb{R}^2$ based on the coordinates X and Y is

$$f(u) = \frac{1}{1-uX}\frac{1}{1-uY} = 1+u(X+Y)+u^2(X^2+XY+Y^2)+u^3(X^3+\cdots$$

$$= \frac{1}{\det\begin{bmatrix} 1-uX & 0 \\ 0 & 1-uY \end{bmatrix}} \tag{11.18}$$

If we are interested only in the number of independent terms of degree d, not in the detailed form of these polynomials, we can drop the coordinate information (X,Y) from this generating function, to obtain

$$f(u) = \frac{1}{\det\left[I_2 - uI_2\right]} \tag{11.19}$$

The monomials are all invariant under the trivial group containing one operation $\mathcal{G} = Id$, so that

$$f(u;\Gamma^{\rm Def}(Id)) = \frac{1}{|Id|}\sum_{g\in Id}\frac{1}{[I_2 - u\Gamma^{\rm Def}(Id)]} \tag{11.20}$$

Extending the symmetry to some larger group, for example $\mathcal{R}_z$ or $\mathcal{C}_3$, requires introduction of the representatives $\Gamma^{\rm Def}(g_i)$ of the additional group operations, as well as averaging by the number of operations in the group.

11.2 GENERATORS AND RELATIONS

From the examples carried out so far, it is clear that the higher degree invariant polynomials are *functionally* dependent on some subset of lower degree invariant polynomials. In general, it is possible to find a small set of invariant polynomials that can be used to construct *any* invariant polynomial through the three operations

- scalar multiplication
- linear superposition
- polynomial multiplication.

Such a subset of invariant polynomials is called an *integrity basis* [25].

11.2.1 Integrity Basis

An integrity basis plays the same role for functions $f(X_1, X_2, \cdots, X_N)$ on $\mathbb{R}^N$ as a linear vector space basis plays for vectors in $\mathbb{R}^N$. The integrity basis for the three representations of the order-2 group $\{I, A\}$ in $\mathbb{R}^3$ are

Group	Integrity Basis	Number
σ_Z	X, Y, Z^2	3
$\mathcal{R}_Z$	Z, X^2, XY, Y^2	4
$\mathcal{P}$	$X^2, Y^2, Z^2, XY, YZ, ZX$	6

(11.21)

The search for an integrity basis is simplified by a nice theorem by Noether. The theorem states that for any equivariance group $\mathcal{G}$ the integrity basis consists of homogeneous invariant polynomials of degree d, $d \leq |\mathcal{G}|$ [25]. For the order-2 groups the integrity basis consists of only first and second degree invariant polynomials.

11.2.2 How to Construct an Integrity Basis

An integrity basis can be constructed from a set of invariant polynomials in an algorithmic way. The algorithm actually constructs a "Gröbner basis" (of functions). A Gröbner basis is a minimal set of polynomials from which all possible polynomials of a certain type can be constructed from the three operations of scalar multiplication, "vector" addition, and "vector" multiplication. The term "vector" in this case refers to polynomial functions. The Gröbner basis is the closest possible analog to the concept of basis that we find so useful for linear vector spaces.

The algorithm for constructing a Gröbner basis from a set of polynomial functions has been thoroughly studied and implemented in a number of symbol manipulation packages. In Fig. 11.2 we show a simple Maple code for computing a Gröbner basis from polynomials invariant under the group $\mathcal{S}_4$. There are nine such polynomials of degree less than or equal to four. Of these, only six are necessary to form a basis for the expansion of all $\mathcal{S}_4$-invariant functions. The first entry loads the Gröbner basis package. The echo shows which subroutines are available. Summaries of each subroutine and protocols for their use can be accessed in an intuitive

```
> with(grobner);
```

$$[finduni, finite, gbasis, gsolve, leadmon, normalf, solvable, spoly]$$

```
> ?gbasis;
> [Coords]:=[X,Y,Z];
> [F]:=[X^2+Y^2,Z^2,X*Y*Z,(X^2-Y^2)*Z,X^4+Y^4,
        X*Y*(X^2-Y^2),X^2*Y^2,(X^2+Y^2)*Z^2,Z^4];
> gbasis([F],[Coords]);
```

$$[XY^3, Y^4, XYZ, ZY^2, Y^2 + X^2, Z^2]$$

Fig. 11.2 Nine polynomials of degree ≤ 4 are invariant under the group $\mathcal{S}_4$. The code segment shown constructs an integrity basis from these nine functions. The basis is six-dimensional. The output polynomials are not necessarily invariant under the group action (e.g., XY^2, Y^4, ZY^2). Their invariant parts, $p_{\rm inv}(X)$, are chosen to be integrity basis functions.

way (`?gbasis`). The coordinates are introduced as the array `[Coords]` and the invariant polynomials of degree $d \leq |\mathcal{G}|$ are introduced as another array, `[F]`. The subroutine `gbasis([F],[Coords])` returns the appropriate Gröbner basis. In this case the output is the set $[XY^3, Y^4, XYZ, ZY^2, Y^2 + X^2, Z^2]$.

Remark 1: The subroutine `gbasis` is designed to construct a minimal basis set — a Gröbner basis. It is not designed to preserve the invariance (under $\mathcal{G}$) property of the input list of polynomials. In some cases the output list may contain polynomials that are not invariant under $\mathcal{G}$. In the case presented, three of the six integrity basis functions are not invariant: XY^3, Y^4, and Y^2Z. The invariant part should be projected out of each noninvariant polynomial in the Gröbner basis set.

Remark 2: It is sometimes obvious that one of the low degree ($d \leq |\mathcal{G}|$) invariant polynomials cannot be a basis polynomial. For example, Z^4 is the square of Z^2, so is not functionally independent of Z^2. As long as Z^2 is in the set of basis polynomials, there is no need for the polynomial Z^4.

11.2.3 Relations

The homogeneous polynomials in an integrity basis are *linearly independent* but not always *functionally independent*. They may satisfy some relation(s) of the form

$$s_\alpha(p_1, p_2, \cdots, p_K) = 0 \tag{11.22}$$

Here $p_1, p_2, \cdots, p_K$ are the K invariant polynomials that constitute an integrity basis and s_α is some polynomial function of its arguments. There may be more than one independent polynomial relation: If so, the different relations are indexed by the subscript α.

Definition: Functional relations of the form (11.22) are called *syzygies* [25].

Table 11.1 The groups σ_Z, $\mathcal{R}_Z$, and $\mathcal{P}$ are three distinct faithful representations of the two-group $\{I, A\}$ in $\mathbb{R}^3$. For each, we identify the invariant polynomials of degree d up to two, the Grobner basis, the dimension of K the Grobner basis, all syzygies, and the equivariant polynomials.

Group	Invariant Polynomials	Grobner Basis	K	Syzygies	Equivariant Polynomials
σ_Z	X, Y X^2, XY, Y^2, Z^2	$p_1 = X$ $p_2 = Y$ $p_3 = Z^2$	3	–	$R_1 = Z$
$\mathcal{R}_Z$	Z X^2, XY, Y^2, Z^2	$p_1 = Z$ $p_2 = X^2$ $p_3 = XY$ $p_4 = Y^2$	4	$s_4 = p_2p_4 - p_3^2$	$R_1 = X$ $R_2 = Y$
$\mathcal{P}$	– X^2, Y^2, Z^2 XY, YZ, ZX	$p_1 = X^2$ $p_2 = Y^2$ $p_3 = Z^2$ $p_4 = YZ$ $p_5 = ZX$ $p_6 = XY$	6	$s_4 = p_1p_2 - p_6^2$ $s_5 = p_2p_3 - p_4^2$ $s_6 = p_3p_1 - p_5^2$ $s_7 = p_1p_4 - p_5p_6$ $s_8 = p_2p_5 - p_6p_4$ $s_9 = p_3p_6 - p_4p_5$	$R_1 = X$ $R_2 = Y$ $R_3 = Z$

In many cases, when there are K polynomials in an integrity basis for functions on $\mathbb{R}^N$ invariant under $\mathcal{G}$, there will be $K - N$ independent functional relations (11.22): $\alpha = N + 1, \cdots, K$. We call these *simple syzygies*. There are instances of group actions on $\mathbb{R}^N$ that produce nonsimple syzygies (e.g., $\mathcal{P}, \mathcal{S}_4$ on $\mathbb{R}^3$).

In Table 11.1, for the three representations of the two-element group $\{I, A\}$ acting faithfully on $\mathbb{R}^3$, we provide information about the invariant polynomials up to degree 2, the Gröbner basis, the dimension K of the Gröbner basis, the syzygies that are satisfied, and the equivariant polynomials, to be discussed in Section 11.3.

The Gröbner basis for σ_Z has dimension $K = 3$, so there are no syzygies. The Gröbner basis for $\mathcal{R}_Z$ has dimension $K = 4$, so there is $4 - 3 = 1$ simple syzygy for $\mathcal{R}_Z$. The group $\mathcal{P}$ has 6 (nonsimple) syzygies.

Construction of syzygies also has a long history, and can therefore be carried out algorithmically. The algorithm is as follows. Introduce one variable for each invariant polynomial $p_i(X)$ in the Gröbner basis. If there are K invariant polynomials, this

```
> p1:=X^2: p2:=Y^2: p3:=Z^2: p4=Y*Z: p5=Z*X:
    p6=X*Y:
> gbasis([p1-a1,p2-a2,p3-a3,p4-a4,p5-a5,p6-a6],
    [X,Y,Z,a1,a2,a3,a4,a5,a6]);
```

$$\cdots, a3a6 - a4a5,\ a2a5 - a4a6,\ a1a4 - a5a6,\ a4^2 - a2a3,\ a5^2 - a1a3,\ a6^2 - a1a2$$

Fig. 11.3 Segment of Maple code suitable for computing syzygies among the six integrity basis polynomials for the group $\mathcal{P}$ acting in $\mathbb{R}^3$. The output shows six syzygies. These syzygies are not simple, since $6 \neq 6 - 3$ (# syzygies $\neq$ Dim. Integrity Basis $-$ Dim $\mathbb{R}^N$).

involves introducing a K-vector $(a_1, a_2, \cdots, a_K)$. Then find the Gröbner basis for the functions $[p_1 - a_1, p_2 - a_2, \cdots, p_K - a_K]$ using `gbasis`$([p_1 - a_1, p_2 - a_2, \cdots, p_K - a_K], [X, Y, Z, a_1, a_2, \cdots a_K])$. The Gröbner basis functions that depend *only* on the variables a_j, $s_\alpha(a_1, a_2, \cdots, a_K)$, are the polynomial constraints that are desired, and

$$s_\alpha(p_1, p_2, \cdots, p_K) = 0 \tag{11.23}$$

are the syzygies. The syzygies for the action of $\mathcal{P}$ on $\mathbb{R}^3$ are determined by the segment of Maple code shown in Fig. 11.3.

There are six polynomial functions depending only on the a_i. They lead directly to the following syzygies:

$$\begin{array}{rcccl}
s_4(p_1, p_2, p_3, p_4, p_5, p_6) & = & p_1 p_2 - p_6^2 & = & 0 \\
s_5(p_1, p_2, p_3, p_4, p_5, p_6) & = & p_2 p_3 - p_4^2 & = & 0 \\
s_6(p_1, p_2, p_3, p_4, p_5, p_6) & = & p_3 p_1 - p_5^2 & = & 0 \\
s_7(p_1, p_2, p_3, p_4, p_5, p_6) & = & p_1 p_4 - p_5 p_6 & = & 0 \\
s_8(p_1, p_2, p_3, p_4, p_5, p_6) & = & p_2 p_5 - p_6 p_4 & = & 0 \\
s_9(p_1, p_2, p_3, p_4, p_5, p_6) & = & p_3 p_6 - p_4 p_5 & = & 0
\end{array} \tag{11.24}$$

When the syzygies are simple, their interpretation is simple. We create from N equivariant coordinates $(X_1, X_2, \cdots, X_N)$ a set of K invariant coordinates $(p_1, p_2, \cdots, p_K)$. We will use these invariant coordinates to describe a K-dimensional space $\mathbb{R}^K(p)$, just as we use the equivariant coordinates to parameterize an N-dimensional space $\mathbb{R}^N(X)$. The mapping $(X_1, X_2, \cdots, X_N) \to (p_1, p_2, \cdots, p_K)$ is a mapping of an N-dimensional space into a K-dimensional space, where $K \geq N$ and usually $K > N$. The mapping $X \to p(X)$ actually maps the space $\mathbb{R}^N(X)$ into an N-dimensional manifold embedded in $\mathbb{R}^K(p)$ (neglecting singularities of lower dimension). When the syzygies are simple, the $K - N$ polynomial relations $s_\mu(p_1, p_2, \cdots, p_K) = 0$ provide $K - N$ nonlinear constraints to define the N-dimensional surface embedded in $\mathbb{R}^K(p)$.

If there are more than $K - N$ syzygies, then they are in some sense not independent. They still must define an N-dimensional subspace in $\mathbb{R}^K(p)$. To see how this comes about, we compute the Jacobian of the matrix $\partial s_\mu / \partial p_\alpha$ for the group $\mathcal{P}$ acting in $\mathbb{R}^3$. The six syzygies s_μ, $\mu = 4, \cdots, 9$, are listed in Table 11.1. There are six invariant

polynomials, so the Jacobian is a 6×6 matrix:

$$\frac{\partial s_\mu}{\partial p_\alpha} = \begin{array}{c} s_4 \\ s_5 \\ s_6 \\ s_7 \\ s_8 \\ s_9 \end{array} \begin{bmatrix} p_2 & p_1 & 0 & 0 & 0 & -2p_6 \\ 0 & p_3 & p_2 & -2p_4 & 0 & 0 \\ p_3 & 0 & p_1 & 0 & -2p_5 & 0 \\ p_4 & 0 & 0 & p_1 & -p_6 & -p_5 \\ 0 & p_5 & 0 & -p_6 & p_2 & -p_4 \\ 0 & 0 & p_6 & -p_5 & -p_4 & p_3 \end{bmatrix} \tag{11.25}$$

This Jacobian is nonsingular if the p_α are considered independent. However, they are not independent. The relations among them are best visualized by replacing the p_α by the corresponding invariant polynomials (e.g., $p_1 \to X^2$). This gives

$$\frac{\partial s_\mu}{\partial p_\alpha} = \begin{bmatrix} Y^2 & X^2 & 0 & 0 & 0 & -2XY \\ 0 & Z^2 & Y^2 & -2YZ & 0 & 0 \\ Z^2 & 0 & X^2 & 0 & -2ZX & 0 \\ YZ & 0 & 0 & X^2 & -XY & -ZX \\ 0 & ZX & 0 & -XY & Y^2 & -YZ \\ 0 & 0 & XY & -ZX & -YZ & Z^2 \end{bmatrix} \tag{11.26}$$

This Jacobian has rank $3 = 6 - 3 = K - N$. A maximal rank submatrix is easily obtained by Gauss-Jordan reduction. It is

$$\begin{bmatrix} X^2 & 0 & 0 & +YZ & -ZX & -XY \\ 0 & Y^2 & 0 & -YZ & +ZX & -XY \\ 0 & 0 & Z^2 & -YZ & -ZX & +XY \end{bmatrix} \tag{11.27}$$

This submatrix corresponds to the three syzygies

$$\begin{array}{lrcccc} s_7: & (X^2)(YZ) - (ZX)(XY) & = & p_1p_4 - p_5p_6 & = & 0 \\ s_8: & (Y^2)(ZX) - (XY)(YZ) & = & p_2p_5 - p_6p_4 & = & 0 \\ s_9: & (Z^2)(XY) - (YZ)(ZX) & = & p_3p_6 - p_4p_5 & = & 0 \end{array} \tag{11.28}$$

Any subset of three syzygies with full rank can be used as constraints to define the 3-dimensional surface embedded in $\mathbb{R}^6(p)$.

Remark: It may be wondered if the syzygies themselves satisfy additonal syzygies. That is, are there secondary relations of the form $\tilde{s}_j(s_4, s_5, \cdots, s_9) = 0$? For the polynomials p_α considered as independent, the primary syzygies $s_\mu(p_1, \cdots, p_K)$ do not satisfy secondary syzygies of the form $\tilde{s}_j(s_4, s_5, \cdots, s_9) = 0$.

11.2.4 How to Read the Generating Function

The generating function $f(u; \Gamma^{\mathrm{Def}}(\mathcal{G}))$ for invariant polynomials contains a great deal of information about the integrity basis and its syzygies, if only one understands how to read it. We illustrate this reading process by considering a number of examples of slowly increasing complexity.

Example 1: The generating function $f(u;\sigma_Z)$ is

$$f(u;\sigma_Z) = \frac{1}{(1-u)^3(1+u)} = \frac{1}{(1-u)^2(1-u^2)} \tag{11.29}$$

There is one factor $\frac{1}{1-u}$ for the monomial X, one factor $\frac{1}{1-u}$ for the monomial Y, and one factor $\frac{1}{1-u^2}$ for the monomial Z^2 in the integrity basis. There are three factors in the denominator, each of the form $1-u^{d_i}$, one for each of the three Gröbner basis polynomials of degree d_i.

We can determine the explicit form of the invariant polynomials by reintroducing information about the Gröbner basis into the generating function:

$$f(u;\sigma_Z) \to \frac{1}{(1-uX)(1-uY)(1-u^2Z^2)} \tag{11.30}$$

The power series expension of this function contains every invariant polynomial that can be constructed from this integrity basis exactly once. The coefficient of u^d identifies the degree of this invariant polynomial. For example, one of the quartic terms in this expansion is u^4XYZ^2.

Example 2: The generating function $f(u;\mathcal{R}_Z)$ is

$$f(u;\mathcal{R}_Z) = \frac{1+u^2}{(1-u)^3(1+u)^2} = \frac{1+u^2}{(1-u)(1-u^2)^2} \tag{11.31}$$

There are three factors in the denominator. The factor $\frac{1}{1-u}$ is for the degree $d=1$ integrity basis polynomial Z. But which two quadratic polynomials X^2, XY, Y^2 do the two factors $\frac{1}{(1-u^2)^2}$ represent? Shouldn't there be another factor $1-u^2$ in the denominator? If there were a third factor $1-u^2$ in the denominator, we could write the product of factors as follows

$$\begin{aligned}\frac{1}{1-u}\frac{1}{(1-u^2)^3} &= \frac{1}{1-u}\frac{1}{(1-u^2)^2}\frac{1}{1-u^2} \\ &= \frac{1}{1-u}\frac{1}{(1-u^2)^2}\left\{1+u^2\underbrace{+u^4+\cdots}\right\}\end{aligned}$$

If this expression is truncated beyond the quadratic terms (the terms within the underbrace are removed), the resulting expression is identical to the generating function $f(u;\mathcal{R}_Z)$ (11.31). This expression is trying to tell us that, at the level of $(u^2)^2$, one of the three quadratic terms is a function of the other two. That is, the syzygy

$$(X^2)(Y^2) = (XY)^2$$

is reflected in the structure of the generating function.

We can restore information about the form of the polynomials that can be constructed from the integrity basis by rewriting the generating function to include information about the integrity basis:

$$f(u;\mathcal{R}_Z) \to \frac{1+u^2XY}{(1-uZ)(1-u^2X^2)(1-u^2Y^2)} = \tag{11.32}$$

$$\sum_{n_1,n_2,n_3} \sum_{d_4} u^{1n_1+2n_2+2n_3+2d_4} (Z)^{n_1} (X^2)^{n_2} (Y^2)^{n_3} (XY)^{d_4} \tag{11.33}$$

In the summation above, the integers n_1, n_2, n_3 can assume any values between 0 and ∞ while the integer d_4 can only assume the two values 0 and 1. The sum includes all possible monomials that can be constructed from the integrity basis exactly once, and excludes no invariant polynomials.

Example 3: The generating function for the inversion group $\mathcal{P}$ acting in $\mathbb{R}^3$ is

$$f(u;\mathcal{P}) = \frac{1+3u^2}{(1-u^2)^3} \tag{11.34}$$

The factor $\frac{1}{(1-u^2)^3}$ tells us that there are three degree-two polynomials that occur to arbitrary powers in the expression for any polynomial. The numerator term can be expressed as

$$\frac{1}{(1-u^2)^3} = 1 + 3u^2 \underbrace{+ 6u^4 + 10u^6 + \cdots} \tag{11.35}$$

There are three other degree $d = 2$ polynomials in the integrity basis. The coefficient 3 in the numerator indicates that there are three syzygies that eliminate three of the six integrity basis polynomials at and beyond the quadratic level. This summarizes the three syzygies:

$$\begin{array}{rcl} (X^2)(Y^2) & = & (XY)^2 \\ (Y^2)(Z^2) & = & (YZ)^2 \\ (Z^2)(X^2) & = & (ZX)^2 \end{array} \tag{11.36}$$

If the integrity basis information is placed back into the generating function, we find

$$f(u;\mathcal{P}) \to 1 + u^2(XY + YZ + ZX)/(1-u^2X^2)(1-u^2Y^2)(1-u^2Z^2) = \tag{11.37}$$

$$\sum_{n_1,n_2,n_3} \sum_{d_1,d_2,d_3} u^{2n_1+2n_2+2n_3+2d_1+2d_2+2d_3} (X^2)^{n_1} (Y^2)^{n_2} (Z^2)^{n_3} (XY)^{d_1} (YZ)^{d_2} (ZX)^{d_3}$$

In this expansion the n_i and d_j have the usual properties: $0 \le n_i < \infty$ and $d_j = 0, 1$.

Example 4: The generating function for $\mathcal{C}_3$ acting in $\mathbb{R}^2$ is

$$f(u;\mathcal{C}_3) = \frac{1-u+u^2}{(1-u)^2(1+u+u^2)} = \frac{1+u^2+u^4}{(1-u^3)^2} \tag{11.38}$$

This last identity is not difficult to show. This form for the generating function tells us that there are two cubic polynomials that must be present in all powers. The numerator term can be reinterpreted as

$$\frac{1}{1-u^2} = 1 + u^2 + u^4 \underbrace{+ u^6 + u^8 + \cdots}$$

When the terms of degree six and higher are neglected, the result is the numerator in the generating function (11.38). If we replace the integrity basis information in the generating function and carry out the standard Taylor series expansion, we find

$$f(u;\mathcal{C}_3) \to \sum_{n_1,n_2} \sum_{d_3} (X^3 - 3XY^2)^{n_1} (3X^2Y - Y^3)^{n_2} (X^2+Y^2)^{d_3} \tag{11.39}$$

According to the generating function, the integers n_1 and n_2 can assume any integer values $0, 1, 2, \cdots, \infty$ but the integer d_3 can assume only the restricted values $0, 1, 2$.

Example 5: The generating function for $\mathcal{C}_3$ in $\mathbb{R}^2$ is

$$f(u;\mathcal{C}_3) = \frac{1 + \cdots + u^{2(3-1)}}{(1-u^3)^2} \tag{11.40}$$

The generating function $f(u;\mathcal{C}_n)$ for $\mathcal{C}_n$ acting in $\mathbb{R}^2$ can be obtained from $f(u;\mathcal{C}_3)$ by the substitution $3 \to n$ everywhere:

$$f(u;\mathcal{C}_n) = \frac{1 + u^2 + \cdots + u^{2(n-1)}}{(1-u^n)^2} \tag{11.41}$$

The interpretation of this generating function, and its implication for the structure of invariant monomials, is essentially the same as for the function $f(u;\mathcal{C}_3)$ given in (11.39), except that now $d_3 = 0, 1, 2 \cdots, n-1$ and the nth degree invariants are the real and imaginary parts of $(X + iY)^n$.

Example 6: The generating function for polynomials invariant under $\mathcal{V}_4$ acting on $\mathbb{R}^3$ is

$$f(u;\mathcal{V}_4) = \frac{1}{4}\left\{\frac{1}{(1-u)^3} + \frac{3}{(1+u)^2(1-u)}\right\} = \frac{1-u+u^2}{(1-u)(1-u^2)^2} \tag{11.42}$$

With a little algebra this rational fraction can be rewritten as

$$f(u;\mathcal{V}_4) = \frac{1+u^3}{(1-u^2)^3} \tag{11.43}$$

In this form we see immediately that an arbitrary polynomial can be expressed as a linear combination of all the invariant polynomials, which have the form

$$\frac{1+u^3(XYZ)}{(1-u^2X^2)(1-u^2Y^2)(1-u^2Z^2)} \to \sum (X^2)^{n_1}(Y^2)^{n_2}(Z^2)^{n_3}(XYZ)^{d_4} \tag{11.44}$$

where as usual $d_4 = 0, 1$ only.

In Fig.11.4 we provide a segment of a Maple code that can be used for constructing the generating function $f(u;\mathcal{G})$ for a group of order $|\mathcal{G}| = n(= 4)$. It is assumed that the matrices $\Gamma(g_i)$ have previously been constructed (e.g., Fig. 11.1). The group used in this example is $\mathcal{C}_4$ acting in $\mathbb{R}^3$.

11.3 EQUIVARIANT POLYNOMIALS

The polynomials in an integrity basis can be used to generate all polynomials invariant under an equivariance group $\mathcal{G}$. Every invariant function $f_{\rm inv}(X_1, X_2, \cdots, X_N)$ can be expressed as a function of the polynomials $p_1(X), p_2(X), \cdots, p_K(X)$ in an integrity basis:

$$f_{\rm inv}(X) = f(p_1(X), p_2(X), \cdots, p_K(X)) \tag{11.45}$$

There are many functions that are not invariant under $\mathcal{G}$. How can they be represented?

```
> n:=4: f:=0:
> for i from 1 to n do
      f:=f+1/det(Id-scalalmul(Gamma[i],u)):
  od:
> simplify(%/n);
```

$$\frac{1+u^4}{(1-u)^3(1+u)^2(1+u^2)}$$

Fig. 11.4 This snippet of Maple code computes the generating function $f(u;\mathcal{C}_4)$ for polynomials of degree d invariant under the group $\mathcal{C}_4$. The four matrices Γ_i are assumed previously defined for the group action of $\mathcal{C}_4$ on $\mathbb{R}^3$.

11.3.1 How Many Equivariant Polynomials Are There?

It is possible to construct a generating function for linearly independent equivariant (i.e., non invariant) polynomials by degree. If $f(u;\mathcal{G})$ is the generating function for invariant polynomials of degree d on $\mathbb{R}^N$, then its complement

$$f_{\rm cov}(u;\mathcal{G}) = \frac{1}{(1-u)^N} - f_{\rm inv}(u;\mathcal{G}) \tag{11.46}$$

is the generating function for equivariant polynomials. The term $1/(1-u)^N$ is the generating function for all polynomials of degree d on $\mathbb{R}^N$. This expression simply says that the total number of independent invariant polynomials and equivariant polynomials of degree d exhaust the polynomials of degree d on $\mathbb{R}^N$.

Examples: For $\mathbb{R}^3$ the generating function for polynomials of degree d is $1/(1-u)^3$. For the groups $\sigma_Z, \mathcal{R}_Z, \mathcal{P}$ the generating functions for invariant and equivarient polynomials are

$\mathcal{G}$	$f_{\rm inv}(u;\mathcal{G})$	$f_{\rm cov}(u;\mathcal{G})$
σ_Z	$\dfrac{1}{(1-u)^3(1+u)^1}$	$\dfrac{u}{(1-u)^3(1+u)^1}$
$\mathcal{R}_Z$	$\dfrac{1+u^2}{(1-u)^3(1+u)^2}$	$\dfrac{2u}{(1-u)^3(1+u)^2}$
$\mathcal{P}$	$\dfrac{1+3u^2}{(1-u)^3(1+u)^3}$	$\dfrac{u(3+u^2)}{(1-u)^3(1+u)^3}$

(11.47)

For $\mathcal{R}_Z$ we find

$$\begin{aligned} f_{\rm cov}(u;\mathcal{R}_Z) = &\quad \frac{2u}{(1-u)(1-u^2)^2} \\ = &\quad 2u + 2u^2 + 6u^3 + 6u^4 + 12u^5 + 12u^6 + 20u^7 + \cdots \end{aligned} \tag{11.48}$$

It is easily verified that the number of invariant (cf. (11.15)) and covariant polynomials of degree d is equal to the total number of linearly independent polynomials of degree d on $\mathbb{R}^3$: $\dfrac{(d+3-1)!}{(3-1)!d!}$.

What fraction of all polynomials of degree less than or equal to d is invariant under $\mathcal{G}$? We answer this by summing the coefficients $n(d)$ for the generating function $f(u;\mathcal{G})$ (in the limit $d \to \infty$ the sum is the generating function) and comparing with a similar sum for the generating function $1/(1-u)^N$ for polynomials on $\mathbb{R}^N$. The limit can be carried out as $u \to 1$. Of course the sums do not converge, but the limit of their ratio is well defined. We find

$$\text{Ratio} = \lim_{u\to 1} \frac{f(u;\mathcal{G})}{1/(1-u)^N} = \lim_{u\to 1} \frac{1}{|\mathcal{G}|} \sum_{g\in\mathcal{G}} \frac{(1-u)^N}{[I_N - u\Gamma^{\text{Def}}(g)]} \tag{11.49}$$

Only the first term in this sum, corresponding to $g = I$, survives the limit. As a result, we find that the ratio of invariant polynomials to all polynomials is $\frac{1}{|\mathcal{G}|}$. This is true for any equivariance group $\mathcal{G}$ acting on any space $\mathbb{R}^N$.

11.3.2 How to Construct Equivariant Polynomials

In order to construct any possible equivariant polynomial it is sufficient to identify just a few—a basis, so to speak ("ring basis") [25]. The remainder can all be constructed by multiplying this small set of equivariant polynomials by invariant polynomials. We will illustrate with several examples.

Example 1: For σ_Z acting in $\mathbb{R}^3$ we construct a list of all polynomials in $\mathbb{R}^3$ up to degree $d = |\sigma_Z| = 2$:

$$\begin{array}{c} \underline{1} \\ \underline{X}, \underline{Y}, Z \\ \underline{X^2}, \underline{XY}, \underline{Y^2}, \underline{Z^2}, XZ, YZ \end{array} \tag{11.50}$$

Next, we remove all invariant polynomials (underlined) from this list. This leaves three polynomials: Z, XZ, YZ. The lowest degree polynomial remaining is Z. This is removed from the list, as well as all products of Z with invariant polynomials. Once these are removed, no polynomials of degree $d \leq 2$ remain, and the process terminates. A basis for the noninvariant polynomials consists of the single equivariant polynomial Z. Every function on $\mathbb{R}^3$ can be written in the form

$$f(X,Y,Z) = f_0(p_1,p_2,p_3)1 + f_1(p_1,p_2,p_3)R_1 \tag{11.51}$$

In this expression the p_i are the invariant polynomials $(p_1,p_2,p_3) = (X,Y,Z^2)$, 1 is the lowest degree invariant polynomial (always uniquely 1), and $R_1 = Z$ is the unique noninvariant generating polynomial for σ_Z in $\mathbb{R}^3$.

This procedure can be followed to construct a ring basis, or basis set of covariant polynomials, for any group $\mathcal{G}$ acting in any space $\mathbb{R}^N$. The ring basis for the three

faithful representations of the two-group $\{I, A\}$ acting in $\mathbb{R}^3$ are

$$\begin{array}{lll} \sigma_Z & 1 & Z \\ \mathcal{R}_Z & 1 & X, Y \\ \mathcal{P} & 1 & X, Y, Z \end{array} \tag{11.52}$$

This information has been collected in Table 11.1.

Example 2: Polynomials up to degree three in two variables are

$$\begin{array}{cccc} & & 1 & \\ & X & & Y \\ X^2+Y^2 & & X^2-Y^2 & & 2XY \\ X^3-3XY^2 & 3XY^2-Y^3 & X(X^2+Y^2) & Y(X^2+Y^2) \end{array}$$

For $\mathcal{C}_3$ acting in $\mathbb{R}^2$ the invariant polynomials are $1, X^2+Y^2, X^3-3XY^2, 3X^2Y-Y^3$. The first-degree polynomials X and Y are not invariant, so $R_1(X,Y) = X$ and $R_2(X,Y) = Y$. Of the three second-degree polynomials, one linear combination is invariant. It is useful to choose two orthogonal linear combinations (under any reasonable inner product) as two additional invariant polynomials:

$$R_3(X,Y) = X^2 - Y^2, \qquad R_4(X,Y) = 2XY \tag{11.53}$$

Two linear combinations of the four cubic terms are invariant. The remaining two can be obtained by multiplying the degree-one covariant polynomials (X, Y) by the degree-two invariant polynomial $X^2 + Y^2$. The ring basis for $\mathcal{C}_3$ acting in $\mathbb{R}^2$ is therefore

$$R_0 = 1, \quad R_1 = X, \quad R_2 = Y \quad R_3 = X^2 - Y^2, \quad R_4 = 2XY \tag{11.54}$$

Example 3: This analysis can be repeated for $\mathcal{C}_n$ acting in $\mathbb{R}^2$. It is simplified by forming complex linear combinations $z = X + iY$ and $\bar{z} = X - iY$. The invariants of degree $k \leq n$ are $1, \bar{z}z, \frac{1}{2}(z^k + \bar{z}^k) = \mathtt{Re}(z^k)$ and $\frac{1}{2i}(z^k - \bar{z}^k) = \mathtt{Im}(z^k)$. The covariant polynomials are the real and imaginary parts of z^k, $k = 1, 2, \cdots, n-1$. The ring basis is

$$R_0 = 1,\ R_{1,2} = \begin{matrix} \mathtt{Re} \\ \mathtt{Im} \end{matrix} z,\ R_{3,4} = \begin{matrix} \mathtt{Re} \\ \mathtt{Im} \end{matrix} z^2,\ \cdots R_{2n-3,2n-2} = \begin{matrix} \mathtt{Re} \\ \mathtt{Im} \end{matrix} z^{n-1} \tag{11.55}$$

Example 4: For $\mathcal{V}_4$ acting in $\mathbb{R}^3$ the integrity basis is X^2, Y^2, Z^2, XYZ. The monomials X, Y, and Z are clearly not invariant. In addition, the degree-two terms XY, YZ, ZX are not invariant. All other covariant polynomials are products of one of these six covariant polynomials with an invariant polynomial. The ring basis is

$$\begin{array}{ll} & R_1 = X \quad R_2 = Y \quad R_3 = Z \\ R_0 = 1 & \\ & R_4 = YZ \quad R_5 = ZX \quad R_6 = XY \end{array} \tag{11.56}$$

Remark: The ring basis/invariant polynomial decomposition is the function space analog of the coset decomposition for groups. A side-by-side comparison illustrates the relation:

$$\begin{array}{cccc} g = \omega_\alpha \times h_i & \omega_\alpha \in \mathcal{G}/\mathcal{H} & h_i \in \mathcal{H} \subset \mathcal{G} & \\ \text{Poly}-\\ \text{nomial} = R_i \times f(p_1,..,p_K) & R_i \in \begin{array}{c}\text{Ring}\\ \text{Basis}\end{array} & p_i(X) \in \begin{array}{c}\text{Integrity}\\ \text{Basis}\end{array} & \end{array} \tag{11.57}$$

This analogy will be made much clearer in the following section. It cannot be pushed too hard, since there is only one combinatorial operation in the group while there are three in the space of functions.

11.4 BASIS SETS FOR IRREDUCIBLE REPRESENTATIONS

When $\mathcal{G}$ acts faithfully on $\mathbb{R}^N$ through the defining matrix representation $\Gamma^{\text{Def}}(\mathcal{G})$, at least one of the coordinates $(X_1, X_2, \cdots, X_N)$ is not an invariant. In general we can divide the N coordinates into two subsets: one subset is invariant under the action of $\mathcal{G}$; the other subset is covariant. The latter subset can be further divided if $\mathcal{G}$ has more than one irreducible representation different from the identity representation.

The two-element group $\{I, A\}$ has two inequivalent irreducible representations. When acting in $\mathbb{R}^3$ it has three inequivalent faithful representations. Invariant polynomials are basis functions for the identity representation $\Gamma^{(1)}$ and the covariant polynomials are basis vectors for the faithful representation $\Gamma^{(2)}$. This information is summarized in the character table

$\{I, A\}$	I	A	σ_Z	$\mathcal{R}_Z$	$\mathcal{P}$
$\Gamma^{(1)}$	1	1	X, Y, Z^2	Z, X^2, XY, Y^2	$X^2, Y^2, Z^2, XY, YZ, ZX$
$\Gamma^{(2)}$	1	-1	Z	X, Y	X, Y, Z

(11.58)

The information in this table is to be interpreted as follows. For the representation $\mathcal{R}_Z$, the generator $A \to R_Z$ acts on the invariant polynomials through the identity representation and acts on the covariant polynomials through the representation $\Gamma^{(2)}(\mathcal{R}_Z)$:

$$\begin{array}{ccccc} Z, X^2, XY, Y^2 & \xrightarrow{R_Z} & Z, (-X)^2, (-X)(-Y), (-Y)^2 & = & Z, X^2, XY, Y^2 \\ X, Y & \xrightarrow{R_Z} & -X, -Y & & \end{array}$$

For the group $\mathcal{C}_3$ acting on $\mathbb{R}^3$ there are three representations. The character table is ($\epsilon = e^{2\pi i/3}$)

$\mathcal{C}_3$	I	A	A^2	Basis Polynomials
$\Gamma^{(0)}$	1	1	1	$Z, X^2+Y^2, (X \pm iY)^3$
$\Gamma^{(1)}$	1	ϵ	ϵ^2	$X+iY, (X-iY)^2$
$\Gamma^{(2)}$	1	ϵ^2	ϵ	$X-iY, (X+iY)^2$

Since the action of $\mathcal{C}_3$ on $\mathbb{R}^3$ is through a real matrix representation, we combine the two complex conjugate representations $\Gamma^{(1)}$ and $\Gamma^{(2)} = \Gamma^{(-1)}$ into a single real 2×2 matrix representation. The character table is

$\mathcal{C}_3$	I	A	A^2	Basis Polynomials
$\Gamma^{(0)}$	1	1	1	$Z, X^2+Y^2, X^3-3XY^2, 3X^2Y-Y^3$
$\Gamma^{(1)}+\Gamma^{(-1)}$	2	-1	-1	$X, Y, X^2-Y^2, 2XY$

The first row contains invariant polynomials. It is sufficient to list only the polynomials in the integrity basis. The covariant polynomials are listed in the second row. It is sufficient to list only the polynomials in the ring basis.

Remark: In writing the character table, we include the trace of the matrices representing the group operations, rather than the full 2×2 matrices themselves.

For the group $\mathcal{C}_4$ acting in $\mathbb{R}^3$ there are four one-dimensional representations that are irrediculble over the complex field. They are given by

$$C_4^j \to \Gamma^{(k)}(C_4^j) = e^{2\pi ijk/4} \tag{11.59}$$

The representation $\Gamma^{(0)}$ is the 1×1 identity representation, and since 4 is even the representation with $k = n/2 = 4/2 = 2$ is also real. The other two representations $\Gamma^{(1)}$ and $\Gamma^{(3)} = \Gamma^{(-1)}$ are complex conjugates. Their direct sum is equivalent to a real faithful 2×2 matrix representation that is irreducible over the real numbers but reducible over the complex numbers. These matrix representations are summarized in the character table

$\mathcal{C}_4$	I	C_4	C_3^2	C_4^3	Basis Polynomials
$\Gamma^{(0)}$	1	1	1	1	$Z,\ X^2+Y^2,\ X^4-6X^2Y^2+Y^4,$ $4X^3Y-4XY^3$
$\Gamma^{(1)}+\Gamma^{(-1)}$	2	0	-2	0	$X,\ Y,\ X^3-3XY^2,\ 3X^2Y-Y^3$
$\Gamma^{(2)}$	1	-1	1	-1	$X^2-Y^2,\ 2XY$

(11.60)

The group $\mathcal{V}_4$ acting in $\mathbb{R}^3$ through rotations around the three coordinate axes has character table and basis functions

$\mathcal{V}_4$	I	R_X	R_Y	R_Z	Basis Polynomials
$\Gamma^{(1)}$	1	1	1	1	X^2, Y^2, Z^2, XYZ
$\Gamma^{(2)}$	1	1	-1	-1	X, YZ
$\Gamma^{(3)}$	1	-1	1	-1	Y, ZX
$\Gamma^{(4)}$	1	-1	-1	1	Z, XY

(11.61)

The integrity basis "carries" the identity representation. The six basic covariant polynomials in the ring basis occur in three pairs. One pair carries each of the three other unfaithful 1×1 matrix representations $\Gamma^{(2)}, \Gamma^{(3)}, \Gamma^{(4)}$. For example, the action of the rotation R_X on the three coordinates is $(X, Y, Z) \xrightarrow{R_X} (+X, -Y, -Z)$. As a

result, I and R_X map X to $+X$ and YZ into $+YZ$, while R_Y and R_Z map X and YZ into $-X$ and $-YZ$, as indicated in the second row of the character table.

Remark: The covariant polynomials can be indexed by the representation that they carry ($R^{(i)},\ i = 2, 3, 4$), and within this representation, by an additional index ($R_j,\ j = 1, 2$). For $\mathcal{V}_4$ we have

$$\begin{array}{lcllcl} R_1^{(2)} & = & X & R_2^{(2)} & = & YZ \\ R_1^{(3)} & = & Y & R_2^{(3)} & = & ZX \\ R_1^{(4)} & = & Z & R_2^{(4)} & = & XY \end{array} \tag{11.62}$$

The invariant polynomials in the integrity basis are indexed by the identity representation: $R_i^{(1)} = p_i(X)$. This information will be useful when establishing the structure that equivariant dynamical systems equations can assume.

These relations are used to construct dynamical systems equations with arbitrary equivariance group in the following chapter.

12

Equivariant Dynamics in R^N

12.1 PROPERTIES OF EQUIVARIANT DYNAMICAL SYSTEMS

The properties of equivariant dynamical systems $\dot{X} = F(X)$ are highly constrained by the symmetry group $\mathcal{G}$. The number of fixed points is to some extent determined by $\mathcal{G}$. The singular set $SS(\mathcal{G})$ is completely determined by the action of $\mathcal{G}$ on $\mathbb{R}^N$ through the defining matrix representation $\Gamma^{\rm Def}(\mathcal{G})$. Most important, the structure of the forcing functions $F(X)$ is determined by $\Gamma^{\rm Def}(\mathcal{G})$, the spectrum of irreducible representations of $\mathcal{G}$, and the ring basis functions $R^{(\alpha)}(X)$ that transform under these irreducible representations.

12.1.1 Fixed Points

The number of fixed points (including degeneracy) of a dynamical system equivariant under a group $\mathcal{G}$ is an integer multiple of $|\mathcal{G}|$.

Example: The Lorenz system has three fixed points. The real nonzero pair $(\pm\sqrt{b(R-1)}, \pm\sqrt{b(R-1)}, R-1)$ is symmetry-related and nondegenerate. The fixed point at the origin $(0,0,0)$ is doubly degenerate. Counting degeneracy, there are $4 = 2|\mathcal{R}_Z|$ fixed points.

Fixed points can be of two types:

1. **Nondegenerate Fixed Points:** If X_0 is a nondegenerate fixed point, the points γX_0 in its orbit under $\gamma \in \Gamma^{\mathrm{Def}}(\mathcal{G})$ are also nondegenerate fixed points. There are $|\mathcal{G}|$ fixed points on the orbit (under $\mathcal{G}$) of any nondegenerate fixed point.
2. **Degenerate Fixed Points:** If X_0 is a degenerate fixed point, there is at least one group operation $g_i \neq Id$ for which $\gamma(g_i)X_0 = X_0$. The set of group operations $g_i \in \mathcal{G}$ that leave X_0 fixed form a subgroup $\mathcal{H}$, $I \subset \mathcal{H} \subseteq \mathcal{G}$. The fixed point is $|\mathcal{H}|$-fold degenerate. The orbit of X_0 under $\mathcal{G}$ is identical to the orbit of X_0 under the coset representatives in $\mathcal{G}/\mathcal{H}$. There are $|\mathcal{G}/\mathcal{H}| = |\mathcal{G}|/|\mathcal{H}|$ $|\mathcal{H}|$-fold degenerate fixed points in the orbit of X_0 under $\mathcal{G}$.

The relation between the order of $\mathcal{G}$ and the number of fixed points of a dynamical system D equivariant under $\mathcal{G}$ has previously been described (cf. Section 10.11).

12.1.2 Flows on $SS(\mathcal{G})$

The singular set $SS(\mathcal{G})$ (cf. Section 10.10) is *invariant*. This means that if one point on a trajectory is in the singular set, the entire trajectory is in the singular set.

Suppose $X_0 = X(t_0) \in SS(\mathcal{G})$. This means that there is at least one linear transformation, $\gamma \in \Gamma^{\mathrm{Def}}(\mathcal{G}),\ \gamma \neq Id$, that maps X_0 into itself:

$$\gamma X_0 = \gamma X(t_0) = X(t_0) \tag{12.1a}$$

After a short interval δt, the initial condition moves to $X(t_0 + \delta t)$, where

$$X(t_0 + \delta t) = X(t_0) + \left.\frac{dX}{dt}\right|_{X_0} \delta t = X(t_0) + F(X_0)\delta t \tag{12.1b}$$

The action of γ on $X(t_0 + \delta t)$ is

$$\gamma X(t_0 + \delta t) = \gamma X(t_0) + \gamma F(X_0)\delta t = X(t_0) + F(\gamma X_0)\delta t =$$

$$X(t_0) + F(X_0)\delta t = X(t_0 + \delta t) \tag{12.1c}$$

In short, if $X(t_0) \in SS(\mathcal{G})$, then $X(t_0 + \delta t) \in SS(\mathcal{G})$.

Example 1: The singular sets of σ_Z, $\mathcal{R}_Z$, and $\mathcal{P}$ acting in $\mathbb{R}^3$ are the X-Y plane $Z = 0$, the Z-axis $X = Y = 0$, and the origin $X = Y = Z = 0$. A point in the $Z = 0$ plane will evolve in the $Z = 0$ plane under a σ_Z-equivariant flow. A point on the Z-axis will move along the Z-axis under an $\mathcal{R}_Z$ equivariant flow. The origin is a fixed point under a $\mathcal{P}$-equivariant flow.

Example 2: The singular set of $\mathcal{V}_4$ acting in $\mathbb{R}^3$ through three mutually orthogonal rotations is the union of the three rotation axes, say the X-, Y-, and Z-axes. The origin is a fixed point. An initial condition on any of the rotation axes will be confined to that axis for all times under a $\mathcal{V}_4$-equivariant flow.

12.1.3 Structure of Equivariant Dynamical Systems

The structure of a dynamical system that is equivariant under a symmetry group $\mathcal{G}$ is rigidly constrained by $\mathcal{G}$. The dynamical system equations are expressed in terms of functions of the

1. Invariant polynomials $p_1(X), p_2(X), \cdots, p_K(X)$
2. Equivariant polynomials $R_i^{(\alpha)}(X)$
3. Defining matrix representation $\Gamma^{\text{Def}}(\mathcal{G})$
4. Irreducible representations $\Gamma^{(\alpha)}(\mathcal{G})$.

We illustrate these concepts with a number of examples.

Example 1: The group σ_Z acts in $\mathbb{R}^3$ through the defining matrix representation given in Section 10.7. There are three invariant polynomials in the integrity basis: $p_1 = X,\ p_2 = Y,\ p_3 = Z^2$. There is one equivariant polynomial $R_1 = Z$ (in the ring basis). There are two irreducible representations $\Gamma^{(1)}$ (identity) and $\Gamma^{(2)}$ (cf. Eq. (10.46)). An $\mathcal{R}_Z$ equivariant dynamical system must have the form

$$\sigma_Z: \qquad \frac{d}{dt}\begin{bmatrix} X \\ Y \\ Z \end{bmatrix} = \begin{bmatrix} f_{10} \\ f_{20} \\ Zf_{31} \end{bmatrix} = \left[\begin{array}{cc|c} f_{10} & 0 & \\ f_{20} & 0 & \\ \hline 0 & & f_{31} \end{array}\right] \left[\begin{array}{c} 1 \\ \hline Z \end{array}\right] \tag{12.2a}$$

In these equations the f_{ij} are invariant functions: they are functions of the invariant polynomials in the integrity basis. Similar reasoning is used to express $\mathcal{R}_Z$ equivariant dynamical systems and $\mathcal{P}$ equivariant dynamical systems in similar form:

$$\mathcal{R}_Z: \quad \frac{d}{dt}\begin{bmatrix} X \\ Y \\ Z \end{bmatrix} = \begin{bmatrix} Xf_{11} + Yf_{12} \\ Xf_{21} + Yf_{22} \\ f_{30} \end{bmatrix} = \left[\begin{array}{c|cc} 0 & f_{11} & f_{12} \\ 0 & f_{21} & f_{22} \\ \hline f_{30} & 0 & 0 \end{array}\right] \left[\begin{array}{c} 1 \\ \hline X \\ Y \end{array}\right] \tag{12.2b}$$

$$\begin{aligned} \mathcal{P}: \quad \frac{d}{dt}\begin{bmatrix} X \\ Y \\ Z \end{bmatrix} &= \begin{bmatrix} Xf_{11} + Yf_{12} + Zf_{13} \\ Xf_{21} + Yf_{22} + Zf_{23} \\ Xf_{31} + Yf_{32} + Zf_{33} \end{bmatrix} \\ &= \left[\begin{array}{c|ccc} 0 & f_{11} & f_{12} & f_{13} \\ 0 & f_{21} & f_{22} & f_{33} \\ 0 & f_{31} & f_{32} & f_{33} \end{array}\right] \left[\begin{array}{c} 1 \\ \hline X \\ Y \\ Z \end{array}\right] \end{aligned} \tag{12.2c}$$

The total number of invariant functions required to specify these three equivariant dynamical systems is

Coupled to	σ_Z	$\mathcal{R}_Z$	$\mathcal{P}$
Invariant 1	2	1	0
Ring Basis	1	4	9
Total	3	5	9

(12.3)

For the Lorenz equations (1.2) the five invariant functions are $f_{11} = -\sigma$, $f_{12} = +\sigma$, $f_{21} = R - Z$, $f_{22} = -1$, $f_{30} = -bZ + XY$.

Example 2: For the group $\mathcal{C}_3$ acting in $\mathbb{R}^3$ the coordinate Z is a basis function for the identity representation $\Gamma^{(0)}$ while the two coordinates X and Y carry the real two-dimensional representation $\Gamma^{(+1)} + \Gamma^{(-1)}$. The four ring basis functions that transform under $\Gamma^{(+1)} + \Gamma^{(-1)}$ are $X,\ Y,\ X^2 - Y^2,\ 2XY$ (cf. (11.60)). The structure of dynamical systems equivariant under $\mathcal{C}_3$ is therefore

$$\mathcal{C}_3: \quad \frac{d}{dt}\begin{bmatrix} X \\ Y \\ Z \end{bmatrix} = \begin{bmatrix} Xf_{11} + Yf_{12} + (X^2 - Y^2)f_{13} + 2XYf_{14} \\ Xf_{21} + Yf_{22} + (X^2 - Y^2)f_{23} + 2XYf_{24} \\ f_{30} \end{bmatrix}$$

The equivariance condition $F(\gamma X) = F(X)$ places constraints on eight of these functions. Specifically, $f_{21} = -f_{12},\ f_{22} = +f_{11},\ f_{23} = +f_{14}$, and $f_{24} = -f_{13}$. The equations of motion are therefore

$$\mathcal{C}_3: \quad \frac{d}{dt}\begin{bmatrix} X \\ Y \\ Z \end{bmatrix} = \left[\begin{array}{c|cccc} 0 & f_{11} & f_{12} & f_{13} & f_{14} \\ 0 & -f_{12} & +f_{11} & +f_{14} & -f_{13} \\ \hline f_{30} & 0 & 0 & 0 & 0 \end{array}\right] \left[\begin{array}{c} 1 \\ \hline X \\ Y \\ X^2 - Y^2 \\ 2XY \end{array}\right] \tag{12.4}$$

The invariant functions f_{ij} depend on the invariant polynomials $p_1 = Z,\ p_2 = X^2 + Y^2,\ p_3 = X^3 - 3XY^2,\ p_4 = 3X^2Y - Y^3$.

Example 3: For the four-group $\mathcal{V}_4$ acting in $\mathbb{R}^3$ by three mutually orthogonal rotations, the polynomials $R_1^{(2)} = X,\ R_2^{(2)} = YZ$ carry the representation $\Gamma^{(2)}$, the polynomials $R_1^{(3)} = Y,\ R_2^{(3)} = ZX$ carry $\Gamma^{(3)}$, and $R_1^{(4)} = Z,\ R_2^{(4)} = XY$ transform under $\Gamma^{(4)}$ (cf. (11.61)). The dynamical systems equations have the form

$$\mathcal{V}_4: \quad \frac{d}{dt}\begin{bmatrix} X^{(2)} \\ Y^{(3)} \\ Z^{(4)} \end{bmatrix} = \begin{bmatrix} Xf_{11} + YZf_{12} \\ Yf_{21} + ZXf_{22} \\ Zf_{31} + XYf_{32} \end{bmatrix} =$$

$$\left[\begin{array}{c|cc|cc|cc} 0 & f_{11}^{(2)} & f_{12}^{(2)} & 0 & 0 & 0 & 0 \\ \hline 0 & 0 & 0 & f_{21}^{(3)} & f_{22}^{(3)} & 0 & 0 \\ \hline 0 & 0 & 0 & 0 & 0 & f_{31}^{(4)} & f_{32}^{(4)} \end{array}\right] \left[\begin{array}{c} 1 \\ \hline R_1^{(2)} \\ R_2^{(2)} \\ \hline R_1^{(3)} \\ R_2^{(3)} \\ \hline R_1^{(4)} \\ R_2^{(4)} \end{array}\right] \tag{12.5}$$

In this case a total of six invariant functions of the four integrity basis functions $X^2,\ Y^2,\ Z^2,\ XYZ$ is required to specify a $\mathcal{V}_4$ equivariant dynamical system.

The general situation can be gleaned from the three examples presented above. Each of the N coordinates $X_1, X_2, \cdots, X_N$ is a basis function for one of the irreducible representations of the equivariance group $\mathcal{G}$. It is useful to include this information with the basis function. For example, if X_i transforms under $\Gamma^{(\alpha)}(\mathcal{G})$, that information can be included by writing X_i as $X_i^{(\alpha)}$, as in Example 3. The time derivative $dX_i^{(\alpha)}/dt$ can only be expressed in terms of the ring basis functions that carry the representation $\Gamma^{(\alpha)}(\mathcal{G})$. As a result, equivariant dynamical systems can be represented in the form

$$\frac{dX_i^{(\alpha)}}{dt} = \sum_s f_{is}^{(\alpha)}(p_1, p_2, \cdots, p_K) R_s^{(\alpha)} \tag{12.6}$$

In this expression, the index i identifies all the distinct coordinates that transform under $\Gamma^{(\alpha)}(\mathcal{G})$ while the index s identifies all distinct the ring basis functions that transform under the same irreducible representation. The functions $f_{is}^{(\alpha)}(p_1, p_2, \cdots, p_K)$ are invariant under the the action of the group. The number of invariant functions required to determine a $\mathcal{G}$-equivariant dynamical system is

$$\# = \sum_\alpha n^{(\alpha)} r^{(\alpha)} \tag{12.7}$$

where $n^{(\alpha)}$ is the number of coordinates $X_i^{(\alpha)}$ $(i = 1, 2, \cdots, n^{(\alpha)})$ that transform under the representation $\Gamma^{(\alpha)}(\mathcal{G})$ and $r^{(\alpha)}$ is the number of ring basis functions $R_s^{(\alpha)}$ $(s = 1, 2, \cdots, r^{(\alpha)})$ that transform under the same irreducible representation of $\mathcal{G}$. The sum extends over all irreducible representations of $\mathcal{G}$, including the identity representation, for which the (invariant) ring basis function is uniquely $R^{(Id)}(\mathcal{G}) = 1$ and $r^{(Id)} = 1$.

It is a simple matter to verify that Eqs. (12.2), (12.4), and (12.5) are special cases of Eq. (12.6), while the dimensions given in Eq. (12.3) are special cases of Eq. (12.7). The number of invariant polynomials required to define $\mathcal{C}_3$-equivariant dynamical systems is $5 = 1 \times 1 + 1 \times 2 + 1 \times 2$, while the number required to determine $\mathcal{V}_4$-equivariant dynamical systems is $6 = 1 \times 0 + 1 \times 2 + 1 \times 2 + 1 \times 2$.

The results (12.6) and (12.7) are consequences of an elegant symmetry. This symmetry will be described more fully in Section 14.1, on Schur symmetries.

12.2 INJECTION $R^N(X) \to R^K(P)$

The mapping of an N-dimensional dynamical system $\dot{X} = F(X)$ on $\mathbb{R}^N(X)$ with symmetry group $\mathcal{G}$ to an N-dimensional dynamical system $\dot{u} = g(u)$ on $\mathbb{R}^N(u)$ that is everywhere locally identical but without any symmetry (or with smaller symmetry group $\mathcal{H} \subset \mathcal{G}$) is conveniently done in two steps. The first step is a $|\mathcal{G}| \to 1$ map that removes the symmetry at the expense of mapping the dynamical system into an intermediate phase space $\mathbb{R}^K(p)$ of larger dimension when $K > N$. The second step is a one to one linear projection of the dynamical system in $\mathbb{R}^K(p)$ into $\mathbb{R}^N(u)$. The

first mapping, $\mathbb{R}^N(X) \to \mathbb{R}^K(p)$, is a $|\mathcal{G}| \to 1$ local diffeomorphism. The second map is many to one as a projection of the K-dimensional phase space down to the N-dimensional phase space $\mathbb{R}^K \downarrow \mathbb{R}^N$ ($K > N$), but it is a one to one projection of the N-dimensional dynamical system embedded in $\mathbb{R}^K(p)$ to an N-dimensional dynamical system in $\mathbb{R}^N(u)$. We discuss each of the two mappings separately before discussing the composition of the two mappings.

12.2.1 Jacobian of the Transformation

The coordinates of a dynamical system $\dot{X} = F(X)$ equivariant under $\mathcal{G}$ are $X_1, X_2, \cdots, X_N$. The invariant polynomials $p_1(X), p_2(X), \cdots, p_K(X)$ are coordinates that are invariant under $\mathcal{G}$. It is useful to choose the polynomials in an integrity basis as coordinates for a locally diffeomorphic dynamical system without symmetry. The dynamical equations of motion in this $|\mathcal{G}| \to 1$ image dynamical system are

$$\frac{dp_\alpha}{dt} = \frac{\partial p_\alpha}{\partial X_i}\frac{dX_i}{dt} = \frac{\partial p_\alpha}{\partial X_i}F_i(X) \tag{12.8}$$

The Jacobian $\partial p_\alpha/\partial X_i$ is a property of the group $\mathcal{G}$ through the defining representation $\Gamma^{\mathrm{Def}}(\mathcal{G})$. It is completely independent of the dynamics. The dynamics in $\mathbb{R}^K(p)$ separates into a kinematic part (i.e., depends on geometry) $\partial p_\alpha/\partial X_i$, and a dynamical part originating from $F_i(X)$.

The Jacobian $\partial p_\alpha/\partial X_i$ is a $K \times N$ matrix whose rows index the integrity basis polynomials and whose columns label the equivariant coordinates. The Jacobians for the equivariance groups σ_Z, $\mathcal{R}_Z$, $\mathcal{P}$, $\mathcal{C}_3$, and $\mathcal{V}_4$ are:

$$\begin{array}{c} \\ X \\ Y \\ Z^2 \end{array}\!\!\begin{array}{c} \sigma_Z \\ \left[\begin{array}{ccc} 1 & 0 & 0 \\ 0 & 1 & 0 \\ 0 & 0 & 2Z \end{array}\right] \end{array} \qquad \begin{array}{c} \\ Z \\ X^2 \\ XY \\ Y^2 \end{array}\!\!\begin{array}{c} \mathcal{R}_Z \\ \left[\begin{array}{ccc} 0 & 0 & 1 \\ 2X & 0 & 0 \\ Y & X & 0 \\ 0 & 2Y & 0 \end{array}\right] \end{array} \qquad \begin{array}{c} \\ X^2 \\ Y^2 \\ Z^2 \\ YZ \\ ZX \\ XY \end{array}\!\!\begin{array}{c} \mathcal{P} \\ \left[\begin{array}{ccc} 2X & 0 & 0 \\ 0 & 2Y & 0 \\ 0 & 0 & 2Z \\ 0 & Z & Y \\ Z & 0 & X \\ Y & X & 0 \end{array}\right] \end{array}$$

$$\begin{array}{c} \\ Z \\ X^2+Y^2 \\ X^3-3XY^2 \\ 3X^2Y-Y^3 \end{array}\!\!\begin{array}{c} \mathcal{C}_3 \\ \left[\begin{array}{ccc} 0 & 0 & 1 \\ 2X & 2Y & 0 \\ 3(X^2-Y^2) & -6XY & 0 \\ 6XY & 3(X^2-Y^2) & 0 \end{array}\right] \end{array} \qquad \begin{array}{c} \\ X^2 \\ Y^2 \\ Z^2 \\ XYZ \end{array}\!\!\begin{array}{c} \mathcal{V}_4 \\ \left[\begin{array}{ccc} 2X & 0 & 0 \\ 0 & 2Y & 0 \\ 0 & 0 & 2Z \\ YZ & ZX & XY \end{array}\right] \end{array} \tag{12.9}$$

Observation 1: All nonzero matrix elements in the Jacobian are *linear* in the ring basis functions. The invariant ring basis function 1 occurs when one or more coordinates $X_i^{(Id)}$ carry the identity representation of the symmetry group $\mathcal{G}$.

Observation 2: Many matrix elements of the Jacobian are zero. If more matrix elements are nonzero than the dimension of the ring basis, then there must be relations among the nonzero matrix elements.

New Algorithm: As a consequence of the first observation, we have an alternative procedure for constructing a basis set for equivariant polynomials: Take all partial derivatives of the integrity basis functions $\partial p_\alpha / \partial X_i$ and choose a linearly independent subset of these derivatives.

Example: For $\mathcal{V}_4$ the integrity basis consists of the four polynomials $X^2,\ Y^2,\ Z^2,\ XYZ$. The set of all possible derivatives consists of those polynomials that appear in the Jacobian for $\mathcal{V}_4$. The derivatives of the invariants with respect to X, namely X and YZ, transform identically and carry the representation $\Gamma^{(2)}(\mathcal{V}_4)$; similarly for the pairs (Y, ZX) and (Z, XY).

12.2.2 Rank

At generic points in $\mathbb{R}^N(X)$ the rank of the Jacobian $\partial p_\alpha / \partial X_i$ is *full*: that is, it is as large as possible, equal to N. This means that the nonlinear mapping $X_i \to p_\alpha(X)$ is locally 1-1 and invertible. However, there are points in $\mathbb{R}^N(X)$ at which the rank drops below N. For the five group actions on $\mathbb{R}^3$ described by the Jacobians in (12.9), we find the following results:

Group	Rank	$\mathrm{Co}-\mathrm{Rank}$	Singular Set
σ_Z	2	1	$Z = 0$
$\mathcal{R}_Z$	1	2	$X = Y = 0$
$\mathcal{P}$	0	3	$X = Y = Z = 0$
$\mathcal{C}_3$	1	2	$X = Y = 0$
$\mathcal{V}_4$	1	2	$X = Y = 0; Y = Z = 0; Z = X = 0$
	0	3	$X = Y = Z = 0$

(12.10)

The Jacobian $\partial p_\alpha / \partial X_i$ provides an analytic expression for the singular set $SS(\mathcal{G})$. The Jacobian is an important bridge between geometry and analysis.

12.2.3 The Inversion Map

Away from the singular set $SS(\mathcal{G})$ the Jacobian $\partial p_\alpha / \partial X_i$ has full rank. This means that the coordinate transformation $(X_1, X_2, \cdots, X_N) \to (p_1, p_2, \cdots, p_K)$ is locally one to one between neighborhoods of generic points in $\mathbb{R}^N(X)$ and suitable N-dimensional neighborhoods of the image points in $\mathbb{R}^K(p)$. Every point in $\mathbb{R}^K(p)$ that is in the image of $\mathbb{R}^N(X)$ but not in the image of $SS(\mathcal{G}) \subset \mathbb{R}^N(X)$ has $|\mathcal{G}|$ inverse images in $\mathbb{R}^N(X)$. The inverse mapping

$$\mathbb{R}^K(p) \longrightarrow \mathbb{R}^N(X) \tag{12.11}$$

has $|\mathcal{G}|$ "sheets."

This is exactly analogous to well-known results from the analysis of complex functions. If z is a complex variable, the cube root function $w = z^{1/3}$ has three covering sheets (Fig. 12.1). Away from the singularity at $z = 0$, z has three distinct cube roots: $w = +z^{1/3} = |z|^{1/3}e^{i\phi}$, $w = |z|^{1/3}e^{i\phi+2\pi/3}$, and $w = |z|^{1/3}e^{i\phi+4\pi/3}$ As z is moved around the circle $|z|^{1/3}e^{i\theta}$, starting from $\theta = \phi$ and moving to $\theta \to 2\pi$, one cube root $|z|^{1/3}e^{i\phi}$ in sheet 0 moves smoothly to the next cube root $|z|^{1/3}e^{i\phi+2\pi/3}$ in sheet 1. As θ increases further from 2π to 4π the covering point moves from the second cube root in sheet 1, $w = |z|^{1/3}e^{i\phi+2\pi/3}$, to the next cube root, $w = |z|^{1/3}e^{i\phi+4\pi/3}$, in sheet 2. A further increase of θ from 4π to 6π returns the third cube root, in sheet 2, to the starting point, in sheet 0. At the same time the point in the z plane traverses the circle in that plane three times. Other fractional powers, $z^{1/n}$, n a positive integer, have n covering sheets. These n-fold covers behave exactly as (in fact, are isomorphic to) the action of the group $\mathcal{C}_n$ in the cover-image problem.

These considerations suggest, correctly, that the multisheet cover-image problem, well known from classical complex analysis, is a particular case of a far more general and powerful mathematical procedure involving arbitrary groups $\mathcal{G}$ which do not necessarily have a single generator and are not necessarily commutative. The preimage problem $z = w^n$ familiar from complex analysis is identical to the group problem when $\mathcal{G} = \mathcal{C}_n$, a group with one generator C_n and one relation: $(C_n)^n = Id$.

When we remove the singular set $SS(\mathcal{G})$ from $\mathbb{R}^N(X)$ we are left with an open set (manifold) in $\mathbb{R}^N(X)$. The coordinate transformation $(X_1, X_2, \cdots, X_N) \to (p_1, p_2, \cdots, p_K)$ provides a $|\mathcal{G}| \to 1$ map of the open set $\mathbb{R}^N(X) - SS(\mathcal{G})$ to a manifold in $\mathbb{R}^K(p)$. This image manifold in $\mathbb{R}^K(p)$ has $|\mathcal{G}|$ covering sheets in $\mathbb{R}^N(X)$. There are no natural boundaries separating one sheet from another. When we follow the inverse image in $\mathbb{R}^N(X)$ of a point in this open manifold in $\mathbb{R}^K(p)$ as p moves around a closed contour, it is never possible to tell when you have left one covering sheet and entered another. The existence of distinct sheets is a "nonlocal" phenomenon. The boundary between sheets is an arbitrary but necessary distinction. We have identified such boundaries for many group actions previously (cf. Section 10.6).

12.3 STRUCTURE OF FLOWS IN $R^K(P)$

The image of the flow in $\mathbb{R}^K(p)$ is invariant under $\mathcal{G}$. The dynamical system equations are

$$\frac{dp_\alpha}{dt} = \frac{\partial p_\alpha}{\partial X_i} F_i(X) = \frac{\partial p_\alpha}{\partial X_i} f_{is}^{(\beta)}(p) R_s^{(\beta)}(X) \tag{12.12}$$

In this expression we have used the resolution (12.6) of the driving functions $F_i(X) = f_{is}^{(\beta)}(p)R_s^{(\beta)}(X)$ as linear superpositions of the ring basis functions $R_s^{(\beta)}(X)$ with invariant coefficients $f_{is}^{(\beta)}(p)$. The matrix elements of the Jacobian $(\partial p_\alpha/\partial X_i)$ and the forcing functions $F_i(X) = f_{is}^{(\beta)}(p)R_s^{(\beta)}(X)$ are both linear in the ring basis functions. As a result, the source terms for the flow dp_α/dt are bilinear in the ring basis functions. Only *invariant* bilinear terms can occur among the forcing functions.

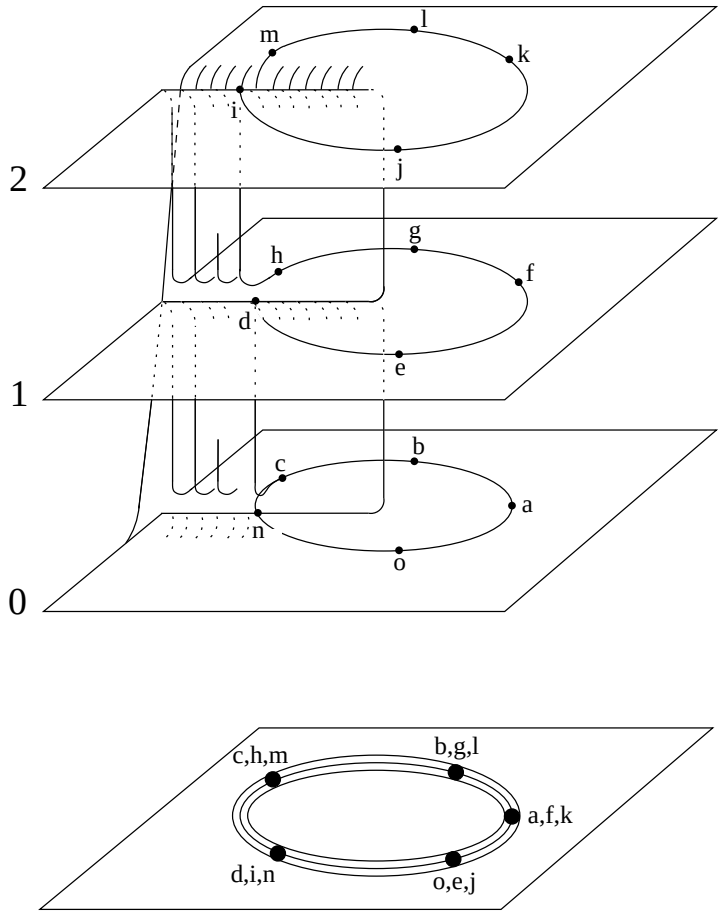

Fig. 12.1 The complex cube root function is a three-sheeted cover of the complex plane. Starting at a one goes around a circle $a \to b \to \cdots \to o$ three times in the z plane, while going around the three sheeted cover only once. Each trip around the circle in the z plane lifts to a different sheet in the cover. The path in the cover begins in sheet 0, proceeds to sheet 1, then sheet 2 before returning to sheet 0. The location of the connection ("cut" or "branch line") between the sheets is arbitrary: It is not possible, locally, to tell when the path has left one sheet and entered another.

12.3.1 Injected Flow is $|\mathcal{G}| \longrightarrow 1$ Image

Since the flow in $\mathbb{R}^K(p)$ is invariant under $\mathcal{G}$, the bilinear terms $(\partial p_\alpha/\partial X_i)R_{is}^{(\beta)}$ must be expressible in terms of the integrity basis functions $p_\alpha(X)$. We illustrate with two examples.

Example 1: For $\mathcal{R}_Z$ acting on $\mathbb{R}^3$, the four invariant polynomials are $p_1 = Z,\ p_2 = X^2,\ p_3 = XY,\ p_4 = Y^2$. The dynamical equations in $\mathbb{R}^4(p)$ are

$$\frac{d}{dt}\begin{bmatrix} p_1 \\ p_2 \\ p_3 \\ p_4 \end{bmatrix} = \begin{bmatrix} 0 & 0 & 1 \\ 2X & 0 & 0 \\ Y & X & 0 \\ 0 & 2Y & 0 \end{bmatrix} \begin{bmatrix} 0 & f_{11} & f_{12} \\ 0 & f_{21} & f_{22} \\ f_{30} & 0 & 0 \end{bmatrix} \begin{bmatrix} 1 \\ X \\ Y \end{bmatrix} =$$

$$\begin{bmatrix} f_{30} & 0 & 0 & 0 & 0 \\ 0 & 0 & 2f_{11} & 2f_{12} & 0 \\ 0 & 0 & f_{21} & f_{11}+f_{22} & f_{12} \\ 0 & 0 & 0 & 2f_{21} & 2f_{22} \end{bmatrix} \begin{bmatrix} 1 \\ p_1 \\ p_2 \\ p_3 \\ p_4 \end{bmatrix} \tag{12.13}$$

For the Lorenz dynamical system (Eq. (12.2b)) this set of equations is equivalent to

$$\frac{d}{dt}\begin{bmatrix} p_1 \\ p_2 \\ p_3 \\ p_4 \end{bmatrix} = \begin{bmatrix} -b & 0 & 1 & 0 \\ 0 & -2\sigma & 2\sigma & 0 \\ 0 & R-Z & -\sigma-1 & \sigma \\ 0 & 0 & 2(R-Z) & -2 \end{bmatrix} \begin{bmatrix} p_1 \\ p_2 \\ p_3 \\ p_4 \end{bmatrix} \tag{12.14}$$

This four-dimensional system is highly dissipative, as the trace of the driving functions is $-b-3(\sigma+1)$ compared with $-b-\sigma-1$ for the Lorenz system itself.

Example 2: For $\mathcal{C}_3$ acting on $\mathbb{R}^3$, the four invariant polynomials are $p_1 = Z,\ p_2 = X^2+Y^2,\ p_3 = X^3-3XY^2,\ p_4 = 3X^2Y-Y^3$. The dynamical equations in $\mathbb{R}^4(p)$ are

$$\frac{d}{dt}\begin{bmatrix} p_1 \\ p_2 \\ p_3 \\ p_4 \end{bmatrix} = \begin{bmatrix} 0 & 0 & 1 \\ 2X & 2Y & 0 \\ 3(X^2-Y^2) & -6XY & 0 \\ 6XY & 3(X^2-Y^2) & 0 \end{bmatrix} \times$$

$$\begin{bmatrix} +f_{11}X + f_{12}Y + f_{13}(X^2-Y^2) + f_{14}(2XY) \\ -f_{12}X + f_{11}Y + f_{14}(X^2-Y^2) - f_{13}(2XY) \\ f_{30} \end{bmatrix}$$

$$= \begin{bmatrix} f_{30} & 0 & 0 & 0 & 0 \\ 0 & 2f_{11} & 2f_{13} & 2f_{14} & 0 \\ 0 & 0 & 3f_{11} & 3f_{12} & 3f_{13} \\ 0 & 0 & -3f_{12} & 3f_{11} & 3f_{14} \end{bmatrix} \begin{bmatrix} 1 \\ p_2 \\ p_3 \\ p_4 \\ p_2^2 \end{bmatrix} \tag{12.15}$$

12.3.2 Invariant Manifold $I^N(0)$

The integrity basis $p_1(X), p_2(X), \cdots, p_K(X)$ provides a mapping of the open set $\mathbb{R}^N(X) - SS(\mathcal{G})$ into an N-dimensional manifold embedded in $\mathbb{R}^K(p)$. Points in this manifold are parameterized in a one to one way by the coordinates $(X_1, X_2, \cdots, X_N)$ in a fundamental domain in $\mathbb{R}^N(X)$.

In general this manifold is not easy to describe. However, when the integrity basis $p_\alpha(X)$ satisfies simple syzygies, the manifold in $\mathbb{R}^K(p)$ is an *algebraic manifold*. It is then very easy to describe.

One or more constaints of the form $s_\mu(p_1, p_2, \cdots, p_K) = 0$ define a submanifold in $\mathbb{R}^K(p)$ provided the Jacobian $\partial s_\mu / \partial X_j$ has full rank. If the functions s_μ are algebraic (polynomial) functions, the manifold defined in this way is called an algebraic manifold.

One smooth function $s_{N+1}(p_1, p_2, \cdots, p_K)$ of K variables places one constraint on the K variables when the function is required to be constant: $s_{N+1}(p_1, p_2, \cdots, p_K) = 0$. The K coordinates are constrained to lie in a $K-1$ dimensional manifold. Two smooth functions place two constraints, and the K coordinates are typically confined to a $K-2$ dimensional manifold. Continuing on in this way, $K-N$ functions restrict the coordinates $(p_1, p_2, \cdots, p_K)$ to lie in an N-dimensional manifold. When the functions s_μ (the syzygies) are simple, the N-dimensional manifold is an algebraic manifold. The injected flow $dp_\alpha/dt = g_\alpha(p)$ is confined to this N-dimensional manifold.

Definition: The set $I^N(0)$ is the N-dimensional subspace in $\mathbb{R}^K(p)$ defined by the $K-N$ simple syzygies $s_\mu(p)$.

Example 1: For $\mathcal{R}_Z$ acting in $\mathbb{R}^3(X)$ there are four integrity basis functions: $p_1 = Z,\ p_2 = X^2,\ p_3 = XY,\ p_4 = Y^2$. There is one syzygy among these four integrity basis functions:

$$s_4 = p_2 p_4 - p_3^2$$

The four coordinates map $\mathbb{R}^3(X) - Z$-axis into a three dimensional manifold $I^3(0)$ in $\mathbb{R}^4(p)$. This surface is an algebraic manifold. It is parameterized by the (X, Y, Z) coordinates in a fundamental domain: for example $X \geq 0$, Y and Z, avoiding the Z-axis $X = Y = 0$. This surface is also an invariant surface: an initial condition in this surface will evolve in this surface under the flow equations. This is easily verified, for

$$\frac{d}{dt}(p_2 p_4 - p_3^2) = p_2 \frac{dp_4}{dt} + p_4 \frac{dp_2}{dt} - 2p_3 \frac{dp_3}{dt} = p_2(2f_{21}p_3 + 2f_{22}p_4) +$$
$$p_4(2f_{11}p_2 + 2f_{12}p_3) - 2p_3(f_{21}p_2 + [f_{11} + f_{22}]p_3 + f_{12}p_4)$$
$$= 2\left(f_{11} + f_{22}\right)\left(p_2 p_4 - p_3^2\right) \tag{12.16}$$

The equation of motion (12.16) for s_4 shows that once $s_4 = p_2 p_4 - p_3^2 = 0$ it remains zero forever. Further, the value of s_4 relaxes exponentially to zero as $e^{-2(\sigma+1)t}$.

Example 2: For $\mathcal{C}_3$ acting in $\mathbb{R}^3$ the invariant polynomials in the integrity basis are $p_1 = Z,\ p_2 = X^2 + Y^2,\ p_3 = X^3 - 3XY^2,\ p_4 = 3X^2Y - Y^3$ and the single

simple syzygy is $s_4 = p_3^2 + p_4^2 - p_2^3$. The equation of motion for this function can be constructed from the flow equations (12.15) and is

$$\frac{ds_4}{dt} = 6f_{11}\left(p_3^2 + p_4^2 - p_2^3\right) = 6f_{11}s_4 \tag{12.17}$$

Remark 1: It is for these reasons that we define the image of $\mathbb{R}^N(X)$ in $\mathbb{R}^K(p)$ as $I^N(0)$: This is the invariant manifold of dimension N defined by the $K-N$ simple syzygies $s_\mu(p) = 0$, $\mu = N+1, \cdots, K$.

Remark 2: As Eqs. (12.16) and (12.17) make clear, when the syzygies are simple they obey equations of motion of the form

$$\frac{ds_\mu}{dt} = h_\mu(s_{N+1}, \cdots, s_K) \tag{12.18}$$

where the functions $h_\mu(s_{N+1}, \cdots, s_K)$ are polynomial in the s_μ with coefficients that are invariant functions and no constant terms, since ds_μ/dt is zero on the invariant surface $I^N(0)$. When the syzygies are not simple, equations of the form (12.18) are still satisfied. Such equations must involve all the syzygies.

Example 3: For the group $\mathcal{P}$ with invariant polynomials p_α and syzygies s_μ as defined in Table 11.1, and dynamics as parameterized in Eq. (12.2c) by the functions f_{ij}, the six syzygies obey the following equations of motion:

$$\tfrac{d}{dt}\begin{bmatrix} s_4 \\ s_5 \\ s_6 \\ s_7 \\ s_8 \\ s_9 \end{bmatrix} =$$

$$\begin{bmatrix} 2(T-f_{33}) & 0 & 0 & 2f_{23} & 2f_{13} & 0 \\ 0 & 2(T-f_{11}) & 0 & 0 & 2f_{31} & 2f_{21} \\ 0 & 0 & 2(T-f_{22}) & 2f_{32} & 0 & 2f_{12} \\ f_{32} & 0 & f_{23} & T+f_{11} & -f_{12} & -f_{13} \\ f_{31} & f_{13} & 0 & -f_{21} & T+f_{22} & -f_{23} \\ 0 & f_{12} & f_{21} & -f_{31} & -f_{32} & T+f_{33} \end{bmatrix} \begin{bmatrix} s_4 \\ s_5 \\ s_6 \\ s_7 \\ s_8 \\ s_9 \end{bmatrix} \tag{12.19}$$

In this expression $T = f_{11} + f_{22} + f_{33}$. These equations are even linear in the six syzygies.

12.3.3 Stratification $I^N(c)$

The phase space $\mathbb{R}^K(p)$ can be "stratified" into a $K-N$ dimensional family of manifolds, each of dimension N. The $K-N$ parameters themselves form a manifold of that dimension. This is analogous to decomposing $\mathbb{R}^3$ into a 1-dimensional family of planes $z = c$. Each point in $\mathbb{R}^3$ can be expressed in terms of a coordinate pair

(x, y) in the "base manifold" $\mathbb{R}^2$ and a coordinate $z = c$ in the one parameter family that defines the stratified planes.

In $\mathbb{R}^K(p)$ the "base manifold" is the N-dimensional manifold $I^N(0)$, parameterized by N coordinates $(X_1, X_2, \cdots, X_N)$ in a fundamental domain in $\mathbb{R}^N(X)$. There is a $K - N$ dimensional family of N dimensional manifolds determined by treating the $K - N$ simple syzygies $s_\mu(p_1, p_2, \cdots, p_K)$ $(\mu = N + 1, \cdots, K)$ as *coordinates*:

$$\begin{array}{rcl} s_{N+1}(p_1, p_2, \cdots, p_K) & = & c_{N+1} \\ \vdots & \vdots & \vdots \\ s_K(p_1, p_2, \cdots, p_K) & = & c_K \end{array} \tag{12.20}$$

Together, the N coordinates $(X_1, X_2, \cdots, X_K)$ in a fundamental domain in $\mathbb{R}^N(X)$ and the $K - N$ "syzygy coordinates" $(c_{N+1}, \cdots, c_K)$ provide a complete parameterization for the K invariant coordinates $(p_1, p_2, \cdots, p_K)$ in $\mathbb{R}^K(p)$:

$$(X_1, X_2, \cdots, X_K; c_{N+1}, \cdots, c_K) \leftrightharpoons (p_1, p_2, \cdots, p_K)$$

For fixed c, each manifold $I^N(c_{N+1}, \cdots, c_K)$ is invariant under the group action

$$(X_1, X_2, \cdots, X_K) \xrightarrow{\mathcal{G}} (X_1^{'}, X_2^{'}, \cdots, X_K^{'})$$

in $\mathbb{R}^N(X)$. However, only the manifold $I^N(0)$ is invariant under the flow $dp_\alpha/dt = g_\alpha(p)$.

12.3.4 Attracting Manifold

Attracting manifolds are important tools for the study of ordinary differential equations.

Definition: A manifold $M^{(m)} \subset \mathbb{R}^N$ $(\dim M^{(m)} = m < N)$ is an *attracting manifold* for a flow if

a. Every point $p \in \mathbb{R}^N$ sufficiently near $M^{(m)}$ is attracted exponentially quickly to $M^{(m)}$, and remains in $M^{(m)}$ once it crosses its boundary.

b. $M^{(m)}$ contains an invariant manifold $\mathcal{IM}$ under the flow.

c. Every point $p \in M^{(m)}$ is attracted exponentially quickly to $\mathcal{IM}$.

Speaking poetically, this means that if an initial condition, $p \in \mathbb{R}^N$, for the flow is sufficiently near $M^{(m)}$ it never gets away from $M^{(m)}$, and if it is in $M^{(m)}$ the flow never gets out of $M^{(m)}$, since it remains forever in $M^{(m)}$ and eventually winds up in $\mathcal{IM}$.

The image $I^N(0)$ of $\mathbb{R}^N(X)$ in $\mathbb{R}^K(p)$,

$$\mathbb{R}^N(X) \longrightarrow I^N(0) \subset \mathbb{R}^K(p)$$

is an attracting manifold for the image of the flow $\dot{X} = F(X)$ in $\mathbb{R}^K(p)$ when the origin $0 \in \mathbb{R}^{K-N}$ is a stable fixed point for the syzygies. We have seen that $I^N(0)$ is

invariant under the flow. Example 1 above (Eq. (12.16)) shows that initial conditions near $M^{(m)}$ are attracted exponentially quickly to $I^N(0)$. The same is true of Eq. (12.17) if $f_{11} < 0$, and of Eq. (12.19) if all the eigenvalues at the origin have negative real parts.

12.3.5 Structure of the Invariant Equations

The dynamical system equations in $\mathbb{R}^K(p)$ assume the form

$$\frac{dp_\alpha}{dt} = g_\alpha(p) \tag{12.21}$$

The forcing functions $g_\alpha(p)$ can be determined in terms of the forcing functions $F_i(X)$ and the ring basis functions $R^\beta_{js}(X)$, as shown in (12.13) and (12.15). The image of $\mathbb{R}^N(X)$ in $\mathbb{R}^K(p)$, namely, the N-dimensional surface $I^N(0)$, is an invariant manifold for the image flow, attracting under suitable conditions.

12.4 PROJECTION $R^K(P) \downarrow R^N(U)$

The second step required to mod out the symmetry of an N-dimensional equivariant dynamical system $D : \dot{X} = F(X)$ in $\mathbb{R}^N(X)$ involves projecting the K-dimensional space $\mathbb{R}^K(p)$ into an N-dimensional space $\mathbb{R}^N(u)$. Since $K \geq N$ and usually $K > N$, this projection is usually many to one. The key to this projection is that it should be one to one between the manifold $I^N(0) \subset \mathbb{R}^K(p)$ and the image Euclidean space $\mathbb{R}^N(u)$. If it is one to one, it is invertible.

12.4.1 Coordinates u and Coordinates p

The proper way to look at $|\mathcal{G}| \to 1$ images of dynamical systems equivariant under a symmetry group $\mathcal{G}$ is as flows in the space $\mathbb{R}^K(p)$ in the manifold $I^N(0)$. This study involves $K \geq N$ first-order ordinary differential equations, of which N are functionally independent. There is a strong prejudice that an N-dimensional dynamical system should be expressed in terms of exactly N first-order ordinary differential equations. To honor this prejudice, it is sufficient to choose N independent functions of the K coordinates p in the manifold $I^N(0)$. Another way to look at this is that we choose a projection of the N-dimensional manifold $I^N(0) \subset \mathbb{R}^K(p)$ to an N-dimensional space $\mathbb{R}^N(u)$. This projection must have suitable properties:

1. The projection $I^N(0) \downarrow \mathbb{R}^N(u)$ must be one to one.
2. The image of $I^N(0)$ should cover as much of $\mathbb{R}^N(u)$ as possible, preferably all.

We impose the first condition to guarantee that the $|\mathcal{G}| \to 1$ nature of the local diffeomorphism is entirely contained in the first map $\mathbb{R}^N(X) \to \mathbb{R}^K(p)$. We introduce the second condition to try to avoid the situation that the image of a dynamical system

in $\mathbb{R}^N(u)$ is constrained to be in some subset of $\mathbb{R}^N(u)$. It is not always possible to satisfy the second condition.

To guarantee the one to one nature of the projection, we require the projection to be linear. It is given explicitly by

$$u_r = \sum_{\alpha=1}^{K} T_{r\alpha} p_\alpha \qquad 1 \le r \le N \tag{12.22}$$

This projection may introduce singularities. These singularities are independent of the singularities in the injection map $\mathbb{R}^N(X) \rightarrow \mathbb{R}^K(p)$, which consists of the topological singular set $SS(\mathcal{G})$. Sometimes these singularities are unavoidable, as in the case $\mathcal{P}$ acting in $\mathbb{R}^3(X)$. The Jacobian of this projection is simply the constant matrix $J(u \leftarrow p) = \partial u_r / \partial p_\alpha = T_{r\alpha}$.

A number of examples will make this projection process clear. For σ_Z equivariant dynamical systems on $\mathbb{R}^3$ no projection is required, since $\mathbb{R}^3(p)$ is 3-dimensional. Projections from $\mathbb{R}^4 \downarrow \mathbb{R}^3$ and $\mathbb{R}^6 \downarrow \mathbb{R}^3$ are required for the other two faithful representations of the two-group in $\mathbb{R}^3$.

Example 1—$\mathcal{R}_Z$: We choose three coordinates (u, v, w) defined in terms of the four invariant coordinates $Z,\ X^2,\ XY,\ Y^2$ in the integrity basis as follows:

$$\begin{bmatrix} u \\ v \\ w \end{bmatrix} = \begin{bmatrix} 0 & 1 & 0 & -1 \\ 0 & 0 & 2 & 0 \\ 1 & 0 & 0 & 0 \end{bmatrix} \begin{bmatrix} p_1 = Z \\ p_2 = X^2 \\ p_3 = XY \\ p_4 = Y^2 \end{bmatrix} = \begin{bmatrix} X^2 - Y^2 \\ 2XY \\ Z \end{bmatrix} \tag{12.23}$$

This projection is invertible from the invariant set $I^3(0) \subset \mathbb{R}^4(p) \leftrightarrow \mathbb{R}^3(u)$, since

$$\begin{aligned} p_1 &= w & p_2 &= \frac{1}{2}\left\{\sqrt{u^2+v^2} + u\right\} \\ p_3 &= \frac{1}{2}v & p_4 &= \frac{1}{2}\left\{\sqrt{u^2+v^2} - u\right\} \end{aligned} \tag{12.24}$$

The positive square root is chosen in this inversion.

Example 2—$\mathcal{C}_3$: We choose three coordinates (u, v, w) defined in terms of the four invariant coordinates $Z,\ X^2+Y^2,\ X^3-3XY^2,\ 3X^2Y-Y^3$ in the integrity basis as follows:

$$\begin{aligned} \begin{bmatrix} u \\ v \\ w \end{bmatrix} &= \begin{bmatrix} 0 & 0 & 1 & 0 \\ 0 & 0 & 0 & 1 \\ 1 & 0 & 0 & 0 \end{bmatrix} \begin{bmatrix} p_1 = Z \\ p_2 = X^2 + Y^2 \\ p_3 = X^3 - 3XY^2 \\ p_4 = 3X^2Y - Y^3 \end{bmatrix} \\ &= \begin{bmatrix} X^3 - 3XY^2 \\ 3X^2Y - Y^3 \\ Z \end{bmatrix} \end{aligned} \tag{12.25}$$

This projection is invertible from the invariant set $I^3(0) \subset \mathbb{R}^4(p) \leftrightarrow \mathbb{R}^3(u)$, since

$$\begin{array}{lllllll} p_1 & = & w & \qquad p_2 & = & (u^2+v^2)^{1/3} \\ p_3 & = & u & & & \\ p_4 & = & v & & & \end{array} \tag{12.26}$$

The real positive cube root is chosen in this inversion. All the other rotation groups $\mathcal{C}_n$ in $\mathbb{R}^3$ are treated the same way. For these groups, we have $p_1 = Z$, $p_2 = X^2 + Y^2$, $p_3 = \mathtt{Re}\,(X+iY)^n$, $p_4 = \mathtt{Im}\,(X+iY)^n$, the new coordinates are $u = p_3, v = p_4, w = p_1$. The inversion is immediate for $p_1,\ p_3,\ p_4$ and for p_2 it is $p_2 = (u^2+v^2)^{1/n}$. The rotation group $\mathcal{R}_Z = \mathcal{C}_2$ can be put into this form also, simply by choosing the integrity basis functions in the same way, as $p_2 = X^2 + Y^2,\ p_3 = X^2 - Y^2,\ p_4 = 2XY$.

Example 3—$\mathcal{P}$: We choose three coordinates (u, v, w) defined in terms of the six invariant coordinates $X^2,\ Y^2,\ Z^2,\ YZ,\ ZX,\ XY$ in the integrity basis as follows:

$$\begin{aligned} \begin{bmatrix} u \\ v \\ w \end{bmatrix} &= \begin{bmatrix} 1 & -1 & 0 & 0 & 0 & 0 \\ 1 & 1 & -2 & 0 & 0 & 0 \\ 0 & 0 & 0 & 1 & 1 & 1 \end{bmatrix} \begin{bmatrix} p_1 = X^2 \\ p_2 = Y^2 \\ p_3 = Z^2 \\ p_4 = YZ \\ p_5 = ZX \\ p_6 = XY \end{bmatrix} \\ &= \begin{bmatrix} X^2 - Y^2 \\ X^2 + Y^2 - 2Z^2 \\ XY + YZ + ZX \end{bmatrix} \end{aligned} \tag{12.27}$$

This projection is invertible on the invariant set. However, this projection introduces singularities beyond those of the singular set $SS(\mathcal{G})$, consisting of the origin. These new singularities are unavoidable.

Example 4—$\mathcal{V}_4$: We choose three coordinates (u, v, w) defined in terms of the four invariant coordinates $X^2,\ Y^2,\ Z^2,\ XYZ$ in the integrity basis as follows:

$$\begin{aligned} \begin{bmatrix} u \\ v \\ w \end{bmatrix} &= \begin{bmatrix} 1 & -1 & 0 & 0 \\ 1 & 1 & -2 & 0 \\ 0 & 0 & 0 & 1 \end{bmatrix} \begin{bmatrix} p_1 = X^2 \\ p_2 = Y^2 \\ p_3 = Z^2 \\ p_4 = XYZ \end{bmatrix} \\ &= \begin{bmatrix} X^2 - Y^2 \\ X^2 + Y^2 - 2Z^2 \\ XYZ \end{bmatrix} \end{aligned} \tag{12.28}$$

This projection is also invertible from $\mathbb{R}^3(u)$ back to $I^3(0)$.

12.4.2 "Radicals"

The inversion formula (12.24) and (12.26) show that expressions for the K invariant coordinates $p_1, p_2, \cdots, p_K$ in terms of the N invariants $u_1, u_2, \cdots, u_N$ can be nonlinear, whereas the forward relation (12.22) is linear. This is true in general.

To show this, it is useful to append to the N linear combinations $u_1, u_2, \cdots, u_N$ a set of $K - N$ additional functions $r_{N+1}, \cdots, r_K$ that are also linear combinations of the p_α. This is done so that a linear transformation relates the K-tuple $(p_1, p_2, \cdots, p_K)$ with the augmented K-tuple $(u_1, u_2, \cdots, u_N; r_{N+1}, \cdots, r_K)$. The simplest way to define these additional functions is by completing the matrix $T_{r\alpha}$ describing the linear transformation $u_r = T_{r\alpha} p_\alpha$ into a square $K \times K$ matrix. It is useful to complete this rectangular matrix to an orthogonal matrix when possible.

Example: For $\mathcal{V}_4$ we introduce one ($K - N = 4 - 3 = 1$) additional function r_4 according to

$$\begin{aligned}
\left[\begin{array}{c} u_1 \\ u_2 \\ u_3 \\ \hline r_4 \end{array}\right] &= \left[\begin{array}{cccc} 1 & -1 & 0 & 0 \\ 1 & 1 & -2 & 0 \\ 0 & 0 & 0 & 1 \\ \hline 1 & 1 & 1 & 0 \end{array}\right] \left[\begin{array}{l} p_1 = X^2 \\ p_2 = Y^2 \\ p_3 = Z^2 \\ p_4 = XYZ \end{array}\right] \\
&= \left[\begin{array}{c} X^2 - Y^2 \\ X^2 + Y^2 - 2Z^2 \\ XYZ \\ \hline X^2 + Y^2 + Z^2 \end{array}\right]
\end{aligned} \tag{12.29}$$

The fourth row in this matrix is orthogonal to the first three, by design. Since the first three rows are mutually orthogonal, the matrix is orthogonal and its inverse is easily computed. We find

$$\left[\begin{array}{l} p_1 = X^2 \\ p_2 = Y^2 \\ p_3 = Z^2 \\ p_4 = XYZ \end{array}\right] = \frac{1}{6} \left[\begin{array}{cccc} 3 & 1 & 0 & 2 \\ -3 & 1 & 0 & 2 \\ 0 & -2 & 0 & 2 \\ 0 & 0 & 6 & 0 \end{array}\right] \left[\begin{array}{c} u_1 \\ u_2 \\ u_3 \\ r_4 \end{array}\right] \tag{12.30}$$

The three integrity basis functions p_1, p_2, p_3 are dependent on the new coordinate r_4.

The new invariant functions are *linearly* independent of the invariant coordinates u_j but they are not *functionally* independent of the u_j. For systems with simple syzygies

$$s_\mu(p_1, p_2, \cdots, p_K) = 0 \qquad \mu = K + 1, \cdots, N$$

the new coordinates r_μ ($\mu = N + 1, \cdots, K$) satisfy $K - N$ polynomial equations. These are derived from the syzygies by expressing the p_α in terms of the K-tuple $(u_1, u_2, \cdots, u_N; r_{N+1}, \cdots, r_K)$ and substituting these expressions into the syzygies. As a result, we obtain a set of $K - N$ polynomial equations in the N variables u and $K - N$ variables r. Since the equations are polynomial, their $K - N$ solutions for

r in terms of the N variables u are called "radicals" even if the equations cannot be solved in closed form by the standard operations $(+, -, \times, \div, \surd)$.

Example: There is one simple syzygy for $\mathcal{V}_4$. It is

$$p_1 p_2 p_3 - p_4^2 = 0 \tag{12.31}$$

Substituting the solutions for p_α in terms of u_1, u_2, u_3, r_4 obtained from (12.29) (e.g., $p_1 = \frac{1}{6}(3u_1 + u_2 + 2r_4)$) into this syzygy, we find the following syzygy for the new coordinates $(u_1, u_2, u_3; r_4)$

$$108 r_4^4 - 4 r_4^3 + (9u_1^2 + 3u_2^2) r_4 + (u_2^3 - 9u_1^2 u_2) = 0 \tag{12.32}$$

This equation can be solved (in principle) for r_4 as a function of (u_1, u_2, u_3) in closed form using the quartic formula. The result is given in terms of "radicals": square roots, cube roots, fourth roots.

12.4.3 Inversion $u \longrightarrow p$

The general procedure for computing the inverse map $(u_1, u_2, \cdots, u_N) \rightarrow (p_1, p_2, \cdots, p_K)$ should now be clear. The radicals $r_{N+1}, \cdots, r_K$ are determined as nonlinear functions of the N variables $(u_1, u_2, \cdots, u_N)$. The linear relation between the K variables p_α and the K variables $(u; r(u))$ is inverted to determine the K variables p_α on the N-dimensional manifold $I^N(0)$ uniquely in terms of the N variables u and the $K - N$ variables $r(u)$, themselves determined by the N variables u.

Example: For $\mathcal{V}_4$, a point in the image space $\mathbb{R}^3(u)$ is determined by the triple of coordinates (u_1, u_2, u_3). The radical r_4 is determined in terms of this triple by the syzygy (12.31), implemented as in (12.32). This value of r_4 is introduced into the matrix inverse relation (12.30) to determine the values of the quartet (p_1, p_2, p_3, p_4) in terms of the triple (u_1, u_2, u_3) and the subsidiary dependent coordinate $r_4(u)$.

12.5 STRUCTURE OF FLOWS IN $R^N(U)$

A $\mathcal{G}$-equivariant dynamical system D: $\dot{X}_i = F_i(X)$ on $\mathbb{R}^N(X)$ is mapped to a dynamical system without residual symmetry $\underline{D}$: $\dot{u}_r = h_r(u; r(u))$ on $\mathbb{R}^N(u)$ by a $|\mathcal{G}| \rightarrow 1$ local diffeomorphism. The local diffeomorphism is constructed in two steps:

$$\begin{array}{ccccc} \mathbb{R}^N(X) & \longrightarrow & I^N(0) & \subset & \mathbb{R}^K(p) \\ & & \downarrow & & \\ & & \mathbb{R}^N(u) & & \end{array} \tag{12.33}$$

The first step is a nonlinear $|\mathcal{G}| \rightarrow 1$ map. The second step is a linear projection of the N-dimensional manifold $I^N(0)$ to the N-dimensional space $\mathbb{R}^N(u)$. The two steps in this mapping have been described in Sections 12.2 and 12.3.

12.5.1 Composition of Jacobians

The Jacobian of the transformation is the composition of the Jacobians of the two separate maps. It is

$$\frac{\partial u_r}{\partial X_i} = \frac{\partial u_r}{\partial p_\alpha}\frac{\partial p_\alpha}{\partial X_i} \tag{12.34}$$

The $K \times N$ matrix $\partial p_\alpha / \partial X_i$ contains information about the topology of the singular set $SS(\mathcal{G})$.

Example 1: For $\mathcal{R}_Z$ acting in $\mathbb{R}^3$ the 3×4 matrix $\partial u_r / \partial p_\alpha$ is given in (12.23) and the 4×3 matrix $\partial p_\alpha / \partial X_i$ is presented in (12.9). The composition is

$$\begin{bmatrix} 0 & 1 & 0 & -1 \\ 0 & 0 & 2 & 0 \\ 1 & 0 & 0 & 0 \end{bmatrix} \begin{bmatrix} 0 & 0 & 1 \\ 2X & 0 & 0 \\ Y & X & 0 \\ 0 & 2Y & 0 \end{bmatrix} = \begin{bmatrix} 2X & -2Y & 0 \\ 2Y & 2X & 0 \\ 0 & 0 & 1 \end{bmatrix} \tag{12.35}$$

The five nonzero matrix elements are expressed in terms of the three ring basis functions $1,\ X,\ Y$. There are two relations: $(\partial u/\partial X)_{11} = 2X = (\partial u/\partial X)_{22}$ and $-(\partial u/\partial X)_{12} = 2Y = (\partial u/\partial X)_{21}$.

Example 2: For $\mathcal{C}_3$ acting in $\mathbb{R}^3$ the 3×4 matrix $\partial u_r / \partial p_\alpha$ is presented in (12.25) and the 4×3 matrix $\partial p_\alpha / \partial X_i$ is given in (12.9). Their composition is

$$\begin{bmatrix} 0 & 0 & 1 & 0 \\ 0 & 0 & 0 & 1 \\ 1 & 0 & 0 & 0 \end{bmatrix} \begin{bmatrix} 0 & 0 & 1 \\ 2X & 2Y & 0 \\ 3(X^2-Y^2) & -6XY & 0 \\ 6XY & 3(X^2-Y^2) & 0 \end{bmatrix} = \begin{bmatrix} 3(X^2-Y^2) & -6XY & 0 \\ 6XY & 3(X^2-Y^2) & 0 \\ 0 & 0 & 1 \end{bmatrix} \tag{12.36}$$

Although the ring basis consists of the $(2\times3-1)$ functions $1,\ X,\ Y,\ X^2-Y^2,\ 2XY$, the Jacobian is a function of only three. There are again symmetries among the five nonzero matrix elements of the Jacobian $\partial u/\partial X$. The symmetries are: $(\partial u/\partial X)_{11} = (\partial u/\partial X)_{22} = 3\mathtt{Re}\,(X+iY)^{3-1}$ and $-(\partial u/\partial X)_{12} = (\partial u/\partial X)_{21} = 3\mathtt{Im}\,(X+iY)^{3-1}$. The results are unchanged for the group $\mathcal{C}_n$ acting in $\mathbb{R}^3$, subject to the replacement $3 \to n$ in the expressions above. The singular set of the Jacobians in all cases is the singular set of the geometric transformation: the Z-axis $X^2 + Y^2 = 0$.

Example 3: For $\mathcal{V}_4$ acting in $\mathbb{R}^3$ the matrices $\partial u_r/\partial p_\alpha$, $\partial p_\alpha/\partial X_i$, and $\partial u_r/\partial X_i$ are:

$$\begin{bmatrix} 1 & -1 & 0 & 0 \\ 1 & 1 & -2 & 0 \\ 0 & 0 & 0 & 1 \end{bmatrix} \begin{bmatrix} 2X & 0 & 0 \\ 0 & 2Y & 0 \\ 0 & 0 & 2Z \\ YZ & ZX & XY \end{bmatrix} = \begin{bmatrix} 2X & -2Y & 0 \\ 2X & 2Y & -4Z \\ YZ & ZX & XY \end{bmatrix} \tag{12.37}$$

The Jacobian is $8(X^2Y^2 + Y^2Z^2 + Z^2X^2)$. The singular set consists of the union of the three rotation axes.

Example 4: For the inversion group $\mathcal{P}$ acting in $\mathbb{R}^3$ we have for the Jacobian

$$\begin{bmatrix} 1 & -1 & 0 & 0 & 0 & 0 \\ 1 & 1 & -2 & 0 & 0 & 0 \\ 0 & 0 & 0 & 1 & 1 & 1 \end{bmatrix} \begin{bmatrix} 2X & 0 & 0 \\ 0 & 2Y & 0 \\ 0 & 0 & 2Z \\ 0 & Z & Y \\ Z & 0 & X \\ Y & X & 0 \end{bmatrix} \tag{12.38}$$

$$= \begin{bmatrix} 2X & -2Y & 0 \\ 2X & 2Y & -4Z \\ Y+Z & Z+X & X+Y \end{bmatrix}$$

The Jacobian is $8\left[XY(X+Y) + YZ(Y+Z) + ZX(Z+X)\right]$. The singular set consists of the union of the one-dimensional sets $X_i = X_j = 0$ and $X_i = X_j + X_k = 0$, $(i \neq j \neq k)$. The topological singular set for this symmetry is $SS(\mathcal{P}) = (0,0,0)$. In this case the algebraic singular set of the local diffeomorphism $\partial u_r/\partial X_i$ does not coincide with the topological singular set of the group $\mathcal{P}$.

12.5.2 Form of Flows

The structure of the image flow, $\underline{D}$, in $\mathbb{R}^N(u)$: $\dot{u}_r = h_r(u; r(u))$, is determined directly from the chain of transformations:

$$\frac{du_r}{dt} = \frac{\partial u_r}{\partial p_\alpha}\frac{\partial p_\alpha}{\partial X_i}\frac{dX_i}{dt} = \frac{\partial u_r}{\partial p_\alpha}\frac{\partial p_\alpha}{\partial X_i}F_i(X) = h_r(u; r(u)) \tag{12.39}$$

The matrix elements $\partial u_r/\partial p_\alpha$ are constants. The matrix elements $\partial p_\alpha/\partial X_i$ are linear in the ring basis functions with coefficients that are invariant functions. The same is true of the forcing functions $F_i(X)$. In general the forcing functions $h_r(u; r(u))$ are bilinear combinations of the ring basis functions. These combinations are invariant under the group action, so can be expressed in terms of the integrity basis functions p_α. These in turn can be expressed *linearly* in terms of the new set of N invariant coordinates $u_1, u_2, \cdots, u_N$ *and* the $K - N$ auxiliary coordinates $r_{N+1}, \cdots, r_K$. As a result, equivariant polynomial forcing functions $F_i(X)$ in the covering dynamical system D map to invariant polynomial forcing functions $h_r(u; r(u))$ in the image dynamical system. The functions $h_r(u; r(u))$ are polynomial *in the coordinates* u *and* r. However, the auxiliary dependent coordinates $r(u)$ are *not* polynomial in the variables u. As a result, the driving functions $h_r(u; r(u))$ are in general not polynomial functions of the N-image coordinates $u_1, u_2, \cdots, u_N$.

Example 1: Dynamical systems equivariant under $\mathcal{C}_3$ have the form shown in (12.4). If the five independent functions f_{ij} are polynomial in the four invariants $p_1 = Z,\ p_2 = X^2 + Y^2,\ p_3 = X^3 - 3XY^2,\ p_4 = 3X^2Y - Y^3$, the equivariant dynamical system is polynomial in the coordinates (X, Y, Z). The image equations

in $I^3(0)$ have the form shown in (12.15). The image dynamical system equations in $\mathbb{R}^3(u)$ for $u = X^3 - 3XY^2, v = 3X^2Y - Y^3, w = Z$ are obtained simply by multiplying from the left by the matrix $\partial u_r/\partial p_\alpha$ in (12.25):

$$\frac{d}{dt}\begin{bmatrix} u \\ v \\ w \end{bmatrix} = \begin{bmatrix} 3f_{11}u + 3f_{12}v + 3f_{13}r_4^2 \\ -3f_{12}u + 3f_{11}v + 3f_{14}r_4^2 \\ f_{30} \end{bmatrix} \qquad u^2 + v^2 = r_4^3 \tag{12.40}$$

These equations are not polynomial in the new coordinates (u, v, w) since r_4 is not polynomial in these coordinates. It is worse: the invariant functions $f_{ij}(p_1, p_2, p_3, p_4)$ depend on the radical: $f_{ij}(u, v, w; r_4)$, so they are also not polynomial. In general the image equations of a $\mathcal{C}_3$ equivariant dynamical system can be expressed in the form

$$\frac{du_r}{dt} = \sum_0^m h_{r,s}(u, v, w) r_4^s \tag{12.41}$$

The upper limit in the sum (m) depends on the syzygy. In the case at hand it is $2 = 3 - 1$, since r_4 and r_4^2 cannot be expressed as polynomial functions of (u, v, w) while r_4^3 can be. The functions $h_{r,s}(u, v, w)$ can be explicitly constructed from the functions f_{ij} that appear in (12.40). Analogous results hold for $\mathcal{C}_n$-equivariant dynamical systems in $\mathbb{R}^3(X)$ and their invariant image equations in $\mathbb{R}^3(u)$: it is only necessary to replace 3 by n in the summation above.

12.5.3 Polynomial Dynamical Systems

Sets of ordinary differential equations are difficult enough to study without looking for additional difficulties. It is for this reason that most modeling in this area is done with polynomial functions. It is this desire for simplicity that has hindered the study of cover and image dynamical systems in two ways.

If the functions $F(X)$ of the equivariant dynamical system are polynomial in the coordinates $(X_1, X_2, \cdots, X_N)$, it is not likely that the forcing functions in the image dynamical system, $h(u; r(u))$, are polynomial in the invariant coordinates $(u_1, u_2, \cdots, u_N)$. The image forcing functions are polynomial in the invariant coordinates $(p_1, p_2, \cdots, p_K)$, but $K - N$ of these must be expressed as radicals, as is apparent in (12.39). It is only when the functions $f_{ij}(p_1, \cdots, p_K)$ have a very special form that radicals do not appear in the image flow. For example, f_{30} must be independent of r_4. For the first equation, $f_{11}u + f_{12}v + f_{13}r_4^2$ can depend only on (u, v, w) and integer powers of r_4^3. As a result, it would be almost a miracle if an equivariant dynamical system with polynomial forcing functions had an image dynamical system that had previously been studied (i.e., with polynomial forcing functions).

The same is true in reverse. It is easy to choose and study image dynamical systems with polynomial forcing functions $h(u_1, u_2, \cdots, u_N)$. However, when such image dynamical systems are lifted to covering dynamical systems with symmetry group $\mathcal{G}$, nonpolynomial terms are also introduced. As a result, the polynomial nature of forcing terms is generally lost under local diffeomorphisms, going in both directions.

13

Covering Dynamical Systems

13.1 IMAGE ATTRACTORS

The image dynamical system is the foundation upon which all its $\mathcal{G}$-equivariant covers are built. It is therefore useful—even imperative—to understand in detail all the most important properties of the image dynamical system.

13.1.1 Phase Space

The variables that describe the image dynamical system are $(u_1, u_2, \ldots, u_N)$. These represent points in an N-dimensional phase space. The phase space is often taken to be $\mathbb{R}^N$. However, the phase space is more generally an N-dimensional manifold $\mathbb{M}^N$. We have already seen that the phase spaces for typical image dynamical systems are N dimensional algebraic submanifolds of $\mathbb{R}^K$ defined by $K-N$ algebraic constraints called syzygies.

13.1.2 Control Parameter Space

In general the flow depends on control parameters $(c_1, c_2, \ldots, c_K)$. The control parameters often model physical operating conditions (e.g., temperature ΔT in a fluid experiment, losses γ in a laser cavity). At a mathematical level there are never enough parameters to represent all possible perturbations of a dynamical system. This is in stark opposition to the study of the simplest dynamical systems governed by Catastrophe heory [32]. In this case a finite, even small, number of parameters is often sufficient to describe *all* possible perturbations of a potential. It is for this reason that topology is the necessary and preferred tool for the analysis of ordinary differential equations.

Example: Imagine a perturbation of the form ϵx^3 added to the forcing term of the first of the Rössler equations $\dot{x} = -y - z$. There is no change in the values of the three control parameters (a, b, c) that can compensate for this cubic perturbation.

13.1.3 Image Dynamical Equations

The dynamical system equations on $\mathbb{M}^N$ have the general form

$$\frac{du_i}{dt} = g_i(\boldsymbol{u}; \boldsymbol{c}) \tag{13.1}$$

where $\boldsymbol{u} = (u_1, u_2, ..., u_N) \in \mathbb{M}^N$ and $\boldsymbol{c} = (c_1, c_2, \ldots, c_K)$. Normally this set of equations is invariant under only the identity operation, independent of the values of the control parameters. However, this is not a necessary condition for any discussions that follow.

The forcing functions $g_i(\boldsymbol{u}; \boldsymbol{c})$ should satisfy a Lipschitz condition over a domain where a strange attractor exists. Typically, the functions $g_i(\boldsymbol{u}; \boldsymbol{c})$ are chosen to be smooth; differentiable or piecewise differentiable; polynomial, analytic, or rational. The functions $g(\boldsymbol{u}; \boldsymbol{c})$ never depend on "radicals" unless they are obtained by modding the symmetry out of an equivariant dynamical system. As a result, when we lift the invariant dynamical system (13.1) to its $\mathcal{G}$-equivariant covers, we cannot expect the forcing terms of the covering dynamical system to be polynomial if the source terms for the invariant dynamical system are polynomial.

13.1.4 Fixed Points

Strange attractors generated by equations of the form (13.1) are organized most strongly by their fixed points. When the functions $g_i(\boldsymbol{u}; \boldsymbol{c})$ are polynomial, their fixed points can be located systematically by algorithms of algebraic topology [25]. Fig. 13.1 presents a Maple worksheet that computes the fixed points of the Lorenz dynamical system.

As with previous Maple codes (cf. Fig. 11.1 and Fig. 11.2) the appropriate packages are read in, followed by the polynomial source terms for the dynamical system, in this case the Lorenz equations. A coordinate system is established, and the `gbasis`

```
> with(linalg):
> with(grobner);
```

$$[finduni, finite, gbasis, gsolve, leadmon, normalf, solvable, spoly]$$

```
> f[1]:=-sigma*x+sigma*y:
> f[2]:=R*x-y-x*z:
> f[3]:=-b*z+x*y:
> [F]:=[f[1],f[2],f[3]];
```

$$F := [-\sigma x + \sigma y, Rx - y - xz, -bz + xy]$$

```
> X:=[x,y,z]:
> gbasis(F,X);
```

$$[-bz + y^2, yz + y - Ry, z^2 + z - Rz, x - y]$$

```
> gsolve(F,X);
```

$$[[[z, y, x], plex(x, y, z), \{\}], [[b - Rb + x^2, -x + y, z + 1 - R], plex(z, y, x), \{\}]]$$

```
> J:=Jacobian(F,[x,y,z]);
```

$$J := \begin{bmatrix} -\sigma & \sigma & 0 \\ R - z & -1 & -x \\ y & x & -b \end{bmatrix}$$

```
> x:=0:y:=0:z:=0:
> eigenvalues(J);
```

$$-b, -\frac{\sigma}{2} - \frac{1}{2} + \frac{\sqrt{\sigma^2 - 2\sigma + 1 + 4R\sigma}}{2}, -\frac{\sigma}{2} - \frac{1}{2} - \frac{\sqrt{\sigma^2 - 2\sigma + 1 + 4R\sigma}}{2}$$

Fig. 13.1 Maple code illustrating how to find fixed points of a dynamical system and eigenvalues at a fixed point.

routine returns the fixed points. The outputs are to be read as each term within the square brackets [ ] being set to zero. The first fixed point, `[x,y,z]`, is the computer's way of saying $x = 0, y = 0, z = 0$. The second output consists of all of the solutions to the equations $b - Rb + x^2 = 0$, $-x + y = 0$, and $z + 1 - R = 0$. It may not seem like a computer is needed to describe this obvious solution. What is significant is that the last equation *always* involves just one coordinate (the last in the coordinate list), so can always be solved by one-dimensional methods. In this case the simple solution is $z = R - 1$. The remaining two solutions are obtained by working right to left to find $x = y$ and $x = \pm\sqrt{b(R-1)}$.

In addition to the number of fixed points and their locations, the stability of each fixed point is an important piece of information. The stability of a fixed point is determined by linearizing the flow in the neighborhood of the fixed point. This produces a Jacobian matrix, as previously discussed. The call to `jacobian` does

this. The eigenvalues determine the stability of the fixed point, and the eigenvectors provide the information about the flow directions in the neighborhood of the fixed point. The call to `eigenvalues` generates the three eigenvalues of the fixed point at the origin. A call to `eigenvectors` would produce the eigenvector for each eigenvalue.

Eigenvalues and eigenvectors at the nontrivial fixed points are treated similarly, but with the following caveat. In those cases the output consists of analytic expressions that are very complicated. Though correct, they are basically useless for interpretive purposes. In such cases it is best to assign numerical (in fact, decimal!) values to all control parameters so that the output consists of real (or complex) numbers. These are always much easier to interpret than analytic expressions that run on for pages.

13.1.5 Symbolic Dynamics

It is enormously useful to have available a description of the flow dynamics in terms of symbol dynamics. In general, symbolic dynamics involves decomposing the phase space into a (relatively) small number of nonoverlapping domains, each labeled by a symbol $\sigma_1, \sigma_2, \ldots, \sigma_s$. Any trajectory under the flow $\dot{u}_i = g_i(\boldsymbol{u}; \boldsymbol{c})$ can then be labeled by a sequence of symbols that reflect the successive regions of the phase space that the trajectory traverses. Ideally, a suitable symbolic dynamics satisfies two conditions:

1. There is one to one correspondence between (infinite) symbol sequences $\ldots \sigma_{i_1}\sigma_{i_2}\sigma_{i_3}\ldots$ and points in the phase space $\mathbb{M}^N$, except possibly for a set of measure 0.
2. A minimal number of symbols is used.

In low dimensional dynamical systems ($d_L < 3$) and very likely in higher dimensional dynamical systems as well, information about the partition of the phase space can be compressed into very small regions of the phase space. This idea is illustrated in Fig. 13.2, which shows the branched manifold for a low dimensional dynamical system that generates Smale horseshoe dynamics. In the projection to the branched manifold all the partition information is contained in the branch line. The branch line is partitioned into two segments labeled 0 and 1. Every trajectory passes through one of these two segments. There is a one-to-one correspondence between trajectories and infinite symbol sequences consisting of 0's and 1's. Finite sequences terminate at a fixed point.

Information about the partition of the three-dimensional phase space $\mathbb{R}^3(\boldsymbol{u})$ is contained in the inverse image of the branch line, specifically, the inverse image of the two segments 0 and 1. The inverse image consists of all points that limit on these segments under the Birman-Williams projection.

13.1.6 Transition Matrices

A trajectory in a region σ_i can evolve directly to some regions σ_j and not to others. The collection of allowed transitions is represented by a *transition matrix* T. This is

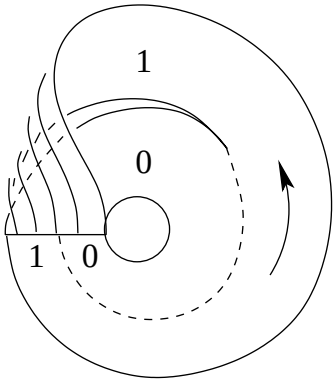

Fig. 13.2 Smale horseshoe branched manifold.

an $s \times s$ matrix defined by

$$\begin{array}{lcll} T_{ij} & = & 1 & \text{if} \quad \ldots\sigma_i\sigma_j\ldots \quad \text{can occur} \\ T_{ij} & = & 0 & \text{if} \quad \ldots\sigma_i\sigma_j\ldots \quad \text{cannot occur} \end{array}$$

Transition matrices for dynamical systems have been used liberally in Part I of this work.

There are some degrees of freedom in the choice of symbols for a dynamical system. For example, the branched manifold for the figure 8 knot (cf. Fig. 14.4) has four branch lines and 8 branches. The symbolic dynamics can either be based on four symbols, each representing a branch line, or on eight symbols, each representing a branch, or flow region. When each branch is uniquely represented by a source branch line and a sink branch line, the two labeling schemes are equivalent. When this is not the case (e.g., Smale horseshoe branched manifold), it is useful to divide each branch line into a number of disjoint segments, each feeding a different branch. Two equivalent transition matrices for the figure 8 knot branched manifold have been presented: an 8×8 matrix in Fig. 14.4 and a 4×4 matrix in Fig. 14.7.

Transition matrices are useful for counting the number of orbits of period p that can exist in a dynamical system. An initial condition on segment i can evolve to segment j, and j to k, if the product of matrix elements $T_{ij}T_{jk} = 1$. If $\sum_j T_{ij}T_{jk} = n$, an initial condition on segment i can propagate to segment k via n intermediate segments j. If $k = i$, there are n period-2 orbits that start and end on segment i and go through various intermediate branchs j. By similar reasoning, if the product of n matrix elements $T_{ij}T_{jk}\cdots T_{mi} = 1$ (no intermediate sums), there is a period-n orbit whose symbol sequence is $(ijk\cdots m)$. The number of period-two orbits, $N(2)$, is related to the trace of T^2 and T, by

$$2N(2) = \mathrm{tr}\, T^2 - \mathrm{tr}\, T \tag{13.2a}$$

A similar result holds for the number of orbits, $N(p)$, of period p and the trace of various powers of the transition matrix T

$$p \times N(p) = \text{tr } T^p - \sum_{k \div p} k \times N(k) \tag{13.2b}$$

The sum is over all values of k (integer) that divide p, $k < p$. This sum removes all orbits of period k that "go around" more than once.

13.1.7 Topological Entropy

An upper bound for the topological entropy of a dynamical system can be constructed from its transition matrix [34]. The topological entropy, h_T, estimates the growth in the number of orbits of period p with the period through

$$N(p) \approx e^{ph_T} \tag{13.3}$$

Since $pN(p) = \text{tr } T^p - \sum_{k \div p} kN(k) \approx \text{tr } T^p$ we have

$$h_T = \lim_{p \to \infty} \frac{1}{p} \log \text{tr } T^p$$

The trace of the matrix is invariant under a similarity transformation. In particular, if T is diagonalized, or at least reduced to upper or lower triangular form with eigenvalues $\lambda_1 \geq \lambda_2 \geq \cdots \geq \lambda_s$, it follows that

$$\text{tr } T^p = \lambda_1^p + \lambda_2^p + \cdots + \lambda_s^p \overset{p \to \infty}{\longrightarrow} \lambda_1^p$$

As a result

$$h_T = \log \lambda_1 \tag{13.4}$$

where λ_1 is the largest eigenvalue of T.

13.1.8 Higher Dimensions

A complete classification theory for low ($d_L = 2 + \lambda_1/|\lambda_3| < 3$) dimensional strange attractors is now available. This involves a hierarchy of four levels of structure:

1. Periodic orbits in strange attractors;
2. Branched manifolds, which organize periodic orbits;
3. Bounding surfaces embedded in $\mathbb{R}^3$ (or $\mathbb{M}^3$) that organize branched manifolds;
4. Intrinsic genus-g surfaces, which organize the extrinsic surfaces embedded in $\mathbb{R}^3$.

This classification will be reviewed in Chapter 15.

We are nowhere near understanding how to describe or even classify chaos in higher dimensions. However, it seems clear that at least two features useful for

the description of low dimensional attractors will carry their usefulness into higher dimensions. These are:

1. Flow Tubes. These are regions of space that carry the flow. In low dimensions these regions limit to branches.
2. Mixing Boxes. These are regions of the space where flows from different parts of phase space get "squeezed together." In low dimensions these regions limit to branch lines and their inflow and outflow branches.

The decomposition of phase space into flow tubes and mixing boxes is compatible with symbolic dynamics in higher dimensional flows and transition matrices to describe allowed symbol sequences.

13.2 LIFTS TO COVERS

A strange attractor $\underline{\mathcal{SA}}$ without symmetry can be lifted to a strange attractor that is equivariant under a symmetry group $\mathcal{G}$. We have studied lifts with many different symmetry groups $\mathcal{G}$ in Part I.

13.2.1 Symmetry Group $\mathcal{G}$

The properties of the lift depend in a crucial way on the properties of the group $\mathcal{G}$. In fact, they depend on different properties on $\mathcal{G}$.

Order: They depend on the order $|\mathcal{G}|$ of $\mathcal{G}$. This is the number of group operations in $\mathcal{G}$. The groups $\mathcal{C}_3$, $\mathcal{C}_4$, $\mathcal{V}_4$ have orders $|\mathcal{C}_3| = 3$, $|\mathcal{C}_4| = 4$, $|\mathcal{V}_4| = 4$. We speak of $|\mathcal{G}|$-fold covers of strange attractors $\underline{\mathcal{SA}}$.

Group/Subgroup Structure: Properties of lifts depend on the group/subgroup structure of $\mathcal{G}$. As an example, the subgroup structure of the two order-4 groups $\mathcal{C}_4$ and $\mathcal{V}_4$ is

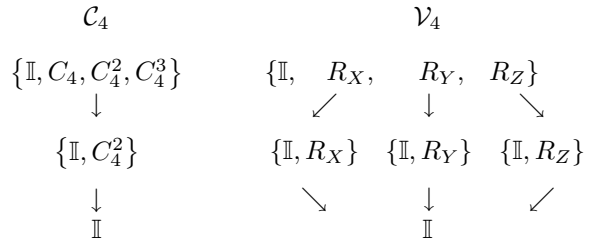

Generators: The properties of lifts are very strongly correlated with the way a group is constructed from its generators. For example, $\mathcal{C}_n$ has one generator γ (cf. Eq. 10.48 with $j = k = 1$). The generator γ obeys the relation $\gamma^n = \mathbb{I}$. In our applications we have chosen γ to represent rotations through $2\pi/n$ radians about a preferred axis. The four-group $\mathcal{V}_4$ has two generators γ_1 and γ_2 that obey the relations $\gamma_1^2 = \gamma_2^2 = \mathbb{I}$, $\gamma_1\gamma_2 = \gamma_2\gamma_1$. The four group operations are $\{\mathbb{I}, \gamma_1, \gamma_2, \gamma_1\gamma_2\}$. In our applications, we have chosen $\gamma_1 = \mathcal{R}_X(\pi)$ and $\gamma_2 = \mathcal{R}_Y(\pi)$, so that $\gamma_1\gamma_2 = \mathcal{R}_Z(\pi)$.

13.2.2 Phase Space

If $\underline{\mathcal{SA}}$ is the strange attractor in an N-dimensional phase space $\mathbb{R}^N(\boldsymbol{u})$ or $\mathbb{M}^N(\boldsymbol{u})$, its $\mathcal{G}$-equivariant covers live in a phase space $\mathbb{R}^N(\boldsymbol{X})$ of the same dimension as long as $|\mathcal{G}|$ is finite.

The group $\mathcal{G}$ can be used to partition phase space into $|\mathcal{G}|$ domains. All the domains are equivalent: each looks like every other. One of these domains can be arbitrarily chosen as the fundamental domain. This is labeled by a group operation: the identity. Points in the fundamental domain can be mapped into the remaining domains by action of the group operators. If $\boldsymbol{x} \in \mathbb{D}_{\mathbb{I}}$, then $g\boldsymbol{x} \in \mathbb{D}_g$. More generally the action of any group operation in any domain is

$$g_\alpha \mathbb{D}_{g_\beta} = g_\alpha g_\beta \mathbb{D}_{\mathbb{I}} = \mathbb{D}_{g_\alpha g_\beta} \tag{13.5}$$

The group operators act to permute the domains among themselves.

The domains partition the phase space

$$\mathbb{R}^n \approx \mathbb{D}_{g_1} \cup \mathbb{D}_{g_2} \cup \cdots \cup \mathbb{D}_{g_{|\mathcal{G}|}} = \bigcup_{g \in \mathcal{G}} \mathbb{D}_g \tag{13.6}$$

where $g_1 = \mathbb{I}$. It is unimportant whether the domains are open or closed.

The most important feature of the domain decomposition of $\mathbb{R}^N$ is adjacency. Two domains are adjacent if the intersection of their closures contains an $N-1$ dimensional boundary component. A trajectory can generically pass from one domain to another if they are adjacent; otherwise it cannot.

13.2.3 Representations

Groups are abstract objects. They act on physically important things—points in phase space, coordinates, equations of motion—through their matrix representations. Often, through carelessness or laziness, we fail to distinguish between an abstract group and its action on physical objects. For example, we sometimes fail to distinguish between the group $\mathcal{R}_Z(\pi)$ and the transformation $(X, Y, Z) \to (-X, -Y, +Z)$. To be precise, there is a two-element group $\{\mathbb{I}, \gamma\}$ and γ acts in $\mathbb{R}^3$ through the matrix representation

$$\gamma \to \begin{bmatrix} -1 & 0 & 0 \\ 0 & -1 & 0 \\ 0 & 0 & +1 \end{bmatrix}$$

This same group has two other faithful matrix representations in $\mathbb{R}^3$ that we identify with the inversion group $\mathcal{P}$ and the reflection group σ_Z.

The point to be made is that the matrix representations of a group are not exactly the same thing as the group itself. For our purposes, the group $\mathcal{G}$ acts on dynamical systems in three different ways through three matrix representations. These three types of matrix representations are inequivalent except in some of the simplest cases.

13.2.3.1 Defining Matrix Representation The action of the group $\mathcal{G}$ in $\mathbb{R}^N$ is defined through its effect on the coordinates of a point in $\mathbb{R}^N$. This group action is specified by the defining matrix representation

$$gX_i = X_j \Gamma^{\mathrm{Def}}_{ji}(g) \qquad g \in \mathcal{G} \tag{13.7}$$

Defining matrix representations of the two-element group $\{\mathbb{I}, \gamma\}$ are given in (10.21), of the three-element group $\{\mathbb{I}, \gamma, \gamma^2\}$ in (10.18), and the two four-element groups $\{\mathbb{I}, \gamma, \gamma^2, \gamma^3\}$ and $\{\mathbb{I}, \gamma_1, \gamma_2, \gamma_1\gamma_2\}$ in (10.24).

13.2.3.2 Irreducible Representations Invariant polynomials play a fundamental role in mapping an equivariant dynamical system to an image dynamical system without any residual symmetry. Invariant polynomials, and functions of them, are acted on ("carry" or "support") the identity representation of a group

$$\begin{aligned} g f_{\mathrm{inv}}(p_1, p_2, \ldots, p_k) &= f_{\mathrm{inv}}(p_1, p_2, \ldots, p_k)\Gamma^{\mathrm{Id}}(g) \\ \Gamma^{\mathrm{Id}}(g) &= [1] \end{aligned}$$

Polynomials that are not invariant—the so-called covariant polynomials—carry the other irreducible representations of $\mathcal{G}$. These representations depend on $\mathcal{G}$ alone, not on the action of $\mathcal{G}$ in $\mathbb{R}^N$. They are well known for all finite groups and have been available for more than one hundred years. The ring basis functions $R^{\alpha}_{i,\mu}(X)$ can be grouped into sets that carry the different irreducible representations of $\mathcal{G}$:

$$gR^{(\alpha)}_{i,\mu}(X) = R^{(\alpha)}_{j,\mu}\Gamma^{(\alpha)}_{ji}(g) \tag{13.8}$$

Example: To illustrate this idea, we discuss the group $\mathcal{C}_n$. This group is commutative, and therefore has one dimensional irreducible representations over the complex numbers. They are

$$\gamma^j \to \Gamma^{(k)}(\gamma^j) = e^{2\pi i j k/n} \tag{13.9}$$

The single generator γ satisfies $\gamma^n = \mathbb{I}$ and describes rotations through $2\pi/n$ radians. The distinct irreducible representations are labeled by the integer k, $k = 0$ (identity representation), 1,2,...,$n-1$, with the relations

$$\begin{aligned} \Gamma^{(k+n)}(g) &= \Gamma^{k}(g) \\ \Gamma^{(n-k)}(g) &= \Gamma^{k}(g)^* \end{aligned} \tag{13.10}$$

If n is even, $\Gamma^{(n/2)}(g)$ is real. All other representations are complex. Since they act on real functions, we would like to construct real representations from these complex one dimensional representations:

$$\Gamma^{(k)}(\theta) + \Gamma^{(n-k)}(\theta) \simeq \begin{bmatrix} \cos k\theta & \sin k\theta \\ -\sin k\theta & \cos k\theta \end{bmatrix} \qquad \theta = \frac{2\pi j}{n} \neq \pi \tag{13.11}$$

These are irreducible over the reals unless $k = 0$ or $n/2$, n even.

Each real 2×2 representation (13.11) with $0 < k < n/2$ has two pairs of basis vectors among the ring basis functions. These are:

	Ring Functions	
Basis Vector	$\mu = 1$	$\mu = 2$
$i = 1$	$R_{1,1} = \mathtt{Re}(X + iY)^k$	$R_{1,2} = \mathtt{Re}(X - iY)^{n-k}$
$i = 2$	$R_{2,1} = \mathtt{Im}(X + iY)^k$	$R_{2,2} = \mathtt{Im}(X - iY)^{n-k}$

13.2.3.3 Regular Representation Every group has a regular representation. It is defined by the action of the group on itself

$$\begin{array}{rcl} g g_\alpha & = & g_\beta \Gamma^{(\mathrm{Reg})}_{\beta\alpha}(g) \\ \Gamma^{(\mathrm{Reg})}_{\beta\alpha}(g) & = & \begin{array}{ccc} 1 & \text{if} & g_\beta = g g_\alpha \\ 0 & \text{if} & g_\beta \neq g g_\alpha \end{array} \end{array} \tag{13.12}$$

The regular representation is a mapping of each group operation into a permutation matrix P. This is a matrix with exactly one element +1 in each row and each column; all other matrix elements are zero.

Example: The Regular representation for $\mathcal{C}_n$ is determined from $\gamma^j \gamma^i = \gamma^{k=j+i} = \gamma^k \Gamma^{\mathrm{Reg}}_{ki}(\gamma^j)$, so that $\Gamma^{\mathrm{Reg}}_{ki}(\gamma^j) = 0$ unless $k = j+i \bmod n$. For $\mathcal{C}_3$, this representation is

$$\begin{array}{ccc} \mathbb{I} & \gamma & \gamma^2 \\ \left[\begin{array}{ccc} 1 & 0 & 0 \\ 0 & 1 & 0 \\ 0 & 0 & 1 \end{array}\right] & \left[\begin{array}{ccc} 0 & 0 & 1 \\ 1 & 0 & 0 \\ 0 & 1 & 0 \end{array}\right] & \left[\begin{array}{ccc} 0 & 1 & 0 \\ 0 & 0 & 1 \\ 1 & 0 & 0 \end{array}\right] \end{array} \tag{13.13}$$

It consists of 3×3 matrices because $|\mathcal{C}_3| = 3$, not because this group (may) act in $\mathbb{R}^3$.

The regular representation plays an important role in the study of equivariant dynamical systems because it describes how the group operations $g_\alpha \in \mathcal{G}$ permute the domains into which the phase space $\mathbb{R}^N$ is decomposed:

$$\begin{array}{rcl} g \mathbb{D}_{g_\alpha} & = & g g_\alpha \mathbb{D}_{\mathbb{I}} = \mathbb{D}_{g g_\alpha} = \mathbb{D}_{g_\beta} \Gamma^{\mathrm{Reg}}_{\beta\alpha}(g) \\ \Gamma^{(\mathrm{Reg})}_{\beta\alpha}(g) & = & \begin{array}{ccc} 1 & \text{if} & g_\beta = g g_\alpha \\ 0 & \text{if} & g_\beta \neq g g_\alpha \end{array} \end{array} \tag{13.14}$$

Here $\mathbb{D}_{\mathbb{I}}$ is the fundamental domain $\mathbb{R}^N(X)/\mathcal{G}$.

13.2.4 Local Diffeomorphism

Image dynamical systems are lifted to covering dynamical systems using local diffeomorphisms. These are mappings relating equivariant coordinates $(X_1, X_2, \ldots, X_N)$ with invariant coordinates $(u_1, u_2, \ldots, u_N)$. If the Jacobian $\frac{\partial u_i}{\partial X_j}$ of this transformation is non singular everywhere, the dynamical systems based on the coordinates $\boldsymbol{u}$ and $\boldsymbol{X}$ are equivalent. Interesting things can only happen when the Jacobian vanishes somewhere in $\mathbb{R}^N(\boldsymbol{X})$. In fact, there are two singular sets:

1. $SS(\mathcal{G})$
2. $SS\left(\dfrac{\partial \boldsymbol{u}}{\partial \boldsymbol{X}}\right)$

The first is the singular set of $\mathcal{G}$. This is the union of the set of points in $\mathbb{R}^N(\boldsymbol{X})$ that are invariant under at least one group operation $g \in \mathcal{G}$, $g \neq \mathbb{I}$. The second is the set of points in $\mathbb{R}^N(\boldsymbol{X})$ on which $\det\left[\dfrac{\partial u_i}{\partial X_j}\right] = 0$. These two singular sets satisfy the inclusion

$$SS(\mathcal{G}) \subseteq SS\left(\frac{\partial \boldsymbol{u}}{\partial \boldsymbol{X}}\right) \tag{13.15}$$

A coordinate transformation $\boldsymbol{X} \to \boldsymbol{u}$ that saturates this inclusion is optimal.

13.3 COVERING ATTRACTORS

When the image flow satisfies (13.1), the covering flow satisfies

$$\frac{dX_j}{dt} = \frac{\partial X_j}{\partial u_i}\frac{du_i}{dt} = \left[\frac{\partial \boldsymbol{X}}{\partial \boldsymbol{u}}\right]^{-1}_{ji} g_i(\boldsymbol{u}(\boldsymbol{X}); \boldsymbol{c}) = F_j(\boldsymbol{X}; \boldsymbol{c}) \tag{13.16}$$

These relations have been discussed many times throughout this work.

The covering flow $\dot{X}_j = F_j(\boldsymbol{X}; \boldsymbol{c})$ is a dynamical system, so should be studied along the lines recommended for the dynamical system $\dot{u}_i = g_i(\boldsymbol{u}; \boldsymbol{c})$. Not surprisingly, the properties of the covering and image dynamical systems are closely related.

13.3.1 Phase Space

The phase space is $\mathbb{R}^N(\boldsymbol{X})$. The fundamental domain $\mathbb{D}_{\mathbb{I}} = \mathbb{R}^N(\boldsymbol{X})/\mathcal{G}$ has a one-to-one correspondence with $\mathbb{R}^N(\boldsymbol{u})$. The other domains are obtained by mapping $\mathbb{D}_{\mathbb{I}}$ under $\mathcal{G}$: $\mathbb{D}_g = g\mathbb{D}_{\mathbb{I}}$.

13.3.2 Control Parameter Space

The control parameter spaces $\mathbb{R}^K(\boldsymbol{c})$ for $g(\boldsymbol{u}; \boldsymbol{c})$ and $F(\boldsymbol{X}; \boldsymbol{c})$ are identical. However, there is the extra freedom of choice for the action of $\mathcal{G}$ on $\mathbb{R}^N(\boldsymbol{X})$. To be more specific, by choosing different displacement coordinates for the axis around which $\mathcal{R}_Z(\pi)$ acted to lift the Rössler system to its $\mathcal{R}_Z(\pi)$ equivariant double covers in Chapter 5, we are able to create several structurally stable double covers and a continuum of structurally unstable double covers. Thus, the choice of how $\Gamma^{\mathrm{Def}}(\mathcal{G})$ acts in $\mathbb{R}^N(\boldsymbol{X})$ can be considered as an additional set of control parameters for the cover, over and above the controls $\boldsymbol{c} \in \mathbb{R}^K$.

13.3.3 Lipschitz Conditions

Even if $g(\boldsymbol{u};\boldsymbol{c})$ obeys a Lipschitz condition, $F(\boldsymbol{X};\boldsymbol{c})$ may not because of the presence of $\left(\frac{\partial \boldsymbol{u}}{\partial \boldsymbol{X}}\right)$ in (13.16) and the existence of a singular set $SS\left(\frac{\partial \boldsymbol{u}}{\partial \boldsymbol{X}}\right)$ in $\mathbb{R}^N(\boldsymbol{X})$. The lack of the Lipschitz condition for the forcing terms presents an opportunity. Existence and uniqueness of (global) solutions is not guaranteed by this no-longer-applicable theorem. Yet they remain true (!) since the theorem is true for the image and lifts of these trajectories into the covers are well defined, unique, and infinitely extendable as long as they avoid $SS\left(\frac{\partial \boldsymbol{u}}{\partial \boldsymbol{X}}\right)$ in $\mathbb{R}^N(\boldsymbol{X})$. This provides an opportunity to sharpen the existence and uniqueness theorem in the future.

13.3.4 Fixed Points

Every fixed point in $\mathbb{R}^N(\boldsymbol{u})$ has $|\mathcal{G}|$ preimage fixed points in $\mathbb{R}^N(\boldsymbol{X})$. In the generic case these $|\mathcal{G}|$ fixed points are all distinct: one occurs in the fundamental domain $\mathbb{D}_{\mathbb{I}} = \mathbb{R}^N(\boldsymbol{X})/\mathcal{G}$, and an image occurs in each of the other domains $\mathbb{D}_g$. In the nongeneric case a fixed point may occur on $SS(\mathcal{G})$, as for example the origin $(X, Y, Z) = (0, 0, 0)$ for the Lorenz system. In such a case a subgroup $\mathcal{H} \subseteq \mathcal{G}$ leaves this point fixed. This fixed point is $|\mathcal{H}|$-fold degenerate. There are $|\mathcal{G}/\mathcal{H}| = |\mathcal{G}|/|\mathcal{H}|$ such fixed points. They may be labeled by the coset representatives of $\mathcal{G}/\mathcal{H}$ when $\mathcal{H} \neq \mathcal{G}$.

In the generic case when $|\mathcal{G}|$ distinct fixed points in $\mathbb{R}^N(\boldsymbol{X})$ cover a fixed point in $\mathbb{R}^N(\boldsymbol{u})$,

1. All fixed points—$|\mathcal{G}|$ in $\mathbb{R}^N(\boldsymbol{X})$ and their image in $\mathbb{R}^N(\boldsymbol{u})$—have the same eigenvalue spectrum.
2. The eigenvectors at the fixed point in $\mathbb{R}^N(\boldsymbol{u})$ are related to the eigenvectors at each of the $|\mathcal{G}|$ fixed points in $\mathbb{R}^N(\boldsymbol{X})$ by the Jacobian matrix.

To show this, we compute the Jacobian $\frac{\partial F_i}{\partial X_j}$ at any of the points p in $\mathbb{R}^N(\boldsymbol{X})$ that cover q in $\mathbb{R}^N(\boldsymbol{u})$

$$\begin{aligned} \frac{\partial F_i}{\partial X_j} &= \frac{\partial}{\partial X_j}\left(\frac{\partial X_i}{\partial u_r}\, g_r\right) = \left.\frac{\partial X_i}{\partial u_r}\right|_p \left.\frac{\partial g_r}{\partial X_j}\right|_p \\ &= \left.\frac{\partial X_i}{\partial u_r}\right|_p \left.\frac{\partial g_r}{\partial u_s}\right|_q \left.\frac{\partial u_s}{\partial X_j}\right|_p \end{aligned} \tag{13.17}$$

All $|\mathcal{G}|$ Jacobians $\left(\frac{\partial F_i}{\partial X_j}\right)\Big|_p$ are related by similarity transformations to the single Jacobian $\left(\frac{\partial g_r}{\partial u_s}\right)\Big|_q$. They all have identical eigenvalue spectra. Their eigenvectors are all related to the eigenvectors of $\left(\frac{\partial g_r}{\partial u_s}\right)\Big|_q$ by the linear transformation $\left(\frac{\partial u_s}{\partial X_j}\right)\Big|_p$.

This argument can be extended to degenerate fixed points with care. The problem is that $\left(\frac{\partial X_i}{\partial u_r}\right)\Big|_p$ becomes singular at a degenerate fixed point, although $\left(\frac{\partial X_i}{\partial u_r}\right)\Big|_p \left(\frac{\partial u_r}{\partial X_s}\right)\Big|_p$

$= \delta_{ij}$ is well defined. This in fact provides constraints on the matrix $\left(\frac{\partial g_r}{\partial u_s}\right)\Big|_q$ at the image of a degenerate fixed point.

More precise statements can be made about the Jacobian $\left(\frac{\partial F_i}{\partial X_j}\right)\Big|_p$ at a degenerate fixed point p:

$$\Gamma_{ij}^{\mathrm{Def}}(g)\left(\frac{\partial F_j}{\partial X_k}\right)_p = \left(\frac{\partial F_i}{\partial X_j}\right)_p \Gamma_{jk}^{\mathrm{Def}}(g) \tag{13.18}$$

where $gp = p$. This intertwining relation forces constraints on the structure of the Jacobian at a degenerate fixed point. These are described in more detail in Section 14.1.

13.3.5 Lyapunov Exponents and Fractal Dimensions

The spectrum of local Lyapunov exponents $\lambda_1, \lambda_2, \ldots, \lambda_N$ at any generic point in $\mathbb{R}^N(\boldsymbol{X})$ is identical to the spectrum of these local exponents at the image point in $\mathbb{R}^N(\boldsymbol{u})$.

The spectrum of fractal dimensions at a point is a local function of the local Lyapunov exponents at that point. The spectrum of Lyapunov exponents for closed periodic orbits is a nonlocal function of the local Lyapunov exponents along that orbit. Essentially, the Lyapunov exponents along a periodic orbit are the integrated local Lyapunov exponents along the orbit.

These observations lead to the following conclusions:

1. "The" fractal dimension (any of them) of a covering attractor at a point $p \in \mathbb{R}^N(\boldsymbol{X})$ is the same as the fractal dimension of the image attractor at the image point $q \in \mathbb{R}^N(\boldsymbol{u})$. This result holds for all points p that cover q.
2. The spectrum of Lyapunov exponents of a covering orbit is equal to the spectrum of Lyapunov exponents of its image.

13.3.6 Symbolic Dynamics

The fundamental domain $\mathbb{R}^N(\boldsymbol{X})/\mathcal{G}$ is homeomorphic with $\mathbb{R}^N(\boldsymbol{u})$, except possibly for measure zero sets on the boundary of $\mathbb{R}^N(\boldsymbol{X})/\mathcal{G}$. The two have homeomorphic decompositions (partitions) into regions labeled by symbols $\sigma_1, \sigma_2, \ldots, \sigma_s$ in $\mathbb{R}^N(\boldsymbol{u})$. In the fundamental domain these s symbols receive also a domain label:

$$\sigma_i \subset \mathbb{R}^N(\boldsymbol{u}) \rightarrow \sigma_{i\mathbb{I}} \subset \mathbb{R}^N(\boldsymbol{X})/\mathcal{G} \tag{13.19}$$

In other domains they receive the appropriate domain label: σ_{ig}, $g \in \mathcal{G}$. As a result, if s symbols are required to partition the phase space $\mathbb{R}^N(\boldsymbol{u})$, $s \times |\mathcal{G}|$ symbols suffice to partition the covering space. These partitions satisfy

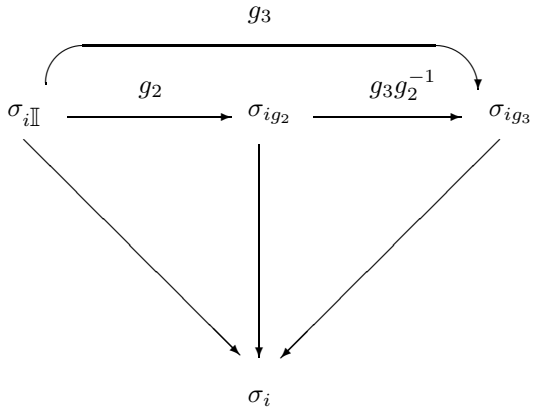

That is, each $\sigma_{ig} \subset \mathbb{D}_g \subset \mathbb{R}^N(\boldsymbol{X})$ maps to the same $\sigma_i \subset \mathbb{R}^N(\boldsymbol{u})$. In addition, the partitions are permuted among themselves by $\mathcal{G}$ exactly as the domains are

$$g\sigma_{ig_\alpha} = \sigma_{ig_\beta}\Gamma^{\mathrm{Reg}}_{\beta\alpha}(g) \tag{13.20}$$

This result is sufficiently important that we emphasize it again: In the symbolic dynamics for the equivariant dynamical system, each symbol σ_{ig} carries two pieces of information:

1. A symbol (i) from the image dynamical system.
2. An operation (g) from the equivariance group $\mathcal{G}$.

13.3.7 Transition Matrices

The image dynamical system has a symbolic dynamics with s symbols and every one of its covers has a symbolic dynamics with $s|\mathcal{G}|$ symbols. Dynamics in the image is encoded by an $s \times s$ transition matrix T_{ij}, $1 \le i, j \le s$. Dynamics in any cover must be encoded by an $s|\mathcal{G}| \times s|\mathcal{G}|$ transition matrix

$$T_{ig_\alpha, jg_\beta} \qquad 1 \le i, j \le s, \;\; 1 \le \alpha, \beta \le |\mathcal{G}|$$

There are two constraints on the transition matrix for any cover

$$\begin{aligned} T_{ig_\alpha, jg_\beta} \quad &\overset{\text{maps to}}{\longrightarrow} \quad T_{ij} \\ T_{ig_\alpha, jg_\beta} \quad &= gT_{ig_\alpha, jg_\beta} = \quad T_{i(gg_\alpha), j(gg_\beta)} \end{aligned} \tag{13.21}$$

The first condition is an expression of the cover-image relation. The second condition expresses the equivalence of the $|\mathcal{G}|$ domains of $\mathbb{R}^N(\boldsymbol{X})$ under the group action.

The second condition can be exploited by setting $g_\alpha = \mathbb{I}$. The first index on the transition matrix then becomes $(i, \mathbb{I})$. That is, it represents the subset in the fundamental domain $\mathbb{D}_{\mathbb{I}}$ that maps to the domain (partition) $\sigma_i \subset \mathbb{R}^N(\boldsymbol{u})$. If $T_{ij} = 1$ (in $\mathbb{R}^N(\boldsymbol{u})$), this subset has an allowed transition to the subset j in *one* of the domains $\mathbb{D}_{g_\beta}$ in the structurally stable case. Thus

$$\begin{aligned} T_{i\mathbb{I}, jg_\beta} &= 1 \\ T_{i\mathbb{I}, jg_\gamma} &= 0 \qquad \gamma \ne \beta \end{aligned} \tag{13.22}$$

By using the transitivity of the group action

$$\begin{array}{rcccl} gT_{i\mathbb{I},jg_\beta} & = & T_{ig,j(gg_\beta)} & = & 1 \\ gT_{i\mathbb{I},jg_\gamma} & = & T_{ig,j(gg_\gamma)} & = & 0 \qquad \gamma \neq \beta \end{array} \tag{13.23}$$

In short, if we know the destination under the flow of each of the s partitions in the fundamental domain $\mathbb{D}_\mathbb{I} = \mathbb{R}^N(\boldsymbol{X})/\mathcal{G}$, we have this information for the s partitions in each of the other domains.

A simple example will clarify this discussion.

Example: An image dynamical system is appropriately encoded by two symbols σ_0 and σ_1. The allowed symbol sequences are described by the 2×2 transition matrix

$$T = \begin{bmatrix} 0 & 1 \\ 1 & 1 \end{bmatrix} \tag{13.24}$$

with $T_{00} = 0$. This dynamical system is lifted to a cover with $\mathcal{C}_3$ symmetry. Symbolic dynamics in any cover involves six symbols $\sigma_{(i,\alpha)}$, $i = 0, 1$, $\alpha = 0, 1, 2$. The 6×6 transition matrix can be expressed as follows

$$T = \begin{array}{cc|cccccc} & & \multicolumn{2}{c}{\mathbb{I}} & \multicolumn{2}{c}{\gamma} & \multicolumn{2}{c}{\gamma^2} \\ & & 0 & 1 & 0 & 1 & 0 & 1 \\ \hline \mathbb{I} & 0 & & & & & & \\ & 1 & & & & & & \\ \hline \gamma & 0 & & & & & & \\ & 1 & & & & & & \\ \hline \gamma^2 & 0 & & & & & & \\ & 1 & & & & & & \end{array} \tag{13.25}$$

We assume in the cover chosen that the partition 0 in the fundamental domain $\mathbb{D}_\mathbb{I}$ maps to the partition 1 in this same domain, but that the partition 1 in $\mathbb{D}_\mathbb{I}$ maps into the domain $\mathbb{D}_\gamma$, where it covers both partitions 0 and 1. This provides the information for the top two rows of T.

$$T = \begin{array}{cc|cccccc} & & \multicolumn{2}{c}{\mathbb{I}} & \multicolumn{2}{c}{\gamma} & \multicolumn{2}{c}{\gamma^2} \\ & & 0 & 1 & 0 & 1 & 0 & 1 \\ \hline \mathbb{I} & 0 & & 1 & & & & \\ & 1 & & & 1 & 1 & & \\ \hline \gamma & 0 & & & & 1 & & \\ & 1 & & & & & 1 & 1 \\ \hline \gamma^2 & 0 & & & & & & 1 \\ & 1 & 1 & 1 & & & & \end{array} \tag{13.26}$$

The top two rows can be mapped to the next two rows by the transitivity of the group action under γ (second constraint, Eq. (13.21)). The last two rows are obtained by acting again with γ.

This matrix can be expressed in a more natural form by permuting the rows and columns

$$T = \begin{array}{cc} & \\ 0 & \\ & \\ 1 & \\ & \end{array} \begin{array}{c} \mathbb{I} \\ \gamma \\ \gamma^2 \\ \mathbb{I} \\ \gamma \\ \gamma^2 \end{array} \left[\begin{array}{ccc|ccc} & 0 & & & 1 & \\ \mathbb{I} & \gamma & \gamma^2 & \mathbb{I} & \gamma & \gamma^2 \\ \hline 0 & 0 & 0 & 1 & 0 & 0 \\ 0 & 0 & 0 & 0 & 1 & 0 \\ 0 & 0 & 0 & 0 & 0 & 1 \\ \hline 0 & 1 & 0 & 0 & 1 & 0 \\ 0 & 0 & 1 & 0 & 0 & 1 \\ 1 & 0 & 0 & 1 & 0 & 0 \end{array}\right]$$

$$= \left[\begin{array}{c|c} T_{00}\Gamma^{\mathrm{Reg}}(g_0^{-1}) & T_{01}\Gamma^{\mathrm{Reg}}(g_0^{-1}) \\ \hline T_{10}\Gamma^{\mathrm{Reg}}(g_1^{-1}) & T_{11}\Gamma^{\mathrm{Reg}}(g_1^{-1}) \end{array}\right] \tag{13.27}$$

In this expression $g_0 = \mathbb{I}$ expresses the condition that the partition 0 in the fundamental domain is mapped back into the fundamental domain; $g_1 = \gamma$ expresses the condition that the partition 1 in the fundamental domain is mapped into domain $\mathbb{D}_\gamma$. The matrices Γ^{Reg} for $\mathcal{C}_3$ are given in (13.13).

This representation of the transition matrix has two strengths:

1. It emphasizes the dynamics in the image system through the matrix elements T_{ij} of the transition matrix.
2. It makes apparent where each of the partitions (0 or 1) in the fundamental domain are mapped to the cover that is chosen.

Example: Transition matrices for the covers of the Rössler system with topological indices (0,1) and (1,1) can be rewritten as

$$(0,1)$$

$$\begin{array}{cc|cccc} & & \mathbb{I} & \mathbb{I} & R_Z & R_Z \\ & & 0 & 1 & 0 & 1 \\ \hline \mathbb{I} & 0 & 1 & 1 & 0 & 0 \\ \mathbb{I} & 1 & 0 & 0 & 1 & 1 \\ R_Z & 0 & 0 & 0 & 1 & 1 \\ R_Z & 1 & 1 & 1 & 0 & 0 \end{array}$$

$$\updownarrow$$

$$\begin{array}{c|cc} & 0 & 1 \\ \hline 0 & \Gamma^{\mathrm{Reg}}(\mathbb{I}^{-1}) & \Gamma^{\mathrm{Reg}}(\mathbb{I}^{-1}) \\ 1 & \Gamma^{\mathrm{Reg}}(R_Z^{-1}) & \Gamma^{\mathrm{Reg}}(R_Z^{-1}) \end{array}$$

$$(1,1)$$

$$\begin{array}{cc|cccc} & & \mathbb{I} & \mathbb{I} & R_Z & R_Z \\ & & 0 & 1 & 0 & 1 \\ \hline \mathbb{I} & 0 & 0 & 0 & 1 & 1 \\ \mathbb{I} & 1 & 0 & 0 & 1 & 1 \\ R_Z & 0 & 1 & 1 & 0 & 0 \\ R_Z & 1 & 1 & 1 & 0 & 0 \end{array}$$

$$\updownarrow$$

$$\begin{array}{c|cc} & 0 & 1 \\ \hline 0 & \Gamma^{\mathrm{Reg}}(R_Z^{-1}) & \Gamma^{\mathrm{Reg}}(R_Z^{-1}) \\ 1 & \Gamma^{\mathrm{Reg}}(R_Z^{-1}) & \Gamma^{\mathrm{Reg}}(R_Z^{-1}) \end{array} \tag{13.28}$$

In these expressions $\Gamma^{\mathrm{Reg}}(\mathbb{I}) = \begin{bmatrix} 1 & 0 \\ 0 & 1 \end{bmatrix}$ and $\Gamma^{\mathrm{Reg}}(R_Z^{-1}) = \begin{bmatrix} 0 & 1 \\ 1 & 0 \end{bmatrix}$.

13.3.8 Topological Entropy

Every covering attractor has the same topological entropy as the image attractor from which it is lifted.

The topological entropy is the logarithm of the largest eigenvalue of the transition matrix. Assume the $s \times s$ transition matrix T for the image system has eigenvector $\boldsymbol{a} = (a_1, a_2, \ldots, a_s)^t$ with largest eigenvalue λ_1, so that

$$T\,\boldsymbol{a} = \lambda_1 \boldsymbol{a} \tag{13.29a}$$

Every $n \times n$ permutation matrix P has maximal eigenvalue +1 with corresponding eigenvector $\boldsymbol{1} = (1, 1, \ldots, 1)^t$:

$$P\,\boldsymbol{1} = 1\boldsymbol{1} \tag{13.29b}$$

The transition matrix for any cover has the form of an outer product

$$T_{i\alpha,j\beta} = T_{ij} P_{\alpha\beta}(i,j) \tag{13.30}$$

where $P_{\alpha\beta}(i,j)$ is a permutation matrix. It is an easy matter to check that the $s|\mathcal{G}| \times 1$ column vector $\boldsymbol{a} \times \boldsymbol{1} = (a_1\boldsymbol{1}^t, a_2\boldsymbol{1}^t, \ldots, a_s\boldsymbol{1}^t)^t$ is an eigenvector of this matrix with eigenvalue λ_1, independent of $P(i,j)$. This is the largest eigenvalue of the transition matrix (13.30). Since every cover has a transition matrix of this form, we conclude that the image and all its covers have the same topological entropy. This conclusion is independent of equivariance group $\mathcal{G}$ and index of the cover.

13.4 INDEX

The examples presented in Section 13.3.7 extend to covers of any image dynamical system with an arbitrary equivariance group $\mathcal{G}$. The dynamics in the image system are governed by s symbols $\sigma_1, \sigma_2, \ldots, \sigma_s$ and determined by an $s \times s$ transition matrix T_{ij}. Symbolic dynamics in the cover is determined by $s|\mathcal{G}|$ symbols. Each symbol carries two labels

$$\underset{\text{Dynamics in the image}}{\sigma_i} \qquad \underset{\text{Symmetry of the cover}}{g_\alpha} \qquad 1 \le i \le s, \quad 1 \le \alpha \le |\mathcal{G}|$$

A structurally stable cover is determined by the image of the partition i in the fundamental domain $\mathbb{D}_i$ under the flow:

$$i \to \mathbb{D}_{g(i)} \tag{13.31}$$

Once the assignments (13.31) have been made, the $s|\mathcal{G}| \times s|\mathcal{G}|$ transition matrix for the covering dynamical system is uniquely determined. It is

$$T_{i\alpha,j\beta} = T_{ij} \Gamma^{\mathrm{Reg}}_{\alpha\beta}\left(g(i)^{-1}\right) \tag{13.32}$$

Definition: The Index for a cover equivariant under $\mathcal{G}$ is an assignment of a group operation to each symbol in the image, that is $\sigma_i \to g(i)$:

$$\sigma_1 \to g(1), \sigma_2 \to g(2), \ldots, \sigma_s \to g(s)$$

Important Remark: The permutation matrix $P(i,j)_{\alpha\beta}$ in the expression (13.30) for the transition matrix for any cover depends only on the first index i. It depends on the group $\mathcal{G}$ through the index component $g(i)$:

$$P(i,j)_{\alpha\beta} = \Gamma^{\rm Reg}_{\alpha\beta}\left[g(i)^{-1}\right]$$

Important Remark: Each symbol can be assigned one of $|\mathcal{G}|$ group operations. There are s symbols. Therefore there are $|\mathcal{G}|^s$ symbol assignments. Each index describes a different cover of the image.

Example: In the image the symbol sequence $\ldots\sigma_i\sigma_j\sigma_k\ldots$ can occur if $T_{ij}T_{jk} \neq 0$. In the cover σ_i lifts to $\sigma_{i,\alpha}$, and likewise for σ_j and σ_k.

$$\sigma_i\sigma_j\sigma_k \xrightarrow{\text{lift}} \sigma_{i,\alpha}\sigma_{j,\beta}\sigma_{k,\gamma}$$

Such a path exists if the product of the transition matrix elements is nonzero

$$\begin{aligned} T_{i\alpha,j\beta}T_{j\beta,k\gamma} &= T_{ij}\Gamma^{\rm Reg}_{\alpha\beta}\left(g(i)^{-1}\right)T_{jk}\Gamma^{\rm Reg}_{\beta\gamma}\left(g(j)^{-1}\right) \\ &= T_{ij}T_{jk}\Gamma^{\rm Reg}_{\alpha\beta}\left(g(i)^{-1}\right)\Gamma^{\rm Reg}_{\beta\gamma}\left(g(j)^{-1}\right) \end{aligned}$$

There is only one path from domain α to domain β, and one from β to γ. To see if there is a path $\alpha \to \gamma$ we sum overall possible intermediate domains to find

$$\sum_\beta T_{i\alpha,j\beta}T_{j\beta,k\gamma} = T_{ij}T_{jk}\Gamma^{\rm Reg}_{\alpha\gamma}\left([g(j)g(i)]^{-1}\right) \tag{13.33}$$

If $T_{ij}T_{jk} \neq 0$ there is a path from $i\alpha$ to $k\gamma$ that covers $\ldots\sigma_i\sigma_j\sigma_k\ldots$ provided that $\Gamma^{\rm Reg}_{\alpha\gamma}\left([g(j)g(i)]^{-1}\right) = 1$.

Remark: It may be disturbing to see that the effect of the symmetry operators appear in the transition matrix through the matrix

$$\Gamma^{\rm Reg}\left(g^{-1}\right) = \Gamma^{\rm Reg}\left(g\right)^t$$

The origin of this slightly uncomfortable feature arises in the different conventions used in Dynamical Systems theory and in Group theory.

In the former a symbol sequence

$$\underset{\ldots\ \sigma_i\ \sigma_j\ \sigma_k\ldots}{\longrightarrow\ t \text{ increasing}}$$

advances (in time) from left to right. In group theory the most popular convention has the sequence of group operations

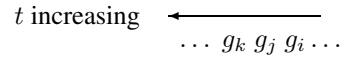

operating from right (first) to left (last). This difference of conventions requires the use of matrix transposes, or equivalently, inverse group operations, in the construction of cover transition matrices.

13.5 SPECTRUM OF COVERS

If the image attractor $\underline{\mathcal{SA}}$ requires s symbols and the equivariance group is $\mathcal{G}$:

1. Every cover requires $s|\mathcal{G}|$ symbols.
2. There are $|\mathcal{G}|^s$ indices, each describing a different cover.

13.5.1 Topological Selection Rules

In the absence of topological "selection rules" there are no index restrictions. However, index assignments are sometimes forbidden by topological considerations. A clear-cut case occurs for $\mathcal{G} = \sigma_Z$ in $\mathbb{R}^3$. In this case the invariant set is the X-Y plane $Z = 0$ and every equivariant cover is disconnected. The only allowed index for the σ_Z-invariant lift of the Smale horseshoe in this case is $(0, 1) \to (I, I)$.

For $\mathcal{R}_Z$ and $\mathcal{P}$ acting in $\mathbb{R}^3$ the singular set has dimension 1 and 0, respectively. Neither provides an obstruction to the flow. Image systems requiring 2, 3, 4, ... symbols for coding have 2^2, 2^3, 2^4, ... distinct indices, and therefore there are as many inequivalent covers with $\mathcal{R}_Z$ or $\mathcal{P}$ symmetry.

13.5.2 Connectedness

Equivariant attractors with different indices are different. However, they fall into broad equivalence classes. One primary discriminant among equivariant covers is their connectivity properties. Connectivity of an attractor can be defined in several different ways. A symmetric attractor is connected if:

1. The attractor's branched manifold is connected (useful for low-dimensional attactors with $d_L < 3$).
2. The closure of the attractor is connected.
3. The attractor's attracting manifold is connected.
4. Some trajectory requires all $s|\mathcal{G}|$ symbols.

Connectivity properties of covering attractors are most easily determined from the last condition. Assume that the index is $g(1), g(2), \cdots, g(s)$. An initial condition in $D_{\mathbb{I}}$ can reach any of the domains $D_{g(i)}$, and from there it can propagate to any of the domains $g(j)D_{g(i)} = G_{g(j)g(i)}$, etc. The group operations in the index $(g(1), g(2), \cdots, g(s))$ generate a subgroup $\mathcal{H} \subseteq \mathcal{G}$ when all possible products are taken in all possible orders. The cover consists of $|\mathcal{G}|/|\mathcal{H}| = |\mathcal{G}/\mathcal{H}|$ disconnected

components. Each component is labeled by a coset representative ω_i in the coset $\mathcal{G}/\mathcal{H}$. Any trajectory $\ldots\sigma_{i\alpha}\sigma_{j\beta}\sigma_{k\gamma}\ldots$ in the identity component of the disconnected cover has an image in the component labeled by the coset representative ω. The image is

$$\ldots\sigma_{i\alpha}\sigma_{j\beta}\sigma_{k\gamma}\cdots \xrightarrow{\text{map by } \omega} \ldots\sigma_{i(\omega g_\alpha)}\sigma_{j(\omega g_\beta)}\sigma_{k(\omega g_\gamma)}\cdots \tag{13.34}$$

If $\mathcal{G} = \mathcal{H}$ the cover consists of one component and it is connected.

13.5.3 Structurally Stable Covers

We have seen in several examples (cf. Chapter 5) that equivariant covers can be structurally stable or structurally unstable. The difference depends on the relation between the partition decomposition and the boundaries of the domain $\mathbb{D}_g$. If the partitions (e.g., branch lines) do not intersect domain boundaries, the cover is structurally stable. If the intersection is nonempty, the cover is structurally unstable. Structurally unstable covers occur naturally in parameterized families of covers. We have seen this in our discussion of peeling bifurcations (Chapter 5), where the location of the $R_Z(\pi)$ rotation axis was parameterized by a "lift control parameter" μ.

In Fig. 13.3 we show arrangement of four branches of covers of the Smale horseshoe branched manifold that are equivariant under $\mathcal{C}_4$ (Fig. 13.3(a)) and $\mathcal{V}_4$ (Fig. 13.3(b)). In both cases the four branches are contained entirely within the domains $\mathbb{D}_g$ that partition $\mathbb{R}^N(\boldsymbol{X})$. The covers, whatever the index, are structurally stable.

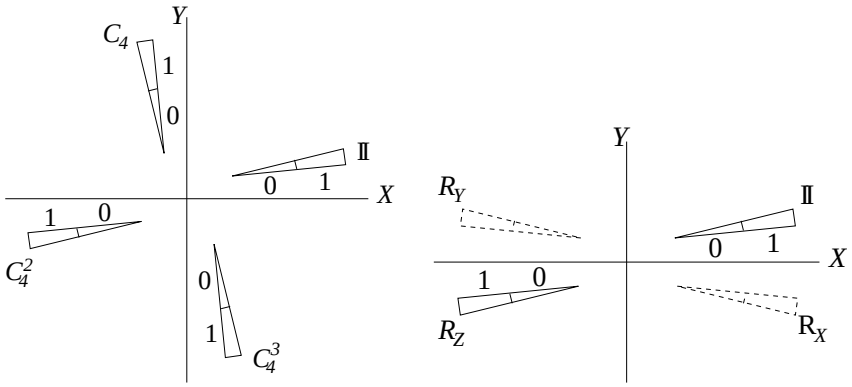

(a) $\mathcal{C}_4$ (b) $\mathcal{V}_4$

Fig. 13.3 Possible arrangement of the branch lines in two different four-fold covers of the Smale horseshoe branched manifold. (a) $\mathcal{C}_4$, (b) $\mathcal{V}_4$. In (b), dashed lines indicate branch line is below the $Z = 0$ plane. The width increases with distance from this plane.

13.5.4 $\mathcal{C}_4$-Equivariant Covers

The cover of the Smale horseshoe with index $(0,1) \to (I, C_4)$ is connected. For this cover $\mathcal{H}$ is generated by I, C_4 and consists of the four group operations $\mathbb{I}, C_4, C_4^2, C_4^3$, so that $\mathcal{H} = \mathcal{G}$ and $|\mathcal{G}|/|\mathcal{H}| = 1$. The cover with index $(0,1) \to (C_4^2, \mathbb{I})$ has two components, since $\mathcal{H} = \{\mathbb{I}, C_4^2\}$. The coset representatives for $\mathcal{G}/\mathcal{H}$ may be chosen as $\{\omega_1, \omega_2\} = \{\mathbb{I}, C_4\}$. One component of the cover is labeled by the group index $\mathbb{I}$. It is the component with branch lines or intervals in $D_{\mathbb{I}}$. The symmetry-related component is labeled by the coset representative C_4. To any trajectory (e.g., a periodic orbit) in the identity component there corresponds a symmetry-related trajectory in the C_4 component. The two symbol sequences are related simply by multiplying by the coset representative:

$$\begin{array}{ll} \text{Component } \mathbb{I} & (s_1, I)(s_2, I)(s_3, C_4^2)(s_4, I)(s_5, C_4^2)\cdots \\ \quad\downarrow & \\ \text{Component } C_4 & (s_1, C_4 I)(s_2, C_4 I)(s_3, C_4 C_4^2)(s_4, C_4 I)(s_5, C_4 C_4^2)\cdots \end{array}$$

An equivariant cover of a strange attractor is defined by the group label assigned to each symbol and used to label orbits in the image attractor. For a strange attractor classified by a branched manifold with two branches, there are $|\mathcal{G}|^2$ structurally stable covers with $|\mathcal{G}|$-fold symmetry.

For the symmetry group $\mathcal{C}_4$ these 16 distinct $\mathcal{C}_4$-invariant covers are organized as follows.

	symbol		group labels										
	0	$\mathbb{I}$	$\mathbb{I}$	C_4^2	C_4^2	$\mathbb{I}$	$\mathbb{I}$	C_4	C_4	C_4^2	C_4	C_4^3
$\mathcal{C}_4$	1	$\mathbb{I}$	C_4^2	$\mathbb{I}$	C_4^2	C_4	C_4^3	C_4^2	C_4^3	C_4^3	C_4	C_4^3
		s.d.	dual pair		s.d.	d.p.	d.p.	d.p.	d.p.	d.p.	s.d.	s.d.
		4 components	2 components			connected covers						

The four-fold cover with index $(0,1) \to (\mathbb{I}, \mathbb{I})$ consists of four disconnected pieces. The cover with index $(0,1) \to (\mathbb{I}, C_4^2)$ consists of two disconnected pieces. Two branch lines, $\mathbb{I}$ and C_4^2, are in one component while the other two, C_4 and C_4^3, lie in the other component. The cover with index $(0,1) \to (C_4^2, \mathbb{I})$ is dual to that with index $(\mathbb{I}, C_4^2)$. Duality is defined by exchanging the sinks for the two sources. The four-fold cover with index $(0,1) \to (C_4^2, C_4^2)$ also consists of two components. It is self-dual. The remaining 12 covers are connected. For each there is a path in the attractor from any branch line to any other branch line. These 12 are divided into five dual pairs $(C_4^i, C_4^j) \leftrightarrow (C_4^j, C_4^i)$, $i \neq j$, i, j not both even, and two self-dual covers $(\mathcal{C}_4^i, \mathcal{C}_4^i)$, $i = 1, 3$. Among these last five dual pairs only one has been presented in the table: the dual partner is easily obtained by the transformation $(g_i, g_j) \leftarrow (0,1) \to (g_j, g_i)$.

Fig. 6.31 shows a structurally stable strange attractor with $\mathcal{V}_4$ symmetry and index $(0,1) \to (\mathbb{I}, R_X)$. Since $\mathcal{H} = \{\mathbb{I}, R_X\}$ the cover is disconnected, consisting of two

components labeled by the coset representative of

$$\mathcal{G}/\mathcal{H} = \{\mathbb{I}, R_X, R_Y, R_Z\}/\{\mathbb{I}, R_X\} = \{\mathbb{I}, R_Y\}$$

The component shown in that figure is identified by its label $\omega = R_Y$.

13.5.5 $\mathcal{V}_4$-Equivariant Covers

The Smale horseshoe branched manifold can be lifted to many different $\mathcal{V}_4$ equivariant covers: $|\mathcal{G}|^2 = 4^2 = 16$ indices are possible. For several choices of indices the following results occur:

Index (g_1, g_2)	Subgroup $\mathcal{H}$	Coset Representatives $\mathcal{G}/\mathcal{H}$	# Components
(I, I)	I	$\{I, R_x, R_Y, R_Z\}$	4
(I, R_X)	$\{I, R_X\}$	$\{I, R_Y\}$	2
(R_Y, R_Y)	$\{I, R_Y\}$	$\{I, R_X\}$	2
(R_X, R_Y)	$\{I, R_X, R_Y, R_Z\}$	I	1

The 16 four-fold covers of the Smale horseshoe branched manifold with $\mathcal{V}_4$ symmetry are partitioned as follows

	symbol		index								
	0	$\mathbb{I}$	$\mathbb{I}$	$\mathbb{I}$	$\mathbb{I}$	R_X	R_Y	R_Z	R_X	R_Y	R_Z
$\mathcal{V}_4$	1	$\mathbb{I}$	R_X	R_Y	R_Z	R_X	R_Y	R_Z	R_Y	R_Z	R_X
		s.d.	3 dual pairs			3 self-dual covers			3 dual pairs		
		4 components	2 components						connected covers		

The cover $(0, 1) \to (\mathbb{I}, \mathbb{I})$ consists of four disconnected components. The next nine consist of two disconnected components. There are three dual pairs: $(\mathbb{I}, R_X) \leftrightarrow (R_X, \mathbb{I})$, etc. and three self-dual covers: e.g., (R_X, R_X). For example, the cover with index $(0, 1) \to (\mathbb{I}, R_Z)$ has one component containing branch lines $\mathbb{I}$ and R_Z, while the symmetry-related component (under either R_X or R_Y) contains branch lines R_X and R_Y. Similarly for the self-dual cover $(0, 1) \to (R_Z, R_Z)$. The three covers with indices $(\mathbb{I}, R_X)$, $(\mathbb{I}, R_Y)$, $(\mathbb{I}, R_Z)$ are related to each other by rotations about the $(1, 1, 1)$ axis by $2\pi/3$ radians, i.e., by the group $\mathcal{C}_3$.

The remaining six covers (three dual pairs) consist of a single connected component. There is a path in each of these branched manifolds from any branch line to any other branch line. There are three dual pairs, such as $(R_X, R_Y) \leftrightarrow (R_Y, R_X)$. In addition, the three (R_X, R_Y), (R_Y, R_Z), $(R_Z, \mathcal{R}_X)$, are mapped into each other under $\mathcal{C}_3$, as are their duals. If we regard the symmetry-related attractors (under $\mathcal{C}_3$) as essentially equivalent, the breakdown of distinct $\mathcal{V}_4$-invariant covers of Smale horseshoe dynamics is

# Components	# Dual Pairs	# Self-Dual Pairs
4	0	$1(\mathbb{I}, \mathbb{I})$
2	$1 \quad (\mathbb{I}, R_X)$	$1 \quad (R_X, R_X)$
1	$1 \quad (R_X, R_Y)$	0

In summary, there are six $(= 2 \times (0 + 1 + 1) + 1 \times (1 + 1 + 0))$ topologically distinct types of double covers of the basic Smale horseshoe branched manifold with $\mathcal{V}_4$ symmetry.

13.6 LIFTS OF ORBITS

An orbit of period p in an image strange attractor $\underline{\mathcal{SA}}$ can be covered by $|\mathcal{G}|$ orbits of period p, $|\mathcal{G}|/2$ orbits of period $2p, \ldots,$ $|\mathcal{G}|/m$ orbits of period mp in $\mathcal{G}$-equivariant covering attractors. The details depend on the orbit chosen and the index of the cover.

When the cover consists of $|\mathcal{G}|$ disconnected components ($\sigma_i \to g(i) = \mathbb{I}$, each i, so $\mathcal{H} = \mathbb{I}$), every orbit in $\underline{\mathcal{SA}}$ has $|\mathcal{G}|$ distinct covers, each with the same period. An orbit of period p in $\underline{\mathcal{SA}}$ can have one covering orbit of period $p|\mathcal{G}|$ only when the covering attractor is connected ($\mathcal{H} = \mathcal{G}$). These are limiting cases.

The general case depends on a the symbol sequence of the image orbit and the index of the cover in a very precise way.

An orbit of period p in $\underline{\mathcal{SA}}$ is represented by product of p transition matrix elements:

$$T_{ab}T_{bc}\ldots T_{op}T_{pa} = 1$$

To see if this orbit is covered by an orbit of period p in the cover, we carry out a similar computation with transition matrices for the cover chosen

$$T_{a\alpha,b\beta}T_{b\beta,c\gamma}\ldots T_{oo,p\rho}T_{p\rho,a\alpha} =$$

$$T_{ab}T_{bc}\ldots T_{op}T_{pa}\Gamma^{\mathrm{Reg}}_{\alpha\alpha}\left([g(a)g(b)\ldots g(o)g(p)]^{-1}\right)$$

This calculation can be carried out at the level of matrix multiplication. This was done explicitly in Section 6.8. The computation can also be carried out at the group level. We do this now.

The matrix element $\Gamma^{\mathrm{Reg}}_{\alpha\alpha}(g(\text{orbit})^{-1})$ is non zero only when the group operator is the identity. This group operator is obtained directly from:

1. the symbol sequence in $\underline{\mathcal{SA}}$
2. the index of the cover.

The algorithm is

$$\begin{array}{ccccccc} a & b & \ldots & o & p & & \\ \downarrow & \downarrow & & \downarrow & \downarrow & & \\ g(a) & g(b) & \ldots & g(o) & g(p) & = g(\text{orbit}) = k \end{array}$$

That is, each symbol in the image orbit is replaced by the appropriate group operation from the index. The product is computed. This identifies a group operation with the orbit: $g(\text{orbit}) = k$. If $k = \mathbb{I}$, $\Gamma^{\mathrm{Reg}}(k) = I_{|\mathcal{G}|}$, tr $\Gamma^{\mathrm{Reg}}(k) = |\mathcal{G}|$, and the image orbit of period p in $\underline{\mathcal{SA}}$ is covered by $|\mathcal{G}|$ orbits, each of period p.

If $k \neq \mathbb{I}$, then k generates a subgroup $\mathcal{K} \subseteq \mathcal{G}$. In fact, $\mathcal{K} \subseteq \mathcal{H} \subseteq \mathcal{G}$. The subgroup $\mathcal{K}$ has one generator and is defined by one relation: $k^m = \mathbb{I}$. The subgroup is $\mathcal{K} = \{\mathbb{I}, k, k^2, \ldots, k^{m-1}\}$.

In this case the original orbit has a covering orbit of period $|\mathcal{K}|p$ in the identity component of the cover. If $\mathcal{K} \subset \mathcal{H}$, there are additional orbits of period $|\mathcal{K}|p$ in the identity component of the cover. These are indexed by the coset representatives of $\mathcal{H}/\mathcal{K}$. The original covering orbit of period $|\mathcal{K}|p$ is mapped into these partner orbits as shown in Eq. (13.34). The set of $|\mathcal{H}|/|\mathcal{K}|$ orbits of period $|\mathcal{K}|p$ in the identity component are mapped into the remaining disconnected components of the cover by the coset representatives of $\mathcal{G}/\mathcal{H}$. The decomposition into covering orbits breaks down as follows:

$$p \xrightarrow{\text{lifts to}} \underbrace{\frac{|\mathcal{G}|}{|\mathcal{H}|}}_{\substack{\#\text{ of disconnected} \\ \text{components of } \mathcal{SA}}} \times \underbrace{\frac{|\mathcal{H}|}{|\mathcal{K}|}}_{\substack{\#\text{ of disconnected cover orbits in identity component of } \mathcal{SA}}} \times \underbrace{|\mathcal{K}|p}_{\substack{\text{period of each} \\ \text{covering orbit}}}$$

Example 1—$\mathcal{C}_4$: We construct lifts of the saddle-node pair 101, 100 in the Smale horseshoe branched manifold. The $\mathcal{C}_4$-equivariant cover is assumed to have index $(0,1) \to (\mathbb{I}, C_4)$. The subgroup $\mathcal{H} = \{\mathbb{I}, C_4, C_4^2, C_4^3\} = \mathcal{C}_4 = \mathcal{G}$, so that covering orbits of period 3, 6, or 12 are possible. To resolve the issue quickly,

$$\begin{array}{cccc} 1 & 0 & 0 & \\ \downarrow & \downarrow & \downarrow & \\ C_4 & \mathbb{I} & \mathbb{I} & = C_4 \end{array} \qquad \begin{array}{cccc} 1 & 0 & 1 & \\ \downarrow & \downarrow & \downarrow & \\ C_4 & \mathbb{I} & C_4 & = C_4^2 \end{array}$$

Since $g(100) = C_4$ and $k^m = \mathbb{I}$ for $m = 4$, $\mathcal{K} = \mathcal{H} = \mathcal{G}$ and 100 has one lift of period 12. Similarly, $g(101) = C_4^2$ and $k^m = \mathbb{I}$ for $m = 2$, so 101 has one lift of period 6 and a partner in the same connected cover. The partner is obtained from the original by multiplying by the coset representative C_4. The symbolic sequences for these lifts are

$$\begin{aligned} 100 \to \quad & \underline{(1,\mathbb{I})}(0,C_4)(0,C_4)\ (1,C_4)(0,C_4^2)(0,C_4^2) \\ & (1,C_4^2)(0,C_4^3)(0,C_4^3)\ (1,C_4^3)(0,\mathbb{I})(0,\mathbb{I})\ \ \underline{(1,\mathbb{I})}\cdots \\ 101 \to \quad & \underline{(1,\mathbb{I})}(0,C_4)(1,C_4)\ (1,C_4^2)(0,C_4^2)(1,C_4^2)\ \ \underline{(1,\mathbb{I})}\cdots \\ & \qquad\qquad\qquad\qquad\qquad\qquad\qquad\qquad \downarrow \\ & \underline{(1,C_4)}(0,C_4^2)(1,C_4^2)\ (1,C_4^3)(0,\mathbb{I})(1,\mathbb{I})\ \ \underline{(1,C_4)}\cdots \end{aligned}$$

Example 2—$\mathcal{V}_4$: The two period-3 orbits 101 and 100 in the Rössler attractor are shown in Fig. 13.4. The lifts of these two orbits into the $\mathcal{V}_4$ -equivariant cover with index $(0,1) \to (R_Y, R_Z)$ are shown in Fig. 13.5.

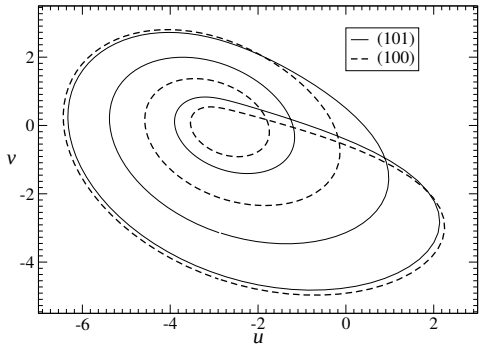

Fig. 13.4 Period-3 orbits embedded within the Rössler attractor.

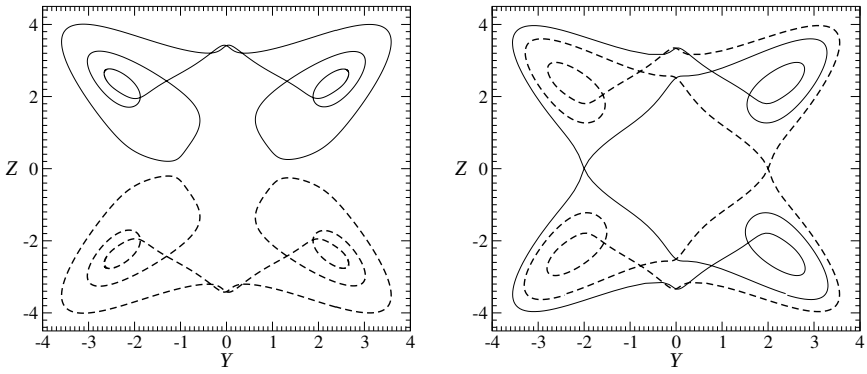

(a) (100) (b) (101)

Fig. 13.5 $\mathcal{V}_4$-fold cover with index $(0 \to R_Y, 1 \to R_Z)$ of the period-three orbits shown in Fig.13.4. Covers of: (a) (100); (b) (101). In both cases the covers consist of two symmetry-related period-6 orbits.

The group operations for these two orbits are obtained as before

$$\begin{array}{cccc} 1 & 0 & 0 & \\ \downarrow & \downarrow & \downarrow & \\ R_Z & R_Y & R_Y & = R_Z \end{array} \qquad \begin{array}{cccc} 1 & 0 & 1 & \\ \downarrow & \downarrow & \downarrow & \\ R_Z & R_Y & R_Z & = R_Y \end{array}$$

so that $g(100) = R_Z$, $g(101) = R_Y$. Both period-3 orbits lift to period-6 orbits in the connected cover. Each has a partner, obtained from the coset representative in $\mathcal{H}/\mathcal{K}$. These figures show that the image orbits are very similar, but their covers are quite dissimilar, as they visit different domains in $\mathbb{R}^3(\boldsymbol{X})$. The covers have symbol

sequences

$$\begin{aligned} 100 \rightarrow \quad & (1,\mathbb{I})(0,R_Z)(0,R_X)\ (1,R_Z)(0,\mathbb{I})(0,R_Y) \\ & \qquad\qquad \downarrow R_X \\ & (1,R_X)(0,R_Y)(0,\mathbb{I})\ (1,R_Y)(0,R_X)(0,R_Z) \end{aligned}$$

$$\begin{aligned} 101 \rightarrow \quad & (1,\mathbb{I})(0,R_Z)(1,R_X)\ (1,R_Y)(0,R_X)(1,R_Z) \\ & \qquad\qquad \downarrow R_Y \\ & (1,R_X)(0,R_Y)(1,\mathbb{I})\ (1,R_Z)(0,\mathbb{I})(1,R_Y) \end{aligned}$$

Table 13.1 provides information about lifts of all the orbits of period $p \leq 5$ in the horseshoe into the $\mathcal{V}_4$-equivariant cover with index $(0,1) \rightarrow (R_X, R_Y)$. This information is simple to compute with the algorithms providing for the computation of the group-subgroup chain $\mathcal{K} \subseteq \mathcal{H} \subseteq \mathcal{G}$.

Remark: The sugroup $\mathcal{K}$ is generated by a single group operation. If $\mathcal{G}$ has two or more generators, $\mathcal{K} \neq \mathcal{G}$. In such a case, no period-p orbit in the image is covered by an orbit of period $|\mathcal{G}|p$ in any of its covers.

13.7 STRUCTURALLY UNSTABLE COVERS

When the image of the singular set in $\mathbb{R}^3(u_1, u_2, u_3)$ intersects the image attractor, the singular set intersects the equivariant covering attractor in $\mathbb{R}^3(\boldsymbol{X})$. The intersection has absolutely no effect on the image attractor but a profound effect on the covering

Table 13.1 Lifts into $\mathcal{V}_4$-equivariant cover with index $(0,1) \rightarrow (R_X, R_Y)$ of horseshoe orbits with $p \leq 5$. The cover is connected since $\mathcal{H} = \mathcal{G}$. P is the period of each of the cover orbits.

Orbit	Symbolic	$\Pi g(i)$	k	$\mathcal{H}/\mathcal{K}$	$\lvert\mathcal{H}/\mathcal{K}\rvert$	m	p	P
1	1	R_Y	R_Y	$\{\mathbb{I}, R_X\}$	2	2	1	2
2	10	$R_Y R_X$	R_Z	$\{\mathbb{I}, R_X\}$	2	2	2	4
4_1	1011	$R_Y R_X R_Y^2$	R_Z	$\{\mathbb{I}, R_X\}$	2	2	4	8
3_1	101	$R_Y R_X R_Y$	R_X	$\{\mathbb{I}, R_Y\}$	2	2	3	6
3_1	100	$R_Y R_X^2$	R_Y	$\{\mathbb{I}, R_X\}$	2	2	3	6
4_2	1001	$R_Y R_X^2 R_Y$	$\mathbb{I}$	$\mathcal{G}$	4	1	4	4
4_2	1000	$R_Y R_X^3$	R_Z	$\{\mathbb{I}, R_X\}$	2	2	4	8
5_1	10111	$R_Y R_X R_Y^3$	R_X	$\{\mathbb{I}, R_Y\}$	2	2	5	10
5_1	10101	$(R_Y R_X)^2 R_Y$	R_Y	$\{\mathbb{I}, R_X\}$	2	2	5	10
5_2	10011	$R_Y R_X^2 R_Y^2$	R_Y	$\{\mathbb{I}, R_X\}$	2	2	5	10
5_2	10100	$(R_Y R_X)^2 R_X$	R_X	$\{\mathbb{I}, R_Y\}$	2	2	5	10
5_3	10001	$R_Y R_X^3 R_Y$	R_X	$\{\mathbb{I}, R_Y\}$	2	2	5	10
5_3	10000	$R_Y R_X^4$	R_Y	$\{\mathbb{I}, R_X\}$	2	2	5	10

attractor. To be precise, the covering attractor is structurally unstable. A perturbation of the location of the intersection changes the periodicity, structure, and organization of many unstable periodic orbits in the cover. The bifurcation due to this structural instability has been named the peeling bifurcation [67].

In the structurally unstable case the flow from one of the intervals of the branch line in the fundamental domain is split into components that flow to two different branch lines in adjacent domains. As an example, we consider a cover of the Smale horseshoe branched manifold with $\mathcal{V}_4$ symmetry and index $(0,1) \rightarrow (\mathbb{I}, R_Y)$. This cover has two disconnected components. Now we displace the image attractor so branch 0 intersects the image of the Z-axis $u_1 = u_3 = 0$, $u_2 \leq 0$. Then the flow from $0(\mathbb{I})$ is split between the branch line in the fundamental domain and the domain R_Z. There is a path from branch line $\mathbb{I}$ to every other branch line. As a result, the structurally unstable attractor is now connected. It is labeled by the index $(0,1) \rightarrow (\mathbb{I} + R_Z, R_Y)$. After the $u_2 \leq 0$ axis passes through branch 0 to the space between the two branches, the cover becomes once again structurally stable, has index $(0,1) \rightarrow (R_Z, R_Y)$, and is connected. The intersection of the half axis $u_1 = u_3 = 0$, $u_2 \leq 0$ with branch 0 causes a global symmetry-restoring bifurcation. In this case the bifurcation is summarized by

$$\begin{array}{lccc} \text{Index} & (0 \rightarrow \mathbb{I}, 1 \rightarrow R_Y) & (0 \rightarrow \mathbb{I} + R_Z, 1 \rightarrow R_Y) & (0 \rightarrow R_Z, 1 \rightarrow R_Y) \\ & \text{structurally stable} & \text{structurally unstable} & \text{structurally stable} \end{array} \tag{13.35}$$

Remark: In structurally unstable cases the flow is split between branch lines in adjacent domains (Fig. 11.1). The connectivity of the structurally unstable cover is determined by computing the subgroup $\mathcal{H}$, now using all appropriate group labels. For example, $\mathcal{H}$ for $(0,1) \rightarrow (\mathbb{I}, R_Y)$ is generated by $\mathbb{I}$ and R_Y and is the two-element group $\mathcal{H} = \{\mathbb{I}, R_Y\}$, whereas in the structurally unstable case $(0,1) \rightarrow (\mathbb{I} + R_Y, R_Z)$, $\mathcal{H}$ is generated by $\mathbb{I}$, R_Z, R_Y and consists of all four group operations: $\mathcal{H} = \{\mathbb{I}, R_X, R_Y, \mathcal{R}_Z\} = \mathcal{G}$. In this case $|\mathcal{G}|/|\mathcal{H}| = 1$ shows that the cover has one connected component.

In a structurally stable $\mathcal{G}$-equivariant cover each $\sigma_i(\mathbb{I})$ provides initial conditions for flows to intervals in the same domain $D_{g(i)}$. When this is not the case, the cover is structurally unstable. In the structurally stable case perturbations of the position of the covering attractor $\mathcal{SA}$ with respect to the (algebraic) singular set of the Jacobian $\partial u_i / \partial X_j$ has no affect on the number, type, and organization of the unstable periodic orbits in $\mathcal{SA}$. In the structurally unstable case, a perturbation has a pronounced affect on all three.

As an example we consider a one-parameter family of local $\mathcal{V}_4$-equivariant diffeomorphisms for which the structurally stable cover has index $(0,1) \rightarrow (I, R_Y)$ in one limit ($s = 0$) and has index $(0,1) \rightarrow (R_Z, R_Y)$ in the other ($s = 1$). In the interval describing structurally unstable covers the index is $(0,1) \rightarrow (I + R_Z, R_Y)$. This means that some initial conditions on the interval 0_I flow to (0_I or 0_{R_Z}) or to (1_I or 1_{R_Z}). The connectivity of the cover is determined by constructing the group $\mathcal{H} \subset \mathcal{G}$

from *all* components of the index:

Index $(0,1)$ $\longrightarrow$	(I, R_Y)	$(I + R_Z, R_Y)$	(R_Z, R_Y)
Group $\mathcal{H}$:	$\{I, R_Y\}$	$\{I, R_X, R_Y, R_Z\}$	$\{I, R_X, R_Y, R_Z\}$
Structural Stability :	Stable	Unstable	Stable
Connectivity :	2 Components	Connected	Connected

On entering the structurally unstable region in parameter space, the cover exhibits a symmetry-restoring bifurcation: the two disjoint components join to form a single connected component. A connected structurally unstable cover with $\mathcal{V}_4$ symmetry and index $(0,1) \to (I, R_Y + R_Z)$ is shown in Fig. 6.31(b).

The analysis of the spectrum, symbolic dynamics, and labeling of covers of periodic orbits in $\underline{\mathcal{SA}}$ in structurally unstable covers proceeds as in Section 13.5. The principal differences are that the groups $\mathcal{H}$ and $\mathcal{K}$ must be replaced by groups $\mathcal{H}', \mathcal{K}'$ generated from all symbols in the index. For example, in the structurally unstable cases described above, $\mathcal{H}'$ is generated by I, R_Z and R_Y, so that $\mathcal{H}' = \{I, R_X, R_Y, R_Z\} = \mathcal{G}$. The structurally unstable cover is connected.

The orbit $001 \subset \underline{\mathcal{SA}}$ lifts to a series of topologically distinct orbits, with distinct symbol sets and even periods, under this family of local diffeomorphisms. These are obtained by assigning the first/second symbols 0 the allowed group labels I, R_Z. The results can be summarized as follows

	Index	
$(I, R_Y) \quad \to$	$(I + R_Z, R_Y) \quad \to$	(R_Z, R_Y)
	Assignment	
$0 \to I$	$0 \to I, 0 \to R_Z$	$0 \to R_Z, 0 \to R_Z$
$0 \to I$	$0 \to R_Z, 0 \to I$	
	Orbit	
$0_I 0_I 1_{R_Y}\ 0_{R_Y} 0_{R_Y} 1_{R_Y}$	$0_I 0_I 1_{R_Z}\ 0_{R_X} 0_{R_X} 0_{R_Y}$	$0_I 0_{R_Z} 1_I\ 0_{R_Y} 0_{R_X} 0_{R_Y}$
	$0_I 0_{R_Z} 1_{R_Z}\ 0_{R_X} 0_{R_X} 0_{R_Y}$	

In this summary, the period-6 orbit that occurs in the structurally unstable cover depends on the order in which the image of the singular set in $\mathbb{R}^3(u)$ passes through the two orbit segments labeled 0. That is:

$$
\begin{array}{ccccc}
 & & & (I, R_Z) & \\
 & & \nearrow & & \searrow \\
00 & \to & (I, I) & & (R_Z, R_Z) \\
 & & \searrow & & \nearrow \\
 & & & (R_Z, I) &
\end{array}
$$

As a rotation axis sweeps through the branch 0 in the image attractor, the period-three orbit 001 lifts to a series of period-six orbits in the structurally unstable $\mathcal{V}_4$-equivariant lift. The lifted orbits deform into each other during the bifurcations induced by this structural instability.

14

Symmetries Due to Symmetry

14.1 SCHUR SYMMETRIES

Schur's lemmas play a fundamental role in the analysis of the representations of groups and algebras. They are powerful tools for the construction of a complete set of irreducible representations of any group. We exploit the first of Schur's lemmas to determine the most general form that a dynamical system in $\mathbb{R}^N$ can have if it is equivariant under a group $\mathcal{G}$. The structure is determined by the representations $\Gamma^{\mathrm{Def}}(\mathcal{G})$ and $\Gamma^{\mathrm{Ring}}(\mathcal{G})$.

14.1.1 Schur's lemmas

Although only one of the two lemmas of Schur is needed for our purposes, the lemmas are so powerful, so pretty, and so similar, we provide the proofs of both. The proofs are summarized in Figs. 14.1 and 14.2.

The essential idea is that groups act on linear vector spaces through linear transformations. These are determined by matrices. The matrices are the group representations.

Definition: A subspace is *invariant* if it is mapped into itself under all linear transformations associated with the matrix representation of the group.

Schur's Lemma #1

$D(x)$	acts in	V
Irreducible		Invariant
	$M\ D(x) = D(x)\ M$	all x

1. Every linear transformation has one nonzero eigenvector.

$$\{M - \lambda I\}\, u = 0 \qquad u \neq 0,\ \text{ some } \lambda$$

2. The vectors u that obey (1) form a subspace $U \subset V$.

3. This linear vector subspace is invariant under $D(x)$:

$$\{M - \lambda I\}\, D(x)u = D(x)\, \{M - \lambda I\}\, u = 0$$

4. V has only two subspaces invariant under $D(x)$. The subspace U is not empty. $U = V$. Therefore

$$\begin{aligned} \{M - \lambda I\}\, U &= \{M - \lambda I\}\, V = 0 \\ M &= \lambda I \end{aligned}$$

Fig. 14.1 The proof of Schur's first lemma is carried out in four steps, summarized above. The proof is very similar to the proof of Schur's second lemma.

When a linear transformation acts on a linear vector space, the linear vector space can be decomposed into invariant subspaces. Every linear vector space always has two invariant subspaces. One consists of the entire linear vector space. The other consists of the zero vector. It may have many other invariant subspaces.

Definition: A matrix representation $\Gamma(\mathcal{G})$ acting on a linear vector space V is *irreducible* if the only two subspaces of V that are invariant under the action of $\Gamma(\mathcal{G})$ on V are the spaces V and 0.

Example 1: The group of orthogonal transformations acting in $\mathbb{R}^3$ is generated by three 3×3 matrices

$$\begin{bmatrix} 1 & 0 & 0 \\ 0 & \cos\theta_x & \sin\theta_x \\ 0 & -\sin\theta_x & \cos\theta_x \end{bmatrix} \begin{bmatrix} \cos\theta_y & 0 & -\sin\theta_y \\ 0 & 1 & 0 \\ \sin\theta_y & 0 & \cos\theta_y \end{bmatrix} \begin{bmatrix} \cos\theta_z & \sin\theta_z & 0 \\ -\sin\theta_z & \cos\theta_z & 0 \\ 0 & 0 & 1 \end{bmatrix} \tag{14.1}$$

The representation of the rotation group generated by the 3×3 matrices above is irreducible.

Schur's Lemma #2

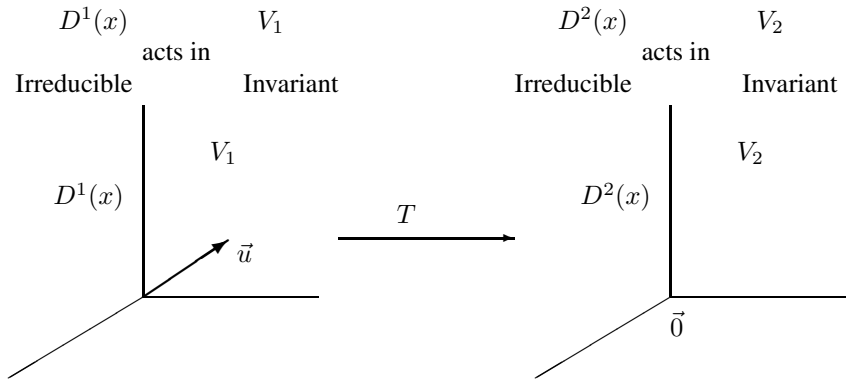

$$T\,D^1(x) = D^2(x)\,T \qquad \text{all } x$$

1. $Tu = 0$ ($u = 0$ Satisfies this.)
2. The vectors u that obey (1) form a subspace $U \subset V_1$.
3. This linear vector subspace is invariant under $D^1(x)$:

$$T\,D^1(x)\,u = D^2(x)\,T\,u = 0$$

4. V_1 has only two subspaces invariant under $D^1(x)$:

$$\begin{array}{lcll} U & = & V_1 & T = 0 \\ U & = & 0 & T \text{ is faithful, } T^{-1} \text{ exists, and} \\ & & & D^2(x) = TD^1(x)T^{-1} \end{array}$$

Fig. 14.2 The proof of Schur's second lemma is carried out in four steps, summarized above. The proof is very similar to the proof of Schur's first lemma.

Example 2: A group $\mathcal{G}$ acts on an n-dimensional linear vector space V through a set of matrices, each of which has the following block-diagonal form:

$$\Gamma^{\text{Red}}(\mathcal{G}) = \begin{bmatrix} A & 0 \\ 0 & B \end{bmatrix} \tag{14.2}$$

Here A is an $n_A \times n_A$ matrix and B is an $n_B \times n_B$ matrix, where $n_A + n_B = n$ and $n_A, n_B > 0$. In this case the $n_A + n_B$ dimensional space V decomposes into two subspaces $V = V_A \oplus V_B$ of dimensions n_A and n_B, respectively. Both subspaces are invariant under the group action through the matrix presentation $\Gamma^{\text{Red}}(\mathcal{G})$.

We now describe the two lemmas of Schur.

Schur's Lemma #1: Assume that the representation $D(x)$ acts on the linear vector space V, and that $D(x)$ is irreducible and V is invariant under $D(x)$. Assume also that a matrix M commutes with $D(x)$, all x:

$$MD(x) = D(x)M \qquad \text{all } x$$

Then M is a multiple of the identity matrix: $M = \lambda I$.

Proof: There is a vector $u \in V$ that satisfies $(M - \lambda I)u = 0$, since every matrix M over an algebraically closed field has a nonzero eigenvector. The vectors u that satisfy this relation form a subspace $U \subset V$. It is easy to check that if two vectors $u_1, u_2 \in V$ satisfy this relation, arbitrary linear combinations $\alpha u_1 + \beta u_2$ of these vectors also satisfy this relation. The linear vector subspace U is invariant under the action $D(x)$, for

$$\{M - \lambda I\}\, D(x)u = D(x)\, \{M - \lambda I\}\, u = 0$$

V has only two invariant subspaces under $D(x)$: V itself and the zero subspace. Since $u \neq 0$, $U = V$. Therefore

$$\{M - \lambda I\}\, U = \{M - \lambda I\}\, V \Rightarrow M = \lambda I$$

This proof of Schur's first lemma is summarized in Fig. 14.1.

Schur's Lemma #2: Assume that the representation $D^1(x)$ acts on the linear vector space V_1, and that $D^1(x)$ is irreducible and V_1 is invariant under $D^1(x)$. Assume the same for $D^2(x)$ acting on V_2. Finally, assume that the linear transformation T (T is a matrix) maps $V_1 \to V_2$ and that

$$TD^1(x) = D^2(x)T, \qquad \text{all } x$$

Then either $T = 0$ or T is one to one (faithful), T^{-1} exists, and $D^2(x) = TD^1(x)T^{-1}$, so that $D^1(x)$ is equivalent to $D^2(x)$.

Proof: There is a vector $u \in V_1$ that satisfies $Tu = 0$. At the very least, the vector $u = 0$ satisfies this. The vectors $u \in V_1$ that satisfy $Tu = 0$ form a linear vector subspace $U \subset V_1$. It is easy to check that if two vectors $u_1, u_2 \in V_1$ satisfy this relation, arbitrary linear combinations $\alpha u_1 + \beta u_2$ of these vectors also satisfy this relation. The linear vector subspace U is invariant under the action $D^1(x)$, for

$$TD^1(x)u = D^2(x)Tu = 0$$

V_1 has only two subspaces invariant under $D^1(x)$, $U = 0$ and $U = V_1$. If $U = V_1$, then the image of every vector in V_1 is zero, so $T = 0$. If $U = 0$, the only vector annihilated by T is the zero vector, so that T is 1-1, faithful, and has an inverse. Multiplying by T^{-1} on the right of the intertwining relation in the statement of the theorem, we find

$$D^2(x) = TD^1(x)T^{-1}$$

In other words, the two representations are related by a similarity transformation, so are equivalent.

This proof of Schur's second lemma is summarized in Fig. 14.2. The proofs of the two lemmas have been designed so they can be given in a parallel fashion.

Remark: In the proofs of the two lemmas given above, we have nowhere used any of the structure available from the group axioms. The proofs involve only the concept of invariant subspace from linear algebra: nothing more, nothing less. It does not even depend on the fact that we are talking about representations of a group. So the conclusions are valid for any kind of a representation: group; algebra; field; semigroup; vector space; even a point set. Schur's lemmas belong to a deeper substratum of algebraic verity than do the concepts they usually are applied to [135].

Example 3: The finite rotation group $\mathcal{C}_n$ acting in the plane R^2 is generated by the operation C_n

$$C_n = \begin{bmatrix} \cos\theta & \sin\theta \\ -\sin\theta & \cos\theta \end{bmatrix} \qquad \theta = \frac{2\pi}{n}, \ \ n \ \text{integer} \tag{14.3}$$

For $n = 2$ this representation is reducible, for the generator commutes with an arbitrary diagonal matrix:

$$\begin{bmatrix} -1 & 0 \\ 0 & -1 \end{bmatrix} \begin{bmatrix} a & 0 \\ 0 & b \end{bmatrix} = \begin{bmatrix} -a & 0 \\ 0 & -b \end{bmatrix} = \begin{bmatrix} a & 0 \\ 0 & b \end{bmatrix} \begin{bmatrix} -1 & 0 \\ 0 & -1 \end{bmatrix}$$

For other values of n this 2×2 matrix representation is also reducible over the complex numbers. The complex invariant subspaces are spanned by the linear combinations $x + iy$ and $x - iy$. In this basis, the matrix representative for C_n is equivalent to

$$C_n \simeq \begin{bmatrix} e^{2\pi i/n} & 0 \\ 0 & e^{-2\pi i/n} \end{bmatrix}$$

and the most general matrix that commutes with this matrix is diagonal, $M = \begin{bmatrix} a & 0 \\ 0 & b \end{bmatrix}$. The groups $\mathcal{C}_n$ have only one-dimensional irreducible representations.

14.1.2 How to Use Schur's Lemmas

In this section we illustrate the power of Schur's first lemma by using it to determine the structure of a matrix defined by a particular relation.

We assume a group $\mathcal{G}$ has inequivalent irreducible representations $\Gamma^{(1)}, \Gamma^{(2)}, \Gamma^{(3)}, \Gamma^{(4)}, \cdots$ of dimensions $n^{(1)}, n^{(2)}, n^{(3)}, n^{(4)}, \cdots$. We also assume that $\mathcal{G}$ has representations $\Gamma^{(L)}$ and $\Gamma^{(R)}$ that may be reducible. It is a remarkable fact that these representations can always be written as direct sums of irreducible representations if $\mathcal{G}$ is finite, discrete, or compact. Thus, we may write these two representations as, for example

$$\Gamma^{(L)} = \begin{bmatrix} \Gamma^{(1)} & 0 & 0 & 0 \\ 0 & \Gamma^{(2)} & 0 & 0 \\ 0 & 0 & \Gamma^{(1)} & 0 \\ 0 & 0 & 0 & \Gamma^{(4)} \end{bmatrix} \qquad \Gamma^{(R)} = \begin{bmatrix} \Gamma^{(1)} & 0 & 0 \\ 0 & \Gamma^{(2)} & 0 \\ 0 & 0 & \Gamma^{(3)} \end{bmatrix} \tag{14.4}$$

Example: A matrix M *intertwines* the two reducible representations $\Gamma^{(L)}$ and $\Gamma^{(R)}$ defined above if: $\Gamma^{(L)}M = M\Gamma^{(R)}$. In order to determine the structure of M, we partition the rows of M according to the structure of the reducible representation $\Gamma^{(L)}$ and the columns of M according to the structure of the reducible representation $\Gamma^{(R)}$:

$$\begin{bmatrix} \Gamma^{(1)} & 0 & 0 & 0 \\ 0 & \Gamma^{(2)} & 0 & 0 \\ 0 & 0 & \Gamma^{(1)} & 0 \\ 0 & 0 & 0 & \Gamma^{(4)} \end{bmatrix} \left[\begin{array}{c|c|c} M_{11} & M_{12} & M_{13} \\ \hline M_{21} & M_{22} & M_{23} \\ \hline M_{31} & M_{32} & M_{33} \\ \hline M_{41} & M_{42} & M_{43} \end{array}\right] = \left[\begin{array}{c|c|c} M_{11} & M_{12} & M_{13} \\ \hline M_{21} & M_{22} & M_{23} \\ \hline M_{31} & M_{32} & M_{33} \\ \hline M_{41} & M_{42} & M_{43} \end{array}\right] \begin{bmatrix} \Gamma^{(1)} & 0 & 0 \\ 0 & \Gamma^{(2)} & 0 \\ 0 & 0 & \Gamma^{(3)} \end{bmatrix} \tag{14.5}$$

In this block submatrix decomposition, the blocks M_{ij} have the appropriate size: For example, the submatrix M_{32} is an $n^{(1)} \times n^{(2)}$ matrix. Eq. (14.5) can be brought to a simpler form by multiplying out the products and subtracting one side from the other:

$$\left[\begin{array}{c|c|c} \Gamma^{(1)}M_{11} - M_{11}\Gamma^{(1)} & \Gamma^{(1)}M_{12} - M_{12}\Gamma^{(2)} & \Gamma^{(1)}M_{13} - M_{13}\Gamma^{(3)} \\ \hline \Gamma^{(2)}M_{21} - M_{21}\Gamma^{(1)} & \Gamma^{(2)}M_{22} - M_{22}\Gamma^{(2)} & \Gamma^{(2)}M_{23} - M_{23}\Gamma^{(3)} \\ \hline \Gamma^{(1)}M_{31} - M_{31}\Gamma^{(1)} & \Gamma^{(1)}M_{32} - M_{32}\Gamma^{(2)} & \Gamma^{(1)}M_{33} - M_{33}\Gamma^{(3)} \\ \hline \Gamma^{(4)}M_{41} - M_{41}\Gamma^{(1)} & \Gamma^{(4)}M_{42} - M_{42}\Gamma^{(2)} & \Gamma^{(4)}M_{43} - M_{43}\Gamma^{(3)} \end{array}\right] = 0 \tag{14.6}$$

Each of the submatrices in (14.5) is zero, if $\Gamma^{(i)} \neq \Gamma^{(j)}$, or else a multiple of the identity if $\Gamma^{(i)} = \Gamma^{(j)}$. In particular, $M_{12} = M_{13} = M_{21} = M_{23} = M_{32} = M_{33} = M_{41} = M_{42} = M_{43} = 0$ while $M_{11} = \lambda_1 I_{n^{(1)}}$, $M_{22} = \lambda_2 I_{n^{(2)}}$, $M_{31} = \lambda_3 I_{n^{(1)}}$. As a result, the matrix M has the explicit structure

$$M = \left[\begin{array}{c|c|c} \lambda_1 I_{n^{(1)}} & 0 & 0 \\ \hline 0 & \lambda_2 I_{n^{(2)}} & 0 \\ \hline \lambda_3 I_{n^{(1)}} & 0 & 0 \\ \hline 0 & 0 & 0 \end{array}\right] \tag{14.7}$$

It is completely determined by the three scalars $\lambda_1, \lambda_2, \lambda_3$ in the appropriate positions.

Remark: Calculations of this type are facilitated by labeling the blocked rows and columns by the irreducible representations contained in the reducible representations

$\Gamma^{(L)}$ and $\Gamma^{(R)}$. For example, for M we find

$$\begin{array}{c} \\ \Gamma^{(1)} \\ \Gamma^{(2)} \\ \Gamma^{(1)} \\ \Gamma^{(4)} \end{array} \begin{array}{c} \begin{array}{ccc} \Gamma^{(1)} & \Gamma^{(2)} & \Gamma^{(3)} \end{array} \\ \left[\begin{array}{ccc} M_{11} & 0 & 0 \\ 0 & M_{22} & 0 \\ M_{31} & 0 & 0 \\ 0 & 0 & 0 \end{array}\right] \end{array} \tag{14.8}$$

Only the submatrices indexed by the same irreducible representations are nonzero, and each such submatrix is a multiple of an appropriate sized identity matrix. The scalar factors λ_i are not related to each other.

Important Remark: If $m^{(\alpha)}$ is the number of times the irreducible representation $\Gamma^{(\alpha)}$ occurs in $\Gamma^{(L)}$ and $n^{(\alpha)}$ is the number of times the irreducible representation $\Gamma^{(\alpha)}$ occurs in $\Gamma^{(R)}$, the number of independent nonzero scalars λ required to define the matrix M is

$$\#\,\text{scalars} = \sum_{\alpha} m^{(\alpha)} n^{(\alpha)} \tag{14.9}$$

For $\Gamma^{(L)}$ these four numbers are $(2,1,0,1)$ and for $\Gamma^(R)$ they are $(1,1,1,0)$. The inner product of these two vectors of integers is $(2,1,0,1)\cdot(1,1,1,0) = 3$.

14.1.3 Application to Equivariant Dynamical Systems

In this section we illustrate how Schur's first lemma is used to determine the structure of a set of equations that is equivariant under the action of a group $\mathcal{G}$ acting in $\mathbb{R}^N$ through the defining matrix representation $\Gamma^{\text{Def}}(\mathcal{G})$. The result is expressed in terms of the defining matrix representation $\Gamma^{\text{Def}}(\mathcal{G})$ and the matrix representation of the group acting on the ring basis functions: $\Gamma^{\text{Ring}}(\mathcal{G})$.

The equations of motion have the form

$$\dot{X}_i = F_i(X) = f_{ir}(p) R_r(X) \tag{14.10}$$

In this expression $\mathbb{R}_r(X)$ are the ring basis polynomials, including the single invariant function 1. The action of a group operation $g \in \mathcal{G}$ on this equation is given by

$$\begin{aligned} g\frac{d}{dt}X_i &= g f_{ir}(p) R_r(X) \\ \Gamma^{\text{Def}}_{ij}(g^{-1})\frac{d}{dt}X_j &= g f_{ir}(p) g^{-1}\, g R_r(X) \\ \Gamma^{\text{Def}}_{ij}(g^{-1})\frac{d}{dt}X_j &= g f_{ir}(p) g^{-1}\, \Gamma^{\text{Ring}}_{rs}(g^{-1}) R_s(X) \end{aligned} \tag{14.11}$$

Since the functions $f_{ir}(p)$ are invariant, $g f_{ir}(p) g^{-1} = f_{ir}(p)$. Now multiply through by the matrix $\Gamma^{\text{Def}}_{ji}(g)$ and sum over dummy indices

$$\frac{d}{dt}X_j = \Gamma^{\text{Def}}_{ji}(g) f_{ir}(p) \Gamma^{\text{Ring}}_{rs}(g^{-1}) R_s(X) \overset{(14.10)}{=} f_{js}(p) R_s(X) \tag{14.12}$$

The basis polynomials $R_s(X)$ are linearly independent, so we can equate their coefficients in the last equality, to find

$$\begin{aligned} \Gamma^{\rm Def}_{ji}(g) f_{ir}(p) \Gamma^{\rm Ring}_{rs}(g^{-1}) &= f_{js} \\ \Gamma^{\rm Def}_{ij}(g) f_{js}(p) &= f_{ir}(p) \Gamma^{\rm Ring}_{rs}(g) \end{aligned} \tag{14.13}$$

This expression is identical in form to Eq. (14.5) under the identifications $\Gamma^{(\rm L)} \leftrightarrow \Gamma^{\rm Def}$, $\Gamma^{(\rm R)} \leftrightarrow \Gamma^{\rm Ring}$, and $M \leftrightarrow f_{ir}$. The structure of the set (matrix) of invariant functions that defines the equivariant equations can simply be determined by the procedure indicated in Eq. (14.8).

Example 1: The group $\mathcal{C}_3$ has only one dimensional irreducible representations. The action of $\mathcal{C}_3$ in R^3 is through a defining 3×3 matrix representation. The basis functions for the irreducible representations are $X+iY$, $X-iY$, and Z. These three functions carry the irreducible representations $\Gamma^{(+1)}$, $\Gamma^{(-1)}$, and $\Gamma^{(0)}$, respectively, where $\Gamma^{(m)}(C_3^n) = e^{2\pi i m n/3}$. There are five functions in the ring basis: The invariant 1, the linear combinations $= X + iY$ and $X - iY$, and the bilinear polynomials $(X-iY)^2 = X^2 - Y^2 - 2iXY$ and $(X+iY)^2 = X^2 - Y^2 + 2iXY$. These last two basis functions carry the irreducible representations $\Gamma^{(+1)}$ and $\Gamma^{(-1)}$. The 3×5 matrix of invariant functions $f_{ir}(p)$ can be partitioned with respect to the coordinate basis functions $X+iY$, $X-iY$, Z and the ring basis functions 1, $X+iY$, $X-iY$, X^2-Y^2-2iXY, X^2-Y^2+2iXY as follows:

$$\begin{array}{c} \\ \Gamma^{(+)} \\ \Gamma^{(-)} \\ \Gamma^{(0)} \end{array} \begin{array}{c} \begin{array}{ccccc} \Gamma^{(0)} & \Gamma^{(+)} & \Gamma^{(-)} & \Gamma^{(+)} & \Gamma^{(-)} \end{array} \\ \left[\begin{array}{ccccc} 0 & f_{11}+if_{12} & 0 & f_{13}+if_{14} & 0 \\ 0 & 0 & f_{11}-if_{12} & 0 & f_{13}-if_{14} \\ f_{30} & 0 & 0 & 0 & 0 \end{array} \right] \end{array} \tag{14.14}$$

The second line is the complex conjugate of the first, so that the complex functions $f_{ij}(p)$ in this line are the conjugates of the complex function in the first row. By taking the real and imaginary parts of the equation for $\frac{d}{dt}(X+iY) = (f_{11}+if_{12})(X+iY) + (f_{13}+if_{14})(X^2-Y^2-2iXY)$ we find the canonical form for the dynamical equations in R^3 that are equivariant under the action of the group $\mathcal{C}_3$. These equations are

$$\frac{d}{dt}\begin{bmatrix} X \\ Y \\ Z \end{bmatrix} = \begin{bmatrix} 0 & f_{11} & -f_{12} & f_{13} & f_{14} \\ 0 & f_{12} & f_{11} & f_{14} & -f_{13} \\ f_{30} & 0 & 0 & 0 & 0 \end{bmatrix} \begin{bmatrix} 1 \\ X \\ Y \\ X^2-Y^2 \\ 2XY \end{bmatrix} \tag{14.15}$$

Example 2: Identical arguments can be applied to study dynamical systems in R^3 that are equivariant under the rotation group $\mathcal{C}_n$. This group has only one dimensional (complex) irreducible representations. These are $\Gamma^{(k)}$, defined by $\Gamma^k(C_n^m) = e^{2\pi i k m/n}$, with the identification $\Gamma^{(k)} = \Gamma^{(k \pm n)}$. The basis functions for the defining matrix representation are $X+iY, X-iY, Z$, so $\Gamma^{\rm Def}$ contains only the three representations $\Gamma^{(+)}, \Gamma^{(-)}, \Gamma^{(0)}$. The ring basis contains the constant 1 and the real and

imaginary parts of $(X \pm iY)^k$, for $k = 1, 2, \cdots, n-1$. The pair $X+iY, X-iY$ carry the representations $\Gamma^{(+)}, \Gamma^{(-)}$. The pair $(X \mp iY)^{n-1}$ also carry the same two representations $\Gamma^{(+)}, \Gamma^{(-)}$. All other ring basis functions $(X \pm iY)^k$, $k = 2, 3, \cdots, n-2$ carry representations that are not equivalent to any of the three representations contained in the defining matrix representation Γ^{Def}. As a result, the equations for $\mathcal{C}_n$ equivariant dynamical systems can be expressed in the form

$$\begin{array}{c} \\ \Gamma^{(+)} \\ \Gamma^{(-)} \\ \Gamma^{(0)} \end{array} \begin{array}{c} \begin{array}{ccccc} \Gamma^{(0)} & \Gamma^{(+)} & \Gamma^{(-)} & \Gamma^{(+)} & \Gamma^{(-)} \end{array} \\ \begin{bmatrix} 0 & f_{11}+if_{12} & 0 & f_{13}+if_{14} & 0 \\ 0 & 0 & f_{11}-if_{12} & 0 & f_{13}-if_{14} \\ f_{30} & 0 & 0 & 0 & 0 \end{bmatrix} \end{array} \tag{14.16}$$

where the rows are indexed by the polynomials $X + iY, X - iY, Z$ and the columns are indexed by the polynomials $1, X+iY, X-iY, (X-iY)^{n-1}, (X-iY)^{n-1}$. The equivariant dynamical systems equations have the form

$$\frac{d}{dt}\begin{bmatrix} X \\ Y \\ Z \end{bmatrix} = \begin{bmatrix} 0 & f_{11} & -f_{12} & f_{13} & f_{14} \\ 0 & f_{12} & f_{11} & f_{14} & -f_{13} \\ f_{30} & 0 & 0 & 0 & 0 \end{bmatrix} \begin{bmatrix} 1 \\ X \\ Y \\ \mathtt{Re}\,(X-iY)^{n-1} \\ \mathtt{Im}\,(X-iY)^{n-1} \end{bmatrix} \tag{14.17}$$

The structure is the same as for $\mathcal{C}_3$ equivariant dynamical systems. All dynamical systems in $\mathbb{R}^3$ that are equivariant under rotation groups $\mathcal{C}_n$ are determined by just five invariant polynomial functions $f_{ij}(p)$, and they appear in the dynamical equations as shown in Eqs. (14.15) and (14.17).

Example 3: For the group $\mathcal{P}$ in $\mathbb{R}^3$ there are two irreducible representations, $\Gamma^{(1)} = Id$ and $\Gamma^{(2)}$. The coordinates X, Y, Z each carry the representation $\Gamma^{(2)}$. The ring basis consists of the invariant 1 and the three polynomials X, Y, Z. A table for the irreducible content of the two representations Γ^{Def} and Γ^{ring} gives

	$\Gamma^{(1)}$	$\Gamma^{(2)}$
Γ^{Def}	0	3
Γ^{Ring}	1	3

(14.18)

As a result, $\mathcal{P}$ equivariant dynamical systems in $\mathbb{R}^3$ are defined by $(0,3) \cdot (1,3) = 0 \times 1 + 3 \times 3 = 9$ invariant functions $f_{ij}(p)$.

14.2 CAUCHY-RIEMANN SYMMETRIES

The Jacobian of the transformation from the equivariant coordinates $(X_1, X_2, \cdots, X_N)$ to the invariant coordinates $(u_1, u_2, \cdots, u_N)$ exhibits symmetries that reduce, for the groups $\mathcal{C}_n$, to well-known symmetries. These are the Cauchy-Riemann relations of classical complex analysis. These symmetries extend to arbitrary equivariance groups. We analyze these symmetries in this section.

14.2.1 Cauchy-Riemann Conditions for Analytic Functions

The classical Cauchy-Riemann symmetries of complex analysis arise as a condition for a complex mapping $z \to w$ to be "analytic." In this mapping z is a complex variable $z = x + iy$ and its image $w = f(z) = u + iv$ is also a complex variable. The real functions $u = u(x, y)$ and $v = v(x, y)$ are functions of the real and imaginary parts of z. The condition that the mapping be analytic is that the derivative dw/dz exists, independent of direction. The derivative can be written as follows

$$\frac{dw}{dz} = \frac{\left(\frac{\partial u}{\partial x}dx + \frac{\partial u}{\partial y}dy\right) + i\left(\frac{\partial v}{\partial x}dx + \frac{\partial v}{\partial y}dy\right)}{dx + i\,dy} \tag{14.19}$$

We unwind this expression as follows

$$w'(dx + idy) = \left[\frac{\partial u}{\partial x} + i\,\frac{\partial v}{\partial x}\right] dx + \left[\frac{\partial v}{\partial y} - i\,\frac{\partial u}{\partial y}\right] i\,dy \tag{14.20}$$

It is useful (as well as correct) to treat the "infinitesimals" dx and dy as linearly independent basis vectors in some sort of linear vector space. This said, we can equate the coefficients of the two basis vectors dx and dy on the two sides of this expression to find

$$w' = \left[\frac{\partial u}{\partial x} + i\,\frac{\partial v}{\partial x}\right] = \left[\frac{\partial v}{\partial y} - i\,\frac{\partial u}{\partial y}\right] \tag{14.21}$$

Equating the real and imaginary parts of these expressions, we find not only the Cauchy-Reimann conditions for a mapping to be analytic:

$$\begin{aligned} \frac{\partial u}{\partial x} &= +\frac{\partial v}{\partial y} \\ \frac{\partial v}{\partial x} &= -\frac{\partial u}{\partial y} \end{aligned} \tag{14.22}$$

but also two equal expressions for the complex derivative, given in Eq. (14.21).

There is another way to look at the Cauchy-Riemann conditions that is ultimately equivalent but in some sense more useful, and certainly more beautiful. In this interpretation, we assume that the line integral of $w(z)$ is independent of the path, and depends only on the endpoints of the path. If this is the case, the line integral that begins and ends at the same point a in the complex plane vanishes, so that

$$\oint w(z)dz = 0$$

This condition can be reexpressed in a form that is familiar from the analysis of vector fields in 2 and 3 dimensions:

$$\oint (u + iv) \cdot (dx + idy) = \oint u\,dx - v\,dy + i \oint v\,dx + u\,dy \tag{14.23}$$

The well-known condition that both the real and imaginary closed contour integrals vanish is given by Stokes' theorem in the plane:

$$\begin{aligned} \oint u\,dx - v\,dy &= 0 \quad \Leftrightarrow \quad -\frac{\partial v}{\partial x} - \frac{\partial u}{\partial y} = 0 \\ \oint v\,dx + u\,dy &= 0 \quad \Leftrightarrow \quad +\frac{\partial u}{\partial x} - \frac{\partial v}{\partial y} = 0 \end{aligned} \tag{14.24}$$

The results on the right are immediate consequences of the requirement that the curl of the vector fields $(u, -v, 0)$ and $(v, u, 0)$ vanish. For example,

$$\nabla\times(u,-v,0) = \begin{vmatrix} \mathbf{i} & \mathbf{j} & \mathbf{k} \\ \frac{\partial}{\partial x} & \frac{\partial}{\partial y} & \frac{\partial}{\partial z} \\ u(x,y) & -v(x,y) & 0 \end{vmatrix} = 0\mathbf{i} + 0\mathbf{j} + \left(-\frac{\partial v}{\partial x} - \frac{\partial u}{\partial y}\right)\mathbf{k} = 0$$

Stokes' theorem guarantees that the closed contour integral vanishes, or that line integrals between the same endpoints are equal, provided that the curl of the vector field vanishes everywhere inside the region of the plane $\mathbb{R}^2$ interior to the closed contour or bounded by the two paths beginning and ending at the same points, and that there are no singularities in this region.

This interpretation of the Cauchy-Riemann conditions is powerful because it allows us to deform contours throughout a plane, provided we do not allow the contour to cross singularities or to enter "forbidden" regions—for example, holes in the plane that transform the region from simply connected to multiply connected. Such a deformation is illustrated in Fig. 14.3. In this figure we show a small closed contour that is gradually expanded until it moves up against the outer closed contour C_0 and the three interior closed contours C_i, $i = 1, 2, 3$. In the region between these contours the function $w = f(z)$ is assumed to be analytic. There are three short curves that connect the outer contour C_0 to each of the three interior contours C_i. The line integral goes along each of these three arcs twice, once in each direction. These six contributions to the total line integral cancel out pairwise, leaving only the contributions around the outer and three interior contours. The contour integral around the original tiny contour is zero, and it remains zero all the while that the contour is deformed. This shows that

$$\oint_{C_0} f(z)dz + \sum_{i=1}^{3} \oint_{C_i} f(z)dz = 0 \tag{14.25}$$

The integral is clockwise around the three contours C_i and counterclockwise around the contour C_0. With this interpretation, it is just a short step to the discussion of Laurent expansions around singularities and the Cauchy integral theorems. These are in some distant sense related to singularities of local diffeomorphisms, a point to which we will not return.

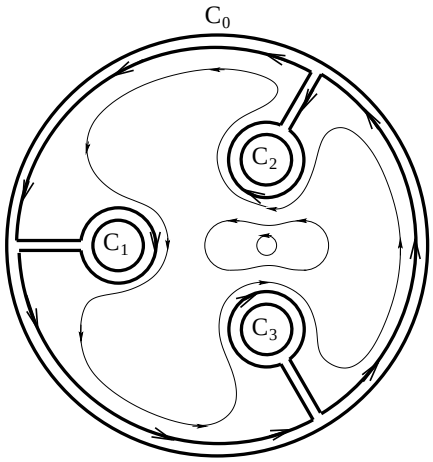

Fig. 14.3 Expansion of a small closed contour into an entire region of the multiply connected complex plane. The expansion can be carried out wherever $f(z) = u(x, y) + iv(x, y)$ satisfies the Cauchy-Riemann, or vanishing curl conditions. The components of the line integrals in opposing directions, connecting the outer contour C_0 with the three inner contours C_i, cancel pairwise. The final result is that the closed contour integral around the outer contour C_0 is equal to the sum of the three closed contour integrals around the three interior holes in the plane, where the integrals are all taken in the clockwise or the counterclockwise direction.

14.2.2 Examples for Analytic Functions

The simplest analytic map is $w = z^2$, for which we find

$$w(z) = u(x, y) + iv(x, y) = (x + iy)^2 = (x^2 - y^2) + i2xy \tag{14.26}$$

From this we conclude that $u(x, y) = x^2 - y^2$ and $v(x, y) = 2xy$. The Cauchy-Riemann conditions are immediately verified:

$$\begin{array}{lcllcl} \dfrac{\partial u}{\partial x} & = & +2x & \dfrac{\partial u}{\partial y} & = & -2y \\ \dfrac{\partial v}{\partial x} & = & +2y & \dfrac{\partial v}{\partial y} & = & +2x \end{array} \tag{14.27}$$

It is useful to treat the Cauchy-Riemann conditions as the Jacobian of the transformation between the variables (u, v) and the variables (x, y):

$$\frac{\partial(u, v)}{\partial(x, y)} = \begin{vmatrix} \dfrac{\partial u}{\partial x} & \dfrac{\partial u}{\partial y} \\ \dfrac{\partial v}{\partial x} & \dfrac{\partial v}{\partial y} \end{vmatrix} \tag{14.28}$$

The Cauchy-Riemann conditions require two symmetries among the four matrix elements: the diagonal matrix elements are equal and the off-diagonal matrix elements

are opposite in sign, so that

$$\frac{\partial(u,v)}{\partial(x,y)} = \begin{vmatrix} \dfrac{\partial u}{\partial x} & \dfrac{\partial u}{\partial y} \\ -\dfrac{\partial u}{\partial y} & \dfrac{\partial u}{\partial x} \end{vmatrix} \xrightarrow{\det} \left(\frac{\partial u}{\partial x}\right)^2 + \left(\frac{\partial u}{\partial y}\right)^2 = \left(\frac{\partial v}{\partial x}\right)^2 + \left(\frac{\partial v}{\partial y}\right)^2 \geq 0$$

The Jacobian is singular only where $\nabla u = \nabla v = 0$.

Example 1: For the complex mapping $w = z^n$, n integer, the derivative is $w' = dw/dz = nz^{n-1}$, from which it is easy to obtain $\frac{\partial u}{\partial x} = \frac{\partial v}{\partial y} = \Re\, n(x+iy)^{n-1}$ and $\frac{\partial v}{\partial x} = -\frac{\partial u}{\partial y} = \Im\, n(x+iy)^{n-1}$. In this example, the z variable provides an n-fold cover of the w variable. There are n values of the variable z, related to each other by phase factor multiplication $z_k = e^{i\phi} z_j$, where z_j and z_k are two of the n distinct values of $z(\neq 0)$ that map to a single value of w, and $e^{i\phi}$ is a phase factor with $\phi = 2\pi/n$ or an integer multiple of this angle. In alternate words, w has n distinct nth roots, one of which belongs to a fundamental domain and the remaining $n-1$ belong to symmetry-related domains, or "sheets" (cf. Fig. 12.1).

Example 2: As a final example of the Cauchy-Riemann conditions in complex analysis, we treat the logarithmic map $w = \ln(z)$. With $r = \sqrt{x^2+y^2}$ and $\phi = \tan^{-1}(y/x)$, we find

$$w = \ln(z) = u + iv = \ln(r\, e^{i(\phi+2\pi k)}) = \frac{1}{2}\ln(x^2+y^2) + i(\phi + 2\pi k)$$

with k integer. From this, we determine

$$\begin{array}{lll} \dfrac{\partial u}{\partial x} = +\dfrac{x}{x^2+y^2} & & \dfrac{\partial u}{\partial y} = +\dfrac{y}{x^2+y^2} \\ \dfrac{\partial v}{\partial x} = -\dfrac{y}{x^2+y^2} & & \dfrac{\partial v}{\partial y} = +\dfrac{x}{x^2+y^2} \end{array} \tag{14.29}$$

In this mapping, w provides an infinite-sheeted cover of the complex variable z: In the z plane the angle ϕ ranges from 0 to 2π, while in the w plane its lift ranges from $-\infty$ to $+\infty$.

14.2.3 Application to Equivariant Dynamical Systems

To illustrate the relation between the Cauchy-Riemann conditions in complex analysis and the analogous relations in the study of local diffeomorphisms, we consider first the Jacobian associated with the symmetry group $\mathcal{R}_Z$ acting in $\mathbb{R}^3$, where the local diffeomorphism is $u = X^2 - Y^2, v = 2XY, w = Z$:

$$\frac{\partial(u,v,w)}{\partial(X,Y,Z)} = \left|\begin{array}{cc|c} 2X & -2Y & 0 \\ 2Y & 2X & 0 \\ \hline 0 & 0 & 1 \end{array}\right| \tag{14.30}$$

The Jacobian must be expressed in terms of the ring basis functions. For this group, these three functions are $1, X, Y$. One of the three coordinates carries the identity representation of this group, so that we can equate one of the new invariant coordinates with one of the original coordinates: $w = Z$. The contribution of this equality to the Jacobian is the ring invariant 1 in the lower right-hand corner of the Jacobian matrix. The matrix elements in the corresponding rows and columns in this matrix are zero. This leaves four matrix elements in the Jacobian of the transformation that are not necessarily zero. These must be expressed in terms of the two remaining (equivariant) ring basis functions. Since $4 - 2 = 2$, there must be two relations among these four remaining matrix elements. The two relations are exactly the Cauchy-Riemann relations — no big surprise since we are working with a complex structure in this local diffeomorphism.

The general situation can be inferred from the preceeding discussion. An equivariance group $\mathcal{G}$ acts in $\mathbb{R}^N(X)$ through the defining matrix representation $\Gamma^{\rm Def}(\mathcal{G})$. This representation contains a spectrum of irreducible representations of $\mathcal{G}$, and in particular, the identity representation is contained $n^{(Id)}$ times in $\Gamma^{\rm Def}(\mathcal{G})$. The implication of this statement is that $n^{(Id)}$ of the new invariant variables can be equated directly to an equal number of the original equivariant variables: $u_j = X_j$, $j = N - n^{(Id)} + 1, \cdots, N$. The ring basis consists of $1 + n^{\rm Ring}$ basis functions, of which one is the invariant 1 and $n^{\rm Ring}$ are equivariant polynomials. The Jacobian of the $|\mathcal{G}| \to 1$ local diffeomorphism $(X_1, X_2, \cdots, X_N) \to (u_1, u_2, \cdots, u_N)$ has the structure

$$\frac{\partial(u_1, u_2, \cdots, u_N)}{\partial(X_1, X_2, \cdots, X_N)} = \left[\begin{array}{c|c} M & 0 \\ \hline 0 & I_{n^{(Id)}} \end{array}\right] \tag{14.31}$$

The $(N - n^{(Id)})^2$ matrix elements of the $(N - n^{(Id)}) \times (N - n^{(Id)})$ matrix M must be expressed in terms of the $n^{\rm Ring}$ equivariant polynomials in the ring basis. Usually there are more matrix elements than equivariant polynomials in the ring basis, so that relations among the matrix elements are forced. In particular, there are

$$\#\,(\text{Cauchy} - \text{Riemann Relations}) = (N - n^{(Id)})^2 - n^{\rm Ring} \tag{14.32}$$

relations among these matrix elements if this difference is positive. Some of the relations may take the form of setting a matrix element equal to zero.

Example 1: For $\mathcal{P}$ acting in $\mathbb{R}^3(X)$, the defining matrix representation has the decomposition $\Gamma^{\rm Def} \simeq 0\Gamma^{(\rm Id)} + 3\Gamma^{(2)}$, so that $N = 3$ and $n^{(Id)} = 0$. The ring basis consists of $1, X, Y, Z$, so that $n^{\rm Ring} = 3$. The number of Cauchy-Riemann relations expected is

$$\#\left(\begin{array}{c}\text{Cauchy-Riemann}\\ \text{Relations}\end{array}\right) = (N - n^{(Id)})^2 - n^{\rm Ring} \to (3-0)^3 - 3 = 6 \tag{14.33}$$

For the local diffeomorphism $u = \frac{1}{2}(X^2 - Y^2), v = \frac{1}{2}(X^2 + Y^2 - 2Z^2), w = XY + YZ + ZX$, the Jacobian is

$$\frac{\partial(u, v, w)}{\partial(X, Y, Z)} = \left[\begin{array}{ccc} X & -Y & 0 \\ X & Y & -2Z \\ Y+Z & Z+X & X+Y \end{array}\right] \tag{14.34}$$

The three matrix elements in the second row can be taken as independent. The remaining six are linear combinations (including 0) of these three independent equivariant ring basis functions. The Cauchy-Riemann relations for $\mathcal{P}$ are

$$\begin{array}{lll} \frac{\partial u}{\partial X} = \frac{\partial v}{\partial X} & -\frac{\partial u}{\partial Y} = \frac{\partial v}{\partial Y} & \frac{\partial u}{\partial Z} = 0 \\ \frac{\partial w}{\partial X} = \frac{\partial v}{\partial Y} - \frac{1}{2}\frac{\partial v}{\partial Z} & \frac{\partial w}{\partial Y} = -\frac{1}{2}\frac{\partial v}{\partial Z} + \frac{\partial v}{\partial X} & \frac{\partial w}{\partial Z} = \frac{\partial v}{\partial X} + \frac{\partial v}{\partial Y} \end{array} \tag{14.35}$$

Example 2: For $\mathcal{V}_4$ acting in $\mathbb{R}^3(X)$, the defining matrix representation has the decomposition $\Gamma^{\mathrm{Def}} \simeq 0\Gamma^{(\mathrm{Id})} + \Gamma^{(2)} + \Gamma^{(3)} + \Gamma^{(4)}$, so that $n^{(Id)} = 0$. The four invariant polynomials in the integrity basis are X^2, Y^2, Z^2, XYZ. In addition to the invariant 1, the equivariant terms in the ring basis consist of all derivatives of the four invariant polynomials with respect to X, Y, and Z, specifically the six polynomials X, Y, Z, YZ, ZX, XY, so that $n^{\mathrm{Ring}} = 6$. The number of Cauchy-Riemann relations expected is

$$\#\,(\mathrm{Cauchy-Riemann\ Rels.}) = (N - n^{(Id)})^2 - n^{\mathrm{Ring}} \rightarrow (3-0)^2 - 6 = 3 \tag{14.36}$$

For the local diffeomorphism $u = \frac{1}{2}(X^2 - Y^2), v = \frac{1}{2}(X^2 + Y^2 - 2Z^2), w = XYZ$, the Jacobian is

$$\frac{\partial(u,v,w)}{\partial(X,Y,Z)} = \begin{bmatrix} X & -Y & 0 \\ X & Y & -2Z \\ YZ & ZX & XY \end{bmatrix} \tag{14.37}$$

One of the three Cauchy-Riemann relations is $\frac{\partial u}{\partial Z} = 0$. The remaining two are $\frac{\partial u}{\partial X} = \frac{\partial v}{\partial X} = X$ and $-\frac{\partial u}{\partial Y} = \frac{\partial v}{\partial Y} = Y$.

14.3 CLEBSCH-GORDAN SYMMETRIES

During the final stages of the construction of the image dynamical system equations from the equivariant equations, the matrix elements of the Jacobian must be combined with the ring basis functions according to the transformation

$$\frac{du_r}{dt} = \frac{\partial u_r}{\partial X_i} f_{is} R_s \tag{14.38}$$

The matrix elements $\partial u_r / \partial X_i$ of the Jacobian are linear in the ring basis functions, as are the source terms $f_{is}R_s$ in the equivariant equations. The construction of invariant driving functions depends on finding bilinear combinations of the ring basis functions that are invariant functions. This is equivalent to coupling basis vectors for direct products of two irreducible representations of a group to form basis vectors for the identity representation of the group. Technically, this is a problem of determining Clebsch-Gordan coupling coefficients.

14.3.1 Clebsch-Gordan Coupling Matrices

Clebsch-Gordan coupling theory is most widely known through its applications in quantum theory, in particular, through the angular momentum coupling coefficients. But it is much more widely applicable. In particular, it applies to the irreducible representations of all groups. To make this explicit, we consider the group $\mathcal{G}$ with irreducible representations Γ^α acting in invariant spaces V^α of dimension n^α. The n^α different basis vectors in V^α are labeled by an index $i = 1, 2, \cdots n^\alpha$. We use Dirac notation to identify the basis vectors in V^α: $\left| \begin{array}{c} \alpha \\ i \end{array} \right\rangle$. The action of $g \in \mathcal{G}$ on these basis vectors is

$$g \left| \begin{array}{c} \alpha \\ i \end{array} \right\rangle = \left| \begin{array}{c} \alpha \\ j \end{array} \right\rangle \left\langle \begin{array}{c} \alpha \\ j \end{array} \right| g \left| \begin{array}{c} \alpha \\ i \end{array} \right\rangle = \left| \begin{array}{c} \alpha \\ j \end{array} \right\rangle \Gamma^\alpha_{ji}(g) \tag{14.39}$$

As usual, intermediate dummy indices are summed over. The direct product linear vector space $V^\alpha \otimes V^\beta$ has as basis vectors the direct product of the basis vectors in each of the two spaces: $\left| \begin{array}{c} \alpha \\ i \end{array} \right\rangle \otimes \left| \begin{array}{c} \beta \\ j \end{array} \right\rangle = \left| \begin{array}{cc} \alpha & \beta \\ i & j \end{array} \right\rangle$. Generally this direct product space is reducible (not invariant). It is useful to decompose this reducible space into the direct sum of irreducible spaces V^γ: $V^\alpha \otimes V^\beta = \sum_\gamma n^\gamma V^\gamma$ where $n^\gamma \geq 0$.

Example: When electrons with orbital angular momenta $l = 2$ and $l = 1$ interact in a spherically symmetric system, the two electron system can have total angular momentum $L = 3, 2, 1$. States with $L = 3$, M in the range $-3 \leq M \leq +3$, are formed by constructing linear combinations of the single electron states according to

$$\left| 2\,1 \begin{array}{c} 3 \\ M \end{array} \right\rangle = \left| \begin{array}{cc} 2 & 1 \\ m_1 & m_2 \end{array} \right\rangle \underbrace{\left\langle \begin{array}{cc} 2 & 1 \\ m_1 & m_2 \end{array} \right| 2\,1 \begin{array}{c} 3 \\ M \end{array} \Big\rangle} \tag{14.40}$$

The sum extends over all intermediate dummy indices (i.e., m_1, m_2). The underlined coefficients in this expression are the angular momentum coupling coefficients: The Clebsch-Gordan coupling coefficients for the rotation group $SO(3)$. They can be worked out, and have been extensively tabulated since they are so useful.

14.3.2 Applications to Finite Groups

For finite groups the coupling scheme is exactly the same:

$$\left| \alpha\beta \begin{array}{c} \gamma \\ k \end{array} \right\rangle = \left| \begin{array}{cc} \alpha & \beta \\ i & j \end{array} \right\rangle \left\langle \begin{array}{cc} \alpha & \beta \\ i & j \end{array} \right| \alpha\beta \begin{array}{c} \gamma \\ k \end{array} \Big\rangle \tag{14.41}$$

If the irreducible representation Γ^γ is contained more than once in the direct product $\Gamma^\alpha \otimes \Gamma^\beta$, an additional index must be inserted in both the ket basis vector $\left| \alpha\beta \begin{array}{c} \gamma \\ k \end{array} , \mu \right\rangle$ and in the Clebsch-Gordan coefficient $\left\langle \begin{array}{cc} \alpha & \beta \\ i & j \end{array} \right| \alpha\beta \begin{array}{c} \gamma \\ k \end{array} , \mu \Big\rangle$ to distinguish among the different subspaces that transform under the same irreducible representation.

For the purposes at hand, we are only interested in pairs of irreducible representations whose direct product contains the identity representation. This information can be teased out of the group character table. We give two examples.

Example 1: The group $\mathcal{C}_3$ has three irreducible representations, $\Gamma^{(i)}$, $i = +, 0, -$. Pairwise products of these three one-dimensional representations are one-dimensional and have the following irreducible representation content:

	$\Gamma^{(0)}$	$\Gamma^{(+)}$	$\Gamma^{(-)}$
$\Gamma^{(0)}$	$\Gamma^{(0)}$	$\Gamma^{(+)}$	$\Gamma^{(-)}$
$\Gamma^{(+)}$	$\Gamma^{(+)}$	$\Gamma^{(-)}$	$\Gamma^{(0)}$
$\Gamma^{(-)}$	$\Gamma^{(-)}$	$\Gamma^{(0)}$	$\Gamma^{(+)}$

(14.42)

From this, we learn the obvious: to construct an invariant we must combine a complex representation with its conjugate, or self-conjugate in the case of the real representation $\Gamma^{(0)}$.

Example 2: The group $\mathcal{T}$ that maps the tetrahedron into itself, excluding reflection operations, consists of 12 group operations. There is one identity operation, three two-fold rotations about the midpoints of opposite edges, and eight three-fold rotations about axes that pass through one vertex and the center of the opposite face. The character table for this group is

$\mathcal{T}$	E	$C_2(3)$	$C_3(4)$	$C_3^2(4)$	Basis Functions
A	1	1	1	1	$x^2+y^2+z^2$
E_1	1	1	ϵ	ϵ^2	$x^2+\epsilon y^2+\epsilon^2 z^2$
E_2	1	1	ϵ^2	ϵ	$x^2+\epsilon^2 y^2+\epsilon z^2$
F	3	-1	0	0	x, y, z

(14.43)

The representations E_1 and E_2 are complex conjugate: their direct sum $E = E_1 \oplus E_2$ is a real 2×2 matrix representation that is irreducible over the real numbers but reducible over the complex field. The two real basis functions for E are equivalent to linear combinations of the complex basis functions for E_1 and E_2: $x^2 - y^2$ and $x^2 + y^2 - 2z^2$. The direct products of the three real representations are given in the table

	A	E	F
A	A	E	F
E	E	$2A+E$	$2F$
F	F	$2F$	$A+E+2F$

(14.44)

For this group there are three cases in which the direct product of two irreducibles produces a representation degeneracy that must be lifted with an additional index μ as described above: $E \otimes E$, $E \otimes F$, and $F \otimes F$. As we are only interested in pairs of irreducible representations that can couple to yield the identity representation, the only tensor products of interest for this group are $A \otimes A$, $F \otimes F$, and $E \otimes E$, and in this last case the two distinct invariants that can be created by coupling pairs of basis

vectors that transform under E must be distinguished by an index. In the case $E \otimes E$ the two sets of functions that transform under the identity representation A can be read directly from the matrix of Clebsch-Gordan coefficients

$$\begin{array}{c} \\ \left| \begin{array}{cc} E & E \\ 1 & 1 \end{array} \right\rangle \\ \left| \begin{array}{cc} E & E \\ 1 & 2 \end{array} \right\rangle \\ \left| \begin{array}{cc} E & E \\ 2 & 1 \end{array} \right\rangle \\ \left| \begin{array}{cc} E & E \\ 2 & 2 \end{array} \right\rangle \end{array} \begin{array}{c} \begin{array}{cccc} \left| \begin{array}{cc} A & 1 \\ 1 & 1 \end{array} \right\rangle & \left| \begin{array}{cc} A & 2 \\ 1 & 2 \end{array} \right\rangle & \left| \begin{array}{c} E \\ 1 \end{array} \right\rangle & \left| \begin{array}{c} E \\ 2 \end{array} \right\rangle \end{array} \\ \left[\begin{array}{cccc} \frac{1}{\sqrt{2}} & 0 & \frac{1}{\sqrt{2}} & 0 \\ 0 & \frac{-i}{\sqrt{2}} & 0 & \frac{-1}{\sqrt{2}} \\ 0 & \frac{i}{\sqrt{2}} & 0 & \frac{-1}{\sqrt{2}} \\ \frac{1}{\sqrt{2}} & 0 & \frac{-1}{\sqrt{2}} & 0 \end{array} \right] \end{array} \tag{14.45}$$

For basis functions $\left\langle \; x \left| \begin{array}{c} E \\ 1 \end{array} \right. \right\rangle = \frac{1}{\sqrt{2}}(x^2 - y^2)$ and $\left\langle \; x \left| \begin{array}{c} E \\ 2 \end{array} \right. \right\rangle = \frac{1}{\sqrt{6}}(x^2 + y^2 - 2z^2)$ the two scalars are

$$\begin{aligned} \left\langle \; x \left| \begin{array}{cc} A & 1 \\ 1 & 1 \end{array} \right. \right\rangle &= \frac{\sqrt{2}}{3}\left[x^4 + y^4 + z^4 - (y^2z^2 + z^2x^2 + x^2y^2)\right] \\ \left\langle \; x \left| \begin{array}{cc} A & 2 \\ 1 & 2 \end{array} \right. \right\rangle &= 0 \end{aligned} \tag{14.46}$$

For the representation F the three basis vectors are (x, y, z). Only one scalar results from the direct product $F \otimes F$: it is the invariant $x^2 + y^2 + z^2$. In fact, for $\mathcal{T}$ this is the only Clebsch-Gordan resolution of interest, since the basis vectors (X, Y, Z) are the equivariant coordinates that define the dynamical system.

14.3.3 Application to Equivariant Dynamical Systems

Most of the groups that we have considered so far are commutative, and therefore have only one-dimensional irreducible representations. For such groups the Clebsch-Gordan coupling problem is rather simple. We illustrate how this works for the commutative group $\mathcal{C}_3$ acting in $\mathbb{R}^3$. We also illustrate how the Clebsch-Gordan symmetry appears in the reduction of equivariant to invariant dynamical systems in more general cases.

In the case of $\mathcal{C}_3$ the nontrivial irreducible representations are complex, so the the equivariant dynamical system equations must be written in complex form to take advantage of the irreducible properties of its representations. In complex form the equivariant equations are

$$\frac{d}{dt}\begin{bmatrix} X + iY \\ X - iY \\ Z \end{bmatrix} = \begin{bmatrix} 0 & f_{11} & 0 & f_{13} & 0 \\ 0 & 0 & f_{11}^* & 0 & f_{13}^* \\ f_{30} & 0 & 0 & 0 & 0 \end{bmatrix} \begin{bmatrix} 1 \\ X + iY \\ X - iY \\ (X - iY)^2 \\ (X + iY)^2 \end{bmatrix} \tag{14.47}$$

The invariant dynamical system equations, in complex form using $(X+iY)^3 = u+iv$, are

$$\frac{d}{dt}\begin{bmatrix} u+iv \\ u-iv \\ w \end{bmatrix} = \begin{bmatrix} 3(X+iY)^2 & 0 & 0 \\ 0 & 3(X-iY)^2 & 0 \\ 0 & 0 & 1 \end{bmatrix} \times \begin{bmatrix} 0 & f_{11} & 0 & f_{13} & 0 \\ 0 & 0 & f_{11}^* & 0 & f_{13}^* \\ f_{30} & 0 & 0 & 0 & 0 \end{bmatrix} \begin{bmatrix} 1 \\ X+iY \\ X-iY \\ (X-iY)^2 \\ (X+iY)^2 \end{bmatrix}$$

$$= \begin{bmatrix} 3(X+iY)^2\left\{f_{11}(X+iY)+f_{13}(X-iY)^2\right\} \\ 3(X-iY)^2\left\{f_{11}^*(X-iY)+f_{13}^*(X+iY)^2\right\} \\ 1\times f_{30}\times 1 \end{bmatrix} \tag{14.48a}$$

$$= \begin{bmatrix} 0 & 3f_{11} & 0 & 3f_{13} \\ 0 & 0 & 3f_{11}^* & 3f_{13}^* \\ f_{30} & 0 & 0 & 0 \end{bmatrix} \begin{bmatrix} w \\ u+iv \\ u-iv \\ r_4^2 \end{bmatrix} \tag{14.48b}$$

In proceeding to the last equation, we have used the relations

$$\begin{bmatrix} Z \\ (X+iY)^3 \\ (X-iY)^3 \\ (X^2+Y^2)^2 \end{bmatrix} = \begin{bmatrix} w \\ u+iv \\ u-iv \\ r_4^2 \end{bmatrix} \tag{14.49}$$

It is no surprise that:

1. In final form the invariant equations are expressed in terms of a small set of nonzero invariant functions f_{ij} whose number is determined by the spectrum of irreducible representations in Γ^{Def} and Γ^{Ring} (cf. Equ. (14.9)).

2. A small set of invariant polynomials w, u, v and the radical r_4.

3. The latter set of functions consists of only those invariant polynomials that can be constructed as invariant bilinear combinations of the ring basis set according to the Clebsch-Gordan series

$$\begin{aligned} \left\langle\, x \,\middle|\, \begin{matrix} A \\ 1 \end{matrix} \,\right\rangle &= \left\langle\, x \,\middle|\, \begin{matrix} \alpha & \beta \\ i & j \end{matrix} \,\right\rangle \left\langle\, \begin{matrix} \alpha & \beta \\ i & j \end{matrix} \,\middle|\, \alpha\beta \begin{matrix} A \\ 1 \end{matrix} \,\right\rangle \\ &= R_i^{(\alpha)}(X) R_j^{(\beta)}(X) \left\langle\, \begin{matrix} \alpha & \beta \\ i & j \end{matrix} \,\middle|\, \alpha\beta \begin{matrix} A \\ 1 \end{matrix} \,\right\rangle \end{aligned} \tag{14.50}$$

For $\mathcal{C}_3$ the ring basis functions and their transformation properties are

Irreducible Representation	Ring Basis
$\Gamma^{(0)}$	$R_1^{(0)} = 1$
$\Gamma^{(+)}$	$R_1^{(+)} = X + iY,\ \ R_2^{(+)} = (X - iY)^2$
$\Gamma^{(-)}$	$R_1^{(-)} = X - iY,\ \ R_2^{(-)} = (X + iY)^2$

The only invariant polynomials that can be constructed from this set are

$$\begin{array}{lcccccl} R_1^{(0)}R_1^{(0)} & = & 1 \times 1 & = & 1 & = & 1 \\ R_1^{(+)}R_1^{(-)} & = & (X+iY)(X-iY) & = & X^2+Y^2 & = & r_4 \\ R_1^{(+)}R_2^{(-)} & = & (X+iY)(X+iY)^2 & = & (X+iY)^3 & = & u+iv \\ R_2^{(+)}R_1^{(-)} & = & (X-iY)^2(X-iY) & = & (X-iY)^3 & = & u-iv \\ R_2^{(+)}R_2^{(-)} & = & (X-iY)^2(X+iY)^2 & = & (X^2+Y^2)^2 & = & r_4^2 \end{array} \tag{14.51}$$

Since only the ring basis functions $R_1^{(0)},\ R_2^{(+)},\ R_2^{(-)}$ occur in the Jacobian, the only invariant functions that can occur in the final expression for the invariant dynamical system are the functions $1,\ u+iv,\ u-iv$, and r_4^2. These results can be summarized in the following table:

Ring / Jacobian	$R_1^{(0)}$	$R_1^{(+)}$	$R_1^{(-)}$	$R_2^{(+)}$	$R_2^{(-)}$
$R_1^{(0)}$	$\begin{matrix}1\\ f_{30}\end{matrix}$	0	0	0	0
$R_2^{(+)}$	0	0	$\begin{matrix}u-iv\\ 3f_{11}^*\end{matrix}$	0	$\begin{matrix}r_4^2\\ 3f_{13}^*\end{matrix}$
$R_2^{(-)}$	0	$\begin{matrix}u+iv\\ 3f_{11}\end{matrix}$	0	$\begin{matrix}r_4^2\\ 3f_{13}\end{matrix}$	0

(14.52)

The column on the left shows the ring basis functions that occur in the Jacobian $\partial u_i/\partial X_j$. Only three ring basis functions occur in the Jacobian, $1,\ (X+iY)^2,\ (X-iY)^2$, so only those three are listed. The top row lists all the ring basis functions that have the appropriate transformation properties. "Appropriate transformation properties" means simply that they transform under the same irreducible representations as occur in $\Gamma^{\mathrm{Def}}(\mathcal{G})$. For $\mathcal{C}_3$ all (linear combinations of) the ring basis functions carry one of the irreducible representations in $\Gamma^{\mathrm{Def}}(\mathcal{C}_3)$, so all five are listed in the top row of this table. The entries in this table are of two types. If the identity representation is not contained in the direct product $\Gamma^{(\alpha)} \times \Gamma^{(\beta)}$, the matrix element is 0. If the identity representation is contained in the direct product $\Gamma^{(\alpha)} \times \Gamma^{(\beta)}$, the invariant(s) constructed from $R_i^{(\alpha)}(X) \times R_j^{(\beta)}(X)$ is listed, together with the invariant function f_{ij} that is coupled to $R_j^{(\beta)}(X)$ in the equivariant dynamical system. The invariants can be expressed in either the invariant coordinate systsem (u, v, w) or the original coordinate system (X, Y, Z).

Remark: For the group $\mathcal{C}_n$, $n > 3$, the analysis proceeds as shown in Eq. (14.51). The invariants in Γ^{Jacob} transform like Γ^0 and $\Gamma^{\pm 1}$. They are 1 and $\begin{matrix}\text{Re}\\ \text{Im}\end{matrix}\ (X \mp iY)^{n-1}$. Although the ring basis has $1 + 2(n-1)$ functions, only five transform under the irreducible representations contained in $\Gamma^{\text{Def}} \simeq \Gamma^0 + \Gamma^+ + \Gamma^-$. These are $R^{(0)} = 1,\ R_1^{(\pm)} = (X \pm iY)^1,\ R_2^{(\pm)} = (X \mp iY)^{n-1}$. Therefore, for $\mathcal{C}_n$ the table in (14.52) is replaced by

Ring / Jacobian	$R_1^{(0)}$	$R_1^{(+)}$	$R_1^{(-)}$	$R_2^{(+)}$	$R_2^{(-)}$
$R_1^{(0)}$	$\begin{matrix}1\\ f_{30}\end{matrix}$	0	0	0	0
$R_2^{(+)}$	0	0	$\begin{matrix}u - iv\\ nf_{11}^*\end{matrix}$	0	$\begin{matrix}r_4^{n-1}\\ nf_{13}^*\end{matrix}$
$R_2^{(-)}$	0	$\begin{matrix}u + iv\\ nf_{11}\end{matrix}$	0	$\begin{matrix}r_4^{n-1}\\ nf_{13}\end{matrix}$	0

(14.53)

The general algorithm should now be clear. The invariant equations are

$$\frac{du_i}{dt} = \frac{\partial u_i}{\partial X^j} F_j(X) \tag{14.54}$$

The driving functions are replaced by their expansion in terms of the appropriate ring basis functions

$$F_j(X) \longrightarrow f_{j;\beta s}(p) R_s^\beta(X) \tag{14.55a}$$

and the Jacobian are expressed in terms of the appropriate ring basis functions

$$\frac{\partial u_i}{\partial X^j} \longrightarrow J_{ij;\alpha r} R_r^\alpha(X) \tag{14.55b}$$

The invariant equations have the form

$$\frac{du_i}{dt} = J_{ij;\alpha r} R_r^\alpha(X) f_{j;\beta s}(p) R_s^\beta(X) = \{J_{ij;\alpha r} f_{j;\beta s}(p)\} \left\{R_r^\alpha(X) \times R_s^\beta(X)\right\} \tag{14.56}$$

The Jacobian matrix elements $J_{ij;\alpha r}$ vanish unless $\Gamma^{(\alpha)} \times \Gamma^{(\beta)}$ contains the identity. If so, these matrix elements are the Clebsch-Gordan coefficients that couple $\left\{R_r^\alpha(X) \times R_s^\beta(X)\right\}$ to the invariant(s) that can be projected out. The coefficient of this invariant is the linear combination of invariant functions $\left\{\sum_j J_{ij;\alpha r} f_{j;\beta s}(p)\right\}$.

14.4 CONTINUATIONS

Analytic continuation of functions of a complex variable plays an important role in pure and applied mathematics, experimental and theoretical physics, and the engineering disciplines. The classical formulation of analytic continuations involves complex

variable $f(z) = u + iv$, where $z = x + iy$, singularities, and some magic involving somehow bypassing or avoiding the singularity in an elegant way. We have found all three ingredients in some of our applications of local diffeomorphisms to the theory of dynamical systems. These have involved the rotation groups $\mathcal{C}_n$. Many other groups can be used to map equivariant to image systems, or lift image systems to equivariant covers. We would therefore expect that the concept of "analytic continuation" can be extended beyond the applications to rotation groups $\mathcal{C}_n$ and the complex variable $z = x + iy$ on which they act.

In this expectation we are correct. Analytic continuation can be extended to a more general setting involving dynamical systems, groups, and topology. In two different ways, in fact. One is "topological continuation", the other is "group continuation." These are illustrated by application to a flow represented by a particular branched manifold—the figure 8 branched manifold, in Sections 14.4.2 and 14.4.3. First, we review the basic idea of analytic continuation so that the resonance between the classical theory of analytic continuation of complex functions and the newer theory of topological and group continuation of flows can be highlighted.

14.4.1 Analytic Continuation

A function of a single complex variable z is said to be *analytic* on a domain if it is differentiable and satisfies the Cauchy-Riemann conditions everywhere on the domain. Analytic functions are very highly constrained: they have a very rich, rigid, beautiful set of properties. The cost for this is that they form a very restricted set of functions defined on the complex plane. Most functions on the complex plane are functions of the complex variable z and its conjugate $\overline{z}$ while analytic functions do not depend on $\overline{z}$.

One of the beautiful properties of analytic functions is the property of analytic continuation. If

- $f_1(z)$ is analytic on a domain D_1 in the complex plane
- $f_2(z)$ is analytic on a domain D_2 in the complex plane
- The domains overlap in an open set: $D_1 \cap D_2 \neq \phi$
- $f_1(z) = f_2(z)$ for all $z \in D_1 \cap D_2$

then $f_1(z)$ is called "the analytic continuation" of $f_2(z)$ to domain D_1, and by symmetry $f_2(z)$ is called the analytic continuation of $f_1(z)$ to domain D_2. If a function has an analytic continuation to some domain, that analytic continuation is unique. There is an "existence and uniqueness" theorem for analytic continuations (if it exists, it is unique).

Example: The factorial function

$$n! = 1 \times 2 \times 3 \times \cdots \times n \tag{14.57a}$$

is one of the workhorses of mathematics and physics. It is defined recursively as a multiplicative function for all the positive integers $n = 1, 2, \ldots$. Its value for $n = (1, 2, 3, 4, 5, \ldots)$ is $n! = (1, 2, 6, 24, 120, \ldots)$. It is also useful to define $0! = 1$.

The first step in generalizing this function is to construct an integral representation for it:

$$(n-1)! = \Gamma_M(n) = \int_0^\infty e^{-t} t^{n-1} dt \qquad n \text{ integer}, n > 0 \tag{14.57b}$$

The second equality is the definition of $\Gamma_M(n)$. The first equality is demonstrated by carrying out a succession of integrations by parts.

This function can be extended from the positive integers to the real numbers by replacing $n \to x$:

$$\Gamma_I(x) = \int_0^\infty e^{-t} t^{x-1} dt \qquad x \text{ real}, x > 0 \tag{14.57c}$$

This reduces to $\Gamma_M(n)$ for $x \to n$.

This gamma function was extended off the real axis into the positive half of the complex plane by Euler, by replacing $x \to z$:

$$\Gamma_E(z) = \int_0^\infty e^{-t} t^{z-1} dt \qquad z \text{ complex}, \ \operatorname{Re} z > 0 \tag{14.57d}$$

The integral over t remains along the positive real axis. The complex function defined by Eq. (14.57d) is analytic.

Euler defined a version of this complex function in the form of a multiplicative limit

$$\Gamma_{EM}(z) = \lim_{n\to\infty} \frac{n^z}{z} \frac{(0+1)(0+2)(0+3)\cdots(0+n)}{(z+1)(z+2)(z+3)\cdots(z+n)} \tag{14.57e}$$

for all values of z except for the negative integers and 0: $z \neq 0, -1, -2, \cdots$. It is possible to show that $\Gamma_{EM}(z) = \Gamma_E(z)$ in the positive half plane. Therefore the multiplicative limit $\Gamma_{EM}(z)$ is an analytic continuation of Euler's gamma function $\Gamma_E(z)$ into the entire complex plane except for $z - 1$ a negative integer.

Obsevation: Each extension $\Gamma_M(n) \to \Gamma_I(x) \to \Gamma_E(z) \to \Gamma_{EM}(z)$ can be regarded as a "continuation". The last is an analytic continuation. The function $\Gamma_{EM}(z)$ is unique although its representation (as a limit) is not. In practice, $\Gamma_{EM}(z)$ is computed by extending $\Gamma_E(z)$ from the positive half plane into the negative half plane by successively applying the continuation formula

$$\Gamma_{EM}(z)\Gamma_{EM}(1-z) = \frac{\pi}{\sin \pi z} \tag{14.57f}$$

The complex gamma function has an elegant representation as a sum over simple poles:

$$\Gamma_{EM}(z) = \sum_{n=0}^{\infty} \frac{A_n}{(z+n)} \qquad (-1)^n n! A_n = 1 \tag{14.57g}$$

It may be objected that this representation of the gamma function is "recursive" in that it is defined in terms of itself ($n!$), but this is not the case, as it is defined in terms of the factorial function defined for the positive integers (and 0) given in Eq. (14.57a).

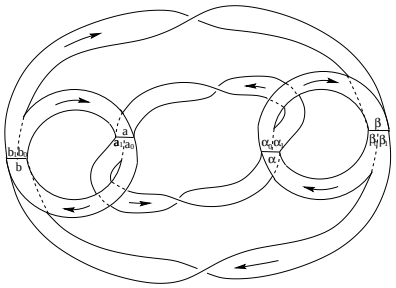

$$
\begin{array}{c}
 \\
\alpha_0 \\
\alpha_1 \\
\beta_0 \\
\beta_1 \\
a_0 \\
a_1 \\
b_0 \\
b_1
\end{array}
\begin{array}{c}
\begin{array}{cccccccc} \alpha_0 & \alpha_1 & \beta_0 & \beta_1 & a_0 & a_1 & b_0 & b_1 \end{array} \\
\left[\begin{array}{cccccccc}
 & & 1 & 1 & & & & \\
 & & & & 1 & 1 & & \\
1 & 1 & & & & & & \\
 & & & & & & 1 & 1 \\
 & & & & & & 1 & 1 \\
1 & 1 & & & & & & \\
 & & & & 1 & 1 & & \\
 & & 1 & 1 & & & &
\end{array}\right]
\end{array}
$$

Fig. 14.4 Branched manifold for the figure 8 knot. This branched manifold describes a dynamical system that is equivariant under the symmetry group $\mathcal{R}_Z(\pi)$. The transition matrix indicates the connectivity of the branches of this template.

14.4.2 Topological Continuation

The very first branched manifold described by Birman and Williams in [15] is the branched manifold of the figure 8 knot. This branched manifold is shown in Fig. 14.4.

This branched manifold arises in a very natural way. Imagine a current flowing through a straight wire. The current flow generates a magnetic field. All magnetic field lines are closed. They are circles in planes perpendicular to the wire. If the wire is deformed, most of the closed field lines (analogous to periodic orbits in a dynamical system) are destroyed. If the wire is deformed into a figure 8 knot, a countable subset of closed field lines is not destroyed. These closed field lines are organized in a very specific way with each other. Their organization can be specified by their mutual linking numbers. In fact, Birman and Williams argue that all closed field lines can be homotoped to the branched manifold shown in Fig. 14.4. Homotoping is a continuous deformation in which the closed lines undergo no self- or mutual intersections. Thus, their topological organization is uniquely specified by the branched manifold.

The figure 8 knot, and its branched manifold, can be exhibited in a way that makes the rotation symmetry explicit. The branched manifold has eight branches, (a_0, a_1), (b_0, b_1), and the symmetry-related branches (α_0, α_1), (β_0, β_1). These are shown in Fig. 14.4. The branch line a is the source for flows through branches a_0 and a_1; similarly for the other three branch lines and six branches. As usual, a trajectory is labeled by the branches through which it travels.

There are four fundamental (lowest period) orbits, which may be taken as $(a_0 b_0)$, $(\alpha_0 \beta_0)$, and $(a_1 \alpha_1)$, $(b_1 \beta_1)$. The linking numbers of these periodic orbits with the

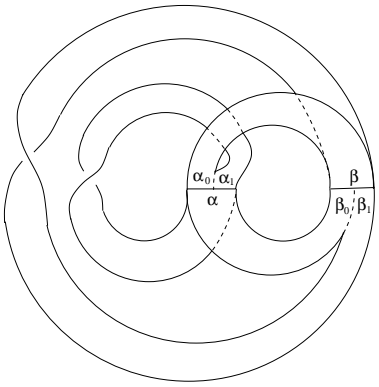

$$\begin{array}{c} \\ \alpha_0 \\ \alpha_1 \\ \beta_0 \\ \beta_1 \end{array} \begin{array}{c} \begin{array}{cccc} \alpha_0 & \alpha_1 & \beta_0 & \beta_1 \end{array} \\ \begin{bmatrix} & & 1 & 1 \\ 1 & 1 & & \\ 1 & 1 & & \\ & & 1 & 1 \end{bmatrix} \end{array}$$

Fig. 14.5 Image of the branched manifold of the figure 8 knot and its transition matrix.

symmetry axis are

$$\begin{array}{cc} a_0 & b_0 \\ \alpha_0 & \beta_0 \\ a_1 & \alpha_1 \\ b_1 & \beta_1 \end{array} \qquad \begin{array}{c} 0 \\ 0 \\ +1 \\ -1 \end{array}$$

The symmetry of this dynamical system can be reduced by modding out the $\mathcal{R}_Z(\pi)$ symmetry. This has the effect of identifying the branches $a \leftrightarrow \alpha$ and $b \leftrightarrow \beta$. The resulting branched manifold without symmetry is shown in Fig. 14.5. The image system has four branches and three fundamental orbits

$$\begin{array}{cc} \alpha_0 & \beta_0 \\ \alpha_1 & \\ \beta_1 & \end{array} \qquad \begin{array}{c} 0 \\ +1 \\ -1 \end{array}$$

The flows on the cover branched manifold in Fig. 14.4 and the image branched manifold in Fig. 14.5 are locally diffeomorphic. There is a $2 \rightarrow 1$ relation between them.

This branched manifold, with four branches and two branch lines, has many inequivalent double covers. One is the original branched manifold of the figure 8 knot. Other inequivalent covers can be constructed by changing the topological index $\bar{\bar{\mathbf{n}}}$, changing the group $\mathcal{G}$, or changing both. The index for the image is three-dimensional: $\bar{\bar{\boldsymbol{n}}} = (n_{(\alpha_0\beta_0)}, n_{\alpha_1}, n_{\beta_1})$.

The image branched manifold shown in Fig. 14.5 has topological index

$$\bar{\bar{\boldsymbol{n}}}(n_{(\alpha_0\beta_0)}, n_{\alpha_1}, n_{\beta_1}) = (0, +1, -1) \tag{14.58}$$

If we construct a double cover of this branched manifold with this index, we recover the original figure 8 branched manifold when $\mathcal{G} = \mathcal{R}_Z$. However, it is possible to

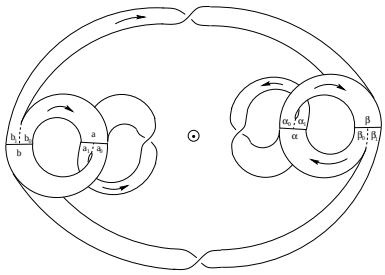

$$
\begin{array}{c}
 \\
\alpha_0 \\
\alpha_1 \\
\beta_0 \\
\beta_1 \\
a_0 \\
a_1 \\
b_0 \\
b_1
\end{array}
\begin{array}{c}
\begin{array}{cccccccc} \alpha_0 & \alpha_1 & \beta_0 & \beta_1 & a_0 & a_1 & b_0 & b_1 \end{array} \\
\left[\begin{array}{cccccccc}
 & & 1 & 1 & & & & \\
1 & 1 & & & & & & \\
1 & 1 & & & & & & \\
 & & & & & & 1 & 1 \\
 & & & & & & 1 & 1 \\
 & & & & 1 & 1 & & \\
 & & & & 1 & 1 & & \\
 & & 1 & 1 & & & &
\end{array}\right]
\end{array}
$$

Fig. 14.6 Another lift of the image branched manifold shown in Fig. 14.5. This cover retains the original symmetry group $\mathcal{R}_Z(\pi)$ of the branched manifold of the figure 8 knot, but has a different topological index. The transition matrix differs from that shown in Fig. 14.4.

place the rotation axis in many other places. For example, if we move the rotation axis so that the topological index is

$$\bar{\bar{\boldsymbol{n}}}(n_{(\alpha_0\beta_0)}, n_{\alpha_1}, n_{\beta_1}) = (0, 0, -1) \tag{14.59}$$

the double cover is topologically distinct from the original branched manifold in Fig. 14.4. The double cover obtained in this way is shown in Fig. 14.6. Its transition matrix is presented also. This branched manifold has: four branch lines; eight branches; and five fundamental orbits—a_1, α_1, (a_0, b_0), (α_0, β_0), (b_1, β_1).

The image branched manifold Fig. 14.5 and its two double covers Fig. 14.4 and Fig. 14.6 are all locally diffeomorphic. The double covers are topological continuations of each other. They both cover the same image and have the same symmetry, but the singular sets of their local diffeomorphisms have different topological indices with the image. The image has many other double covers with $\mathcal{R}_Z$ symmetry, each with a different topological index. All are topological continuations of each other. All have different transition matrices.

14.4.3 Group Continuation

The image branched manifold in Fig. 14.5 can be lifted to a double cover with inversion symmetry $\mathcal{P}$. This lift is shown in Fig. 14.7. Its transition matrix is the same as that of the original figure 8 branched manifold shown in Fig. 14.4. The branched manifolds of Fig. 14.4 and Fig. 14.7, and the flows they represent, are group continuations of each other.

The general case is as follows. Two dynamical systems, $\mathcal{D}_1$ and $\mathcal{D}_2$, with equivariance groups $\mathcal{G}_1$ and $\mathcal{G}_2$, are group continuations of each other if the two groups

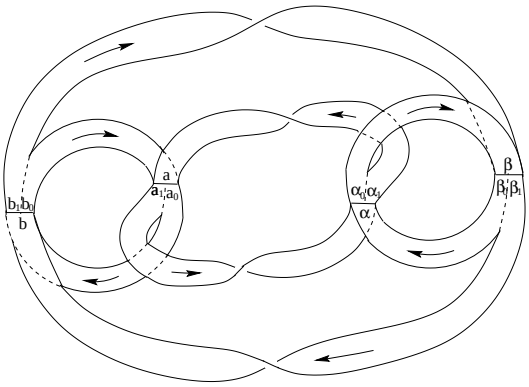

$$\begin{array}{c} \\ a \\ b \\ \alpha \\ \beta \end{array} \begin{array}{c} \begin{array}{cccc} a & b & \alpha & \beta \end{array} \\ \begin{bmatrix} 0 & 1 & 1 & 0 \\ 1 & 0 & 0 & 1 \\ 1 & 0 & 0 & 1 \\ 0 & 1 & 1 & 0 \end{bmatrix} \end{array}$$

Fig. 14.7 A cover of the image branched manifold shown in Fig. 14.5. This cover has symmetry group $\mathcal{P}$. It is a group continuation of the original branched manifold of the figure 8 knot, which has symmetry group $\mathcal{R}_Z(\pi)$ and is shown in Fig. 14.4. Both covers have the same transition matrix. The transition matrices in Fig. 14.4 and this figure are distinct, but equivalent, ways to present the same information.

have the same order and diffeomorphic images $\underline{\mathcal{D}}$ when the symmetry is modded out. These conditions can be represented as follows

$$\frac{\mathcal{D}_1}{\mathcal{G}_1} \rightarrow \underline{\mathcal{D}} \leftarrow \frac{\mathcal{D}_2}{\mathcal{G}_2} \tag{14.60}$$

Part III

Symmetry without Groups: Topology

15

Symmetry without Groups: "Topological Symmetry"

15.1 COVERS AND IMAGES

Cover-image relations occur naturally whenever a $g \to 1$ ($g \geq 2$) local diffeomorphism can be constructed and used to lift a strange attractor in $\mathbb{R}^n$ ($n \geq 3$) to a g-fold cover in $\mathbb{R}^n$. Local diffeomorphisms can be constructed algorithmically whenever a symmetry group of order $g = |\mathcal{G}|$ is identified and its action on $\mathbb{R}^n$ is given through a defining representation (cf. Chapters 3–6).

We have studied the cover-image relation primarily in $\mathbb{R}^3$ for two important reasons. Most of the strange attractors that have been studied so far exist in $\mathbb{R}^3$. More importantly, chaos in three dimensions is reasonably well understood by now [33,34]; this is not the case for chaos in dimensions $n > 3$.

Strange attractors in $\mathbb{R}^3$ are conveniently described by the branched manifold they project to under the Birman-Williams identification. If the branched manifold of an image attractor has m branches $b_1, b_2, \cdots, b_m$ and n branch lines $l_1, l_2, \cdots, l_n$, then its $\mathcal{G}$-equivariant cover is described by a branched manifold with $m \times g$ branches and $n \times g$ branch lines. Each branch in the cover is described by two indices: b_i and g_j. Each of the g branches (b_i, g_j), $j = 1, 2, \cdots, |\mathcal{G}|$ maps to the same branch b_i in the image. Under the action of the symmetry group operation g_k, the branch (b_i, g_j) is mapped to the branch $(b_i, g_k g_j)$:

$$g_k(b_i, g_j) = (b_i, g_k g_j)$$

Similar statements hold for the branch lines in the $\mathcal{G}$-equivariant cover and its image.

A strange attractor can be lifted to many inequivalent covering strange attractors, each with the same equivariance group $\mathcal{G}$. These inequivalent strange attractors can be distinguished by an index. We have introduced the index as a topological quantity, but in fact it is really an algebraic quantity. The index is equivalent to a transition matrix: it specifies the connectivity between the branches (b_i, g_j) and $(b_{i'}, g_{j'})$, or equivalently between the branch lines (l_i, g_j) and $(l_{i'}, g_{j'})$. A transition matrix in the cover is allowed if, under the $g \to 1$ local diffeomorphism to the image, it projects to the transiton matrix describing the image branched manifold. We can rephrase this condition as follows: The index of a cover is a matrix. The spectrum of indices allowed for a cover is the set of inverse images of the transition matrix for the image branched manifold.

The symmetry group $\mathcal{G}$ serves to provide labels that distinguish among the g lifts of each branch b_i and each branch line l_j. Pairs of group elements serve to identify the nonzero matrix elements in the transition matrix for the cover. Transitivity under the group action serves to place constraints on the allowed covers.

There are other ways to achieve these ends. One of them will be described at length in this chapter. In some sense it is more satisfying than the approach using symmetry groups, as the spectrum of indices in the cover is generated by the dynamics itself, rather than by a symmetry.

This alternative approach depends on "bounding tori" [124,125]. These are smooth surfaces that surround strange attractors, or more precisely, the branched manifolds that characterize them. Bounding tori can be constructed algorithmically and enumerated systematically. They organize the branched manifolds that can exist within them in the same way that branched manifolds organize the unstable periodic orbits that they carry ("within them"). There is a much richer variety of bounding tori than equivariant covers. And there are many $g \to 1$ local diffeomorphisms among bounding tori with the proper properties. We turn our attention now to bounding tori.

15.2 BOUNDING TORI

Our description of "equivariance without groups" will be carried out for strange attractors in $\mathbb{R}^3$ because all the apporpriate tools are available in this dimension.

15.2.1 Strange Attractors in R^3

Three-dimensional strange attractors have a spectrum of three Lyapunov exponents that satisfy $\lambda_1 > 0$, $\lambda_2 = 0$, $\lambda_3 < 0$, where the sum of the three exponents is less than zero. As a result, the Lyapunov dimension $d_L = 2 + \epsilon < 3$, where $\epsilon = \lambda_1/|\lambda_3|$.

The Birman-Williams theorem has been a powerful tool for the analysis of such strange attractors. Essentially, this theorem identifies all points with the same future. Equivalently, points along the same stable manifold are projected down along this manifold to a point on an unstable manifold. This projection has two types of singularities: branch lines and splitting points. Flows from different parts of the attractor come together at branch lines, and flows on different "sides" of splitting points go to different parts of the attractor. The image of the flow under the Birman-Williams projection is a semiflow—a flow with a unique future but not a unique past. The semiflow exists on a caricature of the strange attractor—a two-dimensional structure that is a manifold almost everywhere. It is called a branched manifold.

Branched manifolds were originally introduced in order to provide an organizational structure for all the unstable periodic orbits in a strange attractor [14, 15]. Subsequently they have been used to identify and to characterize strange attractors [87, 127]. Information about branched manifolds can be extracted from experimental data [89].

The objective of this section is the construction of two-dimensional boundaries surrounding (or containing) branched manifolds. These boundaries play the same role for branched manifolds as branched manifolds play for periodic orbits in strange attractors. The boundaries are "branched manifold organizers."

15.2.2 Blow-Ups of Branched Manifolds

Strange attractors are generated by vector fields. A vector field, for example, is the set of three forcing functions (f_1, f_2, f_3) that define a deterministic flow in any of the three-dimensional dynamical systems treated so far in this work. Singularities of vector fields are points at which the vector field has a zero (fixed point): $(f_1, f_2, f_3) = (0, 0, 0)$. A singularity is isolated, or nondegenerate, if it does not split into two or more singularities under perturbation. The fixed points of the vector field play a major role in organizing the structure of the flow that is generated by the vector field [100]. When the vector field generates a strange attractor, that attractor can be projected down to a semiflow on a branched manifold. There are no fixed points in the semiflow. In fact, the flow on the branched manifold is everywhere bounded above zero. The structure of the branched manifold is determined to a great extent by the distribution of the singularities of the vector field.

Remark: In the work that follows the only singularities that we consider are the zeroes of the vector field. We explicitly do not consider discontinuities, points of nondifferentiability, or poles of vector fields.

It is useful and also possible to partition $\mathbb{R}^3$ into two parts. One part contains all the singularities of the vector field that generates the flow; the other part contains the branched manifold that is a rigorous caricature of the strange attractor. This is

done as follows [125]. Each point in the branched manifold is surrounded by a small open ball of radius ϵ. The union of these open balls is a three-dimensional manifold because all of the singularities in the branched manifold (splitting points and branch lines) have been eliminated by this smoothing. This three-dimensional manifold fits over the branched manifold like a glove over a hand. This manifold is an *attracting manifold* for the semiflow on the branched manifold. The attracting manifold has the following properties:

Trapping: Once a trajectory enters the attracting manifold, it never escapes.

Relaxing: Points within the attracting manifold approach the attractor exponentially fast.

Singularities: The vector field within the attracting manifold has no singularities.

Boundary Is Orientable: The boundary of the attracting manifold is two-sided. The branched manifold is on the inside and all the singularities of the vector field are on the outside.

15.2.3 The Boundary

The boundary is two-dimensional and two-sided: there is an inside and an outside. The inside contains the attractor. The outside contains the singularities of the flow. Once a trajectory passes through the boundary (only one direction of passage is possible) it is trapped inside forever, and rapidly (exponentially, with exponent λ_3) "falls" to the branched manifold under the flow that limits to the semiflow on the branched manifold.

Since this surface is the boundary of a three-dimensional manifold, it has no boundary itself. This is a result of a powerful theorem of topology: the boundary of a boundary is empty [108].

There is something magic about two-dimensional surfaces without boundaries. They have all been classified [134]. The subset of *orientable* (two-sided) two-dimensional manifolds without boundary consists of the sphere (torus with no holes), the torus (with one hole), and the torus with g holes. These are collectively called tori with g holes, or genus-g surfaces, $g = 0, 1, 2, \cdots$. All tori with g holes are topologically equivalent. "The" torus with g holes is not equivalent to the torus with g' holes, $g \neq g'$. The three-dimensional manifold surrounded by a torus with g holes is called a genus-g *handlebody*.

The branched manifold describing any three-dimensional strange attractor is embedded in a genus-g handlebody that is bounded by a genus-g torus.

This classification is *intrinsic*. A more refined classification describes the extrinsic classification: how the genus-g surface is embedded in $\mathbb{R}^3$ or $\mathbb{M}^3$. At present this is an open problem for genus-g bounding tori. However, this problem has been solved in the genus-one case. The extrinsic classification of genus-one tori will be described in Section 16.5.

15.2.4 Euler Characteristic

There is a beautiful result of a topological nature that allows us to classify these boundaries in a simple and elegant way. This is a topological index (an integer), first proposed by Euler [5]. This index is called the Euler characteristic of a manifold. We describe it briefly for a bounded two-dimensional manifold. It generalizes to higher dimensional bounded manifolds easily.

Every bounded two-dimensional surface can be "triangulated." That is, it is approximated by a series of triangles. Adjacent triangles share common points and edges. The Euler characteristic for a surface is

$$\chi(S) = N_0 - N_1 + N_2 \tag{15.1}$$

The characteristic is the alternating sum of the number of points or vertices (N_0), the number of edges (N_1), and the number of triangles (N_2). In this triangulation, or approximation by simplices, the alternating sum is independent of the triangulation used.

Boundaries of the attracting manifolds constructed above are tori of genus g. All genus-g tori are topologically equivalent. The Euler characteristic of a torus of genus g is [5]

$$\chi(\text{genus } g \text{ torus}) = 2 - 2g$$

This integer plays a fundamental role in our classification of dynamical systems in $\mathbb{R}^3$ whose dynamics is more complicated than simple stretch-and-fold dynamics.

15.2.5 Poincaré-Hopf Index Theorem

The Euler characteristic of a manifold is an incredibly powerful tool, due in part to a theorem by Poincaré, the Poincaré-Hopf index theorem. This theorem relates the singularities of a vector field on a manifold with the topological index of the manifold.

Many different vector fields can be defined on a manifold S. Each vector field on a manifold has an index. This is the sum over the indices of each of its nondegenerate singularities. Each isolated singularity has an index that is related to its stability. The index of an isolated singularity is $(-1)^{n_u}$, where n_u is the number of unstable (positive) eigenvalues of the flow, linearized at the singular point—that is, the Jacobian evaluated at the singularity. The Poincaré-Hopf index theorem states [5]

$$\sum_{\text{all singularities}} (-1)^{n_u} = \chi(S) \tag{15.2}$$

That is, the sum over all isolated singularities of a vector field defined on a manifold S is equal to the Euler characteristic of the manifold. The result is independent of vector field: it holds for all vector fields on S.

This beautiful result is important because it relates dynamics (vector fields) with topology (Euler characteristic). We use this result below to place constraints on the types of flows that can support strange attractors in $\mathbb{R}^3$.

15.2.6 Surface Singularities

Flows can be constructed that limit to the semiflow on the branched manifold. These flows obey the standard conditions on the Lyapunov exponents: $\lambda_1 > 0, \lambda_2 = 0, \lambda_3 < 0$ and $\lambda_1 + \lambda_2 + \lambda_3 < 0$. Since there are no fixed points on the branched manifold, these flows in $\mathbb{R}^3$ have no singularities inside the boundary just constructed, by continuity. However, they can be restricted to the boundary [125]. The flow, restricted to the boundary, usually does have singularities. These occur naturally when the flow intersects the boundary perpendicularly. When this occurs, the flow direction is perpendicular to the boundary, and the flow, restricted to the boundary, appears to have a fixed point on the boundary. This fixed point must be a saddle, since it inherits the remaining two Lyapunov exponents $\lambda_1 > 0$ and $\lambda_3 < 0$ along the eigendirections, locally tangent to the surface at the singularity. As a result, all singularities of the flow, restricted to the two-dimensional genus-g surface, are saddles. This geometry is illustrated in Fig. 15.1 [124, 125].

For our purposes S is the boundary surrounding a branched manifold: a genus-g surface. The Euler characteristic of a genus-g surface is $\chi(\text{genus } g) = 2 - 2g$. The vector field is any that limits to the semiflow on the branched manifold. Such a vector field can have singularities when restricted to the surface S. Every such singularity has index -1 since $n_u = 1$. As a result, the number of singularities on the surface is exactly $2g - 2$, since

$$\sum_{\text{singularities on } S} (-1)^1 = 2 - 2g \tag{15.3}$$

Example: Two representations of the Lorenz attractor are shown in Fig. 15.2. Fig. 15.2(a) shows the standard "masked" branched manifold, surrounded by a torus with two holes. The vector field, restricted to this torus, has singularities at the two points marked $\times$ on the Z-axis. For this representation $g = 2$ and $2g - 2 = 2$. Fig. 15.2(b) shows an "induced" representation of the Lorenz attractor, as previously discussed in Chapter 6. In this case there are no singularities on the outer boundary of this torus. Neither are there any singularities for the flow around the holes on the

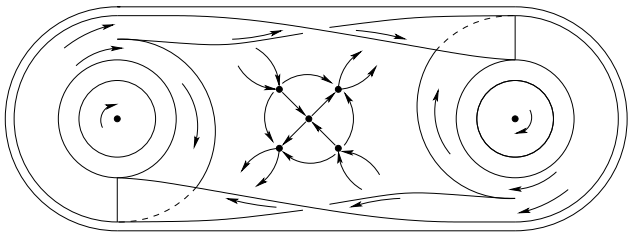

Fig. 15.1 Flows surrounding a branched manifold induce singularities on the torus that encloses the branched manifold. This torus has three holes, two surrounding the foci on the left and the right, one surrounding the regular saddle in the middle.

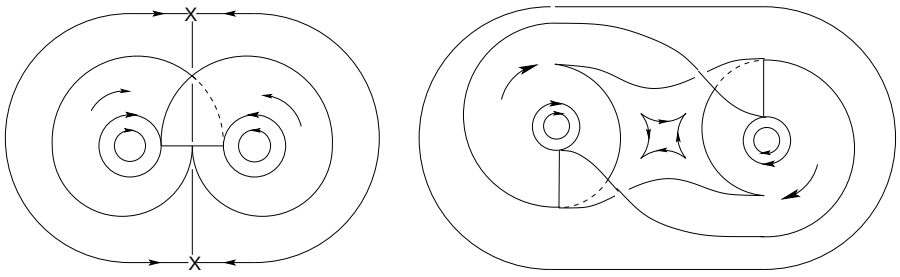

(a) Standard mask (b) Induced representation

Fig. 15.2 Genus-g surfaces surrounding two representations of the Lorenz strange attractor. (a) The branched manifold for the standard masked representation of the attractor is enclosed in a torus with two holes on which the flow has two singularities. The two singularities occur where the Z-axis pierces the genus-2 bounding torus. They occur on the exterior boundary in this projection. (b) The branched manifold for the induced representation of this attractor is enclosed in a torus with three holes. The flow has four singularities on this genus-3 surface. The four singularities have been moved to the edge of the middle inner hole in this projection. The middle hole has been formed by removing a thin tube surrounding the Z-axis from the genus-2 bounding torus, and following the deformation shown in Fig. 15.3. The round holes exclude the two unstable foci from the interior of the bounding torus. The "square hole" excludes the regular saddle at the origin.

left and the right. However, the hole in the middle shows four singularities. These have been emphasized by drawing sharp corners on this hole. This hole is obtained by removing the Z-axis from $\mathbb{R}^3$, and then twisting either of the lobes by π radians in an appropriate direction. For this representation $g = 3$ and $2g - 2 = 4$. The deformation that transforms Fig. 15.2(a) to Fig. 15.2(b) is shown in Fig. 15.3.

15.3 CANONICAL FORM

In this section we develop a useful way to classify flows that generate strange attractors in $\mathbb{R}^3$. Specifically, we introduce a *canonical form* to describe the flow. We use as the prototype of a canonical the bounding torus shown in Fig. 15.2(b).

A canonical form has two aspects: topological and dynamical.

At the topological level we project a genus-g torus onto a plane in such a way that the projection shows a disk boundary with g interior holes. Such a projection can always be constructed by suitably deforming the torus. This projection carries topological information but no dynamical information.

At the second level of detail we dress the projection with flow information. This introduces a dynamical component into the canonical form. In the projection, all singularities occur either on the disk outer boundary (cf. Fig. 15.2(a)) or on one or more interior holes. In the canonical form all singularities are moved to the interior

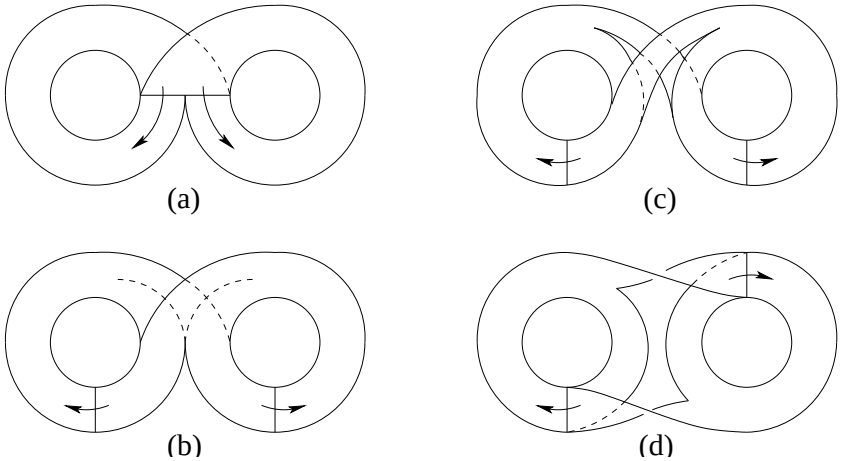

Fig. 15.3 Transformation of the branched manifold for the Lorenz attractor from the standard Lorenz "mask" form to the "induced" form is done by carrying out a series of simple topological transformations (a) → (b) → (c)→ (d).

holes. Specifically, we adopt the following convention for the projection of the flow on a canonically dressed genus-g torus onto a disk with g holes in the plane [124]:

a. There are no singularities on the disk outer boundary. The flow is in a single direction around this exterior boundary.
b. All singularities occur on the interior holes. Holes with singularities have an even number of singularities: $4, 6, \cdots$.
c. The flow around any interior hole without singularities is in the same direction as the flow on the boundary.

The dressed torus in Fig. 15.2(a) is not canonical while that in Fig. 15.2(b) is canonical.

Canonical forms are useful because they can be classified and enumerated. It is always possible to construct a canonical projection. We describe how in a number of different ways, and give several examples.

Each hole in a projection surrounds a point in the vector field on $\mathbb{R}^3$ that has a singularity. For example, the two "round holes" in Fig. 15.2(b) exclude the two foci of the Lorenz flow from the attracting manifold containing the strange attractor. The "square hole" in the middle, with four singularities, excludes the saddle at the origin. More generally, holes without singularities surround foci and holes with singularities surround saddles (four singularities) or degenerate singular points. A degenerate critical point with any kind of n-fold symmetry is surrounded by a hole with $2n$ singularities.

Foci have handedness. If you extend the fingers of your right hand around the focus in the flow direction, your thumb points along the rotation axis in the "positive"

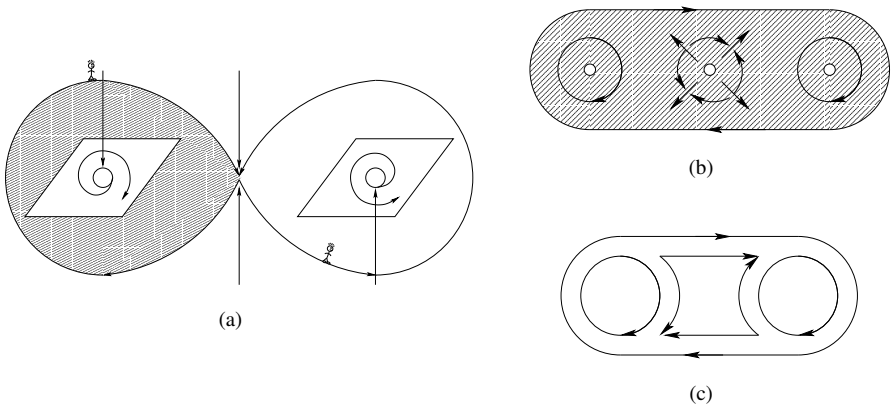

Fig. 15.4 (a) The flow generated by the Lorenz equations can be projected onto a twisted sheet in such a way that the spins of the two foci are on the same side of the sheet. (b) When the twisted sheet is untwisted, the flows around the exterior boundary and the two interior holes without singularities are in the same direction. All four singularities are on the interior hole in the middle. (c) This simple graphic representation serves as a canonical form for the flow restricted to the genus-g boundary of an attracting manifold containing the branched manifold for the Lorenz attractor.

direction (by convention). The plane, or any smooth deformation of it, also has two sides. They can be called up and down, or positive and negative.

A canonical projection can be constructed as shown in Fig. 15.4. Pass a two-sided surface through each of the foci in such a way that the positive axis of each focus is on the positive side of this surface. Then deform the surface to a plane. This automatically generates a canonical form for the flow.

If canonical forms exist for all flows, then even the most complicated branched manifold that we have encountered can be transformed to this form. The prime candidate here is the figure 8 branched manifold, shown in Fig. 15.5. A schematic representation of this branched manifold is shown in Fig. 15.5(a). This schematic representation contains no torsion information. In fact, dressed tori are compatible with many different torsions within each branch or flow region. The torsion information is suppressed mostly to make the figures simpler to draw and easier to understand.

Two of the branches are redrawn in Fig. 15.5(b) to exhibit clearly the periodic boundary conditions that exist in this flow. This allows us to wrap the flow around a cylinder, as shown in Fig. 15.5(c). The representation in Fig. 15.5(c) could have been inferred from that in Fig. 15.5(a) directly, but it is easier through the intermediary shown in Fig. 15.5(b). Looking from along the axis of the cylinder, and flattening the flow down along the line of sight, provides a schematic of the flow as shown in Fig. 15.5(d). A simple pair of moves takes us from there to the representation of Fig. 15.5(e). By moves similar to those given in Fig. 15.4, we obtain Fig. 15.5(f) from Fig. 15.5(e). The canonical form for the flow on the figure 8 branched manifold is a "pinwheel" with four wings [124].

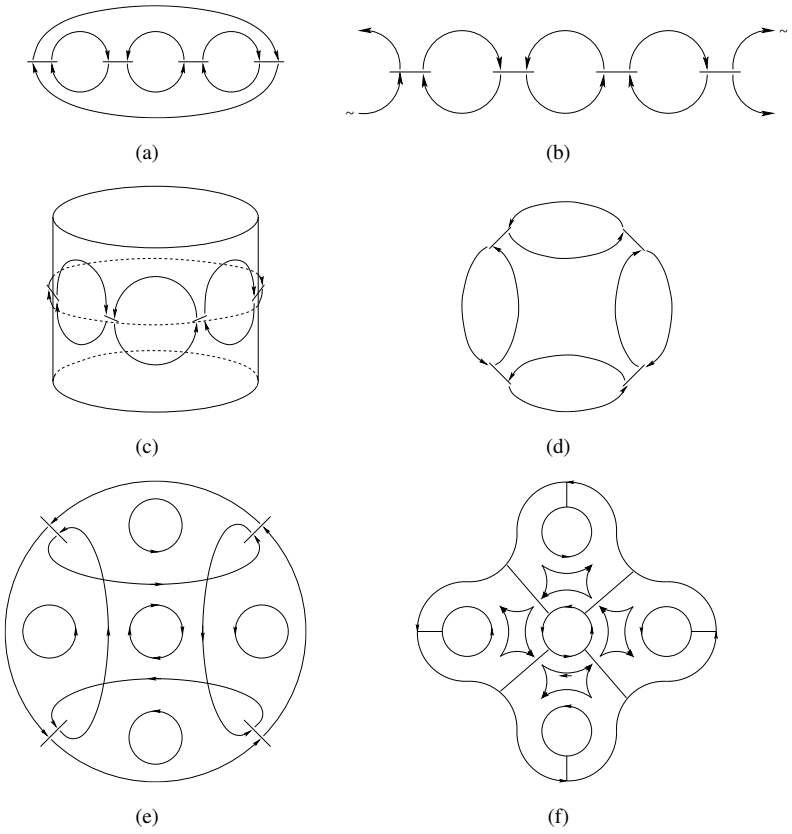

Fig. 15.5 (a) Schematic representation of the figure 8 branched manifold (b) has periodic boundary conditions. This means that the flow (c) can be wrapped around a cylinder, and then (d) flattened when viewed along the axis of the cylinder. (e) Two moves convert this representation into (f) a pinwheel with four wings.

15.4 PROPERTIES OF THE CANONICAL FORM

It is always possible to find a projection of a genus-g surface onto a two-dimensional surface that has a standard form. The standard form consists of a disk with an outer boundary and with g interior holes. Every disk with g holes is equivalent to every other disk with g holes: this is merely a reflection of the fact that all (intrinsic) genus-g surfaces are topologically equivalent.

This equivalence disappears when the genus-g surface is dressed with a flow. A genus-g surface can be dressed in many inequivalent ways with a flow having exactly $2g - 2$ singularities. This is true even for canonically dressed surfaces. However, the

canonically dressed surfaces can be classified, described, and counted. We actually classify the projections of these dressed tori on two-dimensional surfaces.

The enumeration depends on the properties of the canonically dressed surfaces. In fact, canonically dressed surfaces have a rather rigid structure. The structure and properties of these surfaces, and the flows on them, are described in this section.

15.4.1 Disk Boundary

For the canonical form, the flow on the disk outer boundary is unidirectional. There are no singularities on the boundary.

15.4.2 Interior Holes of Two Types

There are g interior holes. All singularities occur on these holes. There are two types of interior holes.

1. There are n_1 holes without singularities. The flow is in a uniform direction around such holes. In the canonical form the flow around these holes is in the same direction as the flow around the disk outer boundary. These interior holes surround part of the vector field on $\mathbb{R}^3$ outside the torus with a singularity of focus type. The circulation around the focus is determined by the flow direction around the hole.
2. There are n_2 holes with singularities. There is always an even number of singularities, starting with 4 [124]. A hole with four singularities surrounds a regular saddle in the vector field external to the torus. Holes with 6, 8, $\cdots$ singularities surround a degenerate saddle, of the type that possesses symmetry group $\mathcal{C}_3$, $\mathcal{C}_4$, $\cdots$. These degenerate critical points perturb to a spectrum of nondegenerate saddles with the same index. All singularities come in pairs: one member (s) of each pair splits flows into two separate regions, the other member (j) shows where flows from two different regions join. A hole with $2n$ singularities is surrounded by n pairs of (s, j) singularities. Each pair is associated with a nearest-neighbor "round" hole.

We show interior holes with 0, 2, 4, and 6 singularities in Fig. 15.6. The hole in Fig. 15.6(a) has no singularities. It separates a focus from the flow. The flow inside the boundary bears an imprint of this focus outside the boundary. The regular saddle shown in Fig. 15.6(c) induces four singularities on the hole surrounding it. This saddle also leaves its imprint on the structure of the flow in its neighborhood. The three-fold degenerate saddle shown in Fig. 15.6(d) induces 2×3 singularities on the surrounding hole. This degenerate saddle also provides an unmistakable imprint on the structure of the flow in the interior of the embedding manifold.

Holes supporting only one (s, j) pair of singularities do not have the same properties as holes with 0, 4, 6, $\cdots$ singularities. As shown in Fig. 15.6(b) they do not leave an imprint on the surrounding flow. They can be removed by "zipping them up." That is, we identify the two boundaries connecting the s and j singularities.

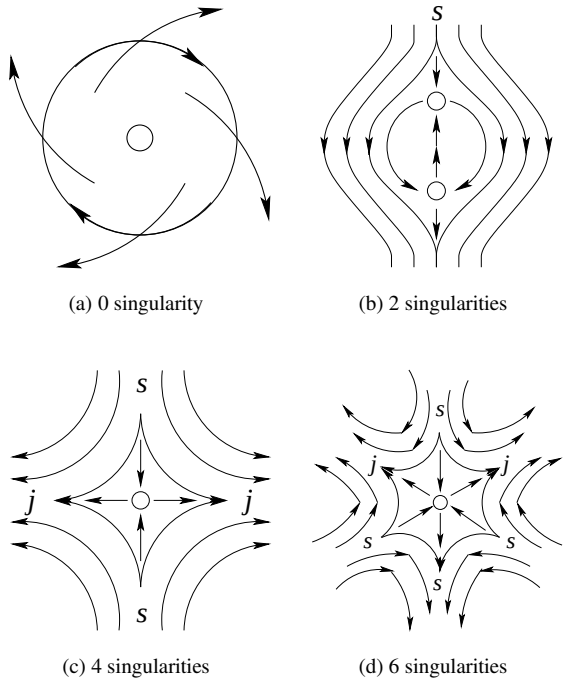

(a) 0 singularity (b) 2 singularities

(c) 4 singularities (d) 6 singularities

Fig. 15.6 Interior holes with (a) 0, (b) 2, (c) 4, and (d) 6 singularities. Only holes with 2 singularities can be removed without changing the asymptotic structure of the flow.

Holes with two singularities can be encountered for a number of reasons. They are often drawn in representations of the standard Smale horseshoe branched manifold to allow easy distinction between the two branches. Such holes do not exist except in the hyperbolic limit, which has never been observed in experimental data, or even in simulations of ordinary differential equations. Such holes can be observed when a large number of orbits have been pruned away. They can be observed in Rössler dynamics and in the Shimizu-Morioka attractor for some parameter values. They are encountered in short data sets. They also occur around real and virtual saddle-node pairs, as shown in Fig. 15.6(b). In all these instances, holes with two singularities can be topologically zipped up. The two singularities and the hole they are on disappear without changing the aysmptotic properties of the flow.

Round holes and "square" holes (i.e., with singularities) show clearly how the flow in the canonically dressed torus is organized. The total number of holes is the genus of the torus:

$$\begin{aligned} n_1 \;+\; n_2 \;&=\; g \\ n_1 \;>\; n_2 \;&\geq\; 1 \end{aligned} \tag{15.4}$$

Two inequivalent canonically dressed genus-5 tori are shown in Fig. 15.7. The canonically dressed torus shown in Fig. 15.7(a) can be regarded as a 4-fold cover of a Smale horseshoe branched manifold with symmetry group $\mathcal{C}_4$. For this cover $n_1 = 4,\ n_2 = 1$. The "square" hole in the middle has eight singularities. One pair is associated with each of the four uniflow holes. In each pair there is a splitting singularity and a joining singularity. The canonically dressed torus shown in Fig. 15.7(b) can also be regarded as a 4-fold cover of a Smale horseshoe branched manifold. It is a double cover of a double cover (cf. Figs. 6.35 and 6.36). For this cover $n_1 = 3,\ n_2 = 2$. The two square holes each have four singularities, or two pairs of singularities. In each pair there is a splitting singularity and a joining singularity. There is no diffeomorphism that maps the flow of Fig. 15.7(a) to that of Fig. 15.7(b).

Remark 1: The two flows are related by topological continuation under certain conditions. Suppose the flow in each of these two genus-5 tori is related to a flow in a genus-1 torus by a $4 \to 1$ local diffeomorphism. Then the flow in (a) can be mapped in a $4 \to 1$ way onto the image flow, and the image flow can be lifted into the $1 \to 4$ cover in (b).

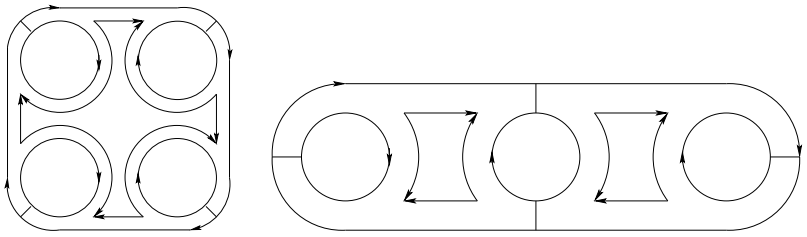

(a) (b)

Fig. 15.7 Two genus-5 dressed tori. (a) One of the four-fold covers of the Smale horseshoe branched manifold, with $\mathcal{C}_4$ symmetry, can be enclosed by this surface. (b) This surface also encloses a four-fold cover of the Smale horseshoe branched manifold. This is a double cover of a double cover (cf. Figs. 6.35 and 6.36). The cover itself has only a two-fold symmetry.

Remark 2: Although there is a vast variety of canonical bounding tori, two classes occur sufficiently often that they deserve labels. One class consists of "cyclic bounding tori" with n round holes and a single hole with $2n$ singularities. Genus-$(n+1)$ bounding tori with this structure are labeled C_n. The bounding torus C_4 is shown in Fig. 15.7(a). The other class is "linear" with n round holes separated by $n-1$ "square holes" with four singularities each. Genus-$(2n-1)$ bounding tori with this structure are labeled A_n. The bounding torus A_3 is shown in Fig. 15.7(b).

15.4.3 Homotopy Group

Of the genus-g surfaces, only the sphere ($g = 0$) is simply connected. All others are multiply connected.

A genus-g surface has a homotopy group with $2g$ generators. The generators can be regarded as simple closed loops in the torus that cannot be continuously deformed to a point. Neither can any be deformed to any other, or to a "linear" combination of others [108, 134].

The $2g$ generators of a homotopy group split into two subsets, each containing g generators. These are called meridians and longitudes. Meridians and longitudes for a genus-g torus are shown in Fig. 15.8.

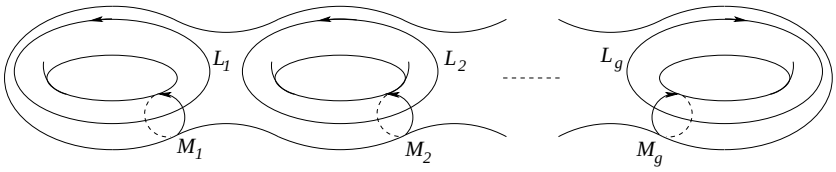

Fig. 15.8 Longitudes L_i and meridians M_j for a genus-g torus.

When the torus is dressed with a flow, the meridians and longitudes pick up a dynamical as well as a topological meaning. When the dressing is canonical, the properties of the generators become very powerful tools for studying the flow.

Meridians and longitudes on genus-g tori have the following properties. These are topological properties, independent of flows.

1. The g meridians can be chosen in such a way that they are pairwise nonintersecting.
2. The g longitudes can be chosen in such a way that they are pairwise nonintersecting.
3. Every longitude intersects each meridian at most once.
4. Every meridian intersects each longitude at most once.
5. Each meridian intersects at least one longitude, and vice versa.

Meridians and longitudes on canonically dressed genus-g tori ($g > 1$) have an additional set of properties. These are dynamical properties, directly related to the flow.

1. One longitude can be chosen around each of the g interior holes.
2. The inner product $\mathbf{v} \cdot d\mathbf{s}$ is positive everywhere along each longitude around a uniflow hole. Here $\mathbf{v}$ is the vector field, restricted to the bounding torus, and $d\mathbf{s}$ is the element of arc length along the longitude.
3. The inner product $\mathbf{v} \cdot d\mathbf{s}$ alternates in sign along a longitude around an interior hole with singularities.
4. All g meridians can be chosen in such a way that they bound two-dimensional surfaces inside the torus on which the flow is everywhere nonzero. In particular, the flow passes through the disk bounded by each meridian always in the same direction, as shown for the genus-1 torus in Fig. 15.9.

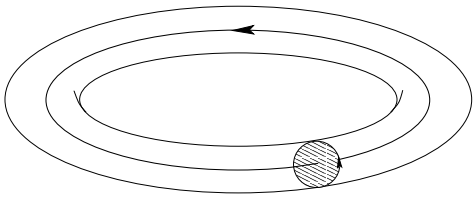

Fig. 15.9 Meridians bound disks that can be chosen transverse to the flow. These disks are components of the global Poincaré surface of section. Longitudes surround each of the g interior holes, and can be chosen to "follow the flow" ($\mathbf{v}\cdot d\mathbf{s} > 0$) around each of the interior uniflow holes.

5. Any trajectory generated by the flow can be specified by the sequence of its intersections with the g surfaces bounded by the g independent meridians. In fact, if $g > 1$, all but one of the g meridians connect a uniflow hole with the boundary. The remaining meridian, and the surface it bounds, provide redundant information and can be eliminated for dynamical purposes.

6. The $g-1$ surfaces bounded by the $g-1$ meridians connecting uniflow holes with the boundary are the $g-1$ components of the Poincaré section for the flow.

Remark: Until now it has not been possible to state with precision what the structure of the Poincaré section of a flow looks like. The last item in the list above makes this clear, at least for flows in $\mathbb{R}^3$: The Poincaré section for a flow that can be enclosed in a genus-g torus consists of the union of $g-1$ disjoint surfaces. Each surface is bounded by a generator of the homotopy group. Specifically, each such generator is a meridian that connects an interior uniflow hole with the disk boundary.

15.4.4 Further Properties

We have introduced bounding tori as branched manifold organizers. So far we have not made much of a connection between branched manifolds and these tori. We now make a useful connection, for the case $g > 1$. All branch lines can be moved so that they occur in one of the $g-1$ components of the Poincaré section.

In schematic representations of canonically dressed tori we will identify the $g-1$ components of the Poincaré section with $g-1$ branch lines for whatever branched manifold is enclosed in the genus-g torus. In Fig. 15.7 these have been represented as straight line segments connecting each internal uniflow hole with the disk exterior boundary. There are four such line segments in each of the two genus-5 canonical forms shown in that figure. A uniflow hole can share more than one line segments with the boundary, as seen in Fig. 15.7(b).

15.5 HOW TO CLASSIFY DRESSED TORI

Canonically dressed tori carry two pieces of information. The topological piece of information is encoded entirely by the genus, g, of the torus. All genus-g tori are topologically the same surface. Genus is the primary descriptor of canonically dressed tori. The dynamical piece of information is encoded in the canonical flow used to dress the genus-g surface. A genus-g torus can be dressed in many inequivalent ways. The objective of this section is to develop methods for distinguishing among genus-g tori that carry nondiffeomorphic dynamical flows. Three methods are presented.

The first method is based on the distribution of singularities among the n_2 holes with singularities. It leads to a partial classification by Young partitions and a complete classification by words of length $g-1$ based on n_2 symbols. The second method is based on uniflow holes and leads to a classification in terms of a sequence of integers $1, 2, \cdots, n_1$ of length $g-1$, with repetitions of some integers. The third approach is based on the $g-1$ components of the Poincaré section, or equivalently the $g-1$ branch lines in these components. It leads to a classification in terms of sequences of length $g-1$ containing the integers $1, 2, \cdots, k$, where $k \leq n_2$.

In any canonically dressed torus the uniflow holes, singular holes, and branch lines are related to each other in a unique way. This means that the three classification schemes are fundamentally equivalent. However, for some purposes one is more useful than the other two. It is for this reason that all three are presented.

Remark: The symbol sequence is generated by a walk around the exterior boundary of the disk in the direction of the flow. This generates an infinite symbol sequence that repeats itself after every $g-1$ symbols. For this reason, we can argue that bounding tori are classified by a "periodic orbit" of period $g-1$.

15.5.1 Singular Holes

The interior holes in the projection of a canonically dressed genus-g torus are of two types. There are n_1 uniflow holes and n_2 holes with singularities, where $n_1 + n_2 = g$. Each hole with singularities has an even number of singularities, starting with 4. The sum of all the singularities is $2g-2$.

The singularities come in pairs. There is one singularity of type s and one of type j between a hole with singularities and each of its nearest neighbor uniflow holes. Since singularities come in pairs, it is more economical to count the number of pairs than the number of singularities. Specifically, a canonically dressed genus-g surface has $g-1$ pairs of singularities in the standard projection.

These pairs can be distributed among the n_2 singular holes so that one hole has λ_1 pairs, another has λ_2, and so forth, with

$$\begin{aligned} \lambda_1 \geq \lambda_2 \geq \cdots \geq \lambda_{n_2} &\geq 2 \\ \lambda_1 + \lambda_2 + \cdots + \lambda_{n_2} &= g-1 \end{aligned} \tag{15.5}$$

These inequalites can be used to further refine the classification of canonically dressed tori.

Example: A torus has genus 9. It can be canonically dressed in a number of different ways. Three different ways are summarized in Table 15.1. The partition of $8 = 9 - 1$ into a nonincreasing set of integers, all greater than 1, contains the following partitions: (8), (6,2), (5,3), (4,4), (4,2,2), (3,3,2), (2,2,2,2). These sets are represented by Young partitions, as is done to classify representations of permutation groups and Lie groups. To each partition there corresponds at least one canonically dressed flow. We note for later reference that for partitions with l rows there is a unique correspondence between Young partitions and canonically dressed tori if $l = 1$ or $l = 2$. We also note that a uniflow hole can be joined to the boundary by no more than l branch lines. Uniflow holes connected to the boundary by 2 [(6,2), (5,3), (4,4)], 3 [(4,2,2)], and 4 [(2,2,2,2)] branch lines are explicitly shown in Table 15.1. The global Poincaré surface of section for each canonical form in this table has eight $(8 = g - 1)$ disjoint components. Only some are shown explicitly.

There are several different ways to encode canonically dressed tori. These encodings are a useful way to discriminate among different canonically dressed tori with the same Young partition.

In one approach a letter is assigned to each hole with singularities. For example, the three singular holes associated with the Young partition $\lambda = (3, 3, 2)$ are labeled a, b, c. Starting on the disk boundary at some point, labeled $\times$ in Fig. 15.10, we encounter all $g = 9$ holes, some more than once. In fact, we alternately encounter uniflow holes and singular holes. Each time a singular hole is encountered its label is written down. The number of times each label is encountered is determined by the Young partition. For the canonical torus, the labeling, and the starting point shown in Fig. 15.10 the sequence of encounters is $abbbccaa$. Continuing around a second time reproduces this set of $8 = 9 - 1$ symbols. In fact, this sequence can be regarded as a periodic orbit of period eight containing $\lambda_1 = 3$ symbols a, $\lambda_2 = 3$ symbols b, and $\lambda_3 = 2$ symbols c. If some reasonable convention is adopted (e.g., alphabetization) one of the eight symbol strings related to each other by cyclic

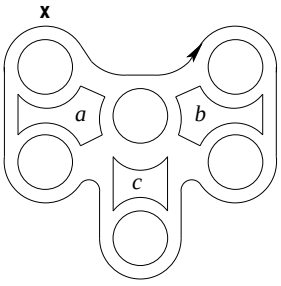

abbbccaa

Fig. 15.10 For the canonical torus, the labeling, and the starting point shown above, the sequence of encounters is $abbbccaa$. Any cyclic permutation of these $8 = g - 1$ symbols serves as a label for this canonical torus. We typically choose the alphabetically earliest symbol sequence to name the canonical form: $aaabbbcc$.

Table 15.1 Canonically dressed tori of genus 8 are described by Young partitions with n_2 rows. One canonically dressed torus is provided for each of the allowed Young partitions with eight boxes.

n_2	λ	Young Partition	Canonical Torus
1	(8)	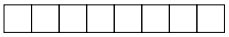	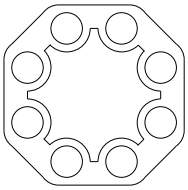
2	(6,2)	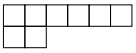	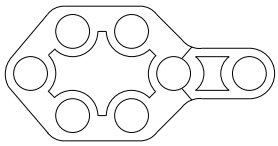
2	(5,3)	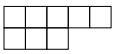	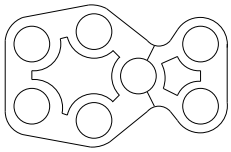
2	(4,4)		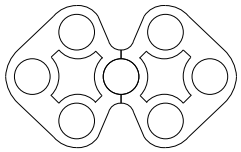
3	(4,2,2)		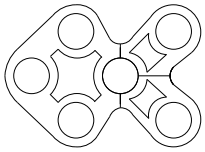
3	(3,3,2)		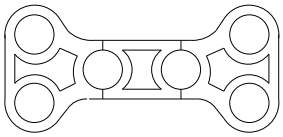
4	(2,2,2,2)		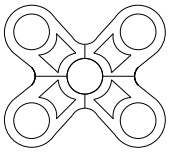

permutation (i.e., changing the starting point) can be used to identify the periodic orbit, and to represent the canonically dressed torus—uniquely! The unique identification for this canonically dressed torus is $aaabbbcc = a^3b^3c^2$, adopting the alphabetical convention.

Other periodic words with 3 a's, 3 b's, and 2 c's can occur. These are summarized in Table 15.2. This table shows the four inequivalent flow distributions associated with the Young partition $\lambda = (3, 3, 2)$. They are uniquely associated with the "periodic orbits" $aaabbbcc$, $aaabbccb$, $aaabccbb$, and $aaacbbbc$. Since $\lambda_1 = \lambda_2$, there is an $a \leftrightarrow b$ equivalence. This equivalence reduces the number of inequivalent flow distributions associated with this (partially degenerate) Young partition.

As Table 15.2 makes clear, there is an isomorphism between the problem of constructing and identifying flow distributions and a polygon partition problem. The problem can be framed in the following delightful way. The owner of an island wants to sell lots on the island. The island has n units of waterfront. How many different ways (up to cyclic permutation) can the owner divide the island into lots so that

1. every lot is connected
2. every lot has at least two units of shorefront.

The rules for allowed words will be presented at the end of this section, in a more sympathetic language.

15.5.2 Uniflow Holes

A dual method for classifying flows with the same partition emphasizes the uniflow holes rather than the singular holes. It is illustrated in Fig. 15.11. The starting point is chosen arbitrarily ($\times$ in this figure). Following the flow on the boundary, the uniflow holes are numbered in the order they are encountered. For the torus shown each of the first five holes encountered was not previously encountered. However, the uniflow hole encountered after hole 5 has already been numbered (3). The next hole

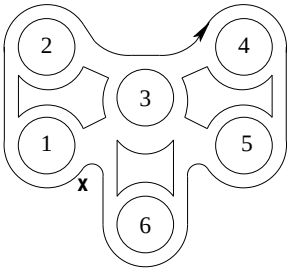

Fig. 15.11 Dual method for classifying flows with the same partition emphasizes the uniflow holes rather than the singular holes. For the labeling and starting point shown, the dual label is (12345363). By changing the starting point and numbering, the lowest possible sequence is (12134156).

Table 15.2 All canonically dressed flows described by words with 3 a's, 3 b's, and 2 c's are shown.

Dressed Flow	Word	Partition of Polygon
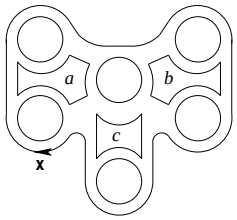	$a\ a\ a\ b\ b\ b\ c\ c$	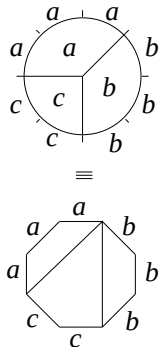
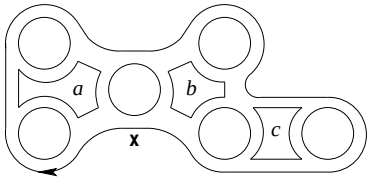	$a\ a\ a\ b\ b\ c\ c\ b$	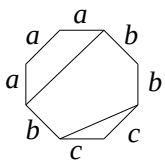
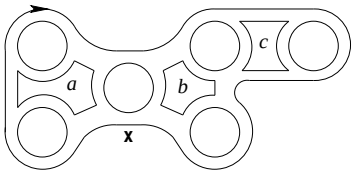	$a\ a\ a\ b\ c\ c\ b\ b$	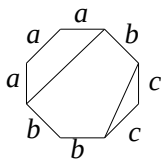
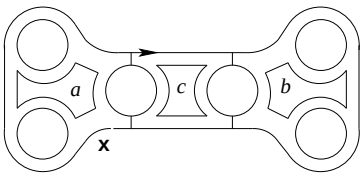	$a\ a\ a\ c\ b\ b\ b\ c$	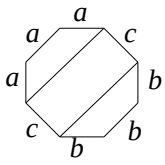

hasn't previously been encountered, and is labeled 6. The last hole to be encountered has already been labeled (3). The sequence for this torus is (12345363). For this torus $n_1 = 6$, so that the largest integer encountered is 6. Moving the starting point produces a different sequence of the integers $1 \rightarrow 6$. One number is encountered three times because one hole (numbered 3 in Fig. 15.11) has three branch lines attached to it. The other integers are encountered once each, indicating that each of the other uniflow holes is attached to a single branch line. By changing the starting point, the lowest possible sequence is (12134156).

The relation between the symbol sequences of the canonically dressed tori associated with Young partition $\lambda = (3, 3, 2)$ based on the singular holes (previous section), uniflow holes (this section), and branch lines (next section) is summarized in Table 15.3.

Remark: It is useful to choose the starting point and the hole labeling scheme to achieve the "lowest possible" sequence. This is obtained for the canonical form shown in Fig. 15.11 by choosing the starting point just above the circle hole 3, and starrting the numbering from this hole. The lowest possible label for this canonical torus is (12314156).

15.5.3 Branch Lines

The Poincaré section for a dressed genus-g torus has $g - 1$ components. In the canonical projection these are represented as branch lines. The branch lines connect uniflow holes with the disk boundary. Since there are $g - 1$ branch lines and $n_1 = g - n_2$ uniflow holes, some of these holes are connected to the boundary by more than one branch line if $n_2 > 1$. None of the holes is connected to the boundary by more than n_2 branch lines. This is a simple consequence of counting.

The third way for identifying canonically dressed tori depends on the observations made in the previous paragraph. Starting at any point on the disk boundary, follow the boundary in the direction of the flow. The algorithm is illustrated in Fig. 15.12. Each time a uniflow hole is encountered, indicate the total number of branch lines connected to that hole. For the starting point indicated by $\times$ and the flow direction indicated

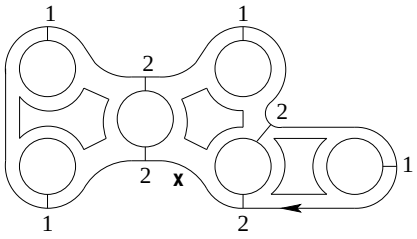

Fig. 15.12 Algorithm for identifying canonically dressed tori. For the labeling and the starting point shown, this torus is identified by the symbol sequence (21121212). The lowest cyclic permutation is (11212122).

by the arrow in this figure, the integer sequence is 21121212. Continuing around this path repeats this integer sequence. This pereiod-8 orbit can be labeled by its "lowest" word ("alphabetic" ordering under cyclic permutation), which is 11212122. The occurrence of the integer 1 four times means that four uniflow holes have one branch line each. The occurrence of the integer 2 four times means that two uniflow holes are connected by two branch lines (each) to the disk boundary. The total number of branch lines is $8 = 9 - 1$ and the total number of uniflow holes is $6 = 4 + 2$. The genus is 9, the word length is 8, the number of singular holes is 3.

For the flows shown in Table 15.2 the encoding by this procedure is given in Table 15.3. This encoding is unique.

Table 15.3 Degeneracies of Young partitions can be lifted by encoding the periodic orbits obtained by walking around the disk boundary in the direction of the flow. Encodings using singular holes, uniflow holes, and branch lines for the Young partition $\lambda = (3, 3, 2)$ are compared.

Singular Holes	Uniflow Holes	Branch Lines
$aaabbbcc$	12134156	11311313
$aaabbccb$	12134536	11212122
$aaabccbb$	12134564	11221212
$aaacbbbc$	12314564	11221122

15.5.4 Allowable Orbits

The results of the previous three subsections make it clear that there is a one to one correspondence between canonically dressed tori of genus-g and periodic orbits of period $g - 1$. It is possible to infer the rules for allowed orbits. These rules are presented for the encoding using branch line information, described in the previous subsection. The rules are:

1. An allowed orbit is a sequence of $g - 1$ integers $1, 2, \cdots, k$, $k \leq [\frac{1}{2}(g - 1)]$.
2. The integer n ($n > 1$) occurs in n-tuples.
3. Between any two successive n's in an n-tuple there must exist at least one integer 1.
4. Multiplets cannot interleave (cf. Fig. 15.13).
5. The smallest representative under cyclic permutation is chosen to represent the periodic orbit.

Example: Fig. 15.14 shows a dressed torus of genus 9. The dressing has Young partition $\lambda = 2^4$. The periodic orbits that describe this canonical form are $aabccddb$,

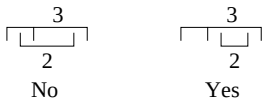

Fig. 15.13 Multiplets cannot interleave.

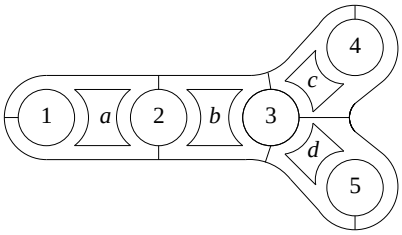

Fig. 15.14 Dressed torus of genus 9. The dressing has Young partition $\lambda = 2^4$. It is identified by the period-8 words: $(aabccddb)$, (12131454), (12313132) under the three coding schemes presented.

12343532, 12313132 in the three coding methods described in the previous three subsections. The third word is the most useful for constructing transition matrices.

Remark: From the projection it is a simple matter to construct the periodic orbit that describes the canonically dressed torus. For the periodic orbit (in any of the three coding schemes) it is almost as simple to recover (uniquely) the canonically dressed torus.

15.6 TRANSITION MATRICES

The $g-1$ components of the Poincaré section play the same role for a canonically dressed torus as the $|\mathcal{G}|$ branch lines do for the $|\mathcal{G}|$-equivariant lifts of an image dynamical system. Whereas the branch lines for the latter are labeled by the group operations $g_1 = Id$, $g_2, \cdots, g_{|\mathcal{G}|}$, the components for the former are labeled by an integer $1, 2, \cdots, g-1$. Just as a transition matrix is useful for describing flows in equivariant covers, transition matrices are useful for describing flows in canonically dressed tori.

When it comes to placing branched manifolds inside canonically dressed tori, we can move each branch line onto one of the components of the Poincaré section. In this case branched manifolds inside a given genus-g bounding torus, including as a special case (topological) lifts of an image attractor, will be labeled by two indices:

1. a symbol from the image branched manifold
2. an integer from the Poincaré section.

Components of the Poincaré section are generalizations of the group operations g_i in equivariant covers. To put this another way: all flows that can be obtained as equivariant covers of an image dynamical system can be obtained as a (small) subset

of the flows that can be described by canonically dressed tori. Specifically, this subset includes only those canonical bounding tori with a symmetry group.

The two canonically dressed tori of genus 5 are shown in Fig. 15.15. Both have a symmetry group: $\mathcal{C}_4$ and $\mathcal{C}_2$, respectively. The two are completely described by their Young partitions (4) and (2,2), since the number of rows is $l \leq 2$. The transition matrix for each torus is presented below the torus. The transition matrix is to be interpreted in the usual way. For example, the flow emerging from the component 2 of the Poincaré section for C_4 flows to components 2 and 3 of the Poincaré section: $T_{22} = 1, T_{23} = 1$.

The transition matrices of Fig. 15.15 reveal a general property of transition matrices for *all* canonically dressed tori. There are two matrix elements $+1$ in each row and each column. All other matrix elements are zero.

The transition matrix for any canonically dressed torus can be written as the sum of two $(g-1) \times (g-1)$ matrices. Roughly and not quite accurately, one describes dynamics and the other describes connectivity (structure):

$$T = T_{\mathrm{Dyn}} + T_{\mathrm{Str}} \tag{15.6}$$

15.6.1 The Cyclic Matrix

If we start at any point on the disk boundary and proceed in the direction of the flow we encounter the $g-1$ branch lines in a specific order. They can be numbered in the

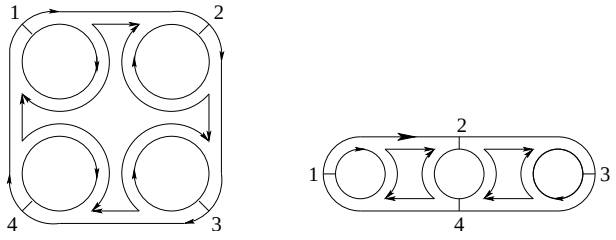

C_4 $\qquad\qquad$ A_3

$$\begin{bmatrix} 1 & 1 & 0 & 0 \\ 0 & 1 & 1 & 0 \\ 0 & 0 & 1 & 1 \\ 1 & 0 & 0 & 1 \end{bmatrix} \qquad \begin{bmatrix} 1 & 1 & 0 & 0 \\ 0 & 0 & 1 & 1 \\ 0 & 0 & 1 & 1 \\ 1 & 1 & 0 & 0 \end{bmatrix}$$

Fig. 15.15 Two canonically dressed tori of genus 5 are completely described by their Young partitions (4) and (2,2).

order in which they are encountered. With this numbering $T_{\rm Dyn}$ is a cyclic matrix:

$$\begin{array}{rcll} (T_{\rm Dyn})_{i,i+1} & = & 1 & 1 \le i, i+1 \le g-1 \\ (T_{\rm Dyn})_{g-1,1} & = & 1 & \end{array} \tag{15.7}$$

All other matrix elements of this cyclic permutation matrix are zero.

In Fig. 15.16 we show one of the canonically dressed tori with genus 9 and Young partition $\lambda = (3,3,2)$. The branch lines are numbered sequentially, $1, \cdots, 8$ in the order in which they are encountered when following the flow around the boundary ("under the dynamics"). The results are independent of the starting point because of cyclic invariance. The dynamical matrix $T_{\rm Dyn}$ is shown below the canonical torus. It is a cyclic matrix, with $T^8_{\rm Dyn} = I_8$.

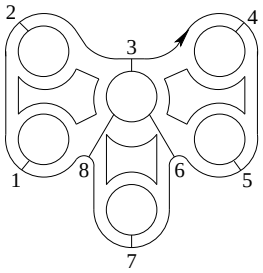

$$T_{\rm Dyn} = \begin{bmatrix} 0&1&0&0&0&0&0&0 \\ 0&0&1&0&0&0&0&0 \\ 0&0&0&1&0&0&0&0 \\ 0&0&0&0&1&0&0&0 \\ 0&0&0&0&0&1&0&0 \\ 0&0&0&0&0&0&1&0 \\ 0&0&0&0&0&0&0&1 \\ 1&0&0&0&0&0&0&0 \end{bmatrix} \qquad T_{\rm Str} = \begin{bmatrix} 1&0&0&0&0&0&0&0 \\ 0&1&0&0&0&0&0&0 \\ 0&0&0&0&0&1&0&0 \\ 0&0&0&1&0&0&0&0 \\ 0&0&0&0&1&0&0&0 \\ 0&0&0&0&0&0&0&1 \\ 0&0&0&0&0&0&1&0 \\ 0&0&1&0&0&0&0&0 \end{bmatrix}$$

Fig. 15.16 One of the canonically dressed tori with Young partition $\lambda = (3,3,2)$.

15.6.2 The Structure Matrix

The structure matrix $T_{\rm Str}$ is in some sense the complement of the cyclic matrix $T_{\rm Dyn}$. We start at the inside boundary of each branch line and see where the flow takes us. For the canonical torus of Fig. 15.16, $1 \to 1$, $2 \to 2$, $3 \to 6 \to 8 (\to 3)$, $4 \to 4$, $5 \to 5$, $7 \to 7$. The connectivity is described by five 1-cycles (1), (2), (4), (5), (7) and one 3-cycle (3,6,8), with $5 \times 1 + 1 \times 3 = 8$. This is reflected in the second matrix shown in Fig. 15.16. It has five matrix elements +1 on the diagonal: $(T_{\rm Str})_{i,i} = 1$, $i = 1, 2, 4, 5, 7$. The remaining three nonzero matrix elements describe the 3-cycle: $(T_{\rm Str})_{3,6} = (T_{\rm Str})_{6,8} = (T_{\rm Str})_{8,3} = 1$.

15.6.3 Encoding the Structure Matrix

The structure matrix is a $(g-1)\times(g-1)$ permutation matrix with only $g-1$ matrix elements different from zero. It becomes useful to assume that the information in this matrix can be encoded using only $g-1$ pieces of information (possibly fewer).

Each branch line is in a k-cycle, $k \leq [\frac{1}{2}(g-1)]$. For each of the $g-1$ branch lines, indicate the length of the cycle it belongs to. For example, for the canonical torus of Fig. 15.16 this representation is

$$1\ 1\ 3\ 1\ 1\ 3\ 1\ 3 \tag{15.8}$$

The three 3's in positions 3, 6, 8 belong to a triplet. The remaining branch lines belong to 1-cycles. The symbol sequence is placed in a $(g-1)\times(g-1)$ matrix, along the diagonal. The diagonal matrix elements that are greater than 1 are moved to the off-diagonal positions that reflect the structure of the n-tuple, as shown below.

$$\begin{bmatrix} 1&0&0&0&0&0&0&0\\ 0&1&0&0&0&0&0&0\\ 0&0&3&0&0&0&0&0\\ 0&0&0&1&0&0&0&0\\ 0&0&0&0&1&0&0&0\\ 0&0&0&0&0&3&0&0\\ 0&0&0&0&0&0&1&0\\ 0&0&0&0&0&0&0&3 \end{bmatrix} \longrightarrow \begin{bmatrix} 1&0&0&0&0&0&0&0\\ 0&1&0&0&0&0&0&0\\ 0&0&0&0&0&1&0&0\\ 0&0&0&1&0&0&0&0\\ 0&0&0&0&1&0&0&0\\ 0&0&0&0&0&0&0&1\\ 0&0&0&0&0&0&1&0\\ 0&0&1&0&0&0&0&0 \end{bmatrix}$$

Remark 1: The symbol sequence is exactly the symbol sequence that classifies the canonically dressed torus, using the prescription given in Section 15.5.4 for classifying these flows. As a result, there is a simple, direct, and unique relation between the periodic orbits that label canonical tori and the transition matrix that describes the structure of the flow.

Remark 2: To determine the structure matrix it is sufficient to indicate the branch lines involved in k-cycles. For the example above this reduces to $(3,6,8)(1)(2)(4)(5)(7)$. Specification of the cycle structure immediately translates into the matrix $T_{\rm Str}$. The cycles identify the nonzero matrix elements. One-cycles correspond to diagonal matrix elements. In fact, these need not be written down explicitly: the branch lines involved are the complement of those specified in the k cycles, $k>1$. As a result, it is sufficient to describe the flow above by the three cycle $(3,6,8)$.

Remark 3: This is similar to the convention adopted in discussions of the permutation group, where group operations are often described by their nontrivial cycles.

15.7 ENUMERATION TO GENUS 9

In this section we describe all canonically dressed tori up to genus $g=9$. We conclude with remarks about entropy.

15.7.1 Genus 1

There is one canonically dressed torus of genus 1. This torus, and its canonical planar projection, are both shown in Fig. 15.9.

A genus-1 surface bounds many of the low-dimensional strange attractors that have been successfully analyzed to date [34]. These analyses have exploited the topological organization of the unstable periodic orbits in the strange attractor, using the fact that they are organized by the same stretch-and-fold mechanism that creates the strange attractor. The tools used include computation of linking numbers of pairs of orbits or their braids [87, 89, 127]. Although the theory of braids is over a century old, it is remarkable that a second, even more refined tool was developed relatively recently for the analysis of braids. This tool is the set of relative rotation rates of either a single orbit or a pair of periodic orbits [116].

15.7.2 Genus $>$ 1

There is no canonically dressed torus of genus 2. This is because the Euler characteristic is -2 but interior holes must have either 0 or 4, 6, 8, $\cdots$ singularities.

For flows in tori with genus $g > 1$ linking numbers still provide a useful tool for teasing out the structure of enclosed branched manifolds. It is not yet clear in exactly what capacity (if any) the relative rotation rates can be used to elicit information about the flow.

15.7.3 Genus 3

There is one canonically dressed genus-3 torus. It is shown in Fig. 15.17 along with three of its codings by periodic orbits. The structure part of its transition matrix is also given.

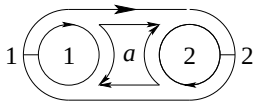

$$\begin{matrix} a\ a \\ 1\ 2 \\ 1\ 1 \end{matrix} \qquad T_{\rm Str} = \begin{bmatrix} 1 & 0 \\ 0 & 1 \end{bmatrix}$$

Fig. 15.17 There is one canonically dressed torus of genus 3.

15.7.4 Genus 4

There is one canonically dressed torus of genus 4. Since $g - 1 = 3$ there is only one possible Young partition: (3). The canonically dressed torus, its three descriptions by periodic orbits of period 3, and the structure part of its transition matrix are shown in Fig. 15.18.

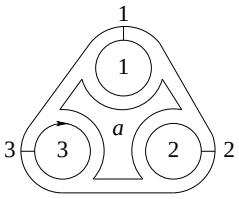

$$\begin{matrix} a\ a\ a \\ 1\ 2\ 3 \\ 1\ 1\ 1 \end{matrix} \qquad T_{\rm Str} = \begin{bmatrix} 1 & 0 & 0 \\ 0 & 1 & 0 \\ 0 & 0 & 1 \end{bmatrix}$$

Fig. 15.18 There is one canonically dressed torus of genus 4.

15.7.5 Genus 5

There are two canonically dressed tori of genus 5. Each one is uniquely described by a Young partition. The allowed partitions are (4) and (2,2). Both are shown in Fig. 15.19.

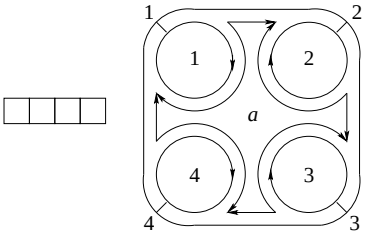

$$\begin{matrix} a\ a\ a\ a \\ 1\ 2\ 3\ 4 \\ 1\ 1\ 1\ 1 \end{matrix} \qquad T_{\rm Str} = \begin{bmatrix} 1 & 0 & 0 & 0 \\ 0 & 1 & 0 & 0 \\ 0 & 0 & 1 & 0 \\ 0 & 0 & 0 & 1 \end{bmatrix}$$

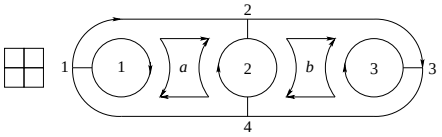

$$\begin{matrix} a\ a\ b\ b \\ 1\ 2\ 3\ 2 \\ 1\ 2\ 1\ 2 \end{matrix} \qquad T_{\rm Str} = \begin{bmatrix} 1 & 0 & 0 & 0 \\ 0 & 0 & 0 & 1 \\ 0 & 0 & 1 & 0 \\ 0 & 1 & 0 & 0 \end{bmatrix}$$

Fig. 15.19 There are two canonically dressed tori of genus 5.

15.7.6 Genus 6

There are two canonically dressed tori of genus 6. Once again each is uniquely described by its Young partition. The two allowed partitions are (5) and (3,2). Both are presented in Fig. 15.20.

15.7.7 Genus 7

At this stage we lose the nondegeneracy between Young partitions and canonically dressed tori that we have seen up to this point. Young partitions have $g-1=6$ boxes. The allowed Young partitions are (6), (4,2), (3,3), and (2,2,2). The last partition, with three rows, allows two distinct, inequivalent canonical flows. This degeneracy is lifted

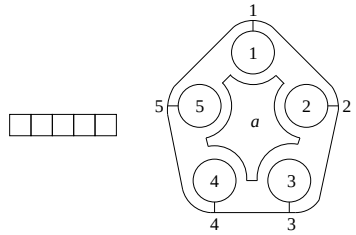

$$\begin{array}{c} a\ a\ a\ a\ a \\ 1\,2\,3\,4\,5 \\ 1\,1\,1\,1\,1 \end{array} \qquad T_{\mathrm{Str}} = \begin{bmatrix} 1 & 0 & 0 & 0 & 0 \\ 0 & 1 & 0 & 0 & 0 \\ 0 & 0 & 1 & 0 & 0 \\ 0 & 0 & 0 & 1 & 0 \\ 0 & 0 & 0 & 0 & 1 \end{bmatrix}$$

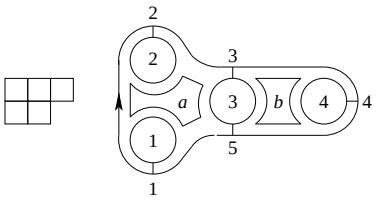

$$\begin{array}{c} a\ a\ a\ b\ b \\ 1\,2\,3\,4\,3 \\ 1\,1\,2\,1\,2 \end{array} \qquad T_{\mathrm{Str}} = \begin{bmatrix} 1 & 0 & 0 & 0 & 0 \\ 0 & 1 & 0 & 0 & 0 \\ 0 & 0 & 0 & 0 & 1 \\ 0 & 0 & 0 & 1 & 0 \\ 0 & 0 & 1 & 0 & 0 \end{bmatrix}$$

Fig. 15.20 Two canonically dressed tori of genus 6.

by the periodic words that describe the two different canonical tori. These statements are summarized in Fig. 15.21.

15.7.8 Genus 8

Genus-8 canonically dressed tori are described by Young partitions with seven boxes. The allowed partitions are (7), (5,2), (4,3), and (3,2,2). Degeneracy enters with the last partition, which describes three inequivalent flows. The spectrum of allowed canonical flows is summarized in Fig. 15.22.

15.7.9 Genus 9

For genus 9 there are 15 canonically dressed tori. There are four partitions with either one or two rows: (8), (6,2), (5,3), and (4,4). Each describes one flow. The two partitions with three rows are (4,2,2) and (3,3,2). Each describes (by accident) four different flows. The four-row partition $(2, 2, 2, 2) = (2^4)$ describes three inequivalent flows. The $15 = 4 + 2 \times 4 + 3$ flows are described by their branch line encoding and Young partition in Table 15.4. The last three flows in this list, all described by the Young partition (2^4), are shown in Fig. 15.23.

15.7.10 Entropy

There is one topological torus of genus g for each g, $g \geq 0$. When dressed with a flow, the number of inequivalent canonically dressed tori increases with g. We have computed the number of canonical bounding tori, $N(g)$, as a function of genus g by

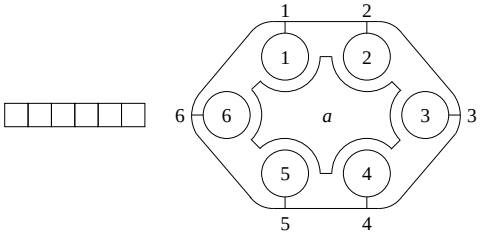

$$a\,a\,a\,a\,a\,a \\ 1\,2\,3\,4\,5\,6 \\ 1\,1\,1\,1\,1\,1$$

$$\begin{bmatrix} 1&0&0&0&0&0\\ 0&1&0&0&0&0\\ 0&0&1&0&0&0\\ 0&0&0&1&0&0\\ 0&0&0&0&1&0\\ 0&0&0&1&0&1 \end{bmatrix}$$

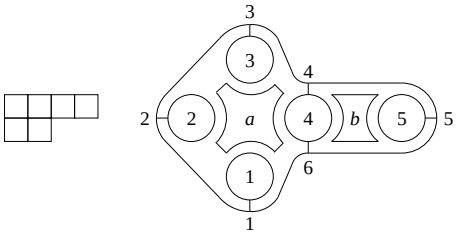

$$a\,a\,a\,a\,b\,b \\ 1\,2\,3\,4\,5\,4 \\ 1\,1\,1\,2\,1\,2$$

$$\begin{bmatrix} 1&0&0&0&0&0\\ 0&1&0&0&0&0\\ 0&0&1&0&0&0\\ 0&0&0&0&0&1\\ 0&0&0&0&1&0\\ 0&0&0&1&0&0 \end{bmatrix}$$

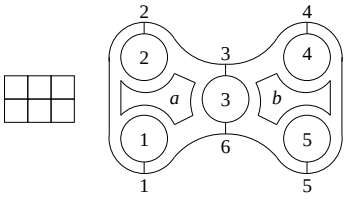

$$a\,a\,a\,b\,b\,b \\ 1\,2\,3\,4\,5\,3 \\ 1\,1\,2\,1\,1\,2$$

$$\begin{bmatrix} 1&0&0&0&0&0\\ 0&1&0&0&0&0\\ 0&0&0&0&0&1\\ 0&0&0&1&0&0\\ 0&0&0&0&1&0\\ 0&0&1&0&0&0 \end{bmatrix}$$

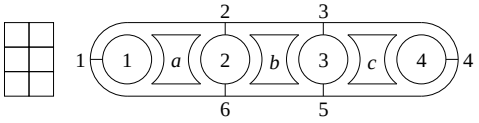

$$a\,a\,b\,c\,c\,b \\ 1\,2\,3\,4\,3\,2 \\ 1\,2\,2\,1\,2\,2$$

$$\begin{bmatrix} 1&0&0&0&0&0\\ 0&0&0&0&0&1\\ 0&0&0&0&1&0\\ 0&0&0&1&0&0\\ 0&0&1&0&0&0\\ 0&1&0&1&0&0 \end{bmatrix}$$

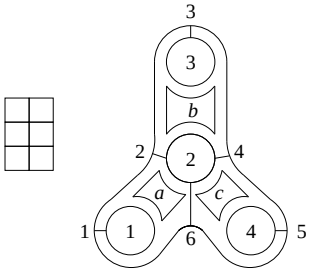

$$a\,a\,b\,b\,c\,c \\ 1\,2\,3\,2\,4\,2 \\ 1\,3\,1\,3\,1\,3$$

$$\begin{bmatrix} 1&0&0&0&0&0\\ 0&0&0&1&0&0\\ 0&0&1&0&0&0\\ 0&0&0&0&0&1\\ 0&0&0&0&1&0\\ 0&1&0&0&0&0 \end{bmatrix}$$

Fig. 15.21 Five canonically dressed tori of genus 7. Two inequivalent flows have Young partitions 2^3. The structure part of the transition matrix is given on the right.

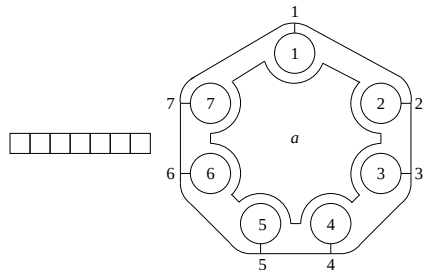

$$\begin{matrix} a\,a\,a\,a\,a\,a\,a \\ 1\,2\,3\,4\,5\,6\,7 \\ 1\,1\,1\,1\,1\,1\,1 \end{matrix} \qquad \begin{bmatrix} 1&0&0&0&0&0&0 \\ 0&1&0&0&0&0&0 \\ 0&0&1&0&0&0&0 \\ 0&0&0&1&0&0&0 \\ 0&0&0&0&1&0&0 \\ 0&0&0&0&0&1&0 \\ 0&0&0&0&0&0&1 \end{bmatrix}$$

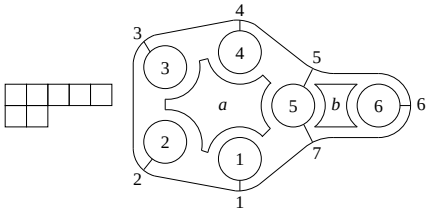

$$\begin{matrix} a\,a\,a\,a\,a\,b\,b \\ 1\,2\,3\,4\,5\,6\,5 \\ 1\,1\,1\,1\,2\,1\,2 \end{matrix} \qquad \begin{bmatrix} 1&0&0&0&0&0&0 \\ 0&1&0&0&0&0&0 \\ 0&0&1&0&0&0&0 \\ 0&0&0&1&0&0&0 \\ 0&0&0&0&0&0&1 \\ 0&0&0&0&0&1&0 \\ 0&0&0&0&1&0&0 \end{bmatrix}$$

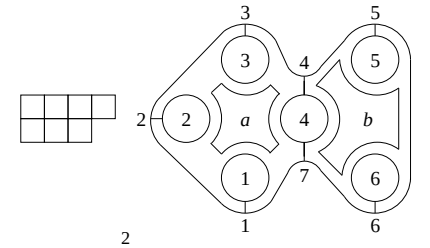

$$\begin{matrix} a\,a\,a\,a\,b\,b\,b \\ 1\,2\,3\,4\,5\,6\,4 \\ 1\,1\,1\,2\,1\,1\,2 \end{matrix} \qquad \begin{bmatrix} 1&0&0&0&0&0&0 \\ 0&1&0&0&0&0&0 \\ 0&0&1&0&0&0&0 \\ 0&0&0&0&0&0&1 \\ 0&0&0&0&1&0&0 \\ 0&0&0&0&0&1&0 \\ 0&0&0&1&0&0&0 \end{bmatrix}$$

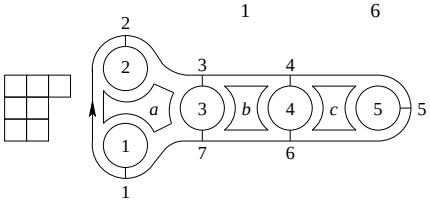

$$\begin{matrix} a\,a\,a\,b\,c\,c\,b \\ 1\,2\,3\,4\,5\,4\,3 \\ 1\,1\,2\,2\,1\,2\,2 \end{matrix} \qquad \begin{bmatrix} 1&0&0&0&0&0&0 \\ 0&1&0&0&0&0&0 \\ 0&0&0&0&0&0&1 \\ 0&0&0&0&0&1&0 \\ 0&0&0&0&1&0&0 \\ 0&0&0&1&0&0&0 \\ 0&0&1&0&0&0&0 \end{bmatrix}$$

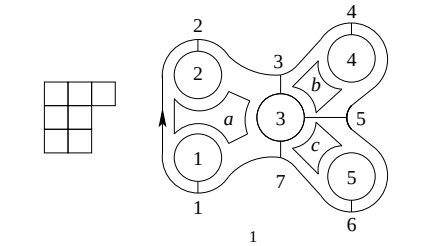

$$\begin{matrix} a\,a\,a\,b\,b\,c\,c \\ 1\,2\,3\,4\,3\,5\,3 \\ 1\,1\,3\,1\,3\,1\,3 \end{matrix} \qquad \begin{bmatrix} 1&0&0&0&0&0&0 \\ 0&1&0&0&0&0&0 \\ 0&0&0&0&1&0&0 \\ 0&0&0&1&0&0&0 \\ 0&0&0&0&0&0&1 \\ 0&0&0&0&0&1&0 \\ 0&0&1&0&0&0&0 \end{bmatrix}$$

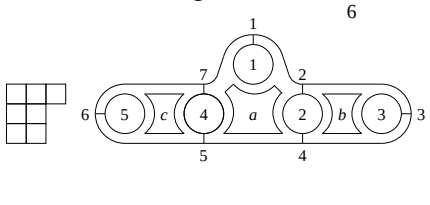

$$\begin{matrix} a\,a\,b\,b\,a\,c\,c \\ 1\,2\,3\,2\,4\,5\,4 \\ 1\,2\,1\,2\,2\,1\,2 \end{matrix} \qquad \begin{bmatrix} 1&0&0&0&0&0&0 \\ 0&0&0&1&0&0&0 \\ 0&0&1&0&0&0&0 \\ 0&1&0&0&0&0&0 \\ 0&0&0&0&0&0&1 \\ 0&0&0&0&0&1&0 \\ 0&0&0&0&1&0&0 \end{bmatrix}$$

Fig. 15.22 There are six canonically dressed tori of genus 8.

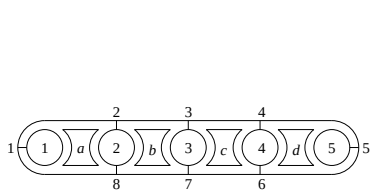

$$a\ a\ b\ c\ d\ d\ c\ b$$
$$1\ 2\ 3\ 4\ 5\ 4\ 3\ 2$$
$$1\ 2\ 2\ 2\ 1\ 2\ 2\ 2$$

$$\begin{bmatrix} 1&0&0&0&0&0&0&0\\ 0&0&0&0&0&0&0&1\\ 0&0&0&0&0&0&1&0\\ 0&0&0&0&0&1&0&0\\ 0&0&0&0&1&0&0&0\\ 0&0&0&1&0&0&0&0\\ 0&0&1&0&0&0&0&0\\ 0&1&0&0&0&0&0&0 \end{bmatrix}$$

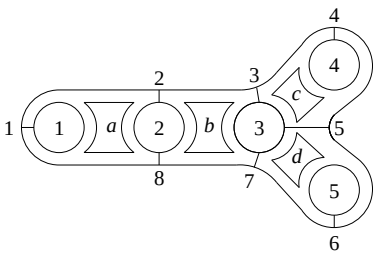

$$a\ a\ b\ c\ c\ d\ d\ b$$
$$1\ 2\ 3\ 4\ 3\ 5\ 3\ 2$$
$$1\ 2\ 3\ 1\ 3\ 1\ 3\ 2$$

$$\begin{bmatrix} 1&0&0&0&0&0&0&0\\ 0&0&0&0&0&0&0&1\\ 0&0&0&0&1&0&0&0\\ 0&0&0&1&0&0&0&0\\ 0&0&0&0&0&0&1&0\\ 0&0&0&0&0&1&0&0\\ 0&0&1&0&0&0&0&0\\ 0&1&0&0&0&0&0&0 \end{bmatrix}$$

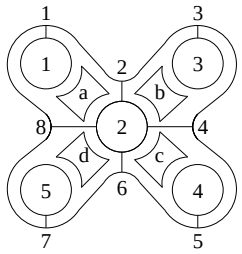

$$a\ a\ b\ b\ c\ c\ d\ d$$
$$1\ 2\ 3\ 2\ 4\ 2\ 5\ 2$$
$$1\ 4\ 1\ 4\ 1\ 4\ 1\ 4$$

$$\begin{bmatrix} 1&0&0&0&0&0&0&0\\ 0&0&0&1&0&0&0&0\\ 0&0&1&0&0&0&0&0\\ 0&0&0&0&0&1&0&0\\ 0&0&0&0&1&0&0&0\\ 0&0&0&0&0&0&0&1\\ 0&0&0&0&0&0&1&0\\ 0&1&0&0&0&0&0&0 \end{bmatrix}$$

Fig. 15.23 Three canonical flows are associated with the Young partition 2^4 of genus 9.

hand up to $g = 11$, and recursively using a FORTRAN code up to $g = 20$ [50]. The results are summarized in Table 15.5.

There appears to be a strong analogy between the growth in the number of unstable periodic orbits, $N(p)$, with period p in a strange attractor, and the growth in the number of canonical bounding tori, $N(g)$, with the genus g. In the former case the growth defines an entropy, the topological entropy, through

$$N(p) \simeq e^{h_{\mathrm{T}} p} \Longrightarrow h_{\mathrm{T}} = \lim_{p\to\infty} \frac{\log(N(p))}{p} \tag{15.9a}$$

Since $N(g)$ also grows rapidly, and since canonical bounding tori are classified by periodic orbits of period $g-1$, it makes intuitive sense to test whether the growth is exponential. We test this hypothesis by estimating $N(g)$ through

$$N(g) \simeq e^{h_{\mathrm{BT}}(g-1)} \overset{?}{\Longrightarrow} h_{\mathrm{BT}} = \lim_{g\to\infty} \frac{\log(N(g))}{g-1} \tag{15.9b}$$

Estimates of h_{BT} up to $g = 20$ are contained in Table 15.5. It is possible to construct rigorous lower and upper bounds on h_{BT}:

$$\log(2) \le h_{\mathrm{BT}} \le \log(3)$$

Table 15.4 Canonical flows that dress a genus-9 torus are listed in "alphabetic" order. Their Young partitions are also given.

	Period-8 Orbit	Young Partition
1	1 1 1 1 1 1 1 1	(8)
2	1 1 1 1 1 2 1 2	(6,2)
3	1 1 1 1 2 1 1 2	(5,3)
4	1 1 1 2 1 1 1 2	(4,4)
5	1 1 1 2 2 1 2 2	(4,2,2)
6	1 1 1 3 1 3 1 3	(4,2,2)
7	1 1 2 1 2 1 2 2	(3,3,2)
8	1 1 2 1 2 2 1 2	(4,2,2)
9	1 1 2 2 1 1 2 2	(3,3,2)
10	1 1 2 2 1 2 1 2	(3,3,2)
11	1 1 3 1 1 3 1 3	(3,3,2)
12	1 2 1 2 1 2 1 2	(4,2,2)
13	1 2 2 2 1 2 2 2	(2,2,2,2)
14	1 2 3 1 3 1 3 2	(2,2,2,2)
15	1 4 1 4 1 4 1 4	(2,2,2,2)

Table 15.5 Number of canonical bounding tori as a function of genus, g.

g	$N(g)$	$\log[N(g)]/(g-1)$	g	$N(g)$	$\log[N(g)]/(g-1)$
3	1	0.000000	12	145	0.452430
4	1	0.000000	13	368	0.492340
5	2	0.173287	14	870	0.520653
6	2	0.138629	15	2211	0.550086
7	5	0.268240	16	5549	0.574758
8	6	0.255966	17	14290	0.597957
9	15	0.338506	18	36824	0.618465
10	28	0.370245	19	96347	0.637540
11	67	0.420469	20	252927	0.654782

In fact, it is possible to construct a closed form expression for $N(g)$. This expression involves the coupling coefficients of the angular momentum algebra—in particular, it counts the number of ways $g-1$ spins $S=1$ can couple to total angular momentum $S_{\rm Tot}=0$. The expression is relatively simple when $g-1$ is prime. Fig. 15.24 shows a plot of $\log(N(g-1))/(g-1)$ vs. $1/(g-1)$ for primes up to 2000. It appears that the limit is the rigorous upper bound: $h_{\rm BT}\rightarrow\log(3)=1.098612$ [50].

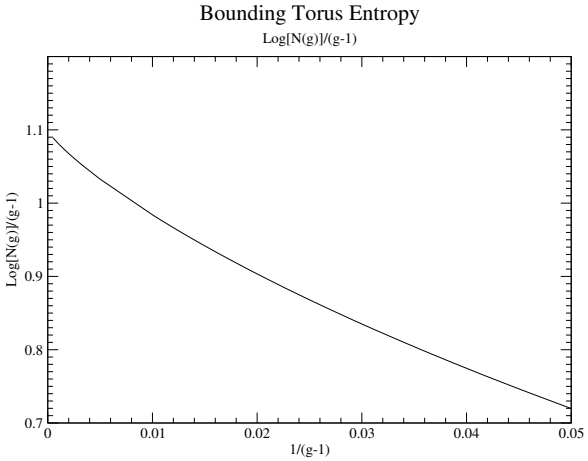

Fig. 15.24 The ratio $\log[N(g)]/(g-1)$ appears to converge at log(3).

15.8 COMPATIBLE BRANCHED MANIFOLDS

Bounding tori are branched manifold organizers in the same way that branched manifolds are periodic orbit organizers. Just as we can specify which orbits can be found on a branched manifold, we can also specify which branched manifolds are compatible with a bounding torus. The object of the present section is to provide this specification.

The most basic condition is that the flow along the individual branches is in the same direction as the flow inside the canonical bounding torus. The second condition is that branches connect components of the Poincaré section that are specified by the transition matrix. More specifically, there is at least one branch connecting each such pair of components. The information about branches is simply represented by a return map.

15.8.1 Return Maps

A genus-g canonical bounding torus has a global Poincaré section with $g-1$ components. Branch lines in any compatible branched manifold within the bounding torus can be moved to the components of the Poincaré section. Any compatible branched manifold has $g-1$ branch lines.

An initial condition on branch line i ($1 \leq i \leq g-1$) flows to two other branch lines, j, j', that are specified by the transition matrix. The cyclic part of the transition matrix, $T_{\rm Dyn}$, provides one value for j. This is $j = i+1 \pmod{g-1}$ in the canonical cyclic numbering of branch lines. The connectivity part of the transition matrix, $T_{\rm Str}$, indicates the other value for j. This is $j = f(i)$ ($\neq i+1$). As an example, one branched manifold that is compatible with the bounding torus C_3 is shown in Fig. 15.25(a). This branched manifold has seven branches. Its return map, shown in Fig. 15.25(b), indicates how the $g-1$ branch lines are mapped among themselves [21, 125]. The return map shows, for example, that an initial condition on branch line 1 is mapped back to branch line 1 for $0 < x <\sim \frac{1}{2}$, where x indicates distance measured along the branch line "from inside to outside." That is, $x = 0$ is on the boundary of the inner circle and $x = 1$ is on the outer disk boundary. For $\sim \frac{1}{2} < x < 1$ an initial condition on branch line 1 flows to branch line 2. Comparable statements hold for the other branches. While representations of the form shown in Fig 15.25(b) (and previously in Figs. 6.9 and 6.15) are convenient, they become profligate as $g-1$ becomes large (larger than 2), since the $(g-1) \times (g-1)$ "matrix" of return maps becomes sparse. A more economical representation of the same information is presented in Fig. 15.26. In this representation only the nonempty "matrix elements" in the return map of Fig. 15.25(b) are presented. The bottom row shows the part of the map described by the matrix $T_{\rm Str}$ and the top shows the part of the map described by the matrix $T_{\rm Dyn}$. There is a total of $g-1$ pairs of maps in this representation. A branched manifold compatible with a canonical genus-g torus has a minimum of $2(g-1)$ branches.

Branched manifolds cannot be reconstructed from return maps without providing additional information. Two pieces of information are required for each branch. One piece of information describes how a branch twists in transition from branch line i to branch line j. This can simply be determined by counting the signed crossings of

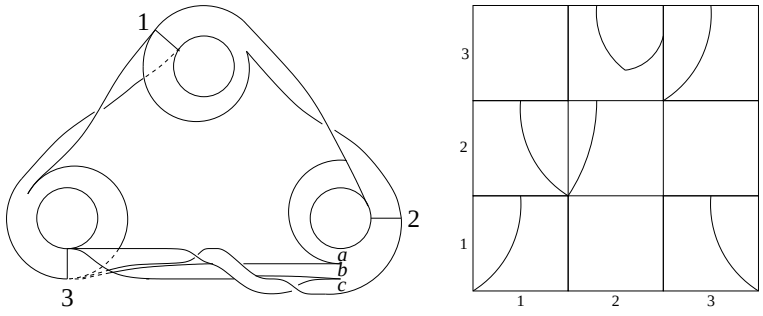

(a) Branched manifold (b) First-return map

Fig. 15.25 (a) Branched manifold with seven branches. This is one of many branched manifolds that are compatible with the bounding torus C_3. (b) Return map for the branches of this branched manifold. Each branch line is mapped to two branch lines. Two branches connect branch lines 2 and 3. For this reason the 3×3 "matrix" of return maps is sparse.

the two edges of each branch. This information can be provided by "dressing" each branch in the return map with this integer. This integer has been attached to each of the seven branches shown in the return map of Fig. 15.26. In particular, the branch from branch line 2 to 2 has zero torsion ($2 \xrightarrow{0} 2$), while the two branches flowing from branch line 2 to 3 have torsions $+1$ and $+2$ ($2 \xrightarrow{+1,+2} 3$).

The other piece of information required for a complete specification of the branched manifold describes how the branches that meet at a branch line are organized. This is the "layering" information. One way to provide this information is shown in Fig. 15.26. Three branches meet at branch line 3: $2 \xrightarrow{+1,+2} 3$ and $3 \xrightarrow{0} 3$. These branches are labeled α, β, γ in the order they are joined at branch line 3, seen from the top down. Ordering information is provided for the branches at the other two branch lines as well. This information can be summarized in a $(g-1) \times (g-1)$ (sparse) matrix, as follows:

3		$+1$ $+2$ α β	0 γ
2	$+1$ α	0 β	
1	0 α		-1 β
Target Source	1	2	3

To determine the torsion of the branches emanating from branch line i (convention: right-hand rule) read the integers vertically. To determine the order in which the branches are connected at branch line j (convention: top to bottom) read the Greek letters across.

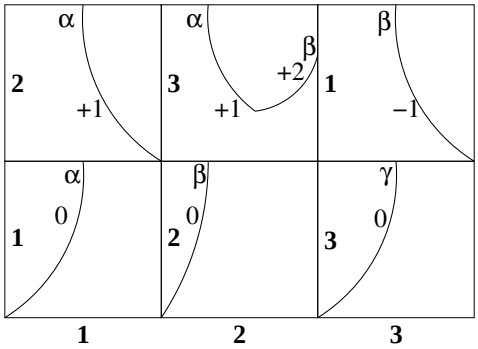

Fig. 15.26 A more economical presentation of return maps for branched manifolds in a genus-g torus. There are only $2 \times (g-1)$ panels in this representation of the return map.

Remark: In reading return maps of the form shown in Fig. 15.25(b) and the table above, the torsion information is organized vertically and the layering information is organized horizontally. Torsion information is attached to branches that originate on a branch line. This information is organized over the source branch line (vertically). Layering information is attached to branches that meet at a branch line. This information is organized across the target branch line (horizontally). Torsion information is obtained by looking forward, in the direction of the flow. Layering information is obtain by looking backward, in the direction the flow comes from.

15.8.2 Selection Rules

These topological tools (torsion and layering information) simultaneously provide rigid constraints on the useful degrees of freedom for the structure of chaotic flows in three dimensions. The rigidity is provided by the selection rules on the twisting and layering properties of the branches in a branched manifold.

The torsions of two branches enamating from adjacent parts of a branch line must obey an atomic physics–like selection rule:

$$\Delta t = \pm 1, 0 \tag{15.10}$$

The three branches emerging from branch line 2 in the example above have torsions $0,\ +1,\ +2$ moving from $x = 0$ (inside) to $x = 1$ (boundary). If we fix the torsion of the branch $2 \xrightarrow{0} 2$ to be 0, the only possibilities for the torsions of these three branches are:

$2 \to 2$	$2 \to 3$	$2 \to 3$
0	$+1$	$+2$
0	$+1$	0
0	0	$+1$
0	0	-1
0	-1	0
0	-1	-2

There are also selection rules for layering information. One involves branches emerging from the same branched line. It is shown in Fig. 15.26. The branch $2 \xrightarrow{+1} 3(\alpha)$ must join branch line 3 above the branch $2 \xrightarrow{+2} 3(\beta)$. The possibility $2 \xrightarrow{+1} 3(\beta)$ $2 \xrightarrow{+2} 3(\alpha)$ is forbidden by continuity considerations.

The other class of selection rules, involving flows to one target branch line from from two different source branch lines, is illustrated in Fig. 15.27. In Fig. 15.27(a) two branches meet at a branch line. One branch comes through each of the two flow tubes feeding the component of the Poincaré section that contains the branch line shown. As a control parameter is increased, one of the branches may expand and fold over. The three branches can meet as shown in Fig. 15.27(b), but if they meet as shown in Fig. 15.27(c) causality will be violated: Points at the intersection of these branches have two different futures.

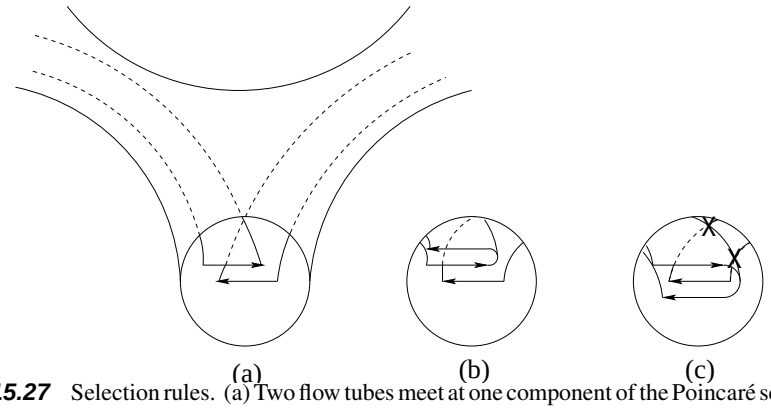

Fig. 15.27 Selection rules. (a) Two flow tubes meet at one component of the Poincaré section. The flow through one flow tube becomes more unstable with change in control parameters, requiring two branches to encode the dynamics. One organization of the three branches is possible (b) while another is not (c). The flow in (c) violates causality where an intersection is forced at the point labeled $\times$.

15.8.3 Perestroikas of Branched Manifolds

Perestroikas of branched manifolds have been described in [75] for flows in a genus-1 torus. We briefly review these results here, because they can be extended without difficulty to flows in higher genus surfaces.

A flow with a genus-1 surface can exhibit chaotic behavior provided it projects under the Birman-Williams identification to a branched manifold with more than one branch. As control parameters change, the number of branches as well as the degree to which they overlap can change. In Fig. 15.28 we show the intersection of a 2-branch manifold with a Poincaré section, and illustrate one possible sequence of events that can occur as control parameters are varied. In this sequence the orientation-preserving branch grows as the control parameter changes.

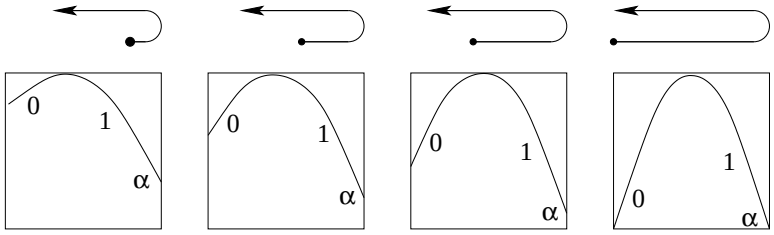

Fig. 15.28 As a control parameter is varied, the branches of a branched manifold can grow or contract. Here the orientation-preserving branch grows in the progression from left to right.

If the control parameter continues to change it is possible for a new branch to be created. Fig. 15.29 shows four possible ways this new branch can be created. The only four possibilities for the perestroika creating a third branch are shown in this

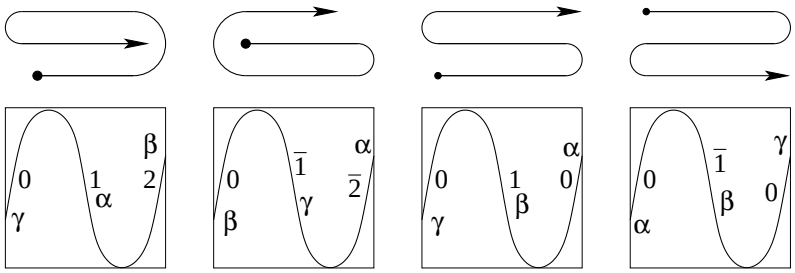

Fig. 15.29 As control parameters continue to increase, a third branch can be added. It can be added in the four ways shown to the two already present in Fig. 15.28. All four three-branch manifolds possess the same (bare) return map. The four return maps are distinguished by the dressing symbols that contain torsion and layering information.

figure. This limited range of possibilities is constrained by continuity arguments. It should be emphasized that the four bare return maps are identical. The four return maps for these three possible three-branch manifolds differ only in their dressing.

If the control parameter continues to change a fourth branch can be added, or one of the three branches already present can be removed. Addition or deletion of single branches can occur only at the extremities. Single branch addition or deletion is subject to constraints imposed by the uniqueness theorem. Two allowed perestroikas and one forbidden perestroika for one of the three-branched manifolds of Fig. 15.29 are shown in Fig. 15.30.

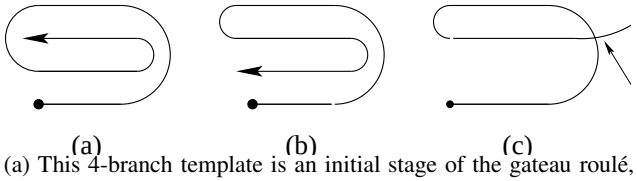

Fig. 15.30 (a) This 4-branch template is an initial stage of the gateau roulé, seen in laser experiments [34] and nerve firing studies [37]. (b) This 4-branch template is seen in the Duffing oscillator [36]. (c) This flow violates causality because of the self-intersection (arrow).

Perestroikas for flows contained in genus-g bounding tori are described similarly. The flow leaving branch line i splits into one component flowing to branch line $i+1$ (under T_{Dyn}) and another part flowing to branch line $f(i)$ (under T_{Str}). The return map over branch line i consists of two panels. One possible perestroika is shown in Fig. 15.31. In this series of return maps tearing [between $f(i)$ and $i+1$] occurs in the transition from one branch line [$f(i)$] to the other [$i+1$]. Within a single branch line only folding is possible. Tearing is indicated by a discontinuity. Folding is indicated by the existence of a two-sided derivative at extrema [21,75].

For a flow in a genus-g bounding torus, the return map consists of $g-1$ panel pairs of the type shown in Fig. 15.31. Each pair can independently exhibit perestroikas as shown in the figure.

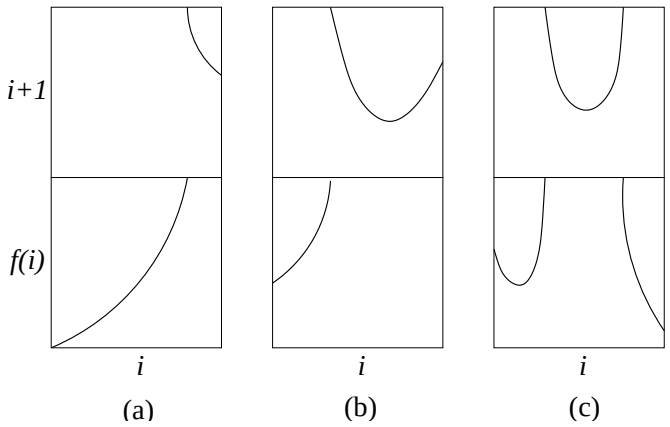

Fig. 15.31 Return map for a branched manifold compatible with a genus-g torus. The return map consists of a set of $g-1$ pairs of panels. Each describes how the flow from branch line i is mapped to the two branch lines allowed by the structure of the bounding torus. Each panel pair can undergo a perestroika of the type shown above. The perestroikas of each panel pair need not be correlated.

Continuity conditions and the uniqueness theorem impose constraints on perestroikas. The change in global torsion on branches originating from adjacent positions on the *same* branch line obeys the "atomic selection rule" $\Delta t = \pm 1, 0$. The layering information must respect the uniqueness condition. When two branch lines are connected by two or more branches, the torsion and layering information must satisfy constraints as illustrated in Fig. 15.30. When three or more branches join at a branch line, they must satisfy constraints of the type illustrated in Fig. 15.27.

15.9 HOW TO EXTRACT FROM EXPERIMENTAL DATA

If the dynamics that governs a physical process generates a low-dimensional ($d_L < 3$) strange attractor contained in a genus-g surface, how is one to know?

Usually all that is available from measurements is a single scalar time series of finite length, with some noise component. In order to "reconstruct" an attractor it is necessary to embed the time series in $\mathbb{R}^3$, or at least some 3-dimensional manifold. There are many ways to embed data: time delay, differential embeddings, integro-differential embeddings, fractional derivatives and integrals constructed from Fourier processing, Hilbert transforms, etc. These have been described in [34].

The traditional embedding into $\mathbb{R}^3$ is the time delay embedding:

$$X(t) \to \mathbf{X}(t) = [X(t), Y(t), Z(t)] = [X(t), X(t-\tau_1), X(t-\tau_2)] \qquad (15.11)$$

This is a two-parameter family of embeddings, depending on the delay parameters τ_1 and τ_2. It is not an embedding (it is an injection) for $\tau_1 = \tau_2$ and for $\tau_1 = 0$ or $\tau_2 = 0$. It is "delay" if $\tau_1 > 0$ and $\tau_2 > 0$. Advance embeddings are also possible:

they are equivalent to delay embeddings with some redefinition of the coordinates. Values of the delays τ_1, τ_2 that provide embeddings exist in open sets in the (τ_1, τ_2) parameter plane. Embedding islands are separated from each other. The topological properties of an embedded attractor can differ from island to island, but only in a systematic way. All embeddings provide the same information about the mechanism that generates chaos. This is discussed in some detail in [126].

We adopt the differential embedding

$$\begin{aligned} X(t) &= X(t) \\ Y(t) &= \dot{X}(t) \\ Z(t) &= \dot{Y}(t) \end{aligned} \tag{15.12}$$

This embedding is related by an affine transformation to the delay embedding with $\tau_2 = 2\tau_1$ and $\tau_1 = \tau$ small. That is, $\dot{X} \sim X(t+\tau) - X(t-\tau)$ and $\ddot{X}(t) \sim X(t+\tau) - 2X(t) + X(t-\tau)$. The dynamics is defined by the single nontrivial equation

$$\dot{Z}(t) = f(X, Y, Z) = f(X, \dot{X}, \ddot{X}) = \frac{d^3X}{dt^3} \tag{15.13}$$

If $X(t)$ is generated by an equivariant dynamical system (i.e., Lorenz attractor with $\mathcal{R}_Z$ symmetry), the function $f(X, Y, Z)$ is of necessity odd:

$$f(-X, -\dot{X}, -\ddot{X}) = -f(X, \dot{X}, \ddot{X}) \tag{15.14}$$

As a result, this type of embedding cannot recover full information about the symmetry of the original system. Specifically, parity and layering information is lost.

The fixed points of the dynamical system in the differential embedding all live on the X axis. In order to recover information about the underlying dynamics the observed scalar time series $X(t)$ must be *generic*. That is, all the fixed points in the underlying dynamics *must* have different X values.

Remark: Since all fixed points in a differential embedding occur along the X-axis, it would appear that the only bounding tori that can be recovered from this type of embedding have the linear structure of the type A_n. That this is not true will be shown in the two examples presented in Figs. 15.32 and 15.33.

The procedure for recovering information about the structure of the underlying flow from a scalar time series is as follows:

1. Construct a differential embedding of the generic time series $X(t)$ in $\mathbb{R}^3$.
2. Project this embedding onto the X-Y = X-$\dot{X}$ plane. The flow circulates clockwise in this plane.
3. Verify that this is an embedding by checking that all crossings are transverse. If any tangencies occur, stop and search for a new time series $X(t)$.
4. Identify the "round" holes in this embedding.
5. Associated with each there is at least one region in which squeezing occurs. These are regions where the flows from two different holes come together. They can be identified by the presence of transverse crossings of flows originating from different regions in the phase space.

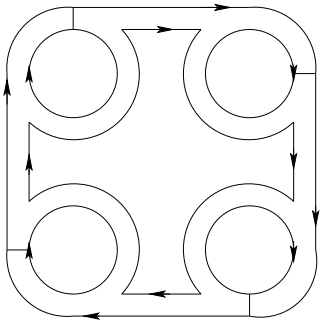

(a) Canonical torus

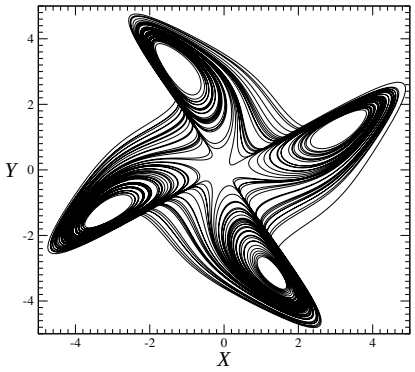

(b) Double cover of the Lorenz system

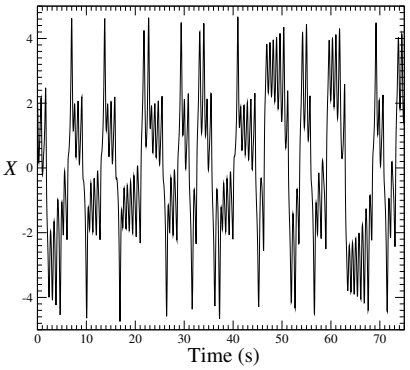

(c) Time series $X(t)$

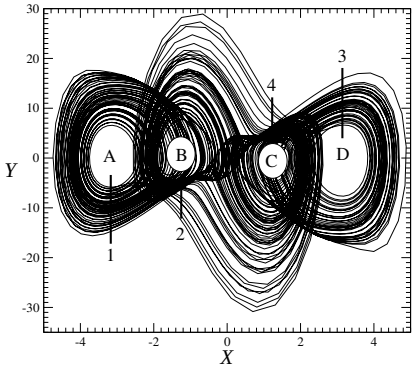

(d) Differential embedding X-$\dot{X}$

$$\begin{bmatrix} 1 & 1 & 0 & 0 \\ 0 & 1 & 1 & 0 \\ 0 & 0 & 1 & 1 \\ 1 & 0 & 0 & 1 \end{bmatrix} \rightarrow \begin{bmatrix} 0 & 1 & 0 & 0 \\ 0 & 0 & 1 & 0 \\ 0 & 0 & 0 & 1 \\ 1 & 0 & 0 & 0 \end{bmatrix} + \begin{bmatrix} 1 & 0 & 0 & 0 \\ 0 & 1 & 0 & 0 \\ 0 & 0 & 1 & 0 \\ 0 & 0 & 0 & 1 \end{bmatrix}$$

(e) Transition matrix

Fig. 15.32 (a) Canonical bounding torus C_4 of genus 5. (b) The double cover of the Lorenz flow with $\mathcal{R}_Z(\pi/2)$ symmetry axis through the saddle in the middle is compatible with this bounding torus. A time series is collected by projecting down onto the horizontal axis. The axis is chosen to maximally separate the foci. (c) Time series $X(t)$ shows four unstable foci visited in a definite order. (d) The projection of the differential embedding onto the X-$\dot{X}$ plane shows four round holes and four squeezing regions. (e) The transition matrix is the sum of a cylcic matrix and one giving the structure of the bounding torus: C_4.

6. Associate a branch line with each of the squeezing regions.
7. Construct the transition matrix for the embedded flow.
8. Reduce the transition matrix to canonical form (cf. Fig. 15.16) by a similarity transformation (permutation matrix). This is facilitated by a clever choice for numbering the squeezing regions. The clever choice is made as follows. Begin anywhere in the flow, and follow around the (outer) boundary until all squeezing regions have been encountered once before returning home. Label the squeezing regions in the order in which they have been encountered. This generates the cyclic part of the transition matrix.
9. Subtract $T_{\rm Dyn}$ from T to recover $T_{\rm Str}$. This describes the structure of the genus-g surface.

We illustrate this algorithm for the flow in two inequivalent genus-5 surfaces: C_4 and A_3. Fig. 15.32(a) shows the canonical form C_4 with genus-5. A flow that is compatible with this canonical form is shown in Fig. 15.32(b). This flow is a double cover of the Lorenz dynamical system with the $\mathcal{R}_Z(\pi/2)$ symmetry axis passing through the origin. A time series $X(t)$ is collected by projecting the flow onto an axis that maximally separates the four foci. This is the X-axis in Fig. 15.32(b). The time series $X(t)$ is plotted in Fig. 15.32(c). It is apparent from the time series that there are four unstable foci, and that they are visited in a definite order. A differential embedding is constructed from the time series $X(t)$. Its projection is shown in Fig. 15.32(d). Four circular holes are apparent in the embedding. These holes are labeled A, B, C, D. Four squeezing regions are identified and labeled sequentially 1, 2, 3, 4, starting from A. The transition matrix is constructed from the X-$\dot{X}$ embedding using the numbering of the squeezing regions. This is shown in Fig. 15.32(e), expressed as the sum of a cyclic matrix $(1 \to 2 \to 3 \to 4 \to 1)$ and a diagonal matrix. This is sufficient to identify the bounding torus as C_4.

As a second example we consider a flow inside the other canonical genus-5 bounding torus: A_3. The canonical form A_3 is shown in Fig. 15.33(a). A flow that is compatible with this canonical form is shown in Fig. 15.33(b). This flow is a double cover of the Lorenz dynamical system with the $\mathcal{R}_Z(\pi)$ symmetry axis passing through a focus. A time series $X(t)$ is collected by projecting the flow onto an axis (again, the X-axis) that maximally separates the three foci. The time series $X(t)$ is plotted in Fig. 15.33(c). It is apparent from the time series that there are three unstable foci. A differential embedding is constructed from the time series $X(t)$. Its projection is shown in Fig. 15.33(d). Three circular holes are apparent in the embedding. These holes are labeled A, B, C. Four squeezing regions are identified and labeled sequentially 1, 2, 3, 4, starting from A. The transition matrix is constructed from the X-$\dot{X}$ embedding using the numbering of the squeezing regions. This is shown in Fig. 15.33(e), expressed as the sum of a cyclic matrix $(1 \to 2 \to 3 \to 4 \to 1)$ and a matrix describing a 2-cycle. This is sufficient to identify the bounding torus as A_3.

We emphasize here that the reconstructed attractor is diffeomorphic with the original attractor. It may not be identical (isotopic) because the folding directions in the embedded attractor are determined by the (anti)symmetry of the function $f(X, \dot{X}, \ddot{X})$, and this may not reflect the symmetry of the original underlying attractor.

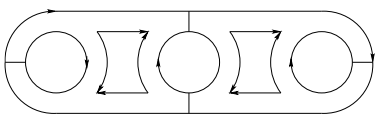

(a) Canonical torus

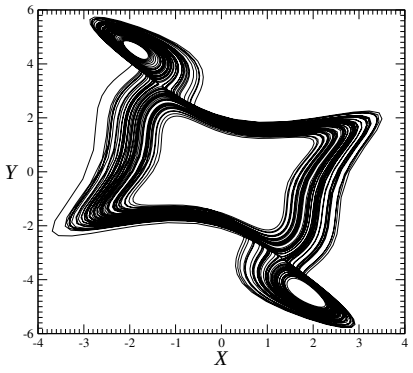

(b) Double cover of the Lorenz system

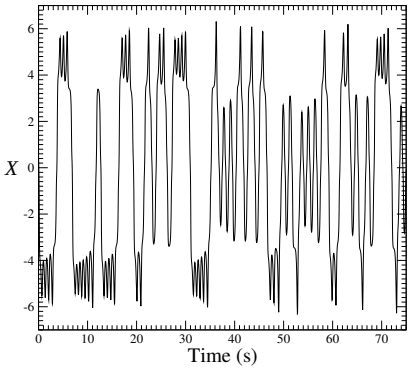

(c) Time series $X(t)$

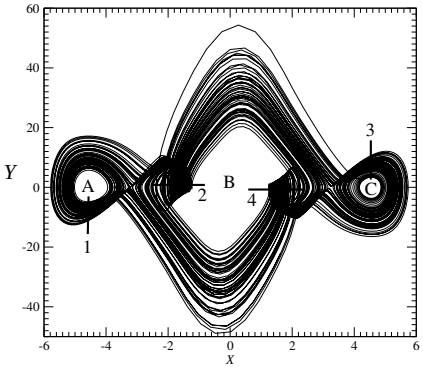

(d) Differential embedding X-$\dot{X}$

$$\begin{bmatrix} 1 & 1 & 0 & 0 \\ 0 & 0 & 1 & 1 \\ 0 & 0 & 1 & 1 \\ 0 & 1 & 0 & 1 \end{bmatrix} \rightarrow \begin{bmatrix} 0 & 1 & 0 & 0 \\ 0 & 0 & 1 & 0 \\ 0 & 0 & 0 & 1 \\ 1 & 0 & 0 & 0 \end{bmatrix} + \begin{bmatrix} 1 & 0 & 0 & 0 \\ 0 & 0 & 0 & 1 \\ 0 & 0 & 1 & 0 \\ 0 & 1 & 0 & 0 \end{bmatrix}$$

(e) Transition matrix

Fig. 15.33 (a) Canonical bounding torus A_3 of genus 5. (b) The double cover of the Lorenz flow with $\mathcal{R}_Z(\pi)$ symmetry axis through either focus is compatible with this bounding torus. A time series is collected by projecting down onto an axis chosen to maximally separate the foci. (c) Time series $X(t)$ shows three unstable foci. (d) The projection of the differential embedding onto the X-$\dot{X}$ plane shows three round holes and four squeezing regions. (e) The transition matrix is the sum of a cyclic matrix and one giving the structure of the bounding torus: A_3.

15.10 PERESTROIKAS OF CANONICAL TORI

Dynamical systems equations are expressed in terms of state variables and control parameters. The systems studied in this work typically involve only three state variables, as the theory of 3-dimensional dynamical systems is well understood, while dynamical systems in higher dimensions are not understood at all. All of the dynamical systems studied so far depend on a finite, in fact a very limited, number of control parameters. As the control parameters are varied, the system responds by changing: its spectrum of periodic orbits as well as their type (all unstable vs. some stable, strange attractor(s) vs. stable fixed points or periodic orbits), the number and labeling of branches needed to describe flows, etc. By varying a limited number of control parameters it is possible to exhibit only a limited number of changes in behavior.

In this section we wish to describe "perestroikas" of dynamical systems—more specifically, of their bounding tori. Perestroika means change. We use as our model for this discussion the methods and theory developed to study the perestroikas of catastrophes: scalar functions (potentials) depending on many variables [32]. As a particular example, we can think of the "Ginzburg-Landau" family of potentials $V(x) = \frac{1}{4}x^4 + \frac{1}{2}ax^2$. This is a one-parameter family of potentials. A very useful question to ask is: How does this family behave under an arbitrary perturbation $V(x) \rightarrow V'(x) = V(x) + f(x)$, where $f(x)$ is arbitrary? The question can be answered locally, in the neighborhood of the critical points (where $dV'(x)/dx = 0$). The answer is that the *most general* perturbation can be encapsulated in the two-parameter family of functions

$$V'(x) = \frac{1}{4}x^4 + \frac{1}{2}ax^2 + bx \tag{15.15}$$

Once the most general unfolding of the original function has been determined, it is a straightforward matter to study the properties—the perestroikas—that this family of functions can undergo.

More generally, there is a theory of "unfoldings" (universal perturbations) of mappings of $\mathbb{R}^m \rightarrow \mathbb{R}^n$ that constitutes the theory of singularities of mappings [6,7,16,38]. This is a generalization of Catastrophe theory. In many cases there is a finite-dimensional unfolding: this means that there is only a finite number of parameters (such as a and b above) involved in the universal perturbation. In all cases the universal perturbation is *local*, valid only in the neighborhood of the critical points.

We would like to create a theory of unfoldings of dynamical systems in order to study the perestroikas that they can exhibit. There is such a theory for the neighborhoods of the fixed points of a flow. However, this is also a local theory—valid only in the neighborhood of the fixed points. This theory can be applied to degenerate fixed points, such as those that give rise to interior holes of a bounding torus with more than four singularities.

We are interested in a larger, much more difficult problem. The problem is: given a dynamical system depending on n state variables and k control parameters, what is the family of perturbations of the source terms that allow us to construct all possible "global perturbations" of that dynamical system. Not only is this vague (what is a

"perturbation"?), but it is at present not possible to answer. We don't even know if the dimension of such a universal perturbation is countable or uncountable. For this reason, we cannot approach this question along the same lines exploited for Catastrophe theory. Our approach must use the most powerful tools currently available—these are topological in nature. In the remainder of this section, and those that follow, we adopt the following approach. We assume that there is some "universal perturbation." Each term in such a perturbation is coupled to some "perturbation parameter" (like b in Eq. (15.15)). We assume one or more perturbation parameters are responsible for producing *any* global perestroika that is topologically possible—not forbidden by topological selection rules. We therefore undertake a study of "topological perestroikas." The unfoldings we exploit are topological in nature.

When perturbation parameters change, lots of exciting things can happen to a strange attractor.

1. Under small changes the symbols that code periodic orbits do not change but the spectrum of periodic orbits does change. This is described by changes in the basis sets of orbits [88], not very well understood for the Smale horseshoe mechanism and basically not understood at all in any other case.
2. Under larger changes the spectrum of symbols does change. This means that branches are added to or deleted from the branched manifold that the chaotic flow projects to [65]. Branched manifold perestroikas have been discussed in Sect. 15.9.
3. Under yet larger changes the topological organization of the branched manifolds may change. This involves changes in the topology of the surface bounding the flow [21,75].

In this section we describe perestroikas of bounding tori. As usual, it is easiest to approach this study by starting with the larger structure and determining how it is reduced in size by reversible transformations. After all, it is easier to see what we can lose than what we can gain.

We approach this study by looking at the flow organized by a genus-g torus. Then we restrict the flow through one of the $2(g-1)$ flow tubes, finally extinguishing the flow. This is responsible for a change in the genus of the torus bounding the flow that remains.

The flow rearrangement depends strongly on whether the flow through an exterior flow tube or an interior flow tube is shut down. We treat the two cases separately.

15.10.1 Exterior Flow Tubes

Exterior flow tubes are described by the cyclic part of the transition matrix. One boundary of an exterior flow tube, in the canonical representation, is the outside boundary of the disk describing the canonical flow.

As usual, we illustrate the concepts by discussing an example. Fig. 15.34 shows a canonical genus-6 torus, with standard labeling of branch lines and holes. The exterior flow tubes describe transitions from branch line i to branch line $i+1$ (or $5 \rightarrow 1$).

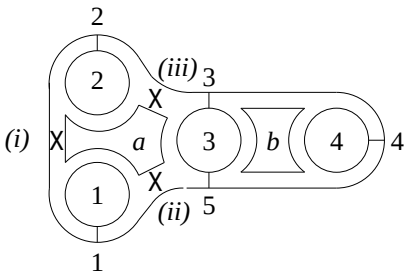

Fig. 15.34 Genus 6 canonical bounding torus 11212, $aaabb$, or 12343. Flows in the exterior flow tubes is cut off successively at i, ii, and iii.

Assume that the flow $1 \to 2$ is gradually restricted and eventually annihilated as some perturbation parameter is changed. This is represented by the $\times$ at (i) in Fig. 15.34. The flow originating from branch line 1 must return to branch line 1. If there is only one branch $1 \to 1$ the flow will settle on a stable limit cycle. In order for a strange attractor to remain, there must be at least two branches from branch line 1 back to branch line 1.

Almost all initial conditions on any other branch line will eventually find their way to branch line 1, where they will be trapped forever around hole 1. A measure-zero set of initial conditions on branch lines 2, 3, 4, 5 define unstable periodic orbits that never encounter branch line 1. All other points on these branch lines provide initial conditions for transient orbits that transit branch lines 2–5 for longer or shorter times before falling into the basin of 1. In other words, closing off the flow $1 \to 2$ creates an attractor (stable limit cycle or strange attractor) around 1 and drains the flow from the neighborhoods of the other foci.

If we now also restrict the flow $5 \to 1$, represented by the $\times$ at (ii) in Fig. 15.34, the flow originating on branch lines 2–5 cannot reach branch line 1. We set up the possibility of a second, disconnected attractor. The flow in this attractor circulates among the branch lines 3, 4, and 5. Initial conditions on branch line 2 provide transients that eventually drain to this second attractor. There may be a set of unstable periodic orbits around hole 2 if there is more than one branch in $2 \to 2$.

Finally, if we restrict the flow $2 \to 3$ (the $\times$ at (iii) in Fig. 15.34) we prevent the escape of the flow from the neighborhood of focus 2, and create conditions for a third disconnected attractor. Once again, this is a stable limit cycle if $2 \to 2$ has one branch, and there may be a strange attractor if $2 \to 2$ supports more than one branch.

When the flow $1 \to 2$ is cut off, the transition matrix undergoes the transformation

$$\begin{bmatrix} 1 & 1 & 0 & 0 & 0 \\ 0 & 1 & 1 & 0 & 0 \\ 0 & 0 & 0 & 1 & 1 \\ 0 & 0 & 0 & 1 & 1 \\ 1 & 0 & 1 & 0 & 0 \end{bmatrix} \xrightarrow[\longrightarrow]{\times \text{ at } (i)} \left[\begin{array}{c|cccc} 1 & 0 & 0 & 0 & 0 \\ \hline 0 & 1 & 1 & 0 & 0 \\ 0 & 0 & 0 & 1 & 1 \\ 0 & 0 & 0 & 1 & 1 \\ 1 & 0 & 1 & 0 & 0 \end{array}\right] \tag{15.16}$$

The transition matrix for the full flow, on the left in (15.16), is *irreducible* as a matrix. No similarity transformation can transform it to a block-diagonal form over the integers 0 and 1. Irreducible for a dynamical system means that any branch line can be reached from any other branch line.

The transition matrix for the restricted flow, on the right in (15.16), is *reducible* as a matrix. This means that in a block submatrix decomposition one of the off-diagonal submatrices is zero while the other is not. The 1×4 off-diagonal submatrix of zeroes reflects the condition that no flow escapes from branch line 1 to other branch lines. The other off-diagonal submatrix is nonzero. Its structure informs us that transients reach branch line 1 via branch line 5.

The concepts of reducible, fully reducible, and irreducible for the matrix representations of groups and algebras apply equally well to flows generated by dynamical systems:

Representation	Property of Dynamical System
Reducible	Transients flow to an attractor.
Fully Reducible	There is a complete set of disjoint attractors and no transients.
Irreducible	There is one attractor, no transients, and anywhere can be reached from anywhere else.

In the example above, the original flow is irreducible. Restricting the flow $1 \to 2$, at (i), produces an attractor at 1 with transients involving branch lines $2, 3, 4, 5$. This flow is reducible. Restricting the flow further at $5 \to 1$, at (ii), isolates the attractor around 1 and produces another attractor involving branch lines $3, 4, 5$ with transients from branch line 2. This flow is also reducible. Finally, restricting the flow out of 2 [$2 \to 3$, at (iii)] produces disjoint attractors around 1, around 2, and around $(3, 4, 5)$. This flow is fully reduced. It consists of irreducible flows bounded by the genus-1 surfaces containing hole 1, hole 2, and the genus-3 surface containing holes $3,\ b,\ 4$. In the latter flow the canonical form is obtained by identifying branch lines 3 and 5. Cutting the flow at (i), (ii), and (iii) is responsible for the transition from the irreducible flow in the orignal genus-6 surrounding torus to a fully reducible flow in $A_1 \cup A_1 \cup A_2$.

We discuss in some more detail what happens when we cut off the flow in an exterior flow tube $i \to i + 1$, where $f(i) \neq i$. An example is shown in Fig. 15.35(a), where the flow $3 \to 4$ is obstructed. In this case transients originate on branch line 4. After transients die out, the flow is restricted to branch lines $5, 1, 2, 3$. What is the nature of the residual attractor? The residual flow has the structure shown in Fig. 15.35(b). To obtain this form, we eliminate branch line 4 and identify branch lines 3 and 5. We keep the inputs to branch line 3 (columns) and the outputs from branch line 5 (rows). The sequence of transition matrices for the full flow, the reducible flow obtained by cutting off the flow $3 \to 4$, and the residual attractor after transients have

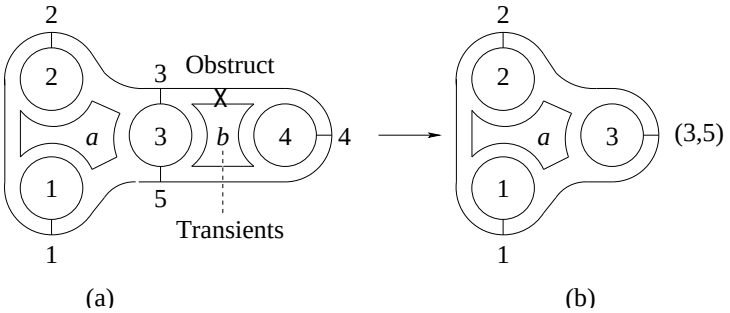

Fig. 15.35 Genus-6 canonical bounding torus 11212, $aaabb$, or 12343. Flow is cut off in the exterior flow tube $3 \to 4$, yielding canonical form C_3. If the flow $4 \to 5$ is also cut off, the canonical form is now fully reduced: $C_3 \cup A_1$.

died out, is:

$$\begin{bmatrix} 1 & 1 & 0 & 0 & 0 \\ 0 & 1 & 1 & 0 & 0 \\ 0 & 0 & 0 & 1 & 1 \\ 0 & 0 & 0 & 1 & 1 \\ 1 & 0 & 1 & 0 & 0 \end{bmatrix} \begin{matrix} \times \\ \longrightarrow \end{matrix} \begin{bmatrix} 1 & 1 & 0 & 0 & 0 \\ 0 & 1 & 1 & 0 & 0 \\ 0 & 0 & 0 & \times & 1 \\ 0 & 0 & 0 & 1 & 1 \\ 1 & 0 & 1 & 0 & 0 \end{bmatrix} \longrightarrow \begin{bmatrix} 1 & 1 & 0 \\ 0 & 1 & 1 \\ 1 & 0 & 1 \end{bmatrix} \begin{matrix} 1 \\ 2 \\ 3+5 \end{matrix} \tag{15.17}$$

The last matrix is obtained by eliminating branch line 4: the column containing the $\times$ in the middle matrix. Row 4 is also eliminated. The adjacent columns (and rows) are combined and identified as $3 + 5$. The column labeled $3 + 5$ contains the *inputs to* branch line 3: $[0, 1, 1]^t$ indicates that the branch lines 2 and $(3 + 5)$ feed $(3 + 5)$. The row labeled $(3 + 5)$ contains the *outputs from* branch line 5: $[1, 0, 1]$ indicates that the output from branch line 5 flows to branch lines 1 and $(3 + 5)$. This transition matrix clearly identifies the bounding torus for this attractor as C_3.

If the flow $4 \to 5$ is also obstructed (Fig. 15.35(a)) the attractor is fully reducible and contained in the union of two bounding tori: $C_3 \cup A_1$.

The general case for constructing the attractor obtained after obstructing the flow $i \to i + 1$ in an exterior flow tube can be deduced from the examples above:

If $f(i) = i$, the attractor, after transients have died out, is contained in A_1 with one branch line.

If $f(i) \neq i$ then $f(i) = j \geq i + 2 \pmod{g - 1}$.

1. Eliminate branch lines $i + 1, \cdots, j - 1$, and corresponding rows and columns in the transition matrix.
2. Identify branch lines i and j as a single branch line (i, j).
3. Column i is input to column (i, j): the inflows to branch line i remain the inflows to the combined branch line (i, j).
4. Row j is input to row (i, j): the outflows from branch line j remain the outflows from the combined branch line (i, j).
5. The residual flow has $g - 1 - (j - i)$ branch lines and lives in a torus of genus $g - (f(i) - i)$.

15.10.2 Interior Flow Tubes

Interior flow tubes are described by the structure part of the transition matrix. Flows through these tubes involve no part of the exterior disk boundary in the canonical projection.

Once again, two cases deserve separate discussions. This time the distinction depends on the hole with singularities that is adjacent to the extinguished flow. The difference depends on whether this hole has more than four singularities or exactly four singularities.

The basic idea is the same in both cases. Removing the flow in an interior flow tube removes an (s, j) pair of singularities from the adjacent hole with singularities. If the hole originally had $2p$ singularities, once the flow has been closed off the adjacent hole has $2p - 2$ singularities. If $2p - 2 \geq 4$, the perestroika removes one round hole and one branch line. On the other hand if $2p - 2 = 2$, this hole can be zipped up and away. The resulting canonical torus has four fewer singularities and two fewer holes. One round hole and one hole with four singularities are removed in this type of perestroika. These ideas are illustrated with a number of examples.

Example 1: The flow in the canonical torus shown in Fig. 15.36 is restricted at $\times$: $1 \rightarrow 1$. Hole a' has two fewer singularities than hole a. Restriction of the flow eliminates the singularity pair (s, j), absorbs hole 1 into hole a, creating hole a' with $6 - 2 = 4$ singularities, and removes branch line 1.

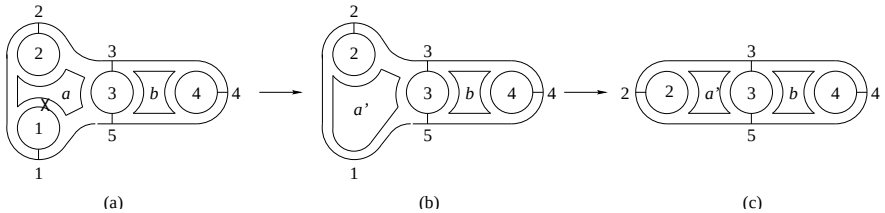

Fig. 15.36 The flow is restricted at interior flow tube $1 \rightarrow 1$. This removes the (s, j) singularity pair, absorbs hole 1 into hole a, producing hole a' with two fewer singularities. When hole 1 is absorbed, branch line 1 disappears.

Example 2: The flow in the same canonical torus is restricted at a different interior flow tube, as shown in Fig. 15.37: $5 \rightarrow 3$. In this case the (s, j) pair is eliminated, hole 3 is absorbed into hole a producing hole a' with 4 singularities, and the flow is rearranged into the canonical form shown at the right in Fig. 15.37. In both this and the previous example the genus is reduced by one, as is the number of branch lines.

Example 3: The flow in the same canonical torus is now restricted at yet another interior flow tube, as shown in Fig. 15.38: $3 \rightarrow 5$. The (s, j) pair is eliminated by this flow restriction and hole 3 is merged into hole b, which now has two singularities. This hole can be zipped away. The remaining flow is of type C_3. It is obtained from the original flow by removing holes 3 and b and the two branch lines (3 and 5) attached to hole 3.

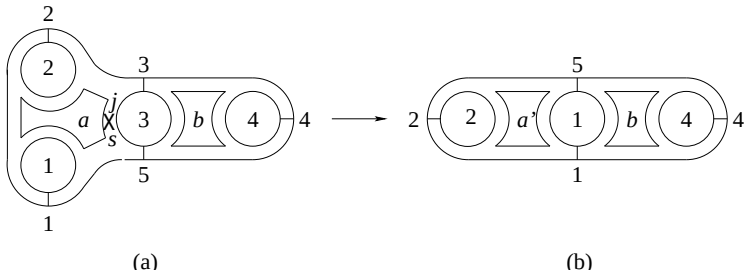

Fig. 15.37 The flow is restricted at interior flow tube $5 \rightarrow 3$. This removes the (s, j) singularity pair, absorbs hole 3 into hole a, producing hole a' with two fewer singularities.

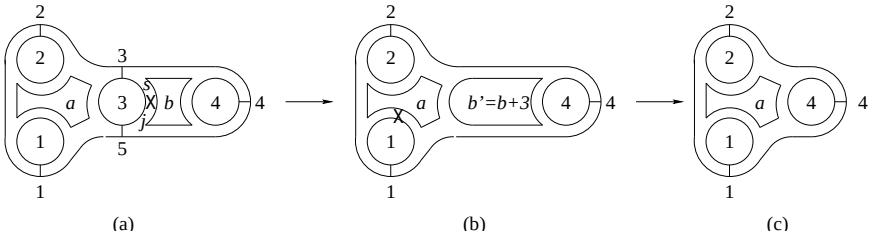

Fig. 15.38 The flow is restricted at interior flow tube $3 \rightarrow 5$. This removes the (s, j) singularity pair, absorbs hole 3 into hole b, producing hole b' with two fewer singularities. This hole is zipped away. When hole 3 is absorbed into b, the two branch lines attached to it are eliminated.

Example 4: The flow in the canonical torus shown in Fig. 15.39 is restricted at the interior flow tube $2 \rightarrow 6$ indicated by the $\times$: $2 \rightarrow 6$. The (s, j) pair shown is thus eliminated and hole 2 is merged into hole b. The new hole $b' = 2 + b$ has 2 singularities, and can be zipped away. The new flow has the canonical form shown at the right in this figure. It has two fewer holes $(2, b)$ and two fewer branch lines $(2, 6)$. These are annihilated when hole 2 is absorbed by hole b.

15.11 "TOPOLOGICALLY EQUIVARIANT" COVERS

In Chapter 6 we studied dynamical systems that were equivariant covers of image dynamical systems. The cover and image systems are related by local diffeomorphisms: there is a $|\mathcal{G}| \rightarrow 1$ local diffeomorphism relating the cover to its image. The flow in the neighborhood of any typical point q in the image can be lifted to neighborhoods of each of the $|\mathcal{G}|$ points p that cover q. The flows in each of these $|\mathcal{G}|$ neighborhoods in the cover are identical to a neighborhood in the image. We have seen examples of $\mathcal{R}_Z(\pi)$ and $\mathcal{P}$ equivariant covers of the Rössler attractor in Fig. 4.6.

"Topologically equivariant" covers also exist. (Group theoretic)-equivariant covers form a (small) subset of this latter, larger class of equivariant covers. The basic idea is the same. A dynamical system bounded by a genus-1 torus can be lifted to a

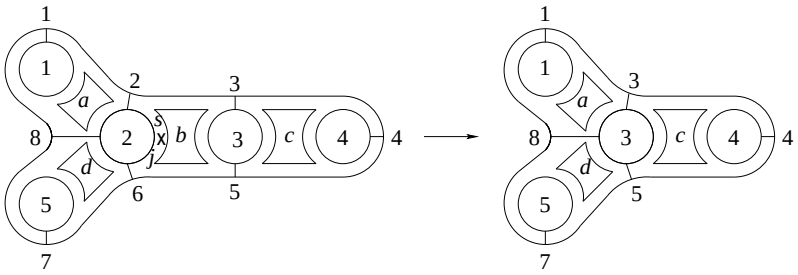

Fig. 15.39 The flow is restricted at interior flow tube $2 \rightarrow 6$. This removes the (s, j) singularity pair, absorbs hole 2 into hole b, producing hole b' with two fewer singularities. This hole is zipped away. When hole 2 is absorbed into b, two of the branch lines attached to it (2 and 6) are eliminated.

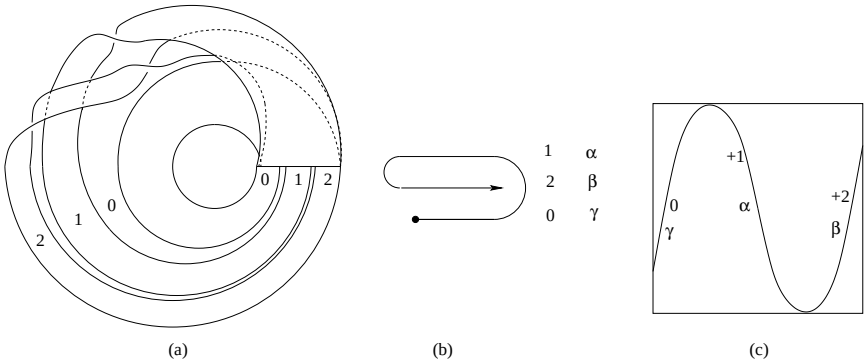

Fig. 15.40 (a) Three-branched manifold shows the initial stages of a gateau roulé. (b) Twisting and layering information as seen as the branch line is approached. (c) Dressed return map includes torsion and layering information shown in (b).

dynamical system enclosed in a genus-g torus using a $(g-1) \rightarrow 1$ local diffeomorphism. We call the "lifted" dynamical system a *topologically equivariant cover*.

We illustrate this idea for a branched manifold that lives in a genus-1 bounding torus. The branched manifold is shown in Fig. 15.40(a). It describes the beginning of a "gateau roulé". The three branches have local torsions 0, +1, +2 and are labeled by these integers. The folding and layering information is suggested in Fig. 15.40(a) and shown more clearly in Fig. 15.40(b). The return map is shown in Fig. 15.40(c). This return map is dressed with torsion $(0, 1, 2)$ and layering (α, β, γ) information. Holes have been drawn between the branches in this representation of the three-branched manifold simply to aid visualization of the branch organization.

Two covers of this branched manifold are shown in Fig. 15.41. Both of these covers can be enclosed in the genus-3 bounding torus A_2. Below each of these two branched manifolds is the return map. The branched manifold in Fig. 15.41(a) has rotation symmetry. This can be deduced from the dressed return map as the three

branches over branch line 1 and the three branches over branch line 2 are dressed the same way: $(0\gamma; +1\alpha; +2\beta)$. On the other hand, the branched manifold shown in Fig. 15.41(b) has inversion symmetry. This can be seen from the branched manifold itself, or from the return map. In this case the dressings over branch lines 1 and 2 are different: $(0\alpha; +1\alpha; +2\beta)$ and $(0\gamma; -1\gamma; -2\beta)$. There are two other covers compatible with the bounding torus A_2 that have not been shown: they are mirror images of the two shown. All four branched manifolds have identical bare return maps: the full return maps differ only in their dressing information.

In the return maps, the torsion information is read vertically and the layering information is read horizontally. Over each branch line there are three branch labels, variously $(0, +1, +2)$ or $(0, -1, -2)$. Feeding into each branch line (each row) there are three layer indices: (α, β, γ). These two pieces of information are redundant in topologically equivariant covers: either piece can be recovered from the other. Essentially, the torsion information is obtained by looking in the forward direction from a branch line, to determine the twist of the outgoing branches. The layering information is obtained by looking backward at each branch line, to determine how the branches approaching a branch line are stacked up. In future representations of return maps in Chapter 16 we will provide mostly the torsion information.

The lesson we take from this example is that the flow, represented by the branches, can twist either to the right or the left in passing from one branch line to another. In the cover, there are two choices for the flow emerging from each branch line. When there are two branch lines there are $2 \times 2 = 2^2$ choices. When there are $g - 1$ branch lines there are 2^{g-1} possibilities. Two of the four possible covers of the gateau roulé were shown in Fig. 15.41. As stated above, there are two additional possibilities. These have flows emerging from branch lines 1 and 2 rotating in the opposite directions from those shown in the figure. Two of these four are equivalent, related by a rotation.

Covers of a flow in a genus-1 bounding torus, or of a branched manifold in such a torus, are simply described as follows. A two-panel return map is constructed. An example of such a return map for the gateau roulé is shown in Fig. 15.42. Part of the flow emerging from branch line i flows to branch line $f(i)$, determined by the network part of the transition matrix $T_{\rm Str}$. The other part flows to branch line $i+1$, determined by the cyclic part of the transition matrix $T_{\rm Dyn}$. The return map over every branch line has the same structure. The only differences are in the directions of the twists that dress each of the branches: $(0, +1, +2)$ or $(0, -1, -2)$. The layering information is uniquely determined by the twisting information, and need not be explicitly specified.

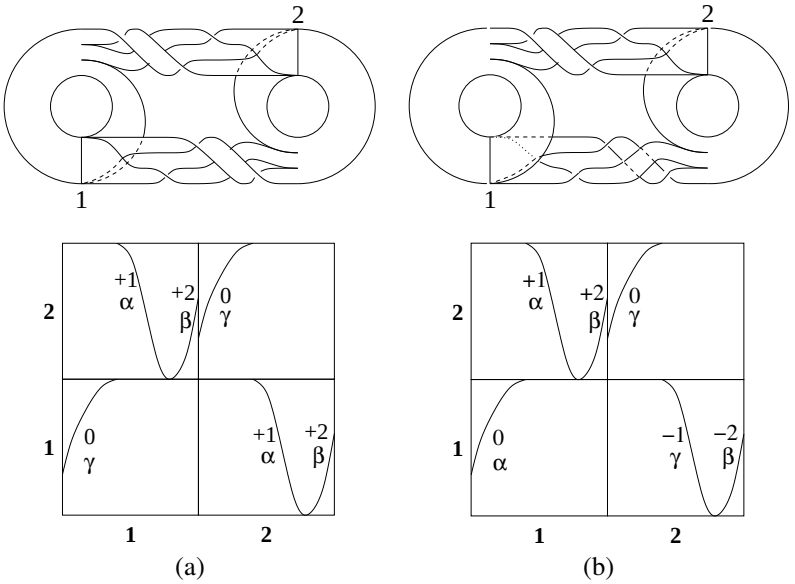

Fig. 15.41 $g-1$ equivariant covers of the gateau roulé branched manifold shown in Fig. 15.40. (a) Invariance under rotations is evident in the branched manifold and its return map. (b) Invariance under inversion is apparent in the branched manifold but less so in the dressing of the return map. Two other branched manifolds that are compatible with the bounding torus A_2 are mirror images of these two branched manifolds.

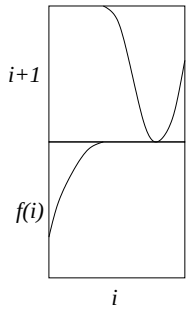

Fig. 15.42 Return maps for topologically equivariant covers of the gateau roulé branch manifold. The undressed return map from each of the $g-1$ branches is identical before being dressed with torsion information. The only possible dressings are $(0,+1,+2)$ and $(0,-1,-2)$. Torsion dressing uniquely determines layering information. Within any specific genus-g bounding torus there are 2^{g-1} locally diffeomorphic covers of the underlying branched manifold in a genus-1 torus. Most of these covers are globally distinct.

16

All the Covers of the Horseshoe

16.1 REVIEW: SOME OF THE COVERS OF THE HORSESHOE

Covers.

This book covers them.

All of them.

As we have progressed through the chapters our understanding and appreciation of covers has become increasingly complex.

At first, covers were dynamical systems with some symmetry that could be mapped to a dynamical systems without symmetry in a locally one to one way. Many examples of such symmetric dynamical systems, and their images, were given in Chapter 3. Fig. 16.1 shows two symmetric attractors, the Lorenz attractor and the Burke and Shaw attractor, and their $2 \to 1$ images, the proto-Lorenz, and the proto–Burke and Shaw attractors. The original attractors are the covers, the proto attractors are the images.

As a next step, the cover-image mapping could be inverted. This allows us to lift an attractor without symmetry, and the dynamical equations that generate that attractor, to attractors with symmetry, and the equations that generate the symmetric

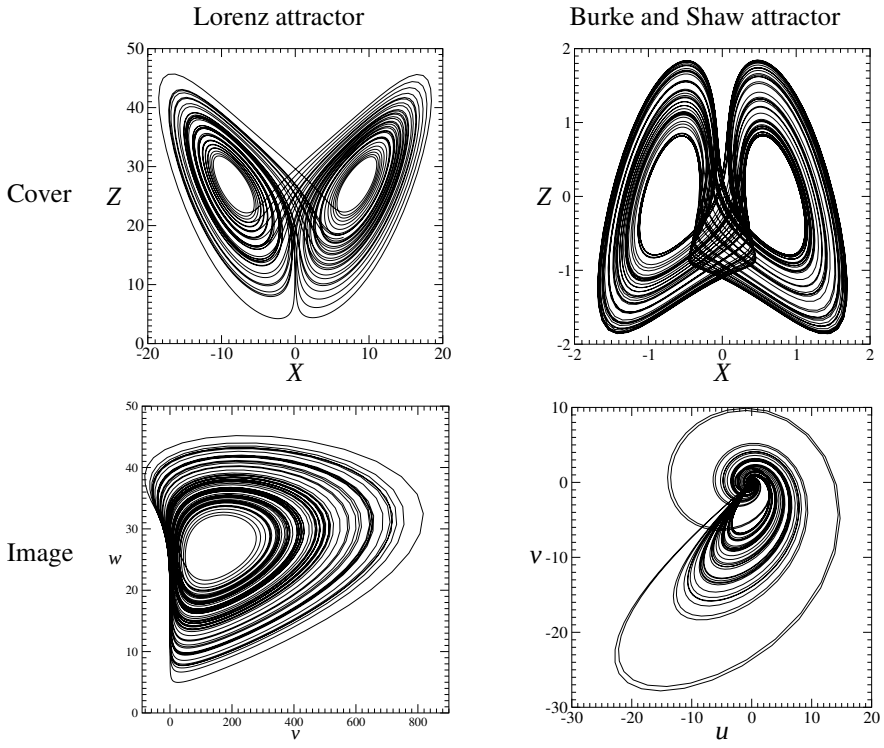

Fig. 16.1 At the simplest level, a covering attractor is a strange attractor with symmetry that projects under a local diffeomorphism to an image attractor without symmetry. Left: Lorenz attractor and its image, the proto-Lorenz attractor. Right: Burke and Shaw attractor covering its image, the proto–Burke and Shaw attractor.

attractors. At this stage we encountered our first enriching experience. It is possible to lift an image to many inequivalent covers, each with the same symmetry group. The topologically inequivalent covers differ from each other by a topological index. In Fig. 16.2 we show four inequivalent lifts of a Smale horseshoe template. These differ by the topological index (n_0, n_1). All exhibit an invariance under the rotation group $\mathcal{R}_Z(\pi)$, with the Z-axis through the spot in the X-Y plane marked with the $\times$.

There is a topological continuation of each of the four $\mathcal{R}_Z(\pi)$ equivariant covers shown in Fig. 16.2 to covers with $\mathcal{P}$ symmetry. For example, the $\mathcal{P}$-equivariant cover with index $(n_0, n_1) = (0, 1)$ differs from that shown in Fig. 16.2(c) by having one of the branches, for example $\hat{1}_l$, twist in the opposite direction from that shown and joining the branch $\bar{0}_r$ from below. This example shows that the branches in a cover can twist in different directions and still map in a locally one to one way down onto an image attractor.

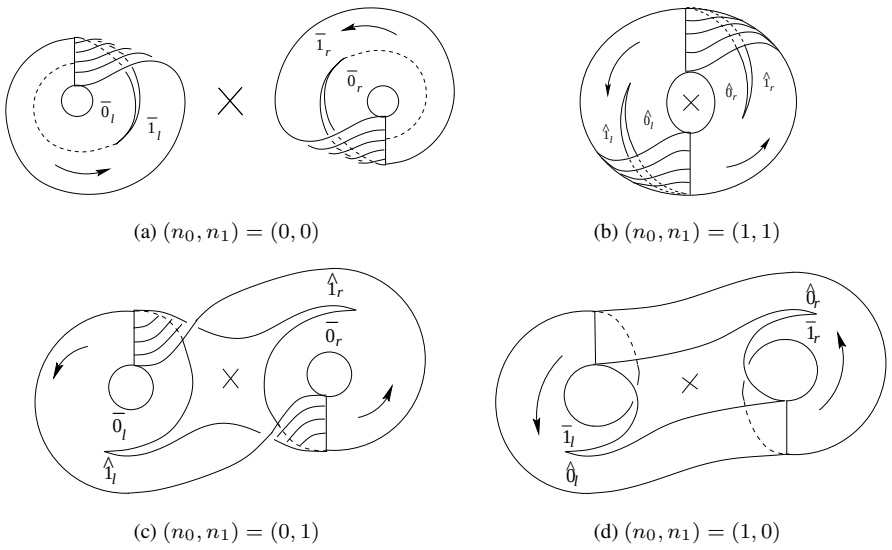

(a) $(n_0, n_1) = (0, 0)$ (b) $(n_0, n_1) = (1, 1)$

(c) $(n_0, n_1) = (0, 1)$ (d) $(n_0, n_1) = (1, 0)$

Fig. 16.2 Four inequivalent double covers of the Smale horseshoe branched manifold are equivariant under the same group $\mathcal{R}_Z(\pi)$.

As a third step in our developing understanding of the range of flexibility of covers, we can construct covers that are not associated with any symmetry group. Two such covers are shown in Fig. 16.3. The covers of the Smale horseshoe template shown in Figs. 16.3(a) and (b) are equivariant under the symmetry group $\mathcal{C}_3$. They differ by their topological indices: $(n_0, n_1) = (0, 1)$ for the cover in Fig. 16.3(a) and $(n_0, n_1) = (1, 1)$ for the cover in Fig. 16.3(b). The two covers below these do not have any symmetry at all. In the cases shown in Figs. 16.3(c) and (d), the branch $\hat{1}_c$ twists in the opposite direction from the twist shown above them in Figs. 16.3(a) and (b), and joins branch line a from below instead of above. These are clearly covers, as we know from similar twist changes in the topological continuations of the $\mathcal{R}_Z(\pi)$ equivariant covers of the Smale horseshoe template to their $\mathcal{P}$ equivariant counterparts.

An image dynamical system can exhibit symmetry. Its cover then exhibits "even more" symmetry, but the symmetry need not be obvious. Fig. 16.4(a) shows a genus-5 double cover of a Lorenz-type attractor, where the rotation axis appears in the central hole. The $2 \to 1$ image is the standard genus-3 canonical form for the Lorenz attractor; *its* $2 \to 1$ image is the genus-1 proto-Lorenz attractor, which is topologically equivalent to the Rössler attractor. In general it is possible to create a complex covering attractor by lifting a simple attractor, for example the Rössler attractor, with a sequence of symmetry groups $\mathcal{G}_1, \mathcal{G}_2, \mathcal{G}_3, \cdots$ as described in Section 6.7. The final cover may exhibit the explicit symmetry of only the last group used to create the lift, yet the cover is a $|\mathcal{G}_1| \times |\mathcal{G}_2| \times |\mathcal{G}_3| \cdots \to 1$ lift of the original

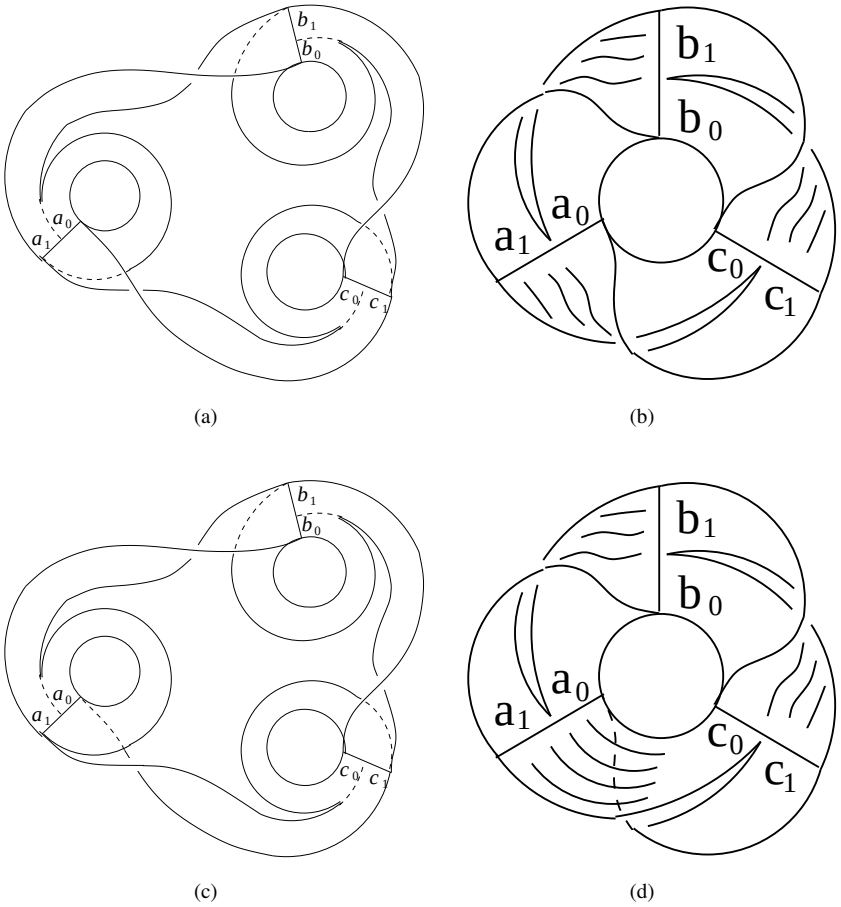

Fig. 16.3 Three-fold covers of the Smale horseshoe with $\mathcal{C}_3$ symmetry and topological indices (a) $(n_0, n_1) = (0, 1)$ and (b) $(n_0, n_1) = (1, 1)$. (c), (d) These three-fold covers of the Smale horseshoe template without any symmetry group are closely related to the covers (a) and (b).

dynamical system. Slight changes in the topology of the cover, as shown in Fig. 16.4(b), creates a cover without any symmetry at all.

As a final step in disassociating the cover-image relation from symmetry, we have introduced topological covers in Chapter 15. In effect, we can lift the dynamics that is constrained by a bounding torus of genus $g = 1$ into any bounding torus of genus g, $g \geq 3$. The properties of topological lifts have been presented for the general case in Chapter 15. In the present chapter we will focus on lifts of the horseshoe template: we will describe all possible lifts of this dynamics.

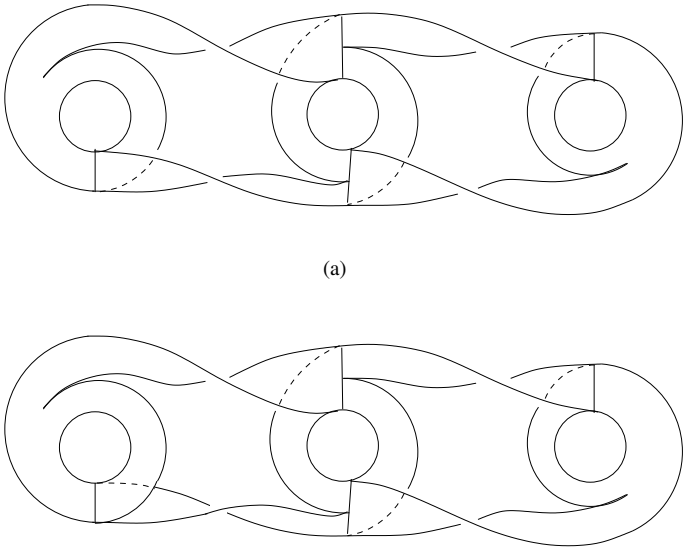

(a)

(b)

Fig. 16.4 (a) Four-fold cover of the Smale horseshoe branched manifold is a two-fold cover of a two-fold cover. (b) This closely related four-fold cover has no symmetry group.

16.2 UNIVERSAL: COVERING GROUPS & IMAGE ATTRACTORS

Group theory has been an enormously useful tool for describing, classifying, and then enumerating covering dynamical systems that are locally, but not globally, diffeomorphic with an image dynamical system. Nevertheless, as the examples in the previous section make clear, many covers cannot be described by equivariance properties.

Although the technical details of group theory cannot be used to classify all covers of strange attractors, the spirit that animates this theory can be.

16.2.1 Cartan's Theorem

To illustrate what we have in mind, we make a slight detour into some technical but beautiful details from the theory of continuous groups.

It has been known for more than a century (contemporary with Poincaré) that a Lie group can be "linearized." The operators that result span a linear vector space and are closed under commutation. They form a Lie algebra. Every Lie group has a Lie algebra. This algebra is unique, up to a change of basis. This relation is not one to one [31]. The most familiar example is encountered in quantum theory. The two Lie groups $SO(3)$ and $SU(2)$ have "the same" (i.e., isomorphic) Lie algebras—the angular momentum algebra—but the two groups are not isomorphic. They are

homomorphic, that is, $SO(3)$ is a $2 \rightarrow 1$ *image* of the *covering* group $SU(2)$. The two groups are *locally* isomorphic but not *globally* isomorphic. The two 2×2 matrices $\pm I_2 \in SU(2)$ map to the single group operation $I_3 \in SO(3)$. This homomorphism, which is a $2 \rightarrow 1$ local isomorphism, is analogous to the $2 \rightarrow 1$ local diffeomorphism mapping the two focal points of the Lorenz attractor down to the image focus in the proto-Lorenz system.

Example: The matrix Lie group $SU(2)$ consists of 2×2 complex matrices M that satisfy $M^\dagger M = I_2$, $\det(M) = +1$. It is three-dimensional. Under linearization, the three independent generators S_i satisfy the commutation relations $[S_i, S_j] = -\epsilon_{ijk} S_k$. The matrix Lie group $SO(3)$ consists of 3×3 matrices O that satisfy $O^t O = I_3$, $\det(O) = +1$. Under linearization, its three independent generators L_i satisfy the commutation relations $[L_i, L_j] = -\epsilon_{ijk} L_k$. These matrices are

$$\begin{array}{cccc} & i=1 & i=2 & i=3 \\ S & \frac{1}{2}\begin{bmatrix} 0 & i \\ i & 0 \end{bmatrix} & \frac{1}{2}\begin{bmatrix} 0 & 1 \\ -1 & 0 \end{bmatrix} & \frac{1}{2}\begin{bmatrix} i & 0 \\ 0 & -i \end{bmatrix} \\ L & \begin{bmatrix} 0 & 0 & 0 \\ 0 & 0 & 1 \\ 0 & -1 & 0 \end{bmatrix} & \begin{bmatrix} 0 & 0 & -1 \\ 0 & 0 & 0 \\ 1 & 0 & 0 \end{bmatrix} & \begin{bmatrix} 0 & 1 & 0 \\ -1 & 0 & 0 \\ 0 & 0 & 0 \end{bmatrix} \end{array}$$

If we exponentiate along the z-axis in the two cases, we find

$$e^{\theta S_3} = \begin{bmatrix} e^{i\theta/2} & 0 \\ 0 & e^{-i\theta/2} \end{bmatrix} \qquad e^{\theta L_3} = \begin{bmatrix} \cos(\theta) & \sin(\theta) & 0 \\ -\sin(\theta) & \cos(\theta) & 0 \\ 0 & 0 & 1 \end{bmatrix}$$

As θ increases from 0 to 2π the real 3×3 matrix moves smoothly from I_3 back to the identity I_3, while the complex 2×2 matrix moves smoothly from $+I_2$ to $-I_2$. The two matrices $\pm I_2$ commute with all matrices in $SU(2)$, they therefore constitute the maximal discrete invariant subgroup of the simply connected covering group $SU(2)$. The nonsimply connected group $SO(3)$ is obtained by modding out the maximal two-element discrete invariant subgroup: $SO(3) = SU(2)/\{I_2, -I_2\}$. This means that each pair of group operations $+I_2 \times M$ and $-I_2 \times M$ in $SU(2)$ is identified with a single element of $SO(3)$.

The local "equality" but global "inequality" is essentially the same for Lie groups as it is for dynamical systems. This suggests that any theorems about local vs. global that are valid for Lie groups might have resonances in the theory of dynamical systems.

There is one very beautiful theorem about such a relation. It is due to Elie Cartan.

Theorem (Cartan): Let $\mathfrak{g}$ be an n-dimensional Lie algebra over the field R of real numbers. Then there is a real simply connected n-dimensional Lie group $\overline{G}$ whose Lie algebra is $\mathfrak{g}$. Every other Lie group G_i with Lie algebra $\mathfrak{g}$ is the quotient of $\overline{G}$ by some subgroup $D_i \subset \overline{G}$. If $D_i \neq I$, the quotient group is not simply connected.

This theorem is illustrated in Fig. 16.5. This figure shows the one to one correspondence between the Lie algebra $\mathfrak{g}$ and the simply connected Lie group $\overline{G}$. All

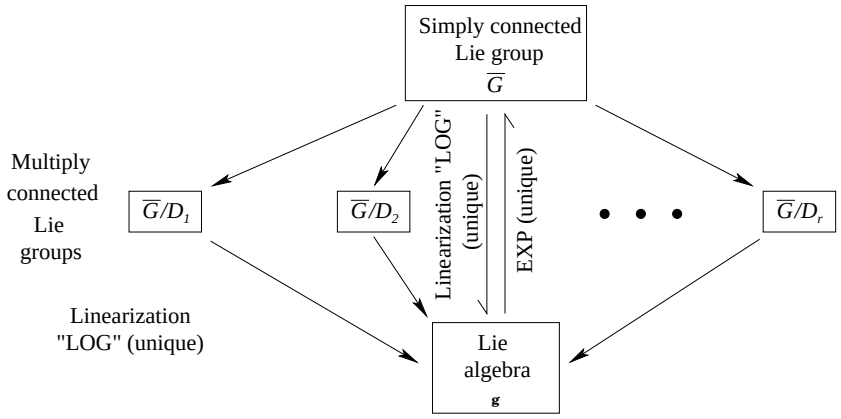

Fig. 16.5 Cartan's Theorem for Lie groups. There is a one to one correspondence between Lie algebras $\mathfrak{g}$ and simply connected universal covering groups $\overline{G}$. All other Lie groups with the same Lie algebra are obtained as quotients of $\overline{G}$ by one of the discrete invariant subgroups of $\overline{G}$.

other Lie groups with the same Lie algebra are "covered" by $\overline{G}$, in the sense that they are obtained from $\overline{G}$ by "modding out" ($\overline{G}/D_i$) by a discrete symmetry group D_i. If $D_i = I$, $\overline{G}/I = \overline{G}$ is simply connected; otherwise $\overline{G}/D_i$ is multiply connected. This gives a complete list of all Lie groups with the same Lie algebra $\mathfrak{g}$, as well as the topological properties of these groups.

Remark: The unique Lie group $\overline{G}$ is called the *universal covering group*.

16.2.2 Groups and Diffeomorphisms

For compact finite-dimensional semisimple Lie algebras $\mathfrak{g}$ there is a maximal discrete invariant subgroup D of $\overline{G}$. As a result there are only a finite number of subgroups $D_i \subseteq D, i = 1, 2, \cdots, \text{finite}$. Thus $\overline{G}$ covers a finite number of nonsimply connected compact Lie groups G_i with the same Lie algebra $\mathfrak{g}$.

In the case of dynamical systems, we have seen that an image dynamical system D, or better for the analogy that we propose, $\underline{D}$, can have many inequivalent covers. Those covers that are equivariant under some (finite) group G are related to the image dynamical system as shown in Fig. 16.6. Here $I_1, I_2, \cdots$ are topological (Chapter 6) or algebraic (Chapter 13) indices that distinguish between topologically inequivalent covers with the same symmetry group.

In some sense, Lie groups and diffeomorphisms are similar. Lie groups and flows are invertible: therefore they are one to one. Homomorphisms are similar to local diffeomorphisms: modding out by a discrete invariant subgroup creates local one to one mappings that are not global one to one mappings. In analogy to *universal covering groups*, we speak in the remainder of this chapter of *universal image dynam-*

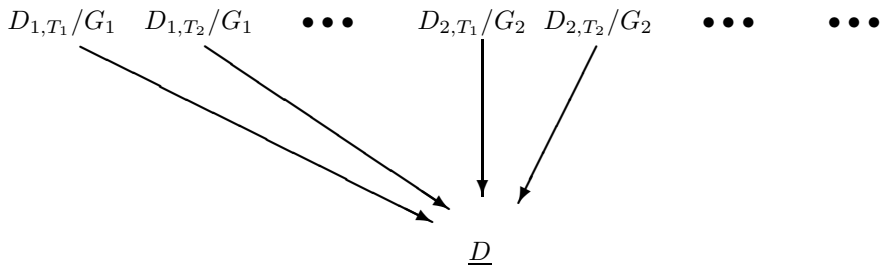

Fig. 16.6 Covering dynamical systems $D_{i,j}$ with symmetry group G_i and topological index I_j have an image dynamical system $\underline{D}$ that is obtained by modding out the symmetry: $\underline{D} = D_{i,j}/G_i$. The dynamical system $\underline{D}$ can be called the "universal image" dynamical system of the covers $D_{i,j}/G_i$.

ical systems, or of *universal image attractors*, or simply *universal images*, in more picturesque language.

16.3 ALL THE COVERS OF THE HORSESHOE

The horseshoe mechanism is a simple stretch-and-fold mechanism for creating chaos. It is responsible for the creation of a strange attractor in Rössler dynamics. A two-branch manifold that the Rössler attractor $(a = 0.398, b = 2.0, c = 4.0)$ projects to, under the Birman-Williams projection, is shown in Fig. 16.7(a). The return map of the branch line back onto itself is shown in Fig. 16.7(b). The dynamics, and the branched manifold that describes it, occurs in a genus-1 torus.

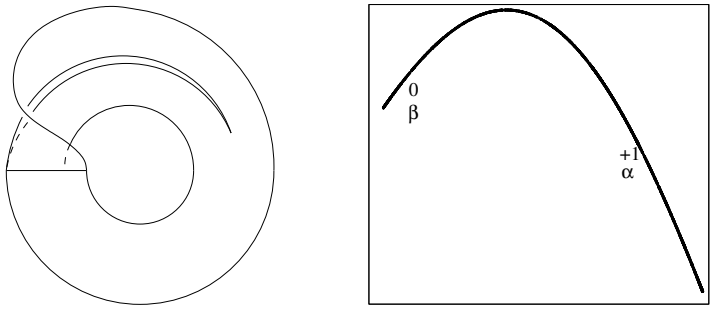

(a) Branched manifold (b) First-return map

Fig. 16.7 (a) Branched manifold for the Rössler attractor and (b) its return map. Control parameter values: $(a, b, c) = (0.398, 2.0, 4.0)$.

We now ask the question: How many "topologically equivariant" covers has the horseshoe?

Part of the answer lies in choosing the particular genus-g torus that the dynamics is lifted to. For any genus, there may be one torus ($g < 5$) or more than one inequivalent tori ($g \geq 5$). To address this question, we first choose a particular canonical bounding torus. For this torus many possible inequivalent covers are possible. As has occurred often before, there are two cases that deserve special discussion. We treat separately the cases where the covers are structurally unstable or structurally stable.

16.3.1 Structurally Unstable Covers

Two types of structurally unstable return maps are shown in Fig. 16.8(a) and (b). Bare return maps for all $g-1$ branches are identical. Dressed return maps differ only by the torsion assignment to each of the $g-1$ branches with torsion: ± 1. The torsion assignments uniquely determine the layering assignments. All told, there are 2^{g-1} possible covers with a single bare return map.

Each of the 2^{g-1} covers with a return map such as the one shown in Fig. 16.8(a) or (b) is structurally unstable. As the location of the splitting point changes, the discontinuity appearing in Fig. 16.8 moves along the branch line, providing return maps of the type shown in Fig. 16.8(a) or (b). This entails large-scale reorganization of the structure of the periodic orbits in the covering dynamical system, as described in Sections 6.3.8 and 6.4.8. We have seen this before, in the structurally unstable lifts of the Rössler attractor with $\mathcal{R}_Z(\pi)$ symmetry. Both parts of branch 0, the one

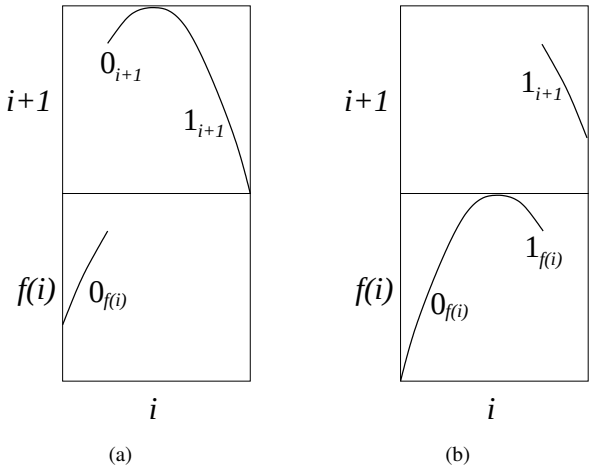

Fig. 16.8 Return map over branch line i of a branched manifold in a genus-g bounding torus. The bare return map is the same over every branch line. Each of the $g-1$ return maps can be dressed in two inequivalent ways. (a) Tearing occurs over branch 0. (b) Tearing occurs over branch 1.

mapping to branch line $f(i)$ ($0_{f(i)}$) and the part mapping to the next branch line (0_{i+1}) have zero torsion. All of the branch with twist (± 1) maps to branch line $i+1$. The three symbols required over branch line i are $0_{f(i)}, 0_{i+1}, 1_{i+1}$.

As the splitting point moves to the neighborhood of the right hand half of the branch lines (Fig. 16.8(b)), the discontinuity occurs in the branch that carries torsion. Once again, dynamics requires three symbols $0_{f(i)}, 1_{f(i)}, 1_{i+1}$ from each branch line.

16.3.2 Structurally Stable Covers

Structurally stable covers are obtained when the splitting points are moved outside the flow, or equivalently do not intersect the branches of the branched manifold. This is equivalent to the statement that branch i is mapped entirely onto either branch $i+1$ or branch $f(i)$. The return maps in these two cases are shown in Fig. 16.9(a) and (b). In both cases the bare return map is confined to one of the two panels and is identical to the return map of the image attractor (Fig. 16.7(b)).

The case shown in Fig. 16.9(a) is equivalent to shutting the flow off in all internal flow tubes. This is illustrated for lifts to the torus 11212 ($aaabb$) shown in Fig. 16.10. When the flow is restricted in the interior flow tubes, indicated by $\times$, the flow circulates through the exterior flow tubes, around the outer boundary of the disk, passing successively through the five branch lines. Two branches meet with a fold (independently left- or right-handed) at each branch line. This means that there are 2^5 locally diffeomorphic, structurally stable covers of this type in this genus-6 torus, some of which are equivalent under rotations. Since the flow occurs in a genus-1

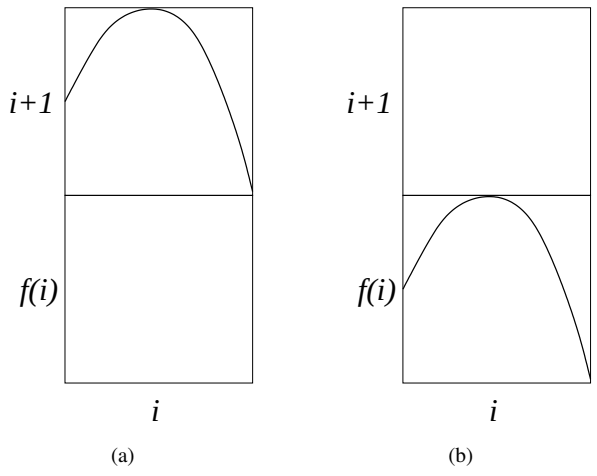

Fig. 16.9 Return maps for structurally stable covers of the horseshoe. (a) The flow moves entirely from branch line i to $i+1$. This is effected by cutting off the flow through all interior flow tubes (Fig. 16.10). (b) The flow moves entirely from branch line i to $f(i)$. This is effected by cutting off the flow through all exterior flow tubes (Fig. 16.11).

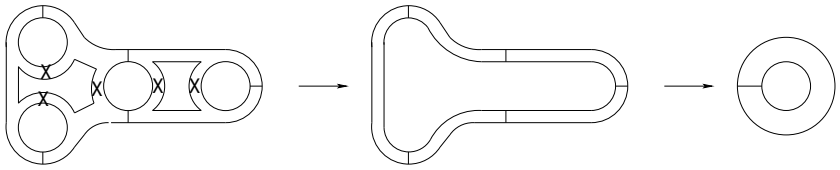

Fig. 16.10 Structurally stable cover. Flow through all interior flow tubes is restricted. The resulting flow follows the exterior boundary, meeting successively the five branch lines, with a fold at each. The flow is restricted to the interior of a single genus-1 torus with one branch line at which 2^{6-1} branches meet.

torus, all the branch lines may be consolidated into a single branch line, where 2^5 branches join.

The other possibility for constructing structurally stable covers is shown in Fig. 16.9(b). This is equivalent to cutting off the flow through all the exterior flow tubes, as shown in Fig. 16.11. Doing this restricts the flow to each of the m interior holes without singularities. The flow is decomposed into a fully reducible flow around the four interior holes without singularities. Three of these carry away one branch line. Each is equivalent to the original image dynamical system, or its mirror image. The fourth carries two branch lines. When consolidated into a single branch line, there are four branches in this component of the fully reducible flow.

These arguments can be applied to any flow, strange attractor, or branched manifold in a torus ($g = 1$) and its lifts to any genus-g bounding torus.

16.4 INTRINSIC EMBEDDINGS

We have searched for an analog of Cartan's theorem for Lie groups in the field of dynamical systems and we have found an analogous result. We have, in fact, determined all the covers of the horseshoe. In this analog the image dynamical

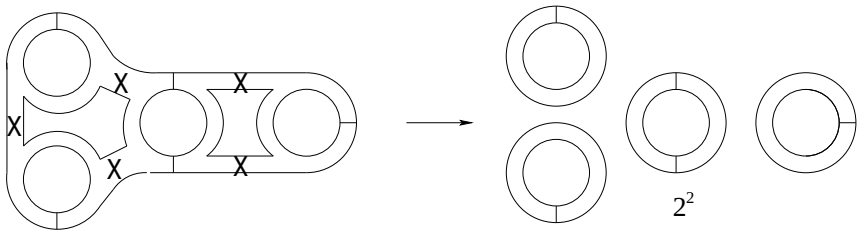

Fig. 16.11 Structurally stable cover. Flow through all exterior flow tubes is restricted. The resulting flow is fully reducible, going around each of the $m = 4$ interior holes without singularities. Three of these holes inherit a single branch line each. The flows in these tori, each of type A_1, have two branches each. The fourth interior hole inherits two branch lines. The branched manifold in this A_1 torus has 2^2 branches.

system plays a role comparable to the covering group in the theory of Lie groups. We are tempted to call the horseshoe a "universal image dynamical system" just as we call a covering group a "universal covering group."

Here the analogy breaks down. The universal covering group is unique up to reparameterization. Reparameterization of this group simply involves an isomorphism. The original group and its reparameterized version have identical properties both at the group level and the topological level. There is no difference between the two.

The same is not true of the "universal image." This is unique up to global diffeomorphism. Under diffeomorphism the flow properties are unchanged but the global topological properties can differ. They can differ in significant ways. In this section we describe intrinsic differences. These depend on how the flow sits inside the bounding genus-1 torus that contains it. In the following section we consider extrinsic differences. These depend on how the genus-1 bounding torus that contains the flow sits inside the ambient space $\mathbb{R}^3$ that contains the dynamics [126,134].

In both sections we treat these differences at two distinct levels. We begin by describing all the branched manifolds that are globally diffeomorphic with a simple stretch-and-fold mechanism in the first subsection. In the following subsection we show explicitly how to embed a time series $X(t)$ from a strange attractor in $D^2 \times S^1$ into a canonical genus-1 bounding torus. In this section the torus is embedded in a natural way in $\mathbb{R}^3$ ("natural embedding"). In the following section the torus is embedded in $\mathbb{R}^3$ following the guiding curve of a knot.

16.4.1 Embeddings of Branched Manifolds

Branched manifolds that describe a simple stretch-and-fold mechanism are shown in Fig. 16.12. We show specifically branched manifolds with global torsion 0, 1, and n, where n (integer) is the number of twists in the return part of the flow. The branched manifold with global torsion one is diffeomorphic with the branched manifold with global torsion zero, but the two are not isotopic. More generally, branched manifolds with global torsions n and n' are diffeomorphic but cannot be isotopic unless $n = n'$. The two branches of a branched manifold with global torsion n have local torsion $2n$ and $2n \pm 1$.

The mirror image of a branched manifold is also a branched manifold. The mirror image of a branched manifold whose branches have local torsions $2n$ and $2n + 1$ has branches with local torsions $-2n$ and $-(2n + 1)$. Further, it describes the same mechanism for generating chaotic behavior as the original. As a result, the mirror images of this set of branched manifolds are also globally diffeomorphic with the zero global torsion branched manifold that we usually use to describe the simple stretch-and-fold mechanism—or also the Rössler system for the usual parameter values.

As a result, embeddings of a branched manifold that describe this mechanism can differ by global torsion and parity (handedness).

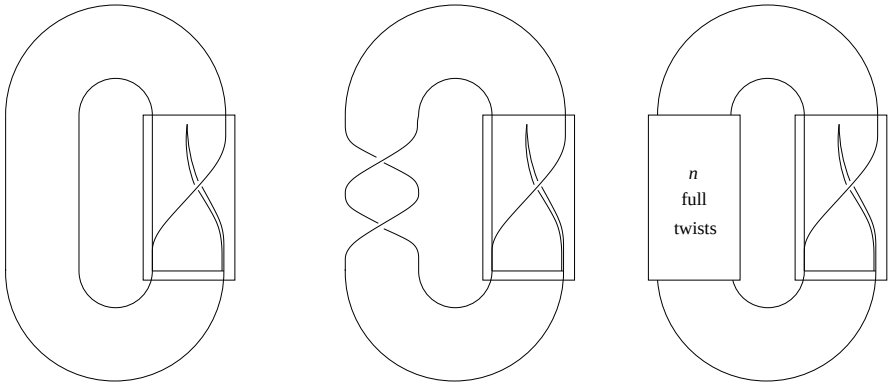

(a) Zero global torsion (b) Global torsion = +1 (c) Global torsion $= n$

Fig. 16.12 Branched manifolds that are globally diffeomorphic. Adjacent branches have local torsions that differ by ± 1. For each branched manifold the box containing the branch line shows the information that is invariant under the embedding (up to handedness).

16.4.2 Embeddings of Flows

In this subsection we illustrate how it is possible to construct an embedding of experimental data generated by a flow in $D^2 \times S^1$ into $\mathbb{R}^3$ in such a way that the embedded attractor projects to any of the branched manifolds described in the previous subsection.

We assume that a time series $X(t)$ is available, and that this time series is generated by a dynamical system that is periodically forced with period T. Further, assume that in any Poincaré section $\phi = 2\pi(t/T \bmod 1) = \text{cst.}$ the attractor exists inside the boundary of a circle of radius a: $X(t)^2 + Y(t)^2 < a^2$. We use as coordinate Y the time derivative of X: $Y(t) = dX(t)/dt$, renormalized, if necessary.

The "natural embedding" of a torus $D^2 \times S^1$ into $\mathbb{R}^3$ is obtained as follows. Choose $R > a$, map the pair $(X(t), Y(t))$ into a circle in a plane rotating around the z-axis in $\mathbb{R}^3$ in a way that is synchronized with the driving period T. The center of the circle is a distance R from the z-axis. The coordinates $(x(t), y(t), z(t))$ of the data embedded in $\mathbb{R}^3$ are related to the coordinates $(X(t), Y(t), t)$ of the data in $D^2 \times S^1$ by:

$$\begin{array}{rcl} x(t) & = & (R - X'(t)) \times \cos(2\pi t/T) \\ y(t) & = & (R - X'(t)) \times \sin(2\pi t/T) \\ z(t) & = & Y'(t) \end{array} \tag{16.1}$$

In the natural embedding $X'(t) = X(t)$ and $Y'(t) = Y(t)$. (Here a prime $'$ does *not* signify a time derivative.) A mirror image embedding is obtained by reversing the sign of either coordinate: $(X', Y') \to (+X, -Y)$ or $(X', Y') \to (-X, +Y)$. An embedding with global torsion n is obtained using the rotation

$$\begin{bmatrix} X'(t) \\ Y'(t) \end{bmatrix} = \begin{bmatrix} \cos(2\pi nt/T) & \sin(2\pi nt/T) \\ -\sin(2\pi nt/T) & \cos(2\pi nt/T) \end{bmatrix} \begin{bmatrix} X(t) \\ Y(t) \end{bmatrix} \tag{16.2}$$

This rotation is synchronized with the driving period and generates a global torison n over and above whatever the intrinsic global torsion of the flow happens to be. If $n = 0$ no additional torsion is added to that already possessed by the flow.

Remark: This procedure is well adapted to create embeddings of periodically driven dynamical systems, such as the van der Pol and the Duffing oscillators described earlier in Chapter 8. It works as well for their images, the proto-systems. It cannot be used directly for autonomous dynamical systems, such as the Rössler system. However, as the Rössler strange attractor lives inside a genus-1 torus for standard control parameter values, it ought to be possible to carry out such an embedding. This can be done if there is a one to one transformation $t \to \phi$, with ϕ measured around the torus containing the strange attractor. If such a diffeomorphism $\mathbb{R}^1 \to \mathbb{R}^1$ can be constucted, so that $dt/d\phi \neq 0$, then the equations of motion can be transformed from $dx_i/dt = f_i(x)$ ($i = 1, 2, 3$, autonomous) to $du_r/d\phi = g_r(u; \phi)$ ($r = 1, 2$, nonautonomous), and the embedding procedure carried out on the two variables $u_1(\phi), u_2(\phi)$.

16.5 EXTRINSIC EMBEDDINGS

From the inside every genus-1 torus looks the same [134]. Each looks like the naturally embedded genus-1 torus described in the previous subsection.

The tori described in Chapter 15 are all intrinsic—as seen from the inside. We do not yet know how to classify how these tori can be embedded in $\mathbb{R}^3$, except in the case of the genus-1 torus.

In this case the embeddings of the genus-1 torus in $\mathbb{R}^3$ are classified by (tame) knots. Every knot can be used as the centerline for a genus-1 torus. There are as many inequivalent embeddings of the genus-1 torus into $\mathbb{R}^3$ as there are knots.

16.5.1 Embeddings of Branched Manifolds

In this subsection we classify all branched manifolds that are diffeomorphic with a simple stretch-and-fold mechanism for generating chaotic behavior.

Start with a zero global torsion right-handed Smale horseshoe branched manifold enclosed in a torus that is naturally embedded in $\mathbb{R}^3$. Cut open the torus, and the branched manifold inside, and straighten it out so it looks like a cylinder. Twist the cylinder n times about its axis, then tie it into a knot before regluing the cylinder (and the branched manifold inside it) at the two ends that were cut. The new branched manifold differs from the original by global torsion and knot type. If we made a mirror image of the cylinder before tying it into a knot, the new and original branched manifolds would differ by global torsion, parity, and knot type [126].

16.5.2 Embeddings of Flows

Knotted embeddings are created most easily using harmonic knots [123]. These are knots parameterized by harmonic functions: sines and cosines. Harmonic knot parameterizations are given by

$$\begin{array}{rcccl} \xi(t) & = & \sum_{j=1}^{k} X_c(j)\cos(2\pi jt/T) & + & \sum_{j=1}^{k} X_s(j)\sin(2\pi jt/T) \\ \eta(t) & = & \sum_{j=1}^{k} Y_c(j)\cos(2\pi jt/T) & + & \sum_{j=1}^{k} Y_s(j)\sin(2\pi jt/T) \\ \zeta(t) & = & \sum_{j=1}^{k} Z_c(j)\cos(2\pi jt/T) & + & \sum_{j=1}^{k} Z_s(j)\sin(2\pi jt/T) \end{array} \tag{16.3}$$

These equations define a space curve $\Upsilon(t) = (\xi(t), \eta(t), \zeta(t))$ of period T. This curve is the core (guiding curve) of the knotted torus. The knotted embedding is obtained by constructing the three-vector $X'(t)\mathbf{N}(t) + Y'(t)\mathbf{B}(t)$ in the plane perpendicular to the tangent vector $\mathbf{T}(t)$ to the knot, and adding this vector to the position vector that defines the coordinates along the knot:

$$\mathbf{x}(t) = (x(t), y(t), z(t)) = \Upsilon(t) + X'(t)\mathbf{N}(t) + Y'(t)\mathbf{B}(t) \tag{16.4}$$

The coordinates $(X'(t), Y'(t))$ have the range of meanings given in the previous subsection (cf. Eq. (16.2)).

The unit tangent vector $\mathbf{T}(t)$ is proportional to the derivative $\frac{d\Upsilon}{dt}$. The unit normal $\mathbf{N}(t)$ is in the plane spanned by $\frac{d\Upsilon}{dt}$ and $\frac{d^2\Upsilon}{dt^2}$. The unit binormal $\mathbf{B}(t)$ is proportional to the cross product of these two vectors: $\mathbf{B}(t) \simeq \frac{d\Upsilon}{dt} \times \frac{d^2\Upsilon}{dt^2}$ The simplest way to construct $\mathbf{N}(t)$ and $\mathbf{B}(t)$ is to construct $\mathbf{B}(t)$ first by normalizing $\frac{d\Upsilon}{dt} \times \frac{d^2\Upsilon}{dt^2}$, and then normalizing $\mathbf{B}(t) \times \frac{d\Upsilon}{dt}$ to construct $\mathbf{N}(t)$.

The conditions necessary for an embedding are the standard no-self-intersection conditions. These have both a local and a global form. Locally, the requirement is that the curvature of the carrier knot is not too large. Specifically, the radius of the osculating circle along the curve must be bounded below by the radius of D^2, that is, greater than a. Globally, it is that the nonzero minima $Min|\Upsilon(t) - \Upsilon(t')|$ must be bounded below by the diameter of D^2: that is, $Min|\Upsilon(t) - \Upsilon(t')| > 2a$.

The *framing* of the knotted torus is a global torsion. It is computed as follows. The linking number of the carrier knot and an offset knot is computed. This is an integer, a global torsion, and the framing of the embedded knotted torus. The offset knot is obtained by setting $(X(t), Y(t)) = (\epsilon, 0)$ in the embedding described above.

The "natural" embedding uses the harmonic knot $\Upsilon(\phi) = (R\cos(\phi), R\sin(\phi), 0)$. For this knot $\mathbf{N}(\phi)$ always points to the origin. This is the reason for the minus signs in Eq. (16.1). The natural embedding has a framing index of zero.

Any knot can be used as a carrier knot for embedding a genus-1 torus in $\mathbb{R}^3$. This includes any periodic orbit encountered in either the Rössler or the Lorenz strange attractors.

We illustrate this idea using one of our canonical examples: the van der Pol oscillator with harmonic drive of period T. A strange attractor created under these conditions is periodic, with period T and angular frequency $\omega = 2\pi/T$. It also possesses an order-two symmetry whose generator is $(X, Y, t) \rightarrow (-X, -Y, t + \frac{1}{2}T)$.

We have created two distinct $2 \to 1$ images of the van der Pol strange attractor by projecting the flow onto "the" van der Pol plane. There are in fact two van der Pol planes. They rotate in opposite directions. The projections are

$$\begin{bmatrix} u(t) \\ v(t) \end{bmatrix} = \begin{bmatrix} \cos(\omega t) & \pm\sin(\omega t) \\ \mp\sin(\omega t) & \cos(\omega t) \end{bmatrix} \begin{bmatrix} X(t) \\ Y(t) \end{bmatrix} \tag{16.5}$$

These projections result in two globally inequivalent proto–van der Pol attractors. They have period $T' = \frac{1}{2}T$, angular frequency $\omega' = 2\omega$, and no other internal symmetry. There is a one to one correspondence between periodic orbits in each of these two proto-attractors but the linking numbers and relative rotation rates of corresponding periodic orbits differ systematically from one attractor to the other. The two proto-attractors are locally diffeomorphic with each other and with the original van der Pol attractor. In fact, the two proto-attractors are globally diffeomorphic but not isotropic.

Either of the proto–van der Pol attractors can be lifted to 2-fold (or n-fold) covers. We describe two classes of lifts.

Lifts around a circle: In one class we use a simple circle as the carrier knot for the bounding torus. The circle is embedded in $\mathbb{R}^3$ as follows:

$$\theta \in T^1 \to R(\cos\theta, \sin\theta, 0) \in \mathbb{R}^3 \tag{16.6}$$

It is necessary that R is greater than the radius of the proto–van der Pol attractor. The coordinates $(u(t), v(t))$ of the image attractor are rotated through an angle ϕ as they are lifted into the bounding torus according to

$$\begin{bmatrix} X(t) \\ Y(t) \end{bmatrix}' = \begin{bmatrix} \cos(\phi) & \sin(\phi) \\ -\sin(\phi) & \cos(\phi) \end{bmatrix} \begin{bmatrix} u(t) \\ v(t) \end{bmatrix} \tag{16.7}$$

The angle ϕ is measured with respect to the local coordinate system $(\mathbf{N}(\theta), \mathbf{B}(\theta))$ established in the plane perpendicular to the guiding knot's unit tangent vector $\mathbf{t} = (-\sin\theta, \cos\theta, 0)$. The unit normal vector always points toward the origin $(0,0,0) \in \mathbb{R}^3$. A double cover is created under the identifications

$$\frac{\theta}{2\pi} \leftrightarrow \frac{t}{n_1 T'} \qquad \phi = n_2\theta \tag{16.8}$$

with $n_1 = 2,\ n_2 = \pm 1$. If the appropriate sign (∓ 1 for n_2) is chosen the double cover produced by the embedding is identical to the original van der Pol attractor, as the rotation matrix in Eq.(16.7) undoes the rotation matrix in Eq.(16.5). If the sign is "inappropriately" chosen (± 1 for n_2), the original van der Pol attractor is *not* recovered. Rather, a globally diffeomorphic but topologically inequivalent attractor is generated.

The strange attractor created by this lift has period $T = 2T'$ and obeys the symmetry $(X, Y, t) \to (-X, -Y, t + \frac{1}{2}T)$.

Remark 1: A whole class of lifts can be created by using the simple circle Eq. (16.6) as the guiding knot for the bounding torus. This is a doubly discrete set indexed

by the integer pair (n_1, n_2) ("quantum numbers for lifts"). In this class n_1 (> 0) is the order of the lift and n_2 indexes the torsion around the guiding knot. The lifted attractor is invariant under $(Z, t) \to (e^{2\pi n_2/n_1} Z, t + T')$, where $Z = X + iY$. The integers n_1 and n_2 are assumed to be relatively prime. If not, the order of the cover is some appropriate divisor of n_1. For $n_1 = 2$ and n_2 odd there is an entire class of double covers with periodicity $T = n_1 T' = 2T'$ and symmetry $(X, Y, t) \to (-X, -Y, t + \frac{1}{2}T)$, while for n_2 even the lifts are one to one with the proto–van der Pol attractors ($1 = n_1/\mathrm{g.c.d}(n_1, n_2)$). This is reminiscent of the $SU(2)$ and $SO(3)$ relation, for good reason.

Remark 2: These remarks apply to *any* knot, not just to the simply embedded circle defined in Eq.(16.6).

Remark 3: If $n_1 = 3$, a three-fold cover of the proto–van der Pol attractor is recovered: This can be regarded as a "$\frac{3}{2}$" cover of the van der Pol attractor.

Remark 4: The van der Pol attractor can be projected in a $2 \to 1$ way onto many more than two rotating van der Pol planes. They are all obtained by replacing $\omega t \to k\omega t$ in Eq. (16.5), with k odd.

Lifts around a cabled torus knot: In the second class we use a "cabled torus knot" as the guiding knot for the bounding torus. This can be regarded as a knot winding around the simple circle (Eq.(16.6)) as the circle (θ) winds around the z-axis in $\mathbb{R}^3$. It is embedded in $\mathbb{R}^3$ according to

$$\theta \in T^1 \to \begin{array}{lcl} x(\theta) &=& (R_1 + R_2 \cos\psi)\cos\theta \\ y(\theta) &=& (R_1 + R_2 \cos\psi)\sin\theta \\ z(\theta) &=& R_2 \sin\psi \end{array} \qquad q\psi = p\theta \tag{16.9}$$

with $R_1 > R_2$. Here R_1 is the radius of the simple circle (Eq.(16.6)) about which the torus knot is cabled (R in Eq.(16.6)), R_2 is the radius of rotation of the torus knot about the simple circle, and p/q is the "winding number" of the torus knot. A simple double cover ($q = 2$) is obtained under the identification

$$\frac{\theta}{2\pi} \leftrightarrow \frac{t}{T'} \qquad \psi = \pm\frac{1}{2}\theta \qquad \phi = \psi \tag{16.10}$$

With this lift of the proto–van der Pol attractor into $\mathbb{R}^3$, the lifted attractor intersects the Poincaré section $\theta =$ constant with period T' but the two intersections are offset by $2R_2$. Further, the two intersections exhibit an inversion symmetry. As a result, the attractor created by this lift possesses exactly the same symmetry as the original van der Pol attractor: $(X, Y, t) \to (-X, -Y, t + \frac{1}{2}T)$. However, it is not equivalent to the original van der Pol attractor. In Fig. 16.13 we show intersections of the attractor lifted using the cabled torus knot defined in Eq.(16.9) and identification given in Eq.(16.10). The two choices ($\psi = \pm\frac{1}{2}\theta$) generate inequivalent attractors that "rotate in opposite directions."

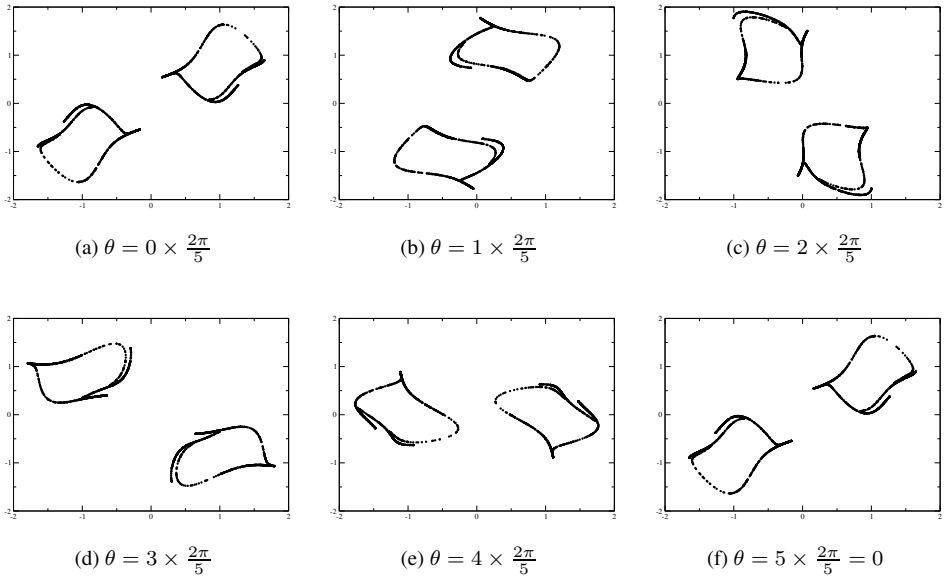

(a) $\theta = 0 \times \frac{2\pi}{5}$ (b) $\theta = 1 \times \frac{2\pi}{5}$ (c) $\theta = 2 \times \frac{2\pi}{5}$

(d) $\theta = 3 \times \frac{2\pi}{5}$ (e) $\theta = 4 \times \frac{2\pi}{5}$ (f) $\theta = 5 \times \frac{2\pi}{5} = 0$

Fig. 16.13 A double cover of the proto–van der Pol attractor. This lift uses a cabled torus knot defined by Eqs.(16.9,16.10). Parameters for the van der Pol oscillator: $a = 0.25,\ b = 0.7,\ c = 1.0,\ d = 10.0,\ \omega = \pi/2,\ T = 4.0$. Parameters for the embedding: $R_1 = 10.0,\ R_2 = 1.2$. Five equally spaced Poincaré sections are shown. They are half-planes hinged on the z-axis separated by dihedral angles $2\pi/5$. The sixth Poincaré section is the same as the first.

Remark 1: An entire class of q-fold lifts can be constructed using cabled torus knots with winding numbers (p/q) and identifications

$$\frac{\theta}{2\pi} \leftrightarrow \frac{t}{T'} \qquad \psi = \frac{p}{q}\theta \qquad \phi = n_2\psi \tag{16.11}$$

For p and q relatively prime the lifted attractor has q intersections on a Poincaré section. Successive intersections ($\Delta\theta = 2\pi, \Delta t = T'$) have centroids rotated through an angle $2\pi p/q$ with respect to the circle $R_1(\cos\theta, \sin\theta, 0)$ and orientations rotated through $2\pi n_2 p/q$ with respect to the centroid, the torus knot.

Remark 2: The lifts around cabled knots just described are classified by three integers, not two as described for lifts using the simple circle. Two of the three integers (p and q) describe the knot, and only one (n_2) is one of the two integer degrees of freedom described earlier. Lifts with quantum numbers (n_1, n_2) can be constructed for the (p, q) torus knot, as for any other knot. We have not done this here.

A trefoil knot is a cabled torus knot with $p/q = 1/3$. A torus embedded in $\mathbb{R}^3$ using the trefoil knot as its guiding curve is shown in Fig. 16.14. The software used

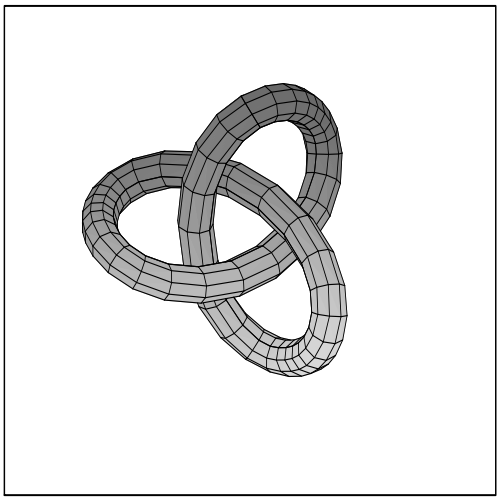

Fig. 16.14 Trefoil knot is a torus knot with $(p, q) = (1, 3)$. This knot has a rotation symmetry.

to draw this knot actually blows up the knot into the torus. This knot has three-fold symmetry. In this class of knots the point drawing the torus knot goes around the torus p times in one direction and q times in the other before closing. If the torus, with its doubly cyclic boundary conditions, is represented as a plane tessellated by squares, the torus knot is represented as a straight line segment from the origin (point $(0, 0)$ in the plane) to the point (p, q) in the plane.

Since torus knots exhibit a symmetry, it is possible to lift a strange attractor from $D^2 \times S^1$ into a torus knotted using a (p, q) torus carrier knot so that the lifted attractor is either diffeomorphic with the original, or else is a q-fold cover of the original strange attractor $(p < q)$, but adjusting the relation between the dynamics (the time t) and the geometry (the angle θ) of the carrier knot.

We close this subsection with a poetic note. The trefoil knot can be cut open, duplicated, and the two copies can be joined. Depending on whether an identical copy or a mirror image is joined with the original, two knots with twice the number of crossings but different symmetries are obtained. These are the granny knot (rotation symmetry $\mathcal{R}_Z(\pi)$) and the square knot (inversion symmetry $\mathcal{P}$). These two knots are shown in Fig. 16.15. Since both knots have two-fold symmetry, a strange attractor can be lifted from $D^2 \times S^1$ into either torus in a straightforward way, or else as a double cover of the original by renormalizing the time parameter of the driven attractor. The parameterizations of these two harmonic knots are presented in Table 16.1.

Fig. 16.16 shows an embedding of chaotic data generated by the periodically driven Duffing oscillator using the granny knot as a carrier knot. Projections on the three coordinate planes of the strange attractors embedded using the granny and the square knots are identical.

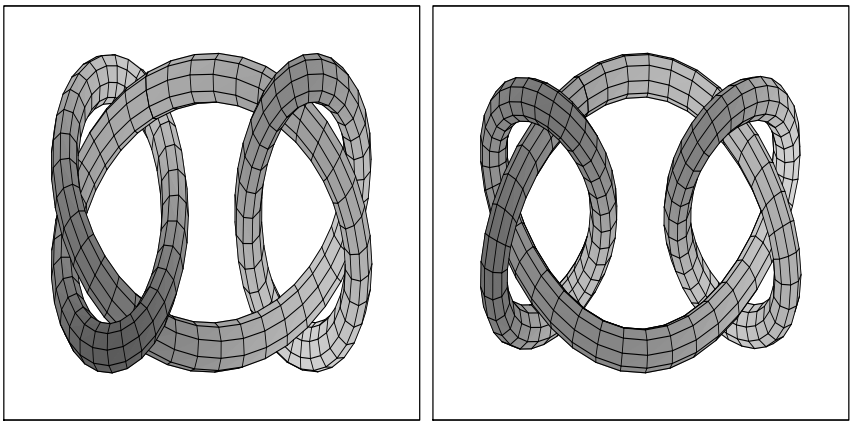

(a) Granny knot (b) Square knot

Fig. 16.15 Two knots obtained by cutting and gluing the trefoil knot either to itself or its mirror image.

Table 16.1 Coefficients in the harmonic parameterizations of the granny knot (top three lines) and the square knot (bottom three lines) [123]. The symmetries of the knots are reflected in their coefficients.

Harmonic	1		2		3		4		5	
Trig. Fun.	cos	sin	cos	sin	cos	sin	cos	sin	cos	sin
x	-22	-128			-44	-78				
y			-10	-27			$+38$	$+46$		
z					$+70$	-40				
x	-22	-128			-44	-78				
y	$+11$	0			-43	0			$+34$	-39
z					$+70$	-40			$+8$	-9

16.6 ONCE A HORSESHOE, ALWAYS A HORSESHOE

Chaotic time series have been generated by a large number of experiments. Typically a scalar time series is available, and a strange attractor must be generated from the scalar time series using some embedding procedure. The algorithm of choice is the time delay embedding [96, 121, 136] although other embedding methods have been

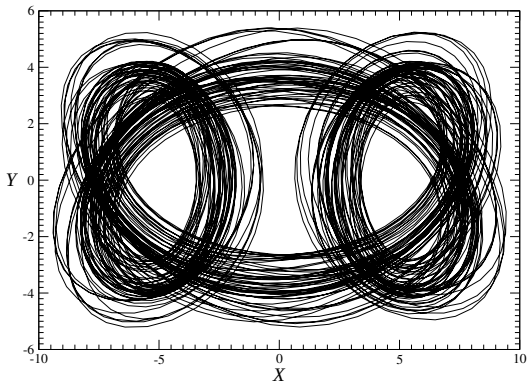

Fig. 16.16 Embedding of chaotic data using a nontrivial embedding of S^1 into $\mathbb{R}^3$. The data are generated by the harmonically driven Duffing oscillator and the granny knot is used as the carrier knot. The projection shown is onto the X-Y plane. The projection of the strange attractor embedded using the square knot as a carrier knot is identical.

used successfully [33,34]. Embeddings are used as a matter of course to "reconstruct" the strange attractor. A major challenge has been to determine exactly to what extent the embedded attractor represents the original, unseen attractor.

The properties of embedded strange attractors have been analyzed using three distinct mathematical approaches: geometric, dynamical, and topological. Geometric analyses involve computing various fractal dimensions [41]. Dynamical analyses involve computation of Lyapunov exponents and the average Lyapunov dimension [137]. Topological analysis concentrates on the organization of the unstable periodic orbits embedded in the attractor, and the global topological properties of the attractor [33,34,87,89,116].

Geometric and dynamical measures are diffeomorphism invariants while topological measures are not. So it would seem that geometric and dynamical measures are more robust tools than topological tools for the analysis of chaotic data. This is one way to look at a comparison of these three approaches to the analysis of chaotic data.

Another way provides more insight. A single attractor can be embedded in $\mathbb{R}^3$ in a variety of different ways, described for genus-1 attractors in the previous two sections. Only topological tools are able to distinguish among these embeddings, for the geometric and dynamical measures are the same, independent of embedding. Only topological tools are able to provide information about the mechanism that creates chaotic behavior. Further, although embeddings can differ by parity, global torsion, and knot type, all diffeomorphic embeddings provide exactly the same information about the mechanism that generates chaos. This information is contained in the number of branches that the chaotic flow projects to and how they are organized as they approach the branch line(s).

It follows from these statements that if a chaotic time series is generated by some unseen stretch-and-fold mechanism acting in a genus-1 torus, distinct embeddings of the data can differ by

- Parity
- Global torsion
- Knot type

but every embedding will reveal the same mechanism (template, cf. Fig. 16.12) [58, 126]. Only topological analysis tools are capable of revealing the mechanism. In particular, in the special case that only two symbols are needed to describe the dynamics, every embedding of these chaotic data will reveal this mechanism is the Smale horseshoe mechanism.

This result is neatly summarized by the aphorism: "Once a horseshoe, always a horseshoe!"

Appendix A
A Potpourri of Equivariant Systems

A.1 THREE-DIMENSIONAL SYSTEMS

A.1.1 Lorenz System

In 1963, Edward Lorenz attempted to understand the lack of long-term predictability in meteorology. For that, he used a severe truncation of the Galerkin decomposition of the Navier-Stokes equations. He obtained the three-dimensional set of ordinary differential equations [78]

$$\begin{aligned} \dot{X} &= -\sigma X + \sigma Y \\ \dot{Y} &= RX - Y - XZ \\ \dot{Z} &= -bZ + XY \end{aligned} \tag{A.1}$$

where σ, b, and R are positive parameters. For $(R, \sigma, b) = (28.0, 10.0, 8/3)$, the Lorenz system has three fixed points: a saddle, F_0, located at the origin of the phase space, and two saddle-foci, $F_\pm$. The two latter are located at

$$\left| \begin{array}{lcl} X_\pm & = & \pm\sqrt{b(R-1)} \\ Y_\pm & = & \pm\sqrt{b(R-1)} \\ Z_\pm & = & R-1 \end{array} \right.$$

The Lorenz system generates a chaotic attractor (Fig. A.1(a)) which is equivariant under a rotation $\mathcal{R}_Z(\pi)$. The associated image is shown in Fig. A.1(b).

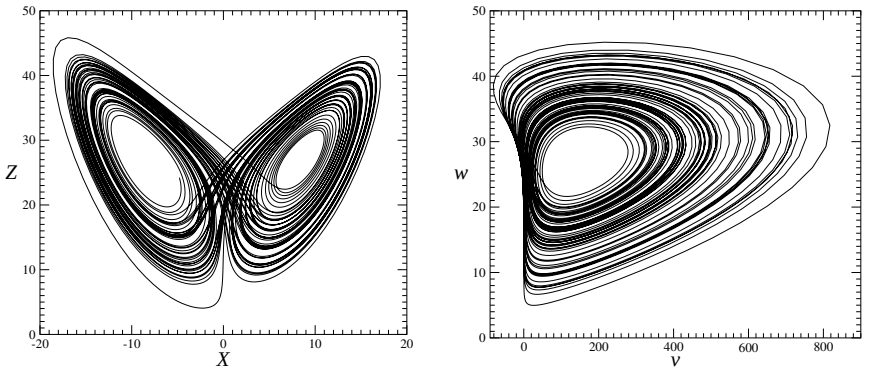

(a) Original dynamics (b) Image system

Fig. A.1 Chaotic solution of the Lorenz system (a) and its image (b). Parameter values: $R = 28$, $\sigma = 10$, and $b = 8/3$.

An algebraically simpler system characterized by the same branched manifold as the Lorenz system has been proposed by Shimizu & Morioka [114]. It is:

$$\begin{aligned} \dot{X} &= Y \\ \dot{Y} &= X - \mu Y - XZ \\ \dot{Z} &= -\alpha Z + X^2 \end{aligned} \tag{A.2}$$

where the control parameters are (α, μ). This system has one fixed point, F_0, located at the origin of the phase space and two fixed points $F_\pm$ located at $(\pm\sqrt{\alpha}, 0, 1)$. For a wide range of parameter values, including those corresponding to a chaotic attractor, F_0 is a saddle and $F_\pm$ are two saddle-foci. The chaotic attractor generated by these equations for $(\alpha, \mu) = (0.375, 0.810)$ is shown in Fig. A.2(a). The associated image is shown in Fig. A.2(b).

In investigating magneto-convection with an imposed vertical magnetic field and convection in a fluid layer rotating uniformly about a vertical axis, Rucklidge [111]

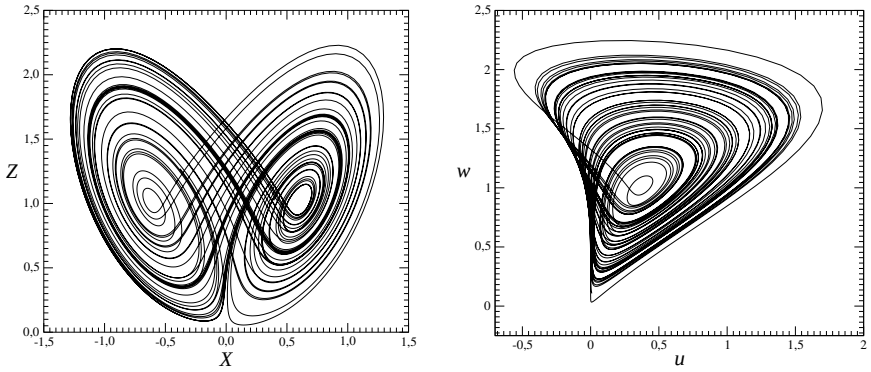

(a) Original dynamics (b) Image dynamics

Fig. A.2 Chaotic behavior (a) generated by the Shimizu & Morioka system for $(\alpha, \mu) = (0.375, 0.810)$ and its image system (b). The chaotic attractor (a) has the same topology as the Lorenz system.

obtained a system with the same algebraic structure as the Shimizu & Morioka equations (A.2). The Rucklidge system is written in the form

$$\begin{aligned} \dot{X} &= Y \\ \dot{Y} &= -\lambda X - \kappa Y - XZ \\ \dot{Z} &= -Z + X^2 \end{aligned} \tag{A.3}$$

where κ and λ are scaled linear combinations of the viscous diffusivity and the magnetic permeability of the fluid. This system is dissipative when $\kappa < 1$. The equivariance property of this system is a manifestation of the invariance of the sense of the flow. Choosing the parameters in an adequate manner leads to an attractor similar to the attractor shown in Fig. A.2.

A.1.2 Thermal Convection Loop

Consider a thermal convection loop constructed from a pipe bent into a torus and standing in the vertical plane as shown in Fig. A.3. Such an experiment was first carried out by Creveling, Pas, Baladi, and Schoenhal [26]. The diameter of the pipe is d and the diameter of the torus is D. θ is the angular location of a point on the torus. The wall temperature of the pipe, $T_{\mathrm{w}}(\theta, t)$, which may vary both with the angular location θ and the time t, is symmetric with respect to the torus axis that is parallel to the gravity vector. Variations in the wall temperature may cause a spatial temperature distribution inside the fluid which, under appropriate conditions, may induce fluid motion in the loop (gravithermal instabilities).

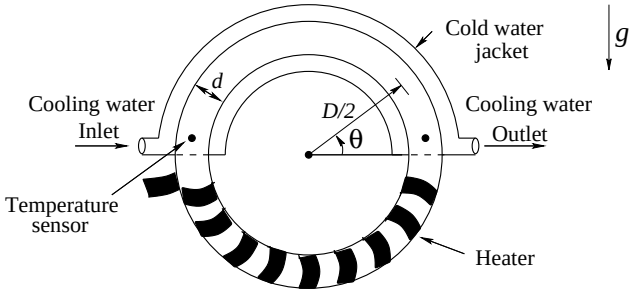

Fig. A.3 Schematic description of the experimental apparatus.

Within the framework of the Boussinesq approximation and using a one-dimensional model consisting of mass, momentum and energy balances [11]:

$$\dot{u} = \frac{1}{\pi}\mathrm{Ra}\sigma \int T(\theta)\cos(\theta)\mathrm{d}\theta - \sigma u \tag{A.4}$$

and

$$\dot{T} = -u\frac{\partial T}{\partial \theta} + B\frac{\partial^2 T}{\partial \theta^2} + (T_{\mathrm{w}}(\theta, t) - T) \tag{A.5}$$

The fluid is incompressible and Newtonian. In these equations, all quantities are nondimensional; $\mathrm{Ra} = \frac{g\beta\Delta T\tau^2}{D\sigma}$ is the loop's Rayleigh number; β is the thermal expansion coefficient; g is the gravitational acceleration; and ΔT is the averaged wall temperature difference between the loop's bottom and top. The time scale is $\tau = \frac{\rho_0 C_p d}{4h}$, where ρ_0 is the fluid's average density, C_p is the thermal capacity, and h is the heat transfer coefficient, here assumed to be constant, between the fluid and the pipe's wall. $\sigma = \frac{32\nu\tau}{d^2}$ is the loop's Prandtl number, where ν is the kinematic viscosity. $B = \left(\frac{d}{D}\right)^2 \frac{1}{\mathrm{Nu}}$ is the Biot number, where Nu is the Nusselt number.

After an expansion of the wall and fluid temperatures in Fourier series in terms of the angle θ, Wang, Singer, and Bau [133] obtained the set of three ordinary differential equations:

$$\begin{aligned} \dot{X} &= -\sigma X + \sigma Y \\ \dot{Y} &= -Y - XZ \\ \dot{Z} &= -Z + XY - \mathrm{Ra} \end{aligned} \tag{A.6}$$

For $(\mathrm{Ra}, \sigma) = (48, 10)$, this model for a thermal convection loop has three fixed points: a saddle, F_0, located at $(X_0, Y_0, Z_0) = (0, 0, -\mathrm{Ra})$, and two saddle-foci, $F_\pm$. The two latter are located at

$$\left| \begin{array}{lcl} X_\pm &=& \pm\sqrt{\mathrm{Ra} - 1} \\ Y_\pm &=& \pm\sqrt{\mathrm{Ra} - 1} \\ Z_\pm &=& -1 \end{array} \right.$$

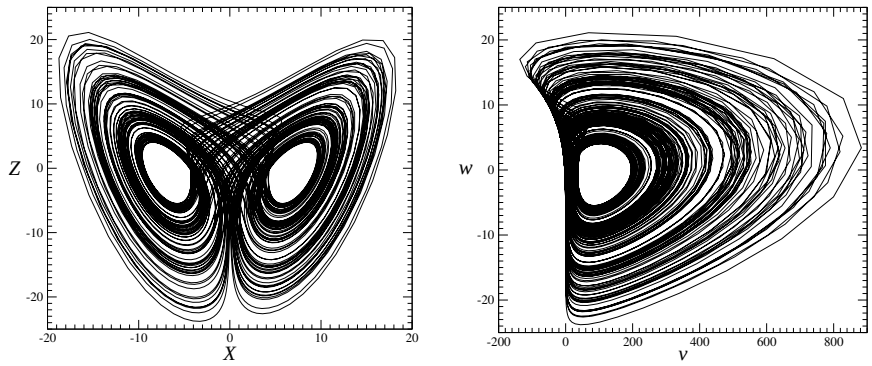

(a) Original dynamics (b) Image dynamics

Fig. A.4 Chaotic behavior (a) generated by the model for a thermal convection loop for $(\mathrm{Ra}, \sigma) = (48, 10)$ and its image system (b). The chaotic attractor (a) has the same topology as the Lorenz system.

The attractor generated by the thermal convection loop equations (A.6) is shown in Fig. A.4(a), as is its image in Fig. A.4(b).

A.1.3 Rikitake System

The paleomagnetic record contains evidence that the Earth's magnetic dipole has reversed its polarity many times in an irregular manner, and the paleomagnetic results indicate that, even while of one sign, its magnitude fluctuates. The reversals have occurred throughout the history of the Earth, but during the last 70 million years they have been very frequent, taking place at least three or four times every million years (cf. Fig. 1.3). As the Earth's magnetic field is caused by electrical currents generated within its deep interior, Bullard [19] introduced a single self-excited disc dynamo as a possible analogy for the nonlinear mechanism responsible for the irregularity of the reversals. But he found that reversals were not possible for such a system. Later, Rikitake [107] introduced the case of two identical coupled disc dynamos in which the current from each disc energizes the coil of the other. In such a case, the current can reverse its sign.

Rikitake's model consists of two identical frictionless disc dynamos connected as shown in Fig. A.5. The dynamos are driven by identical torques, G, to maintain their motion in the face of ohmic losses in the coils and discs. The discs of the model may be taken to represent two large eddies in the Earth's cores. The torques may be likened to buoyancy forces turning the eddies. The retention of resistive dissipation and the neglect of frictional forces reflect the probable dominance of ohmic diffusion over viscous diffusion in the Earth's core. Although these features of the Rikitake model replicate the Earth faithfully, the model is crude in the sense of neglecting

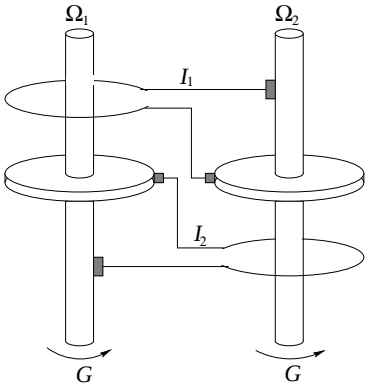

Fig. A.5 Schematic view of Rikitake's dynamo.

other features such as the diffusive and Alfvénic time delays in the communication between eddies in the core, as well as the effects of Coriolis forces.

The equations governing the currents I_1 and I_2 (Fig. A.5) and angular velocities Ω_1 and Ω_2 are

$$\begin{aligned} L\dot{I}_1 + RI_1 &= M\Omega_1 I_2 \\ L\dot{I}_2 + RI_2 &= M\Omega_2 I_1 \\ C\dot{\Omega}_1 &= G - MI_1 I_2 \\ C\dot{\Omega}_2 &= G - MI_1 I_2 \end{aligned}$$

where L is the self-inductance and R the resistance associated with each dynamo and its connecting circuitry, and M is the "mutual inductance" between the dynamo circuits, C is the moment of inertia of a dynamo about its axis, and G is the couple applied about that axis. If follows from the last two equations that the difference in angular velocities is constant

$$\Omega_1 - \Omega_2 = \sqrt{\frac{GL}{CM}}A$$

where A is a constant.

When the equations are put into nondimensional form, they become

$$\begin{aligned} \dot{X}_1 + \mu X_1 &= YX_2 \\ \dot{X}_2 + \mu X_2 &= (Y - \alpha)X_1 \\ \dot{Y} &= 1 - X_1 X_2 \end{aligned}$$

These are conveniently rewritten in the usual form

$$\begin{aligned}\dot{X} &= -\mu X + YZ \\ \dot{Y} &= -\mu Y + (Z-\alpha)X \\ \dot{Z} &= 1 - XY\end{aligned}$$

where α and $\mu = \frac{CR^2}{GLM}$ are two control parameters. This system has two fixed points

$$F_{\pm} = \left| \begin{array}{l} X_{\pm} = \pm\sqrt{\dfrac{\alpha + \sqrt{\alpha^2 + 4\mu^2}}{2\mu}} \\ Y_{\pm} = \pm\sqrt{\dfrac{2\mu}{\alpha + \sqrt{\alpha^2 + 4\mu^2}}} \\ Z = \dfrac{\alpha + \sqrt{\alpha^2 + 4\mu^2}}{2} \end{array} \right.$$

If we set $\alpha = \mu(K^2 - \frac{1}{K^2})$, these coordinates become

$$F_{\pm} = \left| \begin{array}{l} X_{\pm} = \pm K \\ Y_{\pm} = \pm\dfrac{1}{K} \\ Z = \mu K^2 \end{array} \right.$$

This system has been investigated following Lorenz's approach in 1970 by Cook and Roberts [24]. It has a chaotic attractor (Fig. A.6(a)) topologically equivalent to the Lorenz attractor (Fig. A.1(a)) for $\mu = 1.05$ and $K = 1.5$. The image attractor, shown in Fig. A.6(b) is topologically equivalent to the proto-Lorenz system (Fig. A.1(b)).

A.1.4 Homopolar Dynamo

Homopolar dynamo models are used for the understanding of spontaneous magnetic field generation in magnetohydrodynamic flows. In 1979, Moffat [91] proposed a heuristic model of the disk dynamo of Bullard taking into account the field exclusion process necessary to satisfy the Alfvén theorem of flux conservation. This self-consistent model is obtained by a segmentation of the disk, leaving the possibility of azimuthal currents to exclude the magnetic field. An analog of such a dynamo in the electrical engineering science was proposed by Lusseyran and Brancher [81]. It works exclusively in the nonstationary regime. The copper cylinder is first rotated above the critical starting velocity, then connected to the main coil through liquid contacts, and then the kinetic energy of the wheel is transformed to the electric energy.

The generator is formed by a rotating copper ring and tangential coils $\mathcal{E}$ with sliding contacts that can induce a radial magnetic flux $\boldsymbol{B}$through the side of the rotating cylinder (Fig. A.7). The corresponding segmented model allows an azimuthal current

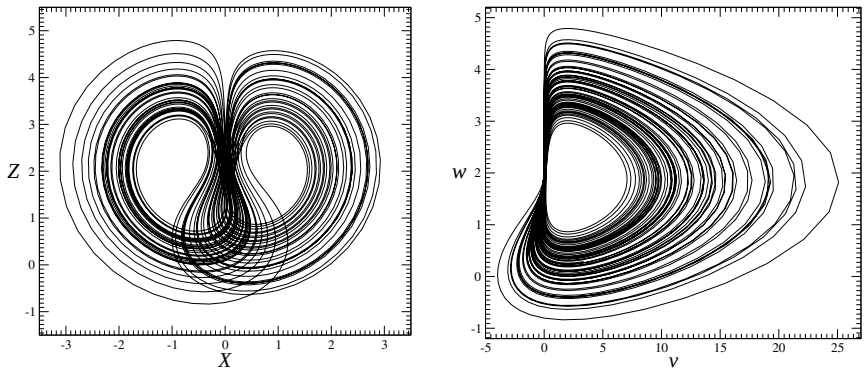

(a) Original dynamics (b) Image system

Fig. A.6 Chaotic attractor (a) of the Rikitake's dynamo model for $\mu = 1.05$ and $K = 1.5$. Its image (b) is topologically equivalent to the proto-Lorenz system.

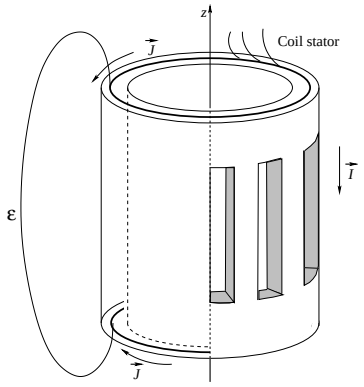

Fig. A.7 Schematic view of the homopolar dynamo.

J and a main current I. The nonlinear system satisfied by the currents and velocity is written in nondimensional form as

$$\dot{X} = \alpha\left[(Z-1)X + (Z+\beta)Y\right]$$

$$\dot{Y} = \alpha\left[(1-Z)X - (Z+\gamma)Y\right]$$

$$\dot{Z} = -XY - X^2 + C - \nu Z$$

where the time is adimensionalized by Rt/L. Dynamical variables are related to physical quantities by

$$X = \frac{M}{R}\sqrt{\frac{L}{4\pi^2 I_2}}I$$
$$Y = \frac{L'}{R'}\sqrt{\frac{L}{4\pi^2 I_2}}J$$
$$Z = \frac{M}{R}\frac{\Omega}{2\pi}$$

where

- L is the self-inductance of the main coil,
- L' is the self-inductance of the rim,
- R and R' are the corresponding resistances,
- M is the mutual inductance of the coil and rim,
- I_2 is the moment of inertia of the rotating part,
- T is the applied torque,
- ν is the friction coefficient,
- Ω is the angular velocity.

The control parameters are

$$\alpha = \frac{LL'}{LL' - M^2} = 1.01$$
$$\beta = \frac{R'M^2}{RL'^2} = 0.1136$$
$$\gamma = \frac{R'L}{RL'} = 11.25$$
$$C = \frac{ML}{R^2}\frac{T}{4\pi^2 I_2} = 93.5$$
$$\nu = 3.0$$

The system has three fixed points

$$F_{\pm} = \begin{vmatrix} \pm\sqrt{C-\nu} \\ 0 \\ 1 \end{vmatrix} \quad \text{and} \quad F_0 = \begin{vmatrix} 0 \\ 0 \\ \dfrac{C}{\nu} \end{vmatrix}$$

for any value of ν different from zero. When $\nu = 0$, the fixed point F_0 is ejected to infinity. The chaotic attractor generated by this homopolar dynamo model, for the control parameter values given above, is shown in Fig. A.8(a) and its image is shown in Fig. A.8(b).

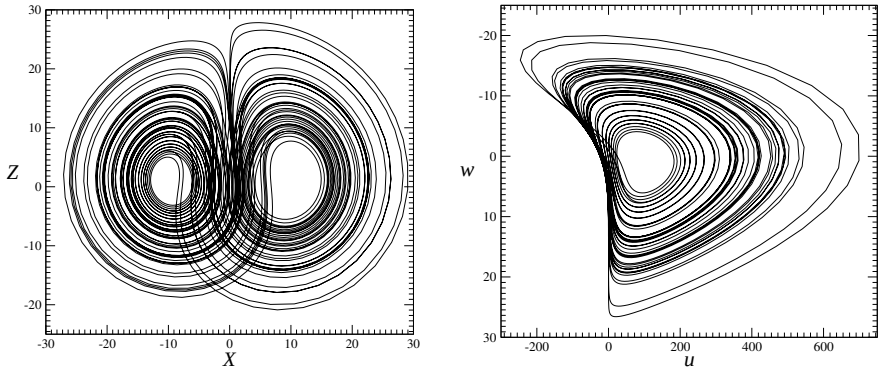

(a) Original dynamics (b) Image system

Fig. A.8 Chaotic attractor (a) of the homopolar dynamo model for $\nu = 3.0$. Its image (b) is topologically equivalent to the image of the Lorenz system. Other parameter values: $\alpha = 1.01$, $\beta = 0.1136$, $\gamma = 11.25$, and $C = 93.5$.

A.1.5 Still Another Lorenz-Like Attractor

In order to investigate the transition to chaotic behavior via a cascade involving bifurcations of stable homoclinic orbits, Arnéodo, Coullet, and Tresser proposed the set of three ordinary differential equations [4]:

$$\begin{aligned} \dot{X} &= aX - aY \\ \dot{Y} &= -4aY + XZ + bX^3 \\ \dot{Z} &= -adZ + XY + cZ^2 \end{aligned} \tag{A.7}$$

For parameter values $(a, b, c, d) = (1.8, 0.02, -0.07, 1.5)$, this system has a chaotic attractor (Fig. A.9(a)) which is topologically equivalent to the Lorenz attractor. Its image is also shown in Fig. A.9(b).

A.1.6 Chen & Ueta System

The Chen and Ueta system [22] reads as:

$$\begin{cases} \dot{X} = -\sigma X + \sigma Y \\ \dot{Y} = (R - \sigma)X + RY - XZ \\ \dot{Z} = -bZ + XY \end{cases} \tag{A.8}$$

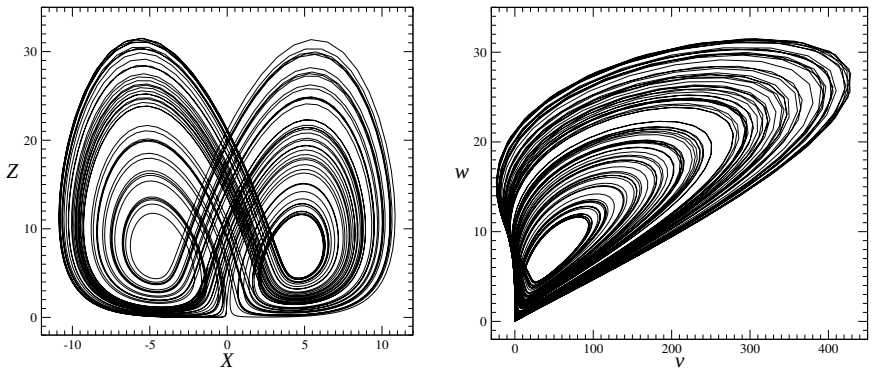

(a) Original dynamics (b) Image system

Fig. A.9 Chaotic attractor (a) of the system proposed for investigating bifurcation of stable homoclinic orbits. Its image (b) is topologically equivalent to the image of the Lorenz system. Parameter values: $(a, b, c, d) = (1.8, 0.02, -0.07, 1.5)$.

This system has three fixed points. One is located at the origin of the phase space $\mathbb{R}^3(X, Y, Z)$. Two are symmetry-related and are defined by:

$$F_{\pm} = \left| \begin{array}{l} x_{\pm} = \pm\sqrt{b(2R - \sigma)} \\ y_{\pm} = \pm\sqrt{b(2R - \sigma)} \\ z = 2R - \sigma \end{array} \right. \tag{A.9}$$

Although there is no diffeomorphism between the Lorenz system and system (A.8) [22], it is possible to find an attractor topologically equivalent to the Lorenz attractor. This is obtained for $(R, \sigma, b) = (22.05, 35, 5)$ (Fig. A.10(a)). Its image (Fig. A.10(b)) is obviously topologically equivalent to the image of the Lorenz attractor.

A.1.7 Burke & Shaw System

Starting from the Lorenz equations, Burke and Shaw [113] proposed the following system:

$$\begin{aligned} \dot{X} &= -S(X + Y) \\ \dot{Y} &= -Y - SXZ \\ \dot{Z} &= SXY + \mathcal{V} \end{aligned} \tag{A.10}$$

where the control parameters are $(S, \mathcal{V})$. This system has only two fixed points, $F_{\pm}$, with coordinates $\left(\pm\sqrt{\frac{\mathcal{V}}{S}}, \mp\sqrt{\frac{\mathcal{V}}{S}}, \frac{1}{S}\right)$. Both are saddle-foci. The attractor is displayed in Fig. A.11(a) with its image in Fig. A.11(b) for $(S, \mathcal{V}) = (10.0, 4.271)$.

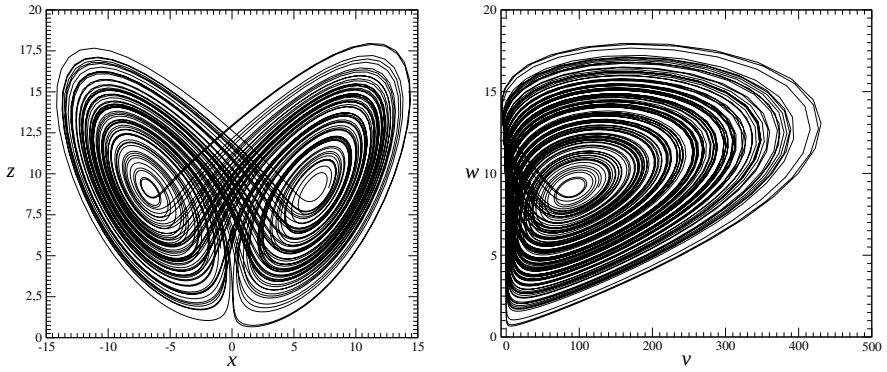

(a) Original dynamics (b) Image system

Fig. A.10 Chaotic attractor (a) of the Chen and Ueta system for $(R, \sigma, b) = (22.05, 35, 5)$. Its image (b) is topologically equivalent to the image of the Lorenz system.

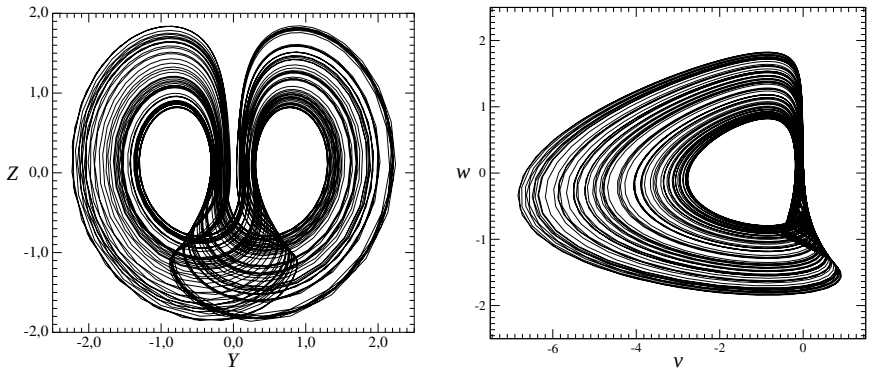

(a) Original dynamics (b) Image system

Fig. A.11 (a) Chaotic attractor for the Burke & Shaw system and (b) its image for $(S, \mathcal{V}) = (10.0, 4.271)$.

In his search for three-dimensional chaotic flows, Sprott [117] found two systems which generate a chaotic attractor topologically equivalent to the Burke & Shaw attractor. These are cases B and C in Table 1 of [117]. The simplest one from an algebraic point of view, case C, is:

$$\begin{aligned} \dot{X} &= -bX + bY \\ \dot{Y} &= XZ \\ \dot{Z} &= a - Y^2 \end{aligned}$$

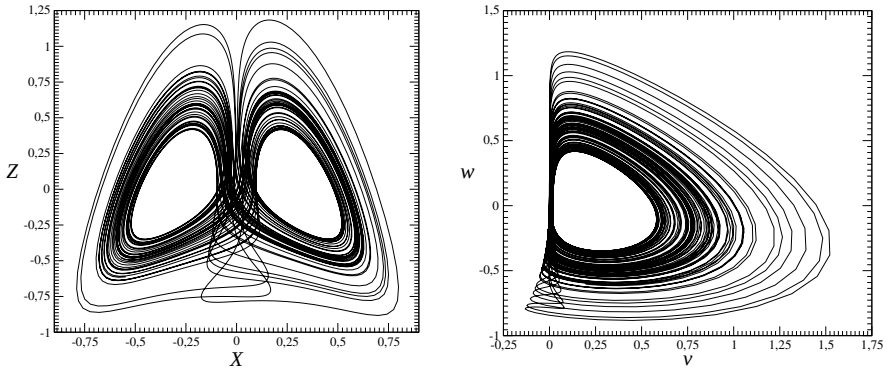

(a) Original dynamics (b) Original dynamics

Fig. A.12 Sprott's system: case C. The chaotic attractor (a) has the same branched manifold as the Burke and Shaw system. Its image (b) is also shown. Parameter values: $(a, b) = (0.097480, 0.64)$.

The corresponding attractor is shown in Fig. A.12(a), along with its image in Fig. A.12(b), for $(a, b) = (0.097480, 0.64)$.

A.1.8 Leipnik and Newton System

Leipnik and Newton proposed a system with three quadratic interactions arising from a modified Euler's rigid body equations by the addition of linear feedback [59]. The equations are

$$\begin{cases} \dot{X} = -aX + Y + 2bYZ \\ \dot{Y} = -X - aY + bXZ \\ \dot{Z} = -bXY + cZ \end{cases} \tag{A.11}$$

This system has five fixed points. One is located at the origin of the phase space and the four others are defined as

$$\begin{aligned} (X, Y, Z) &= \left(\frac{-\lambda c}{b(2\lambda^2 - ac)}, \frac{\lambda}{b}, \frac{-\lambda^2}{b(2\lambda^2 - ac)} \right) \\ \lambda &= \pm\sqrt{\frac{c}{8a}}\sqrt{3 + 4a^2 \pm \sqrt{9 + 8a^2}} \end{aligned} \tag{A.12}$$

This system has $\mathcal{R}_Z(\pi)$ rotation symmetry. For certain parameter values, four attractors coexist in the phase space as shown in Fig. A.13(a). The two attractors observed mainly with positive Z-values are topologically equivalent to the Burke and Shaw attractor observed before the first attractor merging crisis. Two limit cycles also coexist

in the phase space for negative Z-values. They are observed by choosing different initial conditions. These two cycles remain roughly unchanged when the c parameter is increased to 0.152. Contrary to this, the two disconnected attractors for positive Z-values merge into a single attractor (Fig. A.13(b)).

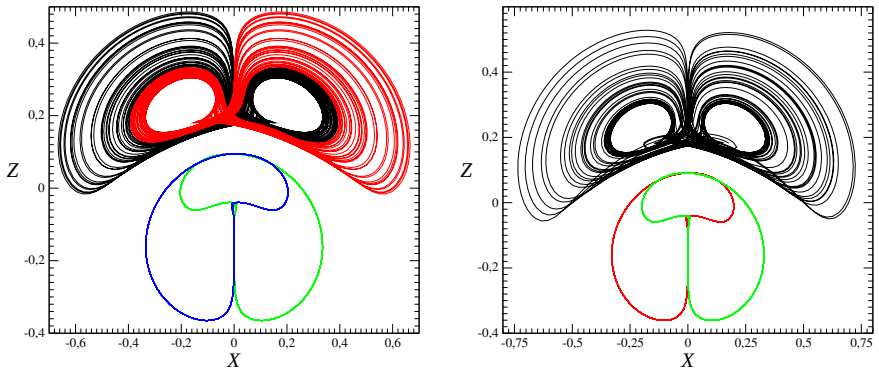

(a) Four disconnected attractors ($c = 0.15134$)

(b) Three disconnected attractors ($c = 0.152$)

Fig. A.13 Disconnected attractors of the Leipnik and Newton system for parameter values $(a, b) = (0.73, 5)$. (a) Two symmetry-related chaotic attractors and (b) one symmetric chaotic attractor. In both cases there are two symmetry-related limit cycles.

The two attractors with negative Z-values, different from the first two attractors with positive Z-values, are obtained because a second symmetry is broken by the factor 2 in the term $2bYZ$ in the first equation of system (A.11). The symmetry can be restored by removing the coefficient 2 from this term. Thus, for slightly different parameter values, four symmetry-related attractors are obtained as shown in Fig. A.14. For values of c greater than 0.1428, the attractors merge and two disconnected attractors remain in the phase space. They are symmetry-related.

A.1.9 Simple Models for Pulsating Stars

In 1966, Moore & Spiegel [92] were interested in describing the irregular pulsations observed in variable stars like Cepheids, among others. In order to do that, they investigated the instability of a sphere of fluid. They obtained a third-order differential equation:

$$\dddot{x} + \ddot{x} + (T - R + Rx^2)\dot{x} + Tx = 0$$

which may be rewritten as three ordinary differential equations

$$\begin{aligned} \dot{X} &= Y \\ \dot{Y} &= Z \\ \dot{Z} &= -Z - (T - R + RX^2)Y - TX \end{aligned} \tag{A.13}$$

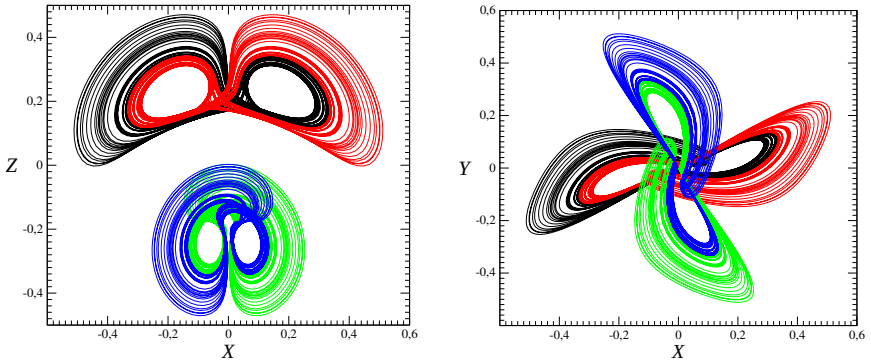

(a) X-Z plane projection (b) X-Y plane projection

Fig. A.14 Four disconnected chaotic attractors of the modified Leipnik and Newton system for parameter values $(a, b, c) = (0.60, 5, 0.1428)$.

where $X = x$. The parameter T is analogous to a Prandtl number multiplied by the Taylor number and R is analogous to a Rayleigh number. They investigated this oscillator for $T = 6.0$ and $R = 20.0$. For these values, a chaotic attractor is obtained (Fig. A.15(a)). They used the term "aperiodic behavior," as Lorenz did in his 1963 paper [78]. This system is equivariant under the inversion $\mathcal{P}$, as are all systems obtained from a differential embedding.

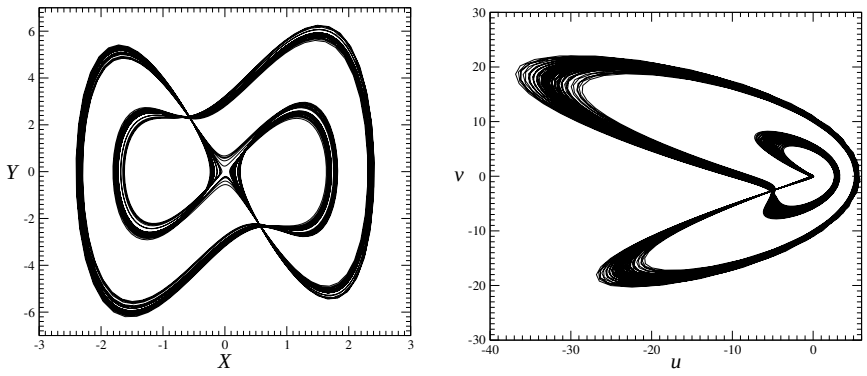

(a) Original dynamics (b) Image system

Fig. A.15 Chaotic attractor (a) solution of the Moore and Spiegel system and its image (b) for $T = 6.0$ and $R = 20.0$.

Later Auvergne and Baglin [9] derived another set of equations from a one-zone model for a pulsating star and obtained the equation

$$\dddot{x} + \ddot{x} + \lambda\left(1 + \alpha x^2\right)\dot{x} + \beta x = 0$$

where $(x = \frac{\delta r}{\bar{r}})$ is the radius relative to the radius at the equilibrium. Coefficients $\alpha,\ \beta$, and λ are defined by

$$\begin{aligned} \alpha &= \frac{\gamma_2(1+\gamma_1)^2}{\gamma_1} \\ \beta &= \frac{B}{A}\,\frac{1}{A^2K^2} \\ \lambda &= \frac{\gamma_1}{A^2K^2} \end{aligned} \tag{A.14}$$

where γ_1 is a function of the adiabatic exponent governing the instability rate and γ_2 depends on the number of ionized elements and on $\eta = \frac{\chi}{kT}$, where χ is the ionization potential. The term A^2K^2 quantifies the departure from adiabaticity and B/A is the energy source term of the star.

System (A.14) may be written as a set of ordinary differential equations:

$$\begin{aligned} \dot{X} &= Y \\ \dot{Y} &= Z \\ \dot{Z} &= -Z - \lambda\left(1 + \alpha X^2\right)Y - \beta X \end{aligned} \tag{A.15}$$

where $X = x$. It thus appears that it is equivalent to the Moore and Spiegel system (A.13) when $\alpha = \frac{R}{T-R}$, $\lambda = T - R$, and $\beta = T$. The Auvergne and Baglin attractor is shown in Fig. A.16(a) for control parameter values $\gamma_1 = -0.3$, $\gamma_2 = 25.0$, $A^2K^2 = 0.01$, and $B/A = 0.125$. Its image is shown in Fig. A.16(b).

A.1.10 Minimal Jerk System

Several papers have been devoted to the search for the "simplest set" of equations which can generate a chaotic behavior [118]. Most of the time, a very simple system may be written in the form of an autonomous third-order differential equation

$$\dddot{x} = \boldsymbol{f}(x, \dot{x}, \ddot{x}) \tag{A.16}$$

Such systems are sometimes called *jerk* equations. Recently, Malasoma [82] proposed the algebraically simplest example of a dissipative equivariant jerk system. It consists of three terms, including one quadratic nonlinearity. It reads as:

$$\dddot{x} = -\alpha\ddot{x} + x\dot{x}^2 - x \tag{A.17}$$

This system can be rewritten as a set of three ordinary differential equations

$$\begin{aligned} \dot{X} &= Y \\ \dot{Y} &= Z \\ \dot{Z} &= -\alpha Z + XY^2 - X \end{aligned} \tag{A.18}$$

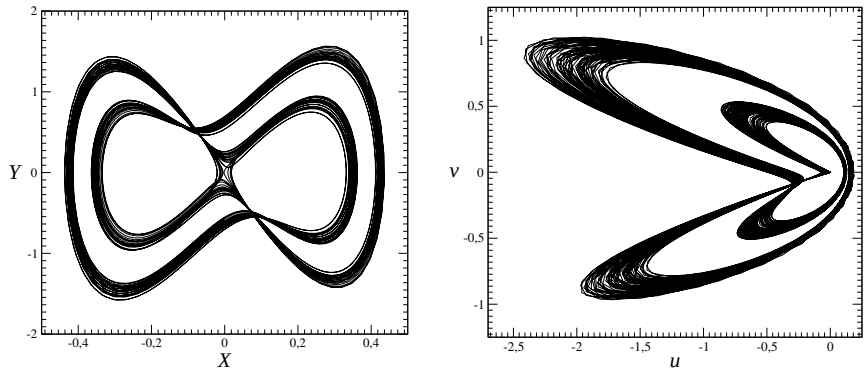

(a) Original dynamics (b) Image system

Fig. A.16 Chaotic attractor (a) solution of the Auvergne and Baglin system and its image (b). Parameter values: $\gamma_1 = -0.3$, $\gamma_2 = 25.0$, $A^2K^2 = 0.01$ and $B/A = 0.125$.

where $X = x$, $Y = \dot{X}$ and $Z = \ddot{X}$. The system (A.18) has a single fixed point F_0 located at the origin of the phase space. It is a saddle-focus with one negative real eigenvalue and two complex conjugate eigenvalues with positive real part. Its image is characterized by a reverse horseshoe branched manifold [72]. This system is a group continuation of the Burke and Shaw system. The Malasoma attractor is shown in Fig. A.17(a) for $\alpha = 2.027717$. The bifurcation diagram of this system is equivalent to the bifurcation diagram of the Burke and Shaw system. The image attractor is shown in Fig. A.17(b).

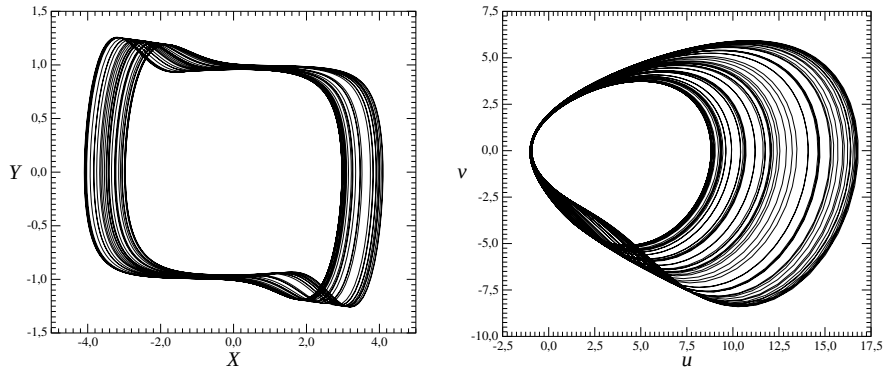

(a) Original dynamics (b) Image dynamics

Fig. A.17 (a) Chaotic attractor generated by the simplest equivariant jerk system just before the attractor merging crisis ($\alpha = 2.027717$). (b) Its image is also represented.

A.1.11 Kremliovsky System

In order to investigate the 22-year solar activity cycle, Kremliovsky realized that a homoclinic orbit to a saddle-focus could be associated with the dynamics underlying the sunspot number [54]. To accomplish that, a symmetry must be added to obtain 22-year cycles from the 11-year cycle observed with the sunspot number. Thus, Kremliovsky modified the Rössler system to obtain an equivariant system. The modified Rössler system, or Kremliovsky system, is:

$$\begin{aligned}\dot{X} &= -Y - Z \\ \dot{Y} &= X + aY \\ \dot{Z} &= bX + Z\left(X^2 - c\right)\end{aligned}$$

where (a, b, c) are the control parameters. This system has two fixed points:

$$F_{\pm} = \left| \begin{array}{l} X_{\pm} = \pm\sqrt{c - ab} \\ \\ Y_{\pm} = \mp\dfrac{\sqrt{c - ab}}{a} \\ \\ Z_{\pm} = \pm\dfrac{\sqrt{c - ab}}{a} \end{array} \right.$$

and a third one, F_0, located at the origin of the phase space. This system is equivariant under an inversion symmetry $\mathcal{P}$. A chaotic attractor is shown in Fig. A.18(a) with its image in Fig. A.18(b) for $(a, b, c) = (0.6, 0.45, 10.0)$.

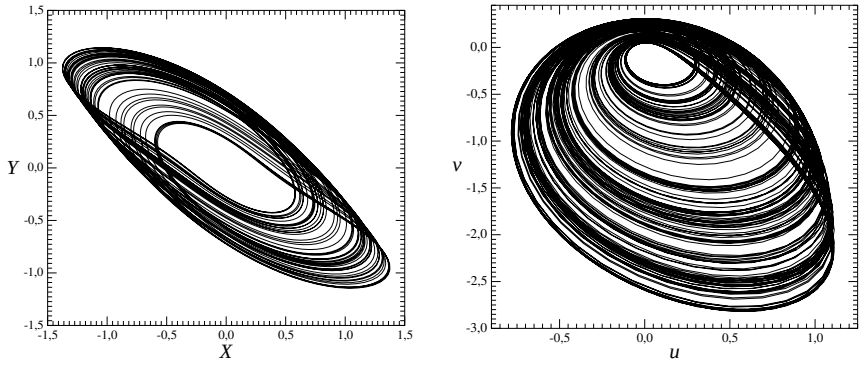

(a) Original dynamics (b) Image attractor

Fig. A.18 Chaotic attractor generated by the Kremliovsky system. Parameter values: $a = 0.6$, $b = 0.45$, and $c = 10.0$.

A.1.12 An Equivariant Rössler System

In his attempt to list the different types of chaos, Rössler proposed a double screw-type chaos, which has in fact the symmetry of Khaikin's "universal" circuit, that is, there are two symmetric foci related by fast jumps. The equations for this double screw-type chaos are [110]:

$$\begin{aligned} \dot{X} &= -aX - Y(1 - X^2) \\ \dot{Y} &= \mu(Y + 0.3X - 2Z) \\ \dot{Z} &= \mu(X + 2Y - 0.5Z) \end{aligned} \tag{A.19}$$

This system is invariant under an inversion symmetry. Two plane projections of the chaotic attractor are shown in Figs A.19(a) and A.19(b). The structure of this attractor is similar to the Matsumoto-Chua circuit [23] (see Section A.1.14) as shown by a first-return map to a Poincaré section (Fig. A.19(c)). The corresponding template therefore has nine branches (not shown).

A.1.13 Duan-Wang-Huang System

A particular kind of chaotic system has been introduced by Duan, Wang, and Huang [27]. They combined a three-dimensional linear system with attraction/repulsion functions developed in the context of "swarm" aggregations. Swarming behaviors have been observed for a long time in certain living systems, such as flocks of birds, schools of fish, herds of animals, etc. The attraction/repulsion function as introduced in this model plays the role of a piecewise nonlinearity. The equations are:

$$\begin{aligned} \dot{X} &= -Y - \mu Z \\ \dot{Y} &= \nu X - 0.6Z \\ \dot{Z} &= -0.2X - 3Z - \rho\left(1 - 20e^{-5\rho^2}\right) \end{aligned}$$

where $\rho = 2X - Y + 0.3Z$. This system is invariant under an inversion symmetry. It has three fixed points

$$F_* = \left| \begin{array}{l} X_* = 0 \\ Y_* = 0 \\ Z_* = 0 \end{array} \right. \quad \text{and} \quad F_\pm = \left| \begin{array}{l} X_\pm = \dfrac{\pm 6\lambda}{12 + \nu(10\mu + 3)} \\ Y_\pm = \dfrac{\mp 10\nu\lambda}{12 + \nu(10\mu + 3)} \\ Z_\pm = \dfrac{\pm 10\nu\lambda}{12 + \nu(10\mu + 3)} \end{array} \right.$$

where

$$\lambda = \frac{1}{5}\sqrt{-5\ln\frac{1}{100}\,\frac{66 + 5\nu(33 + 10\nu)}{12 + \nu(10\mu + 3)}}$$

From initial conditions $(X_0 = -0.1, Y_0 = 1.5, Z_0 = -2)$, a chaotic attractor can be obtained. It is shown in Fig. A.20(a) with its image in Fig. A.20(b).

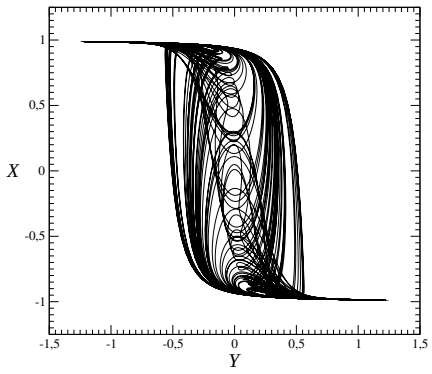

(a) Y-X plane

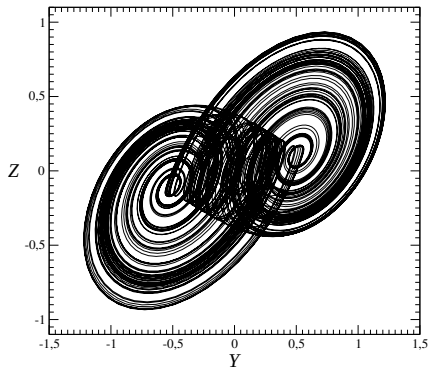

(b) Y-Z plane

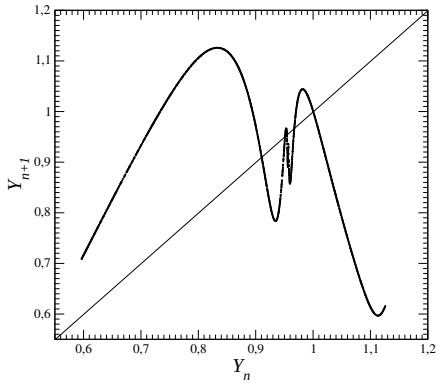

(c) First-return map

Fig. A.19 Phase portrait and first-return map associated with a chaotic behavior solution to system (A.19). Parameter values: $a = 0.03$ and $\mu = 0.1$ (and not 10 as reported in Rössler's paper [110]). Initial conditions: $X_0 = -1$, $Y_0 = 0.55$, and $Z_0 = 0.12$.

A.1.14 Matsumoto-Chua System

A.1.14.1 Piecewise Nonlinearity The system is an electronic circuit whose block diagram is shown in Fig. A.21. The circuit consists of a nonlinear amplifier N which transforms the input voltage $X(t)$ into the output $\alpha f(X)$. The parameter α characterizes the gain of N around $X = 0$. The nonlinear amplifier has a linear feedback which contains a series connection to a low pass filter (RC_1) and to an LC_2 resonance branch. Chua's equations model the dynamics of such an electronic circuit

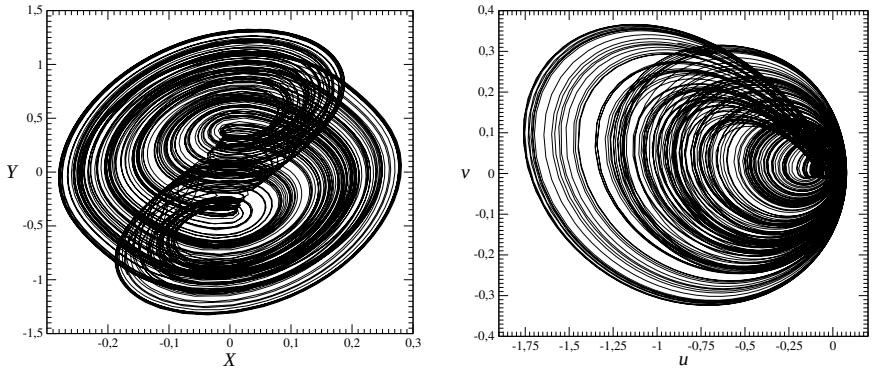

(a) Original dynamics (b) Image attractor

Fig. A.20 Chaotic attractor generated by the Duan-Wang-Huang system. Parameter values: $\mu = 1.0$ and $\nu = 20.2$.

[23]. It consists of a set of three ordinary differential equations:

$$\dot{X} = \alpha \left[Y - X - h(X) \right]$$

$$\dot{Y} = X - Y + Z$$

$$\dot{Z} = -\beta Y$$

where the nonlinearity is

$$h(x) = m_1 X + \frac{(m_0 - m_1)}{2} \left[|X + 1| - |X - 1| \right]$$

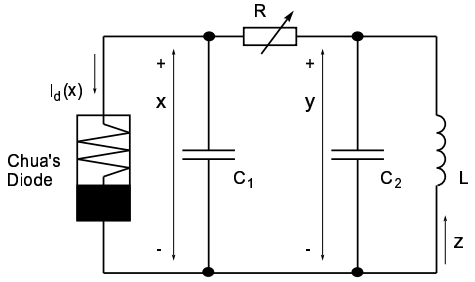

Fig. A.21 Typical block diagram for a Matsumoto-Chua circuit with a nonlinear function that is piecewise linear with two breaks.

The control parameters of the system are fixed to $\beta = 100/7$, $m_0 = -8/7$, $m_1 = -5/7$ while α is a variable control parameter. The vector field defined by these equations is equivariant under the inversion symmetry $\mathcal{P}$.

After an attractor merging crisis, the connected chaotic attractor generated by this system is globally invariant under the inversion $\mathcal{P}$. Such an attractor is shown in Fig. A.22 with its image. Other numerical systems similar to that one as well as experimental data recorded on such an electronic circuit are investigated taking into account their symmetry properties in [70].

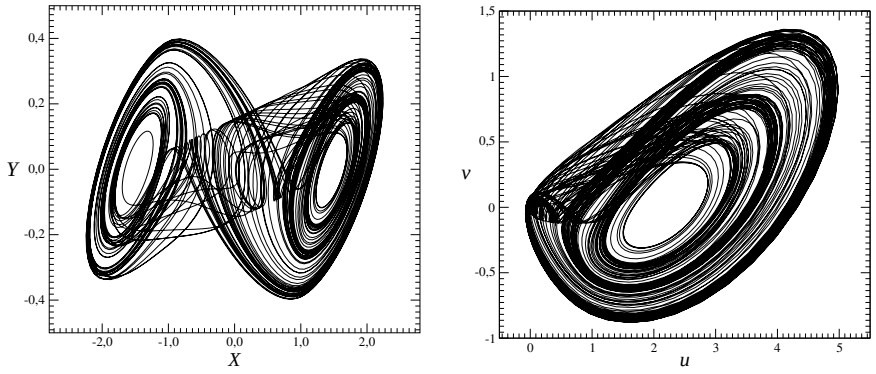

(a) Original dynamics (b) Image dynamics

Fig. A.22 (a) Matsumoto-Chua chaotic attractor and (b) its image. Parameter values: $(\beta, m_0, m_1, \alpha) = (100/7, -8/7, -5/7, 18.9)$.

A.1.14.2 Smooth Polynomial Nonlinearity As seen in the previous system, the nonlinearity is often expressed under the form of a piecewise continuous function. Nevertheless, a real circuit never reproduces such a piecewise nonlinearity, and a smooth nonlinearity might be preferred. Moreover, a real circuit never ejects a trajectory to infinity. Such a feature may be produced by a model with a piecewise smooth nonlinearity. A system with an everywhere differentiable nonlinear function has been proposed [23,51]:

$$\begin{aligned}\dot{X} &= \alpha\,[Y - \varphi(X)]\\ \dot{Y} &= X - Y + Z\\ \dot{Z} &= -\beta Y\end{aligned}$$

where the nonlinear function is expressed as a polynomial

$$\varphi(X) = K_0 + K_1 X + K_2 X^2 + K_3 X^3$$

Using the control parameters

$$\begin{aligned} K_0 &= 0.0 \\ K_1 &= -1/6 \\ K_2 &= 0.0 \\ K_3 &= 1/16 \end{aligned}$$

ensures that the nonlinear function $\varphi(X)$ is odd. This allows to obtain an equivariant dynamical system under an inversion symmetry $\mathcal{P}$.

The system has three fixed points:

$$S_0 = \left| \begin{array}{l} X = 0 \\ Y = 0 \\ Z = 0 \end{array} \right. \quad \text{and} \quad S_\pm = \left| \begin{array}{l} X = \pm q \\ Y = 0 \\ Z = \mp q \end{array} \right.$$

where $q = \sqrt{8/3} \approx 1.63$ is the positive root of the equation $\varphi(X) = 0$. Thus, the location of periodic points does not depend on the control parameters α and β. Different types of behaviors are shown in Fig. A.23.

A.1.15 Multispiral Attractors

From the Chua's circuit, it is possible to build the so-called multispiral attractors using a piecewise-linear characteristic [10, 119]. The dynamical system is thus a Chua circuit slighlty modified:

$$\begin{aligned} \dot{X} &= \alpha \left[Y - \varphi_N(X) \right] \\ \dot{Y} &= X - Y + Z \\ \dot{Z} &= -\beta Y \end{aligned}$$

where $\varphi_N(X)$ is the piecewise-linear characteristic. N designates the number of "spiral attractors" which will be observed. For $N = 2$, we have

$$\varphi_2(X) = \left| \begin{array}{lll} m_0 X + \ \text{sgn}(X)\xi_0 & \text{if} & |X| < s_0 \\ m_1 X + \ \text{sgn}(X)\xi_1 & \text{if} & |X| \geq s_0 \end{array} \right.$$

where

$$\begin{aligned} \alpha &= 9.2 \\ \beta &= \tfrac{100}{7} \\ m_0 &= -\tfrac{8}{7} \\ m_1 &= -\tfrac{5}{7} \\ s_0 &= 1 \\ \xi_0 &= 0 \\ \xi_1 &= (m_0 - m_1)s_0 + \xi_0 \end{aligned}$$

This system corresponds to the usual Chua circuit (Fig. A.24(a)). When $N = 3$, we obtain

$$\varphi_3(X) = \left| \begin{array}{lll} m_0 X + \ \text{sgn}(X)\xi_0 & \text{if} & |X| < s_0 \\ m_1 X + \ \text{sgn}(X)\xi_1 & \text{if} & s_0 \leq |X| < s_1 \\ m_0 X + \ \text{sgn}(X)\xi_2 & \text{if} & |X| \geq s_1 \end{array} \right.$$

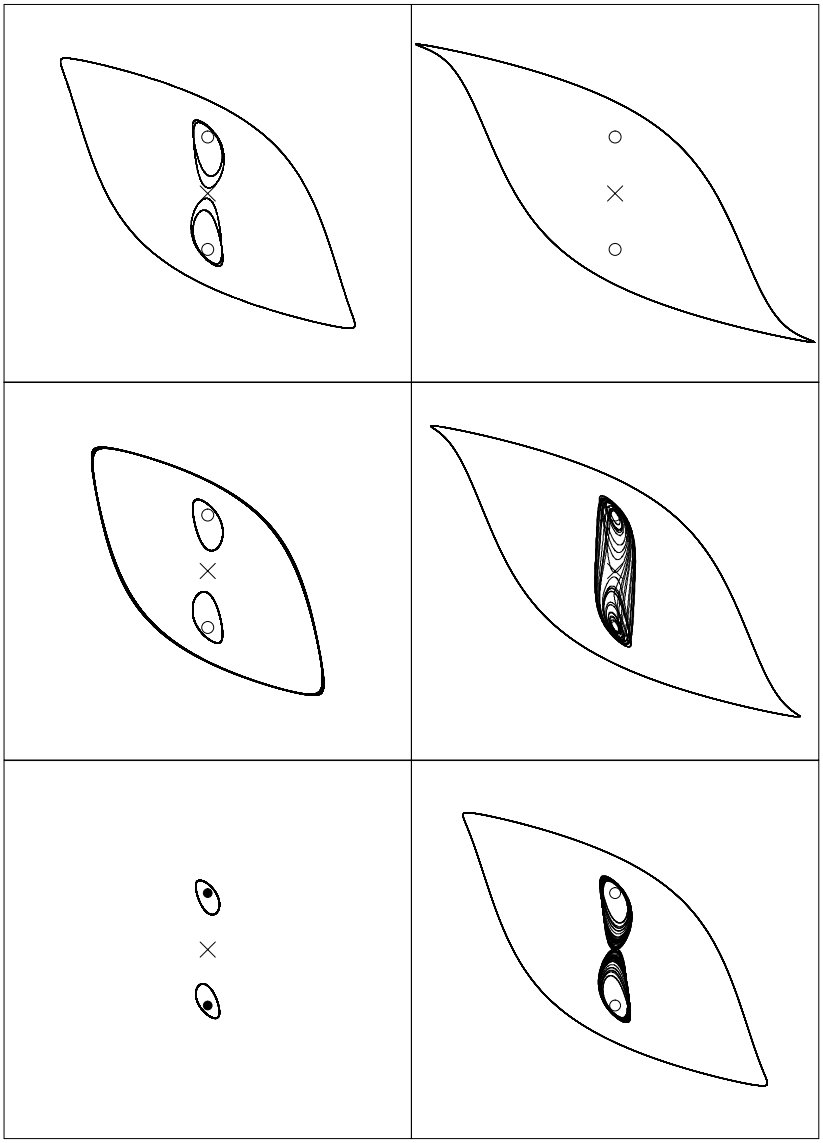

Fig. A.23 Different types of behaviors generated by the smooth Chua system for different control parameter values α. Fixed points are designated by "$\bullet$" when they are stable, "$\circ$" when they are instable and "$\times$" when they are unstable with one positive real eigenvalue. Limit cycles and strange attractors are also shown. Other parameter value: $\beta = 14.0$.

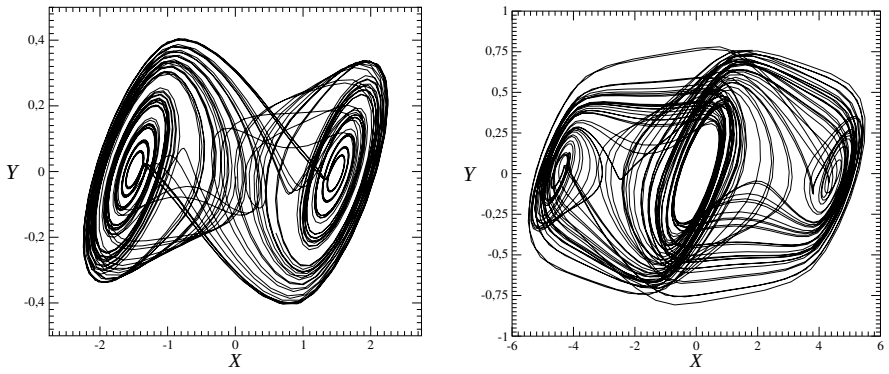

(a) Two spirals (b) Three spirals

Fig. A.24 Chaotic attractors generated by the multispiral Chua system. Initial conditions are $(X_0 = 0.1, Y_0 = 0, Z_0 = 0)$. (a) Two spirals and (b) three spirals. These can be enclosed in genus-3 and genus-5 bounding tori.

where

$$\begin{aligned}
\alpha &= 11.4 \\
\beta &= \tfrac{100}{7} \\
m_0 &= -\tfrac{5}{7} \\
m_1 &= -\tfrac{8}{7} \\
s_0 &= 1 \\
s_1 &= 4 \\
\xi_0 &= 0 \\
\xi_1 &= (m_0 - m_1)s_0 + \xi_0 \\
\xi_2 &= (m_1 - m_0)s_1 + \xi_1
\end{aligned}$$

A chaotic attractor with three spirals is shown in Fig. A.24(b). The strange attractors shown in Fig. A.24 can be enclosed in genus-3 and genus-5 bounding tori A_2 and A_3. Those with "N spirals" can be enclosed in genus-$(2N-1)$ linear bounding tori A_N.

A.1.16 Thomas Systems

A.1.16.1 A System with an $\mathcal{S}_6$ Symmetry A system with an $\mathcal{S}_6$ symmetry has been proposed by Thomas [122]:

$$\begin{aligned}
\dot{X} &= -bX + aY - Y^3 \\
\dot{Y} &= -bY + aZ - Z^3 \\
\dot{Z} &= -bZ + aX - X^3
\end{aligned} \tag{A.20}$$

The control parameter b is fixed to 0.3. In order to have a better representation of the symmetry properties, we may use the coordinate transformation:

$$\begin{aligned} X &= \frac{\sqrt{3}}{2}(y-x) \\ Y &= z - \frac{x+y}{2} \end{aligned} \tag{A.21}$$

This plane projection will help us to exhibit the nature of the symmetry. This is exemplified in the case where there is a single attractor in the phase space (Fig. A.25(a)). A projection of the image (Fig. A.25(b)) may be obtained using the coordinate transformation:

$$\begin{aligned} u &= \Re(X+iY)^6 = X^6 - 15X^4Y^2 + 15X^2Y^4 - Y^6 \\ v &= \Im(X+iY)^6 = 6X^5Y - 20X^3Y^3 + 6XY^5 \end{aligned} \tag{A.22}$$

The $6 \mapsto 1$ image attractor is shown in Fig. A.25(c).

A.1.16.2 A System with an Inversion Symmetry

Thomas proposed another system with an inversion symmetry $\mathcal{P}$ [122]:

$$\begin{aligned} \dot{X} &= -Y \\ \dot{Y} &= X + aY - Z \\ \dot{Z} &= Y^3 - bZ \end{aligned} \tag{A.23}$$

It has a single fixed point located at the origin of the phase space. A chaotic attractor is shown in Fig. A.26(a) with its image in Fig. A.26(b) for $(a, b) = (3.3, 4.0)$.

A.1.17 Liu and Chen System

Liu and Chen proposed a system with $\mathcal{V}_4$-symmetry [77]:

$$\begin{aligned} \dot{X} &= aX + YZ \\ \dot{Y} &= -bY - XZ \\ \dot{Z} &= -cZ - XY \end{aligned} \tag{A.24}$$

We hold $a = 0.5$ and $b = 12.0$ fixed and treat c as a bifurcation parameter. It has one degenerate fixed point located at the origin of the phase space. Its eigenvalues are $\lambda_1 = a$, $\lambda_2 = -b$, and $\lambda_3 = -c$. It is a saddle. There are four other fixed points located at

$$\begin{aligned} X_\pm &= \pm\sqrt{bc} \\ Y_\pm &= \pm\sqrt{ac} \\ Z_\pm &= \pm\sqrt{ab} \end{aligned} \tag{A.25}$$

where the product of these three coordinates is negative. If a, b, or c is negative, the fixed points are imaginary. If a, b, and c are positive, they are saddle-foci with one negative real eigenvalue. With $c = 4$, two attractors coexist in the phase space (Fig. A.27(a)). Their images are shown in Fig. A.27(b).

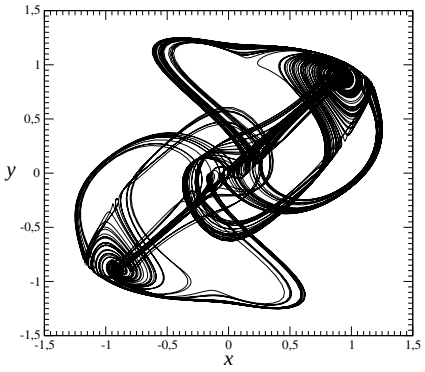

(a) Plane projection $\mathbb{R}^2(x, y)$

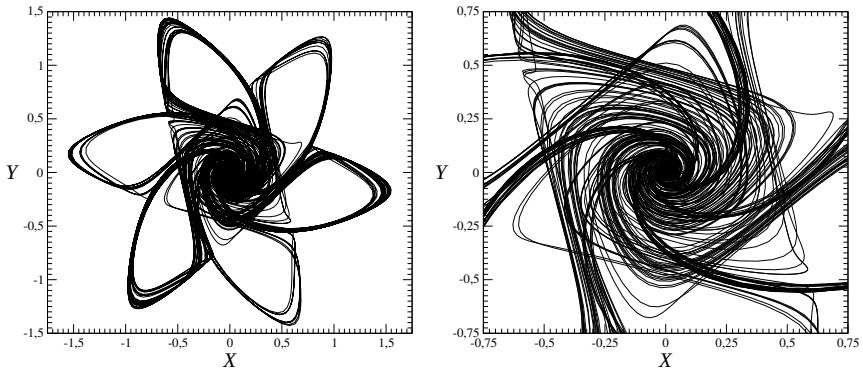

(b) Plane projection $\mathbb{R}^2(X, Y)$

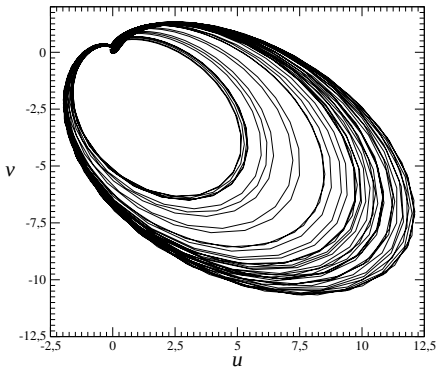

(c) Image space $\mathbb{R}^2(u, v)$

Fig. A.25 Different representations of the chaotic attractor of the Thomas system. Parameter values: $(a, b) = (1.1, 0.3)$.

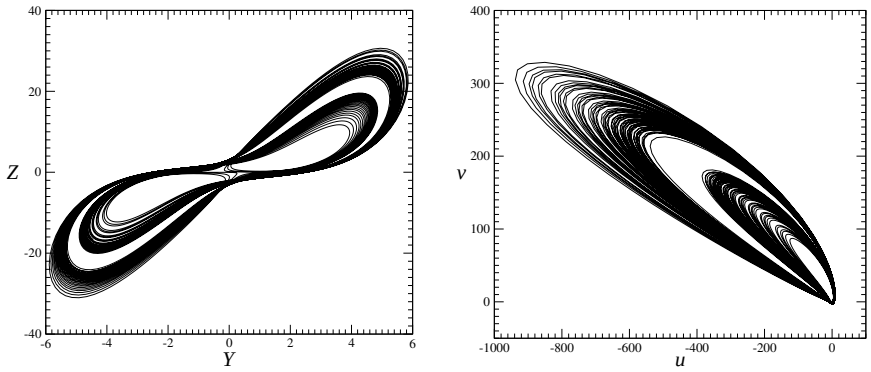

(a) Original phase portrait (b) Image phase portrait

Fig. A.26 (a) Chaotic attractor generated by the Thomas system with an inversion symmetry. (b) Image attractor. Parameter values: $a = 3.3$ and $b = 4.0$.

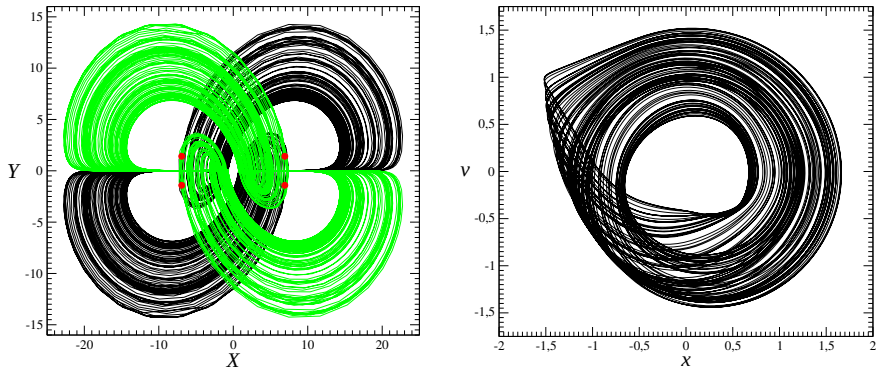

(a) Original phase portrait (b) Differential embedding

Fig. A.27 Chaotic attractors for the Liu-Chen system for two disconnected components (a). Both have the same image (b). Parameter values: $(a, b, c) = (0.5, 12.0, 4.0)$.

A.1.18 Lü, Chen, and Cheng System

Chen and co-workers proposed another system with a $\mathcal{V}_4$ symmetry (if $\nu = 0$) [80]. The equations are

$$\begin{aligned} \dot{X} &= -\frac{ab}{a+b}X - YZ \\ \dot{Y} &= aY + XZ + \nu \\ \dot{Z} &= bZ + XY \end{aligned} \tag{A.26}$$

This system has five fixed points (for $\nu = 0$). One is located at the origin of the phase space $\mathbb{R}^3(X, Y, Z)$. The four other fixed points are symmetry related and are defined as:

$$F_{1,\pm} = \left| \begin{array}{l} X_\pm = \sqrt{ab} \\ Y_\pm = \pm|b|\sqrt{\dfrac{a}{a+b}} \\ Z_\mp = \pm a\sqrt{\dfrac{b}{a+b}} \end{array} \right. \tag{A.27}$$

and

$$F_{2,\pm} = \left| \begin{array}{l} X_\pm = -\sqrt{ab} \\ Y_\pm = \pm|b|\sqrt{\dfrac{a}{a+b}} \\ Z_\mp = \mp a\sqrt{\dfrac{b}{a+b}} \end{array} \right. \tag{A.28}$$

The parameters are $a = -10$. This system has a $\mathcal{V}_4$ symmetry only when $\nu = 0$. Parameter b can be varied over the interval $[-5.604; -2.34]$. When $b = -2.4170$, a chaotic attractor with four components is observed (Fig. A.28(a)). The disconnected chaotic attractors are then topologically equivalent to the Burke and Shaw attractor before the attractor merging crisis [69]. When b is decreased, an attractor merging crisis occurs and an attractor with two disconnected components remains in phase space (Fig. A.28(b)). Each connected component of the attractor is topologically equivalent to the Burke and Shaw attractor characterized by a four-branch return map.

When parameter b is further decreased, the attractor continues to grow as observed for the Burke and Shaw system. Note that the trajectory never crosses the plane defined by $Z = 0$ (Fig. A.29(a)). This is only permitted when a perturbation is added. For instance, when $\nu = 1.0$, the trajectory may then cross the plane $Z = 0$, a one component attractor is observed (Fig. A.29(b)). Equivalently, such a property of the system is very fragile and a noise contamination could be sufficient to restore a one component attractor as shown in Fig. A.29(b). It is sufficient since the trajectory travels in the neighborhood of the plane $Z = 0$.

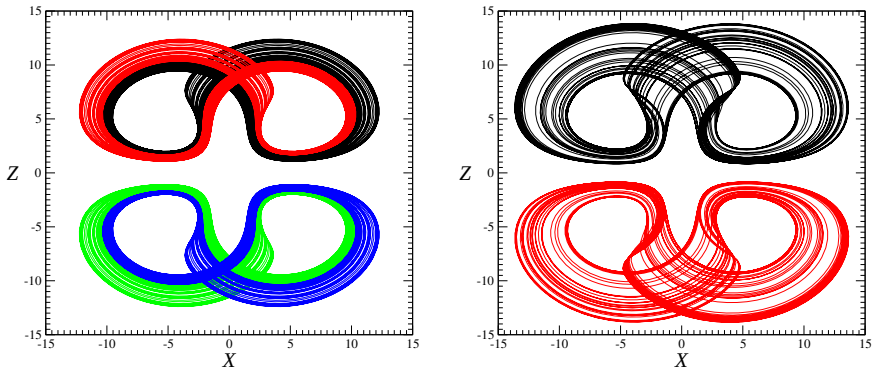

(a) Four components ($b = -2.4170$) (b) Two components ($b = -2.5305$)

Fig. A.28 Chaotic attractors for the Lü-Chen-Cheng system for (a) four and (b) two components. Parameter values: $(a, \mu, \nu) = (-10, 0, 0)$.

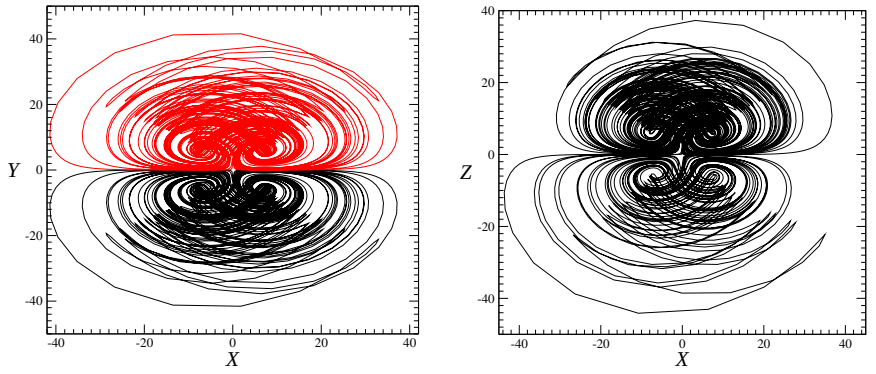

(a) Four components ($\nu = 0.0$) (b) Two components ($\nu = 1.0$)

Fig. A.29 Chaotic attractors for the Lü-Chen-Cheng system for (a) two components and (b) one component when the symmetry is broken ($\nu \neq 0$). Parameter values: $(a, b, \mu) = (-10, -4.417, 0)$.

A.2 HIGHER DIMENSIONAL SYSTEMS

A.2.1 4D Chaotic System

In their search for new chaotic systems, Qi, Du, Chen, Chen, and Yuan [103] found a four-dimensional chaotic system with a four-group symmetry. The equations are

$$\begin{aligned}
\dot{X}_1 &= a(X_2 - X_1) + X_2 X_3 X_4 \\
\dot{X}_2 &= b(X_1 + X_2) - X_1 X_3 X_4 \\
\dot{X}_3 &= -cX_3 + X_1 X_2 X_4 \\
\dot{X}_4 &= -dX_4 + X_1 X_2 X_3
\end{aligned} \tag{A.29}$$

This system has one fixed point at the origin of the phase space and four others. This system is equivariant under a four-group symmetry whose generators are $(X_1, X_2, X_3, X_4) \mapsto (-X_1, -X_2, X_3, X_4)$ and $(X_1, X_2, X_3, X_4) \mapsto (X_1, X_2, -X_3, -X_4)$. It may produce a chaotic attractor topologically equivalent to the Lorenz attractor (in spite of its jittery shape) as shown in Fig. A.30.

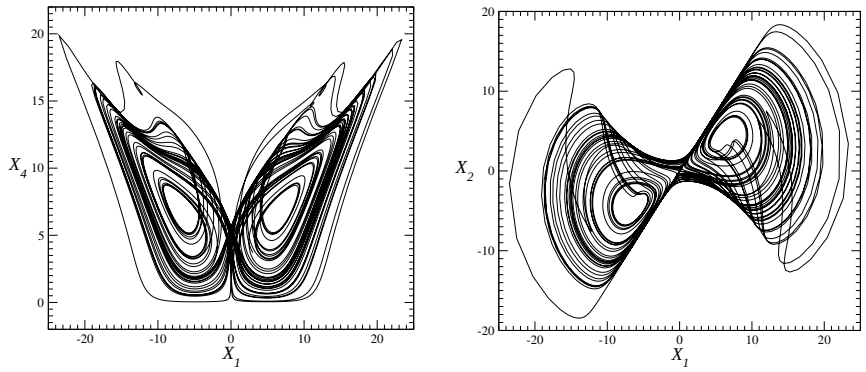

(a) X_1-X_4 plane projection (b) X_1-X_2 plane projection

Fig. A.30 Chaotic attractors for the Qi-Du-Chen-Chen-Yuan system. Parameter values: $(a, b, c, d) = (30, 8, 100, 10)$.

A.2.2 5D Laser Model by Zeghlache & Mandel

In 1975, Haken [43] showed that the equations of a laser system derived in the semi-classical approach are equivalent to the Lorenz equations [78]. The main weakness of these equations is that chaotic behaviors are predicted for the weak cavity limit and high intensity in spite of experiments showing that these behaviors occur for low intensity.

This laser model is extensively discussed in Section 9.2.1. When the detuning δ between the normalized steady-state laser frequency and the molecular resonance frequency ($\delta \in [0; 1]$) is taken into account, the amplitude equations become [139]

$$\begin{array}{rcl} \dot{X}_1 & = & -\sigma(X_1 + \delta X_2 - Y_1) \\ \dot{X}_2 & = & -\sigma(X_2 - \delta X_1 - Y_2) \\ \dot{Y}_1 & = & RX_1 - Y_1 + \delta Y_2 - X_1 Z \\ \dot{Y}_2 & = & RX_2 - Y_2 - \delta Y_1 - X_2 Z \\ \dot{Z} & = & -\gamma Z + X_1 Y_1 + X_2 Y_2 \end{array} \tag{A.30}$$

where R is the pumping rate, σ is the ratio of the cavity decay rate of the field to the relaxation constant of the polarization, and γ is the relaxation rate of the normalized population inversion, Z [139]. (X_1, X_2) are the real and imaginary parts of the electric field and (Y_1, Y_2) are the real and imaginary parts of the polarization amplitude. These amplitude equations are invariant under the symmetry group $U(1)$: $(X = X_1 + iX_2, Y = Y_1 + iY_2, Z) \rightarrow (Xe^{i\theta}, Ye^{i\theta}, Z)$. The system (A.30) has one fixed point F_0 located at the origin and a continuous set of fixed points defined by

$$Z = R - (1 + \delta^2) \quad |X| = \sqrt{\gamma Z} \quad Y = (1 - i\delta)X$$

This set of fixed point defines a circle which is invariant under continuous rotations. The case of the continuous rotation symmetry is explicitly discussed in Section 9.2.1. The chaotic attractor generated by the Zeghlache-Mandel equations is shown in Fig. A.31(a) for control parameter values $\delta = 0.002$, $R = 20.0$, $\gamma = 0.25$ and $\sigma = 2.0$. Its image is shown in Fig. A.31(b).

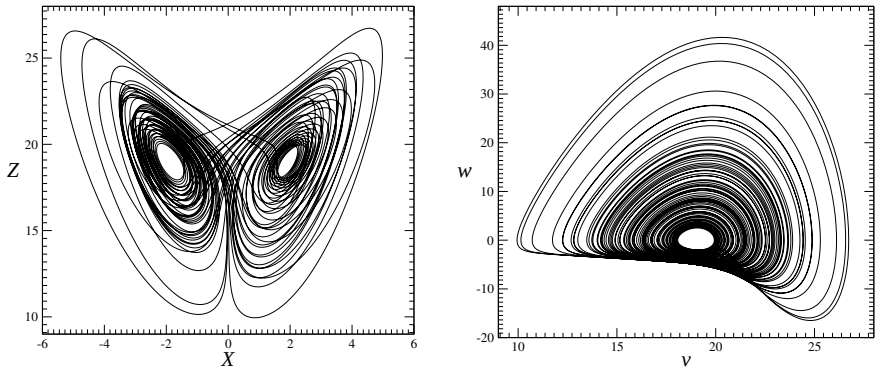

(a) Original dynamics (b) Image system

Fig. A.31 Chaotic attractor of the Zeghlache and Mandel equations (a) and its image (b). The detuning is slighltly different from zero ($\delta = 0.002$) to show the effect of the continuous rotation on the Lorenz-like attractor. Other parameter values: $R = 20.0$, $\gamma = 0.25$, and $\sigma = 2.0$.

A.2.3 6D Chaotic Model for Solar Activity

The magnetic activity of a lower main-sequence star depends upon its rotation rate. As the star ages, it loses angular momentum, owing to magnetic braking, and so becomes less active. Magnetic cycles are found in middle-aged stars like the Sun, which are relatively inactive. The cycles of the sunpot numbers have periods around 11 years and are modulated on a longer time scale. This modulation leads to intervals of reduced activity (grand minima). The Sun's magnetic history can be traced back for the last 10,000 years, and the proxy record derived from abundances of cosmogenic isotopes such as ^{14}C and ^{10}Be demonstrates that the Maunder minimum of the seventeenth century—when sunspots were very rarely observed—was preceded by numerous similar episodes. The last three grand minima—the Spörer minimum (1415–1535), the Maunder minimum (1645–1715) and the abortive Dalton minimum (1795–1825)—were separated by intervals of 100-200 years [12] and the ^{14}C record displays a characteristic time scale of about 200 years; however, the record is aperiodic and the intervals between successive grand minima show considerable variation about this mean value. There is also evidence that up to 30 % of solar-type stars may be undergoing similar grand minima at any time: indeed, one star (HD3651) seems to have been caught in the act of entering a grand minimum.

The spatial structure of these magnetic fields can only be determined for the Sun. Since the end of the Maunder minimum the incidence of sunspots has been symmetrical about the equator, with minor statistical fluctuations. Magnetic fields have only been measured since the beginning of this century and the azimuthally averaged toroidal field, which emerges in sunspots and active regions, is antisymmetric about the equator and reverses after each 11-year activity cycle. The corresponding poloidal field can be derived from a vector potential that is roughly symmetric about the equator; thus it has the symmetry of a dipole. It is generally accepted that magnetic cycles in a star like the Sun are produced by a dynamo located at, or near, the base of its convection zone. These stellar dynamos differ from the geodynamo (which maintains the same polarity for times much longer than the ohmic diffusion time for the Earth's core) in that their magnetic fields reverse on a much shorter time scale. The measured modulation of the solar cycle is aperiodic and might have a deterministic cause. The available record was not long enough to distinguish between these two possibilities until a global model was obtained from the sunspot numbers.

An appropriate sixth-order system that contains the minimal number of terms with relevant symmetries was introduced by Knobloch and Landsberg [52, 53]. The interaction of oscillatory dipole and quadrupole modes under the action of instantaneous nonlinearities are taken into account. The complex variable z_1 represents the dipole mode while z_2 is the quadrupole mode. A fourth-order system consistent with the symmetries of a rotating star was derived [52]. In addition to the pure dipole and quadrupole solutions, the system possesses mixed-mode solutions (periodic but asymmetric dynamos), as well as several different types of quasiperiodic dynamos, of both pure and mixed parity [53].

The driving of velocity perturbations by the magnetic field (both dipole and quadrupole modes) are included in the model by decomposing the velocity into com-

ponents that are symmetric, v, and antisymmetric, w, with respect to the equator. The sixth-order model is

$$\begin{aligned}
\dot{z}_1 &= (\mu + \sigma + i\omega_1)z_1 + a|z_1|^2 z_1 + a|z_2|^2 z_1 + b|z_2|^2 z_1 + (\epsilon v + \delta v^2)z_1 + \beta w z_2 \\
\dot{z}_2 &= (\mu + i\omega_2)z_2 + a'|z_2|^2 z_2 + a'|z_1|^2 z_2 + b'|z_1|^2 z_2 + (\epsilon' v + \delta' v^2)z_2 + \beta' w z_1 \\
\dot{v} &= -\tau_1 v + e_1(|z_1|^2 + |z_2|^2) \\
\dot{w} &= -\tau_2 w + e_2(z_1\bar{z}_2 + z_2\bar{z}_1)
\end{aligned}$$

where $(\mu + \sigma, \mu)$ are the linear growth rates of the dipole and quadrupole modes, respectively, and (ω_1, ω_2) are their frequencies. The nonlinear pure modes are controlled by the complex coefficients a and a'. The complex coefficients b and b' quantify the nonlinear couplings of the two modes. The decay rates of the symmetric velocity v and the anti-symmetric velocity w are controlled by the real parameters τ_1 and τ_2. The real coefficients e_1 and e_2 quantify the contribution of the mixed mode solutions, that is, solutions with both dipole and quadrupole components. The parameters are

$$\begin{array}{lllllllll}
\mu & = & 1.9 & \sigma & = & -0.361 & a & = & 0.5 + i0.5 \\
a' & = & 0.38 + i0.38 & b & = & -1.8 & b' & = & -2.2 \\
\epsilon & = & 1.1 - i1.1 & \delta & = & -0.965 + i0.965 & \delta' & = & -1.0 + i \\
\eta & = & 1.39 - i1.25 & \beta' & = & 0.43 + i0.43 & \tau_1 & = & 1.0 \\
\tau_2 & = & 1.1 & e_1 & = & 1.31 & e_2 & = & 2.0
\end{array}$$

and the initial conditions are

$$\begin{array}{lllll}
z_1 & = & 0.1 + i0.2 & v & = & 1.1 \\
z_2 & = & 0.1 + i0.1 & w & = & 1.1
\end{array}$$

A chaotic attractor obtained for $\mu = 1.9$ is shown in Fig. A.32(a) and its image is shown in Fig. A.32(b).

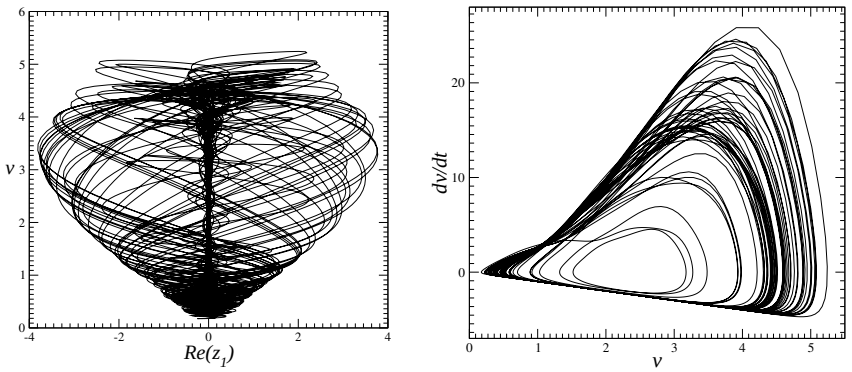

(a) Chaotic attractor (b) Image attractor

Fig. A.32 $\Re(z_1) - v$ plane projection of the chaotic attractor for solar activity generated for $\mu = 1.9$ (a) and its image phase portrait (b).

A.2.4 9D Model for a Rayleigh-Bénard Convection

The experiments considered by Lorenz [78] concern fluid motion occurring in a layer of fluid of uniform depth H, when the temperature difference between the upper and lower surfaces is maintained at a constant value ΔT. In the present case, the experiments concern a fluid motion occurring in a square cell. Reiterer [105] demonstrated that, in the case where the horizontal boundaries are free surfaces, the governing equations may be written as:

$$\begin{aligned} \frac{\partial \boldsymbol{w}}{\partial t} - \nabla \wedge (\boldsymbol{v} \cdot \boldsymbol{w}) &= \mathrm{Pr}\, \nabla^2 \boldsymbol{w} + \mathrm{Pr}\, \nabla \wedge (\theta \boldsymbol{e}_z) \\ \frac{\partial \theta}{\partial t} + (\boldsymbol{v} \cdot \nabla)\theta &= \nabla^2 \theta + \frac{R}{\pi^4} w \end{aligned} \tag{A.31}$$

where $\boldsymbol{w} = \nabla \wedge \boldsymbol{v}$ and $\boldsymbol{v} = \nabla \wedge \mathcal{A}$. Here, $\mathcal{A}$ is a vector potential and θ is the departure of temperature from that occurring in the motionless state. The problem is three-dimensional and convection cells are organized as displayed in Fig. A.33. A translation along the x- or y-axis by π/a reverses the convection flow, leaving invariant the temperature dependence.

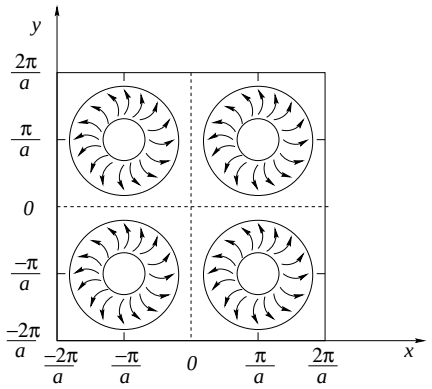

Fig. A.33 Spatial organization of convection cells in the x-y plane. No symmetry is observed along the z-axis. Two cells are exhibited along x- and y-axis.

The partial differential equations (A.31) may be reduced to a set of ordinary differential equations by expanding $\mathcal{A}$ and θ in Fourier series in x, y and z. Reiterer

retained a set of nine modes C_i such as:

$$\begin{aligned}
\mathcal{A}_1 &= C_1\,\tfrac{1+2a^2}{a}\sin(2ay)\sin(2z) + \quad C_2\,\tfrac{2\sqrt{2}\left(1+2a^2\right)}{a}\cos(ax)\sin(ay)\sin(z)\\
\mathcal{A}_2 &= C_3\,\tfrac{1+2a^2}{a}\sin(2ax)\sin(2z) + \quad C_4\,\tfrac{2\sqrt{2}\left(1+2a^2\right)}{a}\sin(ax)\cos(ay)\sin(z)\\
\mathcal{A}_3 &= C_5\,\tfrac{1+2a^2}{a^2}\sin(2ax)\sin(2ay)\\
\theta &= C_6\tfrac{\left(1+2a^2\right)^3}{a^2}\sin(2z) + \qquad C_7\,\tfrac{\left(1+2a^2\right)^3}{a^2}\cos(2ay)\sin(2z)\\
&\quad + C_9\,\tfrac{\sqrt{2}\left(1+2a^2\right)^3}{a^2}\cos(ax)\cos(ay)\sin(z) + C_8\,\tfrac{\left(1+2a^2\right)^3}{a^2}\cos(2ax)\sin(2z)
\end{aligned}$$

By inspecting the coefficients of the nine modes, one may observe that the mode C_6 is only related to a z-dependence and, consequently, it is not associated with a symmetry property. Modes C_5 and C_9 are associated with x and y variables and, consequently, are involved in a symmetry. The six remaining modes can be paired as (C_1, C_3), (C_2, C_4), and (C_7, C_8) according to their coefficients for which x (resp. y) is replaced by y (resp. x). They are also related to a symmetry. Once again, an exact relationship between modes cannot be exhibited without a complete derivation of the set of ordinary differential equations [105]:

$$\begin{aligned}
\dot{C}_1 &= -\text{Pr}\, b_1 C_1 - C_2 C_4 + b_4 {C_4}^2 + b_3 C_3 C_5 - \text{Pr}\, b_2 C_7\\
\dot{C}_2 &= -\text{Pr}\, C_2 + C_1 C_4 - C_2 C_5 + C_4 C_5 - \text{Pr}\, C_9/2\\
\dot{C}_3 &= -\text{Pr}\, b_1 C_3 + C_2 C_4 - b_4 {C_2}^2 - b_3 C_1 C_5 + \text{Pr}\, b_2 C_8\\
\dot{C}_4 &= -\text{Pr}\, C_4 - C_2 C_3 - C_2 C_5 + C_4 C_5 + \text{Pr}\, C_9/2\\
\dot{C}_5 &= -\text{Pr}\, b_5 C_5 + {C_2}^2/2 - {C_4}^2/2\\
\dot{C}_6 &= -b_6 C_6 + C_2 C_9 - C_4 C_9\\
\dot{C}_7 &= -b_1 C_7 - R C_1 + 2 C_5 C_8 - C_4 C_9\\
\dot{C}_8 &= -b_1 C_8 + R C_3 - 2 C_5 C_7 + C_2 C_9\\
\dot{C}_9 &= -C_9 - R C_2 + R C_4 - 2 C_2 C_6 + 2 C_4 C_6 + C_4 C_7 - C_2 C_8
\end{aligned} \tag{A.32}$$

where $\dot{C}_i$ denotes the derivative of C_i with respect to t. Here Pr is the Prandtl number and R is the reduced Rayleigh number

$$R = \frac{R_\alpha}{R_c} \tag{A.33}$$

where R_c is the critical Rayleigh number for the onset of instabilities. The constant parameters b_i measure the geometry of the square cell, and are defined by:

$$\begin{aligned}
b_1 &= 4\frac{1+a^2}{1+2a^2} \qquad & b_2 &= \frac{1+2a^2}{2\left(1+a^2\right)} \qquad & b_3 &= 2\frac{1-a^2}{1+a^2}\\
b_4 &= \frac{a^2}{1+a^2} \qquad & b_5 &= \frac{8a^2}{1+2a^2} \qquad & b_6 &= \frac{4}{1+2a^2}
\end{aligned}$$

Several attractors are plotted in Fig. A.34 along the line Pr $= 0.5, a = 0.25, 14.22 \leq R \leq 15.0$ in the control parameter space. This sequence shows an "inverse attractor halving bifurcation," as a 4-component attractor ($R = 14.22$) becomes a 2-component attractor ($R = 14.30$) and finally a single-component attractor ($R = 15.10$).

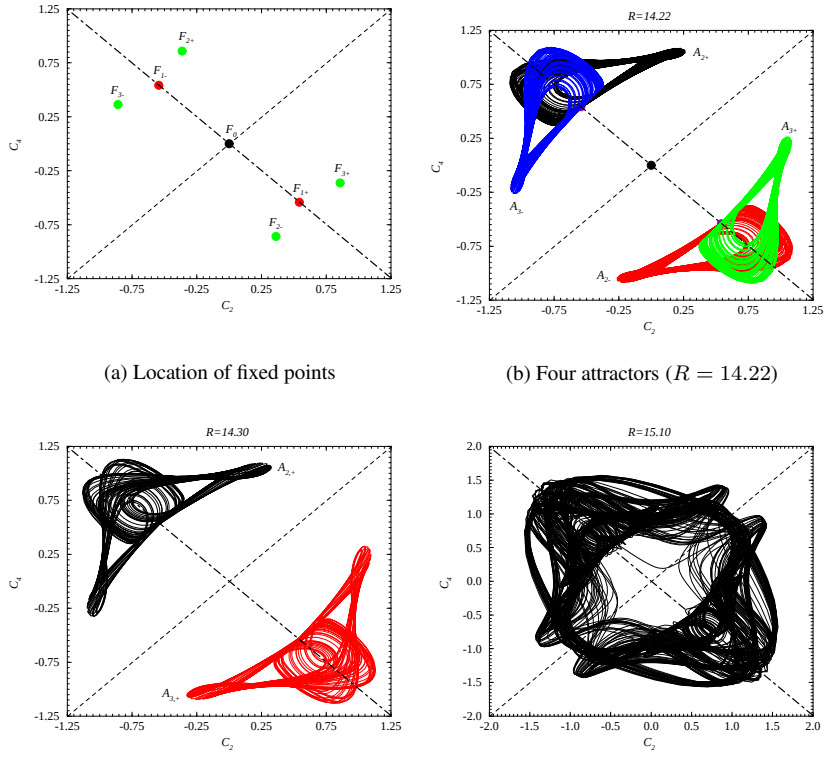

(a) Location of fixed points

(b) Four attractors ($R = 14.22$)

(c) Two attractors ($R = 14.30$)

(d) A single attractor ($R = 15.10$)

Fig. A.34 Different coexisting attractors generated by a 9-mode truncation of the Rayleigh-Bénard convection problem. For these attractors the control parameters are Pr $= 0.5$, and $a = 0.25$. The bifurcation parameter is R.

A.2.5 10D Model for Wave-Wave Interaction in a Plasma

Another interesting equivariant model comes from plasma physics. In the solar wind before the bow shock, there are relatively high electric fields which are turbulent. The source of energy for these fields comes from the reinjection of high energy electron beams in the solar wind. The "turbulence" so created is nothing else than an attempt of the plasma to return to thermodynamic equilibrium. These processes are investigated through a simplified model which corresponds to an interaction between energetic electrons and electromagnetic waves propagating in a plasma, but without collisions. A typical configuration is the case of electrons accelerated in the solar coronal zone which are ejected in the solar wind.

The model consists of five complex amplitude equations [56]

$$\begin{aligned}
\dot{a}_1 &= -\nu_1 a_1 + a_2 a_4 e^{-i\Delta t} \\
\dot{a}_2 &= -\nu_2 a_2 - a_1 a_4^* e^{i\Delta t} + a_3 a_4 e^{-i\delta t} \\
\dot{a}_3 &= -\nu_3 a_3 - a_2 a_4^* e^{i\delta t} \\
\dot{a}_4 &= -2\nu_4 a_4 + 2i(a_4 - a_5) \\
\dot{a}_5 &= -\nu_4 a_4 - a_1 a_2^* e^{-i\Delta t} - a_2 a_3^* e^{-i\delta t}
\end{aligned}$$

which correspond to a ten-dimensional real dynamical system. This system has a continuous rotation symmetry. It phase portrait is shown in Fig. A.35(a) with its image in Fig. A.35(b).

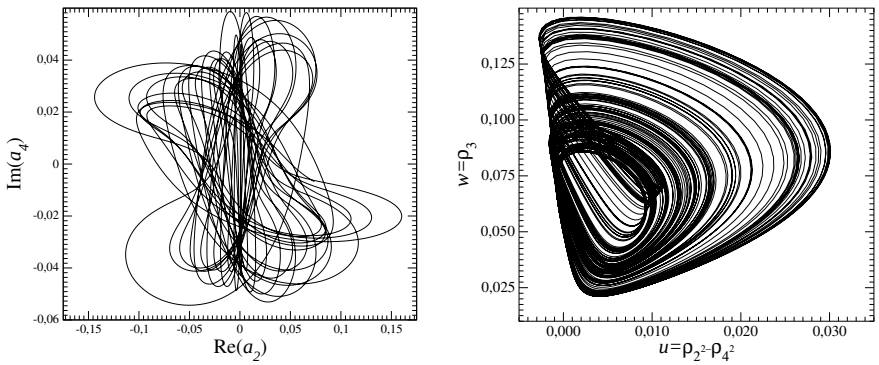

(a) Original dynamics (b) Image attractor

Fig. A.35 Chaotic attractor generated by the ten-dimensional model for four wave in interaction in a plasma. Parameter values: $\nu_1 = 0.050$, $\nu_2 = -0.0343$, $\nu_3 = 0.03$, $\nu_4 = 0.05$ and $\Delta = \delta = 0.0$.

A.3 NONAUTONOMOUS SYSTEMS

A.3.1 van der Pol System

The historic study of forced oscillators dealt exclusively with periodic and almost periodic solutions. The original impetus which led to the discovery of several coexisting periodic solutions was an experimental study by van der Pol and van der Mark [130]. The electric circuit which they used is shown in Fig. A.36, where Ne repesents a glow discharge tube filled with neon gas, E a battery (≈ 200 volts), R a resistor (several megohms), and E_0 (≈ 10 volts) is the amplitude of an applied periodic electric field. In the absence of the electric field the period of the system increases with increasing capacitance, C. They discovered the production of 40 or more subharmonics ($\frac{\omega}{n}$) of the applied frequency, ω. These subharmonics were found to be entrained, in the sense that the frequency of the system remained fixed while the capacitance was varied over a limited range. As C was further varied, the frequency changed discontinuously to another subharmonic. They also observed bands of "noise" in the regions of many transitions of the frequency, which they regarded as "a subsidiary phenomena." Also they clearly showed a hysteresis effect, hence a bistability in their experiments, but they did not provide any comment on that.

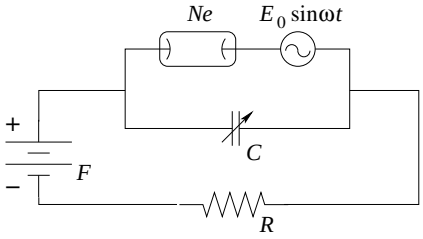

Fig. A.36 Electric circuit investigated by van der Pol & van der Mark in 1927.

For this type of experiment, van der Pol had earlier proposed an equation which may be written in the form [129]

$$\ddot{X} - \mu(1 - X^2)\dot{X} + X = 0 \tag{A.34}$$

for $\omega = 0$. In such a case, the asymptotic behavior may be a limit cycle. When $\omega \neq 0$ the equation becomes

$$\ddot{X} - \mu(1 - X^2)\dot{X} + X = B\cos\omega t \tag{A.35}$$

These equations may be rewritten as an autonomous system:

$$\begin{aligned} \dot{X} &= Y \\ \dot{Y} &= \mu(1 - X^2)Y - X + Z \\ \dot{Z} &= W \\ \dot{W} &= -\omega^2 Z \end{aligned} \tag{A.36}$$

A van der Pol attractor is shown in Fig. A.37(a), along with its $2 \mapsto 1$ image in Fig. A.37(b).

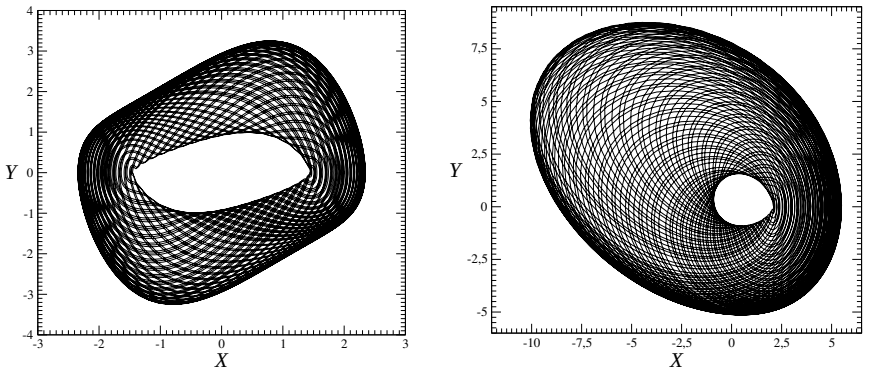

(a) Original dynamics (b) Image attractor

Fig. A.37 Quasi-periodic regime generated by the van der Pol system. Parameter values: $\mu = 0.5$, $\omega = 2.0$. Initial conditions: $X_0 = 0.1$, $Y_0 = 0.1$, $Z_0 = 1.5$, and $W_0 = 0.0$.

A.3.2 Duffing System

The Duffing-Ueda equations were first investigated by Duffing [28] and later extensively investigated using analogic and numerical simulations by Ueda [128]. The corresponding electrical circuit is shown in Fig. A.38. In this circuit, nonlinear oscillation takes place due to the saturable-core inductance $L(\phi)$ under the impression of the alternating voltage $E_0 \sin \omega t$. The resistor R is parallel with the capacitor C, so that the circuit is dissipative.

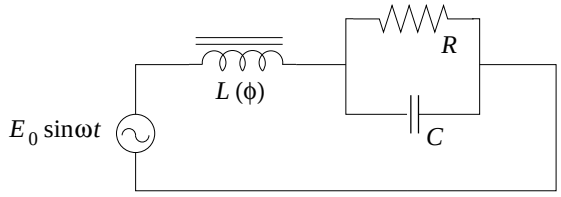

Fig. A.38 Series-resonance circuit with nonlinear inductance.

These equations are nonautonomous, i.e., the time appears explicitly. The Duffing equations are:

$$\ddot{X} + a\dot{X} + X^3 = A\cos(\omega t + \varphi) \tag{A.37}$$

They may be rewritten as:

$$\begin{aligned} \dot{X} &= Y \\ \dot{Y} &= -aY - X^3 + A\cos(\omega t + \varphi) \end{aligned} \tag{A.38}$$

The external sinusoidal driving force $A\cos(\omega t + \varphi)$ is generated by a second-order differential equation. The nonautonomous Duffing system may be rewritten as an autonomous four-variable system:

$$\begin{aligned} \dot{X} &= Y \\ \dot{Y} &= -aY - X^3 + U \\ \dot{U} &= V \\ \dot{V} &= -\omega^2 U \end{aligned} \tag{A.39}$$

An attractor generated by these equations for $(a, A, \omega) = (0.05, 7.5, 1.0)$ is shown in Fig. A.39 (a). The image attractor is shown in Fig. A.39 (b).

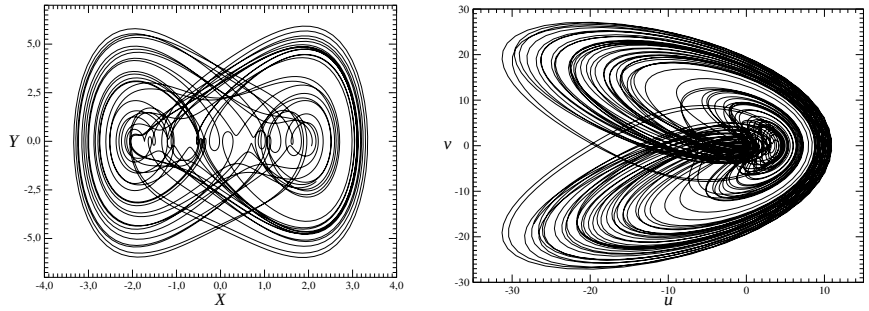

(a) Original dynamics (b) Image attractor

Fig. A.39 Chaotic attractor generated by the Duffing system with its image. Parameter values: $(a, A, w) = (0.05, 7.5, 1)$.

A.4 OTHER CASES

A.4.1 Three Hamiltonian Flows

Non dissipative flows on classical phase space are divergence-free. Phase space volume elements are conserved under Hamiltonian flows:

$$\dot{q}_i = +\frac{\partial \mathcal{H}}{\partial p_i}$$

$$\dot{p}_i = -\frac{\partial \mathcal{H}}{\partial q_i}$$

where $\mathcal{H}$ is the Hamiltonian function . For two-degrees-of-freedom Hamiltonian systems, the Hamiltonian function $\mathcal{H}(p_1, p_2, q_1, q_2)$ depends on the position coordinates (q_1, q_2) and the canonical momenta (p_1, p_2). Three systems with different symmetry properties are defined by the Hamiltonian functions [49]:

$$\mathcal{H}_1 = \frac{1}{2}\left(p_1^2 + p_2^2\right) + \frac{1}{2}\left(q_1^2 + q_2^2\right) - \epsilon q_1^2 q_2^2$$
$$\mathcal{H}_2 = \frac{1}{2}\left(p_1^2 + p_2^2\right) + \frac{1}{2}\left(q_1^2 + q_2^2\right) - \epsilon q_1 q_2^2$$
$$\mathcal{H}_3 = \frac{1}{2}\left(p_1^2 + p_2^2\right) + \frac{1}{2}\left(q_1^2 + q_2^2 - \frac{2}{3}q_2^3\right) - \epsilon q_1^2 q_2$$

The system will be designated by their Hamiltonian functions $\mathcal{H}_i$. All of them may be written under the form

$$\mathcal{H}_i(p_1, p_2, q_1, q_2) = \frac{1}{2}\left(p_1^2 + p_2^2\right) + \mathcal{U}_i(q_1, q_2)$$

where $\mathcal{U}_i(q_1, q_2)$ are the potential functions of the systems. Note that, in each case, the Hamiltonian function is of the form

$$\mathcal{H} = \mathcal{H}_0 + \epsilon\mathcal{H}'$$

with $\mathcal{H}_0$ integrable and $\epsilon\mathcal{H}'$ a nonintegrable correction. The parameter ϵ is taken to be non negative but it is not necessarily assumed to be small. These Hamiltonian systems are rather different in the sense they have potential functions $\mathcal{U}_i(q_1, q_2)$ possessing different symmetries. Potential $\mathcal{U}_1$ is invariant under eight-element group of the square. This consists of the four-element group $\{\mathbb{I}, \gamma_4, \gamma_4^2, \gamma_4^3\}$, reflections in the x- and y- axis γ_x and γ_y, and reflections in the two diagonals. The matrices representing the action of γ_4, γ_x and γ_y in the plane are

$$\gamma_4 = \begin{bmatrix} 0 & 1 \\ -1 & 0 \end{bmatrix} \qquad \gamma_x = \begin{bmatrix} 1 & 0 \\ 0 & -1 \end{bmatrix} \qquad \gamma_y = \begin{bmatrix} -1 & 0 \\ 0 & 1 \end{bmatrix}$$

Potential $\mathcal{U}_2$ is invariant under the two-element group of reflections in the x-axis, with generator γ_x, and $\mathcal{U}_3$ is invariant under reflections in the y-axis, with generator γ_y, unless $\epsilon = -1$. In this case the symmetry group has an additional generator

$$\gamma_3 = \begin{bmatrix} \cos\frac{2\pi}{3} & \sin\frac{2\pi}{3} \\ -\sin\frac{2\pi}{3} & \cos\frac{2\pi}{3} \end{bmatrix}$$

of rotations around the Z-axis. The full symmetry group is $\mathcal{S}_6 = \mathcal{R} \times \mathcal{C}_3$ with two generators γ_x, γ_3 and relations $\gamma_x^2 = \gamma_3^3 = \mathbb{I}$. These symmetries may be easily recognized from equipotential surfaces shown in Fig. A.40. For $\epsilon = -1, \mathcal{U}_3$ reduces to the Hénon-Heiles potential [46]. Typical trajectories in the position subspace $\mathbb{R}^2(X, Y)$ are shown in Fig. A.41 for the three potentials $\mathcal{U}_1, \mathcal{U}_2$, and $\mathcal{U}_3$.

In 1964, Michel Hénon and Carl Heiles were searching for a third constant of motion, added to the conservation of energy and angular momentum. Their problem

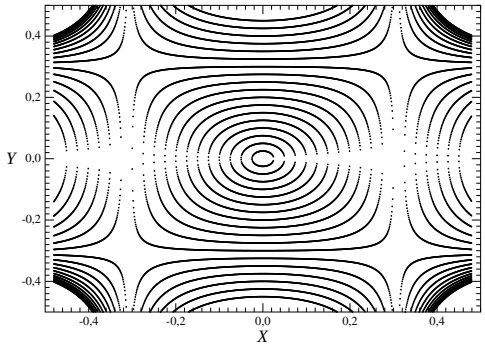

(a) $\mathcal{U}_1(x, y)$ with $\epsilon = 5.25$

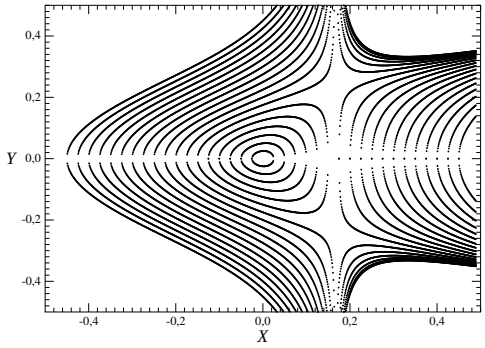

(b) $\mathcal{U}_2(x, y)$ with $\epsilon = 3.0$

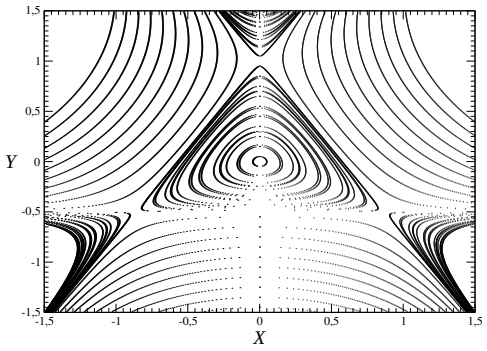

(c) $\mathcal{U}_3(x, y)$ with $\epsilon = -1.0$

Fig. A.40 Equipotential surfaces of the potentials $\mathcal{U}_i(X, Y)$.

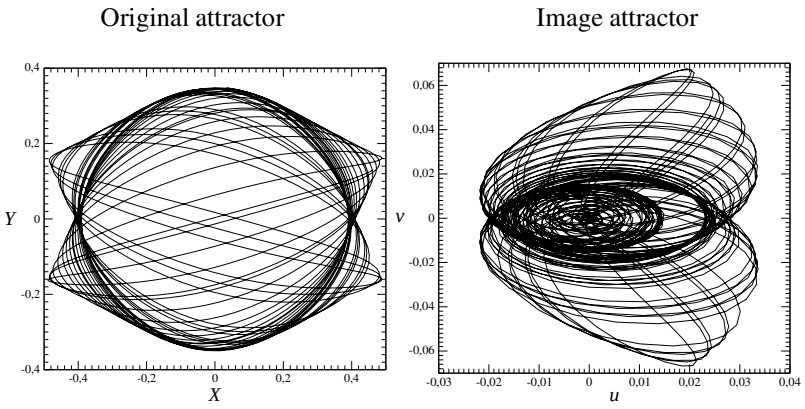

(a) $\mathcal{U}_1(X, Y)$ with $\epsilon = 5.25$

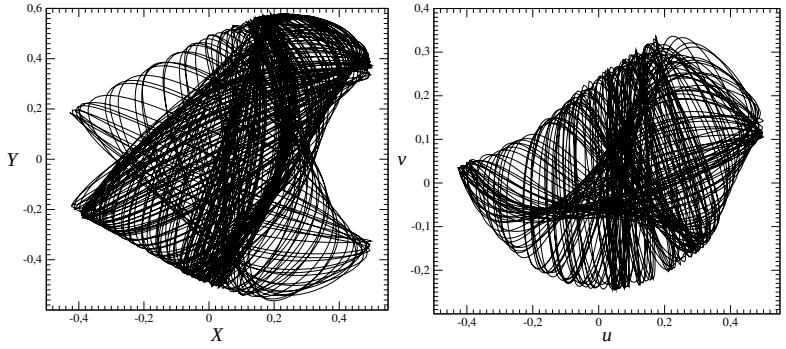

(b) $\mathcal{U}_2(X, Y)$ with $\epsilon = 1.0$

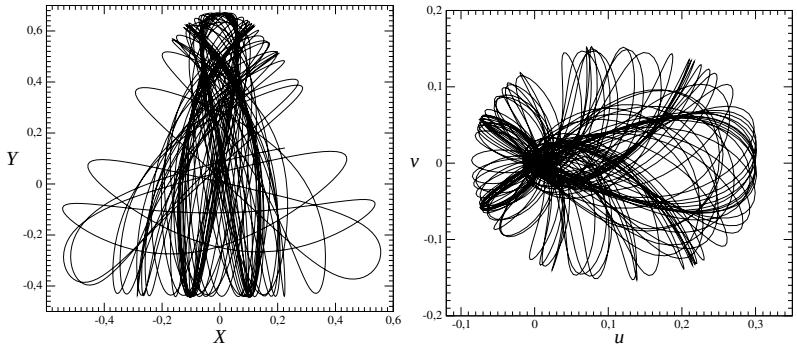

(c) $\mathcal{U}_3(X, Y)$ with $\epsilon = -1.0$

Fig. A.41 Chaotic trajectories of the Hamiltonian systems for the three different potentials. The images are with respect to the three groups $\mathcal{C}_4$, σ_y, and $\mathcal{C}_3$.

was the motions of galaxies. They were thinking that, under specific conditions, one additional constant of motion might be obtained. In order to simplify their problem, they investigated a problem with two degrees of freedom X and Y associated with the position. The phase space is therefore the 2×2-dimensional space $\mathbb{R}^4(X, Y, V_X, V_Y)$ where the V_X and V_Y are the components of the velocity. The equations of the system constructed from $\mathcal{H}_3$ are [46]:

$$\begin{aligned}
\dot{X} &= V_X \\
\dot{Y} &= V_Y \\
\dot{V}_X &= -X + 2\epsilon XY \\
\dot{V}_Y &= -Y + \epsilon X^2 + Y^2
\end{aligned}$$

The energy

$$E = \frac{1}{2}\left[\left(V_X^2 + V_Y^2\right) + \left(X^2 + Y^2 - 2\epsilon X^2 Y - \frac{2}{3}Y^3\right)\right] \tag{A.40}$$

of the system is a constant of the motion. The system is therefore *Hamiltonian*. In this system, Kepler's second law cannot be applied since the potential is not central. One constant of motion is therefore missing to ensure the integrability of the system. Hénon and Heiles were thus confrontated to a similar problem they faced in the context of the galaxy motions: another constant of motion was to be obtained.

A.4.2 1-D Delay Differential Equation

If a dynamical system has a finite dimension, this means that there is a finite set of dynamical variables which is sufficient to fully describe in a nonambiguous way any state of the system. When a delay differential equation has the form

$$\dot{x}(t) = F\left(x(t), x(t-\tau)\right) \tag{A.41}$$

where τ is a time delay, a function of $x(t)$ on the interval $[t-\tau, t]$ must be used to compute $x(t)$ at each time t. Thus, such equations have, mathematically speaking, an infinite dimension. In principle, a phase space with an infinite dimension must be used to represent the dynamics. Nevertheless, when the dynamical system is dissipative, a chaotic attractor may be obtained and it may be possible to represent the phase portrait in a low-dimensional space.

An example of a delay differential equation invariant under an inversion is [79]:

$$\dot{X} = aX - b\left(|X_\tau + 1| - |X_\tau - 1|\right) + c\left(|X_\tau + d| - |X_\tau - d|\right) \tag{A.42}$$

where $X_\tau = X(t-\tau)$. Control parameters are given by:

$$\begin{cases} b = 3.8 \\ c = 2.85 \\ d = \frac{4}{3} \end{cases}$$

Parameter a may be considered as the bifurcation parameter. The embedding dimension may be estimated by using the false nearest neighbors technique [1]. A three-dimensional space should be sufficient to describe the dynamics without any ambiguity for $a = -0.001$. Since we have a single dynamical variable, the phase portrait can only be represented using delay coordinates. A two-dimensional plane projection is shown in Fig. A.42 with its image.

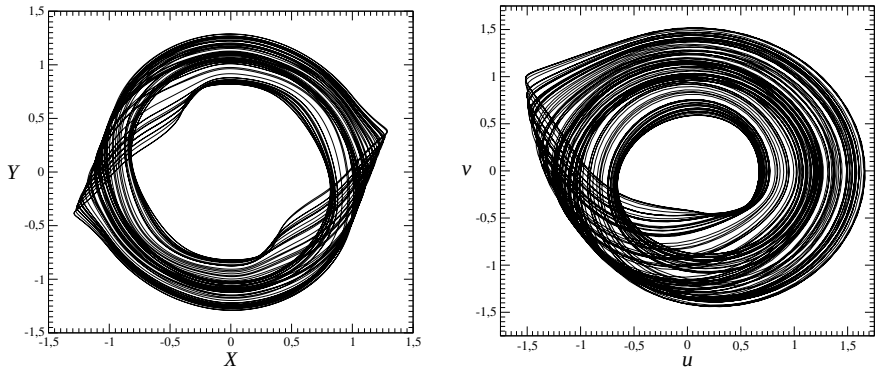

(a) Original dynamics (b) Image attractor

Fig. A.42 (a) Chaotic attractor using a delay embedding $Y(t) = X(t - \tau_1)$ of the delay differential equation (A.42) with $a = -0.001$. An inversion symmetry may be identified. (b) The image is also shown. Parameter values: $(a, b, c, d) = (-0.001, 3.8, 2.85, 4/3)$. For the delay differential equation, $\tau = 0.1$ s and the delay for the embedding is $\tau_1 = 1.0$ s.

A.4.3 3D Discontinuous System

In investigating the possibilities for having a Lorenz-like dynamics with a single nonlinearity, Elwakil, Özoğuz, & Kennedy [29] proposed a discontinuous system with a single parameter σ. In fact, the nonlinearities are replaced with piecewise linear functions. They proposed the set of equations

$$\begin{aligned} \dot{X} &= -\sigma X + \sigma Y \\ \dot{Y} &= -KZ \\ \dot{Z} &= +|X| - 1.0 \end{aligned} \tag{A.43}$$

where

$$K = \begin{array}{ll} +1 & \text{if} \quad X \geq 0 \\ -1 & \text{if} \quad X < 0 \end{array} \tag{A.44}$$

The nonlinearity XY of the third equation of the Lorenz system has been replaced with the absolute value function $|X|$ and the nonlinearity YZ of its second equation

with K, effectively equal to sgn(X). Compared to the Lorenz system, the threshold effect performed by the term $-bZ$ in the third equation has been replaced by the absolute value $|X|$. The threshold induced by the term RX in the second equation is removed. Hence, the system is controlled via the remaining single parameter σ. Despite the nonanalytic nature of the two singularities, the equations (A.43) exhibit an $\mathcal{R}_Z(\pi)$ symmetry. This system has two fixed points at

$$F_{\pm} = \left| \begin{array}{rcl} X_{\pm} & = & \pm 1 \\ Y_{\pm} & = & \pm 1 \\ Z_{\mp} & = & 0 \end{array} \right. \tag{A.45}$$

Written in that form, system (A.43) is invariant under a $\mathcal{R}_Z(\pi)$ rotation symmetry. This is evident in Fig. A.43.

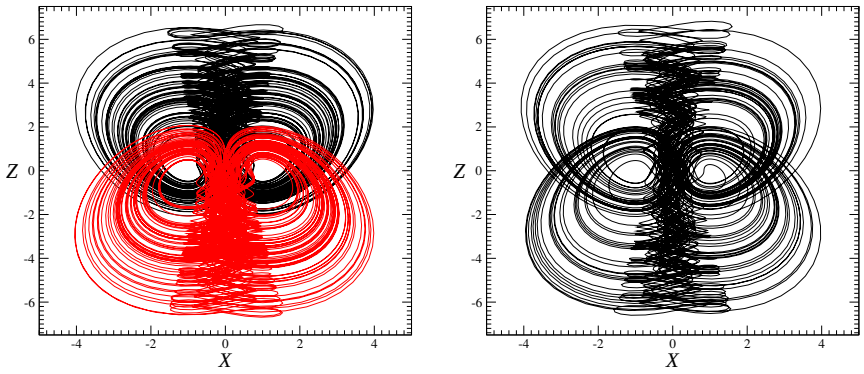

(a) Two coexisting attractors

(b) Connected attractor

Fig. A.43 Two coexisting chaotic attractors (a) and one connected attractor (b) for the discontinuous system (A.43). Both exhibit $\mathcal{R}_Z(\pi)$ symmetry. Parameter value: $\sigma = 0.55$.

In fact, this system has a dual system which can be written as

$$\begin{aligned} \dot{X} &= -\sigma X + \sigma Y \\ \dot{Y} &= +KZ \\ \dot{Z} &= -|X| + 1.0 \end{aligned} \tag{A.46}$$

This second system can be denoted S(Y_+, Z_-) while the system (A.43) is designated by S(Y_-, Z_+). The attractor solution of system S(Y_+, Z_-) is symmetry-related to the attractor solution of the system S(Y_-, Z_+) with respect of the plane $Z = 0$. This is therefore a mirror symmetry.

References

1. H. D. I. ABARBANEL, R. BROWN, J. J. SIDOROWICH & L. TSIMRING, Coping with chaos, *Reviews of Modern Physics*, **65**, 1331–1392, 1993.

2. C. ADAMS, *The Knot Book*, New York: Freeman, 1994.

3. R. C. ADLER, A. C. KONHEIM & M. H. ANDREW, Topological entropy, *Transactions American Mathematical Society*, **114**, 309–319, (1965).

4. A. ARNÉODO, P. COULLET & C. TRESSER, A possible mechanism for the onset of turbulence, *Physics Letters A*, **81** (4), 197–201, 1981.

5. V. I. ARNOL'D, *Ordinary Differential Equations*, Cambridge, MA: MIT Press, 1989.

6. V. I. ARNOL'D, A. VARCHENKO & S. GOUSSEIN-ZADE, *Singularit´es des applications differentiables 1. Classifi cation des points critiques des caustiques et des fronts d'onde*, Moscou: MIR, 1984 (French translation 1986).

7. V. I. ARNOL'D, A. VARCHENKO & S. GOUSSEIN-ZADE, *Singularit´es des applications differentiables 2. Monodromie et comportement asymptotique des integrales*, Moscou: MIR, 1984 (French translation 1986).

8. D. K. ARROWSMITH & C. M. PLACE, *An Introduction to Dynamical Systems*, Cambridge: Cambridge University Press, 1990.

9. M. AUVERGNE & A. BAGLIN, A dynamical instability as a driving mechanism for stellar oscillations, *Astronomy-Astrophysics*, **142**, 388–392, 1985.

10. M. A. AZIZ-ALAOUI, Differential equations with multispiral attractors, *International Journal of Bifurcation and Chaos*, **9** (6), 1009–1039, 1999.

11. H. H. BAU & K. E. TORRANCE, Transient and steady behavior of an open symmetrically-heated, free convection loop, *International Journal of Heat and Mass Tranfer*, **24**, 597–609, 1981.

12. J. BEER, S. M. TOBIAS & N. O. WEISS, An active sun throughout the Maunder minimum, *Solar Physics*, **181** (1), 237–249, 1998.

13. P. BERGÉ, Y. POMEAU & C. VIDAL, *Order within Chaos. Towards a Deterministic Approach to Turbulence*, New York: Wiley, 1984.

14. J. S. BIRMAN & R. F. WILLIAMS, Knotted periodic orbits in dynamical systems I : Lorenz' equations, *Topology*, **22**, 47–82, 1983.

15. J. S. BIRMAN & R. F. WILLIAMS, Knotted periodic orbits in dynamical systems II : Knot holders for fibered knots, *Contemporary Mathematics*, **20**, 1–60, 1983.

16. J. M. BOARDMAN, Singularities of differentiable maps, *Publications Math´ematiques de l'Institut des HautesÉtudes Scientifi ques*, **33**, 21–57, 1967.

17. R. I. BOGDANOV, Versal deformations of a singular point of a vector field on the plane in the case of two zero eigenvalues, *Functional Analysis and its Applictions*, **9** (2), 144–145, 1975.

18. G. F. BRISSON, K. M. GARTZ, B. J. MCCUNE, K. P. O'BRIEN & C. A. REITER, Symmetric attractors in three-dimensional space, *Chaos, Solitons & Fractals*, **7** (7), 1033–1049, 1996.

19. E. C. BULLARD, The stability of a homopolar dynamo, *Proceedings of the Cambridge Philosophical Society*, **51**, 744–760, 1955.

20. F. H. BUSSE, Magnetohydrodynamics of the earth's dynamo, *Annual Review of Fluid Mechanics*, **10**, 435–462, 1978.

21. G. BYRNE, R. GILMORE & C. LETELLIER, Distinguishing between folding and tearing mechanisms in strange attractors, *Physical Review E*, **70**, 056214, 2004.

22. G. CHEN & T. UETA, Yet another chaotic attractor, *International Journal of Bifurcation and Chaos*, **9**, 1465–1466, 1999.

23. L. O. CHUA, M. KOMURO & T. MATSUMOTO, The double scroll family, *IEEE Transactions on Circuits and Systems*, **33**, 1073–1118, 1986.

24. A. E. COOK & P. H. ROBERTS, The Rikitake two-disc dynamo system, *Proceeding of the Cambridge Philosophical Society*, **68**, 547–569, 1970.

25. D. Cox, J. Little & D. O'Shea, *Ideals, Varieties, and Algorithms. An Introduction to Computational Algebraic Geometry and Commutative Algebra*, New York: Springer-Verlag, 1996.

26. H. F. Creveling, J. F. de Paz, J. Y. Baladi & R. H. Schoenhals, Stability characteristics of a single thermal convection loop, *Journal of Fluid Mechanics*, **67**, 65–84, 1975.

27. Z. Duan, J.-Z. Wang & L. Huang, Attraction/repulsion functions in a new class of chaotic systems, *Physics Letters A*, **335**, 139–149, 2005.

28. G. Duffing, *Erzwungene Schwingungen bei ver¨anderlicher Eigenfrequenz und ihre technische Bedeutung*, Braunschweig: Vieweg-Verlag, 1918.

29. A. S. Elwakil, S. Özoğuz & M. P. Kennedy, Creation of a complex butterfly attractor using a novel Lorenz-type system, *IEEE Transactions on Circuits and Systems—1: Fundamental Theory and Applications*, **49** (4), 527–530, 2002.

30. M. Finardi, L. Flepp, J. Parisi, R. Holzner, R. Badii & E. Brun, Topological and metric analysis of heteroclinic crisis in laser chaos, *Physical Review Letters*, **68**, 2989–2991, 1992.

31. R. Gilmore, *Lie Groups, Lie Algbebras, and Some of Their Applications*, New York: Wiley-Interscience, 1974 (reprinted Dover, 2006).

32. R. Gilmore, *Catastrophe Theory for Scientists and Engineers*, New York: Wiley-Interscience, 1981 (reprinted Dover, 1993).

33. R. Gilmore, Topological analysis of chaotic dynamical systems, *Reviews of Modern Physics*, **70** (4), 1455–1529, 1998.

34. R. Gilmore & M. Lefranc, *The Topology of Chaos*, New York: Wiley-Interscience, 2002.

35. R. Gilmore & C. Letellier, Dressed symbolic dynamics, *Physical Review E*, **67**, 036205, 2003.

36. R. Gilmore & J. W. L. McCallum, Structure in the bifurcation diagram of the Duffing oscillator, *Physical Review E*, **51** (2), 935–956, 1995.

37. R. Gilmore, X. Pei & F. Moss, Topological analysis of chaos in neural spike train bursts, *Chaos*, **9** (3), 812–817, 1999.

38. M. Golubitsky & V. Guillemin, *Stable Mappings and Their Singularities*, New York: Springer-Verlag, 1973.

39. M. Golubitsky & D. Schaeffer, *Singularities and Groups in Bifurcation Theory, Volume 1*, New York: Springer-Verlag, 1985.

40. P. GRASSBERGER & H. KANTZ, Generating partitions for the dissipative Hénon map, *Physics Letters A*, **113**, 235–238, 1983.

41. C. GREBOGI, E. OTT & J. A. YORKE, Unstable periodic orbits and the dimensions of multifractal chaotic attractors, *Physical Review A*, **37**, 1711–1724, 1988.

42. J. GUCKENHEIMER & P. HOLMES, *Nonlinear Oscillations, Dynamical Systems, and Bifurcations of Vector Fields*, New York: Springer-Verlag, 1983.

43. H. HAKEN, Analogy between higher instabilities in fluids and laser, *Physics Letters A*, **53**, 77–78, 1975.

44. T. HALL, Weak universality in two-dimensional transitions to chaos, *Physical Review Letters*, **71** (1), 58–61, 1993.

45. T. HALL, The creation of horseshoes, *Nonlinearity*, **7**, 861–924, 1994.

46. M. HÉNON & C. HEILES, The applicability of the third integral of motion: Some numerical experiments, *Astrophysical Journal*, **69**, 73–79, 1964.

47. I. ITO, Chaos in the Rikitake two-disc dynamo system, *Earth Planet. Sciences Letters*, **51**, 451–456, 1980.

48. E. A. JACKSON, *Perspectives in Nonlinear Dynamics, Volumes 1 and 2*, Cambridge: Cambridge University Press, 1990.

49. H. E. KANDRUP, C. SIOPIS, G. CONTOPOULOS & R. DVORAK, Diffusion and scaling in escapes from two-degrees-of-freedom Hamiltonian systems, *Chaos*, **9**, 381–392, 1999.

50. J. KATRIEL & R. GILMORE, Entropy of bounding tori, *preprint*.

51. A. I. KHITNIK, D. ROSE & L. O CHUA, On periodic orbits and homoclinic bifurcations in Chua's circuit with a smooth nonlinearity, *International Journal of Bifurcation and Chaos*, **3** (2), 363–384, 1993.

52. E. KNOBLOCH & A. S. LANDSBERG, A new chaotic model for the sun, *Monthly Notices of the Royal Astronomical Society*, **278**, 294–302, 1996.

53. E. KNOBLOCH, S. M. TOBIAS & N. O. WEISS, Modulation and symmetry changes in stellar dynamos, *Monthly Notices of the Royal Astronomical Society*, **297**, 1123–1138, 1998.

54. M. KREMLIOVSLY, Can we understand time scales of solar activity?, *Solar Physics*, **151**, 351–370, 1994.

55. K. R. LANG, *The Sun from Space*, New York: Springer-Verlag, 2000.

56. B. LEFEBVRE & V. KRANOSEL'SKIKH, Nonlinear interaction of four electrostatic waves in a plasma, *Physica D*, **152–153**, 742–751, 2001.

57. M. LEFRANC, P. GLORIEUX, F. PAPOFF, F. MOLESTI & E. ARIMONDO, Combining topological analysis and symbolic dynamics to describe a strange attractor and its crises, *Physical Review Letters*, **73** (10), 1364–1367, 1994.

58. M. LEFRANC, R. GILMORE & N. ROMANAZZI, Once a horseshoe - Always a horseshoe, *preprint*.

59. R. B. LEIPNIK & T. A. NEWTON, Double strange attractors in rigid body motion with linear feedback control, *Physics Letters A*, **86** (2), 63–67, 1981.

60. C. LETELLIER, Modding out a continuous rotation symmetry for disentangling a laser dynamics, *International Journal of Bifurcation and Chaos*, **13** (6), 1573–1577, 2003.

61. C. LETELLIER & L. A. AGUIRRE, Investigating nonlinear dynamics from time series: The influence of symmetries and the choice of observables, *Chaos*, **12**, 549–558, 2002.

62. C. LETELLIER, L. A. AGUIRRE, J. MAQUET & R. GILMORE, Evidence for low dimensional chaos in sunspot cycles, *Astronomy and Astrophysics*, **449**, 379–387, 2006.

63. C. LETELLIER, L. A. AGUIRRE, J. MAQUET & B. LEFEBVRE, Analogy between a 10D model for nonlinear wave-wave interaction in a plasma and the 3D Lorenz dynamics, *Physica D*, **179**, 33–52, 2003.

64. C. LETELLIER, P. DUTERTRE & G. GOUESBET, Characterization of the Lorenz system taking into account the equivariance of the vector field, *Physical Review E*, **49** (4), 3492–3495, 1994.

65. C. LETELLIER, P. DUTERTRE & B. MAHEU, Unstable periodic orbits and templates of the Rössler system : Toward a systematic topological characterization, *Chaos*, **5** (1), 271–281, 1995.

66. C. LETELLIER, P. DUTERTRE, J. REIZNER & G. GOUESBET, Evolution of multimodal map induced by an equivariant vector field, *Journal of Physics A*, **29**, 5359–5373, 1996.

67. C. LETELLIER & R. GILMORE, Covering dynamical systems I: Two-fold covers, *Physical Review E*, **63**, 016206, 2001.

68. C. LETELLIER & G. GOUESBET, Topological characterization of a system with high-order symmetries: The proto-Lorenz system, *Physical Review E*, **52** (5), 4754–4761, 1995.

69. C. LETELLIER & G. GOUESBET, Topological characterization of reconstructed attractors modding out symmetries, *Journal de Physique II*, **6**, 1615–1638, 1996.

70. C. LETELLIER, G. GOUESBET & N. RULKOV, Topological analysis of chaos in equivariant electronic circuits, *International Journal of Bifurcation and Chaos*, **6** (12B), 2531–2555, 1996.

71. C. LETELLIER, L. LE SCELLER, P. DUTERTRE, G. GOUESBET, Z. FEI & J. L. HUDSON, Topological characterization and global vector field reconstruction from experimental electrochemical system, *Journal of Physical Chemistry*, **99**, 7016–7027, 1995.

72. C. LETELLIER & J.-M. MALASOMA, Unimodal order in the image of the simplest equivariant jerk system, *Physical Review E*, **64**, 067202, 2001.

73. C. LETELLIER, J. MAQUET, H. LABRO, L. LE SCELLER, G. GOUESBET, F. ARGOUL & A. ARNÉODO, Analyzing chaotic behaviour in a Belousov-Zhabotinskii reaction by using a global vector field reconstruction, *Journal of Physical Chemistry A*, **102**, 10265–10273, 1998.

74. C. LETELLIER, O. MÉNARD & L. A. AGUIRRE, Validation of selected global models, *Modeling and Forecasting Financial Data: Techniques of Nonlinear Dynamics*, Ed. A. Soofi & L. Cao, Boston, MA: Kluwer Academic Publisher, pp. 283–302, 2002.

75. C. LETELLIER, T. D. TSANKOV, G. BYRNE & R. GILMORE, Large-scale structural reorganization of strange attractors, *Physical Review E* **72** (1), 026212, 2005.

76. C. LETELLIER, P. WERNY, J.-M. MALASOMA & R. GILMORE, Multichannel intermittencies induced by symmetries, *Physical Review E*, **66** (3), 036220, 2002.

77. W. LIU & G. CHEN, A new chaotic system and its generation, *International Journal of Bifurcation and Chaos*, **13** (1), 261–267, 2003.

78. E. N. LORENZ, Deterministic nonperiodic flow, *Journal of Atmospheric Science*, **20**, 130–141, 1963.

79. H. LU, Y. HE & Z. HE, A chaos generator: Analyses of complex dynamics in a cell equation in delayed cellular networks, *IEEE Transactions on Circuits Systems*, **45**, 178–181, 1998.

80. J. LÜ, G. CHEN & D. CHENG, A new chaotic system and beyond: The generalized Lorenz-like system, *preprint*.

81. F. LUSSEYRAN & J. P. BRANCHER, Some results on simple dynamo systems, *IEEE Transactions on Magnetics*, **26** (5), 2875–2879, 1990.

82. J.-M. MALASOMA, What is the simplest dissipative chaotic jerk equation which is parity invariant?, *Physics Letters A*, **264**, 383–389, 2000.

83. P. MANNEVILLE & Y. POMEAU, Intermittency and the Lorenz model, *Physics Letters A*, **75**, 1–2, 1979.

84. M. W. MCELHINNY & P. L. MCFADDEN, Paleomagnetism: continents and oceans, *International Geophysics Series*, **73**, New York: Academic Press, 2000.

85. O. MÉNARD, C. LETELLIER, J. MAQUET, L. LE SCELLER & G. GOUESBET, Analysis of a non synchronized sinusoidally driven dynamical system, *International Journal of Bifurcation and Chaos*, **10** (7), 1759–1772, 2000.

86. M. METROLPOLIS, M. L. STEIN & P. R. STEIN, On finite limit sets for transformations on the unit interval, *Journal of Combinatorial Theory*, **15**, 25–44, 1973.

87. G. B. MINDLIN, X.-J. HOU, H. G. SOLARI, R. GILMORE & N. B. TUFILLARO, Classification of strange attractors by integers, *Physical Review Letters*, **64** (20), 2350–2353, 1990.

88. G. B. MINDLIN, R. LOPEZ-RUIZ, H. G. SOLARI & R. GILMORE, Horseshoe implications, *Physical Review E*, **48**, 4297–4304, 1993.

89. G. B. MINDLIN, H. G. SOLARI, M. A. NATIELLO, R. GILMORE & X.-J. HOU, Topological analysis of chaotic time series data from the Belousov-Zhabotinski reaction, *Journal of Nonlinear Sciences*, **1**, 147–173, 1991.

90. R. MIRANDA & E. STONE, The proto-Lorenz system, *Physics Letters A*, **178**, 105–113, 1993.

91. H. K. MOFFAT, A self-consistent treatment of simple dynamo systems, *Geophysical and Astrophysical Fluid Dynamics*, **14**, 147–166, 1979.

92. D. W. MOORE & E. A. SPIEGEL, A thermally excited non-linear oscillator, *Astrophysical Journal*, **143** (3), 871–887, 1966.

93. T. ONDARÇUHU, G. B. MINDLIN, H. L. MANCINI & C. PÉREZ-GARCÍA, Dynamical patterns in Bénard-Marangoni convection in a square container, *Physical Review Letters*, **70** (2), 3892–3895, 1993.

94. V. I. OSELEDEC, A multiplicative ergodic theorem: Lyapunov characteristic numbers for dynamical systems, *Transactions of the Moscow Mathematical Society*, **19**, 197, 1968.

95. E. OTT, *Chaos in Dynamical Systems,* Cambridge: Cambridge University Press, 1993.

96. N. H. PACKARD, J. P. CRUTCHFIELD, J. D. FARMER & R. S. SHAW, Geometry from a time series, *Physical Review Letters*, **45**, 712–715, 1980.

97. F. PAPOFF, A. FIORETTI, E. ARIMONDO, G. B. MINDLIN, H. G. SOLARI & R. GILMORE, Structure of chaos in the laser with a saturable absorber, *Physical Review Letters*, **68**, 1128–1131, 1992.

98. L. M. PECORA & T. L. CARROLL, Synchronization in chaotic systems, *Physical Review Letters*, **64**, 821–824, 1990.

99. J. PLUMECOQ & M. LEFRANC, From template analysis to generating partitions I: Periodic orbits, knots and symbolic encodings, *Physica D*, **144**, 231–258, 2000.

100. H. POINCARÉ, *Les Methodes nouvelles de la m´ecanique c´eleste*, Paris: Gauthier-Villars, 1892.

101. Y. POMEAU & P. MANNEVILLE, Intermittent transitions to turbulence in dissipative dynamical systems, *Communications in Mathematical Physics*, **74**, 189–197, 1980.

102. W. H. PRESS, B. P. FLANNERY, S. A. TEUKOLSKY & W. T. VETTERLING, *Numerical Recipes*, Cambridge: Cambridge University Press, 1986.

103. G. QI, S. DU, G. CHEN, Z. CHEN & Z. YUAN, On a four dimensional chaotic system, *Chaos, Solitons & Fractals*, **23**, 1671–1682, 2005.

104. L. RAYLEIGH (J. W. STRUTT), On maintained vibrations, *Philosophical Magazine*, **XV**, 229–232, 1883.

105. P. REITERER, *Zur Dynamik dreidimensionaler quadratischer Konvektionszellen*, Diploma thesis, Technical University at Graz, Austria, 1996.

106. P. REITERER, C. LAINSCSECK, F. SCHÜRRER, C. LETELLIER & J. MAQUET, A nine-dimensional Lorenz system to study high-dimensional chaos, *Journal of Physics A*, **31**, 7121–7139, 1998.

107. T. RIKITAKE, Oscillations of a system of disk dynamos, *Proceedings of the Cambridge Philosophical Society*, **54**, 89–105, 1958.

108. D. ROLFSEN, *Knots and Links*, Providence, RI: AMS Chelsea Publishing, 2003.

109. O. E. RÖSSLER, An equation for continuous chaos, *Physics Letters A*, **57** (2), 397–398, 1976.

110. O. E. RÖSSLER, Chemical turbulence: a synopsis, In *Synergetics* (H. Haken, ed.), *Proceedings of the International Workshop on Synergetics* at Schloss Elmau (Bavaria, May 2–7, 1977), New York: Springer-Verlag, pp. 174–183, 1977.

111. A. M. RUCKLIDGE, Chaos in models of double convection, *Journal of Fluid Mechanics*, **237**, 209–229, 1992.

112. B. SALTZMAN, Finite amplitude free convection as an initial value problem — I, *Journal of Atmospheric Science*, **19**, 329–341, 1962.

113. R. SHAW, Strange attractor, chaotic behavior and information flow, *Zeitschrift f¨ur Naturforschung*, **36** (a), 80–112, 1981.

114. T. SHIMIZU & N. MOROIKA, On the bifurcation of a symmetric limit cycle to an asymmetric one in a simple model, *Physics Letters A*, **76**, 201–204, 1980.

115. R. H. SIMOYI, A. WOLF & H. SWINNEY, One-dimensional dynamics in a multicomponent chemical reaction, *Physical Review Letters*, **49**, 245–248, 1982.

116. H. G. SOLARI & R. GILMORE, Relative rotation rates for driven dynamical systems, *Physical Review A*, **37**, 3096–3109, 1988.

117. J. S. SPROTT, Some simple chaotic flows, *Physical Review E*, **50** (2), 647–650, 1994.

118. J. C. SPROTT & S. J. LINZ, Algebraically simple chaotic flows, *International Journal of Chaos Theory and Applications*, **5** (2), 3–22, 2000.

119. J. A. K. SUYKENS & J. VANDEWALLE, Generation of n-double scrolls ($n = 1, 2, 3, 4, ..$), *IEEE Transactions Circuits Systems*, **40** (11), 861–867, 1993.

120. F. TAKENS, Singularities of vector fields, *Publications Math´ematiques de l'Institut des Hautes Études Scientifi ques*, **43**, 47–100, 1974.

121. F. TAKENS, Detecting strange attractors in turbulence, *Lecture Notes in Mathematics*, Vol. 898, (D. A. Rand and L.-S. Young, eds.), New York: Springer-Verlag, pp. 366–381, 1981.

122. R. THOMAS, Deterministic chaos seen in terms of feedback circuits: Analysis, synthesis, "labyrinth chaos", *International Journal of Bifurcation and Chaos*, **9** (10), 1889–1905, 1999.

123. A. K. TRAUTWEIN, < http://www2.carthage.edu/˜trautwn/ >.

124. T. D. TSANKOV & R. GILMORE, Strange attractors are classified by bounding tori, *Physical Review Letters*, **91** (13), 134104, 2003.

125. T. D. TSANKOV & R. GILMORE, Topological aspects of the structure of chaotic attractors in $\mathbb{R}^3$, *Physical Review E*, **69** (13), 056206, 2004.

126. T. D. TSANKOV, A. NISHTALA & R. GILMORE, Embeddings of a strange attractor into $\mathbb{R}^3$, *Physical Review E*, **69**, 056215, 2004.

127. N. B. TUFILLARO, H. G. SOLARI & R. GILMORE, Relative rotation rates: Fingerprints for strange attractors, Physical Review A, **41**, 5717–5720, 1990.

128. Y. UEDA, *Some Problems in the Theory of Nonlinear Oscillations*, Doctoral dissertation, Kyoto University, 1965. Reprinted in *Road to Chaos*, Santa Cruz, CA: Aerial Press, 1991.

129. B. VAN DER POL, On oscillation hysteresis in a simple triode generator, *Philosophical Magazine*, **43** (6), 700–719, 1926.

130. B. VAN DER POL & J. VAN DER MARK, Frequency demultiplication, *Nature*, **120**, 363–364, 1927.

131. F. J. VINE, Spreading of the ocean floor: New evidence, *Science*, **154**, 1405–1415, 1966.

132. F. J. VINE & D. H. MATTHEWS, Magnetic anomalies over oceanic ridges, *Nature*, **199**, 947–949, 1963.

133. Y. WANG, J. SINGER & H. H. BAU, Controlling chaos in a thermal convection loop, *Journal of Fluid Mechanics*, **237**, 479–498, 1992.

134. J. R. WEEKS, *The Shape of Space*, New York: Marcel Dekker, 2002.

135. H. WEYL, *The Classical Groups, Their Invariants and Representations*, Princeton: University Press, 1946.

136. H. WHITNEY, Differentiable manifolds, *Annals of Mathematics*, **37**, 645–680, 1936.

137. A. WOLF, J. B. SWIFT, H. L. SWINNEY & J. A. VASTANO, Determining Lyapunov exponents from a time series, *Physics D*, **16**, 285–317, 1985.

138. V. E. ZAKHAROV, Collapse of Langmuir waves, *Soviet Physics JETP*, **35** (5), 908–914, 1972.

139. H. ZEGHLACHE & P. MANDEL, Influence of detuning on the properties of laser equations, *Journal of Optical Society of America B*, **2**, 18–22, 1985.

Index